Dissertation zur Erlangung des Doktorgrades
der Fakultät für Chemie und Pharmazie
der Ludwig-Maximilians-Universität München

Transmission electron microscopy and properties of thermoelectric chalcogenides and luminescent oxonitridosilicates

Tobias Christopher Rosenthal

aus

Starnberg, Deutschland

2014

Erklärung

Diese Dissertation wurde im Sinne von § 7 der Promotionsordnung vom 28. November 2011 von Herrn Prof. Dr. O. Oeckler betreut.

Eidesstattliche Versicherung

Diese Dissertation wurde eigenständig und ohne unerlaubte Hilfe erarbeitet.

München,

.....

(Tobias Rosenthal)

Dissertation eingereicht am	20.05.2014
1. Gutachter:	Prof. Dr. O. Oeckler
2. Gutachter:	Prof. Dr. W. Schnick
Mündliche Prüfung am	17.06.2014

Acknowledgement

I want to thank Prof. Dr. Oliver Oeckler for the very interesting topic and his constant support at all times. I am grateful that he gave me the opportunity to present my results and those of our group at a variety of international and national conferences. His review and conceptual input greatly improved the quality of the publications. During the course of this thesis he was always there when his advice was needed and always took the time for constructive discussions concerning all aspects of life.

I would like to express my gratitude to Prof. Dr. Wolfgang Schnick who made this work possible by his generous support. I would also like to thank him for taking the time for being my second referee.

I would also like to thank Prof. Dr. Wolfgang Schmahl, Prof. Dr. Hans-Christian Böttcher, Prof. Dr. Konstantin Karaghiosoff and Prof Dr. Dirk Johrendt for taking the time to evaluate my thesis and participate on the examiners committee during the oral examination for the doctor's degree.

My special thanks go to Dr. Markus Döblinger for the practical TEM training and his trustfulness in my ability to operate them self-reliant. Without his constant support in the early days this work would not have been possible. I also want to thank Steffen Schmidt for the maintenance of the TEM and the sample preparation facilities as well as the help with technical problems of the TEM.

My deepest gratitude goes to my fellow PhD student from lab D2.100 who made even the longest nights enjoyable. I would like to thank Matthias Schneider with whom I began from my journey into the depths of chemistry more than 10 years ago. I am grateful for the very pleasant and effective cooperation during various projects with Thorsten Schröder and his support during the last years. We were a great team! Special thanks go to Markus Seibald for the enlightening co-operations that did not only yield very interesting results but were also very joyful on and off campus.

Lukas Neudert and Felix Fahrnbauer who began as research interns and later joined our group were a constant help and greatly enriched the time of my doctoral thesis. The support of our

constantly growing group at the IMKM in Leipzig was a great help, especially Simon Welzmiller and Philipp Urban. Frank Heinke, Robert Schlegel, Peter Schultz, Stefan Schwarzmüller and Daniel Souchay as well as Dr. Gerald Wagner with whom I had fruitful discussions, gave new impulses to our growing group.

The constant and prompt support by Wolfgang Wünschheim with all IT-related problems, by Christian Minke concerning REM-EDX experiments and by Thomas Miller regarding single-crystal as well as temperature-programmed powder diffraction experiments were crucial in realizing this work. Thank you all very much for taking the time and for the good working atmosphere. I would like to thank Olga Lorenz in Munich as well as Sylvia Proksch in Leipzig for the help with the organization of the administrative issues

Furthermore I am indebted to the research interns Peter Wagatha, Kathleen Nimmrich, Pirmin Ganther, Edgar Uhl and Ludwig Schenk who worked with great enthusiasm on their projects under my supervision. They were able to execute the practical work mostly independent after the initial practice. This was a great support especially during the synthesis of the often very fragile samples for thermoelectric characterization.

I am also grateful to Nadja Gießbrecht, Markus Nentwig and Stefan Mayer who performed thermoelectric measurements at the California Institute of Technology. In this respect I also want to thank Prof. Dr. Jeff Snyder and his group for the possibility of using the facilities at Caltech.

Discussions with Alexander Zurawski, Martin Zeuner and Sandro Pagano highly enriched the early days of my M. Sc. and doctorate work. The same is true for the always friendly and constructive atmosphere in our lab D2.100 with Saskia Lupart and Frauke Thienel as well as my time in the lab D2.110. I would also like to thank all members of the groups of Professor Schnick, Professor Jorendt, Professor Lotsch, Dr. Hoch and Professor Schmedt auf der Günne for the solidarity that was always inherently present.

In addition to these great people that shaped my development at university I would like to thank my parents, family and friends for their constant support and for giving me the chance of focussing on the scientific subjects when necessary and for distraction when I needed it. This holds especially true for Katharina who supported me from the early days of my studies.

Table of contents

1 Introduction 1

1.1 Dealing with the energy problem 1

1.2 Thermoelectrics 2

1.3 Luminescent materials 4

2 TEM investigations of nanostructured germanium antimony tellurides and related compounds with respect to their thermoelectric properties 6

2.1 Overview 6

2.2 Thermoelectric germanium antimony tellurides 11

2.2.1 From phase-change materials to thermoelectrics? 11

2.2.1.1 Introduction 12

2.2.1.2 Structure of metastable GST bulk materials with different GeTe content and their thermoelectric properties 15

2.2.1.2.1 Structural aspects 15

2.2.1.2.2 Thermoelectric properties 21

2.2.1.3 Conclusion 22

2.2.1.4 Experimental 23

2.2.1.5 References 26

2.2.2 Real structure and thermoelectric properties of GeTe-rich germanium antimony tellurides 29

2.2.2.1 Introduction 30

2.2.2.2 Experimental Section 32

2.2.2.3 Results and Discussion 34

2.2.2.3.1 Stability of the phases $Sb_2Te_3(GeTe)_n$ ($3 \leq n \leq 17$) 34

2.2.2.3.2 Influence of thermal treatment on the nanostructure 36

2.2.2.3.3 Influence of the composition on the nanostructure of quenched $Sb_2Te_3(GeTe)_n$ samples 39

2.2.2.3.4 Structural relaxation around the defect layers in $Sb_2Te_3(GeTe)_{12}$. 40

2.2.2.3.5 Influence of the microstructure on the thermoelectric characteristics of $Sb_2Te_3(GeTe)_n$ ($n = 3$-19) 40

2.2.2.4 Conclusion 44

2.2.2.5 References 45

2.3 Influencing properties and nanostructures of germanium antimony tellurides by substitution 47

2.3.1 The solid solution series $(GeTe)_{12}M_2Te_3$ (M = Sb, In): nanostructures and thermoelectric properties 47

2.3.1.1 Introduction 47

2.3.1.2 Experimental Section 48

2.3.1.3 Results and Discussion 50

2.3.1.3.1 Crystal structure of quenched $Ge_{12}(Sb_{1-x}In_x)_2Te_{15}$ phases 50

2.3.1.3.2 Influence of In substitution on strain and on the phase transition temperatures 53

2.3.1.3.3 Influence of the In substitution on the nanostructure 55

2.3.1.3.4 Influence of the In substitution on the thermoelectric properties 56

2.3.1.4 Conclusion 58

2.3.1.5 References 58

2.3.2 Nanostructures and thermoelectric properties of the solid solution series $(Ge_{1-x}Sn_xTe)_nSb_2Te_3$ (n = 4, 7, 12; $0 \le x \le 1$) 60

2.3.2.1 Introduction 60

2.3.2.2 Experimental 62

2.3.2.3 Results and discussion 64

2.3.2.3.1 Composition, and average structure of (pseudo-)cubic quenched phases 64

2.3.2.3.2 Thermal behavior of quenched phases 68

2.3.2.3.3 Influence of the Sn substitution on the nanostructure 70

2.3.2.3.4 Thermoelectric properties 73

2.3.2.4 Conclusion 76

2.3.2.5 Supplementary Information 77

2.3.2.6 References 79

2.3.3 Enhancing the thermoelectric properties of germanium antimony tellurides by substitution with selenium in compounds $Ge_nSb_2(Te_{1-x}Se_x)_{n+3}$ ($0 \le x \le 0.5$; $n \ge 7$) 81

2.3.3.1 Introduction 82

2.3.3.2 Experimental Section 84

2.3.3.3 Results and Discussion 87

2.3.3.3.1 Structure and existence ranges of Se-substituted GST materials $Ge_nSb_2(Te_{1-x}Se_x)_{n+3}$ ($0 \leq x \leq 0.5$; $7 \leq n \leq 19$) *87*

2.3.3.3.2 Influence of Se substitution on the phase transitions of GST materials *95*

2.3.3.3.3 Influence of Se substitution on the nanostructure of GST materials and the lateral extension of defect layers *98*

2.3.3.3.4 Influence of Se substitution on the thermoelectric properties of GST materials *101*

2.3.3.4 Conclusion 104

2.3.3.5 Supplementary Information 106

2.3.3.6 References 113

3 Real - structure property relationships in thermoelectric chalcogenides 116

3.1 Overview 116

3.2 Nanostructures in metastable $GeBi_2Te_4$ obtained by high-pressure synthesis and rapid quenching and their influence on physical properties 119

3.2.1 Introduction 119

3.2.2 Experimental details 122

3.2.3 Results and discussion 125

3.2.3.1 Structure of quenched HP-$GeBi_2Te_4$ *125*

3.2.3.2 Nucleation mechanism and nanostructuring *129*

3.2.3.3 Influence of the nanostructure on the electrical resistivity *131*

3.2.4 Conclusion 139

3.2.5 References 141

3.3 Structural features and physical properties of $In_2Bi_3Se_7I$, $InBi_2Se_4I$ and BiSeI 143

3.3.1 Introduction 143

3.3.2 Results and Discussion 144

3.3.2.1 Synthesis and stability of $In_2Bi_3Se_7I$ and In_2BiSe_4I *144*

3.3.2.2 Crystal structure of In_2BiSe_4I *146*

3.3.2.3 Structure of $In_2Bi_3Se_7I$ *148*

3.3.2.4 Common structural features in the systems Bi-In-Se-I and X-Bi-Se (X = alkali metal) *150*

3.3.2.5 Thermoelectric Properties *151*

3.3.3 Conclusion 153
3.3.4 Experimental Section 154
3.3.5 Supplementary Information: 156
3.3.6 References 158
3.4 A high-pressure route to thermoelectrics with low thermal conductivity: the solid solution series $AgIn_xSb_{1-x}Te_2$ (x = 0.1 - 0.6) 159
3.4.1 Introduction 159
3.4.2 Experimental 161
3.4.3 Results and discussion 163
3.4.3.1 Crystal structure 163
3.4.3.2 Thermal behavior 167
3.4.3.3 Electron microscopy of $AgIn_{0.5}Sb_{0.5}Te_2$ 167
3.4.3.4 Thermoelectric properties 169
3.4.4 Conclusion 172
3.4.5 Supplementary information 173
3.4.6 References 174
3.5 TAGS-related indium compounds and their thermoelectric properties – the solid solution series $(GeTe)_xAgIn_ySb_{1-y}Te_2$ (x = 1 – 12; y = 0.5 and 1) 176
3.5.1 Introduction 176
3.5.2 Experimental 178
3.5.3 Results and Discussion 181
3.5.3.1 Sample characterization and optimal conditions for syntheses 181
3.5.3.2 Crystal structure 181
3.5.3.3 Electron microscopy and diffraction 186
3.5.3.4 Thermal behavior 188
3.5.3.5 High-temperature thermoelectric properties of $(GeTe)_{5.5}AgIn_{0.5}Sb_{0.5}Te_2$ 191
3.5.3.6 Low-temperature thermoelectric properties of $(GeTe)_{5.5}AgInTe_2$ 192
3.5.4 Conclusion 194
3.5.5 Supplementary information 195
3.5.6 References 196

3.6 Nanostructures in TAGS thermoelectric materials induced by phase transitions associated with vacancy ordering 198

3.6.1 Introduction 199

3.6.2 Experimental 200

3.6.3 Results and discussion 202

3.6.3.1 Overview and sample characterization 202

3.6.3.2 Crystal structures of the quenched compounds 203

3.6.3.3 Transmission electron microscopy 207

3.6.3.4 Stability ranges and phase transitions 209

3.6.3.5 Thermoelectric properties of $Ge_{0.53}Ag_{0.13}Sb_{0.27}\square_{0.07}Te_1$ and $Ge_{0.61}Ag_{0.11}Sb_{0.22}\square_{0.06}Te_1$ 211

3.6.4 Conclusion 213

3.6.5 Supplementary information 215

3.6.6 References 218

4 Synergism of electron microscopy and synchrotron diffraction methods 220

4.1 Overview 220

4.2 Complementary use of electron microscopy and synchrotron diffraction for structure analysis 222

4.3 Novel superstructure of the rocksalt type and element distribution in germanium tin antimony tellurides 226

4.3.1 Introduction 226

4.3.2 Experimental 229

4.3.3 Results and discussion 231

4.3.3.1 Overview and strategy 231

4.3.3.2 Superstructure of the rocksalt type 232

4.3.3.3 Domain size and hierarchical structure in $Ge_2Sn_2Sb_2Te_7$ 237

4.3.3.4 Element distribution $Ge_3SnSb_2Te_7$ 239

4.3.4 Conclusion 243

4.3.5 Supplementary Information 244

4.3.6 References 248

4.4 Layered germanium tin antimony tellurides: element distribution, nanostructures and thermoelectric properties 250

4.4.1 Introduction 250

4.4.2 Results and Discussion 252

4.4.2.1 The solid solution series $(Ge_{1-x}Sn_x)Sb_2Te_4$ (x = 0-1) *252*
4.4.2.2 Mixed crystals $(Ge_{1-x}Sn_x)_2Sb_2Te_5$ (x= 0.35, 0.5) *258*
4.4.2.3 Thermoelectric properties *263*
4.4.3 Conclusion 264
4.4.4 Experimental Section 265
4.4.5 Supplementary Information 269
4.4.6 References 272
5 Complementary use of electron and X-ray methods for the structure elucidation of luminescent oxonitridosilicates 275
5.1 Overview 275
5.2 New polymorph of the highly efficient LED-phosphor $SrSi_2O_2N_2:Eu^{2+}$ – polytypism of a layered oxonitridosilicate 279
5.2.1 Introduction 280
5.2.2 Experimental Section 281
5.2.3 Results and Discussion 283
5.2.3.1 Synthesis and chemical analysis *283*
5.2.3.2 Single-Crystal Structure Analysis *283*
5.2.3.3 Lattice Energy Calculations *285*
5.2.3.4 Rietveld Refinement *286*
5.2.3.5 Transmission Electron Microscopy and Electron Diffraction *287*
5.2.3.6 Luminescence *289*
5.2.5 Conclusion 291
5.2.6 References 292
5.3 Unexpected luminescence properties of $Sr_{0.25}Ba_{0.25}Si_2O_2N_2:Eu^{2+}$ – a narrow blue emitting oxonitridosilicate with cation ordering 294
5.3.1 Introduction 294
5.3.2 Results and Discussion 296
5.3.2.1 Synthesis and Chemical Analysis *296*
5.3.2.2 Electron Microscopy *297*
5.3.2.3 Single-Crystal Structure Analysis *300*
5.3.2.4 Cation Ordering as Derived from HRTEM *301*
5.3.2.5 Luminescence *304*
5.3.3 Conclusion 305
5.3.4 Experimental Section 306

5.3.5 References 307
6 Conclusion and prospects 309
7 Summary 313
8 Appendix 322
8.1 Publications within this thesis 322
8.2 Publications not reprinted as part of this thesis 328
8.3 Contributions to conferences 330
Curriculum Vitae 338

1 Introduction

1.1 Dealing with the energy problem

The sustainable transformation, storage and allocation of energy is one of the major issues of our time. The scarcity of fossil fuel and the current drawbacks of alternative energy sources drive the search for increased energy-usage efficiency. Great potential unfolds from the usage of waste heat. Although this has been done for many years in industrial processes, e.g. by recuperative heat exchangers, the development of highly efficient thermoelectric materials yields many new possible applications (Chapter 1.2). Due to the direct conversion of heat to electricity, thermoelectric materials are especially suited for non-stationary waste-heat recovery.

Great energy-saving potential has already been unleashed in the illumination sector (Chapter 1.3). New concepts for the conversion of energy to visible light, e.g. phosphor-converted light-emitting diodes (pc-LEDs), result in dramatically increased efficiencies. The comprehensive structural characterization of the luminescent oxonitridosilicates $Sr_{1-x}Ba_xSi_2O_2N_2:Eu^{2+}$ made it possible to reveal unknown compounds as well as the real-structure effects present, which leads to an advanced understanding of the luminescence properties (Chapter 5).

In thermoelectric materials, real-structure phenomena often have a strong impact on the thermoelectric performance, especially on the phononic contribution to thermal conductivity (κ_{ph}). In germanium antimony telluride (GST) based materials and structurally related tellurides, phase transitions can be used to introduce nanostructures whose extent depends on thermal treatment and composition (Chapters 2 and 3). Therefore, the profound understanding of the structural chemistry is the basis of specifically influencing thermoelectric properties by substitutions and thermal treatment.

Both the systematic development of new compounds for pc-LEDs and the improvement of thermoelectric materials are model cases of the fact that the detailed understanding of structural features is important for the explanation of properties. In both fields of research, the correlation between the nanostructure and the properties has received growing attention in recent years as the improvement of analytical methods resulted in significantly higher accuracy of real-structure determination. Electron microscopy is ideally suited for the analysis of most real-structure phenomena. It enables the direct observation of individual domains and

defects with atomic resolution and the determination of the degree of disorder with high spatial resolution. Statistical information about the frequency of occurrence of such phenomena can be obtained by evaluating the diffuse intensities present in X-ray diffraction patterns. The combination of electron and synchrotron X-ray methods enables the structure elucidation of microcrystalline materials with low scattering power (Chapter 4). The long-term objective is the development of real-structure property relationships that allow a systematic optimization of thermoelectric or luminescent materials.

1.2 Thermoelectrics

Thermoelectric generators (TEG) enable the direct conversion of heat that is present at temperature gradients into electricity. The efficiency of this conversion process is determined by the individual thermoelectric figures of merit (*ZT*) of the p- and n- doped semiconductors of which the TEG is composed. The *ZT* value describes the thermoelectric efficiency and is determined by the Seebeck coefficient (*S*), which is the material property that describes the magnitude of the voltage induced by a thermal gradient across a material, as well as the electrical conductivity (σ) and the thermal conductivity (κ): $ZT = S^2 \cdot \sigma \cdot T \cdot \kappa^{-1}$.[1,2] According to the Wiedeman-Franz law, σ is linked with the electronic contribution to the lattice thermal conductivity (κ_e) by the heat transport of the electrons. Both properties are also correlated with *S* since they all depend on the charge-carrier concentration. Therefore, recent approaches to optimizing the *ZT* values tend to focus on reducing the κ_{ph}, which is the only property that can be changed, to a certain extend, without altering the electronic properties.[3,4] The reduced phonon proliferation is often realized by nanostructuring, e.g. introduction of nanoscale precipitates and grain boundaries. This is a textbook example for the changing focus of solid-state chemistry away from ideal crystal structures towards materials where real-structure effects determine the properties. This explains the increased use of electron microscopy, which renders the local determination of structural effects on the atomic level possible.

In cars and airplanes with increasingly complex electronic systems, for instance, the production of electrical energy for on-board systems by the generators consumes a significant amount of the engine's energy. It is already possible to reduce the fuel consumption of automotives by up to 1.2% when waste heat from the combustion is "harvested" by TEGs.[5,6] Further improved TEGs could result in the replacement of the alternator, which would significantly reduce the fuel consumption. The reasonable efficiency of TEGs down to the microwatt power level results in new applications.[7] The turbine heat in airplanes can already

be utilized to produce the energy for sensors, resulting in notably lower weight.[8] One of the major issues that prohibit the proliferation of TEGs is their low efficiency. *ZT* values of 1.5 – 2 or more are necessary for the development TEGs that are competitive with conventional mechanical engines for applications in non-stationary waste heat recovery, while actually used materials often exhibit $ZT < 1$. Higher *ZT* values would also pave the way for new applications of Peltier-type cooling or heating devices. Even higher *ZT* values of 4 or more would be necessary for TEGs to be competitive in industrial waste-heat recovery.[3,7,9] However, even with rather low efficiencies the mechanical advantages already drive the substitution of classical cooling devices by Peltier elements. These are silent and require little maintenance due to the absence of moving parts. They are easily scalable and the direction of the heat transport can be altered by changing the direction of the applied electrical voltage. Diverse applications require optimal conversion efficiencies in different temperature regions and new energy-saving concepts like the automated start-stop mechanism of engines in modern cars demand high stability of the TEGs during repetitive cooling and heating cycles. Tellurides are prominent candidates that exhibit a combination of properties that render them promising materials for thermoelectric applications. For high-temperature applications, thermoelectric tellurides like PbTe are the best investigated materials. Among other materials, germanium antimony telluride (GST) compounds, which are well known for their application as phase-change materials, might be well suited as thermoelectric materials. It has been shown that, for example, the substitution with GeTe has a positive influence on the thermoelectric properties of Sb_2Te_3.[10] It also turned out that the thermal treatment has an impact on the thermoelectric performance of $Ge_2Sb_2Te_5$ and $GeSb_2Te_4$.[11] This indicates the possibility to influence the properties of GST materials by the thermal treatment as well as by varying the composition. The use of GST and silver indium antimony telluride (AIST) materials as phase-change materials indicates that it might be possible to apply similar concepts to both systems. The transfer of the insights derived from these PCMs to similar systems, like $(GeTe)_nAgSbTe_2$ (TAGS materials)[12], which exhibit high *ZT* values is a promising approach for the further optimization of thermoelectric materials. These ideas present the motivation of many projects discussed in this thesis.

1.3 Luminescent materials

Due to the enormous amount of waste heat created by incandescent lamps (up to 90 % of the used electrical energy), the use of thermoelectric materials would not improve their overall energy efficiency to a competitive level as major improvements in lighting technology have been achieved in last decades. Compared to incandescent lamps, compact fluorescent lamps (CFLs), where ultraviolet light is emitted by an activator (Hg) and converted to visible light by a phosphor blend, were a remarkable improvement. However, the higher efficiency of CFLs comes with certain drawbacks. They contain Hg which makes their disposal difficult and raises health concerns by customers. The rather long warm-up time until the maximum brightness is reached reduces the convenience especially for applications where only short-time lighting is required. These drawbacks are overcome and even higher efficiencies can be achieved with pc-LEDs. These are mostly based on blue emitting $In_{1-x}Ga_xN$ semiconductor pump-LEDs.[13] White pc-LEDs are obtained by additive color mixing with additional phosphors (green-yellow, orange-red) applied on top of such primary LEDs. Due to their energy-saving potential, long life cycle and non-toxicity, pc-LEDs are replacing traditional lighting solutions in a constantly growing number of applications. The conversion of light by the phosphors is achieved through a two-step process that involves rare-earth ions such as Eu^{2+}.[14-16] Here the UV to blue radiation from the pump-LED excites 4f electrons of Eu^{2+} atoms to higher energy levels (5d). For Eu^{2+} phosphors, the emission can be very intense due to the parity allowed $4f^6(^7F)5d^1 \rightarrow 4f^7(^8S_{7/2})$ transition and thereby energy is re-emitted as light with a longer wavelength compared to the absorbed one. The Stokes shift, which is defined as the difference between the excitation-band maximum and the emission-band maximum, depends on the ligands and the characteristics of the chemical bonds between the ligands and the rare-earth atom. Therefore, the crystal structure of the host lattice is crucial for the conversion properties of the phosphor material. In order to achieve high quantum efficiencies, rigid host lattices are desirable. Compounds with highly condensed substructures exhibit low thermal quenching, which would reduce the quantum efficiency at the application temperatures of the corresponding pc-LED. The rigid silicate substructure built up of condensed $Si(O,N)_4$ tetrahedra in combination with high thermal and chemical stability make (oxo)nitridosilicates well suited as host lattices for rare-earth atoms for the use in pc-LEDs. The layered oxonitridosilicates $Sr_{1-x}Ba_xSi_2O_2N_2:Eu^{2+}$ ($0 \leq x \leq 1$) discussed in this thesis are highly interesting for the application in pc-LED devices as they show intense emission from blue to yellow depending on the composition, combined with high quantum efficiencies. Due

to the presence of pronounced real-structure effects in this class of materials, the elucidation of the local structure is crucial for the understanding of the luminescence properties. Therefore, a significant synergism arises from the combined analysis of the average and local structure by means of X-ray and electron methods, respectively.

References

[1] D. Rowe, ed., *CRC handbook of thermoelectric materials*, CRC Press, **2005**.

[2] A. Shakouri, *Annu. Rev. Mater. Res.* **2011**, *41*, 399.

[3] M. Martín-González, O. Caballero-Calero, P. Díaz-Chao, *Renew. Sustain. Energy Rev.* **2013**, *24*, 288.

[4] M. H. Elsheikh, D. A. Shnawah, M. F. M. Sabri, S. B. M. Said, M. H. Hassan, M. B. A. Bashir, M. Mohamad, *Renew. Sustain. Energy Rev.* **2014**, *30*, 337.

[5] R. Saidur, M. Rezaei, W. K. Muzammil, M. H. Hassan, S. Paria, M. Hasanuzzaman, *Renew. Sustain. Energy Rev.* **2012**, *16*, 5649.

[6] D. Crane, J. Lagrandeur, V. Jovovic, M. Ranalli, M. Adldinger, E. Poliquin, J. Dean, D. Kossakovski, B. Mazar, C. Maranville, *J. Electr. Mater.* **2013**, *42*, 1582.

[7] C. B. Vining, *Nat. Mater*. **2009**, *8*, 83.

[8] N. D. Hiller, AIRBUS SAS (EADS-C), Patent Number FR2947529-A1. **2013**

[9] H. Kawamoto, *Science&Technology Trends: Quarterly Review* **2009**, *30*, 54.

[10] J. L. Cui, H. Fu, X. L. Liu, D. Y. Chen, W. Yang, *Curr. Appl. Phys.* **2009**, *9*, 1170.

[11] F. Yan, T. J. Zhu, X. B. Zhao, S. R. Dong, *Appl. Phys.* **2007**, *A88*, 425.

[12] G. C. Christakudis, S. K. Plachkova, L. E. Shelimova, E. S. Avilov, *Phys. Status Solidi A* **1991**, *128*, 465.

[13] S. Nakamura, M. Senoh, T. Mukai, *Appl. Phys. Lett*. **1993**, *62*, 2390.

[14] G. Blasse, B. C. Grabmaier, *Luminescent Materials*, 1st edition, Springer, Berlin, **1994**.

[15] C. R. Ronda, *Luminescence*, 1st edition, Wiley-VCH Verlag, **2007**.

[16] R.-J. Xie, Y. Q. Li, N. Hirosaki, H. Yamamoto, *Nitride phosphors and solid-state lighting*, Taylor & Francis, **2011.**

2 TEM investigations of nanostructured germanium antimony tellurides and related compounds with respect to their thermoelectric properties

2.1 Overview

Metastable germanium antimony tellurides (GST materials) are the predominant materials used in rewritable optical storage media like DVDs and BluRay discs. They are also well suited for PCRAM devices, where the switch between the amorphous and the crystalline state is triggered by electrical resistance heating. [1-7] The information is stored as a binary code by switching between an amorphous state with low reflectivity and high resistance and a crystalline state with high reflectivity and low resistance. The metastable crystalline phase involved exhibits a disordered rocksalt-type structure which is in fact thermodynamically stable at high temperature (HT). The corresponding trigonal structure, which is thermodynamically stable at room temperature (RT), does not play a role in phase-change data storage. However, "partial" transitions from the cubic HT phase to the trigonal RT phase can be utilized to induce nanostructures. During these phase transitions, the rearrangement of the defects is crucial. There are various analogies concerning the required material properties for PCMs and thermoelectrics that render GST materials promising candidates for high thermoelectric figures of merit (*ZT*) (Chapter 2.2.1). For high storage density, small recording marks are required. Therefore, a low thermal conductivity (κ) is necessary in order not to affect the neighbouring recording marks. For the application in PCRAM devices, intermediate electrical conductivities (σ) are necessary which also render high Seebeck coefficients (*S*) possible. The introduction of nanostructures, which can be easily obtained in GST materials by quenching the HT phase, is a common approach to improving thermoelectric materials by reducing their phononic contribution to the thermal conductivity (κ_{ph})

The members of the homologous series $(GeTe)_nSb_2Te_3$ represent the pseudo-binary line between tetradymite-type Sb_2Te_3[8] and the layered structure of GeTe. Like Sb_2Te_3 itself, the resulting long-range ordered layered structures (space groups $P\bar{3}m1$ or $R\bar{3}m$) consist of rocksalt-type slabs as building blocks, which are interconnected by van der Waals gaps between the Te atom layers terminating the slabs. The stacking sequence of the Te atom layers across the van der Waals gaps is hexagonal (ABAB) and the distance of the Te atoms is shorter than the sum of the van der Waals radii, which indicates partially covalent

bonding.[9,10] The thickness of the rocksalt-type slabs depends on the GeTe content (n). GeTe was discovered in 1934;[11] its α-GeTe structure type with the space group *R*3*m* [12] is a binary variant of the gray As type with alternating cationic and anionic layers. This corresponds to a rocksalt-type structure with a metric distortion along the cubic <111> directions and a Peierls-like distortion that leads to the formation of layers. Above 705 K, a cubic rocksalt-type HT structure is formed.[13] For GST materials with $n \geq 3$, a comparable rocksalt-type HT phase exists with Te on the anion position and a mixed occupation of Ge, Sb and vacancies on the cation position.[14] The thermal treatment has a huge impact on the nanostructures formed and thereby on the thermoelectric properties of GST materials (Chapter 2.2.2). Temperature programmed powder X-ray diffraction (PXRD) reveals that metastable pseudo-cubic phases are obtained by quenching (Figure 1). In these phases, short-range defect ordering leads to defect layers perpendicular to the <111> directions. Intersecting defect layers with different orientations form a parquet-like nanostructure. At higher temperatures the increased mobility results in the formation of the layered trigonal phase that is thermodynamically stable at room temperature. This phase is also formed when the cubic HT phase is slowly cooled. In the pseudocubic phase the parquet-like structure is associated with lower κ and higher *ZT* values compared to the trigonal structure; probably the parquet-like structure hinders the phonon proliferation more efficiently. This results in *ZT* values of up to 1.5 at 450 °C for $(GeTe)_nSb_2Te_3$ (n = 12, 19).

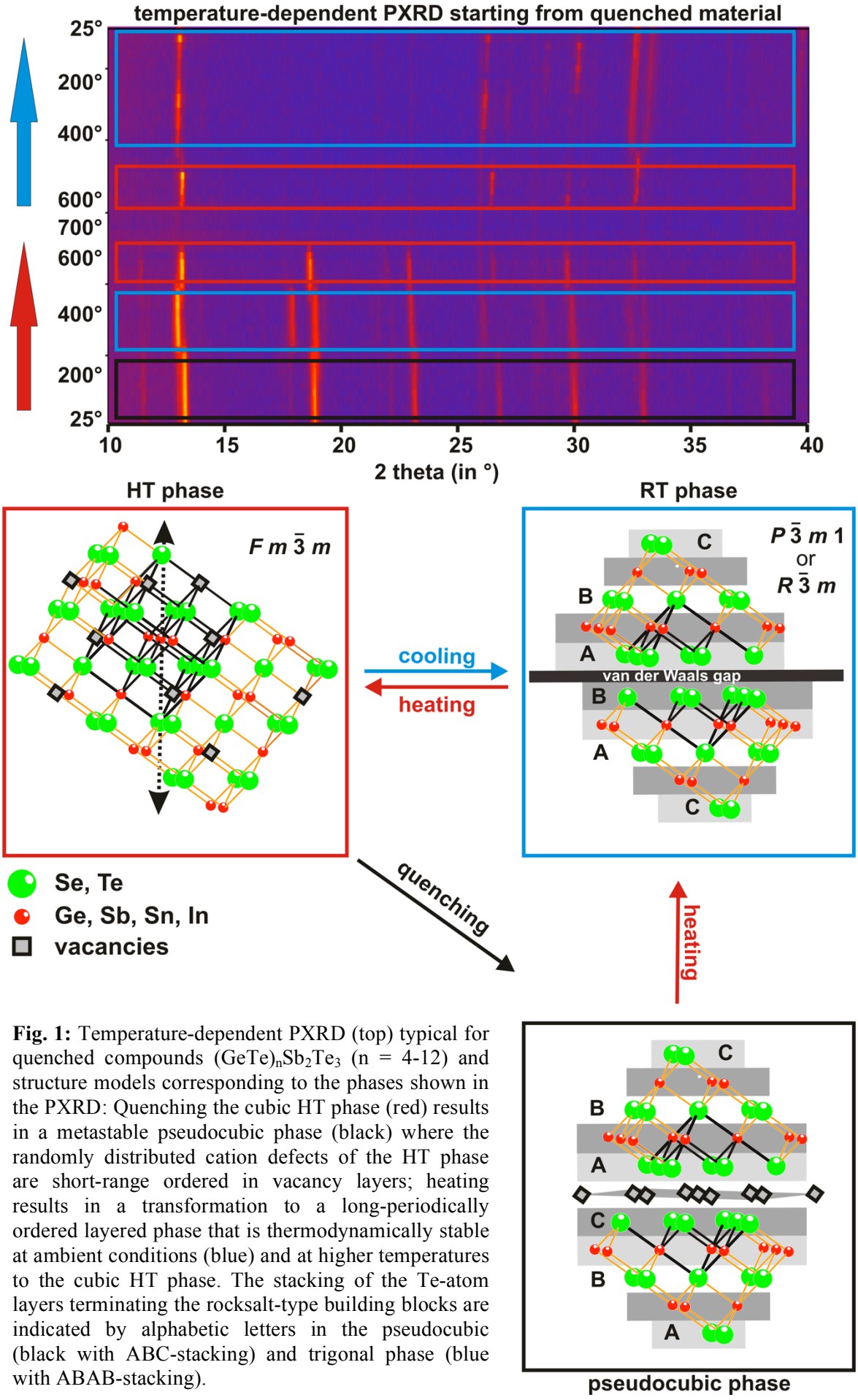

Fig. 1: Temperature-dependent PXRD (top) typical for quenched compounds $(GeTe)_nSb_2Te_3$ (n = 4-12) and structure models corresponding to the phases shown in the PXRD: Quenching the cubic HT phase (red) results in a metastable pseudocubic phase (black) where the randomly distributed cation defects of the HT phase are short-range ordered in vacancy layers; heating results in a transformation to a long-periodically ordered layered phase that is thermodynamically stable at ambient conditions (blue) and at higher temperatures to the cubic HT phase. The stacking of the Te-atom layers terminating the rocksalt-type building blocks are indicated by alphabetic letters in the pseudocubic (black with ABC-stacking) and trigonal phase (blue with ABAB-stacking).

For GST materials with substitutions by In or Sn on the cation position or Se on the anion position, comparable parquet-like structures are obtained when the samples are quenched from the cubic HT phase. The thermal conductivities In-substituted compounds are comparable to unsubstituted GST materials due to the similar differences of the atomic masses on the anion and cation position and the presence of analogous nanostructures. The *ZT* values of the In-substituted compounds are higher below 200 °C due to higher Seebeck coefficients (Chapter 2.3.1). The substitution of Ge with Sn results in a more pronounced parquet-like structure, especially for lower GeTe contents (n), compared to unsubstituted compounds with similar defect concentrations. Higher *ZT* values of the substituted samples with n = 4 and 7 result from higher σ and *S* values (Chapter 2.3.2). Substitution with Se results in increased *S* and reduced κ, especially at high temperatures, due to the additional disorder by the mixed occupation on the anion position (Chapter 2.3.3). These effects are most pronounced for the materials with 20 % substitution rate and result in an overall increase of the *ZT* value up to 400 °C.

Substitutions also affect the phase transition temperatures and the extent of the metrics distortion before or after the phase transition, respectively. Compared to unsubstituted GST materials, In-substituted compounds yield pseudo-cubic phases for higher vacancy concentration at lower quenching rates, since the metrics of the layered phases remains closer to cubic one (Chapter 2.3.1 and ref.[15]). The transition temperatures between the trigonal phase and the cubic HT phase are lower for the substituted compounds, especially for those with Se (Chapter 2.3.3). They exhibit a lower lateral extension of the defect layers as visible in HRTEM images and concluded from the broadening of the diffuse intensities in reciprocal lattice sections calculated from single-crystal data and in SAED patterns. This reflects the shorter time available for diffusion processes and lower mobility of the atoms and vacancies during the quenching process, as a result of lower phase-transition temperatures. The variety of possibilities to influence the properties of GST materials in combination with their usually low κ and intermediate σ values, render these well established PCMs promising candidates for thermoelectric application. The phononic contribution to the thermal conductivity can be optimized by changing the nanostructure via the variation of vacancy concentration and different thermal treatment as well as the variation of the transition temperatures by substitution. Of course, the substitutions might additionally be used for the optimization of electronic properties.

References

[1] M. Wuttig, N. Yamada, *Nat. Mater.* **2007**, *6*, 824.

[2] T. Siegrist, P. Merkelbach, M. Wuttig, *Annu. Rev. Condens. Matter Phys.* **2012**, *3*, 215.

[3] M. Wuttig, S. Raoux, *Z. Anorg. Allg. Chem.* **2012**, *638*, 2455.

[4] W. Bensch, M. Wuttig, *Chem. Unserer Zeit* **2010**, *44*, 92.

[5] S. Raoux, R. M. Shelby, J. Jordan-Sweet, B. Munoz, M. Salinga, Y.-C. Chen, Y.-H. Shih, E.-K. Lai, M.-H. Lee, *Microelectron. Eng.* **2008**, *85*, 2330.

[6] S. Raoux, W. Welnic, D. Ielmini, *Chem. Rev.* **2010**, *110*, 240.

[7] Y. Gu, S. Song, Z. Song, S. Bai, Y. Cheng, Z. Zhang, B. Liu, S. Feng, *Appl. Phys. Lett.* **2013**, *102*, 103110.

[8] T. L. Anderson, H. B. Krause, *Acta Crystallogr Sect, B* **1974**, *30*, 1307.

[9] L. E. Shelimova, O. G. Karpinsky, M. A. Kretova, V. I. Kosyakov, V. A. Shestakov, V. S. Zemskov, F. A. Kuznetsov, *Inorg. Mater.* **2000**, *36*, 768.

[10] O. G. Karpinsky, L. E. Shelimova, M. A. Kretova, J.-P. Fleurial, *J. Alloy. Compd.* **1998**, *268*, 112.

[11] W. Klemm, G. Frischmuth, *Z. Anorg. Allg. Chem.* **1934**, *218*, 249.

[12] J. Goldak, C. S. Barrett, D. Innes, W. Youdelis, *J. Chem. Phys.* **1966**, 44, 3323.

[13] T. Chattopadhyay, J. Boucherle, H. G. von Schnering, *J. Phys. C* **1987**, *20*, 1431.

[14] T. Matsunaga, H. Morita, R. Kojima, N. Yamada, K. Kifune, Y. Kubota, Y. Tabata, J.-J. Kim, M. Kobata, E. Ikenaga, K. Kobayashi, *J. Appl. Phys.* **2008**, *103*, 093511.

[15] F. Fahrnbauer, P. Urban, S. Welzmiller, T. Schröder, T. Rosenthal, O. Oeckler, *Solid State Sci.* **2013**, *208*, 20.

2.2 Thermoelectric germanium antimony tellurides

2.2.1 From phase-change materials to thermoelectrics?

M. N. Schneider, T. Rosenthal, C. Stiewe, O. Oeckler

Z. Kristallogr. **2010**, *225,* 463-470.

Abstract

Metastable tellurides play an important role as phase-change materials in data storage media and non-volatile RAM devices. The corresponding crystalline phases with very simple basic structures are not stable as bulk materials at ambient conditions, however, for a broad range of compositions they represent stable high-temperature phases. In the system Ge/Sb/Te, rocksalt-type high-temperature phases are characterized by a large number of vacancies randomly distributed over the cation position, which order as 2D vacancy layers upon cooling. Short-range order in quenched samples produces pronounced nanostructures by the formation of twin domains and finite intersecting vacancy layers. As phase-change materials are usually semimetals or small-bandgap semiconductors and efficient data storage requires low thermal conductivity, bulk materials with similar compositions and properties can be expected to exhibit promising thermoelectric characteristics. Nanostructuring by phase transitions that involve partial vacancy ordering may enhance the efficiency of such thermoelectrics. We have shown that germanium antimony tellurides with compositions close to those used as phase-change materials in rewritable Blu-Ray Discs, e.g. $(GeTe)_{12}Sb_2Te_3$, exhibit thermoelectric figures of merit of up to ZT = 1.3 at 450 °C if a nanodomain structure is induced by rapidly quenching the cubic high-temperature phase. Structural changes have been elucidated by X-ray diffraction and high-resolution electron microscopy.

2.2.1.1 Introduction

2.2.1.1.1 Thermoelectrics

In the past decade, an increasing number of research projects have focused on both the synthesis and the optimization of thermoelectric materials. These may be used to reversibly interconvert thermal and electrical energy, the ultimate goals being electric power generation from waste heat and the construction of efficient cooling devices. In this context, structure-property relationships concerning thermoelectricity have received increasing attention of materials scientists as understanding the phenomenon on the atomic as well as the nanoscale is the basis for any targeted optimization. Efficient thermoelectrics should combine high electrical conductivity (σ) and high Seebeck coefficients (S). Furthermore, the thermal conductivity (κ) should be as low as possible. The interplay of these specifications is represented by the dimensionless figure of merit $ZT = S^2T\sigma\kappa^{-1}$ which is directly related to the efficiency of thermoelectric generators.

All relevant properties depend on the charge carrier concentration and cannot be altered independently. Concerning σ and κ, the best compromise are small-bandgap semiconductors or semimetals. As the electronic part of κ is proportional to σ, only its phononic part can be somehow independently varied.

Table 1. Comparison of tellurides used as thermoelectrics or as phase-change materials. Compounds without references are discussed in reviews.[1-5, 31-40]

thermoelectric materials	phase-change materials
M-Te (M = Ge, In, Ga, Pb, Bi, Sb) $GeTe_4$,[19] $InTe_4$,[20] $GaTe_4$,[20] PbTe, Bi_2Te_3, Sb_2Te_3, $(Bi_2)_m(Bi_2Te_3)_n$,[21], $(Sb_2)_m(Sb_2Te_3)_n$ [22]	**M-Te (M = Au, Ge, Sb)** Au_5Te_{95},[23] GeTe, $GeTe_4$,[23] Sb_2Te, Sb_7Te_3
M-Sb-Te (M = Ag, Ge, Ag/Ge, Ga, Pb) $AgSbTe_2$, $(GeTe)_n(Sb_2Te_3)_m$ (GST),[24,25] $(AgSbTe_2)_{1-x}(GeTe)_x$ (TAGS), $Ga_mSb_nTe_{1.5(m+n)}$,[26] $Pb_2Sb_6Te_{11}$, $GeSb_{100}Te_{150}$ [27]	**M-Sb-Te (M = Ag, Ge, Sn, In)** $AgSbTe_2$,[28] $(GeTe)_n(Sb_2Te_3)_m$ (GST), $SnSb_2Te_4$, $Ge_{7.1}Sb_{76.0}Te_{16.9}$ In_3SbTe_2 [29]
M-Bi-Te (M = Ge, Sn, Pb, Cs) $(GeTe)_n(Bi_2Te_3)_m$ (GBT),[30], $(SnTe)_n(Bi_2Te_3)_m$,[30] $(PbTe)_n(Bi_2Te_3)_m$,[30] $CsBi_4Te_6$	**M-Bi-Te (M = Ge)** $(GeTe)_n(Bi_2Te_3)_m$ (GBT)
M-Tl-Te (M = Ag, Sn, Bi) Ag_9TlTe_6, Tl_2SnTe_5, Tl_9BiTe_6	**M-In-Sb-Te (M = Ag)** $Ag_5In_5Sb_{60}Te_{30}$, $Ag_{3.4}In_{3.7}Sb_{76.4}Te_{16.5}$ (AIST)
M- Pb- (M')-Sb-Te (M = Ag, Na, K; M' = Sn) $AgPb_mSbTe_{2+m}$ (LAST), $AgPb_mSn_nSbTe_{2+m+n}$ (LASTT), $NaPb_mSbTe_{2+m}$ (SALT), $NaPb_mSn_nSbTe_{2+m+n}$ (SALTT), KPb_mSbTe_{2+m} (PLAT)	**M-M'-Sn-Te (M = Au M'=Ge)** $Au_{25}Ge_4Sn_{11}Te_{60}$

One way to increase *ZT* is the incorporation of atoms that are located in voids that are larger than necessary to accommodate them. These so-called 'rattling' atoms may effectively scatter phonons and thus reduce κ. Several classes of compounds such as skutterudites (e.g., $CoSb_3$), clathrates (e.g., Na_8Si_{46}) or half Heusler alloys (e.g., TiNiSn) provide promising candidates as summed up in various recent reviews.[1–5] However, practical applications are still dominated by tellurides such as PbTe or Bi_2Te_3 which show a sufficient concentration of carriers and exhibit a rather low thermal conductivity owing to the presence of heavy atoms. Based on these conventional thermoelectrics with *ZT* in the range of ~1, a broad range of new tellurides with promising properties has been prepared (see Table 1). Most of these materials exhibit a high degree of disorder on various length scales. Nanostructuring by partial decomposition or exsolution on the nanoscale led to *ZT* values up to ~2, the most prominent examples being $AgPb_mSbTe_{2+m}$ (LAST-*m*) or $NaPb_mSbTe_{2+m}$ (SALT-*m*).[6,7] Other examples such as $Pb_2Sb_6Te_{11}$ exhibit layered structures.[8] Precipitates and domain or grain boundaries, respectively, are essential as corroborated by thermoelectrics which combine high power factors $S^2\sigma$ with drastically reduced lattice thermal conductivity due to increased phonon scattering at interfaces. This approach has successfully been demonstrated for layer-like systems such as Sb_2Te_3/Bi_2Te_3 superlattices, PbTe/PbSe quantum dot superlattices or nanocomposites of crystalline GeTe in an amorphous matrix with overall composition $GeTe_4$.[9–11] Such approaches (recent reviews [12–18]): strongly depend on the interplay of thermodynamics and kinetics and always mean approaching (but not reaching) the equilibrium state from a metastable one. Unstable but kinetically inert tellurides obviously offer a good starting point to follow this concept.

2.2.1.1.2 Phase-change materials

Metastable tellurides play another important role as phase-change materials (PCMs) in the recording layers of many rewritable data storage media (e.g., DVD-RW, DVD-RAM, BD-RE) and novel non-volatile random-access memory (RAM) devices.[31–40] PCMs allow switching between amorphous and crystalline modifications which differ in optical and electrical properties, respectively. According to theoretical calculations and X-ray absorption fine structure (EXAFS) investigations,[41–48] Ge/Sb–Te–Ge/Sb–Te squares and even-membered larger rings are present in the amorphous modification. Although distorted octahedral coordination is predominant for most atoms, tetrahedral coordination of Ge has been evidenced and led to the hypothesis of an 'umbrella-flip' mechanism for the phase

change between the amorphous and crystalline phases.[49–53] The metastable crystalline modifications of various PCMs exhibit simple average structures, such as the A7 (gray As) type (e.g., $Ag_{3.4}In_{3.7}Sb_{76.4}Te_{16.5}$ or $Ge_{7.1}Sb_{76.0}Te_{16.9}$) [39] or the rocksalt type (e.g., $GeSb_2Te_4$ or $Ge_2Sb_2Te_5$) [54–56] which may be rhombohedrally distorted towards a GeTe-type structure (e.g., $Ge_8Sb_2Te_{11}$).[57] These simple average structures are accessible from amorphous ones via short diffusion pathways, which is a requirement for the fast phase transition. As chemically very different atom types share the same Wyckoff position, the question of short-range ordering arises, both concerning of the elements and the vacancies, including the accompanying local distortion and relaxation, respectively. Vacancies are crucial for the stabilization of these materials and a statistical distribution as well as an arrangement in planar defect planes have been discussed.[58–64] The stable phases formed upon annealing of the metastable crystalline materials often exhibit ordered layered structures such as 21*R*-$GeSb_2Te_4$, 21*R*-$GeBi_2Te_4$ or 9*P*-$Ge_2Sb_2Te_5$.[65–69] These structures can be described as a stacking sequence of distorted rocksalt-type slabs with van der Waals gaps in between Te layers terminating the slabs. These gaps can be viewed as 2D infinite layers of cation vacancies associated with relaxation. However, in other cases equilibrium conditions correspond to a mixture of two or more different phases. For example, GeTe-rich GST materials do not form single-phase materials when reaching the thermodynamically stable state but separate into the long-periodically ordered compound $Ge_9Sb_2Te_{12}$ and an additional phase with a GeTe-type structure.[57] Although the stable modifications do not occur during the write-erase cycle, they need to be taken into consideration as they are the ‘thermodynamic trap’ to be avoided. The kinetic inertness of metastable tellurides is essential for PCMs.

The properties of the materials depend, of course, on the electronic structure of the materials. The reversible phase transition amorphous to metastable crystalline is either induced by laser irradiation or by an electric current. In general, small-bandgap semiconductors or semimetals are required. Especially in RAM devices, intermediate electrical conductivity ensures sufficient currents but still allows ‘resistance heating’. The writing process involves the amorphization of small recording marks in a crystalline matrix, whereas erasing means recrystallization. For the sake of high spatial resolution and short write and erase times, low thermal conductivity of the PCMs is important in order to obtain high temperatures in very small areas. The metastability of both modifications is essential and ensures the reversibility of the process which would be interrupted once the stable phases are formed.

Several reviews show impressively that tellurides dominate the field of PCMs.[31–40] For example, $Ag_5In_5Sb_{60}Te_{30}$ and $Ag_{3.4}In_{3.7}Sb_{76.4}Te_{16.5}$ are used for DVD-RW media, whereas

germanium antimony tellurides (GST materials) are employed in CD-RWs (e.g. $Ge_{7.1}Sb_{76}Te_{16.9}$), DVD-RAMs ($GeSb_2Te_4$ or $Ge_2Sb_2Te_5$) and Blu-Ray Discs (GeTe-rich materials like $Ge_8Sb_2Te_{11}$). The relevant materials are summarized in Table 1, which also contains further examples that exhibit rapid phase-change behavior but are currently not used due to slightly inferior properties. Interestingly, the combinations of elements used for efficient PCMs are rather similar to those employed in thermoelectrics with high figures of merit. This fact is reflected in several basic properties. For both applications, semimetals or small-bandgap semiconductors with low thermal conductivity are required. For a few examples, such as $AgSbTe_2$, $Ge_2Sb_2Te_5$ or $GeTe_4$, more or less stable modifications have been shown to possess interesting thermoelectric properties,[3,25] whereas their metastable modifications are well known PCMs. The striking similarities between both classes of materials rise the question if metastable modifications of PCMs are intriguing precursors for efficient thermoelectrics. Whereas the formation of thermodynamically stable modifications is a drawback concerning PCM applications, the partial equilibration by exsolution or short-range vacancy ordering might be associated with the formation of nanostructures in bulk material. Such processes may yield interesting thermoelectrics, however, not much is known about the thermoelectric properties of PCMs and materials obtained from such ‘precursors’ by approaching stable states.

2.2.1.2 Structure of metastable GST bulk materials with different GeTe content and their thermoelectric properties

2.2.1.2.1 Structural aspects

Concerning the investigation of thermoelectric properties, it is a drawback that most metastable phases of PCMs are only accessible as thin films prepared by sputtering techniques. Therefore, it is desirable to find compounds whose metastable modifications are accessible as bulk material. Most GST materials with metastable, slightly distorted rocksalt-type average structures correspond to compositions that lie on the pseudobinary line $(GeTe)_n(Sb_2Te_3)_m$, i.e. all elements exhibit normal valence states. Rewriting the formula so that it reflects the cation and anion positions of the rocksalt-type shows that the concentration of vacancies decreases with decreasing Sb content: $(Ge_{n/(3m+n)}Sb_{2m/(3m+n)}\square_{m/(3m+n)})Te$, whereas the cation to anion ratio converges to 1 when approaching pure GeTe as shown in Fig. 1 for $m = 1$.

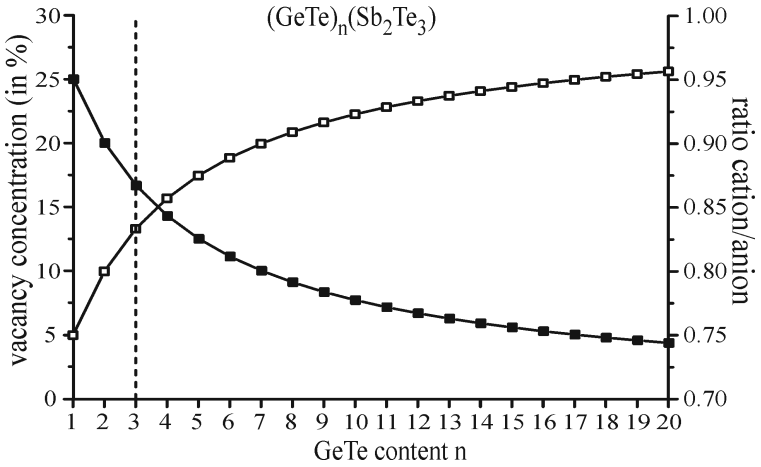

Fig. 1: Concentration of vacancies in metastable rocksalt-type structures with compositions $(GeTe)_nSb_2Te_3$ (solid squares) and anion/cation ratio (empty squares) depending on the GeTe content n in the range n = 1 – 20. For n ≥ 3 (broken line), there are stable cubic high-temperature modifications.

The vacancy concentration has an impact on the existence and stability of different atomic as well as nanostructures. The spacing between van der Waals gaps that can be viewed as 2D extended cation defect planes in the stable modifications increases with increasing GeTe content; the overall stacking sequence (Ramsdell symbol) depends on *n* and *m*.[69,70] On the other hand, the average structure of metastable crystalline GeTe-rich PCM phases produced by magnetron sputtering corresponds to the rocksalt type for $n \leq 6$, whereas phases with $n \geq 8$ exhibit a rhombohedrally distorted rocksalt-type resembling the structure of GeTe.[57] Similar to GeTe, these phases have a cubic rocksalt-type modification at high temperatures. If this high-temperature phase is rapidly quenched to room temperature, the transition to the stable layered phase is hindered due to the multiple twinning associated with a cubic → rhombohedral phase transition. Stresses between the nanoscale rhombohedral twin domains impede lattice relaxation and long-range two-dimensional defect ordering.[71] The metrics remain almost cubic but short-range layer formation takes place. Concerning the use of this partial phase transition to optimize the thermoelectric properties of $(GeTe)_nSb_2Te_3$ compounds, it is interesting to determine the range of *n* in which a stable cubic high-temperature modification does exist and in which cases it can be quenched to pseudocubic metastable bulk material.

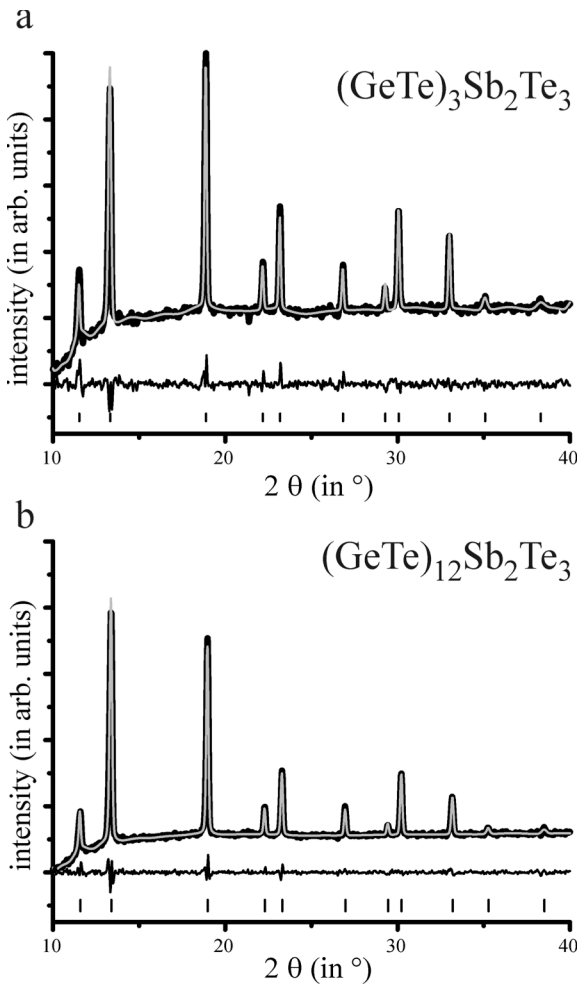

Fig. 2: Result of Rietveld fits (gray) of experimental powder diffraction patterns (black) measured at 600 °C (background from the furnace subtracted) of (a) $(GeTe)_3Sb_2Te_3$ and (b) $(GeTe)_{12}Sb_2Te_3$ with difference curve and reflection markers (bottom).

For the most prominent PCMs $GeSb_2Te_4$ and $Ge_2Sb_2Te_5$ (i.e., $n < 3$), no phase transition from their stable 21*R* type and 9*P* type structures to cubic high temperature modifications has been reported in the literature. This is in accordance with temperature-dependent X-ray powder diffraction and DTA experiments which we performed in the course of this study. No phase transitions were observed up to the melting points. However, for the stable ambient temperature phase of 33*R*-$Ge_3Sb_2Te_6$ ($n = 3$), which was obtained by annealing a sample at 500 °C, both methods indicate a phase transition to a cubic phase at ~575 °C, which melts at ~615 °C. The rocksalt-type of the high-temperature phase was confirmed by a Rietveld refinement on a powder diffraction pattern recorded at 600 °C (cf. Fig. 2a), assuming that Te occupies the anion position and Ge, Sb and vacancies share the cation position. Details of the structure refinement are given in Table 2. Whereas slow cooling from the melt yields long-range ordered 33*R*-$Ge_3Sb_2Te_6$, rapid quenching in air or liquid nitrogen does neither yield the stable modification nor a homogenous distorted rocksalt-type structure. Powder diffraction patterns of quenched samples indicate a mixture of a cubic and a layered rhombohedral phase. However, the rhombohedral phase is strongly disordered as indicated by the diffuse broadening of its reflections. Upon heating this material, the cubic phase vanishes at ~270 °C, whereas 33*R*-$Ge_3Sb_2Te_6$ forms from the disordered rhombohedral phase at ~420 °C as shown in Fig. 3a. The cubic phase forms at ~575 °C and transforms back to 33*R*-$Ge_3Sb_2Te_6$ without significant hysteresis.

Table 2. Experimental details and results of the Rietveld refinements for the high-temperature phases of $(GeTe)_nSb_2Te_3$ with n = 3 and 12, respectively.

	$(GeTe)_3Sb_2Te_3$	$(GeTe)_{12}Sb_2Te_3$
sum formula	$Ge_3Sb_2Te_6$	$Ge_{12}Sb_2Te_{15}$
structure type	NaCl (B1)	
crystal system	cubic	
space group	$Fm\bar{3}m$	
temperature	600 °C	
lattice parameters	a = 6.1140(6) Å	a = 6.0826(5) Å
cell volume	228.54(7) Å^3	225.04(6) Å^3
formula weight	1226.87 g/mol	3028.58 g/mol
Z	2/3	4/15
observed reflections	22	
refined parameters	62	
diffractometer	Stoe STADI P, Ge(111) monochromator	
radiation	Mo $K_{\alpha1}$ (λ = 0.7093 Å)	
2θ range	10 – 50°	
background function	Shifted Chebyshev (48 parameters)	
R_p	0.029	0.026
wR_p	0.044	0.041

$(GeTe)_{12}Sb_2Te_3$ exhibits an analogous rocksalt-type high-temperature phase (cf. Table 2) which has also been confirmed by a Rietveld refinement (Fig. 2b) using data measured at 600 °C. In contrast to $(GeTe)_3Sb_2Te_3$, rapid quenching of this phase (or directly quenching the melt) yields a homogeneous (stress-stabilized) pseudo-cubic phase whose average structure corresponds to a rhombohedrally distorted rocksalt-type. Slow cooling as well as annealing at 400 °C, however, leads to a relaxed rhombohedral layered structure. Temperature dependent powder diffraction (cf. Fig. 3b) starting from quenched samples indicate a transformation to the relaxed structure at ~325 °C and the phase transition to the cubic high-temperature phase at ~475-500 °C, which is significantly lower than for $(GeTe)_3Sb_2Te_3$.

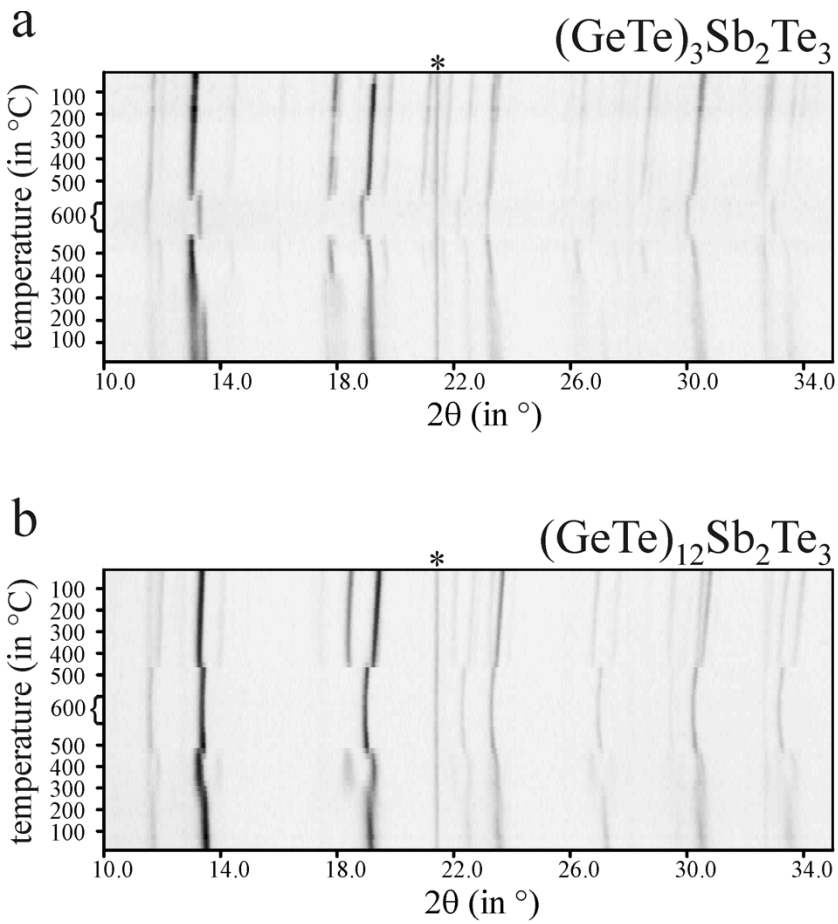

Fig. 3: Comparison of in situ temperature dependent powder diffraction patterns (heating and subsequent cooling shown from bottom to top): (a) a sample of $(GeTe)_3Sb_2Te_3$ quenched from the melt after heating to 950 °C; (b) a sample of $(GeTe)_{12}Sb_2Te_3$ quenched after annealing at 500 °C for 20 h (samples of $(GeTe)_{12}Sb_2Te_3$ quenched from the melt are not significantly different). The asterisk marks a reflection from the furnace. The reflections of the (pseudo-)cubic quenched phases (bottom) can be identified by comparison with those of the cubic high-temperature phase (middle): they are the only ones observed for quenched $(GeTe)_{12}Sb_2Te_3$ whereas they correspond to a minor phase for $(GeTe)_3Sb_2Te_3$. Note that the reflection broadening for the main phase in quenched $(GeTe)_3Sb_2Te_3$ vanishes around 420 °C.

Single crystals of $(GeTe)_{12}Sb_2Te_3$ (composition verified by EDX) were grown from starting material with the same composition by chemical transport in the stability region of the high temperature and subsequently quenched to room temperature. Their structure is similar to that of GeTe-rich single crystals isolated from pseudo-cubic bulk material.[71] The average structure is rhombohedral (GeTe type, $R\bar{3}m$, a = 4.237(3) Å, c = 10.29(1) Å) with pseudo-cubic metrics due to stresses resulting fourfold twinning. Their diffraction patterns exhibit pronounced diffuse streaks along the pseudocubic <111> directions as shown in Fig. 4a. Very similar diffraction patterns have been obtained by selected-area electron diffraction (SAED). Figure 5 shows that these correspond to nanostructured crystals as described in detail recently.[71] The corresponding high-resolution images show that vacancies tend towards

short-range order in finite layers that extend perpendicular to the (pseudo-)cubic <111> directions. This involves a (local) symmetry reduction, however, the corresponding twin domains are very small.

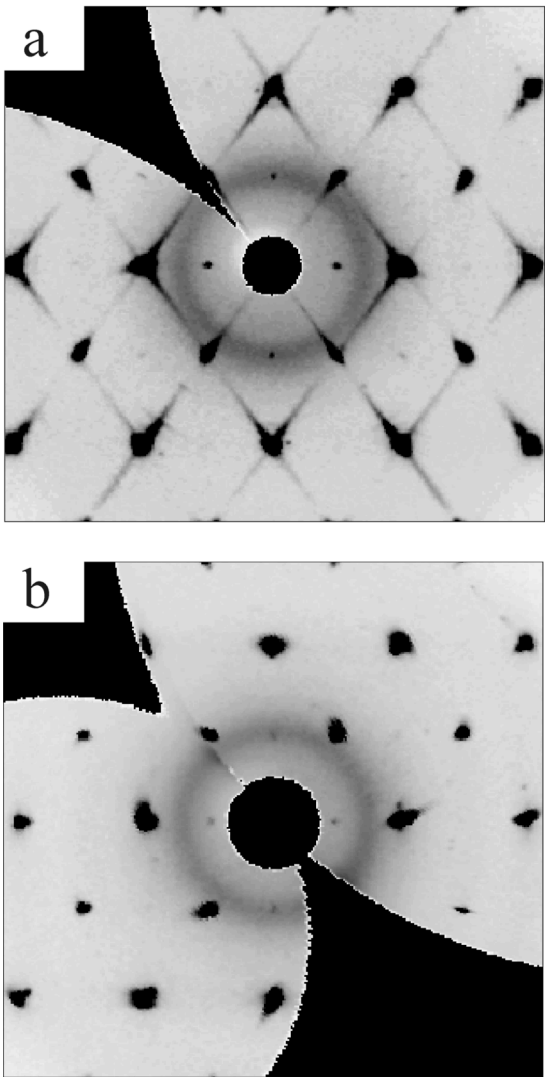

Fig. 4: Reciprocal lattice sections *hhl* (with respect to pseudocubic indexing) reconstructed from area-detector data of a $(GeTe)_{12}Sb_2Te_3$ single crystal grown by chemical transport: (a) quenched crystal at room temperature with diffuse streaks along <111>; (b) measurement at 550 °C (cubic high-temperature phase, no diffuse streaks).

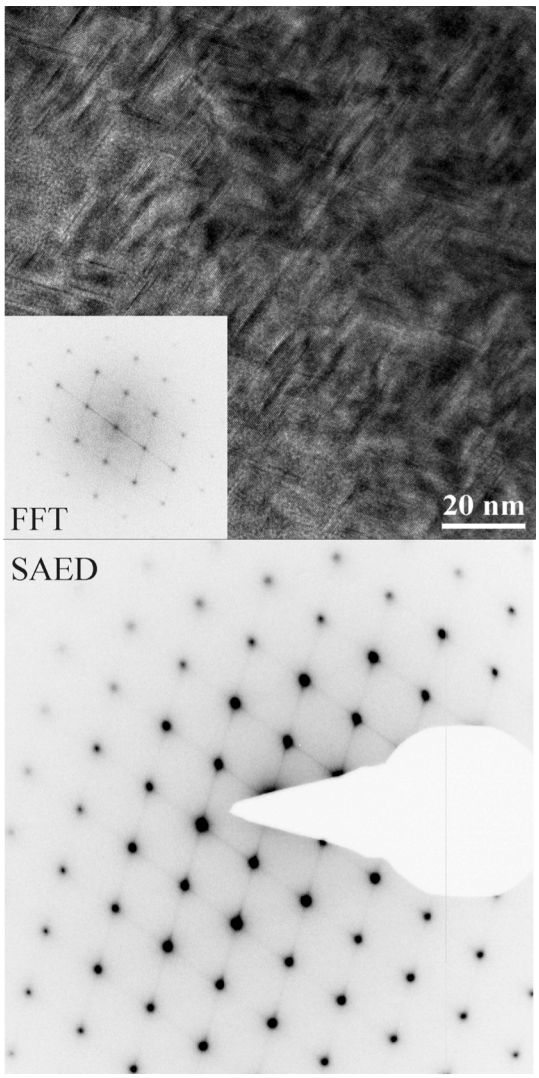

Fig. 5: SAED pattern (bottom) and HRTEM image (top, with corresponding Fourier transform) of quenched $(GeTe)_{12}Sb_2Te_3$. The zone axis [110] (pseudocubic indexing) corresponds to the reciprocal lattice sections *hhl*.

However, X-ray diffraction patterns recorded in the stability range of the high temperature phase (550 °C, cf. Fig. 4b) do not show diffuse streaks. This indicates that at this temperature there are no planar defects, i.e., no significant short-range ordering of vacancies. Ge, Sb and vacancies are probably randomly distributed over all cation sites.

2.2.1.2.2 Thermoelectric properties

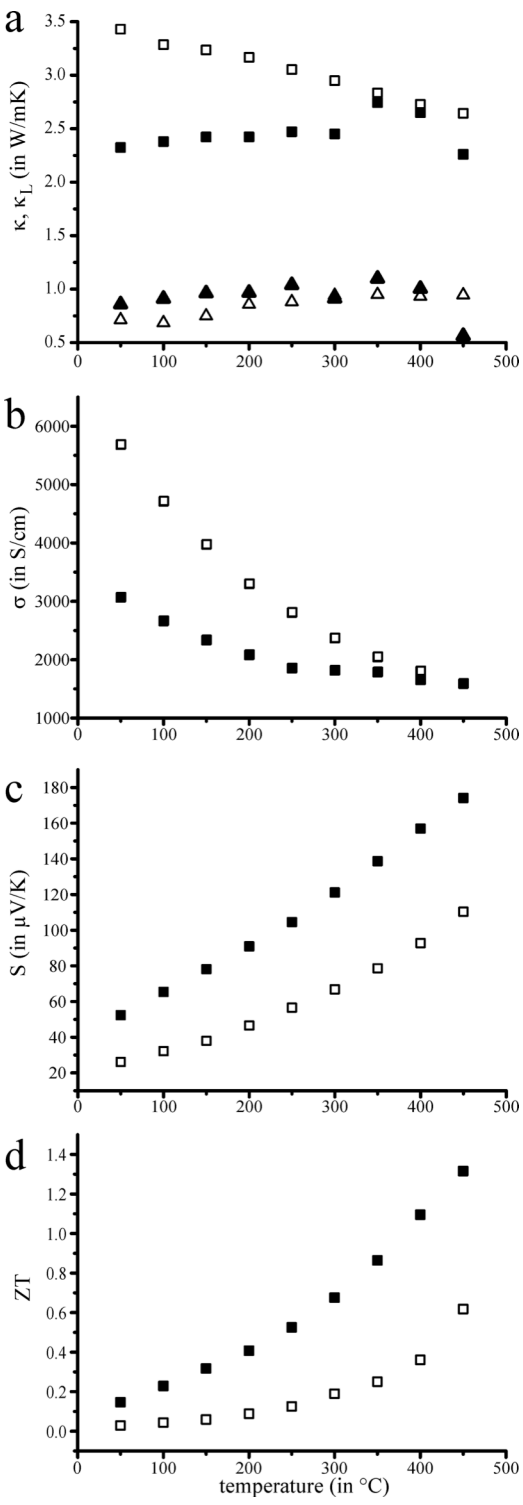

Fig. 6: Thermoelectric characteristics for $(GeTe)_{12}Sb_2Te_3$ (solid squares) and $(GeTe)_3Sb_2Te_3$ (empty squares): (a) thermal conductivity (additional triangles represent the lattice part κ_L); (b) electrical conductivity; (c) Seebeck coefficient; (d) overall thermoelectric figure of merit.

The nanostructuring by planar defect planes in quenched material as indicated by HRTEM and diffuse scattering can be expected to reduce the thermal conductivity of the materials and increase the thermoelectric efficiency. Very high electrical conductivities were measured for both of the samples (Fig. 6b), with lower values for $(GeTe)_{12}Sb_2Te_3$, probably due to a more pronounced scattering of charge carriers because of the nanodomain structure. The temperature dependences of the electrical conductivities show metallic behavior, corresponding to highly doped semiconductors.

The Seebeck coefficient for both samples is positive over the complete temperature range under investigation, proving the deficiency electrons (holes) as the major charge carriers (Fig. 6c). At each temperature, the Seebeck coefficient values of $(GeTe)_{12}Sb_2Te_3$ are almost double compared to $(GeTe)_3Sb_2Te_3$. This surprising result has been checked in a repeated measurement run to improve the reliability. The reason for this behavior of the Seebeck coefficient is not yet completely

understood and will be investigated in more detail in further studies. The overall thermal conductivity matches the picture of the electrical conductivity with smaller values for $(GeTe)_{12}Sb_2Te_3$. Calculating the electrical contribution of the thermal conductivity using the Wiedemann-Franz law for non-degenerate semiconductors allows the identification of the lattice thermal conductivity as displayed in Fig. 6a. No significant difference in κ_L could be found between both samples. Although the domain structure is more pronounced for $(GeTe)_{12}Sb_2Te_3$, the higher concentration of vacancies in $(GeTe)_3Sb_2Te_3$ probably compensates for the higher degree of long-range order. Therefore, the difference in the overall thermal conductivity is due to the difference in the electrical one, leading to an almost uninfluenced ratio of σ/κ.

Both compounds exhibit rather high overall figures of merit *ZT* as compared to long-range ordered stable GST phases, where maximum *ZT* values of about ~0.2 have been measured.[24,25] The high value of *ZT* = 1.3 at 450 °C for $(GeTe)_{12}Sb_2Te_3$ is due to the increased Seebeck coefficient, as can be seen from Fig. 6c and d, making this class of materials very promising for thermoelectric applications.

2.2.1.3 Conclusion

Several conclusions can be drawn from the comparison of GeTe-poor and GeTe-rich $(GeTe)_nSb_2Te_3$ materials. Only materials with $n \geq 3$ exhibit a stable cubic high-temperature modification with randomly distributed cation defects. 2D vacancy ordering is energetically favored, therefore, the transition temperature to the high-temperature phase is higher for compounds with high vacancy concentrations (~575 °C for $n = 3$ vs. ~500 °C for $n = 12$). If the vacancy concentration is rather high (e.g., $(GeTe)_3Sb_2Te_3$), the high-temperature modification cannot be completely quenched to a pseudocubic phase, in contrast to phases with fewer vacancies like $(GeTe)_{12}Sb_2Te_3$ which require longer diffusion pathways to reach the stable layered compounds. The pseudocubic phases are kinetically inert as stresses impede metric relaxation and vacancy diffusion.[71] The partial transition from the randomly disordered high-temperature phase to the layered stable phase can be used to induce nanostructuring which influences both the thermal as well as the electric conductivity. The composition of $(GeTe)_{12}Sb_2Te_3$ is close to that of PCMs employed in rewritable BluRay-Discs. As pointed out in the introduction, the requirements for PCMs and thermoelectrics are comparable. If the cubic phases of PCMs are used as precursors for nanostructured thermoelectrics, one can expect efficient materials. We have shown this for quenched $(GeTe)_{12}Sb_2Te_3$, which exhibits promising *ZT* values at high temperatures, and, to a lesser

extent, for $(GeTe)_3Sb_2Te_3$. We believe that this is a promising concept for the search of new nanostructures chalcogenide or pnictide thermoelectrics.

2.2.1.4 Experimental

2.2.1.4.1 Synthesis

Bulk samples of $(GeTe)_3Sb_2Te_3$ (= $Ge_3Sb_2Te_6$) and $(GeTe)_{12}Sb_2Te_3$ (= $Ge_{12}Sb_2Te_{15}$) were prepared by melting stoichiometric amounts of the elements Ge (99.999%, Sigma Aldrich), Sb (99.999%, Smart Elements) and Te (99.999%, Alfa Aesar) in sealed silica glass ampoules under Ar atmosphere. After melting the mixtures at 950 °C (ca. 2 h), the ampoules were quenched in water. The nanostructured samples were obtained by reheating to 500 °C for 20 h and quenching in water again. Other samples were annealed at the temperatures given in the text.

Single crystals of $(GeTe)_{12}Sb_2Te_3$ were grown by chemical transport using iodine as transport agent. Stoichiometric $(GeTe)_{12}Sb_2Te_3$ (ca. 110 mg, see above) was sealed in evacuated silica ampoules of approximate 20 cm in length and 15 mm diameter as starting material. Small amounts (ca. 10 mg) of SbI_3 were added to generate I_2 by decomposition at elevated temperatures (a similar procedure has been used for $GeSb_4Te_7$ [72]). The octahedral single crystals grew in a temperature gradient from 600 to 550 °C (i.e., in the stability range of the high-temperature phase) within 15-20 h and were subsequently quenched to room temperature by removing the ampoule from the furnace.

Ingots for the measurement of thermoelectric properties were prepared by melting stoichiometric mixtures of the elements under inert atmosphere in ampoules with flat base which allow to solidify the melts into disc-shaped ingots with diameter of approximately 15 mm and thickness of 3-6 mm. After melting at 950 °C and quenching, these ingots were annealed at 500 °C for 20 h and quenched to room temperature in air. For thermoelectric measurements, they were polished to flat plates. Powder diffraction patterns of these materials do not differ significantly from those of the corresponding samples used for the other investigations.

2.2.1.4.2 Scanning electron microscopy and chemical analysis

Energy dispersive X-ray spectroscopy was done with a JSM-6500F (Jeol, USA) scanning electron microscope (SEM) equipped with an energy-dispersive X-ray (EDX) detector (model 7418, Oxford Instruments, Great Britain). The compositions of the bulk samples were confirmed by averaging three point analyses on crystallites isolated from bulk material. The resulting atom ratios Ge : Sb : Te are 29 : 18 : 53 for $(GeTe)_3Sb_2Te_3$ (calculated: 27.3 : 18.2 : 54.6) and 48 : 5 : 47 for $(GeTe)_{12}Sb_2Te_3$ (calculated: 41.4 : 6.8 : 51.7), the deviations are within the usual error limits for samples with rough surfaces. The composition of single crystals $(GeTe)_{12}Sb_2Te_3$ grown by transport reactions was determined as Ge : Sb : Te = 43 : 7 : 50 by analyzing flat crystal faces. No iodine impurities were detected.

2.2.1.4.3 X-ray diffraction

X-ray powder patterns were recorded on a Huber G670 Guinier camera equipped with a fixed imaging plate and integrated read-out system using Cu-$K_{\alpha 1}$ radiation (Ge monochromator, λ = 1.54051 Å). Specimens were prepared by fixing powdered parts of the samples on Mylar foils using silicone grease. Temperature-dependent powder patterns were recorded using a STOE Stadi P powder diffractometer with a linear position-sensitive detector (PSD) using Mo-$K_{\alpha 1}$ radiation (Ge monochromator, λ = 0.71093 Å) equipped with a graphite furnace. The powdered sampled were filled into silica glass capillaries with 0.3 mm diameter which were sealed with silicone grease under argon atmosphere. During the measurements, the samples were heated up to 600 °C (5 °C/min), where several measurements were carried out (at least 90 min altogether) and then cooled to room temperature with a rate of 5 °C/min. Powder patterns were evaluated using WIN^{XPOW}.[73] Rietveld pattern fitting was carried out using the program TOPAS.[74]

Single crystals obtained from chemical transport reactions were sealed in silica glass capillaries under argon atmosphere and checked for quality by Laue photographs on a Buerger precession camera. Intensity data were collected on a Stoe IPDS I diffractometer using Mo-K_α radiation (graphite monochromator, λ = 0.71073 Å). High temperature measurements were performed using a heated gas flow around the crystals (Stoe Heatstream). Reciprocal space sections were reconstructed using the diffractometer software.

2.2.1.4.4 Transmission electron microscopy

Finely ground samples were dispersed in ethyl alcohol suspension and subsequently dispersed on copper grids coated with holey carbon film. The grids were mounted on a double tilt holder with a maximum tilt angle of 30°. Selected-area electron diffraction (SAED) and high-resolution electron microscopy (HRTEM) were carried out on a FEI Titan 80-300 equipped with a field emission gun operating at 300 kV. The images were recorded using a Gatan UltraScan 1000 (2k x 2k) camera.

2.2.1.4.5 Thermal analysis

The thermal behavior of the samples was studied up to 700 °C by differential thermal analysis and thermo-gravimetry (DTA-TG) with a Setaram TG-92 instrument. The measurement was conducted under helium at a scanning rate of 10 $K \cdot min^{-1}$ using alumina crucibles. In this temperature range, the weight loss was not significant.

2.2.1.4.6 Thermoelectric properties

The temperature dependence of the electrical and thermal conductivity as well as the Seebeck coefficient and the figure of merit were investigated in the range from room temperature up to approx. 500 °C under vacuum using various facilities, both commercial and in-house-built ones. The electrical conductivity was measured by a four-point-probe setup above room temperature using an AC method in order to avoid Peltier influences on the measurement. Seebeck coefficient investigation was performed using a small temperature gradient across the sample while slowly changing the environment temperature. This way Seebeck coefficient values for each mean sample temperature are obtained. The thermal conductivity was calculated from measurements of the thermal diffusivity by a Laser Flash Apparatus (Netzsch LFA 427) and heat capacity determined by Differential Scanning Calorimetry (Netzsch DSC 404).

Acknowledgment

The authors thank Dr. M. Döblinger for help with TEM operation, Dr. A. Sattler for DTA measurements, C. Minke for SEM operation and EDX analyses, and T. Miller for the temperaturedependent powder diffraction experiments. Furthermore, we are indebted to Prof. Dr. W. Schnick for his generous support of this work. This investigation was funded by the Deutsche Forschungsgemeinschaft (grant OE530/1–1).

2.2.1.5 References

[1] G. S. Nolas, J. Poon, M. G. Kanatzidis, *MRS Bull*. **2006,** *31*, 199.

[2] T. M. Tritt, M. A. Subramanian, *MRS Bull*. **2006**, *31*, 188.

[3] J. R. Sootsman, D. Y. Chung, M. G. Kanatzidis, *Angew. Chem. Int. Ed*. **2009**, *48*, 8616.

[4] V. A. Shevelkov, *Russ. Chem. Rev*. **2008**, *77*, 1.

[5] G. J. Snyder, E. S. Toberer, *Nat. Mater*. **2008**, *7*, 105.

[6] A. C. Bruce, J. K. Matthew, L. H. Joel, H. Mi-Kyung, C. Duck-Young, G. K. Mercouri, *Adv. Funct. Mater*. **2009**, *19*, 1254.

[7] P. F. P. Poudeu, J. D'Angelo, A. D. Downey, J. L. Short, T. P. Hogan, M. G. Kanatzidis, *Angew. Chem. Int. Ed*. **2006**, *45*, 3835.

[8] T. Ikeda, V. A. Ravi, L. A. Collins, S. M. Haile, G. J. Snyder, *J. Electron. Mater*. **2007**, *36*, 716.

[9] R. Venkatasubramanian, E. Siivola, T. Colpitts, B. O'Quinn, *Nature* **2001**, *413*, 597.

[10] H. Böttner, G. Chen, R. Venkatasubramanian, *MRS Bull*. **2006**, *31*, 211.

[11] T. J. Zhu, F. Yan, X. B. Zhao, S. N. Zhang, Y. Chen, S. H. Yang, *J. Phys*. **2007**, *D40*, 6094.

[12] J. Sommerlatte, K. Nielsch, H. Böttner, *Phys. J*. **2007**, *6*, 35.

[13] A. Bulusu, D. G. Walker, *Superlattice Microst*. **2008**, *44*, 36.

[14] A. Majumdar, *Science* **2004**, *303*, 777.

[15] M. S. Dresselhaus, G. Chen, M. Y. Tang, R. Yang, H. Lee, D. Wang, Z. Ren, J.-P. Fleurial, P. Gogna, *Adv. Mater*. **2007**, *19*, 1.

[16] D. L. Medlin, G. J. Snyder, *Curr. Opin. Colloid Interface Sci*. **2009**, *14*, 226.

[17] M. G. Kanatzidis, *Chem. Mater*. **2010**, *22*, 648.

[18] Y. C. Lan, A. J. Minnich, G. Chen, Z. F. Ren, *Adv. Funct. Mater*. **2010**, *20*, 357.

[19] T. J. Zhu, F. Yan, X. B. Zhao, S. N. Zhang, Y. Chen, S. H. Yang, *J. Phys*. **2007**, *D40*, 6094.

[20] S. K. Hsiung, R. Wang, *J. Appl. Phys*. **1978**, *49*, 280.

[21] J. W. G. Bos, H. W. Zandbergen, M.-H. Lee, N. P. Ong, R. J. Cava, *Phys. Rev*. **2007**, *B75*, 195203.

[22] P. F. P. Poudeu, M. G. Kanatzidis, *Chem. Commun*. **2005**, *21*, 2672.

[23] T. Shima, T. Kikukawa, T. Nakano, J. Tominaga, *Jpn. J. Appl. Phys*. **2006**, *45*, 136.

[24] P. P. Konstantinov, L. E. Shelimova, E. S. Avilov, M. A. Kretova, V. S. Zemskov, *Inorg. Mater*. **2001**, *37*, 662.

[25] F. Yan, T. J. Zhu, X. B. Zhao, S. R. Dong, *Appl. Phys. A* **2007**, *88*, 425.

[26] J. L. Cui, X. L. Liu, W. Yang, D. Y. Chen, H. Fu, P. Z. Ying, *J. Appl. Phys*. **2009**, *105*, 063703

[27] J. L. Cui, H. Fu, X. L. Liu, D. Y. Chen, W. Yang, *Curr. Appl. Phys*. **2009**, *9*, 1170.

[28] R. Detemple, D. Wamwangi, M. Wuttig, G. Bihlmayer, *Appl. Phys. Lett*. **2003**, *83*, 2572.

[29] Y. Maeda, H. Andoh, I. Ikuta, H. Minemura, *J. Appl. Phys*. **1988**, *64*, 1715.

[30] L. E. Shelimova, O. G. Karpinskii, P. P. Konstantinov, E. S. Avilov, M. A. Kretova, V. S. Zemskov, *Inorg. Mater*. **2004**, *40*, 451.

[31] M. Wuttig, *Nat. Mater*. **2005**, *4*, 265.

[32] D. Lencer, M. Salinga, B. Grabowski, T. Hickel, J. Neugebauer, M. Wuttig, *Nat. Mater*. **2008**, *7*, 972.

[33] M. Wuttig, C. Steimer, *Appl. Phys. A* **2007**, *87*, 411.

[34] M. Wuttig, N. Yamada*, Nat. Mater*. **2007**, *6*, 824.

[35] S. Raoux, R. M. Shelby, J. Jordan-Sweet, B. Munoz, M. Salinga, Y.-C. Chen, Y.-H. Shih, E.-K. Lai, M.-H. Lee, *Microelectron. Eng*. **2008**, *85*, 2330.

[36] S. Raoux, *Annu. Rev. Mater. Res*. **2009**, *39*, 9.1.

[37] S. Raoux, W. Wojciech, D. Ielmini, *Chem. Rev*. **2009**, *110*, 240.

[38] M. Frumar, B. Frumarova, T. Wagner, M. Hrdlicka, *J. Mater. Sci: Mater .Electron* **2007**, *18*, 169.

[39] T. Matsunaga, N. Yamada, *Jpn. J. Appl. Phys*. **2004**, *43*, 4704.

[40] T. Matsunaga, N. Yamada, *Jpn. J. Appl. Phys*. **2002**, *41*, 1674.

[41] P. Jóvári, I Kaban, J. Steiner, B. Beuneu, A. Schöps, A. Webb, *J. Phys.: Condens. Matter* **2007**, *19*, 335212.

[42] S. Caravati, M. Bernasconi, T. D. Kuhne, M. Krack, M. Parrinello, *Appl. Phys. Lett*. **2007**, *91*, 171906.

[43] K. Kohary, V. M. Burlakov, D. G. Pettifor, *Phys. Rev. B* **2005**, *71*, 235309.

[44] F. Sava, A. Lörinczi, *J. Ovonic Res*. **2006**, *2*, 4.

[45] S. Hosokawa, T. Ozaki, K. Hayashi, N. Happo, M. Fujiwara, K. Horii, P. Fons, A. V. Kolobov, J. Tominaga, *Appl. Phys. Lett*. **2007**, *90*, 131913.

[46] J. Akola, R. O. Jones, S. Kohara, S. Kimura, K. Kobayashi, M. Takata, T. Matsunaga, R. Kojima, N. Yamada, *Phys. Rev. B* **2009**, *80*, 020201.

[47] J. Akola, R. O. Jones, *Phys. Rev. B* **2007**, *76*, 235201.

[48] J. Akola, R. O. Jones, *Phys. Rev. B* **2009**, *79*, 134118.

[49] A. V. Kolobov, P. Fons, A. I. Frenkel, A. L. Ankudinov, J. Tominaga, T. Uruga, *Nat. Mater*. **2004**, *3*, 703.

[50] A. V. Kolobov, P. Fons, J. Tominaga, A. I. Frenkel, A. L. Ankudinov, T. Uruga, *J. Ovonic Res*. **2005**, *1*, 21.

[51] V. A. Kolobov, P. Fons, J. Tominaga, T. Uruga, *J. Non-Cryst. Solids* **2006**, *352*, 1612.

[52] E. T. Kim, J. Y. Lee, Y. T. Kim, *Appl. Phys. Lett*. **2007**, *91*, 101909.

[53] W. Wenic, M. Wuttig, *Materials Today* **2008**, *11*, 20.

[54] T. Matsunaga, N. Yamada, *Phys. Rev. B* **2004**, *69*, 104111.

[55] T. Matsunaga, N. Yamada, Y. Kubota, *Acta Crystallogr. Sect. B* **2004**, *60*, 685.

[56] T. Matsunaga, R. Kojima, N. Yamada, K. Kifune, Y. Kubota, Y. Tabata, M. Takata, *Inorg. Chem*. **2006**, *45*, 2235.

[57] T. Matsunaga, H. Morita, R. Kojima, N. Yamada, K. Kifune,Y. Kubota, Y. Tabata, J.-J. Kim, M. Kobata, E. Ikenaga, K. Kobayashi, *J. Appl. Phys*. **2008**, *103*, 093511.

[58] W. Wenic, A. Pamungkas, R. Detemple, C. Steimer, S. Blugel, M. Wuttig, *Nat. Mater*. **2006**, *5*, 56.

[59] M. Wuttig, D. Lüsebrink, D. Wamwangi, W. Wenic, M. Gilleßen, R. Dronskowski, *Nat. Mater*. **2007**, *6*, 122.

[60] Z. Sun, J. Zhou, R. Ahuja, *Phys. Rev. Lett*. **2006**, *96*, 055507.

[61] Z. Sun, S. Kyrsta, D. Music, R. Ahuja, J. M. Schneider, *Solid State Commun*. **2007**, *143*, 240.

[62] S. Shamoto, N. Yamada, T. Matsunaga, T. Proffen, J. W. Richardson, J.-H. Chung, T. Egami, *Appl. Phys. Lett*. **2005**, *86*, 081904.

[63] S. I. Shamoto, K. Kodama, S. Iikubo, T. U. Taguchi, N. Yamada, T. Proffen, *Jpn. J. Appl. Phys*. **2006**, *45*, 8789.

[64] J.-H. Eom, Y.-G. Yoon, C. Park, H. Lee, J. Im, D.-S. Suh, J.-S. Noh, Y. Khang, J. Ihm, *Phys. Rev. B* **2006**, *73*, 214202.

[65] O. G. Karpinskii, L. E. Shelimova, M. A. Kretova, V. S. Zemskov, *Inorg. Mater*. **2000**, *36*, 1108.

[66] O. G. Karpinsky, L. E. Shelimova, M. A. Kretova, J.-P. Fleurial, *J. Alloys Compd*. **1998**, *268*, 112.

[67] O. G. Karpinsky, L. E. Shelimova, M. A. Kretova, J.-P. Fleurial. *J. Alloys Compd*. **1998**, *265*, 170.

[68] L. E. Shelimova, O. G. Karpinsky, P. P. Konstantinov, M. A. Kretova, E. S. Avilov, V. S. Zemskov, *Inorg. Mater*. **2001**, *37*, 342.

[69] L. E. Shelimova, O. G. Karpinsky, M. A. Kretova, V. I. Kosyakov, V. A. Shestakov, V. S. Zemskov, F. A. Kuznetsov, *Inorg. Mater*. **2000**, *36*, 768.

[70] M. N. Schneider, O. Oeckler, *Z. Anorg. Allg. Chem*. **2008**, *634*, 2557.

[71] M. N. Schneider, P. Urban, A. Leineweber, M. Doeblinger, O. Oeckler, *Phys. Rev. B* **2010**, *81*, 184102.

[72] M. Frumar, L. Tichy, M. Matyas, J. Zelizko, *Phys. Stat. Sol*. **1974**, *22*, 535.

[73] *WINXPOW*, *v2.12 ed*., Stoe & Cie GmbH, Darmstadt, Germany, **2005**.

[74] *TOPAS-Academic*, *V. 4.1*, Coelho Software, Brisbane, Australia, **2007**.

2.2.2 Real structure and thermoelectric properties of GeTe-rich germanium antimony tellurides

T. Rosenthal, M. N. Schneider, C. Stiewe, M. Döblinger, O. Oeckler
Chem. Mater. **2011**, *23*, 4349-4356**.**

Abstract

Quenched Ge-Sb-Te (GST) compounds exhibit strongly disordered metastable structures whose average structure corresponds to a distorted rocksalt type with trigonal symmetry. Depending on the composition and thermal treatment, the metrics remain more or less pseudocubic. The corresponding stable phases show regular sequences of distorted rocksalt-type blocks that formally result from layer-like cation defect ordering. These thermodynamically stable layered phases can gradually be approached by annealing the metastable (pseudo)cubic compounds that are accessible by quenching high-temperature phases. The relaxation of Te atoms in the vicinity of the defect layers leads to van der Waals gaps rather than defect layers in an undistorted matrix. The partially ordered phases obtained show defect layers with an average distance and arrangement depending on the composition and the thermal treatment of the samples. This variation of the nanostructure influences the lattice thermal conductivity (κ_L) and thus the thermoelectric figure of merit (ZT). This results in *ZT* values up to 1.3 at 450 °C for bulk samples of $Sb_2Te_3(GeTe)_n$ (n = 12 and 19). The stability ranges of the various phases have been examined by temperature programmed X-ray powder diffraction and can be understood in conjunction with the changes of the nanostructure involved. The real structure of phases $Sb_2Te_3(GeTe)_n$ (n = 3-19) has been investigated by high-resolution electron microscopy (HRTEM) and scanning transmission electron microscopy (STEM)-high-angle annular dark-field (HAADF) with respect to the stoichiometry and synthesis conditions. The correlation of the nanostructure with the thermoelectric properties opens an interesting perspective for tuning thermoelectric properties.

2.2.2.1 Introduction

2.2.2.1.1 Tellurides as thermoelectrics

Tellurides have been the predominant materials for thermoelectric applications in the past decade. PbTe, Bi_2Te_3, and Sb_2Te_3 are well-established examples that still dominate the market.[1] In order to secure the future energy supply, the sustainable usage of energy is becoming increasingly important.[2] Thermoelectric materials make electric power generation from waste heat possible, e.g., in cars and airplanes, leading to lower fuel consumption. In addition, they may become increasingly popular in energy-efficient cooling and heating devices. The bottleneck for all applications is the efficiency of the transformation between heat and electric energy, which depends on the thermoelectric figure of merit (*ZT*) of the material used. At a given temperature T, it is defined as:

$$ZT = \frac{S^2\sigma}{\kappa}T$$

The major problem is the interdependence of the material properties determining *ZT*. The electrical conductivity (σ) and the electronic part of the thermal conductivity (κ_e), which corresponds to heat transport by electrons, are linked by the Wiedemann-Franz law. Both properties correlate with the Seebeck coefficient (*S*), as all these properties depend on the charge carrier concentration. The phononic part of the thermal conductivity (κ_L) reflects the heat that is transported by phonons. Since it depends on various structural features, it seems to be the most promising approach to reduce κ_L by increased phonon scattering. Therefore, many new approaches rely on nanostructuring and doping. Novel element combinations, e.g., Ag/Sb/Pb/Te (LAST, *ZT* up to 2)[3] or Ag/Ge/Sb/Te (TAGS, *ZT* up to 1.5[4]), and structuring processes (e.g., spin-milled, ball-milled and hot pressed crystalline ingots of Bi-Sb-Te alloys with *ZT* up to 1.4[5]) have led to drastic improvements in recent years. However, there is still an urgent need for bulk materials with high *ZT* values at various temperatures.

2.2.2.1.2 $Sb_2Te_3(GeTe)_n$ as phase-change materials

For rewritable optical data storage media, GST (Ge-Sb-Te) materials have been used for more than a decade[6,7] because the fast reversible phase change between metastable crystalline and amorphous phases can be induced in a favorable energy range. Compared to rewritable DVDs, the GeTe content has been increased for rewritable Blu-Ray discs in order to (1) optimize the bit

density by enhancing the difference in reflectivity between both phases and (2) obtain higher stability of the amorphous phase (recording marks), corresponding to a longer life cycle.[8] The fast reversible phase change can also be induced by electric pulses, and the structural states can be identified by their different resistivity.[9,10] As the information is preserved by structural changes, GST materials are very promising candidates for nonvolatile PC-RAM devices.[11-14] Besides this well-known phase change between amorphous and metastable crystalline phases, GeTe-rich GST materials exhibit another phase transformation between a rocksalt-type high-temperature and a layered low-temperature modification.

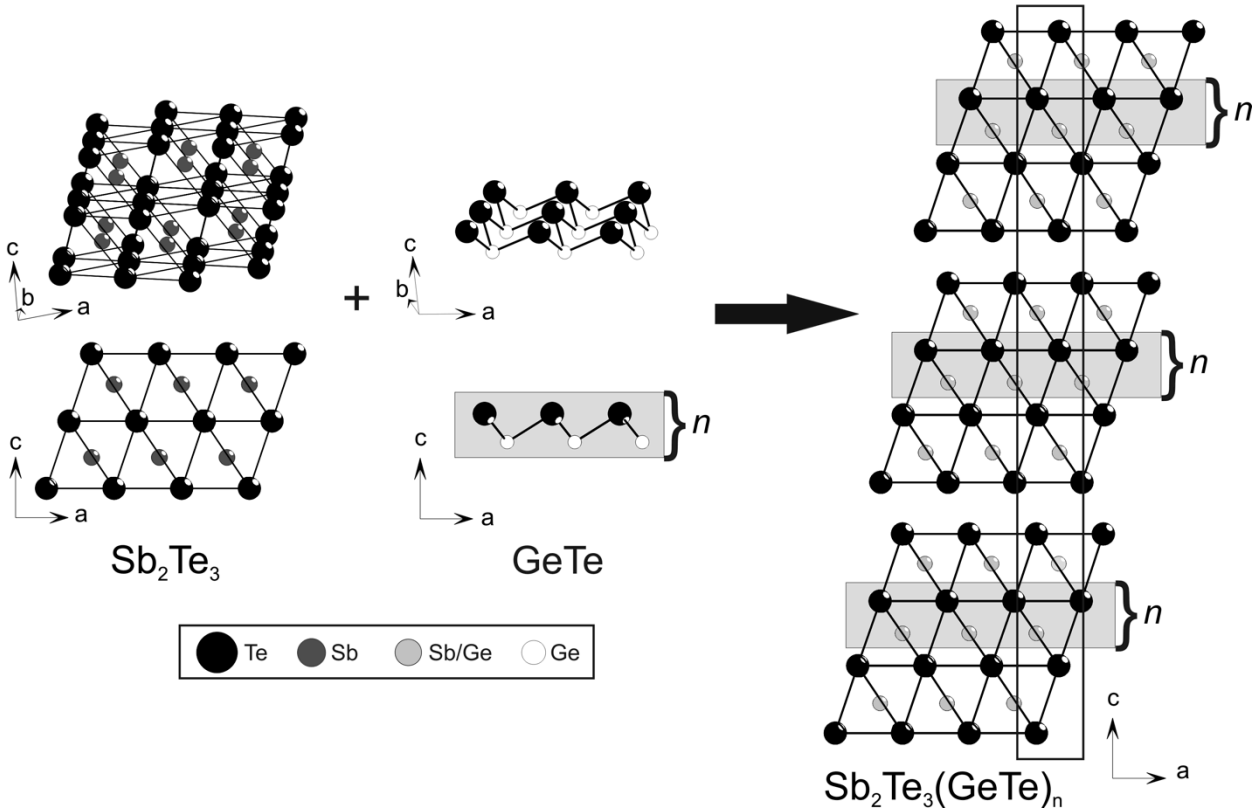

Fig. 1: Tetradymite-like Sb_2Te_3 slabs (left) are formally enlarged by inserting GeTe-type layers in the blocks. The resulting structure (right) consists of distorted rocksalt-type building blocks with a thickness depending on the GeTe content n (the crosses indicate the position of the formal "vacancies" in the van der Waals gaps). For Sb_2Te_3 itself, *n* equals 0.

2.2.2.1.3 Structure and properties of $Sb_2Te_3(GeTe)_n$

The structures of materials with the composition $Sb_2Te_3(GeTe)_n$ can be described as a combination of tetradymite-type Sb_2Te_3[15] and GeTe, a binary variant of the A7 (gray arsenic) structure type. The tetradymite-like Sb_2Te_3 blocks can formally be enlarged by inserting GeTe, resulting in the pseudobinary homologous series $Sb_2Te_3(GeTe)_n$ with distorted rocksalt-type building blocks of a thickness depending on n (Figure 1). These blocks are separated by van der

Waals gaps between the Te layers terminating the individual building blocks. The distance between these Te layers and the following cation layers are rather short, leading to a 3 + 3 coordination of these cations and an arrangement resembling that in GeTe itself. The Te-Te distances between adjacent building blocks are significantly shorter than the sum of the van der Waals radii and indicate partially covalent bonding. Although these trigonal, thermodynamically stable phases contain no structural vacancies, the strongly distorted octahedral voids between these Te layers can formally be viewed as layer-like ordered cation-position "vacancies".[16,17] The cubic rocksalt-type high-temperature phases are highly disordered with Ge, Sb, and vacancies occupying the cation positions and Te occupying the anion positions. The vacancy concentration depends on the ratio $GeTe/Sb_2Te_3$ (n).[18,19] In GeTe rich (n > 3) GST phase-change materials, the structure of the crucial metastable crystalline phase is similar to the high-temperature rocksalt-type phase. It is kinetically inert at ambient conditions, providing long-time data storage on rewriteable optical media.

In recent years, the thermoelectric behavior of some GST materials has been investigated.[20] HRTEM investigations of spark plasma sintered $Sb_2Ge_{0.02}Te_3$ revealed a large number of randomly distributed nanodomains, coupled with a 0.3 W/mK decrease in thermal conductivity compared to pure Sb_2Te_3. Consequently, the *ZT* value of Sb_2Te_3 increases from 0.74 to 0.84 at 492 K when doped with small amounts of Ge.[21] Recent investigations indicate ZT values up to 1.3 at 720 K for Ge-rich compositions (n ~ 12).[22]

2.2.2.2 Experimental Section

Bulk samples of $Sb_2Te_3(GeTe)_n$ ($3 \leq n \leq 19$) were prepared by melting (950 °C, 2 h) stoichiometric amounts of the elements Ge (99.999%, Sigma Aldrich), Sb (99.999%, Smart Elements), and Te (99.999%, Alfa Aesar) in silica glass ampules sealed under Ar atmosphere. Nanostructured samples were obtained by annealing the initially quenched samples at 500-550 °C (i.e., in the stability range of the cubic high-temperature phase) for 2 days and quenching in water. The relaxed (trigonal) samples with less pronounced nanostructuring were annealed for 2 days at 400 °C and slowly cooled in the furnace (2 h). A fraction of each sample was used for electron microscopy.

Ingots for thermoelectric measurements were prepared under analogous conditions in silica glass ampules with flat bottom. The ingots obtained were disk-shaped with a diameter around 15 mm and a thickness of 2-6 mm. They were polished to obtain flat discs with a constant thickness. X-ray powder diffraction patterns matched those from corresponding samples used for other investigations.

The composition of the samples was verified by energy-dispersive X-ray spectroscopy (EDX). Typical analyses deviate less than 5 atom % from values corresponding to the starting mixture. Data acquisition was done using a JSM-6500F (Jeol, Japan) scanning electron microscope equipped with an EDX detector (model 7418, Oxford Instruments, UK).

For transmission electron microscopy, samples were finely ground, dispersed in ethanol, and subsequently transferred on a copper grid coated with holey carbon film. Selected area electron diffraction (SAED) and high-resolution electron microscopy (HRTEM) were done on a JEM2011 (Jeol Ltd., Japan) with an tungsten thermal emitter and an acceleration voltage of 200 kV equipped with a TVIPS CCD camera (model 114, resolution: 1k x 1k). Further HRTEM, SAED, EDX, and scanning transmission electron microscopy (STEM) using a high-angle annular dark-field (HAADF) detector was done on a Titan 80-300 (FEI, USA) with a field emission gun operated at 300 kV equipped with a TEMTOPS 30 EDX spectrometer (EDAX, Germany). Images were recorded on an UltraScan 1000 camera (Gatan, USA, resolution: 2k x 2k). HRTEM and SAED data were evaluated using the Digital Micrograph[23] and EMS[24] software; for STEM and EDX data, the program ES Vision[25] was used.

X-ray powder diffraction (XRPD) patterns were recorded from ground samples fixed on Mylar foils using silicone grease. Data were collected on a G670 Guinier camera (Huber, Germany) equipped with a fixed imaging plate detector with an integrated read-out system using Cu $K_{\alpha 1}$ radiation (Ge monochromator, λ = 1.54051 Å).

Temperature programmed XRPD patterns were collected using powdered samples filled into silica glass capillaries with a diameter of 0.3 mm and sealed with silicone grease under Ar. Data were collected using a Stadi P powder diffractometer (Stoe & Cie. GmbH, Germany) with a linear position-sensitive detector (PSD) and a graphite furnace using Mo $K_{\alpha 1}$ radiation (Ge monochromator, λ = 0.71093 Å). The samples were heated from room temperature to 600 °C (10°/min) and subsequently cooled to room temperature in the same way. Data were collected every 25 °C with 10 min acquisition time. Powder patterns were analyzed with WIN^{XPOW}.[26]

Thermoelectric properties were measured up to 450 °C under vacuum using commercial and in-house-built facilities of the DLR (Cologne, Germany). The Seebeck coefficient was measured by establishing a small temperature gradient across the sample while the temperature was changed slowly and continuously. Type-R thermocouples attached directly to the sample's surface were used for both temperature measurement (T1 and T2) and Seebeck voltage (U_S) pickup via the Pt lines. The sample's Seebeck coefficient was then calculated as

$$S_{sample} = \frac{U_S}{\Delta T} - S_{Pt} \qquad \Delta T = \left| T_2 - T_1 \right|$$

Electrical conductivity σ was calculated from the sample's resistance R, measured using an AC method in order to reduce Peltier influences and a four-point-probe setup to avoid cable and contact resistances affecting the measurement. When the cross-section A of the sample and the distance l of the probe tips are taken into account, the electrical conductivity follows as $\sigma = l/A\ R$. Thermal conductivity κ was calculated from measurements of the thermal diffusivity D_{th} using a laser-flash apparatus (LFA 427, Netzsch GmbH & Co., Germany), the heat capacity c_p in a differential scanning calorimeter (DSC 404, Netzsch GmbH & Co., Germany), and the density ρ using a Mohr's balance: $\kappa = D_{th} \cdot \rho \cdot c_p$.

2.2.2.3 Results and Discussion

2.2.2.3.1 Stability of the phases $Sb_2Te_3(GeTe)_n$ ($3 \leq n \leq 17$)

Temperature-dependent XRPD investigations of quenched samples of $Sb_2Te_3(GeTe)_n$ ($3 \leq n \leq 17$) were performed in order to determine the existence range of the different phases (Table 1). Two changes occur when the quenched samples are heated (T1, T2) (Figure 2) and one during cooling (T3) (Table 1). All transformation temperatures depend on the composition, indicating the influence of the thickness of the distorted rocksalt-type building blocks and the vacancy concentration on the stability of each phase, respectively. Starting from quenched pseudocubic samples, diffusion processes occur at T1 when the quenched sample with short-range ordered vacancies relaxes to the thermodynamically stable trigonal phase (see below), which transforms to the cubic high-temperature phase when the sample reaches the latter's stability region (T2). When it is slowly cooled below that stability range, the transformation from the cubic to the trigonal phase occurs (T3). This phase transition is delayed because the high-temperature phase can be undercooled (T3 < T2).

Table 1. Phase transformation temperatures of $Sb_2Te_3(GeTe)_n$ ($3 \leq n \leq 17$) from temperature programmed XRPD

Composition	T1 (in °C)	T2 (in °C)	T3 (in °C)
$Sb_2Te_3(GeTe)_3$	375	560	550
$Sb_2Te_3(GeTe)_7$	250-320	500	460
$Sb_2Te_3(GeTe)_{12}$	325	475-500	460
$Sb_2Te_3(GeTe)_{14}$	325	450	320
$Sb_2Te_3(GeTe)_{17}$	300	410	250-275

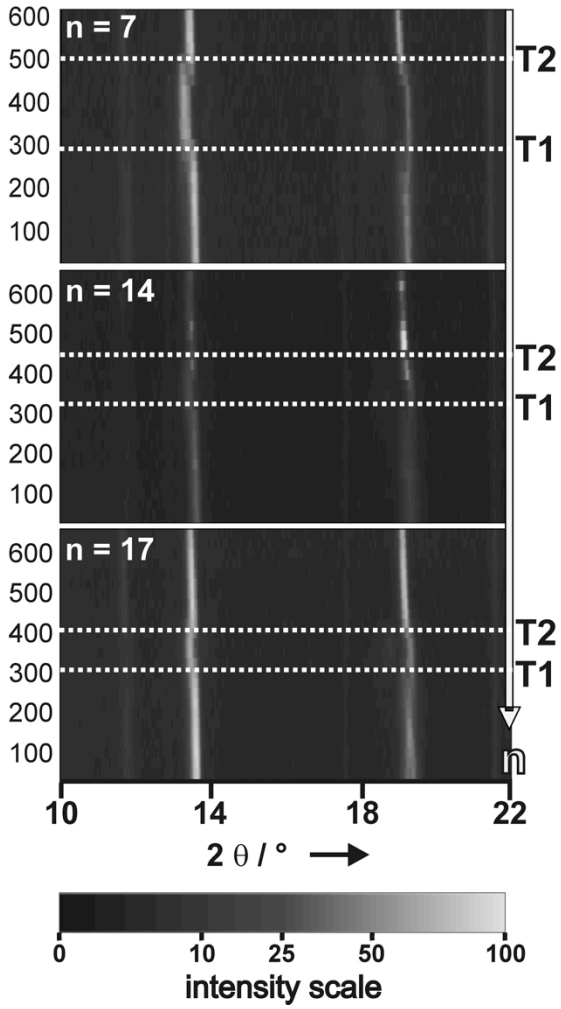

Fig. 2: Heating section of the temperature-dependent PXRD of different $Sb_2Te_3(GeTe)_n$ samples with the transition temperatures T1 and T2 (left: temperatures in °C).

With increasing GeTe content n, the cubic phase obviously becomes more stable and more inert at lower temperatures: it is reached at lower temperatures (T2) upon heating and can be increasingly undercooled (T3 decreases). GeTe itself cannot be undercooled as it exhibits no vacancies.[27] Its transition temperature (ca. 390 °C for slightly Te-rich samples) between the rhombohedral and the cubic phase continues the trend given by samples with increasing n.

The diffusion pathways required to reach the trigonal phase with more or less equidistant van der Waals gaps depend on the block size. Due to the long diffusion pathways involved, the cubic phase can be increasingly undercooled and partially retained at room temperature by quenching the samples if the GeTe content is higher (i.e., thicker blocks). The transition from the trigonal to the cubic phase requires a rearrangement of the Te substructure and the introduction of randomly distributed structural vacancies on cation positions. This process is governed by thermodynamics rather than by kinetics. Trigonal phases of all samples investigated can be long-time annealed at 400 °C without phase transition to the cubic high-temperature phase.

2.2.2.3.2 Influence of thermal treatment on the nanostructure

The microstructure of $Sb_2Te_3(GeTe)_{12}$ samples with different thermal treatment have been investigated by TEM. Samples quenched from temperatures in the existence range of the cubic high-temperature phase show intersecting defect layers perpendicular to all pseudocubic <111> directions in the HRTEM images. A parquet-like structure is formed, and corresponding diffuse intensities are observed in the SAED patterns (Figure 3). The defect layers are directly imaged by Z contrast in STEM-HAADF images (electron-rich areas appear brighter). A similar HRTEM investigation of samples that were annealed in the existence range of the trigonal phase (400 °C) show parallel van der Waals gaps with irregular distances, which can only formally be viewed as "defect layers". Accordingly, the corresponding SAED patterns show diffuse intensities only in the direction orthogonal to the layers (Figure 3). Slowly cooled samples resemble those obtained by annealing quenched ones.

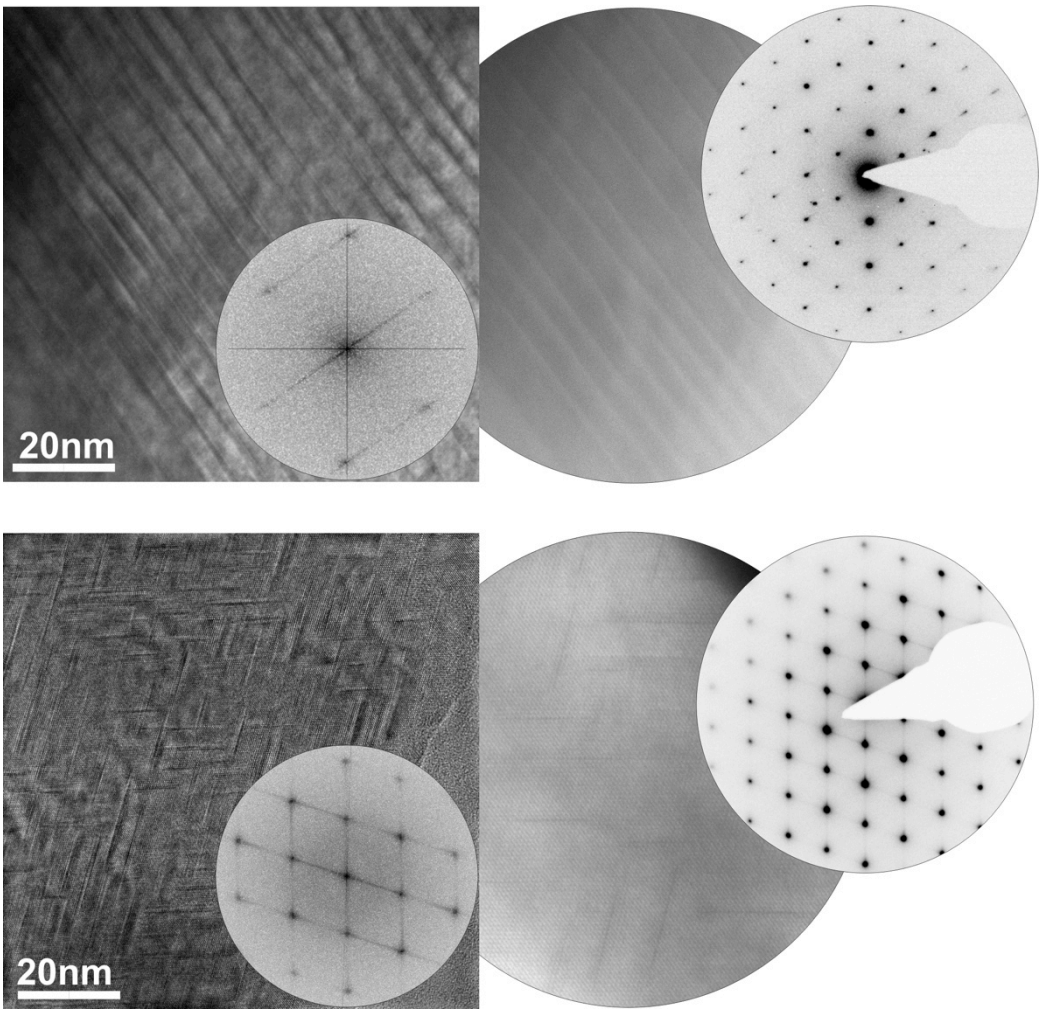

Fig. 3: Comparison of two samples of $Sb_2Te_3(GeTe)_{12}$ with different thermal treatment (top: annealed at 400°C for 20h; bottom: quenched from 500 °C); each with HRTEM image (left, insert: corresponding Fourier transform), STEM-HAADF image (middle) and SAED (right).

The different arrangements of the defect layers or van der Waals gaps, respectively, are a consequence of the diffusion processes that occur during the phase changes associated with the thermal treatment. The disorder-order phase transition from the cubic high-temperature phase with random distribution of the vacancies to the long-range ordered trigonal structures, which are thermodynamically stable at room-temperature, requires a reconstructive phase transition including a rearrangement of the anion substructure. During this phase transformation, the short-range order gradually increases when the vacancies are arranged in two-dimensional layers by diffusion in the solid state. In quenched phases, the defect layers are finite and arranged perpendicular to all <111> directions of the original cubic phase, forming the parquet-like structure consisting of multiple intersecting defect layers. Annealing quenched phases leads to further diffusion and thus to an extension of the defect layers toward the thermodynamically stable trigonal phase with an ideally symmetric, equidistant arrangement of van der Waals gaps. Summing up, the structure of the quenched phases combines features of both stable (low and high temperature) phases even though it cannot be observed as an intermediate state during the phase transition at equilibrium conditions.

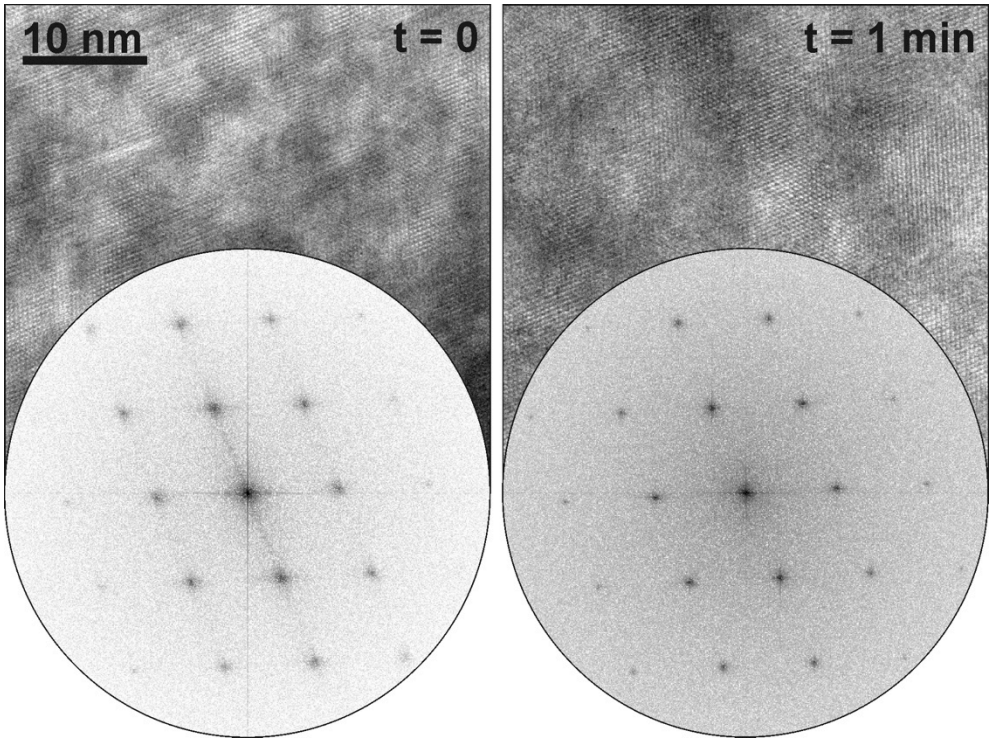

Fig. 4: Quenched sample with diffuse intensities in the corresponding Fourier transform and defect layers in HRTEM (left); after prolonged exposition (1 min) to the electron beam, there are no diffuse intensities in the Fourier transform and no defect layers in HRTEM (right).

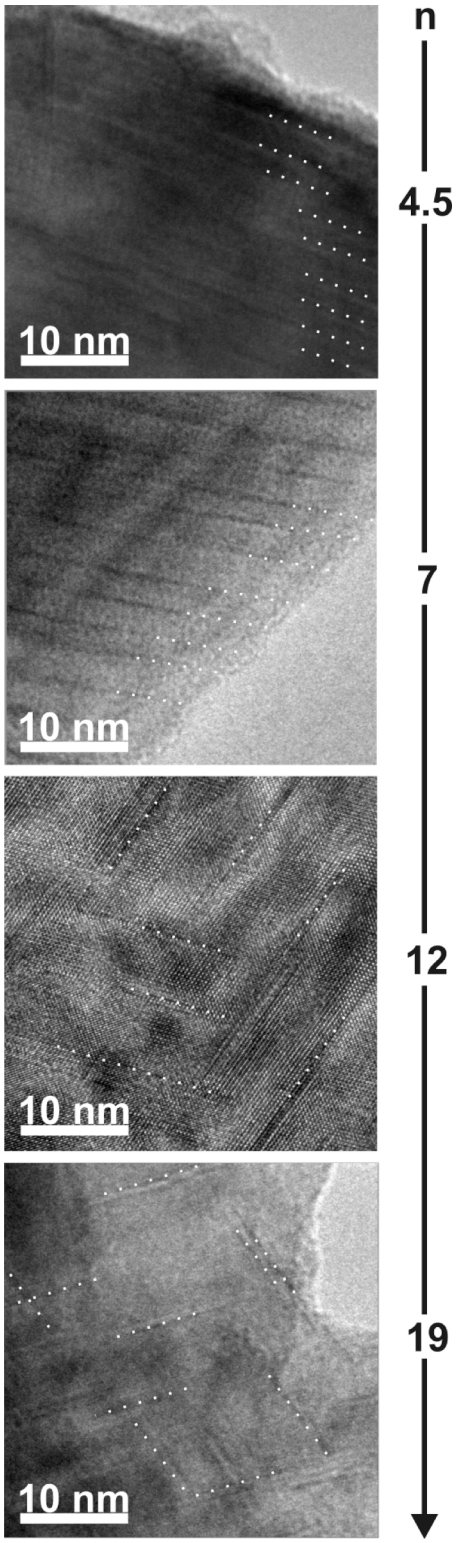

Fig. 5. HRTEM images of different $Sb_2Te_3(GeTe)_n$ samples with similar thermal treatment (top to bottom n = 4.5; 7; 12; 19; the defect layers are highlighted with white dotted lines) – they become fewer and less regularly spaced with increasing n.

Investigations of the phase diagram Ge-Sb-Te showed that such samples need up to 8 months of annealing to reach the trigonal thermodynamically stable phase.[28] Therefore, it is possible to obtain various stages between the structure of quenched samples and the stable phase by controlling the annealing conditions. This transformation is hindered because the cubic structure is locally preserved, owing to stresses caused by multiple twinning that is unavoidable in quick transitions from the cubic high-temperature to the rhombohedral phase (translationengleiche group-subgroup relationship).[30] When the quenched pseudocubic samples are heated, the mobility of vacancies increases and stresses are relieved during the transformation to the stable trigonal structure (T1 in Table 1).

In situ TEM experiments show that the defect layers present in samples quenched from the cubic high-temperature phase disappear when the sample is exposed to the highly energetic electron beam for about 1 min (Figure 4). This is similar to the behavior described for $Ge_2Sb_2Te_5$.[29]

2.2.2.3.3 Influence of the composition on the nanostructure of quenched $Sb_2Te_3(GeTe)_n$ samples

The nanostructure of $Sb_2Te_3(GeTe)_n$ (n = 4.5-19) samples quenched from the cubic phase not only depends on the thermal treatment but also on the composition (n) of the samples. Higher GeTe contents result in fewer defects in the high-temperature phase and larger blocks in the trigonal phase with strongly varying thicknesses. Higher defect concentrations at lower GeTe contents correspond to an increased number of van der Waals gaps with more regular spacing (Figure 5). This change in the variance of the spacing results from the increasing diffusion pathways which are necessary to reach the ideal, thermodynamically stable trigonal phase. Samples with a higher GeTe content must be annealed much longer in order to reach this state, and therefore, the block thickness distribution is more irregular as compared to samples with the same thermal treatment and a lower GeTe content.

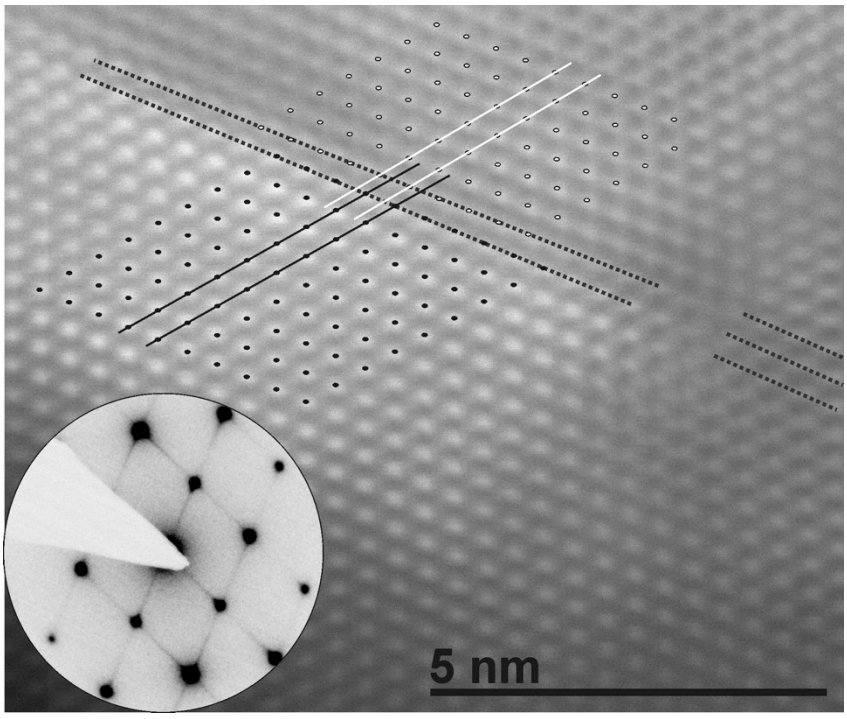

Fig. 6: HAADF-STEM image (pseudocubic zone axis <110>, with corresponding SAED of the whole crystallite) of $Sb_2Te_3(GeTe)_{12}$; the atom rows on either side of the defect layer are marked (gray and white dotted lines); at the defect layer the structure is shifted by 1/3 of the distance between the atom rows parallel to the defect layer; the image also shows the relaxation of the defect layer (black lines).

Increased diffusion pathways have a second effect on the microstructure. The probability of intersecting defect layers with different orientations increases when the diffusion pathways necessary to form the stable phase increase. Therefore, the fraction of domains with intersecting defect layers forming parquet-like structures increases with the GeTe content. Thus, in addition

to the thermal treatment, the composition is an important factor that determines the nanostructure of $Sb_2Te_3(GeTe)_n$.

2.2.2.3.4 Structural relaxation around the defect layers in $Sb_2Te_3(GeTe)_{12}$.

We reported in earlier works that the relaxation and/or shift of Te atom layers upon "vacancy ordering" leads to van der Waals gaps rather than defect layers in an undistorted matrix.[22,30] High-resolution imaging both by HRTEM and STEM-HAADF shows that the magnitude of relaxation between the distorted rocksalt-like building blocks depends on the lateral extension of the "vacancy" layers. Where they terminate, the relaxation is hindered by the surrounding bulk and the Te atom positions of the rocksalt-type phase are approximately retained. For the same reason, no relaxation occurs if the defect layers extend over just a few unit cells. Whenever defect layers extend over larger areas, Te-Te contacts are formed and the structure is partially relaxed (Figure 6). The relaxation includes a shift of 1/3 of the distance between the rows of atom columns parallel to the defect layers. This shift corresponds to the structure around the van derWaals gaps in stable trigonal phase (compare Figure 1), whose structures were derived from single-crystal data.[31,32] This proves the van der Waals character of extended defect layers whereas less extended ones are rather similar to "point defects" (point defect = a type of defect as opposed to a planar defect or a line defect) with little influence on the surrounding lattice.

2.2.2.3.5 Influence of the microstructure on the thermoelectric characteristics of $Sb_2Te_3(GeTe)_n$ (n = 3-19)

The thermoelectric properties of $Sb_2Te_3(GeTe)_n$ (n = 3, 4.5, 7, 12, 19) samples, each quenched from its cubic high-temperature phase, show that the nanostructures resulting from different compositions (Figure 7) have diverse and, in part, complex consequences.

For all samples of $Sb_2Te_3(GeTe)_n$ with n = 3-19, the Seebeck coefficients (S) are quite similar and increase continuously with the temperature reaching 100-200 μVK^{-1} at 450 °C. They correspond to p-type semiconductors. For n = 19, the increase with the temperature is most pronounced. Such values are common for materials with high ZT values, e.g., TAGS (Te-Ag-Ge-Sb) compounds with S = 160-220 μV/K at 450 °C, the exact values depending on the composition and sample treatment.[33,34] Water quenched and rapidly solidified (melt-spun) samples of layered $Sb_2Te_3(GeTe)_n$ with n = 1or 2 reach S = 60-110 μV/K at 450 °C.[35]

The temperature dependence of the electrical conductivity (σ) corresponds to metallic behavior. Upon heating, σ decreases down to 800-2000 S/cm at 450 °C, which is also similar to TAGS compounds (800-1200 S/cm at 450 °C)[33,34] and optimized $Sb_2Te_3(GeTe)_n$ (n = 1, 2) (1500-2000 S/cm at 450 °C).[35] The electrical conductivity decreases with the GeTe content for n = 3, 4.5, 7, probably as a consequence of the increasingly inhomogeneous spacings between defect layers (see above). Further increasing the GeTe content (n = 12, 19) increases σ, probably because the defect layer concentration gets rather small and its influence on the metallic character becomes less dominant. The fact that $Sb_2Te_3(GeTe)_{12}$ exhibits the maximal electrical conductivity is probably the result of a complex interplay of different factors.

As the positive effect of a high electrical conductivity σ is compensated by a higher electronic part of the thermal conductivity κ_e, the phononic part (lattice thermal conductivity κ_L) is crucial for *ZT*. The overall thermal conductivities of the compounds $Sb_2Te_3(GeTe)_n$ (n = 3-19) range from 1 to 3.5 W/mK, the lattice part amounts to 0.2-1.3 W/mK at 450 °C. For TAGS, the overall thermal conductivity ranges from 1.5 to 2.8 with a lattice part around 0.4 at 450 °C.[33,34]

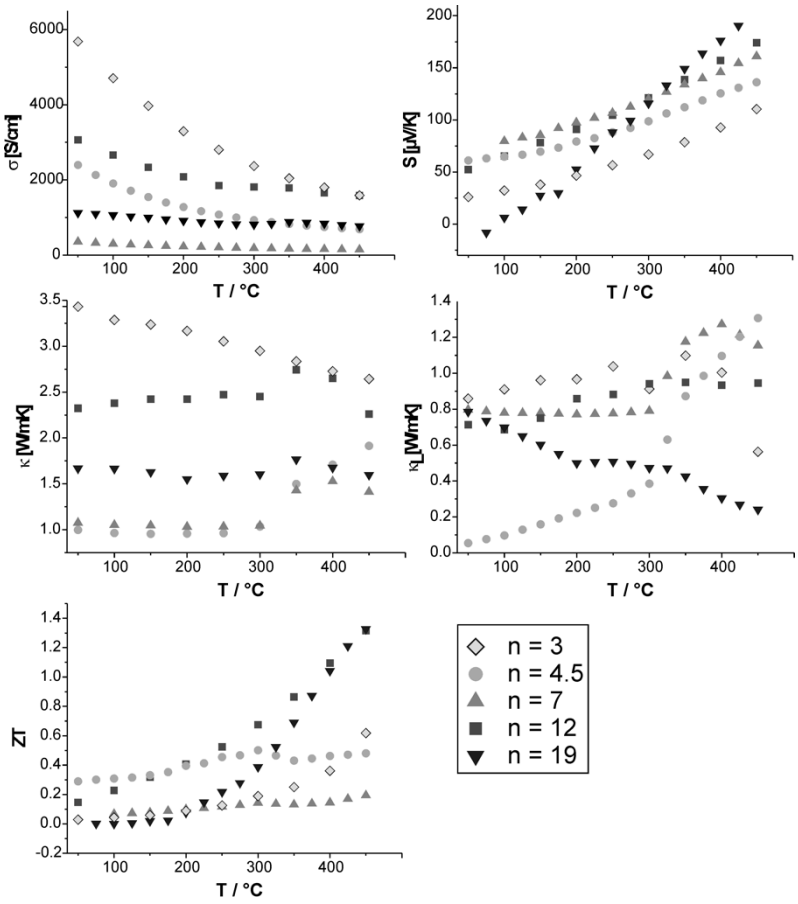

Fig. 7: Thermoelectric characteristics of quenched $Sb_2Te_3(GeTe)_n$ (n = 3 – 19) samples; electric conductivity (σ) (top left); Seebeck coefficient (*S*) (top right); thermal conductivity (κ) (middle left); lattice thermal conductivity (κ_L) (middle right) and the resulting thermoelectric figure of merit (*ZT*, bottom).

In general, more pronounced nanostructuring is expected to cause more phonon scattering and thus reduce κ_L, thereby increasing *ZT*. Higher defect concentrations should have a similar effect. $Sb_2Te_3(GeTe)_3$ has the highest overall thermal conductivity of the samples investigated. Its cubic high-temperature phase exhibits a maximum cation defect concentration; however, it cannot be quenched to a pseudocubic one with highly disordered defect planes. Therefore, quenched samples of $Sb_2Te_3(GeTe)_3$ are not significantly different from annealed ones and exhibit an almost completely ordered trigonal structure with equidistant van der Waals gaps. Since such an ordered arrangement has less potential to suppress the phonon proliferation, $Sb_2Te_3(GeTe)_3$ has the highest lattice (κ_L) and overall (κ) thermal conductivity. This results in a relatively low *ZT* value. Therefore, the rather low *ZT* of more or less long-range ordered phases $Sb_2Te_3(GeTe)_n$ with n = 1 or 2 (~0.2 at 450 °C)[35] is not surprising.

Since *ZT* of all compounds investigated increases with temperature, the temperature dependence of κ_L is crucial. $Sb_2Te_3(GeTe)_{4.5}$ has a very low κ_L and thus the highest *ZT* at roomtemperature, probably due to the high defect concentration combined with disorder. However, in this case, the diffusion pathways are rather short so that the transition to the stable trigonal phase causes κ_L to increase significantly with the temperature. That outweighs the increasing Seebeck coefficient and results in a comparably low *ZT* at higher temperatures. The same effect is observed for $Sb_2Te_3(GeTe)_7$ which has a higher κ_L at room temperature due to the reduced defect concentration and therefore a lower *ZT* value. The overall low thermal conductivity is not helpful as it comes with a low electrical conductivity. The lower defect concentration also means less pronounced effects of structural changes at higher temperatures since the diffusion pathways are significantly increased compared to $Sb_2Te_3(GeTe)_{4.5}$. The compounds with higher GeTe contents (n = 12, 19) increasingly show the parquet-like structure, owing to intersecting finite defect layers as a result of the even longer diffusion pathways hypothetically required to form the thermodynamically stable trigonal phase. The diffusion processes are, of course, more pronounced at higher temperatures, which results in an increased κ_L, except for $Sb_2Te_3(GeTe)_{19}$, where there is little diffusion due to the low defect concentration. The strongly increasing Seebeck coefficient of the compounds with n = 12 and 19 leads to the steep increase of *ZT* at higher temperatures. As a result, the *ZT* values reach 1.3 at 450 °C for both $Sb_2Te_3(GeTe)_{19}$ and $Sb_2Te_3(GeTe)_{12}$.

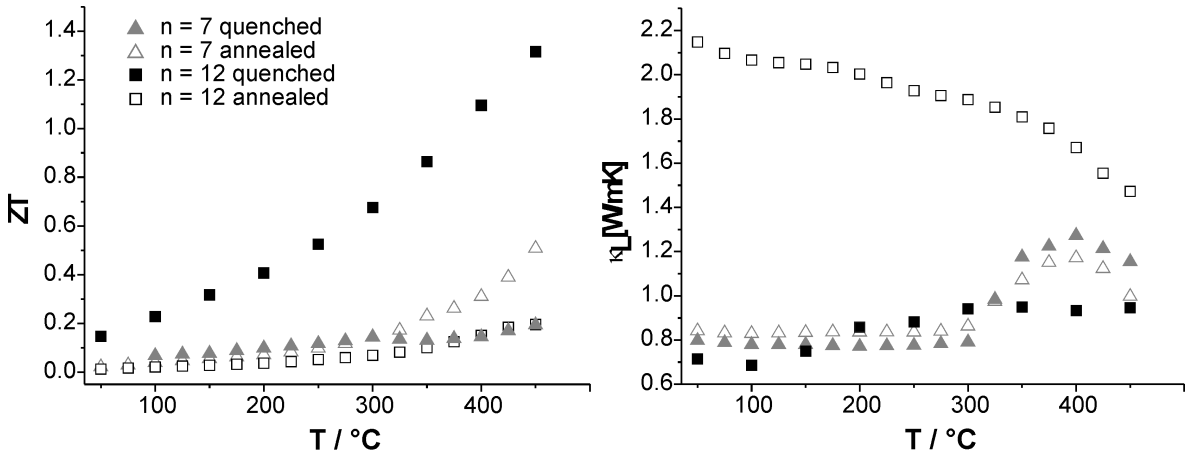

Fig 8: Comparison of the thermoelectric characteristics of quenched samples of $Sb_2Te_3(GeTe)_n$ (n = 7, 12) with those of annealed and slowly cooled ones; left side: thermoelectric figure of merit (*ZT*); right side: lattice thermal conductivity.(κ_L).

In order to analyze the influence of the nanostructure on the thermoelectric properties independent of the chemical composition and the associated carrier concentration, samples with identical composition but different thermal treatment were investigated. Quenched samples of $Sb_2Te_3(GeTe)_{12}$ and $Sb_2Te_3(GeTe)_7$ have a higher *ZT* value at room temperature than those annealed at 400 °C (in the stability range of the trigonal phase) and slowly cooled afterward (Figure 8). The Seebeck coefficients are influenced very little by the thermal treatment and almost identical for the samples investigated. Up to 300 °C, i.e., in the temperature range where diffusion effects are negligible, the lattice thermal conductivity of the quenched samples is significantly lower, reflecting the high degree of phonon scattering by the finite defect layers with irregular spacings. This effect is much more pronounced in $Sb_2Te_3(GeTe)_{12}$ than it is in $Sb_2Te_3(GeTe)_7$. This is obviously due to the parquet-like structure of quenched $Sb_2Te_3(GeTe)_{12}$ which is neither present in annealed samples nor in quenched $Sb_2Te_3(GeTe)_7$.

The electrical conductivity σ of annealed and slowly cooled $Sb_2Te_3(GeTe)_{12}$ is lower than that of quenched samples. For $Sb_2Te_3(GeTe)_7$, however, σ nearly doubles between 300 and 400°C, resulting in a higher ZT value at high temperatures than that of quenched samples. The slowly cooled samples exhibit a structure that is closer to the thermodynamically stable layered structure than that of the quenched sample. Most defect layers in slowly cooled $Sb_2Te_3(GeTe)_{12}$ are already ordered and form van der Waals gaps, which results in long diffusion pathways for the remaining disordered defects. This results in a decreasing lattice thermal conductivity with increasing temperatures, comparable to the situation in quenched $Sb_2Te_3(GeTe)_{19}$. Thus, the high *ZT* value of quenched $Sb_2Te_3(GeTe)_{12}$ is a consequence of the reduced thermal conductivity in combination with a high electrical conductivity.

2.2.2.4 Conclusion

The nanostructure of $Sb_2Te_3(GeTe)_n$ (n = 3-19) can be tuned both by varying the composition and by changing the thermal treatment of the samples. Cation defects tend to form layers, which become van der Waals gaps if they are extended enough to allow the relaxation of the surrounding structure. Quenching from highly disordered cubic high-temperature phases leads to finite intersecting defect layers forming a parquet-like structure, which (especially for n = 12) leads to a significant reduction of the lattice thermal conductivity. The concentration and arrangement of the defect layers have substantial influence on the thermoelectric properties. The temperature dependence of the individual contributions varies in a rather complicated way. Although this makes predictions rather difficult, the complex interplay of different structural features correlates with the properties and is very valuable for an a posteriori understanding of many observed effects.

The Seebeck coefficient of all compounds investigated rises with increasing temperature, especially for high GeTe contents, and indicates p-type semiconductors. Materials with intermediate n such as $Sb_2Te_3(GeTe)_7$ have the lowest electric conductivity. As their lattice thermal conductivity increases with temperature, they interestingly exhibit the lowest *ZT* values at high temperatures, in addition to those (e.g., n = 3) that exhibit fully ordered structures independent of the thermal treatment. A high defect concentration leads to a relatively homogeneous arrangement of parallel “defect layers” which correspond to van der Waals gaps and result in an increased electric conductivity. The high defect concentrations induces a low lattice thermal conductivity in case enough disorder remains in quenched pseudocubic samples. This holds for GeTe contents as low as n = 4.5; further decreasing n is not helpful as short diffusion pathways usually yield highly ordered structures (as shown for n = 3). The increased mobility of the atoms at higher temperatures emphasizes the importance of order-disorder effects and causes a more or less pronounced transition to the thermodynamically stable phase with equidistant van der Waals gaps around ~300 °C. In compounds with higher GeTe contents, the reduced defect concentration increases the electrical conductivity while the long diffusion pathways required to form extended defect layers result in intersecting finite defect layers and a more pronounced nanostructure, decreasing the lattice thermal conductivity (especially for n = 19). Therefore, the compounds $Sb_2Te_3(GeTe)_{12}$ and $Sb_2Te_3(GeTe)_{19}$ have rather low *ZT* values at room temperature but reach the highest *ZT* values up to 1.3 in the high-temperature range. Although due to limited long-time stability above ~300 °C, this value has little meaning for the application in actual devices;the *ZT* values of about 0.7 in the temperature interval where the nanostructures are long-time stable still seems promising. Probably, the properties can be further

enhanced by doping with additional elements, even if such efforts might further complicate the situation. In contrast to other multinary telluride systems, germanium antimony tellurides do not tend to exhibit phase separation (e.g., precipitates) and, despite the nanostructuring, remain chemically homogeneous.

Acknowledgment

The authors thank Christian Minke (LMU Munich) for SEM operation and EDX analyses, Thomas Miller (LMU Munich) for the temperature-dependent powder diffraction experiments and Werner Schönau (DLR Cologne) for temperature-dependent thermal analysis. Furthermore, we are indebted to Prof. Dr. W. Schnick (LMU Munich) for his generous support of this work. This investigation was funded by the Deutsche Forschungsgemeinschaft (grants OE530/1-1 and OE530/1-2).

2.2.2.5 References

[1] G. J. Snyder, E. S. Toberer, *Nat. Mater*. **2008**, *7*, 105.

[2] F. Schüth, *Positionspapier Koordinierungskreis Chemische Energieforschung*, **2009**.

[3] K. F. Hsu, S. Loo, F. Guo, W. Chen, J. S. Dyck, C. Uher, T. Hogan, E. K. Polychroniadis, M. G. Kanatzidis, *Science* **2004**, *303*, 818.

[4] J. P. Heremans, V. Jovovic, E. S. Toberer, A. Saramat, K. Kurosaki, A. Charoenphakdee, S. Yamanaka, G. J. Snyder, *Science* **2008**, *321*, 554.

[5] B. Poudel, Q. Hao, Y. Ma, Y. Lan, A. Minnich, B. Yu, X. Yan, D. Wang, A. Muto, D. Vashaee, X. Chen, J. Liu, M. S. Dresselhaus, G. Chen, Z. Ren, *Science* **2008**, *320*, 634.

[6] M. Wuttig, N. Yamada, *Nat. Mater.* **2007**, *6*, 824.

[7] S. Raoux, *Annu. Rev. Mater. Res*. **2009**, *39*, 9.1.

[8] L. van Pieterson, M. H. R. Lankhorst, M. van Schijndel, A. E. T. Kuiper, J. H. J. Roosen, *J. Appl. Phys.* **2005**, *97*, 083520.

[9] S. R. Ovshinsky, *Phys. Rev. Lett.* **1968**, *21*, 1450.

[10] W. Welnic, M. Wuttig, *Mater. Today* **2008**, *11*, 20.

[11] S. Raoux, R. M. Shelby, J. Jordan-Sweet, B. Munoz, M. Salinga, Y.-C. Chen, Y.-H. Shih, E.-K. Lai, M.-H. Lee, *Microelectron. Eng*. **2008**, *85*, 2330.

[12] M. Wuttig, C. Steimer, *Appl. Phys. A: Mater. Sci. Process*. **2007**, *87*, 411.

[13] A. L. Lacaita, D. Wouters, *J. Phys. Status Solidi A* **2008**, *205*, 2281.

[14] M. Terao, T. Morikawa, T. Ohta, *Jpn. J. Appl. Phys.* **2009**, *48*, 080001.

[15] T. L. Anderson, H. B. Krause, *Acta Crystallogr.* **1974**, *C47*, 1141.

[16] O. G. Karpinsky, L. E. Shelimova, M. A. Kretova, J.-P. Fleurial, *J. Alloys Compd.* **1998**, *268*, 112.

[17] L. E. Shelimova, O. G. Karpinsky, M. A. Kretova, V. I. Kosyakov, V. A. Shestakov, V. S. Zemskov, F. A. Kuznetsov, *Inorg. Mater.* **2000**, *36*, 768.

[18] T. Matsunaga, H. Morita, R. Kojima, N. Yamada, K. Kifune, Y. Kubota, Y. Tabata, J.-J. Kim, M. Kobata, E. Ikenaga, K. Kobayashi, *J. Appl. Phys*. **2008**, *103*, 093511.

[19] S: Raoux, W. Wojciech, D. Ielmini, *Chem. Rev.* **2010**, *110*, 240.

[20] F. Yan, T. J. Zhu, X. B. Zhao, S. R. Dong, *Appl. Phys. A: Mater. Sci. Process.* **2007**, *88*, 425.

[21] J. L. Cui, H. Fu, X. L. Liu, D. Y. Chen, W. Yang, *Curr. Appl. Phys*. **2009**, *9*, 1170.

[22] M. N. Schneider, T. Rosenthal, C. Stiewe, O. Oeckler, *Z. Kristallogr*. **2010**, *225*, 463.

[23] *DigitalMicrograph 3.6.1*, Gatan Software, Pleasanton, USA, **1999**.

[24] P. A. Stadelmann, *Ultramicroscopy* **1987**, *21*, 131.

[25] *ESVision*, *4.0.164*, Emispec Systems Inc., Tempe, USA, **1994-2002**.

[26] *WINXPOW*, *v2.12 ed*., Stoe & Cie GmbH, Darmstadt, Germany, **2005**.

[27] T. Chattopadhyay, J. X. Boucherle, H. G. von Schnering, *J. Phys. C: Solid State Phys*. **1987**, *20*, 1431.

[28] S. Bordas, M. T. Clavaguera-Mora, B. Legendre, C. Hancheng, *Thermochim. Acta* **1986**, *107*, 239.

[29] B. J. Kooi, W. M. G. Groot, J. T. M. De Hosson, *J. Appl. Phys.* **2004**, *95*, 924.

[30] M. N. Schneider, P. Urban, A. Leineweber, M. Döblinger, O. Oeckler, *Phys. Rev. B* **2010**, *81*, 184102.

[31] K. A. Agaev, A. G. Talybov, *Sov. Phys. Cryst*. **1966**, *11*, 400.

[32] M. N. Schneider, O. Oeckler, *Z. Anorg. Allg. Chem*. **2008**, *634*, 2557.

[33] Y. Chen, T. J. Zhu, S. H. Yang, S. N. Zhang, W. Miao, X. B. Zhao, *J. Electron. Mater*. **2010**, *39*, 1719.

[34] S. H. Yang, T. J. Zhu, C. Yu, J. J. Shen, Z. Z. Yin, X. B. Zhao, *J. Electron. Mater.* **2011**, *40*, 1244.

[35] F. Yan, T. J. Zhu, X. B. Zhao, S. R. Dong, *Appl. Phys. A: Mater. Sci. Process*. **2007**, *88*, 425.

2.3 Influencing properties and nanostructures of germanium antimony tellurides by substitution

2.3.1 The solid solution series $(GeTe)_{12}M_2Te_3$ (M = Sb, In): nanostructures and thermoelectric properties

T. Rosenthal, S. Welzmiller, O. Oeckler

Solid State Sci. **2013**, *25*, 118-123.

Abstract

Quenching rocksalt-type high-temperature phases of members of the solid solution series $Ge_{12}M_2Te_{15}$ (M = Sb, In) results in nanostructured (pseudo-)cubic materials as shown by high-resolution electron microscopy. The transition temperatures between the thermodynamically stable trigonal phases and the cubic high-temperature phases decrease with increasing In content. Due to a pronounced increase of the Seebeck coefficient, the thermoelectric figure of merit (*ZT*) of $Ge_{12}SbInTe_{15}$ (average structure: $Fm\bar{3}m$, a = 5.9603(1), R_{Bragg} = 0.024) is higher than that of $Ge_{12}Sb_2Te_{15}$ up to 300 °C. This effect is even more pronounced for metastable $Ge_{12}In_2Te_{15}$ (average structure: $Fm\bar{3}m$, a = 5.94723(4), R_{Bragg} = 0.048).

2.3.1.1 Introduction

Germanium antimony tellurides, so called GST materials, are commonly used as thin-film phase-change materials in optical data storage media such as rewritable DVDs and BluBay discs and also as electrically switchable non-volatile PC-RAM devices.[1-4] Tuning the nanostructure of bulk material with similar chemical compositions by utilizing phase transitions between a cubic disordered rocksalt-type high-temperature (HT) phase and a layered trigonal phase, which is stable at ambient temperature, yields thermoelectric materials with figures of merit (*ZT*) up to 1.3.[5,6] During this phase transition, the randomly distributed vacancies present in the cubic phase form defect layers with limited lateral extension perpendicular to the cubic <111> directions. This represents a “transition state” towards the layered phase where rocksalt-type blocks are separated by van der Waals gaps whose formation involves relaxation processes of the adjacent Te-atom layers when the lateral

extension of the defect layers increases.[5,6] The thermoelectric properties of these $(GeTe)_nSb_2Te_3$ compounds depend on their GeTe content (n) and the synthesis conditions (temperature, annealing time and cooling rate). Furthermore, the thermoelectric properties can be influenced by doping, e.g. with Se and Sn.[7] Despite the different chemical behavior of In and Sb in most of their compounds, the combination of In_3SbTe_2 and $Ge_2Sb_2Te_5$ in thin films was performed successfully and shown to influence the characteristics of the phase transition in In-Ge-Sb-Te thin films.[8] Doping thin GST films with In results in retarded crystallization, partially as a result of phase separation and the increased transition temperature between the amorphous and the metastable crystalline (NaCl-type) phase.[9-11] This altered crystallization behavior probably also affects the formation of nanostructures upon quenching the HT phase and might influence the kinetic stability of the nanostructure in In-doped GST bulk samples. It has been shown by resonant X-ray diffraction – which allows one to distinguish elements with very similar electron counts such as Te, Sb and In – that In can substitute Sb in trigonal 33*R*-$Ge_3InSbTe_6$.[12] This can be explained by the similar ionic radii of both elements in octahedral coordination (Sb^{3+} 76 pm; In^{3+} 80 pm).[13] Such substitutions, of course, influence the electronic band structure as well as the phonon scattering and may provide a simple way to tune the thermoelectric properties. Here we report on the synthesis and thermoelectric characterization of bulk samples of solid solutions between $Ge_{12}Sb_2Te_{15}$ and $Ge_{12}In_2Te_{15}$.

2.3.1.2 Experimental Section

2.3.1.2.1 Synthesis

$Ge_{12}(Sb_{1-x}In_x)_2Te_{15}$ (x = 0, 0.5, 0.75, 1) samples were prepared by melting stoichometric amounts of the elements Ge (99.999%, Sigma Aldrich), Sb (99.999%, Smart Elements), Te (99.999%, Alfa Aesar) and In (99.999%, Smart Elements) in silica glass ampoules sealed under Ar atmosphere at 950 °C for 2 hours. The samples were quenched in water and annealed at 590 °C for 3 days and subsequently quenched in water. For thermoelectric characterization, disc-shaped pellets with 20 mm diameter were prepared using ampoules of appropriate dimensions and grinding the ingots to a thickness of 3-4 mm.

2.3.1.2.2 Powder X-ray diffraction

Powder diffraction experiments were carried out with a G670 Guinier camera (Huber, Germany) with a fixed imaging-plate detector and an integrated read-out system using Cu-$K\alpha_1$ radiation (Ge monochromator, λ = 1.54051 Å). Temperature-programmed investigations

were done using a Stadi P powder diffractometer (Stoe & Cie. GmbH, Germany) with a imaging plate detector system and a graphite furnace using Mo-Kα_1 radiation (Ge monochromator, λ = 0.71093 Å) in Debye-Scherrer geometry. The samples were heated from room temperature up to 700 °C with 10 °C/min in silica glass capillaries and data were collected every 25°C with 10 minutes acquisition time. Rietveld refinements of the powder patterns were carried out using the program package TOPAS-Academic.[14]

2.3.1.2.3 Electron microscopy

Energy dispersive X-ray spectroscopy (EDX) was done using a Jeol JSM-6500F scanning electron microscope (SEM) with a Si/Li EDX detector (Oxford Instruments, model 7418). Electron diffraction patterns (SAED, selected area electron diffraction) and high-resolution transmission electron micrographs (HRTEM) were recorded on a FEI Titan 80-300 transmission electron microscope with a field emission gun (acceleration voltage 300 keV). The images were recorded on a Gatan UltraScan 1000 camera with a resolution of 2k x 2k. Additional EDX measurements were performed in the TEM using a TEM TOPS 30 EDX spectrometer (EDAX). The data were evaluated using the software Digital Micrograph[15] and ES Vision[16].

2.3.1.2.4 Thermoelectric measurements

Thermoelectric measurements were done up to 450 °C under vacuum conditions using in-house-built (DLR, Cologne, Germany) and commercial facilities (LSR-3 for S and σ, LFA 1000 for κ, both Linseis GmbH, Germany; as well as LFA 427 for κ, Netzsch GmbH & Co., Germany). The determination of the thermal conductivity κ was followed by the combined measurement of the Seebeck coefficient S and the electrical conductivity σ.

The values of σ were calculated from the resistance R taking into account the cross-section A of the sample and the distance l of the probe tips: $\sigma = 1/A\ R^{-1}$. In order to reduce Peltier influences, the resistance was measured using an AC method; to avoid cable and contact resistances affecting the measurement a four-point-probe setup was used. Seebeck coefficients were measured by slowly and continuously changing the environmental temperature in the presence of a small temperature gradient across the sample. Temperatures measurement (T_1 and T_2) and Seebeck voltage (U_S) pickup were carried out with the Pt lines of type-R

thermocouples attached directly to the samples. The sample's Seebeck coefficient was then calculated as $S_{sample} = U_s/\Delta T - S_{Pt}$ with $\Delta T = |T_2 - T_1|$.

The thermal diffusivity D_{th} was measured using laser-flash apparatuses and the heat capacity c_p was measured by differential scanning calorimetry (DSC 404, Netzsch GmbH & Co. or DSC PT10, Linseis GmbH, Germany). The densities ρ determined using a Mohr's balance were consistent with the X-ray densities. The thermal conductivities κ were calculated from these measurements according to: $\kappa = D_{th} \cdot \rho \cdot c_p$. The thermoelectric figure of merit (ZT) results from these properties according to $ZT = S^2 \cdot \sigma \cdot \kappa^{-1} \cdot T$; where T is the absolute temperature.

2.3.1.3 Results and Discussion

2.3.1.3.1 Crystal structure of quenched $Ge_{12}(Sb_{1-x}In_x)_2Te_{15}$ phases

Rietveld refinements and EDX analyses of samples quenched from the cubic HT phase prove the existence of a solid solution series of quenched (pseudo-)cubic $Ge_{12}(Sb_{1-x}In_x)_2Te_{15}$ ($0 \leq x \leq 1$) phases. The composition of the samples was verified by a minimum of 4 individual SEM-EDX measurements for each sample (Table 1).

The powder diffraction patterns of the samples $Ge_{12}(Sb_{1-x}In_x)_2Te_{15}$ ($0 < x \leq 1$) were fitted with a cubic NaCl-type structure model, similar to the one described for metastable crystalline phases of phase-change materials.[17] Te anions occupy the 4*a* position and Sb, Ge, In and vacancies share the 4*b* cation position. A fit with a GeTe-type model[18] (space group *R*3*m*, atoms on 3*a* (0, 0, *z*), Te at the origin ($z = 0$), cations and vacancies at $z = \sim 0.5$) showed no significant deviations of the metrics and the coordination polyhedra from the cubic structure. However, both reflection profiles and atomic displacement parameters indicate that the cubic model represents a good, yet still approximate description of the average structure, as strain distortions and concentration gradients may be present. For $Ge_{12}Sb_2Te_{15}$ ($x = 1$), the refinement of a trigonal GeTe-type structure revealed a significant deviation from the cubic metrics with an *a/c* ratio of 2.4680 (ideal value for the trigonal setting of cubic metrics: 2.4498), which is also obvious as the "pseudocubic" 200 reflection (at ca. 30° 2ϑ) is much sharper than others that split when there is a trigonal distortion. The trigonal symmetry is corroborated by the clear 3+3 coordination of the atoms as suggested in ref. [19]

For all refinements of the cubic structure model, the same parameter set was used. Site occupation factor were derived from the nominal composition verified by EDX and not

refined. Equal displacement parameters were employed for the cations sharing one position. Reflection profiles were described by a fundamental parameter approach as a direct convolution of parameters of the experimental setup, anisotropic microstrain and crystallite size effects. Preferred orientation was taken into account using spherical harmonics. The results of the Rietveld refinements are shown in Fig. 1, crystallographic data are given in Tables 2 and 3, respectively. Further details of the crystal structure investigations may be obtained from Fachinformationszentrum Karlsruhe, 76344 Eggenstein-Leopoldshafen, Germany (fax: (+49)7247-808-666; e-mail: crysdata@fiz-karlsruhe.de, http://www.fiz-karlsruhe.de /request_for_deposited_data.html) on quoting the depository numbers CSD-426029, CSD-426031 and CSD-426030 for x = 0.5, 0.75 and 1, respectively (data for $Ge_{12}Sb_2Te_{15}$ cf. reference [5]).

Table1. Results from SEM-EDX measurements (calculated for the nominal composition/measured, in atom %).

sample	Ge	Sb	In	Te
$Ge_{12}Sb_2Te_{15}$	41.4 / 41(2)	6.9 / 7.5(7)	0 / 0	51.7 / 51.7(9)
$Ge_{12}SbInTe_{15}$	41.4 / 42(1)	3.45 / 3.3(3)	3.45 / 3.5(1)	51.7 / 51.1(8)
$Ge_{12}Sb_{0.5}In_{1.5}Te_{15}$	41.4 / 42(1)	1.7 / 1.6(3)	5.2 /5.5(3)	51.7 / 51.2(8)
$Ge_{12}In_2Te_{15}$	41.4 / 41.6(7)	0 / 0	6.9 / 7.4(3)	51.7 / 51.0(5)

The refinements show that the cubic lattice parameter *a* decreases with increasing In content (x), the value for x = 0.75 corresponds to the average of those for x = 0.5 and 1, which is consistent with Vegard's law and yields a linear fit $a = 5.9733(5) - 0.02614(7)\ x$. This would result in $a = 5.9733$ Å for x = 0 which is in good agreement with the cube root of the volume of the trigonal cell (5.9727 Å). In addition, a cubic sample with x = 0.1, which was not investigated in further detail, yielded $a = 5.9727$ Å in good agreement with 5.9707 Å as calculated from the Vegard relationship.

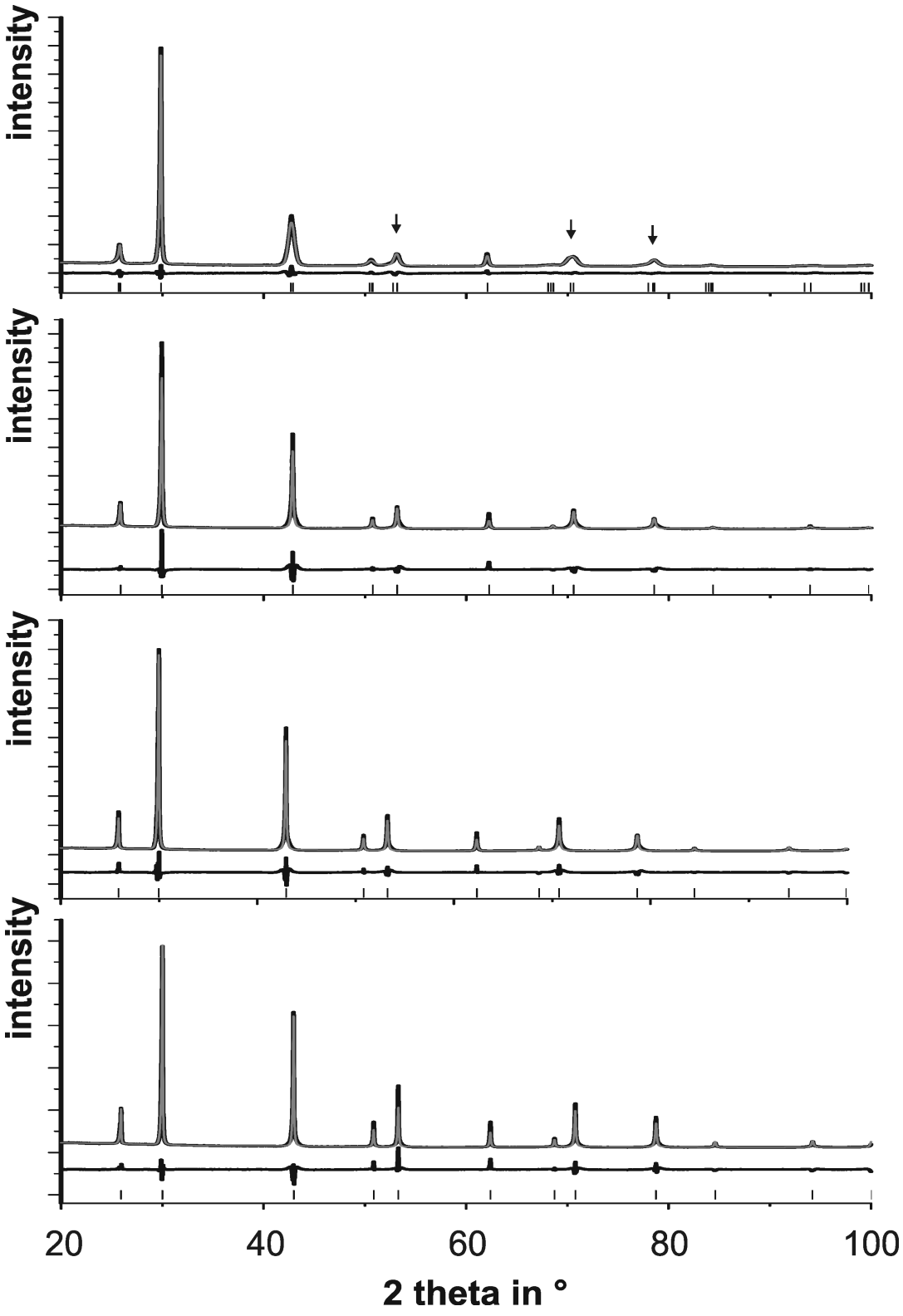

Fig. 1: Rietveld refinements of $Ge_{12}(Sb_{1-x}In_x)_2Te_{15}$: from top to bottom for x = 0, 0.5, 0.75, 1; experimental (black) and simulated (gray) powder patterns, difference plot (below) and reflection markers (black, bottom); the scaling of the 2ϑ axis is the same for all plots, the intensity scale is normalized according to the strongest reflection (same scaling for pattern and difference plot); for x = 0, arrows mark some of the reflections that are broadened due to the rhombohedral symmetry of the GeTe type of this compound.

Table 2. Atom coordinates and isotropic displacement parameters for $Ge_{12}(Sb_{1-x}In_x)_2Te_{15}$ (in Å².); space groups see Table 3.

	Te			cations and vacancies			
	position		U_{iso}	position		occupancy	U_{iso}
$Ge_{12}Sb_2Te_{15}$	3*a*	0 0 0	1.01(2)	3*a*	0 0 0.4818(5)	0.8 Ge, 0.133 Sb	1.85(7)
$Ge_{12}SbInTe_{15}$	4*a*	0 0 0	1.50(3)	4*b*	½ ½ ½	0.8 Ge, 0.067 Sb, 0.067 In	3.36(5)
$Ge_{12}Sb_{0.5}In_{1.5}Te_{15}$	4*a*	0 0 0	1.46(2)	4*b*	½ ½ ½	0.8 Ge, 0.033 Sb, 0.1 In	3.26(3)
$Ge_{12}In_2Te_{15}$	4*a*	0 0 0	0.42(2)	4*b*	½ ½ ½	0.8 Ge, 0.133 In	2.87(3)

Table 3. Details of the Rietveld refinements for the quenched $Ge_{12}(Sb_{1-x}In_x)_2Te_{15}$ phases.

	$Ge_{12}Sb_2Te_{15}$	$Ge_{12}SbInTe_{15}$	$Ge_{12}Sb_{0.5}In_{1.5}Te_{15}$	$Ge_{12}In_2Te_{15}$
M (in g mol^{-1})	3029.20	3022.26	3018.79	3015.12
F(000)	337.6	337.1	336.8	336.4
crystal system / space group (no.)	trigonal / *R*3*m* (160)		cubic / $Fm\bar{3}m$ (225)	
lattice parameters (in Å)	*a* = 4.2128(1) *c* = 10.3971(7)	*a* = 5.9603(1)	*a* = 5.95346(6)	*a* = 5.94723(4)
cell volume (in $Å^3$)	159.80(1)	211.74(1)	211.012(6)	210.350(4)
density (X-ray, in g/cm³)	6.295	6.320	6.334	6.347
radiation	Cu-$K_{\alpha 1}$ (λ = 1.540596 Å)			
2θ range (in °)	$20 \leq 2\theta \leq 100$			
parameters (thereof background)	30 (6)	20 (12)	20 (12)	20 (12)
R_p / R_{wp}	0.025 / 0.035	0.061 / 0.092	0.055 / 0.081	0.042 / 0.068
GooF / R_{Bragg}	1.399 / 0.009	4.087 / 0.024	3.590 / 0.027	2.844 / 0.048

2.3.1.3.2 Influence of In substitution on strain and on the phase transition temperatures

The misfits in the difference plot of the Rietveld refinements are a consequence of reflection broadening. According to the refined fundamental parameters, this is due to anisotropic microstrain as well as domain size (microstructure) effects[19] and probably also local chemical variations. With increasing In content, the reflections in the powder patterns become sharper and more Lorentz-shaped, indicating less microstrain as the local deviations from cubic metrics become smaller and the situation remains closer to that of the cubic HT phase. In addition, strain effects are probably less pronounced due to the lower transition temperature between the trigonal phase and the cubic HT phase in In substituted samples as shown by temperature-dependent powder X-ray diffraction (cf. Fig. 2 and Table 4). As the stability region of the cubic phase extends towards lower temperatures with increasing x, quenching yields samples whose structure is more similar to the HT phase. Yet, the general thermal behavior of In-substituted samples corresponds to that of unsubstituted ones.[6]

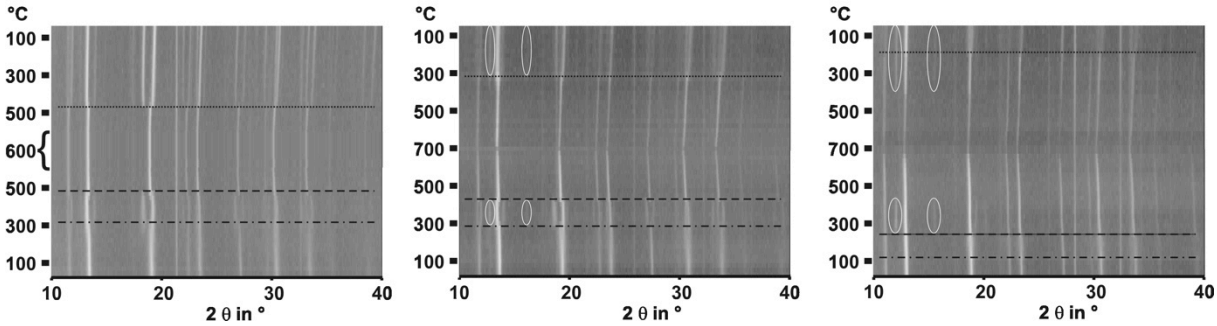

Fig. 2: Temperature-dependent powder diffraction patterns of $Ge_{12}(Sb_{1-x}In_x)_2Te_{15}$ with x = 0 (left), 0.5 (middle) and 1 (right); heating (bottom to middle) and cooling (middle to top). The strongest reflections of In_2Te_3 phase are marked with white ellipses and the transition temperatures are indicated by horizontal lines: pseudo-cubic → trigonal (dot-and-dashed); trigonal → cubic (during heating, dashed) and cubic → trigonal (during cooling, dotted).

Table 4. Phase transition temperatures of $Ge_{12}(Sb_{1-x}In_x)_2Te_{15}$ ($0 \leq x \leq 1$) from the experiments shown in Fig. 2 (for $Ge_{12}Sb_2Te_{15}$, also see ref. [6]).

phase transition	$Ge_{12}Sb_2Te_{15}$	$Ge_{12}SbInTe_{15}$	$Ge_{12}In_2Te_{15}$
pseudo-cubic → trigonal	325 °C	290 °C	~130 °C
trigonal → cubic (heating)	475 °C	440 °C	~260 °C*
cubic → trigonal (cooling)	460 °C	310 °C	190 °C
melting point	~700 °C	700 °C	690 °C

The increasing mobility at higher temperatures leads to the transition from the quenched pseudocubic phase to the thermodynamically stable trigonal phase. The cubic HT phase is formed when its existence region is reached and is stable up to the melting point. When the melt is slowly cooled, the cubic HT phase forms and upon further cooling transforms to the trigonal phase.

In the case of $Ge_{12}In_2Te_{15}$, the transition to a trigonal GeTe-type phase during heating is indicated by reflection broadening only. In addition, the segregation of a binary or doped indium telluride occurs at 260 °C when the HT phase is formed. Such a segregation has also been reported for In substituted thin-film $Ge_2Sb_2Te_5$.[10] The binary phase is present up to 430 °C when it probably dissolves in the HT phase of $Ge_{12}In_2Te_{15}$ which then is stable up to the melting point at 690 °C. When the melt is slowly cooled, a homogeneous cubic phase reappears, only below 380 °C the segregation is observed. The remaining In-substituted main phase distorts to a trigonal GeTe-type phase below 190 °C. This distortion is much less pronounced than that of $Ge_{12}(Sb_{1-x}In_x)_2Te_{15}$ (x = 0, 0.5) described above, which involves the formation of van der Waals gaps. Very small amounts of In_2Te_3 also occur when the trigonal phase of $Ge_{12}InSbTe_{15}$ is formed. Thus, the quaternary phases are only stable at high

temperatures as a cubic phase and metastable, respectively, as the pseudocubic phase accessible by quenching. The thermodynamically stable state at ambient conditions is a mixture of In_2Te_3 and trigonal $Ge_{12}Sb_2Te_{15}$ probably doped with In.

2.3.1.3.3 Influence of the In substitution on the nanostructure

TEM investigations of $Ge_{12}(Sb_{1-x}In_x)_2Te_{15}$ (x = 0, 0.5, 1) samples reveal their rocksalt-type average structure with pronounced layer-like short-range ordering of the defects forming a parquet-like nanostructure as reported for $Ge_{12}Sb_2Te_{15}$ (cf. Fig. 3).[5,6] This leads to characteristic diffuse intensities in SAEDs and Fourier transforms of HRTEM images; and the defect layers are clearly visible in the HRTEM images themselves. It turned out that, in general, their relative arrangement is not significantly affected by the In substitution. The nanostructure of GST thermoelectrics depends significantly on the vacancy concentration (as discussed in detail in ref. [6]) which is given by n in $(GeTe)_n(Sb,In)_2Te_3$ and does not change upon substitution with In. The cooling rate, which was not varied in the present investigation, further determines the structural features of GST thermoelectrics.[19] Substitution influences the existence regions of the different phases and thus the diffusion processes and, consequently, the nanostructures formed. For Se-substituted GST samples, the lower transition temperatures between the cubic HT phase and the trigonal phase are correlated to smaller average lateral extensions of the defect layers.[7] This effect also explains their slightly different average extension in the HRTEM images of $Ge_{12}(Sb_{1-x}In_x)_2Te_{15}$ with different x. Lower phase transition temperatures, especially for $Ge_{12}In_2Te_{15}$, mean less time for vacancy diffusion during quenching and lead to less extended defect layers. Thus, the phase transition temperatures influence strain effects and the layer-like short-range ordering of the vacancies but do not have a significant impact on the principal arrangement of the defect layers.

Both for $Ge_{12}SbInTe_{15}$ and $Ge_{12}In_2Te_{15}$, TEM-EDX measurements do not show significant chemical variation within crystallites and between individual crystallites. The average composition was determined as $Ge_{12.2(2)}Sb_{1.2(3)}$ $In_{1.2(1)}Te_{15}$ and $Ge_{12.4(5)}In_{2.2(1)}Te_{15}$, respectively.

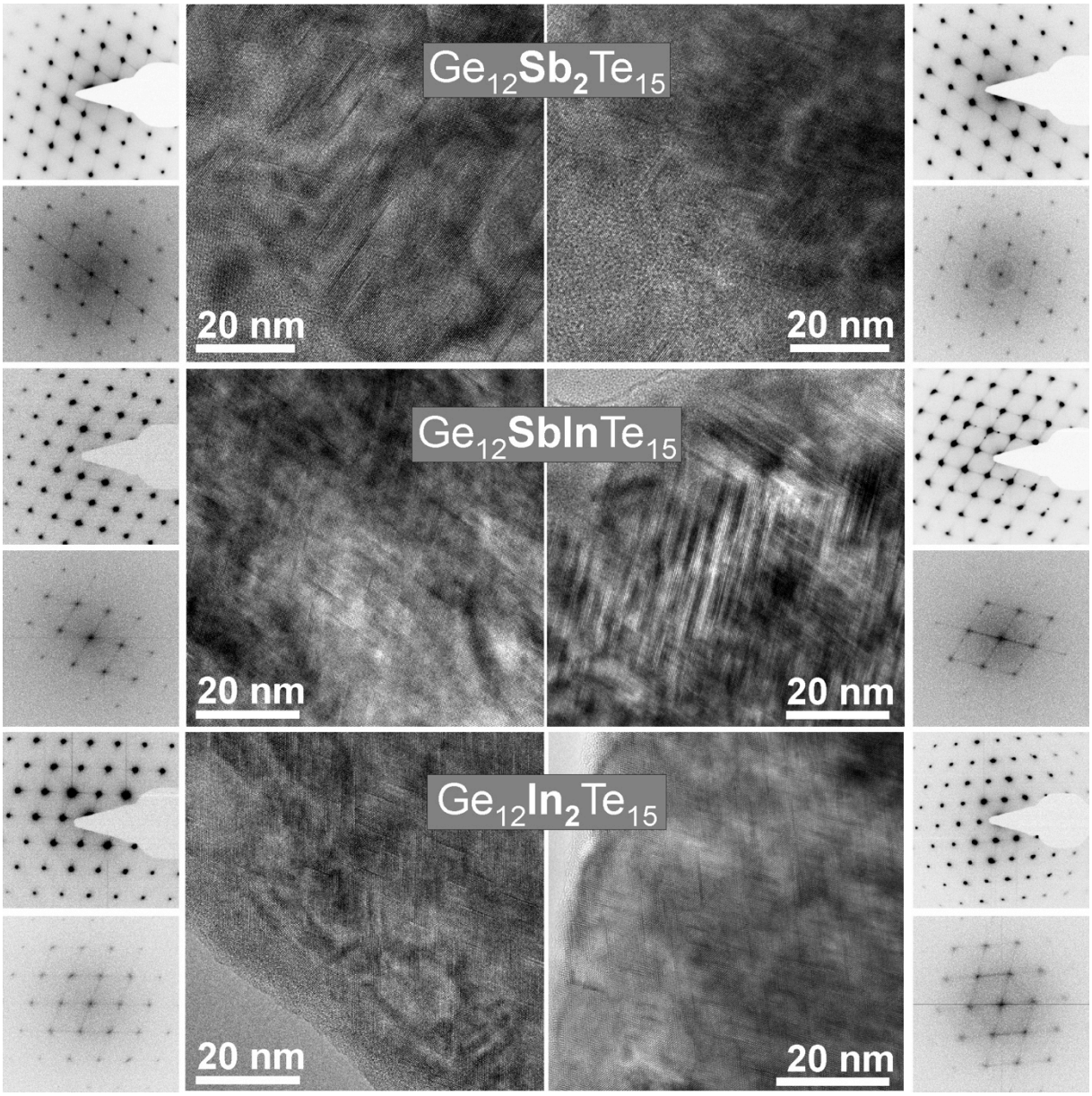

Fig. 3: HRTEM images for the cubic <100> zone axis with corresponding SAED patterns (with beam stop) and Fourier transforms of the images; for each composition, images for two different representative crystals are shown.

2.3.1.3.4 Influence of the In substitution on the thermoelectric properties

The difference in the thermoelectric properties of $Ge_{12}Sb_2Te_{15}$ compared to $Ge_{12}SbInTe_{15}$ and $Ge_{12}In_2Te_{15}$ (Fig. 4) is most significant concerning the much higher Seebeck coefficients of the In-containing samples, which exhibit only minor changes with temperature. Therefore, at temperatures below 300 °C the *ZT* value of the substituted samples is higher. However, the high values for $Ge_{12}In_2Te_{15}$ are not long-time stable and also depend on the measurement procedure as the compound tends to decompose as described above.

The higher Seebeck coefficients of the semiconducting compounds $Ge_{12}In_2Te_{15}$ and - even more pronounced - $Ge_{12}SbInTe_{15}$ are reflected in their lower electrical conductivities as both

quantities are related by the charge carrier concentration, which is apparently reduced by In substitution. At 450 °C, the absolute electrical conductivity of $Ge_{12}InSbTe_{15}$ is 580 S/cm, which is comparable to that of $Ge_{19}Sb_2Te_{22}$ (769 S/cm) with ZT = 1.3 [6] and Se substituted samples, e.g. $Ge_7Sb_2Te_5Se_5$ (400 S/cm, ZT = 1.0) [7]. The electrical conductivity of $Ge_{12}In_2Te_{15}$ at 450 °C is 960 S/cm. The higher electrical conductivity of $Ge_{12}Sb_2Te_{15}$, especially at low temperatures, is associated with metallic characteristics.

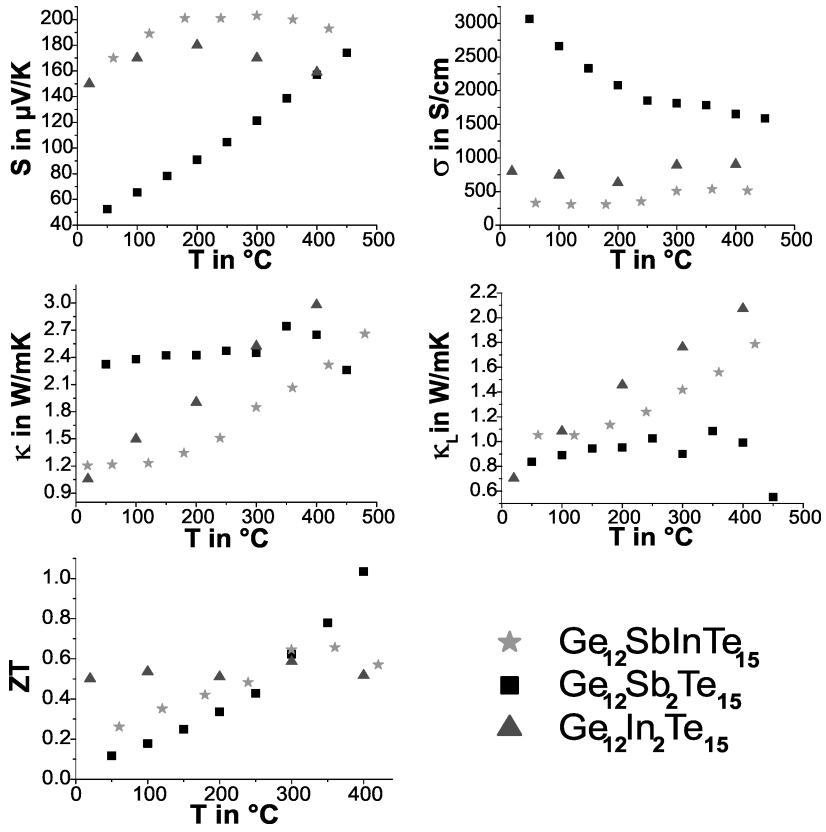

Fig. 4: Thermoelectric characteristics of quenched $Ge_{12}(Sb_{1-x}In_x)_2Te_{15}$ samples: Seebeck coefficient (S) top left, electrical conductivity (σ) top right, thermal conductivity (κ) middle left, lattice thermal conductivity (κ_L, calculated from σ with L = 1.48 $\cdot 10^{-8}$ WΩK^{-2}) middle right, and the resulting thermoelectric figure of merit (ZT) bottom. The values for $Ge_{12}Sb_2Te_{15}$ have been taken from ref. [6].

As suggested by the Wiedemann-Franz law, the compounds with higher electrical conductivities also exhibit higher thermal conductivities which increase with temperature. It is difficult to assess the lattice parts of the thermal conductivity (κ_L) as semiconductors and metals may exhibit significantly different Lorenz numbers L.[20] Assuming a constant L of 1.48 $\cdot 10^{-8}$ WΩK^{-2}, which is typical for degenerate semiconductors like Ag_2Te[21], the κ_L values of all compounds at low temperatures are similar as suggested by the similar nanostructures and similar masses of In and Sb atoms. The low κ_L at low temperatures, especially for $Ge_{12}In_2Te_{15}$, contributes to the high ZT value at room temperature.

2.3.1.4 Conclusion

In contrast to binary GeTe, in which only a few percent of InTe can be solved due to the different structures of the binary phases[22], quenched rocksalt-type $Ge_{12}Sb_2Te_{15}$ forms a complete solid solution series with the corresponding In compound. Substituting Sb with In lowers the transition temperature between the trigonal phase stable at ambient conditions and the cubic HT phase. Upon quenching, the metrics remains closer to cubic and strain effects are less pronounced than in pure GST materials. However, the short-range defect ordering is almost independent of the In content. This results in the parquet-like nanostructure which is well known from GST materials. Therefore, the lattice thermal conductivity remains approximately the same at low temperature, so that the electronic properties can be varied independently up to a certain extent. The substitution involves a change from metallic to semiconducting behavior of the electrical conductivity that strongly increases the Seebeck coefficient at low temperatures. This increases the *ZT* values of $Ge_{12}SbInTe_{15}$ and $Ge_{12}In_2Te_{15}$ as compared to $Ge_{12}Sb_2Te_{15}$ below ~300°C, where their parquet-like nanostructure is stable.

Acknowledgements

The authors thank Jörg Frohrig (Linseis GmbH, Selb, Germany), Christian Stiewe, Johannes de Boor (both German Aerospace Center, Cologne, Germany) as well as Felix Fahrnbauer (Leipzig University, Germany) for thermoelectric measurements. Christian Minke and Thomas Miller (both LMU Munich) are acknowledged for SEM operation and for temperature-dependent powder diffraction experiments, respecitvely. Special thanks go to Prof. Dr. W. Schnick (LMU Munich) for his generous support of this work. This investigation was funded by the Deutsche Forschungsgemeinschaft (grant OE530/1-2).

2.3.1.5 References

[1] T. Siegrist, P. Merkelbach, M. Wuttig, *Annu. Rev. Condens. Matter Phys.* **2012**, *3*, 215.

[2] T. Matsunaga, H. Morita, R. Kojima, N. Yamada, K. Kifune, *J. Appl. Phys.* **2008**, *103*, 093511.

[3] D. Loke, T. H. Lee, W. J. Wang, L. P. Shi, R. Zhao, Y. C. Yeo, T. C. Chong, S. R. Elliott, *Science* **2012**, *336*, 1566.

[4] S. Raoux, G. W. Burr, M. J. Breitwisch, C. T. Rettner, Y.-C. Chen, R. M. Shelby, M. Salinga, D. Krebs, S.-H. Chen, H.-L. Lung, C. H. Lam, *IBM J. Res. & Dev.* **2008**, *52*, 465.

[5] M. N. Schneider, T. Rosenthal, C. Stiewe, O. Oeckler, *Z. Kristallogr.* **2010**, *225*, 463.

[6] T. Rosenthal, M. N. Schneider, C. Stiewe, M. Döblinger, O. Oeckler, *Chem. Mater.* **2011**, *23*, 4349.

[7] S. Welzmiller, T. Rosenthal, T. Schröder, P. Urban, F. Fahrnbauer, C. Stiewe, O. Oeckler, *Acta Crystallogr. Sect. A* **2012**, *68*, 50.

[8] S. J. Park, M. H. Jang, M.-H. Cho, D.-H. Ko, *Appl. Surface Sci.* **2012**, *258*, 9786.

[9] M. H. R. Lankhorst, L. van Pieterson, M. van Schijndel, B. A. J. Jacobs, J. C. N. Rijpers, *Jpn. J. Appl. Phys.* **2003**, *42*, 863.

[10] K. Wang, C. Steimer, D. Wamwangi, S. Ziegler, M. Wuttig, J. Tomforde, W. Bensch, *Microsyst. Technol.* **2007**, *13*, 203.

[11] K. Wang, C. Steimer, D. Wamwangi, S. Ziegler, M. Wuttig, *Appl. Phys. A* **2005**, *80*, 1611.

[12] O. Oeckler, S. Welzmiller, T. Rosenthal, T. Schröder, F. Fahrnbauer, *Z. Anorg. Allg. Chem.* **2012**, *638*, 1561.

[13] R. D. Shannon, *Acta Crystallogr. Sect. A*, **1976**, *32*, 751.

[14] *TOPAS-Academic*, *V. 4.1*, Coelho Software, Brisbane, Australia, **2007**.

[15] *DigitalMicrograph 3.6.1*, Gatan Software, Pleasanton, USA, **1999**.

[16] *ESVision*, *4.0.164*, Emispec Systems Inc., Tempe, USA, **1994-2002**.

[17] T. Matsunaga, R. Kojima, N. Yamada, K. Kifune, Y. Kubota, Y. Tabata, M. Takata, *Inorg. Chem.* **2006**, *45*, 2235.

[18] T. K. Chattopadyay, J. X. Boucherle, H. G. Von Schnering, *J. Phys. C: Solid State Phys.* **1987**, *20*, 1431.

[19] M. N. Schneider, P. Urban, A. Leinweber, M. Döblinger, O. Oeckler, *Phys. Rev. B* **2010**, *81*, 184102.

[20] R. T Delves, *Proc. Phys. Soc.* **1959**, *73*, 572.

[21] G. S. Kumar, G. Prasad, R. O. Pohl, *J. Mater. Chem.* **1993**, *28*, 4261.

[22] A. D. Bigvava, E. D. Kunchuliya, V. K. Korobov, R. R. Shvangiradze, *Inorg. Mater.* **1983**, *19*, 1170.

2.3.2 Nanostructures and thermoelectric properties of the solid solution series $(Ge_{1-x}Sn_xTe)_nSb_2Te_3$ (n = 4, 7, 12; $0 \leq x \leq 1$)

T. Rosenthal, L. Neudert, P. Ganter, J. de Boor, C. Stiewe, O. Oeckler

J. Solid State Chem. **2014**, *215*, 231 -240.

Abstract

Solid solutions $(Ge_{1-x}Sn_xTe)_nSb_2Te_3$ (n = 4, 7, 12; $0 \leq x \leq 1$) represent stable high-temperature phases and can be obtained as metastable compounds by quenching. High-resolution transmission electron microscopy reveals that the quenched (pseudo-)cubic materials exhibit parquet-like nanostructures comparable to, but especially for n = 4 more pronounced than in $(GeTe)_nSb_2Te_3$ (GST materials). The temperature-dependent phase transitions are comparable; however, substitution with Sn significantly lowers the transition temperatures between cubic high-temperature phase and the long range ordered layered phases that are stable at ambient conditions. In addition, the metrics of the quenched Sn-containing materials remains closer to cubic, especially for samples with n = 7 or 12. For samples with high defect concentrations (n = 4, 7), Sn-substituted samples exhibit electrical conductivities up to 3 times higher than those of corresponding GST materials. Since the difference in thermal conductivity is much less pronounced, this results in a doubling of the thermoelectric figure of merit (*ZT*) at high temperatures for $(Ge_{0.5}Sn_{0.5}Te)_4Sb_2Te_3$ as compared to $(GeTe)_4Sb_2Te_3$. Sn doping in $(GeTe)_7Sb_2Te_3$ increases the *ZT* value by a factor of up to 4 which is also due to an increased Seebeck coefficient.

2.3.2.1 Introduction

The increased awareness for the responsible use of energy has led to major improvements in the efficiency of production processes and combustion engines; however, there is still a lot of waste heat. This might be utilized by employing thermoelectric generators on a large scale; however, restrictions concerning their efficiency have to be overcome. Thus, the improvement of thermoelectric properties is an important field of research. The thermoelectric performance is characterized by the dimensionless *ZT* value which depends on the Seebeck coefficient *S*, the electrical conductivity σ and the thermal conductivity κ: $ZT = S^2\sigma T\kappa^{-1}$. The interdependence of the thermal and electrical conductivities as described by the Wiedemann-

Franz law constitutes a major problem for the optimization of *ZT* and in addition, both properties correlate with *S* via the charge carrier concentration.[1,2] Therefore, improvements of one property are often at least partially compensated by less favorable values of the other crucial ones. Yet, this holds mainly for the electronic contribution (κ_{el}) to κ, whereas the phononic contribution κ_L is not directly related to σ.

Germanium antimony tellurides (GST materials) and substitution variants thereof offer many possibilities for optimization. The nanostructure and, in part as a consequence, the thermoelectric properties of $(GeTe)_nSb_2Te_3$ can be influenced by changing the vacancy concentration which is directly related to the GeTe content (n) as well as by altering the thermal treatment.[3] The thermodynamically stable phase at room temperature (RT) is a layered trigonal phase with van der Waals gaps connecting rocksalt-type slabs while the high-temperature (HT) phase corresponds to a defect rocksalt-type structure with randomly distributed vacancies.[4] These vacancies form defect layers with limited lateral extension when the samples are quenched. These are oriented perpendicular to the cubic rocksalt type's <111> directions. This is associated with metric distortion. The frequency and lateral extension of the defect layers and the variance of their spacing are determined by diffusion processes and by the total defect concentration. These defect layers may intersecting each other and form a rather isotropic nanostructure that hinders the phonon proliferation effectively. Thus, quenching the cubic HT phase of $(GeTe)_nSb_2Te_3$ with $n > 3$ yields materials with *ZT* values up to 1.3. [3,5]

Substituting Sb with In in quenched samples of $(GeTe)_{12}Sb_2Te_3$ results in materials with similar nanostructures but improved Seebeck coefficients at temperatures below 400 °C.[6] Substitution of Te by Se leads to a reduction of the lattice part of κ (κ_L) due to the mixed occupation of the anion site.[7,8] Due to a significant improvement of *S*, *ZT* values up to 6 times higher than those of $(GeTe)_7Sb_2Te_3$ (n = 7) can be achieved.

Doping with Sn influences the properties of $(GeTe)_2Sb_2Te_3$ thin films which are widely used as phase-change materials.[9-15] Such thin films consisting of $(GeTe)_nSb_2Te_3$ with different GeTe contents (n) have also been substituted with Sn which, for example, results in higher crystallization speeds for $Ge_{2.7}Sn_{1.3}Sb_2Te_7 = (Ge_{0.672}Sn_{0.325}Te)_4Sb_2Te_3$ [16] (n = 4) while $SnGe_7Sb_2Te_7Se_4$ (n = 8) exhibits an increased band gap in the amorphous state.[17] Investigations of the element distribution in bulk samples of layered phases of $(Ge_{0.65}Sn_{0.35}Te)_2Sb_2Te_3$ and $(Ge_{0.6}Sn_{0.4}Te)Sb_2Te_3$ showed that Sn has a slight preference to occupy the cation positions near the van der Waals gaps.[18] In these studies, resonant X-ray diffraction data were used due to the similar electron counts of Sn, Sb and Te.[19] Similar investigations were performed on 39*R*-$M_{0.067}Sb_{0.667}Te_{0.266}$ (M=Ge, Sn)[20] and 21*R*-$SnSb_2Te_4$

= $(SnTe)Sb_2Te_3$.[21] The substitution of Ge by Sn in TAGS materials $(AgSbTe_2)_{100-x}(GeTe)_x$ (x = 80, 85, 90, 95) results in higher hole mobility in $(AgSbTe_2)_{100-x}(SnTe)_x$ and in low κ (0.3 W/m K for x = 85 at RT).[22] The compounds $(Ge_{0.65}Sn_{0.35}Te)_2Sb_2Te_3$ and $(Ge_{0.6}Sn_{0.4}Te)Sb_2Te_3$ also exhibit lower κ and higher *ZT* values compared to $(GeTe)_2Sb_2Te_3$ and $(GeTe)Sb_2Te_3$, respectively.[18] However, in these cases *ZT* values reach a maximum of only 0.25 at 400 °C since the low GeTe content is associated with a less favorable parallel arrangement of the defect layers and low Seebeck coefficients (max. 85 μV/K at 400 °C). Since compounds $(GeTe)_nSb_2Te_3$ with higher GeTe contents (n = 7, 12, 19) exhibit higher Seebeck coefficients,[3] the substitution with Sn should result in a better thermoelectric performance for these materials.

2.3.2.2 Experimental

Ternary and quarternary bulk samples of $(Ge_{1-x}Sn_xTe)_nSb_2Te_3$ (n = 4, 7, 12; $0 \leq x \leq 1$) were synthesized under Ar in sealed silica glass ampoules. Stoichometric mixtures of the elements Ge (99.999%, Sigma Aldrich), Sn (99.999%, Smart Elements), Sb (99.999%, Smart Elements) and Te (99.999%, Alfa Aesar) were melted (minimum 1h at 900-950 °C) and quenched in water. The compact metallic gray ingots were annealed in the existence range of the cubic HT phases, i.e. between 560 °C and 610 °C, for up to 10 d and quenched in water. Details of the synthesis conditions are given in the Supplementary Information Table S1. Disc-shaped ingots for thermoelectric characterization were prepared under Ar in flat-bottom ampoules. The air-quenched melts where annealed at 590 °C for 2 days and subsequently quenched by removing from the furnace. The resulting ingots with a diameter of 20 mm were polished to a thickness of 2 - 5 mm. The products were analyzed by Rietveld refinements of the powder X-ray diffraction patterns (PXRD) and the composition was verified by energy-dispersive X-ray spectroscopy (EDX) as discussed below. All samples were obtained as single phased metallic gray ingots.

For EDX analysis, a JSM-6500F (Jeol, Japan) scanning electron microscope (SEM) equipped with an EDX detector (model 7418, Oxford Instruments, UK) was used. Additional EDX analyses as well as high-resolution transmission electron microscopy (HRTEM), selected-area electron diffraction (SAED), and scanning transmission electron microscopy (STEM) using a high-angle annular dark-field (HAADF) detector were carried out with a Titan 80-300 (FEI, USA) equipped with a TEM TOPS 30 EDX spectrometer (EDAX, Germany). The field emission gun was operated at 300 kV. An UltraScan 1000 camera (Gatan, USA, resolution 2k

x 2k) was used to record SAED patterns and HRTEM images which were evaluated using Digital Micrograph[23] and EMS.[24] For STEM and EDX data, the program ES Vision[25] was used. For TEM investigations, finely ground pieces of the samples were dispersed in ethanol and distributed onto a copper grid coated with holey carbon film by drop casting.

For PXRD, the samples were ground in a agate mortar and fixed on Mylar foils with small amounts of vacuum grease. Data were collected using a Guinier camera (G670, Huber, Germany) equipped with a fixed imaging plate detector and an integrated read-out system using Cu-Kα_1 radiation (Ge(111) monochromator, λ = 1.54051 Å). Temperature-programmed PXRD was carried out on powdered samples filled into silica glass capillaries with a diameter of 0.3 mm and sealed with silicone grease under Ar atmosphere. The samples were heated from RT up to 750 °C with 10 °C/min and subsequently cooled to RT with the same rate. Data were collected every 25°C with 10-20 minutes acquisition time. These investigations were carried out with a Stadi P powder diffractometer (Stoe & Cie. GmbH, Germany) with an imaging plate detector system using Mo-Kα_1 radiation (Ge(111) monochromator, λ = 0.7093 Å), equipped with a graphite furnace. Rietveld refinements were performed using the program package TOPAS-Academic.[26]

A fundamental parameter approach taking into account the experimental setup was used to describe the reflection profiles in all refinements. Lorentzian and Gaussian crystallite size broadenings as well as Lorentzian microstrain broadening were taken into account for all samples. The pronounced asymmetry of the reflection profiles of $(GeTe)_4Sb_2Te_3$ was empirically described by anisotropic microstrain and crystallite size broadening using the LeBail-Jouanneaux algorithm.[27] This effect may be due to local distortions as a result of the high vacancy concentration. Preferred orientation was taken into account using 4th order spherical harmonics.

For the characterization of the thermoelectric properties up to 450° C, commercial and in-house-built facilities of the DLR (Cologne, Germany) were used. The thermal conductivity (κ) was measured first, followed by a combined measurement of σ and S. Datapoints at comparable temperatures were obtained from the different measurements by linear interpolation. The electrical conductivity was determined by an in-line four-point-probe setup to avoid influences of cable and contact resistance. Peltier influences were reduced by using an AC method with a frequency of 7 Hz. The electrical conductivity σ was calculated from the resistance R according to $\sigma = 1/(2\pi\, s \cdot R \cdot G)$, taking into account the distance of the voltage probes s and the sample geometry, given by a correction factor G. Temperatures as well as the Seebeck voltage (U_S) were determined by type-N thermocouples attached to the sample by

spring-loaded pressure contacts. For the measurement of S, a variable temperature difference ΔT was used. S was calculated according to: $S = \partial U_S / \partial \Delta T - S_{Nicrosil}$ with $S_{Nicrosil}$ the Seebeck coefficient of the corresponding thermocouple wires. Detailed information about the S measurement is given in ref. [28]; information about the hardware and the σ measurements can be found in ref. [29]. A laser-flash apparatus (LFA 427, Netzsch GmbH & Co., Germany) was used to measure the thermal diffusivity (D_{th}). κ was calculated according to $\kappa = D_{th} \cdot \rho \cdot c_p$. The specific heat capacity c_p was determined by differential scanning calorimetry (DSC 404, Netzsch GmbH & Co., Germany). The results of the c_p and D_{th} measurement are provided in the Supplementary Information Table S2. The densities ρ were determined using Mohr's balance; the maximum deviation from the X-ray densities was 1 %. The thermoelectric figure of merit (ZT) was calculated from the individual properties according to $ZT = S^2 \cdot \sigma \cdot \kappa^{-1} \cdot T$ where T is the absolute temperature.

2.3.2.3 Results and discussion

2.3.2.3.1 Composition, and average structure of (pseudo-)cubic quenched phases

The samples $(Ge_{1-x}Sn_xTe)_nSb_2Te_3$ (n = 4, 7, 12; x = 0, 0.25, 0.5, 0.75, 1) prepared by quenching the HT phase were single-phase according to the Rietveld refinements discussed below. In addition, the composition of many representative samples was verified by REM-EDX and TEM-EDX (cf. Supplementary Information, Tables S3 and S4). The crystal structures were refined from PXRD data by the Rietveld method. These analyses confirm a rocksalt-type structure with Te on the anion position and Sb, Sn, Ge and vacancies on the cation position. The occupancies were derived from the nominal composition and not refined. Due to the random distribution of the cations and vacancies, the isotropic displacement parameters of the cations are rather large compared to the anions. Therefore, this effect is less pronounced for samples with lower vacancy concentrations (higher n).The profile fits from the refinements for compounds with x = 0.5 and 1.0 are shown in Fig. 1; the corresponding plots for all other samples can be found in the Supplementary Information (Fig. S1). Crystal data and details of all refinements are given in Tables 1-3, the refined atom parameters are given in Tables 4-6. Further details of the crystal structure investigations may be obtained from Fachinformationszentrum Karlsruhe, 76344 Eggenstein-Leopoldshafen, Germany (fax: (+49)7247-808-666; e-mail: crysdata@fiz-karlsruhe.de, http://www.fiz-

karlsruhe.de/request_for_deposited_data.html) on quoting the depository numbers provided in Tables 1, 3 and 5.

In contrast to all other samples discussed here, new refinements (not shown) fully confirmed that quenched $(GeTe)_{12}Sb_2Te_3$ (n = 12, x = 0) exhibits a trigonal GeTe-type average structure as described earlier.[30] The volume of that trigonal cell is 159.80(1) Å^3, the cube root of the volume (213.07 Å^3) of the corresponding pseudocubic cell is 5.9727 Å. This value was used in Fig. 2, which shows Vegard plots for the tree solid solution series investigated. The cubic lattice parameter *a* increases in a linear fashion when more Ge is substituted by the larger Sn. This confirms the existence of solid solution series of quenched phases $(Ge_{1-x}Sn_xTe)_nSb_2Te_3$ for n = 4, 7 and 12 based on samples with x = 0, 0.25, 0.5, 0.75 and 1.

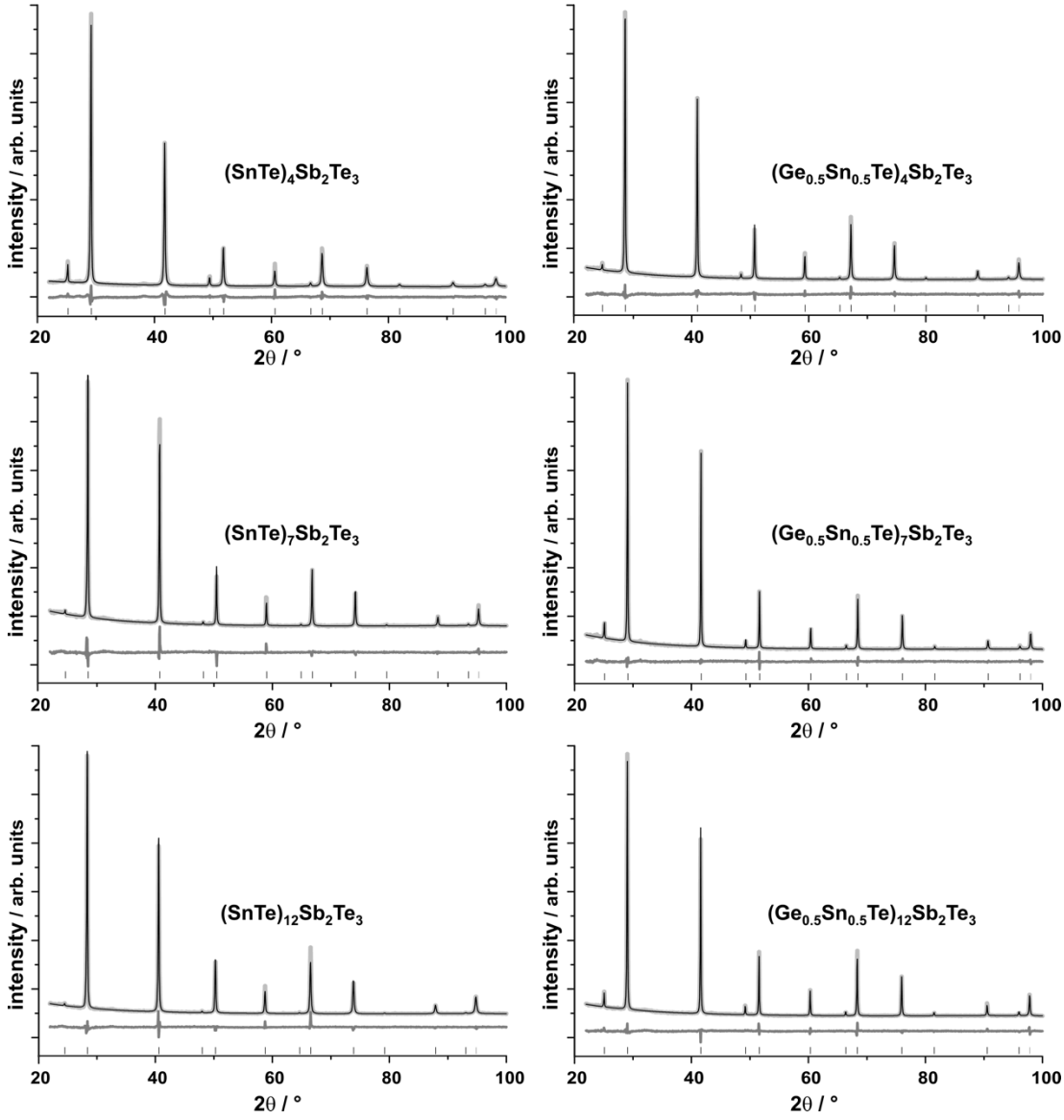

Fig. 1: Profile fits from the Rietveld refinements of $(Ge_{1-x}Sn_xTe)_nSb_2Te_3$ with n = 4, 7, 12 (top to bottom) and x = 1 (left) and x = 0.5 (right); experimental (light gray) and simulated (black) powder patterns, difference plot (below) and reflection markers (black, bottom); the scaling of the 2θ axis is the same for all plots.

Table 1. Details of the Rietveld refinements for $(Ge_{1-x}Sn_xTe)_4Sb_2Te_3$ phases obtained by quenching the HT phase.

sum formula	$Ge_4Sb_2Te_7$	$Ge_3SnSb_2Te_7$	$Ge_2Sn_2Sb_2Te_7$	$GeSn_3Sb_2Te_7$	$Sn_4Sb_2Te_7$
$(Ge_{1-x}Sn_xTe)_4Sb_2Te_3$	x = 0	x = 0.25	x = 0.5	x = 0.75	x = 1
CSD	426870	426869	426866	426861	426862
asymmetric unit	$Ge_{0.571}Sb_{0.286}Te$	$Ge_{0.429}Sb_{0.286}Sn_{0.143}Te$	$Ge_{0.286}Sb_{0.286}Sn_{0.286}Te$	$Ge_{0.143}Sb_{0.286}Sn_{0.429}Te$	$Sb_{0.286}Sn_{0.571}Te$
formula weight asymmetric unit (in g mol^{-1})	203.87	210.45	217.04	223.63	230.22
F(000)	339.4	349.7	360.0	370.4	380.5
crystal system / space group (no.)	cubic / $Fm\bar{3}m$ (225)				
lattice parameters (in Å)	a = 5.988(2)	a = 6.0437(3)	a = 6.10480(17)	a = 6.16579(7)	a = 6.22175(8)
cell volume (in $Å^3$)	214.7(2)	220.75(3)	227.517(19)	234.405(8)	240.845(9)
X-ray density (in g/cm^3)	6.307	6.333	6.337	6.337	6.349
radiation	Cu-$K_{\alpha1}$ (λ = 1.540596 Å)				
2θ range (in °)	22 ≤ 2θ ≤ 100				
parameters (thereof background)	26(6)*		16(6)		
R_p / R_{wp}	0.0287 / 0.0432	0.0278 / 0.0411	0.0313 / 0.0429	0.0248 / 0.0349	0.0196 / 0.0273
GooF / R_{Bragg}	1.550 / 0.0104	1.496 / 0.0111	1.600 / 0.009	1.354 / 0.0103	0.994 / 0.0102

*** with LeBail-Jouanneaux anisotropic broadening**

Table 2. Details of the Rietveld refinements for $(Ge_{1-x}Sn_xTe)_7Sb_2Te_3$ phases obtained by quenching the HT phase.

sum formula	$Ge_7Sb_2Te_{10}$	$Ge_{5.25}Sn_{1.75}Sb_2Te_{10}$	$Ge_{3.5}Sn_{3.5}Sb_2Te_{10}$	$Ge_{1.75}Sn_{5.25}Sb_2Te_{10}$	$Sn_7Sb_2Te_{10}$
$(Ge_{1-x}Sn_xTe)_7Sb_2Te_3$	x = 0	x = 0.25	x = 0.5	x = 0.75	x = 1
CSD	426859	426871	426867	426865	426863
asymmetric unit	$Ge_{0.7}Sb_{0.2}Te$	$Ge_{0.525}Sb_{0.2}Sn_{0.175}$ Te	$Ge_{0.35}Sb_{0.2}Sn_{0.35}Te$	$Ge_{0.175}Sb_{0.2}Sn_{0.525}Te$	$Sb_{0.2}Sn_{0.7}Te$
formula weight asymmetric unit (in g mol^{-1})	202.76	210.85	218.92	226.98	235.05
F(000)	338.4	351.0	363.6	376.2	388.8
crystal system / space group (no.)	cubic / $Fm\bar{3}m$ (225)				
lattice parameters (in Å)	a = 5.99160(6)	a = 6.05668(5)	a = 6.12377(7)	a = 6.19206(11)	a = 6.25520(11)
cell volume (in $Å^3$)	215.094(7)	222.179(6)	229.645(7)	237.414(13)	244.751(13)
X-ray density (in g/cm^3)	6.262	6.303	6.332	6.350	6.379
radiation	Cu-$K_{\alpha1}$ (λ = 1.540596 Å)				
2θ range (in °)	22 ≤ 2θ ≤ 100				
parameters (thereof background)	16 (6)				
R_p / R_{wp}	0.0255 / 0.0371	0.0196 / 0.0278	0.0160 / 0.0222	0.0195 / 0.0268	0.0210 / 0.0333
GooF / R_{Bragg}	1.394 / 0.0267	1.009 / 0.0196	0.785 / 0.0029	0.958 / 0.0059	1.199 / 0.0307

Table 3. Details of the Rietveld refinements for $(Ge_{1-x}Sn_xTe)_{12}Sb_2Te_3$ phases obtained by quenching the HT phase; for $Ge_{12}Sb_2Te_{15}$, see ref. [30].

sum formula	$Ge_9Sn_3Sb_2Te_{15}$	$Ge_6Sn_6Sb_2Te_{15}$	$Ge_3Sn_9Sb_2Te_{15}$	$Sn_{12}Sb_2Te_{15}$
$(Ge_{1-x}Sn_xTe)_{12}Sb_2Te_3$	x = 0.25	x = 0.5	x = 0.75	x = 1
CSD	426860	426858	426868	426864
asymmetric unit	$Ge_{0.6}Sb_{0.133}Sn_{0.2}Te$	$Ge_{0.4}Sb_{0.133}Sn_{0.4}Te$	$Ge_{0.2}Sb_{0.133}Sn_{0.6}Te$	$Sb_{0.133}Sn_{0.8}Te$
formula weight asymmetric unit (in g mol^{-1})	211.13	220.35	229.58	238.80
F(000)	352.0	366.4	380.8	395.2
crystal system / space group (no.)	cubic / $Fm\bar{3}m$ (225)			
lattice parameters (in Å)	a = 6.05352(4)	a = 6.13145(6)	a = 6.21548(12)	a = 6.27778(9)
cell volume (in $Å^3$)	221.832(4)	230.510(7)	240.118(14)	247.411(11)
X-ray density (in g/cm^3)	6.322	6.350	6.350	6.411
radiation	Cu-$K_{\alpha1}$ (λ = 1.540596 Å)			
2θ range (in °)	$22 \le 2\theta \le 100$			
parameters (thereof background)	16(6)			
R_p / R_{wp}	0.0207 / 0.0301	0.0167 / 0.0245	0.0187 / 0.0265	0.0193 / 0.0291
GooF / R_{Bragg}	1.168 / 0.0137	0.872 / 0.0129	0.962 / 0.0114	1.047 / 0.0224

Table 4. Atom coordinates, site occupancies and isotropic displacement parameters (in Å²) for $(Ge_{1-x}Sn_xTe)_4Sb_2Te_3$ samples obtained by quenching the HT phase.

		Te			cations and vacancies			
	x	position		B_{iso}	position		occupancy	B_{iso}
$(GeTe)_4Sb_2Te_3$	0	4*a*	½ ½ ½	1.67(8)	4*b*	0 0 0	4/7 Ge, 2/7 Sb	3.81(11)
$(Ge_{0.75}Sn_{0.25}Te)_4Sb_2Te_3$	0.25	4*a*	½ ½ ½	1.52(10)	4*b*	0 0 0	3/7 Ge, 1/7 Sn, 2/7 Sb	3.71(14)
$(Ge_{0.5}Sn_{0.5}Te)_4Sb_2Te_3$	0.5	4*a*	½ ½ ½	1.71(6)	4*b*	0 0 0	2/7 Ge, 2/7 Sn, 2/7 Sb	3.75(9)
$(Ge_{0.25}Sn_{0.75}Te)_4Sb_2Te_3$	0.75	4*a*	½ ½ ½	1.00(4)	4*b*	0 0 0	1/7 Ge, 3/7 Sn, 2/7 Sb	2.84(6)
$(SnTe)_4Sb_2Te_3$	1	4*a*	½ ½ ½	0.98(5)	4*b*	0 0 0	4/7 Sn, 2/7 Sb	2.52(7)

Table 5. Atom coordinates, site occupancies and isotropic displacement parameters (in Å²) for $(Ge_{1-x}Sn_xTe)_7Sb_2Te_3$ samples obtained by quenching the HT phase.

		Te			cations and vacancies			
	x	position		B_{iso}	position		occupancy	B_{iso}
$(GeTe)_7Sb_2Te_3$	0	4*a*	½ ½ ½	0.70(4)	4*b*	0 0 0	7/10 Ge, 1/5 Sb	2.55(5)
$(Ge_{0.75}Sn_{0.25}Te)_7Sb_2Te_3$	0.25	4*a*	½ ½ ½	1.07(4)	4*b*	0 0 0	21/40 Ge, 7/40 Sn, 1/5 Sb	2.84(6)
$(Ge_{0.5}Sn_{0.5}Te)_7Sb_2Te_3$	0.5	4*a*	½ ½ ½	1.57(5)	4*b*	0 0 0	7/20 Ge, 7/20 Sn, 1/5 Sb	3.08(7)
$(Ge_{0.25}Sn_{0.75}Te)_7Sb_2Te_3$	0.75	4*a*	½ ½ ½	0.89(7)	4*b*	0 0 0	7/40 Ge, 21/40 Sn, 2/5 Sb	2.31(9)
$(SnTe)_7Sb_2Te_3$	1	4*a*	½ ½ ½	1.41(8)	4*b*	0 0 0	7/10 Sn, 1/5 Sb	2.82(10)

Table 6. Atom coordinates, site occupancies and isotropic displacement parameters (in Å²) for $(Ge_{1-x}Sn_xTe)_{12}Sb_2Te_3$ samples obtained by quenching the HT phase.

		Te			cations and vacancies			
	x	position		B_{iso}	position		occupancy	B_{iso}
$(Ge_{0.75}Sn_{0.25}Te)_{12}Sb_2Te_3$	0.25	4*a*	½ ½ ½	0.80(3)	4*b*	0 0 0	9/15 Ge, 3/15 Sn, 2/15 Sb	2.65(4)
$(Ge_{0.5}Sn_{0.5}Te)_{12}Sb_2Te_3$	0.5	4*a*	½ ½ ½	1.02(4)	4*b*	0 0 0	6/15 Ge, 6/15 Sn, 2/15 Sb	2.59(6)
$(Ge_{0.25}Sn_{0.75}Te)_{12}Sb_2Te_3$	0.75	4*a*	½ ½ ½	0.80(6)	4*b*	0 0 0	3/15 Ge, 9/15 Sn, 2/15 Sb	1.88(8)
$(SnTe)_{12}Sb_2Te_3$	1	4*a*	½ ½ ½	0.89(6)	4*b*	0 0 0	12/15 Sn, 2/15 Sb	1.92(8)

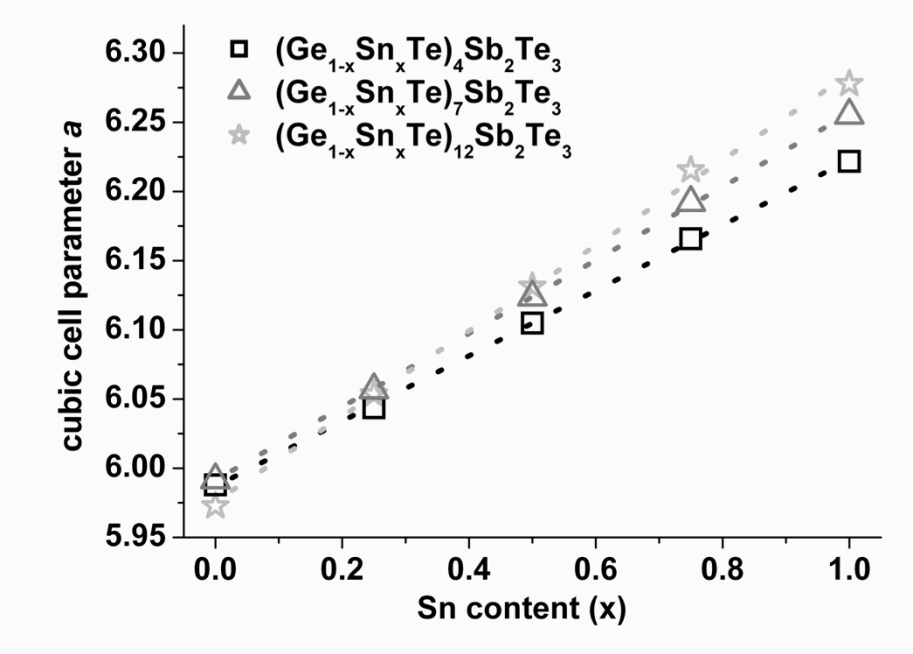

Fig. 2: Vegard plots for (pseudo-)cubic phases $(Ge_{1-x}Sn_xTe)_nSb_2Te_3$ with linear least-squares fits for n = 4 (black triangles and line), 7 (gray squares and line), 12 (light gray stars and line): lattice parameters vs. increasing Sn-content x (for $Ge_{12}Sb_2Te_{15}$ [30] the cube root of the volume of the trigonal cell was used).

2.3.2.3.2 Thermal behavior of quenched phases

Temperature-dependent X-ray investigations reveal the influence of the Sn doping on the phase transition temperatures (Fig. 3 and Table 7). Starting from the quenched (pseudo-)cubic $(Ge_{1-x}Sn_xTe)_nSb_2Te_3$ samples with short-range ordered vacancies (see TEM investigation below), two structural changes occur when the samples are heated and one upon subsequent cooling. All transformations depend on the vacancy concentration. Upon heating to T1, the vacancies undergo re-ordering processes that lead to the thermodynamically stable trigonal phase with parallel defect planes extended in 2D (i.e., van der Waals gaps). This involves a trigonal distortion whose temperature, as a rule, neither depends significantly on the vacancy concentration nor on the Sn content; it occurs at 260 °C. The transformation from this trigonal phase to the cubic HT phase sets in at T2, when the latter's stability region is reached. This starts at lower temperatures for samples with lower vacancy concentrations (i.e. higher n) since this means less anions with low coordinaton numbers. Rocksalt-type phases become less favorable with very high defect concentrations as these involve many "under-coordinated" Te atoms. With increasing Sn content x, T2 becomes lower as shown for n = 4. For x = 0.5, T2 is up to 100 °C lower than for unsubstituted samples which exhibit T2 of 500 °C and 460 – 500 °C for n = 7, 12, respectively.[3]

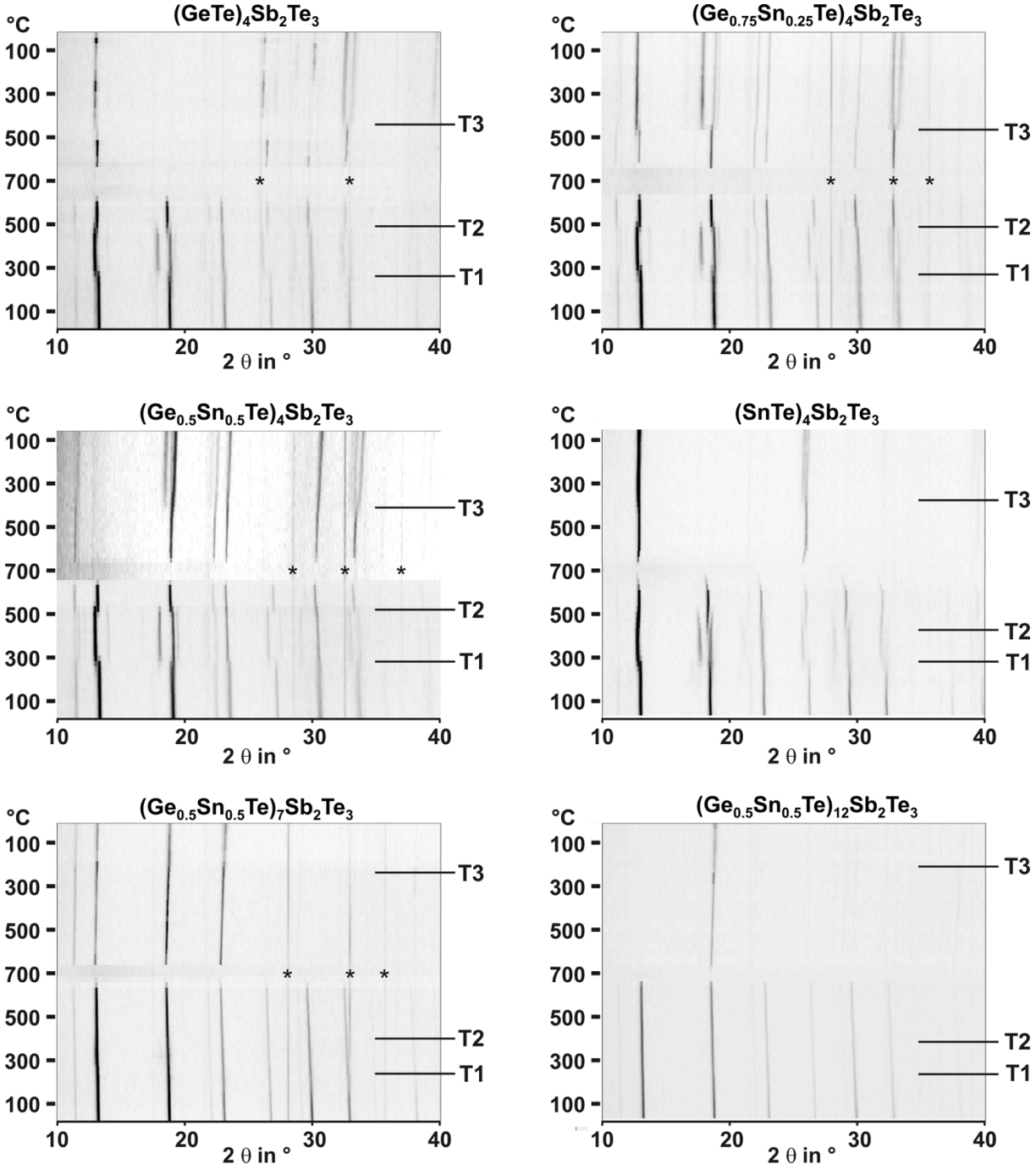

Fig. 3: Temperature-dependent X-ray powder diffraction patterns of quenched samples of $(Ge_{1-x}Sn_xTe)_nSb_2Te_3$: heating and cooling (bottom to middle and middle to top, respectively, in each image; reflections originating from the furnace are marked with asterisks, *); the phase transition temperatures T1, T2 and T3 (see the text) are highlighted with black horizontal lines. The reduced number and intensities of certain reflections during cooling results from preferred orientation as a result of recrystallization from the melt in small capillaries.

When the samples are slowly cooled down below the stability range of the cubic HT phase, the transformation from the cubic to the rhombohedral phase occurs at T3. In analogy to T2, T3 is lower for higher Sn contents x. For higher GeTe contents n, samples with x = 0.5 exhibit

lower T3 (by up to 250 °C) in comparison to GST samples with T3 = 460 °C for n = 7 and 12.[3] Due to the lower phase transition temperatures T2 and T3, which are expected for mixed crystals, it is easier to obtain the (pseudo-)cubic phase by quenching samples with higher Sn contents x and lower vacancy concentrations (i.e. higher n).

For higher GeTe contents, the trigonal distortion of slowly cooled phases $(Ge_{0.5}Sn_{0.5}Te)_nSb_2Te_3$ (n = 4, 7, 12) is less pronounced, i.e. the metrics remains closer to cubic. This is more pronounced for Sn-containing samples. The formation of the trigonal layered phase during heating is only obvious from reflection splittings for n = 4, while $(Ge_{0.5}Sn_{0.5}Te)_7Sb_2Te_3$ and $(Ge_{0.5}Sn_{0.5}Te)_{12}Sb_2Te_3$ show only a minor splitting or broadening, of the corresponding reflections upon slow cooling. The melting points increase with higher GeTe contents (as for unsubstituted samples), while the Sn substitution decreases the melting point only very little.

Table 7. Phase transition temperatures for $(Ge_{1-x}Sn_xTe)_nSb_2Te_3$ (see text).

phase transition	n = 4 x = 0	n = 4 x = 0.25	n = 4 x = 0.5	n = 4 x = 1	n = 7 x = 0.5	n = 12 x = 0.5
pseudo-cubic → trigonal (T1)	260 °C	260 °C	260 °C	260 °C	260 °C	260 °C
trigonal → cubic (heating) (T2)	490 °C	470 °C	460°C	410 °C*	410 °C	390 °C
cubic → trigonal (cooling) (T3)	470 °C	465 °C	460 °C	420 °C	260 °C	220 °C
melting point	630°C	610 °C	610 °C	610 °C	640 °C	660 °C

* cubic and trigonal phase coexist from 410 to 510 °C in the TPXRD due to time-dependent effects.

2.3.2.3.3 Influence of the Sn substitution on the nanostructure

TEM investigations show how the Sn substitution influences the nanostructure of pseudocubic quenched materials $(Ge_{1-x}Sn_xTe)_nSb_2Te_3$ (n = 4, 7, 12, x = 0, 0.5). The composition of the investigated regions was verified by TEM-EDX (cf. Supplementary Information Table S4). STEM-HAADF images (Fig. 4) show that Sn substituted GST contains intersecting vacancy layers comparable to those in GST itself.[3,30] HRTEM images reveal the parquet-like structure in all of these samples (Fig. 5). Similar to unsubstituted GST, $(Ge_{0.5}Sn_{0.5}Te)_nSb_2Te_3$ samples exhibit less vacancy layers for higher n, i.e. for lower defect concentrations. However, $(Ge_{0.5}Sn_{0.5}Te)_4Sb_2Te_3$ exhibits a more pronounced parquet-like structure than the corresponding $(GeTe)_4Sb_2Te_3$ and occasionally a tendency towards superstructure formation. Yet, the SAED patterns shown in Fig. 5 are typical and indicate no long-range order. Slight differences between GST and Sn-substituted variants may be a consequence of kinetic effects due to the lower bonding energy Sn-Te (359.8 kJ/mol) in comparison to Ge-Te (397 kJ/mol) which makes structural rearrangements easier.[31,32]

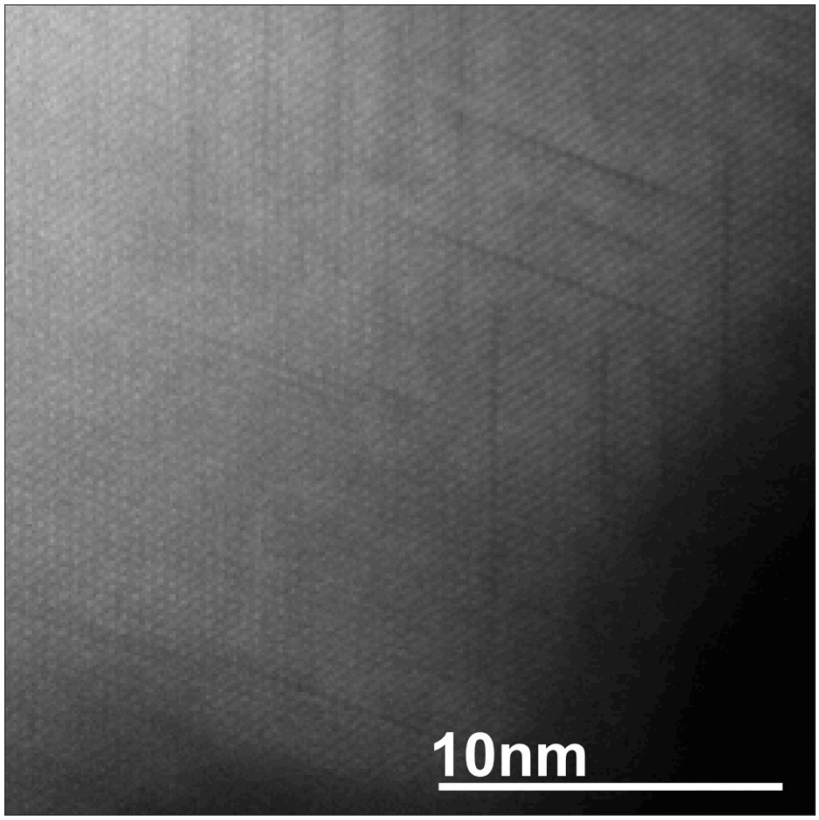

Fig. 4: Z-contrast image (STEM -HAADF) of the parquet-like structure of a quenched sample with the nominal composition $(Ge_{0.5}Sn_{0.5}Te)_4Sb_2Te_3$.

Although Rietveld refinements show a cubic average structure of the quenched phases, some SAED patterns reveal slight metric distortions as evidenced by angles down to 88.2° between the (pseudo-)cubic [110] and [001] directions. The cubic metrics is probably a result of stresses in the quenched samples after the "incomplete" phase transition. In the very thin fringes suitable for TEM, a certain metric relaxation towards rhombohedral structures may occur. Comparable effects of stress and strain in GST samples have been shown to depend on the crystallite size.[30]

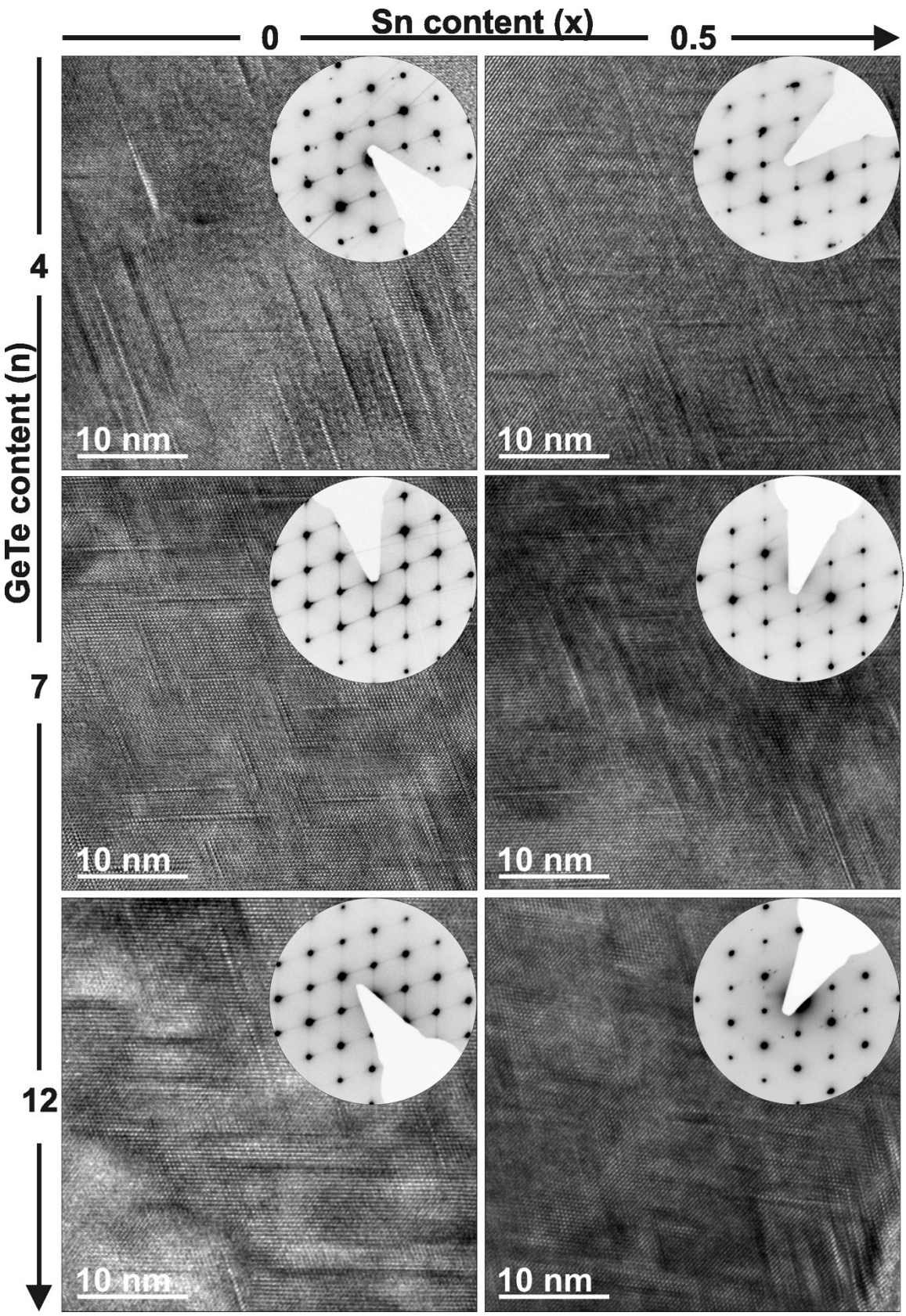

Fig. 5: HRTEM images and corresponding SAED patterns (insets) of $(Ge_{1-x}Sn_xTe)_nSb_2Te_3$ with x = 0 (left) and x = 0.5 (right); from top to bottom with n = 4, 7, 12.

2.3.2.3.4 Thermoelectric properties

The influence of the Sn substitution and its interplay with the defect concentration on the thermoelectric properties was investigated for $(Ge_{0.5}Sn_{0.5}Te)_nSb_2Te_3$ with n = 4, 7, 12 (cf. Fig. 6). For comparison, results of comparable samples of $(GeTe)_7Sb_2Te_3$ and $(GeTe)_{12}Sb_2Te_3$ were taken from Ref. [3]; data for $(GeTe)_4Sb_2Te_3$ were obtained in the present study (cf. Supplementary Information Fig. S2). The phase purity of the ingots used for thermoelectric measurements was verified by Rietveld refinements with the same parameters as described in Section 2 (details of these refinements are given in Supplementary Information Table S5; for $(GeTe)_4Sb_2Te_3$ and $(Ge_{0.5}Sn_{0.5}Te)_4Sb_2Te_3$ the use of anisotropic microstrain and crystallite size broadening was necessary). These Rietveld refinements are inferior to the ones shown above as the reflections of the samples used for thermoelectric measurements are broadened as a consequence of lower quenching rates due to the larger sample volumes, especially for $(Ge_{0.5}Sn_{0.5}Te)_4Sb_2Te_3$.

The values for σ and S in consecutive measurement cycles (except during the initial heating) are similar, they are shown for $(Ge_{0.5}Sn_{0.5}Te)_{12}Sb_2Te_3$ in the Supplementary Information (Fig. S4). The Seebeck coefficient S of $(Ge_{0.5}Sn_{0.5}Te)_nSb_2Te_3$ with n = 4 is lower that those for n = 7 and 12. All samples show positive values of S that increase with temperature, corresponding to p-type semiconductors. The values, including the effects associated with the phase transition, are very similar to those of the corresponding unsubstituted GST materials except for $(Ge_{0.5}Sn_{0.5}Te)_7Sb_2Te_3$, whose S is higher than that of $(GeTe)_7Sb_2Te_3$[3] over the whole temperature range (up to 30 μV/K). Both for GST itself[3] and for $(Ge_{0.5}Sn_{0.5}Te)_nSb_2Te_3$, σ is lowest for the intermediate defect concentration with n = 7. Decreasing form 810 S/cm to 560 S/cm from 50 °C to 450 °C, respectively, the values for $(Ge_{0.5}Sn_{0.5}Te)_7Sb_2Te_3$ are much higher than those of $(GeTe)_7Sb_2Te_3$ which exhibits the lowest σ of all (pseudo-)cubic GST samples investigated so far (decreasing from 350 S/cm at 50 °C to 150 S/cm at 450 °C). For the other samples the difference is less pronounced: σ of $(Ge_{0.5}Sn_{0.5}Te)_4Sb_2Te_3$ is comparable to that of $(GeTe)_4Sb_2Te_3$ at elevated temperatures (cf. Supplemantary Information Fig. S2) while $(Ge_{0.5}Sn_{0.5}Te)_{12}Sb_2Te_3$ exhibits a lower σ compared to $(GeTe)_{12}Sb_2Te_3$.

While κ of all $(Ge_{0.5}Sn_{0.5}Te)_nSb_2Te_3$ samples converges at HT, $(Ge_{0.5}Sn_{0.5}Te)_7Sb_2Te_3$ has a much lower κ up to 250 °C than $(Ge_{0.5}Sn_{0.5}Te)_{12}Sb_2Te_3$. Whereas κ of $(Ge_{0.5}Sn_{0.5}Te)_4Sb_2Te_3$ is not reversible after the first heating cycle, for $(Ge_{0.5}Sn_{0.5}Te)_7Sb_2Te_3$ and $(Ge_{0.5}Sn_{0.5}Te)_{12}Sb_2Te_3$ it is only slightly lower during cooling than during heating. This reflects the strong influence of the high defect concentration and the tendency to form a long-

range ordered structure in $(Ge_{0.5}Sn_{0.5}Te)_4Sb_2Te_3$. $(Ge_{0.5}Sn_{0.5}Te)_{12}Sb_2Te_3$ and $(GeTe)_{12}Sb_2Te_3$ exhibit comparable κ during heating; however, the values for $(Ge_{0.5}Sn_{0.5}Te)_4Sb_2Te_3$ and $(Ge_{0.5}Sn_{0.5}Te)_7Sb_2Te_3$ are significantly higher than for pure GST (below 250 °C: 1.2 -1.3 W/mK vs. 0.8 W/mK and 1.4 – 1.5 W/mK vs. 1.0 W/mK, respectively). This is due to the higher σ and the resulting higher electronic contribution (κ_{el}) to κ of the Sn-containing samples. The phononic part κ_L, which is more characteristic for real-structure effects was calculated using a Lorenz number of $1.48 \cdot 10^{-8}$ $W\Omega K^{-2}$ for all samples, which is a typical value for degenerate semiconductors.[33] There is little difference in κ_L for the samples with n = 7 and 12 (cf. Supplementary Information Fig. S3) whereas for n = 4, it is significantly lower during the initial heating cycle. Above ~250 °C and after cooling, the parquet-like nanostructure is not present; consequently κ_L of all $(Ge_{1-x}Sn_xTe)_nSb_2Te_3$ samples (n = 4, 7, 12, x = 0, 0.5) then converges to ~ 1.0 W/mK. All changes in κ and κ_L start around 250 °C where the transition from the parquet-like nanostructure to the trigonal phase sets in (T1 = 260° C). A comparable effect was observed for quenched $(GeTe)_nSb_2Te_3$ (n = 7, 12) which exhibit significantly lower κ_L and consequently higher *ZT* values than slowly cooled or annealed samples with the same composition.[3]

The comparison of the *ZT* values of $(Ge_{1-x}Sn_xTe)_nSb_2Te_3$ in Fig. 7 shows that Sn substitution is most beneficial for defect-rich $(Ge_{1-x}Sn_xTe)_nSb_2Te_3$ (i.e., n = 4, 7) where the higher electrical conductivity results in higher *ZT* values. Compared to $(GeTe)_7Sb_2Te_3$, the combination of the increased σ with a higher *S* results in a strong increase of *ZT* for $(Ge_{0.5}Sn_{0.5}Te)_7Sb_2Te_3$, reaching 0.7 at 400 °C.

Whereas we report on chemically homogeneous samples, improved thermoelectric properties, especially a reduction of the thermal conductivity has also been achieved with nanostructured bulk materials, e.g. in systems based on GeTe and PbTe, often with additional Sb_2Te_3.[34-37] In the system PbTe/PbS[38,39], temperature-induced nucleation leads to nanoprecipitates which are very beneficial due to the reduction of lattice thermal conductivities in bulk samples. Although the annealing processes involved seem very similar to the ones we describe, in GST materials and substitution variants thereof, annealing results in a higher degree of order in a chemically homogeneous system and thus is not beneficial. Long-range order in annealed samples hinders phonon proliferation less effectively compared to the short-range ordered nanostructures in the quenched samples. Thus, prolonged annealing is expected to reduce *ZT*, yet, several months would be required to reach the thermodynamical equilibrium.[40]

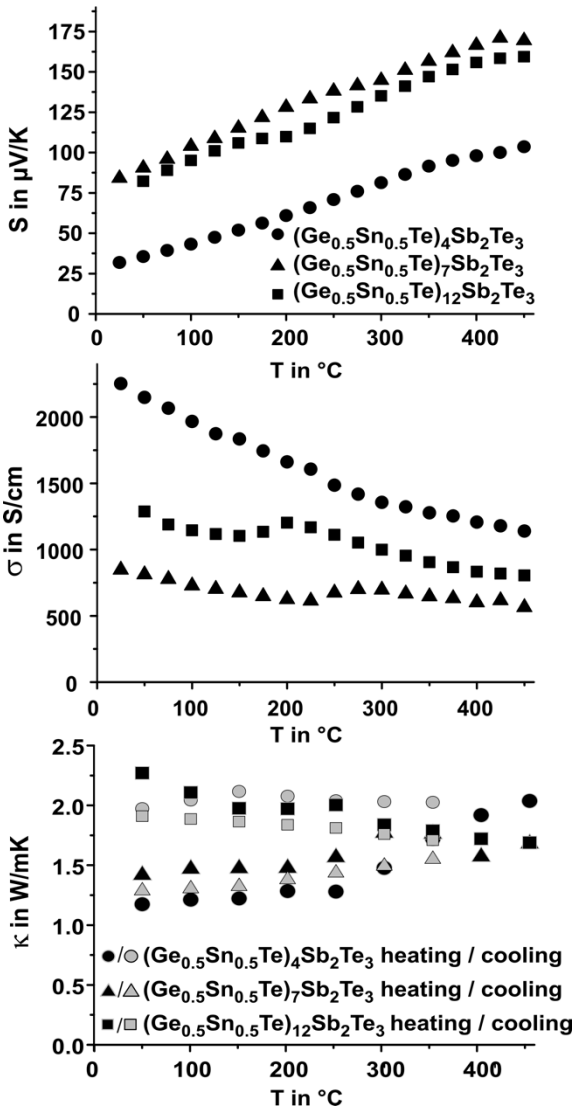

Fig. 6: Thermoelectric properties of $(Ge_{0.5}Sn_{0.5}Te)_nSb_2Te_3$ with n = 4 (circles), 7 (triangles) and 12 (squares); from top to bottom: Seebeck coefficient (*S*), electrical conductivity (σ) and thermal conductivity (κ, black symbols heating, gray symbols cooling); for *S* and σ the average of the heating and cooling curve is shown (these curves do not differ significantly).

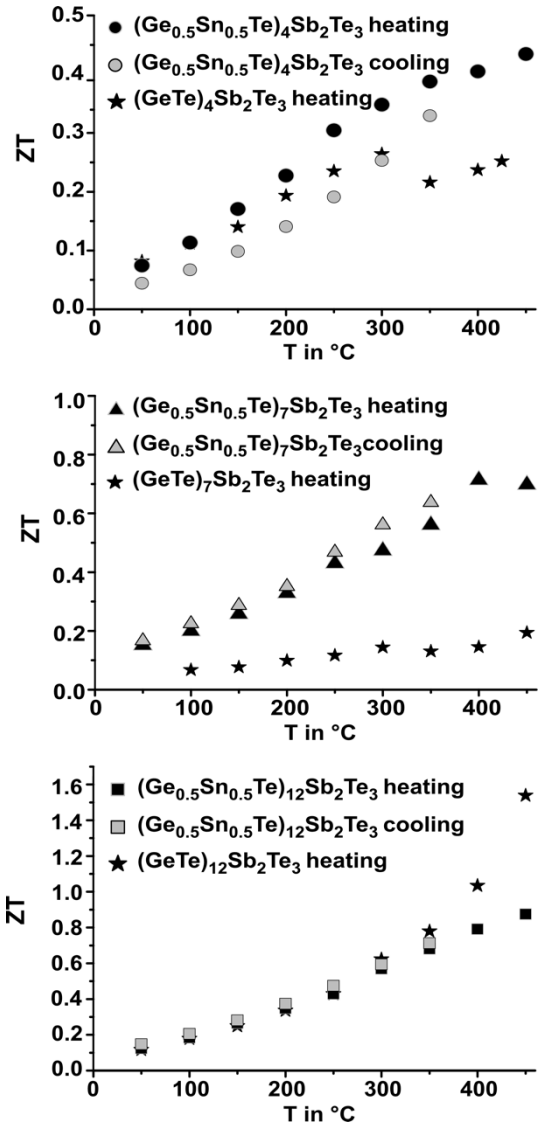

Fig. 7: Thermoelectric figure of merit ZT of $(Ge_{1-x}Sn_xTe)_nSb_2Te_3$) with x = 0 (asterisks) and x = 0.5 (n = 4: circles, left; n = 7: triangles, middle, n = 12: squares, right); for *S* and σ the average of the heating and cooling curves (as shown in Fig. 6) was used; for $(Ge_{0.5}Sn_{0.5}Te)_nSb_2Te_3$ *ZT* was calculated separately with the κ values of the heating and cooling cycle. The values for $(GeTe)_7Sb_2Te_3$ and $(GeTe)_{12}Sb_2Te_3$ are taken from measurements identical to those in Ref. [3]. For these samples - and also for $(GeTe)_4Sb_2Te_3$ - only heating curves for κ were measured.

2.3.2.4 Conclusion

Pseudocubic sample of the solid solutions $(Ge_{1-x}Sn_xTe)_nSb_2Te_3$ exhibit 2-3 times higher electrical conductivities for samples with high defect concentrations (i.e., n = 4, 7), which result in higher thermoelectric figures of merit *ZT*. The phase transitions observed by PXRD are comparable to those of GST materials but occur at significantly lower temperatures. These transitions are often seen in temperature-dependent conductivity measurements, too. The nanostructure of quenched Sn-containing samples is characterized by intersecting defect layers and thus comparable to that of GST materials. For high vacancy concentrations, however, the parquet-like arrangement of defect layers becomes more pronounced upon Sn substitution. In combination with the improved Seebeck coefficient this results in *ZT* values of up to 0.7 at 400 °C for $(Ge_{0.5}Sn_{0.5}Te)_7Sb_2Te_3$ compared to 0.2 for $(GeTe)_7Sb_2Te_3$. Since the nanostructures develop during quenching, long-range ordered phases do not form when diffusion rates are rather low. Therefore, in general, low transition temperatures are desirable. Comparable to In-substituted samples, the metrics of the layered structures that are thermodynamically stable at ambient conditions are closer to cubic in Sn-containing samples, especially for lower vacancy concentrations (n = 7, 12). This probably contributes to the fact that pseudocubic phase can be obtained more easily in quaternary phases. Such changes in the phase stabilities might be utilized to improve the phase-change properties of GST materials for data storage devices.

Acknowledgments

The authors thank T. Miller (LMU Munich) for the acquisition of temperature-dependent powder diffraction patterns, C. Minke (LMU Munich) for SEM-EDX analyses and W. Schönau (DLR Cologne) for the temperature-dependent measurements of D_{th} and c_p. The generous support of this work by Prof. Dr. W. Schnick and the funding by the Deutsche Forschungsgemeinschaft (grant OE530/1-2) are greatly appreciated.

2.3.2.5 Supplementary Information

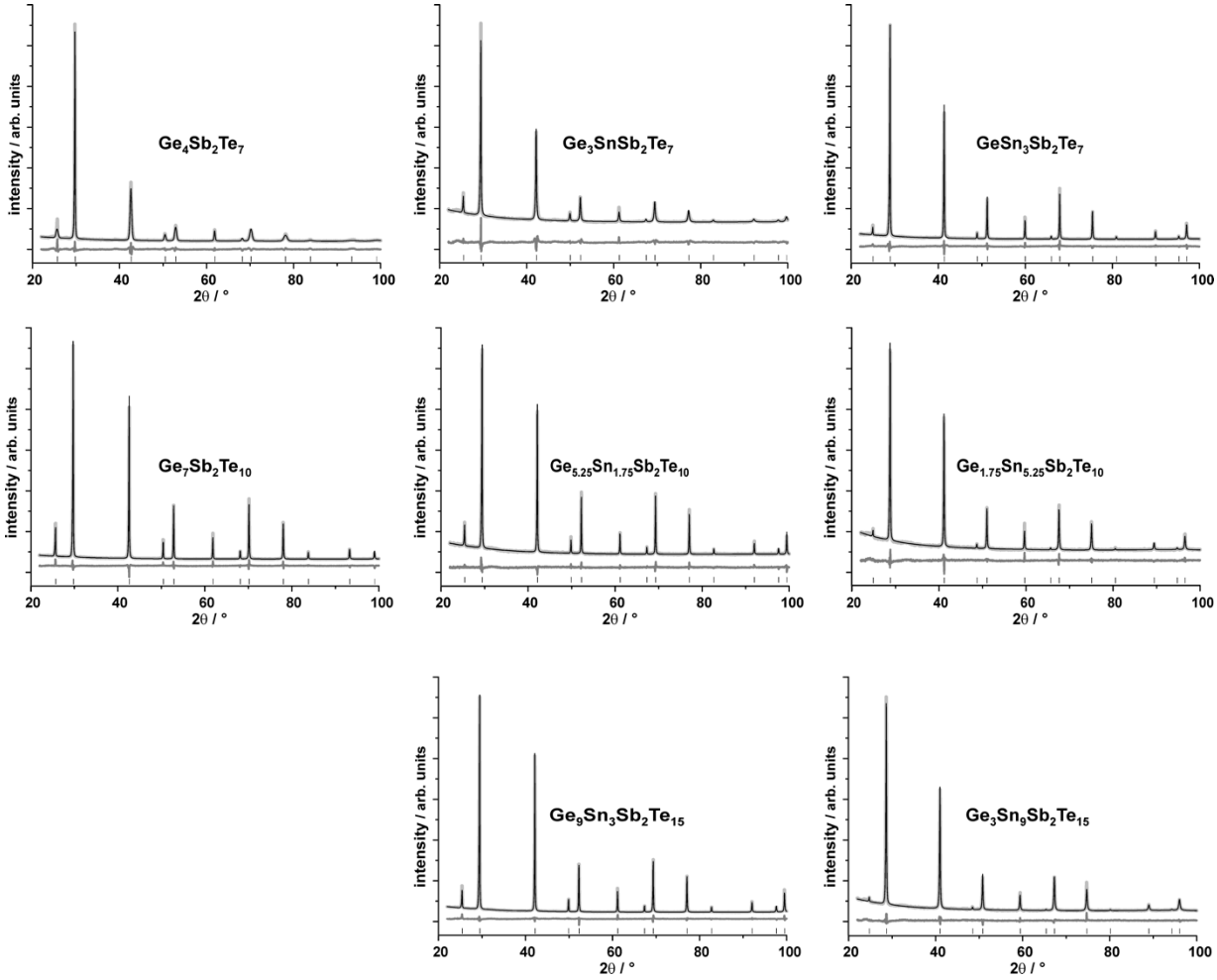

Fig. S1: Profile fits from the Rietveld refinements of $(Ge_{1-x}Sn_xTe)_nSb_2Te_3$ for n = 4, 7, 12 (top to bottom) with x = 0 (left), x = 0.25 (middle) and x = 0.75 (right); measured (light gray) and simulated (black) powder patterns, difference plot (below) and reflection markers (black, bottom); the scaling of the 2ϑ axis is the same for all plots.

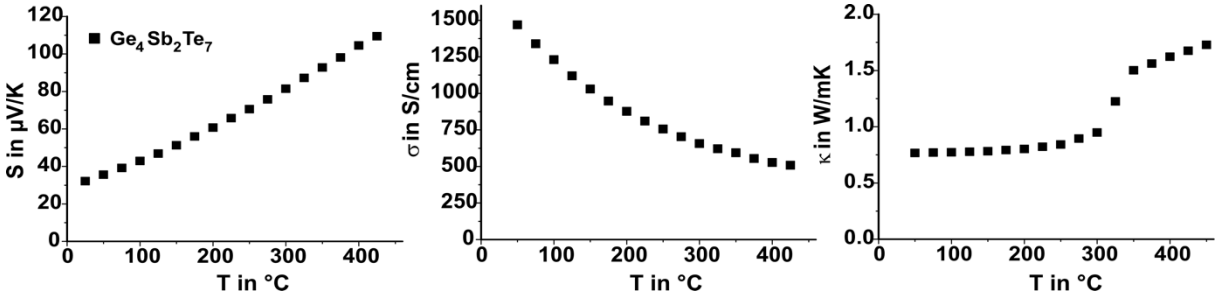

Fig. S2: Thermoelectric properties of $Ge_4Sb_2Te_7$: Seebeck coefficient (left) and electrical conductivity (middle) as interpolated and averaged values from heating and cooling measurements, heating measurement for the thermal conductivity (experimental procedure analogous to the measurements shown in the text).

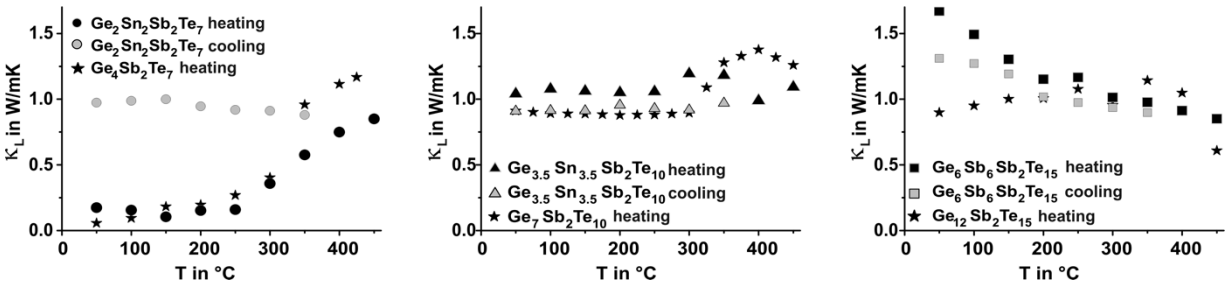

Fig. S3: Lattice part of the thermal conductivity of $(Ge_{1-x}Sn_xTe)_nSb_2Te_3$ with x = 0 (asterisks) and x = 0.5 (n = 4: circles, left side; n = 7: triangles, middle, n = 12: squares, right side) calculated from the heating and cooling curves of κ combined with the averaged heating and cooling curves (which do not differ significantly!), the same Lorenz number of $1.48 \cdot 10^{-8}$ $W\Omega K^{-2}$ was used for all samples. The electrical and thermal conductivities for $Ge_7Sb_2Te_{10}$ and $Ge_{12}Sb_2Te_{15}$ are taken from T. Rosenthal, M. N. Schneider, C. Stiewe, M. Döblinger, O. Oeckler, *Chem. Mater.* **2011**, *23*, 4349-4356; for these samples - and also for $Ge_4Sb_2Te_7$ - only heating curves for κ were measured.

Table S1. Detailed synthesis conditions for the samples $(Ge_{1-x}Sn_xTe)_nSb_2Te_3$ (n = 4, 7, 12; $0 \leq x \leq 1$) discussed in the text.

composition	used for	melting temp. / time	annealing temp. / time
$Ge_4Sb_2Te_7$	Rietveld, TEM, TPXRD	950 °C, 1h	590 °C , 2.5 d
	TE	950 °C, 1h	590 °C, 2.5 d
$Ge_3SnSb_2Te_7$	Rietveld, TPXRD	950 °C, 9d	590 °C, 20 h
$Ge_2Sn_2Sb_2Te_7$	Rietveld, TEM, TPXRD	950 °C, 1.5 h	590 °C, 20 h
	TE	900 °C, 4h	600 °C, 2d
$GeSn_3Sb_2Te_7$	Rietveld, TPXRD	950 °C, 9d	600 °C, 20 h
$Sn_4Sb_2Te_7$	Rietveld, TPXRD	900 °C, 5h	600 °C, 10d
$Ge_7Sb_2Te_{10}$	Rietveld, TEM	950 °C, 4.5 h	590 °C, 2d
$Ge_{5.25}Sn_{1.75}Sb_2Te_{10}$	Rietveld	950 °C, 2h	566 °C, 10 d
$Ge_{3.5}Sn_{3.5}Sb_2Te_{10}$	Rietveld, TPXRD	950 °C, 4d	566 °C, 2d
	TE, TEM	900 °C, 5d	590 °C, 2d
$Ge_{1.75}Sn_{5.25}Sb_2Te_{10}$	Rietveld	950 °C, 2.5h	566 °C, 10 d
$Sn_7Sb_2Te_{10}$	Rietveld	950 °C, 2.5h	566 °C, 10 d
$Ge_{12}Sb_2Te_{15}$	TEM	950 °C, 4h	500 °C, 20 h
$Ge_9Sn_3Sb_2Te_{15}$	Rietveld	900 °C, 3 h	590 °C, 3d
$Ge_6Sn_6Sb_2Te_{15}$	Rietveld, TPXRD	950 °C, 20h	560 °C, 1d
	TEM	950 °C, 15h	610 °C, 1d
	TE	900 °C, 4d	590 °C, 2d
$Ge_3Sn_9Sb_2Te_{15}$	Rietveld	950 °C, 20h	570 °C, 30h
$Sn_{12}Sb_2Te_{15}$	Rietveld	950 °C, 4.5h	605 °C, 10d

Table S2. REM-EDX results for selected $(Ge_{1-x}Sn_xTe)_nSb_2Te_3$ samples

sample	calculated composition (at.-%)	measured composition (at.-%)
$Ge_{5.25}Sn_{1.75}Sb_2Te_{10}$	$Ge_{27.6}Sn_{9.2}Sb_{10.5}Te_{52.6}$	$Ge_{28.2(8)}Sn_{9.2(2)}Te_{10.7(1)}Te_{51.8(5)}$ (3 points)
$Ge_{3.5}Sn_{3.5}Sb_2Te_{10}$	$Ge_{18.4}Sn_{18.4}Sb_{10.5}Te_{52.6}$	$Ge_{17.3}Sn_{18.7}Sb_{11.5}Te_{52.5}$(1 point)
$Ge_{1.75}Sn_{5.25}Sb_2Te_{10}$	$Ge_{9.2}Sn_{27.6}Sb_{10.5}Te_{52.6}$	$Ge_{10.3(2)}Sn_{29.0(3)}Sb_{9.8(5)}Te_{50.9(6)}$ (3 points)
$Sn_7Sb_2Te_{10}$	$Sn_{36.8}Sb_{10.5}Se_{52.6}$	$Ge_{39.2(4)}Sb_{9.1(2)}Te_{51.6(2)}$ (3 points)
$Sn_{12}Sb_2Te_{15}$	$Sn_{41.4}Sb_{6.9}Te_{51.7}$	$Sn_{44.3(5)}Sb_{4.7(6)}Te_{51.0(3)}$ (3 points)
$Ge_6Sb_6Sb_2Te_{15}$	$Ge_{20.7}Sn_{20.7}Sb_{6.9}Te_{51.7}$	$Ge_{21.5(3)}Sn_{21.3(3)}Sb_{5.7(3)}Te_{51.6(5)}$ (3 points)
$Ge_3Sn_9Sb_2Te_{15}$	$Ge_{10.3}Sn_{31.0}Sb_{6.9}Te_{51.7}$	$Ge_{10.2(2)}Sn_{34.1(1)}Sb_{5.5(4)}Te_{50.1(2)}$ (2 points)

Table S3. TEM-EDX results for $(Ge_{1-x}Sn_xTe)_nSb_2Te_3$ for all samples investigated by TEM

sample	calculated composition (at.-%)	measured composition (at.-%)
$Ge_4Sb_2Te_7$	$Ge_{30.8}Sb_{15.4}Te_{53.8}$	$Ge_{32.3(5)}Sb_{14.9(9)}Te_{52.8(1.3)}$ (3 points)
$Ge_2Sn_2Sb_2Te_7$	$Ge_{15.4}Sn_{15.4}Sb_{15.4}Te_{53.8}$	$Ge_{14.1(5)}Sn_{17.5(8)}Te_{15.9(9)}Te_{52.5(6)}$ (2 points)
$Ge_7Sb_2Te_{10}$	$Ge_{36.8}Sb_{10.5}Se_{52.6}$	$Ge_{36.1(4.0)}Sb_{9.4(8)}Te_{54.5(3.1)}$ (2 points)
$Ge_{3.5}Sn_{3.5}Sb_2Te_{10}$	$Ge_{18.4}Sn_{18.4}Sb_{10.5}Te_{52.6}$	$Ge_{18.5(2)}Sn_{19.2(1.3)}Sb_{9.9(1)}Te_{52.3(1.6)}$ (2 points)
$Ge_{12}Sb_2Te_{15}$	$Ge_{41.4}Sb_{6.9}Te_{51.7}$	$Ge_{41.9(1.3)}Sb_{5.4(1)}Te_{52.8(1.2)}$ (2 points)
$Ge_6Sb_6Sb_2Te_{15}$	$Ge_{20.7}Sn_{20.7}Sb_{6.9}Te_{51.7}$	$Ge_{20.5}Sn_{19.3}Sb_{9.8}Te_{50.4}$ (1 point)

Table S4. Details of the Rietveld refinements for the samples used for thermoelectric measurements of quenched $(Ge_{1-x}Sn_xTe)_nSb_2Te_3$ phases.

	$Ge_4Sb_2Te_7$	$Ge_2Sn_2Sb_2Te_7$	$Ge_{3.5}Sn_{3.5}Sb_2Te_{10}$	$Ge_6Sn_6Sb_2Te_{15}$
asymmetric unit	$Ge_{0.571}Sb_{0.286}Te$	$Ge_{0.286}Sb_{0.286}Sn_{0.286}Te$	$Ge_{0.35}Sb_{0.2}Sn_{0.35}Te$	$Ge_{0.4}Sb_{0.133}Sn_{0.4}Te$
formula weight of the asymmetric unit (in g mol^{-1})	203.87	217.04	218.92	220.35
F(000)	339.43	360.00	363.60	366.4
crystal system / space group (no.)	cubic / $Fm\bar{3}m$ (225)			
lattice parameters (in Å)	a = 5.974(2)	a = 6.045(2)**	a = 6.1180(2)	a = 6.1322(2)
cell volume (in $Å^3$)	213.2(2)	220.9(2)	229.00(3)	230.60(2)
density (X-ray, in g/cm^3)	6.351(6)	6.527(6)	6.3496(7)	6.3473(5)
radiation	Cu-$K_{\alpha1}$ (λ = 1.540596 Å)			
2θ range (in °)	$22 \le 2\theta \le 100$			
parameters (thereof background)	26(6)*		16(6)	
R_p / R_{wp}	0.030 / 0.044	0.049 / 0.071	0.029 / 0.040	0.022 / 0.032
GooF / R_{Bragg}	1.585 / 0.007	2.793 / 0.040 **	1.527 / 0.008	1.239 / 0.007

* Le Bail-Jouanneaux treatment of anisotropic peak broadening and anisotropic peak shape.
** Due to broadened reflections, the fit is not optimal and the lattice parameter determination is imprecise (thus the values seems to from that of other samples discussed in the text - in fact it is just an approximate value).

2.3.2.6 References

[1] L.-D. Zhao, V. P. Dravid, M. G. Kanatzidis, *Energy Environ. Sci* **2014**, *7,* 251.

[2] J. R. Sootsman, D. Y. Chung, M. G. Kanatzidis, *Angew. Chem. Int. Ed.* **2009**, *48,* 8616.

[3] T. Rosenthal, M. N. Schneider, C. Stiewe, M. Döblinger, O. Oeckler, *Chem. Mater.* **2011,** *23*, 4349.

[4] T. Matsunaga, H. Morita, R. Kojima, N. Yamada, K. Kifune, Y. Kubota, Y. Tabata, J.-J. Kim, M. Kobata, E. Ikenaga, K. Kobayashi, *J. Appl. Phys.* **2008,** *103*, 093511.

[5] M. N. Schneider, T. Rosenthal, C. Stiewe, O. Oeckler, *Z. Kristallogr.* **2010**, *225*, 463.

[6] T. Rosenthal, S. Welzmiller, O. Oeckler, *Solid State Sci.* **2013**, *25,* 118.

[7] T. Rosenthal, P. Urban, K. Nimmrich, L. Schenk, J. de Boor, C. Stiewe, O. Oeckler, *Chem. Mater.* **2014**, *26*, 2567.

[8] S. Welzmiller, T. Rosenthal, T. Schröder, P. Urban, F. Fahrnbauer, C. Stiewe, O. Oeckler, *Acta Crystallogr. Sect. A* **2012**, *68*, 50.

[9] C. Xu, B. Liu, Z.-T. Song, S.-L. Feng, B. Chen, *Chin. Phys. Lett.* **2005**, *22*, 2929.

[10] D.-H. Kim, F. Merget, M. Laurenzis, P. H. Bolivar, H. Kurz, *J. Appl. Phys.* **2005**, *97*, 083538.

[11] T. J. Park, D. H. Kim, S. M. Yoon, K. J. Choi, N. Y. Lee, B. G. Yu, S. Y. Choi, *Jpn. J. Appl. Phys.* **2006**, *45*, L1273.

[12] W. D. Song, L. P. Shi, X. S. Miao, T. C. Chong, *Appl. Phys. Lett*. **2007**, *90*, 091904.

[13] M. L. Lee, K. T. Yong, C. L. Gan, L. H. Ting, S. B. M. Daud, L. P. Shi, *J. Phys. D: Appl. Phys.* **2008**, *41*, 215402.

[14] M. L. Lee, K. T. Yong, C. L. Gan, L. H. Ting, L. P. Shi, *Jpn. J. Appl. Phys*. **2009**, *48,* 03A063.

[15] J. Xu, F. Rao, Z. Song, M. Xia, C. Peng, Y. Gu, M. Zhu, L. Wu, B. Liu, S. Feng, *Electrochem. Solid-State Lett.* **2012**, *15*, H59.

[16] R. Kojima, N. Yamada, *Jpn. J. Appl. Phys.* **2001**, *40*, 5930.

[17] S. Buller, C. Koch, W. Bensch, P. Zalden, R. Sittner, S. Kremers, M. Wuttig, U. Schürmann, L. Kienle, T. Lichtweiß, J. Janek, B. Schönborn, *Chem. Mater.* **2012**, *24*, 3582.

[18] S. Welzmiller, T. Rosenthal, P. Ganter, L. Neudert, F. Fahrnbauer, P. Urban, C. Stiewe, O. Oeckler, *Dalton Trans.* **2014**, http://dx.doi.org/10.1039/c4dt00336e

[19] S. Welzmiller, P. Urban, F. Fahrnbauer, L. Erra, O. Oeckler, *J. Appl. Crystallogr.* 2013, *46*, 769.

[20] M. N. Schneider, F. Fahrnbauer, T. Rosenthal, M. Döblinger, C. Stiewe, O. Oeckler, *Chem. Eur. J.* **2012**, *18*, 1209.

[21] O. Oeckler, M. N. Schneider, F. Fahrnbauer, G. Vaughan, *Solid State Sci.* **2011**, *13*, 1157.

[22] X. Shi, J. R. Salvador, J. Yang, H. Wang, *Sci. Adv. Mater.* **2011**, *3*, 667.

[23] *DigitalMicrograph 3.6.1*, Gatan Software, Pleasanton, USA, **1999**.

[24] P. A. Stadelmann, *Ultramicroscopy* **1987**, *21*, 131.

[25] *ESVision*, *4.0.164*, Emispec Systems Inc., Tempe, USA, **1994-2002**.

[26] *TOPAS-Academic*, *V. 4.1*, Coelho Software, Brisbane, Australia, **2007**.

[27] A. Le Bail, A. Jouanneaux, *J. Appl. Crystallogr.* **1997**, *30,* 265.

[28] J. de Boor, E. Müller, *Rev. Sci. Instrum.* **2013**, *84*, 065102.

[29] J. de Boor, C. Stiewe, P. Ziolkowski, T. Dasgupta, G. Karpinski, E. Lenz, F. Edler, E. Müller, *J. Electron. Mater.* **2013**, *42,* 1711.

[30] M. N. Schneider, P. Urban, A. Leinweber, M. Döblinger, O. Oeckler, *Phys. Rev. B* **2010**, *81,* 184102.

[31] R. F. Barrow, E. E. Vago, *Proc. Phys. Soc. Lond.* **1944**, *56*, 78.

[32] P. A. G. O'Hare, *J. Chem. Thermodyn*. **1995**, *27*, 921.

[33] G. S. Kumar, G. Prasad, R. O. Pohl, *J. Mater. Chem.* **1993**, 28, 4261.

[34] Z.-G- Chen, G. Han, L. Yang, L. Cheng, J. Zou, *Prog. Nat. Sci: Mater Int.* **2012**, *22*, 535.

[35] S. N. Girard, T. C. Chasapis, J. He, X. Zhou, E. Hatzikraniotis, C. Uher, K. M. Paraskevopoulos, V. P. Dravid, M. K. Kanatzidis, *Energy. Environ. Sci.* **2012**, *5*, 8716.

[36] Y. Pei, J. Lensch-Falk, E. S. Toberer, D. L. Medlin, G. J. Snyder, *Adv. Funct. Mater.* **2011**, *21*, 241.

[37] Y. Rosenberg, Y. Gelbstein, M. P. Dariel, *J. Alloys Compd.* **2012**, *526*, 31.

[38] S. N. Girard, J. He, C. Li, S. Moses, G. Wang, C. Uher, V. P. Dravid, M. G. Kanatzidis, *Nano Lett.* **2010**, *10*, 2825.

[39] S. N. Girard, K. Schmidt-Rohr, T. C. Chasapis, E. Hatzikraniotis, B. Njegic, E. M. Levin, A. Rawal, K. M. Paraskevopoulos, M. G. Kanatzidis, *Adv. Funct. Mater.* **2013**, *23*, 747.

[40] S. Bordas, M. T. Clavaguera-Mora, B. Legendre, C. Hancheng, *Thermochim. Acta* **1986**, *107*, 239.

2.3.3 Enhancing the thermoelectric properties of germanium antimony tellurides by substitution with selenium in compounds $Ge_nSb_2(Te_{1-x}Se_x)_{n+3}$ ($0 \leq x \leq 0.5$; $n \geq 7$)

T. Rosenthal, P. Urban, K. Nimmrich, L. Schenk, J. de Boor, C. Stiewe, O. Oeckler

Chem. Mater. **2014**, *26*, 2567-2578.

Abstract

Quenched pseudocubic germanium antimony tellurides (GST compounds) exhibit promising thermoelectric properties. These are related to the nanostructures which can be influenced by varying the composition and the thermal treatment. The substitution of Te by Se in bulk samples of $Ge_nSb_2Te_{n+3}$ with high thermoelectric figures of merit (*ZT*) is possible over a wide compositional range. This results in solid solution series $Ge_nSb_2(Te_{1-x}Se_x)_{n+3}$ with $0 < x < 0.75$ for $n \geq 7$. Se substitution reduces the average lateral extension of the defect layers in quenched samples. This is a consequence of the reduced mobility during the quenching process due to the lower cubic to trigonal phase transition temperatures of Se-substituted samples. Most pronounced for n = 7, Se doping increases the transition temperatures between the nanostructured (pseudo)cubic modification of quenched samples and their layered trigonal phase. This increases the temperature ranges in which the materials can be employed without altering their nanostructures and properties. When Se is introduced, the Seebeck coefficient increases and the thermal conductivity decreases. The *ZT* value of $Ge_7Sb_2Te_8Se_2$, for instance, increases up to 1.2 at 425 °C, which is 6 times higher than that of $Ge_7Sb_2Te_{10}$. Similarly, the *ZT* value of $Ge_{12}Sb_2(Te_{1-x}Se_x)_{15}$ increases up to a factor of 2 for x = 0.2 at temperatures below 400 °C. The most promising thermoelectric properties (*ZT* = 1.2 at 425 °C for n = 7, and *ZT* = 1.1 at 350 °C for n =12) are observed for x = 0.2 whereas higher Se substitution rates result in a less pronounced effect. The average structures were determined by powder as well as single crystal X-ray diffraction (SCXRD). The real structure of quenched $Ge_nSb_2(Te_{1-x}Se_x)_{n+3}$ ($0 \leq x \leq 0.5$; $n \geq 7$) bulk material was investigated by high-resolution electron microscopy (HRTEM) with respect to the degree of substitution (x) and correlated with the resulting changes of the thermoelectric properties. The decrease of the lateral extension of the defect layers with increasing Se content as found by HRTEM and electron diffraction is confirmed by SCXRD data for $Ge_{\sim 5}Sb_2(Te_{0.13}Se_{0.87})_{\sim 8}$.

2.3.3.1 Introduction

Thermoelectric generators are intriguing devices for the improvement of the efficiency of energy conversion processes by utilizing waste heat and may also advance new cooling and heating concepts. Their proliferation depends on the economic feasibility which is strongly related to the thermoelectric figure of merit (*ZT*), defined as $ZT = S^2 \cdot \sigma \cdot T \cdot \kappa^{-1}$, which determines the efficiency of thermoelectric generators. The most favorable materials combine high Seebeck coefficients (*S*) and high electrical conductivities (σ) with low thermal conductivities (κ). New synthetic approaches and element combinations have been developed in recent years, resulting in a significant enhancement of *ZT* values.

Germanium antimony tellurides (GST materials), which are well-known because of their applications as phase-change materials in optical data storage media and nonvolatile RAM devices,[1-5] have recently been shown to exhibit very interesting thermoelectric properties.[6,7] These are related to the nanostructure which can be influenced by utilizing characteristic phase transitions of GST materials. At ambient temperature, the thermodynamically stable pseudobinary compounds of the homologous series $Ge_nSb_2Te_{n+3}$ consist of tetradymite-type Sb_2Te_3[8] slabs that are formally enlarged by n additional GeTe layers. The crystal structure of these compounds thus consists of layer-like distorted rocksalt-type building blocks separated by van der Waals gaps between the Te atom layers terminating the individual slabs. These Te atoms formally surround distorted octahedral voids, so that the van der Waals gaps can be viewed as layer-like ordered cation defects (cf. Figure 1).[9,10] At high temperatures (HT), these defects are randomly disordered in a cubic rocksalt-type phase with Ge, Sb and vacancies occupying the cation positions and Te occupying the anion positions. Therefore, both the vacancy concentration in the cubic HT phase and the thickness of the slabs in the layered ambient-temperature phase are given by n in the formula $Ge_nSb_2Te_{n+3}$.[11,12] In GeTe-rich samples with $n \geq 3$, quenching the cubic HT phase yields a metastable pseudocubic phase.[11] In this material, short-range ordering of the defects in finite layers perpendicular to the cubic <111> directions often leads to pronounced nanostructuring. While the average spacing of the defect layers exclusively depends on n, the variance of the spacing and the sizes of discrete domains with parallel defect layers in addition depend on the thermal treatment. Individual defect layers may intersect, forming parquet-like structures.[7] Across defect layers with limited lateral extension, the cubic stacking of the HT phase is preserved, while structural relaxation towards a hexagonal stacking (comparable to the situation in layered phase) occurs when the lateral extension is larger.[7,13] The lack of long-range order of the defect layers in quenched pseudocubic GST materials results in a lower lattice thermal

conductivity and higher *ZT* values (up to 1.3 at 450° C for $Ge_{12}Sb_2Te_{15}$) as compared to annealed samples with a parallel arrangement of the defect layers (*ZT* up to 0.2 at 450° C for $Ge_{12}Sb_2Te_{15}$).[7]

The substitution of tellurium by the isovalence-electronic selenium is often possible. In some telluride-based thermoelectrics, the partial substitution of Te by Se led to improved *ZT* values, probably due to reduced lattice thermal conductivity (κ_L) as a consequence of Se/Te anion disorder. For example, Se-doped LAST materials $AgPb_{18}SbTe_{20-x}Se_x$ ($x = 1, 2, 4$) exhibit a lower thermal conductivity at all temperatures investigated and, at low temperatures, a higher power factor than the corresponding Se-free material $AgPb_{18}SbTe_{20}$.[14] Se substitution in $AgSbTe_2$ has been investigated in detail. The solid solution series $AgSbTe_{2-x}Se_x$ ($0 < x < 2$) obeys Vegard's law; the cubic cell parameter *a* deceases with increasing Se content.[15,16] The highest *ZT* values are found for small values of x; they mainly result from the reduced κ_L.[17-19] For example, *ZT* of p-type $AgSbSe_xTe_{2-x}$ (x = 0.02-0.04) is 1.37 at 292 °C, i.e. 26% higher than that of undoped $AgSbTe_2$.[19] $Co_4Sb_{11.3}Te_{0.6}Se_{0.1}$, a Te-doped skutterudite-type $CoSb_3$ additionally doped by Se, exhibits *ZT* values 15% higher than those of $Co_4Sb_{11.4}Te_{0.6}$, again due to a significantly lower κ_L.[20] The Se and Te doping is supposed to increase both point-defect phonon scattering and electron-phonon interaction. Moderate doping with Se leads to a lower charge carrier concentration in n-type $Co_4Sb_{11.3}Te_{0.7-x}Se_x$ ($0 \le x \le 0.3$), and thus a lower σ.[21] Similarly, for $Co_4Sb_{11}Ge_{0.2}Te_{0.7}Se_{0.1}$, a maximum *ZT* value of 0.99 is obtained at 502 °C, 16% higher than that of $Co_4Sb_{11}Ge_{0.2}Te_{0.8}$ at the same temperature.[22] Therefore, the substitution of Te with small amounts of Se should also be a promising approach to increasing the thermoelectric performance of telluride thermoelectrics in general and GST materials in particular.

The correlation of the nanostructure with the thermoelectric properties opens an interesting perspective for tuning these properties as partially substituting Te with Se changes phase transition temperatures. This has also been investigated for phase-change materials; e.g., in thin films of $Ge_8Sb_2Te_{11}$, where the substitution of Te by Se has been shown to increase the temperature of the amorphous to crystalline phase change.[23] In nanostructured thermoelectric materials, on the other hand, phase transitions influence the defect ordering upon cooling or quenching. Therefore, varying the transition temperatures constitutes an intriguing aspect for optimizing the performance of GST bulk thermoelectrics by Se doping. Limitations are indicated by the fact that at ambient conditions GeSe crystallizes in a binary variant of the black phosphorus structure type [24] while the structure of α-GeTe is a binary variant of the structure type of gray arsenic.[25-28] Even though at HT both compounds exhibit a rocksalt-

type structure, the ternary phase diagrams Ge/Sb/Te [29] and Ge/Sb/Se [30] are significantly different. There is no homologous series of layered compounds "$Ge_nSb_2Se_{3+n}$" corresponding to those on the pseudo-binary line Sb_2Te_3/GeTe. Therefore, complete solid solution series between selenides and tellurides are unlikely. However, there are solid solutions $Sb_2Te_{3-x}Se_x$ with x up to 1.25.[31] Furthermore, Te was substituted with Se in thin films like $GeSb_2Te_3Se$ and $Ge_2Sb_2Te_{5-x}Se_x$ [32] as well as $Ge_8Sb_2Te_6Se_5$.[23]

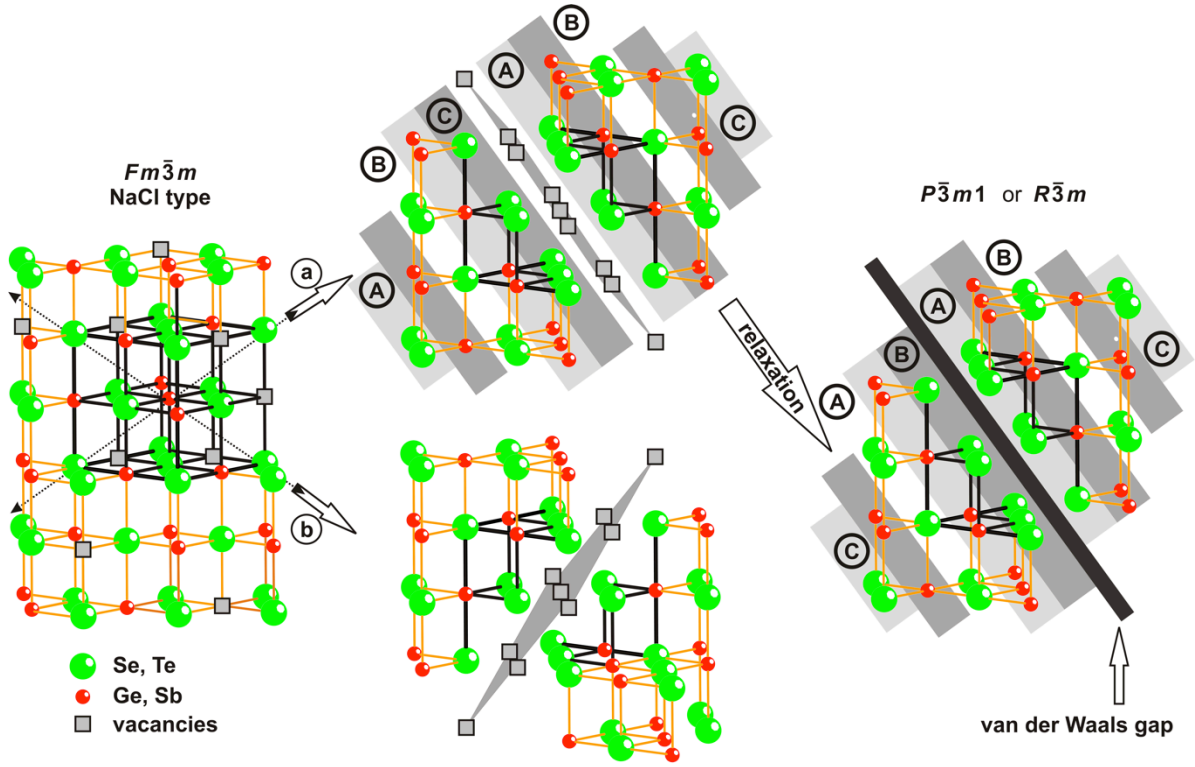

Fig. 1: Rocksalt-type HT phase of $Ge_nSb_2(Te_{1-x}Se_x)_{n+3}$ with random distribution of the vacancies on the cation position (left);. quenching results in rhombohedral distortion along $<111>_{cubic}$ which is accompanied by short range ordering of the vacancies in defect layers between distorted rocksalt-type slabs (middle, two of four possible distortions are shown, a and b); when the lateral extension of the defect layers is sufficient, relaxation occurs and the stacking sequence across the vacancy layers becomes hexagonal (right).

2.3.3.2 Experimental Section

For the synthesis of bulk samples $Ge_nSb_2(Te_{1-x}Se_x)_{n+3}$ ($0 < x \leq 0.5$; $7 \leq n \leq 19$), stoichiometric amounts of the elements Ge (99.999%, Sigma Aldrich), Sb (99.999%, Smart Elements), Te (99.999%, Alfa Aesar) and Se (99.999%, Alfa Aesar) were melted in silica glass ampoules sealed under Ar atmosphere for 2 h at 950 °C and then quenched in water. Subsequently, the samples were annealed for 2 days in the stability range of the cubic high-temperature phase (~ 580 °C; except $Ge_{19}Sb_2(Te_{0.8}Se_{0.2})_{22}$: 630 °C) and quenched in water again. All samples

were obtained as homogenous compact metallic gray ingots without any visible impurities. For thermoelectric measurements, ingots were prepared under analogous conditions (but quenched in air) in silica glass ampoules with a flat bottom. After polishing, the disc-shaped ingots exhibit a diameter of ca. 20 mm and a thickness of 2-6 mm. The phase purity of the samples was verified by Rietveld refinements based on the X-ray powder diffraction patterns. Representative refinements are shown in Section 3.1, further refinement results are given in the Supporting Information (for the ingots used for thermoelectric measurements cf. Figure S1 and Tables S1 and S2, for the samples $Ge_{12}Sb_2(Te_{1-x}Se_x)_{15}$ used for the Vegard plot cf. Figure S2 and Tables S3 and S4, respectively). For comparison, unsubstituted samples $Ge_nSb_2Te_{n+3}$ ($7 \leq n \leq 19$) were synthesized as described in ref. [7]. The single crystal was obtained by melting a stoichiometric mixture of $Ge_2Sb_2TeSe_4$ at 950 °C in a sealed silica glass ampoule under dry Ar, quenching it in water and keeping the ampoule at 650 °C for 69 h followed by quenching it again in ice water. Octahedral crystals were isolated from the ampoule wall.

The chemical composition of the samples, including two representative single crystals, was determined by energy-dispersive X-ray spectroscopy (EDX) using a JSM-6500F (Jeol, Japan) scanning electron microscope (SEM) equipped with an EDX detector (model 7418, Oxford Instruments, UK).

For transmission electron microscopy (TEM), finely ground pieces of the samples were dispersed in ethanol and distributed onto a copper grid coated with holey carbon film by drop casting. High-resolution transmission electron microscopy (HRTEM), selected-area electron diffraction (SAED), and energy dispersive X-ray spectroscopy (EDX) were done on a Titan 80-300 (FEI, USA). The microscope was equipped with a field emission gun operated at 300 kV and a TEM TOPS 30 EDX spectrometer (EDAX, Germany). The SAED and HRTEM images (recorded on an UltraScan 1000 camera, Gatan, USA, resolution 2k x 2k) were evaluated using Digital Micrograph[33] and EMS,[34] for STEM and EDX data the program ES Vision[35] was used.

X-ray patterns of powdered pieces of the ingots fixed on Mylar foils (by means of vacuum grease) were collected on a G670 Guinier camera (Huber, Germany) equipped with a fixed imaging plate detector and an integrated read-out system using Cu-Kα_1 radiation (Ge(111) monochromator, λ = 1.54051 Å). For temperature programmed X-ray powder diffraction, a Stadi P powder diffractometer (Stoe & Cie. GmbH, Germany) with an imaging plate detector system was used with Mo-Kα_1 radiation (Ge(111) monochromator, λ = 0.7093 Å). The diffractometer was equipped with a graphite furnace (details cf. Supplementary Information). Powder patterns were analyzed with WIN^{XPOW}.[36] For phase analysis and the determination of

lattice parameters, Rietveld refinements were performed using the program package TOPAS-Academic.[37]

Single crystal data were acquired with an IPDS-I diffractometer (Stoe & Cie GmbH, Germany) with Ag-Kα radiation (λ = 0.56085 Å) and with a heavy-duty diffractometer (Huber, Germany) equipped with a FReLoN2K CCD detector (dynamical range 2^{16}) [38] at the materials science beamline ID11 [39] (ESRF, Grenoble, France) near the absorption edges of Te (λ = 0.38979 Å; 31.808 keV) and Sb (λ = 0.40681 Å; 30.477 keV), respectively. Dispersion correction terms $\Delta f'$ and $\Delta f''$ near the absorption edges of Sb and Te were calculated from wavelength-dependent fluorescence measurements (Rontec X-Flash detector) with CHOOCH.[40] Laboratory single crystal data were processed with the diffractometer software,[41] numerical absorption correction was performed with X-RED32[42] and X-SHAPE[43] taking into account the Laue symmetry $m\bar{3}m$. Synchrotron diffraction data were indexed with SMART[44] and integrated with SAINT;[45] semiempirical absorption correction as well as scaling and merging the different datasets for each wavelength was performed with SADABS.[46] The final structure refinements were performed with JANA2006.[47] Additional test refinements were also done with SHELX-97.[48]

The thermoelectric properties were measured up to 450° C under inert conditions (see below) using commercial and in-house-built facilities of the DLR (Cologne, Germany). The combined measurement of the electrical conductivity (σ) and the Seebeck coefficient (S) was performed after the measurement of the thermal conductivity (κ). The raw data were treated as described in the Supplementary Information. For the measurement of the electrical resistivity, an in-line four-point-probe setup was used to avoid influences of cable and contact resistance; an AC method with a frequency of 7 Hz was employed to reduce Peltier influences. The values of σ were determined from the resistance R using $\sigma = 1/(2\pi\, s \cdot R \cdot G)$, where s is the distance of the voltage probes and the correction factor G takes into account the sample geometry. Type-N thermocouples attached directly to the sample were used to measure the temperatures (T_1 and T_2) and the Seebeck voltage (U_s). The Seebeck coefficient was determined from a variable temperature gradient using $S = \partial U_s / \partial \Delta T - S_{\text{Nicrosil}}$ with $\Delta T = |T_2 - T_1|$ and S_{Nicrosil} the Seebeck coefficient of the thermocouple wires. More details on the hardware and the electrical conductivity measurements can be found in ref. [49], while the details of the Seebeck measurement are given in ref. [50].

The thermal conductivity (κ) was calculated from the thermal diffusivity (D_{th}), taking into account the heat capacity (C_p) and the density (ρ) of the sample: $\kappa = D_{\text{th}} \cdot \rho \cdot C_p$. The densities were determined using Mohr's balance; the deviation from the X-ray densities was ≤

1%. D_{th} was measured with a laser-flash apparatus (LFA 427, Netzsch GmbH & Co., Germany) and C_p was determined by differential scanning calorimetry (DSC 404, Netzsch GmbH & Co., Germany). The lattice part of the thermal conductivity (κ_L) was calculated as the difference of the total thermal conductivity and the electronic contribution to the thermal conductivity (κ_e), which is related to the electrical conductivity according to the Wiedemann-Franz law: $\kappa_e / \sigma = LT$ (with the absolute temperature T and the Lorenz number L). For all samples, $L = 1.48 \cdot 10^{-8}$ $W\Omega K^{-2}$ was used; this value is typical for degenerate semiconductors.[51] The thermoelectric figure of merit (ZT) was calculated from these properties according to $ZT = S^2 \cdot \sigma \cdot T \cdot \kappa^{-1}$.

2.3.3.3 Results and Discussion

2.3.3.3.1 Structure and existence ranges of Se-substituted GST materials $Ge_nSb_2(Te_{1-x}Se_x)_{n+3}$ ($0 \le x \le 0.5$; $7 \le n \le 19$)

a) (pseudo)cubic mixed crystals of quenched $Ge_nSb_2(Te_{1-x}Se_x)_{n+3}$ ($0 \le x \le 0.5$; $7 \le n \le 12$)

Se-substituted samples exhibit phase transitions comparable to those of the ternary GST compounds as described in the Introduction, e.g., a layered structure thermodynamically stable at ambient conditions and a cubic HT phase. Quenching the cubic HT phase of solid solutions $Ge_nSb_2(Te_{1-x}Se_x)_{n+3}$ ($0 \le x \le 0.5$; n = 7, 12) results in pseudocubic samples whose powder patterns do not indicate significant deviations from the cubic metrics. Following Vegard's law, the volume of the (pseudo)cubic unit cell of $Ge_{12}Sb_2(Te_{1-x}Se_x)_{15}$ (x = 0.05, 0.067, 0.133, 0.2, 0.333, 0.5, 0.6, 0.733) decreases with increasing x, i.e., when Te is substituted with the smaller Se (cf. Figure 2).

The chemical composition of the products $Ge_nSb_2(Te_{1-x}Se_x)_{n+3}$ (x = 0.2, 0.5; n = 7, 12) corresponds to that of the weighted samples with deviations of less than 2 atom% according to TEM-EDX (for samples used for TEM investigations) and SEM-EDX (for the samples used for thermoelectric characterization and the Vegard plot, Figure 2). The results of these measurements are given in the Supporting Information (Tables S5 and S6). In contrast to the quarternary compounds $Ge_{12}Sb_2(Te_{1-x}Se_x)_{15}$ ($x < 0.75$), quenching the ternary selenium compounds (x = 1) does not yield a pseudocubic single-phase product; instead, a mixture of Sb-doped GeSe and (possibly Ge-doped) Sb_2Se_3 is formed.

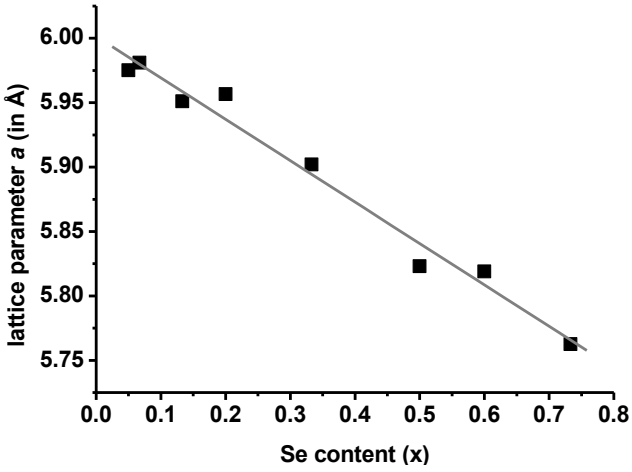

Fig. 2: Decrease of the cubic lattice parameter *a* with the Se content (x) in quenched samples of $Ge_{12}Sb_2(Te_{1-x}Se_x)_{15}$ (Vegard's plot) with linear least-squares fit (a = 6.001(8) – 0.321(19) x , gray line).

The lattice parameters of the quenched (pseudo-)cubic samples $Ge_nSb_2(Te_{1-x}Se_x)_{n+3}$ ($0 \leq x < 0.75$; n = 7, 12) were determined by Rietveld refinements using the powder diffraction patterns. A fundamental parameter approach based on the experimental setup was employed to describe the reflection profiles. For n = 7, Lorentzian microstrain broadening was taken into account; for n = 12, anisotropic microstrain and crystallite size broadening (using the LeBail-Jouanneaux method)[52] were considered and significantly improved the fit due to the pronounced asymmetry of the reflection profiles. Preferred orientation (using spherical harmonics) was taken into account for all samples discussed. Site occupation factors were derived from the nominal composition. Common displacement parameters were employed for the cations and anions, respectively. The isotropic displacement parameters of the cations are rather large due to the variance of the surrounding atoms that results from the mixed occupancy of the anion position with Se and Te as well as the random distribution of the cations and vacancies.

The results of the refinements for $Ge_nSb_2(Te_{1-x}Se_x)_{n+3}$ (x = 0.2, 0.5 and n = 7, 12) are shown in Figure 3, crystal data and details on the refinements are given in Table 1, the atomic parameters are listed in Table 2. These compositions were also used for the determination of the nanostructure by TEM and measurements of thermoelectric properties. Further details of the crystal structure investigations may be obtained from Fachinformationszentrum Karlsruhe, 76344 Eggenstein-Leopoldshafen, Germany (fax: (+49)7247-808-666; e-mail: crysdata@fiz-karlsruhe.de, http://www.fiz-karlsruhe.de /request_for_deposited_data.html) on quoting the depository numbers CSD-426896 ($Ge_7Sb_2Te_8Se_2$), CSD-426895 ($Ge_7Sb_2Te_5Se_5$), CSD-426892 ($Ge_{12}Sb_2Te_{12}Se_3$), and CSD-426897 ($Ge_{12}Sb_2Te_{7.5}Se_{7.5}$), respectively (data for $Ge_{12}Sb_2Te_{15}$ cf. ref. [6] and for $Ge_7Sb_2Te_{10}$ cf. ref. [53]).

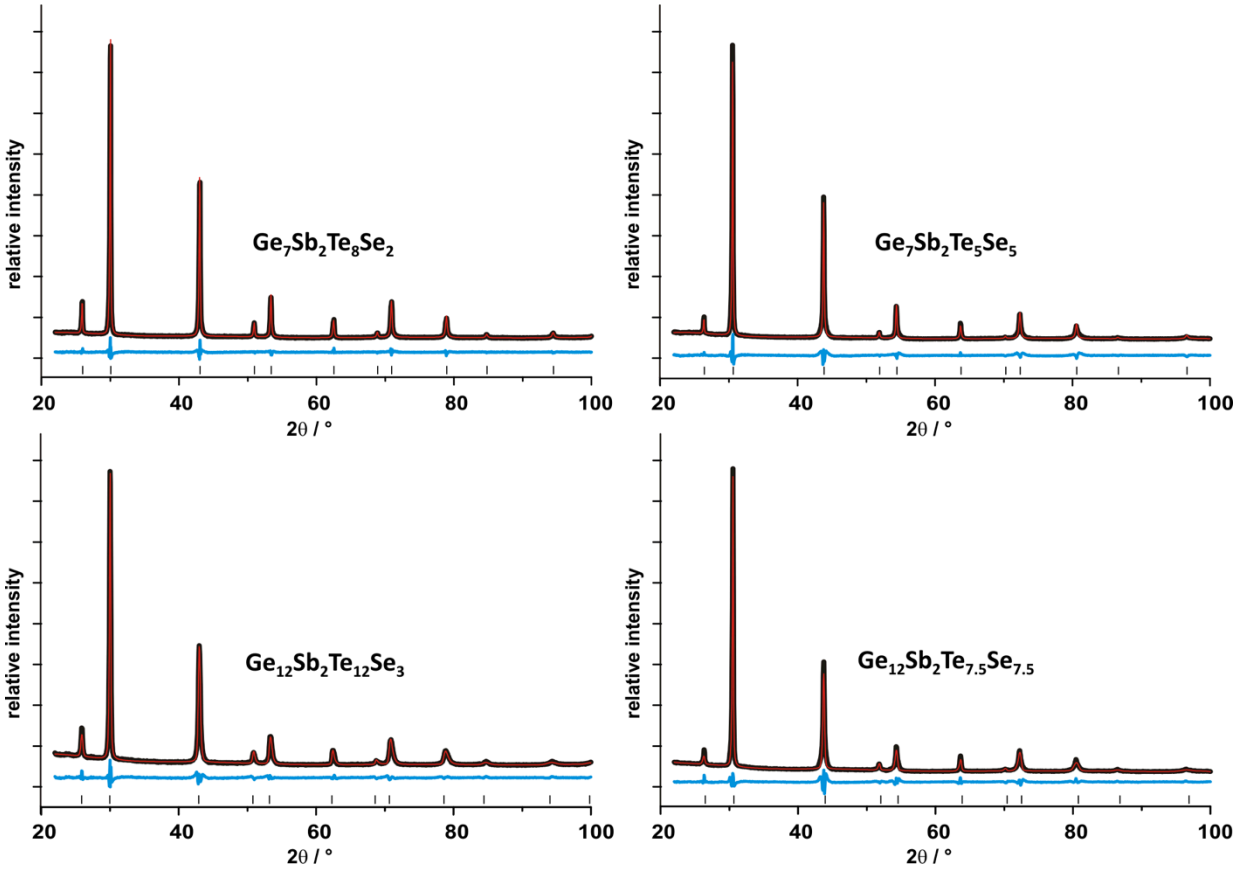

Fig. 3: Profile fits from the Rietveld refinements of $Ge_7Sb_2Te_8Se_2$ (top left), $Ge_7Sb_2Te_5Se_5$ (top right), $Ge_{12}Sb_2Te_{12}Se_3$ (bottom left) and $Ge_{12}Sb_2Te_{7.5}Se_{7.5}$ (bottom right): experimental (black) and simulated (red) powder patterns, difference plots (blue) and reflection markers (black, bottom); the scaling of the 2θ axis is the same for all plots and the intensities were normalized according to that of the strongest reflection of the experimental powder pattern.

Table 1. Details of the Rietveld refinements for $Ge_nSb_2(Te_{1-x}Se_x)_{n+3}$ (n = 7, 12) phases obtained by quenching the HT phase.

	$Ge_7Sb_2Te_8Se_2$	$Ge_7Sb_2Te_5Se_5$	$Ge_{12}Sb_2Te_{12}Se_3$	$Ge_{12}Sb_2Te_{7.5}Se_{7.5}$
asymmetric unit	$Ge_{0.7}Sb_{0.2}Se_{0.2}Te_{0.8}$	$Ge_{0.7}Sb_{0.2}Se_{0.5}Te_{0.5}$	$Ge_{0.8}Sb_{0.133}Se_{0.2}Te_{0.8}$	$Ge_{0.8}Sb_{0.133}Se_{0.5}Te_{0.5}$
formula weight of the asymmetric unit (in g mol^{-1})	193.05	178.46	192.15	177.56
F(000)	324.0	302.4	323.1	301.5
crystal system / space group (no.)	cubic / $Fm\bar{3}m$ (225)			
lattice parameters (in Å)	a = 5.93511(11)	a = 5.8326(2)	a =5.9566(6)	a = 5.8231(10)
cell volume (in $Å^3$)	209.067(12)	198.42(2)	211.35(6)	197.45(10)
density (X-ray, in g/cm^3)	6.13	5.97	6.04	5.97
radiation	Cu-$K_{\alpha1}$ (λ = 1.540596 Å)			
2θ range (in °)	$22 \le 2\theta \le 100$			
parameters (thereof background)	20(12)		33(12)*	
R_p / R_{wp}	0.0231 / 0.0317	0.0362 / 0.0535	0.0251 / 0.0356	0.0318 / 0.0519
GooF / R_{Bragg}	1.192 / 0.0085	2.110 / 0.0079	1.386 / 0.0068	2.034 / 0.0094

*with LeBail-Jouanneaux anisotropic broadening [52]

Table 2. Atom coordinates, site occupancies and isotropic displacement parameters (in Å²) for $Ge_nSb_2(Te_{1-x}Se_x)_{n+3}$ (n = 7, 12) samples obtained by quenching the HT phase.

	anions				cations and vacancies			
	position		occupancy	B_{iso}	position		occupancy	B_{iso}
$Ge_7Sb_2Te_8Se_2$	4*a*	1/2 1/2 1/2	4/5 Te, 1/5 Se	1.42(4)	4*b*	0 0 0	7/10 Ge, 2/10 Sb	3.48(6)
$Ge_7Sb_2Te_5Se_5$	4*a*	1/2 1/2 1/2	1/2 Te, 1/2 Se	2.03(8)	4*b*	0 0 0	7/10 Ge, 2/10 Sb	3.60(11)
$Ge_{12}Sb_2Te_{12}Se_3$	4*a*	1/2 1/2 1/2	4/5 Te, 1/5 Se	1.13(6)	4*b*	0 0 0	12/15 Ge, 2/15 Sb	3.67(8)
$Ge_{12}Sb_2Te_{7.5}Se_{7.5}$	4*a*	1/2 1/2 1/2	1/2 Te, 1/2 Se	1.50(9)	4*b*	0 0 0	12/15 Ge, 2/15 Sb	3.93(13)

b) single-crystal structure determination of $Ge_{\sim 5}Sb_2(Te_{0.13}Se_{0.87})_{\sim 8}$

Diffraction data of a single crystal of $Ge_{\sim 5}Sb_2(Te_{0.13}Se_{0.87})_{\sim 8}$ have been obtained with synchrotron radiation near the *K* absorption edges of Sb and Te in order to enhance the scattering contrast between these elements. At such wavelengths, the atomic form factor $f(\lambda,\theta) = f^0(\sin\theta/\lambda) + \Delta f'(\lambda) + i\Delta f''(\lambda)$ (dependent on the diffraction angle θ and the wavelength λ) is characterized by large dispersion correction terms Δf' and Δf'', which are rather small when wavelengths far from absorption edges are used.[54-56] The structure was refined simultaneously on 3 datasets (near the Sb-*K* and Te-*K* edges and far off the edges with Ag-K_α radiation). The dispersion correction terms of Sb and Te at their respective absorption edges were calculated from fluorescence data. The remaining dispersion correction terms were taken as they are implemented in JANA2006.[57] The values used for the structure refinement are listed in Table 3. Ge and Sb were refined on a shared cation position and Se and Te on a shared anion position, respectively. Common displacement parameters were used for each shared position. Full site occupancy of the anion position was assumed so that the refined ratio Se/Te requires one parameter. Concerning the occupancy of the cation position, an electroneutrality constraint was applied, assuming that the cation position is occupied by Ge^{2+}, Sb^{3+} and vacancies; this way one additional parameter suffices to describe the cation distribution without assuming full occupancy. EDX measurements of two crystals from the same batch yield an average composition that is in good agreement with the composition $Ge_{\sim 5}Sb_2(Te_{0.13}Se_{0.87})_{\sim 8}$ refined from the single crystal data (in atom-%: calculated $Ge_{33.3}Sb_{13.3}Se_{6.9}Te_{46.4}$, measured $Ge_{33.4(6)}Sb_{13.9(3)}Se_{6.8(3)}Te_{45.9(6)}$). The lattice parameter *a* =5.708 Å of the single crystal also corresponds to a very high Se content. Since the influence of the GeTe content n on the lattice parameter is much less pronounced than that of the Se content x (cf. Table 1), Figure 2 may be used to estimate x ~ 0.9, which is in good agreement with the refined composition. The results of the joint refinement and crystal data are shown in Tables 4 and 5, respectively. Further details of the crystal structure

investigations may be obtained from Fachinformationszentrum Karlsruhe, 76344 Eggenstein-Leopoldshafen, Germany (fax: (+49)7247-808-666; e-mail: crysdata@fiz-karlsruhe.de, http://www.fiz-karlsruhe.de/ request_for_deposited_data.html) on quoting the depository number CSD-426726.

The structure can be described as a rocksalt-type one with mixed cation and anion sites and additional vacancies on the cation position. The diffraction pattern exhibits diffuse intensities around the Bragg reflections (cf. Fig. 7 top right). Streak-like but rather broad and weak maxima next to the Bragg reflections indicate short-range vacancy ordering in defect layers as described for $(GeTe)_nSb_2Te_3$ ($3 < n < 15$).[6,58] The corresponding nanostructure and the influence of the Se substitution are described in Section 3.3.

Table 3. Dispersion correction terms used for the structure refinement of $Ge_{\sim 5}Sb_2(Te_{0.13}Se_{0.87})_{\sim 8}$.

λ / Å	element	$\Delta f'$ / e	$\Delta f''$ / e
0.56085	Ge	0.302	1.190
	Sb	-1.055	1.010
	Se	0.237	1.483
	Te	-0.971	1.096
0.40681	Ge	0.279	0.670
	Sb	-5.790	0.630
	Se	0.289	0.843
	Te	-2.574	0.623
0.38979	Ge	0.268	0.619
	Sb	-2.214	3.303
	Se	0.281	0.780
	Te	-6.950	0.710

Table 4. Crystal data and results of the joint refinement of $Ge_{\sim 5}Sb_2(Te_{0.13}Se_{0.87})_{\sim 8} = Ge_{0.625}Sb_{0.25}Se_{0.87}Te_{0.133}$.

refined composition (per formula unit)	$Ge_{0.64(4)}Sb_{0.24(2)}Se_{0.866(9)}Te_{0.133}$		
molecular mass	161.1 $gmol^{-1}$		
temperature	293 K		
crystal size	0.08 · 0.10 · 0.17 mm^3		
lattice parameter	a = 5.7078(18) Å		
cell volume	185.95(10) $Å^3$		
crystal system	cubic		
space group	$Fm\ \bar{3}m$		
$\rho_{calc.}$	5.751 gcm^{-3}		
Z	4		
F(000)	276		
diffractometer	IPDS-I	ID11 (ESRF)	
radiation	Ag-Kα	synchrotron	
λ	0.56085 Å	0.40681 Å	0.38979 Å
reflections (independent)	321 (48)	1116 (65)	1221 (60)
R_{int} (all)	0.0355	0.0221	0.0217
μ	17.31 mm^{-1}	7.15 mm^{-1}	10.79 mm^{-1}
sinθ/λ	0.89 $Å^{-1}$	1.02 $Å^{-1}$	1.00 $Å^{-1}$
absorption correction	numerical	semiempirical	
parameters	8 (3 constraints, *cf.* text)		
weighting scheme	$w = 1/[\sigma^2(F_o) + 0.000225(F_o^2)]$		
R1 [I > 3σ(I)]	0.0320	0.0227	0.0257
wR [I > 3σ(I)]	0.0391	0.0309	0.0370
R1 (all)	0.0362	0.0227	0.0257
wR (all)	0.0401	0.0309	0.0370
	for all data in all datasets		
R1 [I > 3σ(I)]	0.0267		
wR [I > 3σ(I)]	0.0352		
R1 (all)	0.0280		
wR (all)	0.0354		
GooF (all)	1.91		
$\Delta\rho_{min}$ / $\Delta\rho_{max}$	-2.96 / +0.93		

Table 5. Atomic coordinates, site occupancies and isotropic displacement parameters (in $Å^2$) of $Ge_{\sim 5}Sb_2(Te_{0.13}Se_{0.87})_{\sim 8}$.

Atom	Wyckoff position	x	y	z	sof	U_{iso}
Ge1	4*a*	0	0	0	0.64(4)	0.0366(2)
Sb1					0.24(2)	
Se2	4*b*	0.5	0.5	0.5	0.866(9)	0.02172(18)
Te2					0.134	

c) GeTe-type average structure of $Ge_{19}Sb_2(Te_{1-x}Se_x)_{22}$

While quenching the HT phases of $Ge_nSb_2(Te_{1-x}Se_x)_{n+3}$ with n = 7, 12 yields samples with a cubic average structure, quenching samples with lower defect concentrations (i.e., higher GeTe contents) yields materials whose powder patterns indicate a rhombohedral average structure. Samples of $Ge_{19}Sb_2(Te_{1-x}Se_x)_{22}$ (x = 0.2, 0.5) quenched from the cubic HT phase exhibit an α-GeTe-type structure (i.e., the binary variant of the A7 structure type of gray arsenic)[25] according to Rietveld refinements. HRTEM images (cf. Figure 6 in Section 3.3) reveal only few defect layers comparable to those in the (pseudo)cubic quenched samples of $Ge_nSb_2(Te_{1-x}Se_x)_{n+3}$ (x = 0.2, 0.5) with n = 7, 12. Thus, the non-centrosymmetric average α-GeTe-type structure model mainly reflects A7-type layers with cation-anion ordering within the domains that are free of defect layers, and not an average over multiple domains (which would be centrosymmetric).[59] The short-range defect ordering is not visible in the PXRD pattern since there are only few layers with limited lateral extension so that diffuse intensities are very weak and cannot be distinguished from the background. In analogy to the refinements of the (pseudo)cubic samples (Section 3.1 a), a fundamental parameter approach for reflection profiles was used, and anisotropic microstrain and crystallite size boadening (LeBail-Jouanneaux method)[52] as well as preferred orientation (using spherical harmonics) were taken into account. Site occupancies and displacement parameters were treated in the same way as for the cubic samples. The results of the Rietveld refinements are given in Figure 4 as well as Tables 6 and 7. Further details of these crystal structure investigations may be obtained from Fachinformationszentrum Karlsruhe, 76344 Eggenstein-Leopoldshafen, Germany (fax: (+49)7247-808-666; e-mail: crysdata@fiz-karlsruhe.de, http://www.fiz-karlsruhe.de/ request_for_deposited_data.html) on quoting the depository numbers CSD-426894 ($Ge_{19}Sb_2Te_{17.6}Se_{4.4}$) or CSD- 426893 ($Ge_{19}Sb_2Te_{11}Se_{11}$), respectively.

During cooling or quenching, the α-GeTe-type structure is formed when the metrics of the cubic HT phase is distorted by an elongation along one of the the cubic <111> directions and A7-type-analogous anion/cation layers are formed in quenched $Ge_{19}Sb_2(Te_{1-x}Se_x)_{22}$. The c/a ratios of both samples are very similar: 2.544 for x = 0.2 and 2.543 for x = 0.5, respectively (cf. Table 6). This is between the value of the trigonal setting of a cubic unit cell (2.532) and that of binary GeTe (2.559). In addition to the significant distortion of the cubic metrics, the A7-layer formation leads to a 3 + 3 coordination, with bond lengths of 2.8336(7) Å and 3.1140(9) Å for x = 0.2 and 2.8016(9) Å and 3.0567(11) Å for x = 0.5, respectively. This is typical for the α-GeTe-type structure and follows from the deviation of the z coordinates of the anions from z = ½ which would correspond to equal bond lengths (Table 7). The anion-

cation ordering of the HT cubic phase is preserved, which is in good agreement with the temperature dependent X-ray investigations that basically indicate a displacive phase transition during cooling.

Table 6. Crystal data and details of the Rietveld refinements for quenched $Ge_{19}Sb_2(Te_{1-x}Se_x)_{22}$ (x = 0.2, 0.5) with α-GeTe-type average structure.

	$Ge_{19}Sb_2Te_{17.6}Se_{4.4}$	$Ge_{19}Sb_2Te_{11}Se_{11}$
asymmetric unit	$Ge_{0.86}Sb_{0.091}Se_{0.2}Te_{0.8}$	$Ge_{0.86}Sb_{0.091}Se_{0.5}Te_{0.5}$
formula weight of the asymm. unit (in g mol^{-1})	191.69	177.10
F(000)	242.1	225.9
crystal system / space group (no.)	trigonal / *R*3*m* (160)	
lattice parameters (in Å)	*a* = 4.14306(12) *c* = 10.5387(3)	*a* = 4.0823(2) *c* = 10.3825(6)
cell volume (in $Å^3$)	156.661(12)	149.85(2)
density (X-ray, in g/cm³)	6.09	5.89
radiation	Cu-$K_{\alpha1}$ (λ = 1.540596 Å)	
2θ range (in °)	22 ≤ 2θ ≤ 100	
parameters (thereof background)	48(12)	
R_p / R_{wp}	0.0192 / 0.0267	0.0191 / 0.0274
GooF / R_{Bragg}	1.030 / 0.0071	1.069 / 0.0063

Table 7. Atom coordinates, site occupancies and isotropic displacement parameters (in Å²) for $Ge_{19}Sb_2(Te_{1-x}Se_x)_{22}$ (x = 0.2, 0.5).

	anions				cations and vacancies			
	position		occupancy	B_{iso}	position		occupancy	B_{iso}
$Ge_{19}Sb_2Te_{17.6}Se_{4.4}$	4*a*	0 0 0	0.8 Te, 0.2 Se	1.00(1)	4*b*	0 0 0.47748(13)	19/22 Ge, 2/22 Sb	1.84(3)
$Ge_{19}Sb_2Te_{11}Se_{11}$	4*a*	0 0 0	0.5 Te, 0.5 Se	1.15(2)	4*b*	0 0 0.47920(16)	19/22 Ge, 2/22 Sb	2.23(4)

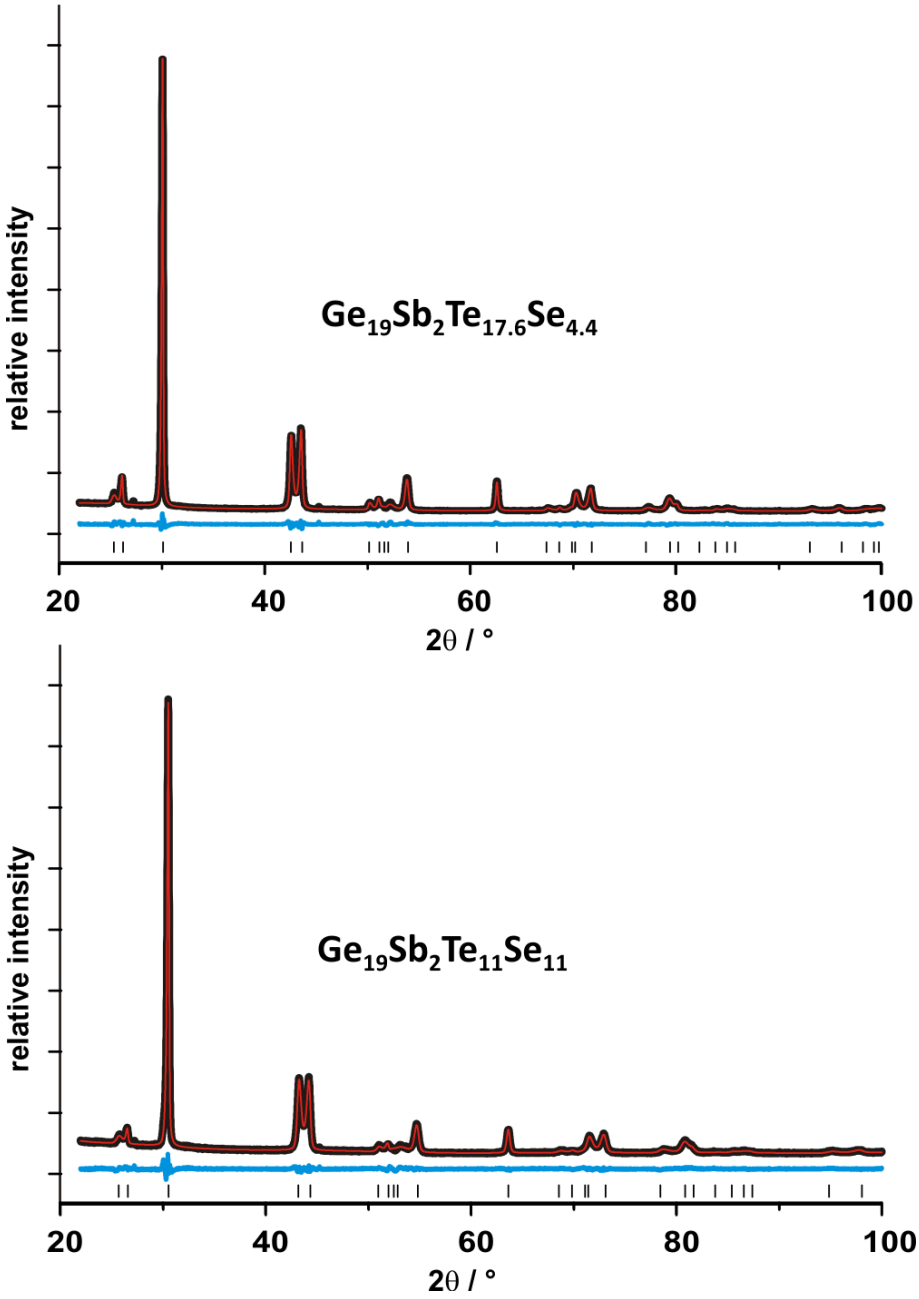

Fig. 4: Results of the Rietveld refinements for $Ge_{19}Sb_2Te_{17.6}Se_{44}$ (top) and $Ge_{19}Sb_2Te_{11}Se_{11}$ (bottom): experimental powder diffraction pattern (black), calculated pattern (red), difference plot (blue) and reflection markers (bottom).

2.3.3.3.2 Influence of Se substitution on the phase transitions of GST materials

Temperature-programmed X-ray powder diffraction (TPXRD) investigations of pseudocubic bulk samples of $Ge_nSb_2(Te_{1-x}Se_x)_{n+3}$ ($0 \leq x \leq 0.5$; $n \geq 7$) obtained by quenching the cubic HT phase were performed in order to determine the existence range of the different crystalline phases (Figure 5). In general, Se-substituted samples exhibit phase transitions similar to those known from quenched unsubstituted GST samples ($3 \leq n \leq 17$).[7] Upon heating, two transformations (temperatures T1 and T2, respectively) occur whereas during cooling there is

only one (T3). The increased atom mobility at elevated temperatures enables a vacancy re-ordering process that leads from the metastable quenched pseudocubic material towards the thermodynamically stable trigonal layered phase with 2D extended van der Waals gaps at T1 (cf. Figure 1, right). When the temperature reaches the stability region of the cubic HT phase, the random distribution of the vacancies in a rocksalt-type phase becomes favorable (T2). When the sample is slowly cooled down below the stability range of the cubic HT phase, only one transition is observed at T3 (cf. Table 8), where the stable trigonal layered phase is formed. The transformation temperatures of individual samples depend on the GeTe content. The difference in the cubic ←→ trigonal transition temperatures during heating (T2) and cooling (T3) show that the cubic HT phase can be undercooled.

The diffusion pathways required for complete vacancy ordering, i.e., the formation of van der Waals gaps "infinitely" extended in 2D, depend on the slab thickness and thus increase with the GeTe content (n). However, in contrast to unsubstituted GST, the transformation temperature T1 of Se-substituted materials decreases with increasing n; probably because the trigonal phase remains very close to cubic in Se-containing compounds (see below) and therefore the transition process requires less strain relaxation. Upon heating, the cubic phase of substituted and unsubstituted GST materials is reached at lower temperatures (T2) with increasing n; and T3 also decreases. Thus, with increasing n, the cubic HT phase obviously becomes stable at lower temperatures. This is probably due to the higher local coordination numbers in structures with fewer vacancies. Therefore, this effect is more pronounced for the more ionic Se-substituted samples. From the point of view of kinetics, however, the long diffusion pathways at higher n mean that it becomes easier to undercool the cubic HT phase and partially retain it at room temperature by quenching.

As a rule, the metrics of the trigonal phase remains closer to cubic for the Se-substituted samples. For compounds $Ge_{12}Sb_2(Te_{1-x}Se_x)_{15}$ (x = 0.2, 0.5), the cubic metrics is nearly preserved both at room and at elevated temperatures. This effect is visible in the less pronounced splitting of the cubic reflections 220, 222 and 420 (at 2θ = ~19°, ~26° and ~32°, respectively) compared to the corresponding pure GST materials.[7] With increasing Se contents x, the transition temperatures T1 from the pseudocubic nanostructured phase to the thermodynamically stable layered phase increase for samples with n = 7. Thus, the substituted material can be kept at higher temperatures without altering its nanostructure or properties. This may again be due to the more ionic character that involves higher activation energies for diffusion processes. As a rule, the lower trigonal-cubic transition temperatures T2, and more pronounced T3, indicate that the stability range of the cubic HT phase is reached at lower

temperatures with increasing Se contents. This results in a reduced mobility at the transition temperature, especially during quenching, which influences the short-range defect order and the metrics of the quenched samples. Altogether, the existence ranges of the trigonal phases are narrower for samples with higher Se contents. The melting points of the compounds show a tendency to decrease with increasing relative Se contents.

Table 8. Phase transformation temperatures and melting points (mp) in °C of $Ge_nSb_2(Te_{1-x}Se_x)_{n+3}$ ($0 \leq x \leq 0.5$; n = 7, 12) from temperature programmed PXRD; T1, T2 and T3 of $Ge_7Sb_2Te_{10}$ and $Ge_{12}Sb_2Te_{15}$ taken from ref (7).

Composition	T1	T2	T3	mp
$Ge_7Sb_2Te_{10}$	250-320	500	460	650
$Ge_7Sb_2Te_8Se_2$	325	450	360	640
$Ge_7Sb_2Te_5Se_5$	380	460	330	600
$Ge_{12}Sb_2Te_{15}$	325	475-500	460	~700*
$Ge_{12}Sb_2Te_{12}Se_3$	150	280	265	640
$Ge_{12}Sb_2Te_{7.5}Se_{7.5}$	150	260	240	600

* The material is solid up to 650 °C and liquid at 700 °C.

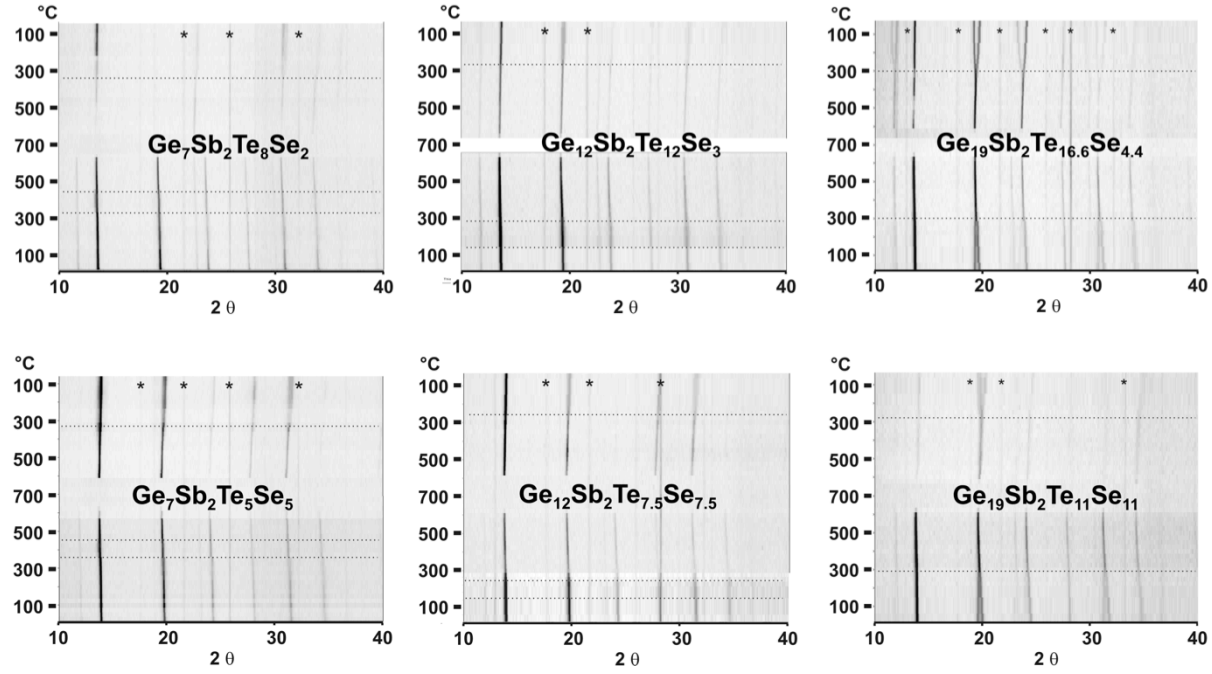

Fig. 5: Temperature-dependent PXRD: heating and cooling (bottom to middle and middle to top, respectively, in each image; $Ge_{12}Sb_2Te_{12}Se_3$ was only heated up to 650 °C, the white bar represents the interval where no data was measured) of $Ge_nSb_2(Te_{1-x}Se_x)_{n+3}$ with x = 0.2 (top) and x = 0.5 (bottom) quenched form the cubic HT phase, with increasing GeTe content from left to right (n = 7, 12, 19); transition temperatures from the pseudocubic to the trigonal layered phase (T1), from the trigonal to the cubic HT phase (T2) and from the cubic HT to trigonal during cooling (T3) are marked with dotted lines; reflections originating from the furnace are marked with asterisks (*).

For Se-substituted samples $Ge_{19}Sb_2(Te_{1-x}Se_x)_{22}$ (x = 0.2 and 0.5), quenching does not yield a pseudocubic phase but an *α*-GeTe-type layered structure with very little partial defect ordering as shown above. Upon heating, the transition to the cubic HT phase (comparable to T2 of pseudocubic samples) occurs at 300 and 290 °C for x = 0.2 and 0.5, respectively (Figure 5). Upon cooling, the transition to the trigonal phase (T3) occurs at 300 and 280 °C for x = 0.2 and 0.5, respectively. In contrast to the pseudocubic samples, there is no difference between phase transition temperatures during heating (T2) and cooling (T3). This may be explained by the fact that this is a second-order phase transition comparable to that of GeTe itself which involves only a negligible degree of vacancy ordering. The main effect is the formation of layers in the disordered structure via a Peierls-type transition; thus, the HT phase cannot be undercooled.

2.3.3.3.3 Influence of Se substitution on the nanostructure of GST materials and the lateral extension of defect layers

a) domain structure

For unsubstituted GST compounds $Ge_nSb_2Te_{n+3}$ (n = 4.5 - 19), an increasing GeTe content n results in an increasing average spacing of the defect layers, which are formed by short-range ordering of the randomly distributed defects during quenching the cubic HT phase, and a higher variance of these spacings. Due to the longer diffusion pathways that are required to form long-range ordered layered structures with extended defect layers at higher values of n, the probability of intersecting defect layers with different orientation increases, resulting in more pronounced parquet-like structures with intersecting defect layers.[7] Since the substitution with Se does not alter the defect concentration in mixed crystals $Ge_nSb_2(Te_{1-x}Se_x)_{n+3}$, a similar trend is visible for the substituted samples (Figure 6). For a given Se fraction x, the average spacing of the defect layers increases with n; and the decreasing average sizes of the domains with parallel defect layers result in more pronounced parquet-like structures. However, at very high GeTe contents (e.g., n = 19), the situation is different: Quenching yields compound with an α-GeTe-type average structure (cf. Section 3.1c) and only a very limited number of finite defect layers is present.

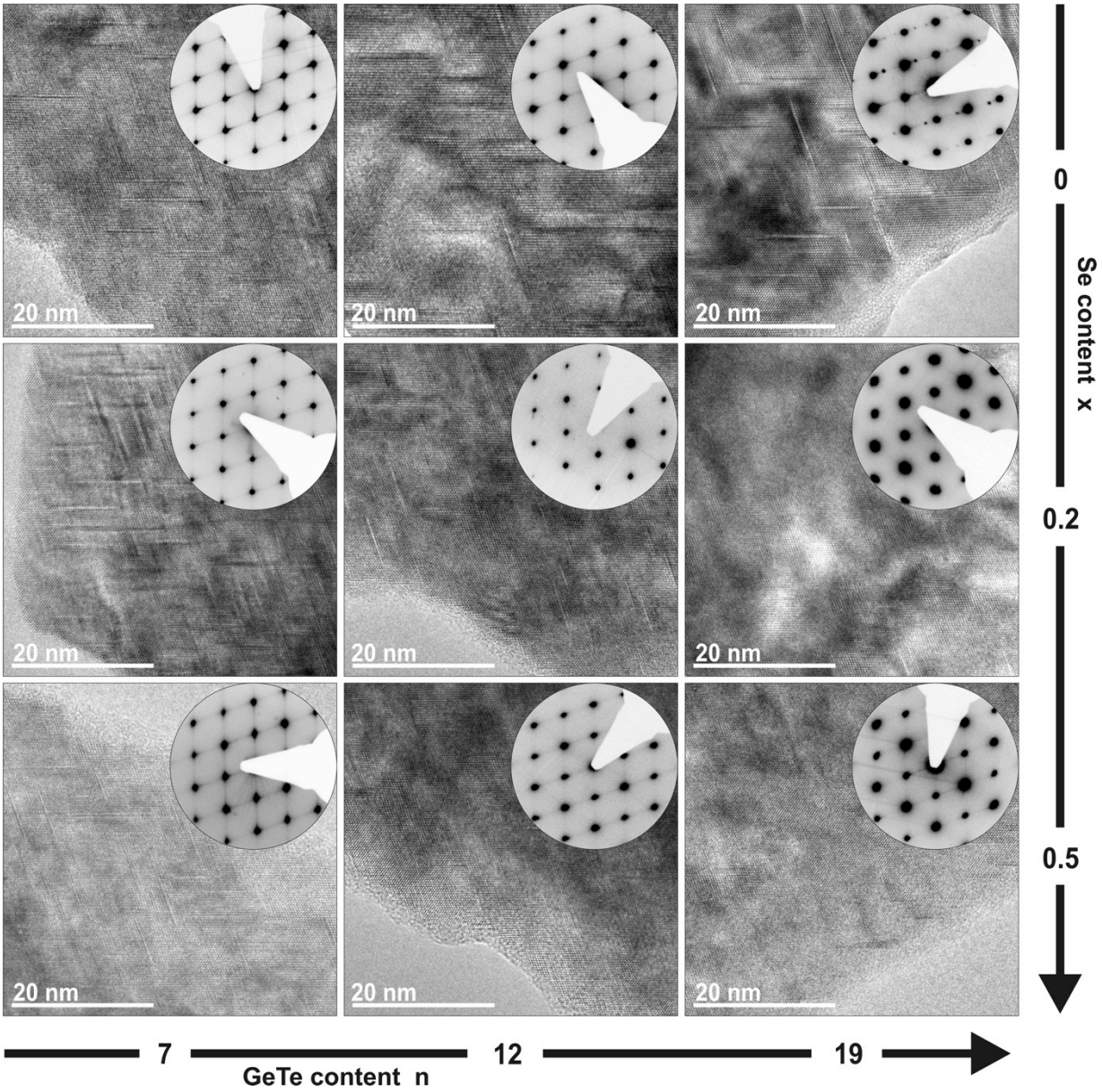

Fig. 6: HRTEM images (zone axis <110> according to (pseudo)cubic setting); all of them have the same magnification) and SAED patterns (insets) of $Ge_{12}Sb_2(Te_{1-x}Se_x)_{n+3}$; with increaseing Se content (x) from top to bottom and increasing GeTe content (n) from left to right.

b) lateral extension of defect layers

The lower transition temperature from the cubic HT phase to the trigonal one (T3) and the less pronounced metric distortion of the trigonal phase in Se-substituted samples influence the short-range ordering of defects as the mobility of atoms and vacancies is lower during the quenching process. For comparable quenching rates, there is less time for diffusion processes that are necessary to form defect layers from randomly disordered defects. Thus, the lateral extension of the defect layers in the pseudocubic phase is smaller for higher Se contents. This

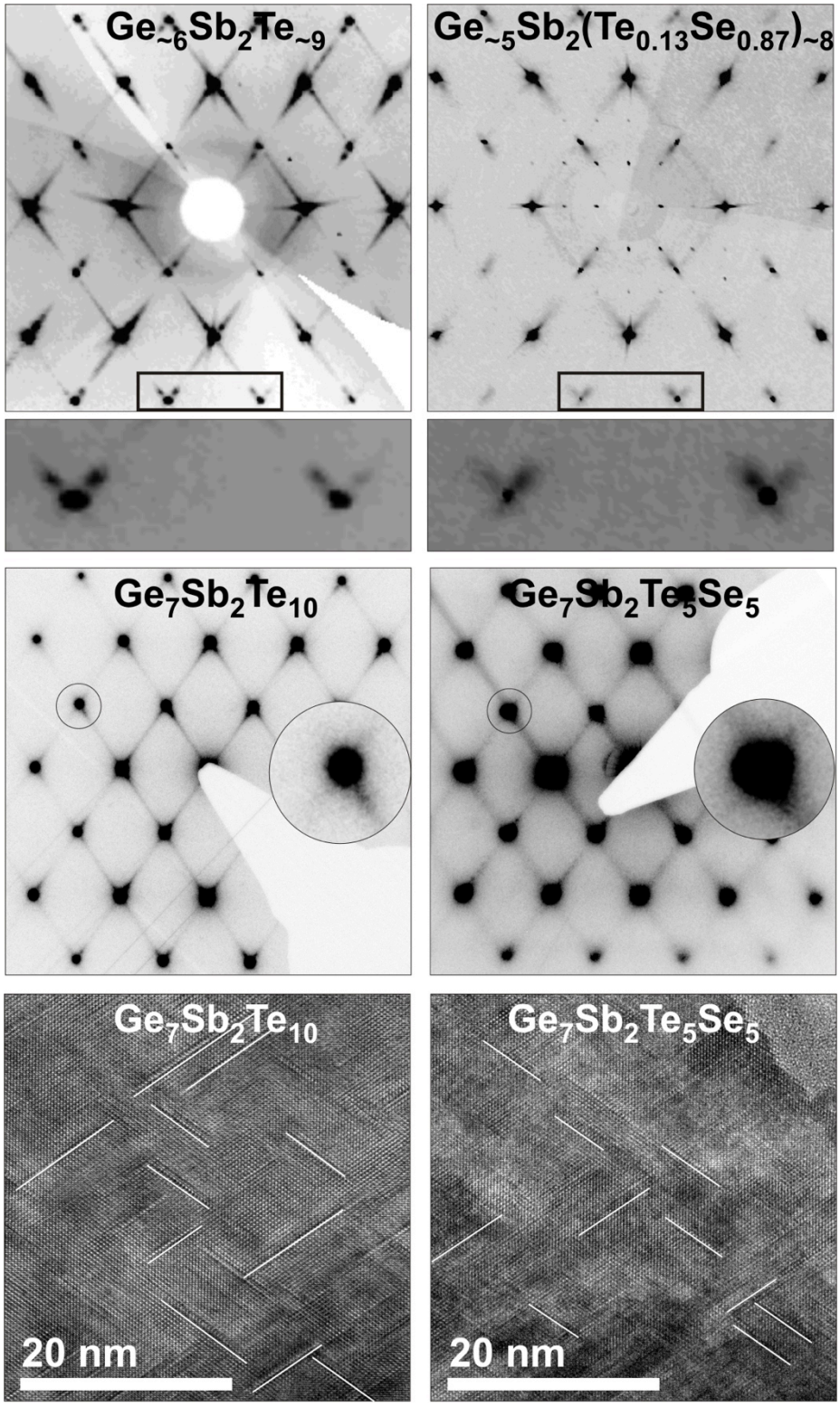

Fig. 7: Comparison of the real structures of unsubstituted (left) with Se-substituted (right) GST crystals; from top to bottom: reconstructed reciprocal lattice section *hhl* of single crystal X-ray data of $Ge_{\sim 6}Sb_2Te_{\sim 9}$ and $Ge_{\sim 5}Sb_2(Te_{0.13}Se_{0.87})_{\sim 8}$, respectively, measured at the Te-K absorption edge (enlarged section with diffuse scattering around Bragg reflections); SAED patterns of the <110> zone axes of $Ge_7Sb_2Te_{10}$ and $Ge_7Sb_2Te_5Se_5$, respectively, with enlarged reflection surrounded by diffuse intensity and HRTEM images (<110> zone axis) showing defect layers (some highlighted by white lines).

is visible in the HRTEM images and reflected in the broadening of the diffuse streaks both in the SAED and in the single-crystal X-ray diffraction patterns in Figure 7. The enlarged reflections depicted in the reciprocal lattice sections reconstructed from X-ray data as well as the SAED patterns show that the diffuse scattering of unsubstituted GST samples is localized on thin diffuse streaks between the Bragg reflections. The Se-substituted sample rather exhibits diffuse clouds whose diameter is larger than that of the Bragg reflections. This clearly indicates less pronounced 2D ordering, i.e., a smaller lateral extension of the defect layers, and is also obvious from the corresponding HRTEM images (Figures 6, 7, and additional data): the average lateral extension of the defect layers of the unsubstituted samples is 11(3) nm for n = 7 and 17(6) nm for n = 12, while the values found for the samples with x = 0.5 are 7(1) nm for n = 7 and 7(2) nm for n = 12, respectively.

2.3.3.3.4 Influence of Se substitution on the thermoelectric properties of GST materials

Thermoelectric measurements were performed starting with chemically homogeneous disc-shaped ingots of quenched pseudocubic $Ge_nSb_2(Te_{1-x}Se_x)_{n+3}$ (cf. Supporting Information, Figure S1, Tables S1 and S2). Their composition corresponds to the weighted samples (cf. Supporting Information Table S5), and the lattice parameters differ slightly from those of smaller samples due to minor variations of cooling rates; however, there is no indication for different nanostructures in samples with the same composition. The substitution with Se alters the phase transition temperatures and, as a consequence, the nanostructure of $Ge_nSb_2(Te_{1-x}Se_x)_{n+3}$ (see above) and thus strongly influences the thermoelectric properties (Figure 8). For $Ge_{12}Sb_2Te_{12}Se_3$, the thermal conductivity κ during cooling does not differ significantly from that during the heating process, thus the measured values were averaged. For the other samples multiply measured heating curves were averaged (cf. Supporting Information Figure S3). For σ and S, some of the heating and cooling measurements differ more than the experimental error since in some cases there are partially irreversible structural changes (see above). Still, the values are comparable and were averaged in order not to over-interpret very small time-dependent changes. Heating and cooling curves of the σ and S measurements of $Ge_{12}Sb_2Te_{12}Se_3$ further show that there is no significant change in a second measurement cycle. Therefore, the averaged σ and S curves show realistic values for materials in application.

For $Ge_{12}Sb_2Te_{15}$, σ and κ are significantly higher than for $Ge_7Sb_2Te_{10}$ and all samples containing Se. The latter exhibit electrical conductivities between 100 and 600 S/cm. Whereas

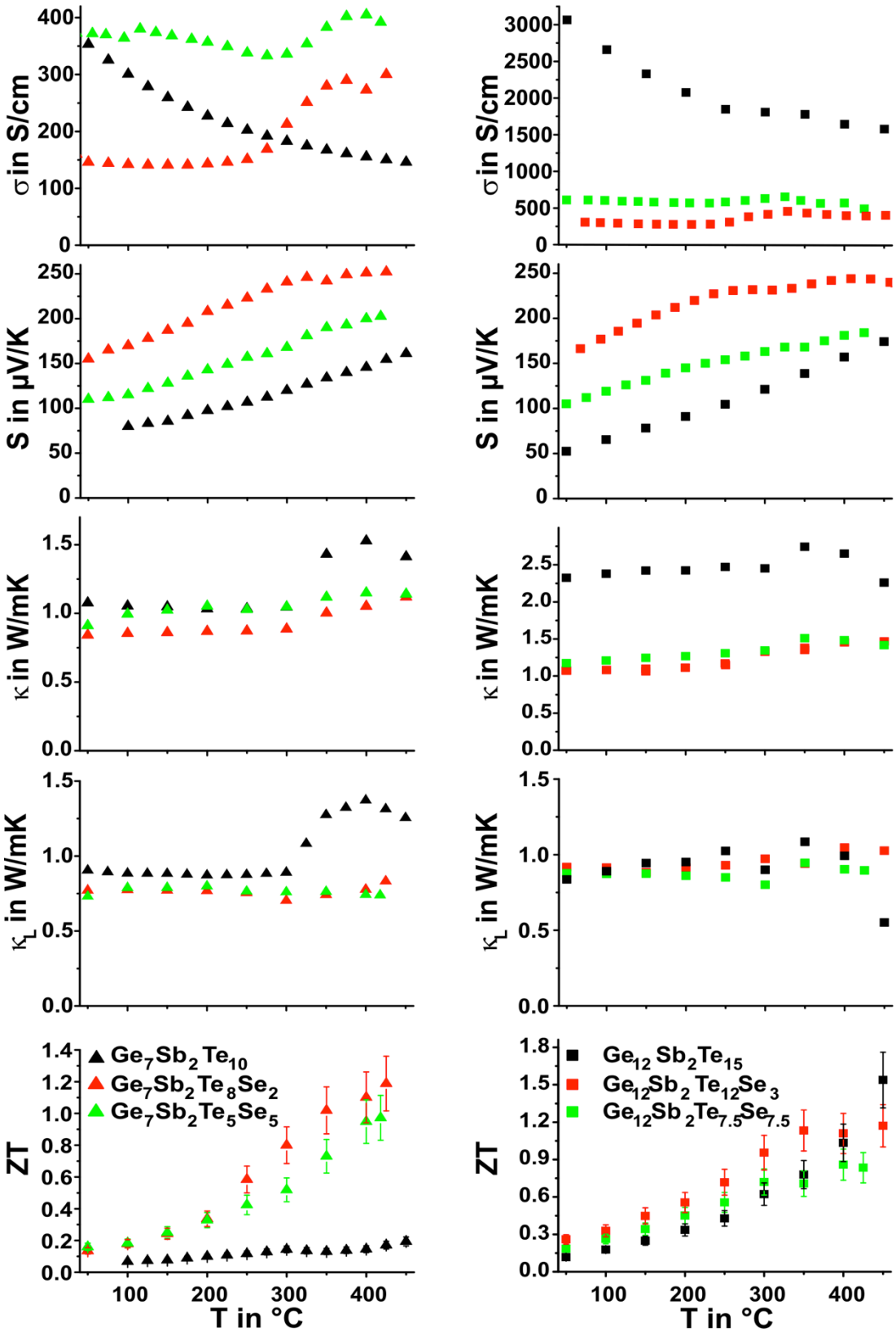

Fig. 8: Thermoelectric characteristics of quenched $Ge_nSb_2(Te_{1-x}Se_x)_{n+3}$ samples with n = 7 (left) and n = 12 (right); from top to bottom: electrical conductivity (σ), Seebeck coefficient (S), thermal conductivity (κ), lattice part of thermal conductivity (κ_L), and the resulting ZT values; averaged values of heating and cooling curves were used for S and σ. The error bars for the ZT values were calculated from those of the individual measurements as detailed in the Supporting Information.

for Se-free samples, the temperature dependence of σ corresponds to metallic behavior, σ of $Ge_nSb_2(Te_{1-x}Se_x)_{n+3}$ (x = 0.2, 0.5) changes little with temperature up to 300 °C for n = 7 and over the whole temperature range for n = 12. Se doping increases the ionicity so that σ of samples $Ge_{12}Sb_2(Te_{1-x}Se_x)_{15}$ with x > 0 is much lower (1/5 at RT; 1/3 at 430 °C) than for $Ge_{12}Sb_2Te_{15}$. When the trigonal layered phase is formed, Se-substituted samples with n = 7 become semiconducting; this effect is much less pronounced for n = 12. Probably the van der Waals gaps, which are more closely spaced for n = 7, impede metallic electron conduction. Thus, the samples $Ge_7Sb_2(Te_{1-x}Se_x)_{10}$ (x = 0.2, 0.5) are better electrical conductors at higher temperatures compared to metallic $Ge_7Sb_2Te_{10}$ whose σ decreases with temperature.

The lowest thermal conductivities are found for the samples $Ge_nSb_2(Te_{1-x}Se_x)_{n+3}$ with x = 0.2. For samples with n = 7, and for the Se-substituted ones with n = 12, the overall thermal conductivity κ as well as the lattice part κ_L are similar up to the phase transition temperature (~300 °C) for all values of x. $Ge_{12}Sb_2Te_{15}$ exhibits similar κ_L values but different κ due to the higher electronic contribution. The Se-substituted samples show a tendency for lower absolute values of κ_L, especially above 300 °C when the unsubstituted samples (especially $Ge_7Sb_2Te_{10}$) exhibit an increase in κ_L (and κ). Se-containing samples exhibit only a small increas in κ at higher temperatures, reflecting their increasing σ (especially for n = 7), while κ_L remains constant above 300°C probably due to the higher phonon scattering caused by the Se/Te anion disorder.

The Seebeck coefficient of all samples $Ge_nSb_2(Te_{1-x}Se_x)_{n+3}$ investigated is positive, i.e., the compounds are p-type materials. *S* increases with the temperature in the same way as it does for the unsubstituted samples that reach 110 - 180 μV K^{-1} at 450 °C.[7] *S* of samples with Se contents of x = 0.2 is on average by 100 μV K^{-1} higher than for the correspon+ding pure GST materials. This has a strong influence on the thermoelectric performance given the fact that high efficiency thermoelectrics like TAGS (Te-Ag-Ge-Sb)[60,61] compounds have a maximum *S* of 160 - 220 μV/K and *ZT* depends on the square of *S*. The highest values of up to 250 μV/K are reached for x = 0.2, i.e., moderate Se doping. Additional investigations on $Ge_{12}Sb_2Te_{15}$ (shown in the Supporting Information Figure S4) reveal typical charge carrier concentrations that increase form $0.6 \cdot 10^{[21]}$ at 25 °C to $1.2 \cdot 10^{21}$ at 300 °C and charge carrier mobilities that decrease from 14 $cm^2/(V \cdot s)$ at 25 °C to ~ 2 $cm^2/(V \cdot s)$ at 500 °C.

In general, the substitution with small amounts of Se leads to the most favorable combination of high *S* and low κ with a relatively high σ. The high *S* is the crucial quantity behind the higher maximal *ZT* values (at 425 °C) of Se-substituted $Ge_7Sb_2(Te_{1-x}Se_x)_{10}$ (maximal *ZT* ~ 1.0 for x = 0.5 and *ZT* ~ 1.2 for x = 0.2) compared to the unsubstituted sample (maximal *ZT* ~

0.2). This is due to the less pronounced metallic character resulting from the incorporation of electronegative Se. Around 250 °C, the *ZT* value of the Se-containing samples increases much faster compared to the unsubstituted ones due to a strong increase of σ upon forming the trigonal phase that is not fully compensated by the less pronounced increase in κ. For n = 12, the reduced κ cannot compensate the very high σ of $Ge_{12}Sb_2Te_{15}$ so that an increased *ZT* value is observed only at temperatures below 300 °C for x = 0.5 and 400 °C for x = 0.2. At higher temperature, the ”convergence” of *S* in combination with the still rather large difference in σ results in higher *ZT* vales of the unsubstituted sample (*ZT* ~ 1.5 at 450 °C) while the substituted ones exhibit a slower increase of *ZT* ($Ge_{12}Sb_2Te_{7.5}Se_{7.5}$) or no increase at all ($Ge_{12}Sb_2Te_{12}Se_3$ with *ZT* = 1.1 – 1.2 between 350°C and 450 °C). As a rule (up to 300 – 400 °C), the *ZT* values of the substituted $Ge_nSb_2(Te_{1-x}Se_x)_{n+3}$ samples with x = 0.2 is signficantly higher than those of unsubstituted ones and or those of samples with a higher degree of substitution (x = 0.5) due to their higher *S*.

2.3.3.4 Conclusion

Our experiments have shown that Te in pseudocubic quenched GST bulk materials $Ge_nSb_2Te_{3+n}$ ($7 \leq n \leq 19$) can be partially replaced by Se; however, it is not possible to synthesize single phase quenched pseudocubic samples of ternary $Ge_nSb_2Se_{3+n}$. Quenching Se-substituted samples with n = 19 yields α-GeTe-type structures, which exhibit a pronounced deviation from cubic metrics. Samples with higher Se substitution rates exhibit lower transition temperatures between the cubic HT and the layered trigonal phase; thereby the diffusion processes during the quenching processes are more limited. As a consequence, the average lateral extension of the defect layers is smaller and the nanostructure of pseudocubic quenched samples is stable up to higher temperatures for increasing Se concentrations. This result may also be important for thin-film phase-change materials. Moreover, thermoelectric devices using compounds with higher Se content could be used up to higher temperatures without altering the nanostructure and properties. The best thermoelectric performance is achieved for low Se substitution rates (20 %). The resulting compounds exhibit a lower thermal conductivity due to the nanostructure and the additional disorder by the mixed occupation of the anion position. In combination with a higher *S* but lower σ due to the less metallic character (increased ionicity) compared to the unsubstituted samples, this results in up to 6 times higher *ZT* values when 20% of the Te is substituted with Se in $Ge_7Sb_2Te_{10}$. However, at higher substitution rates (50%), the effect of the substitution on σ and *S* is less pronounced than for lower substitution rates. This could be a result of the

change in band structure and the mobility of the charge carriers. The influence of the substitution on the thermoelectric performance is more pronounced for samples with lower GeTe content (n = 7 vs. n =12). The well understood influence of the GeTe/Sb_2Te_3 ratio and the thermal treatment on the nanostructure and thermoelectric properties of GST materials can be combined with Se substitution. This results in Se-substituted nanostructured GST materials with improved thermoelectric properties and an increased thermal stability which offer various approaches for further optimization.

Acknowledgments

The authors thank Christian Minke (LMU Munich) for SEM operation and EDX analyses, Thomas Miller (LMU Munich) for the temperature-dependent powder diffraction experiments and Werner Schönau (DLR Cologne) for temperature-dependent thermal analysis. Dr. Loredana Erra and Dr. Gavin Vaughan helped with synchtotron measurements at the ESRF, Grenoble (project HS4363). We thank Dr. G. J. Snyder (California Institute of Technology) and Stefan Maier (LMU Munich) or the Hall measruement shown in the Supporting Information. Furthermore, we are indebted to Prof. Dr. W. Schnick (LMU Munich) for his generous support of this work. This investigation was funded by the Deutsche Forschungsgemeinschaft (grant OE530/1-2).

2.3.3.5 Supplementary Information

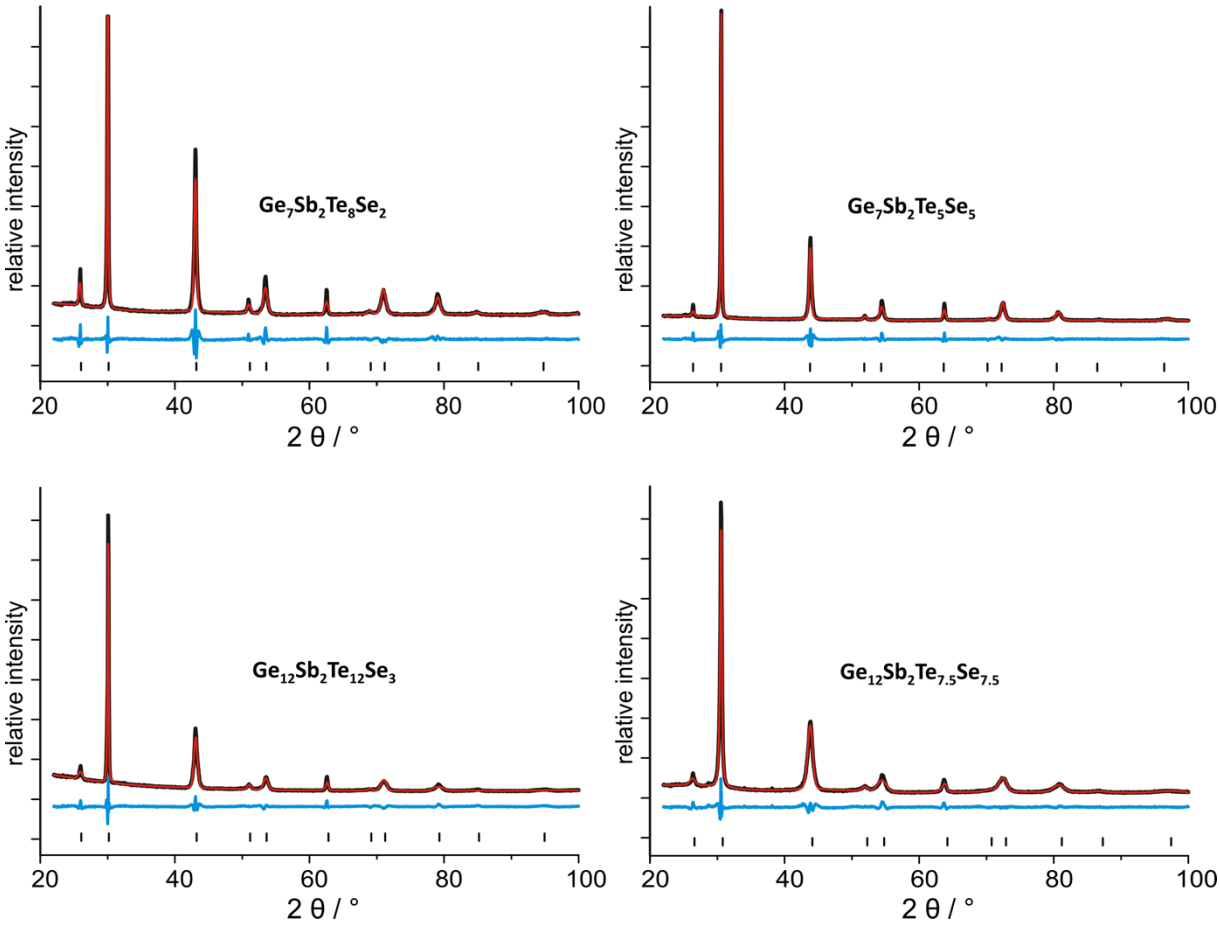

Fig. S1: Profile fits for the Rietveld refinements (cf. Table T1) for powders that were obtained by grinding small parts of the ingots used for thermoelectric measurements of $Ge_nSb_2(Te_{1-x}Se_x)_{n+3}$; experimental (black) and simulated (red) powder patterns, difference plot (blue) and reflection markers (black, bottom); the scaling of the 2 θ axis is the same for all plots and the intensities have been normalized according to the intensity of the strongest reflection of the experimental powder pattern.

Table S1. Details of the Rietveld refinements for powder diffraction data of the quenched $Ge_nSb_2(Te_{1-x}Se_x)_{n+3}$ samples used for thermoelectric measurements (obtained by grinding small parts of the ingots)

	$Ge_7Sb_2Te_8Se_2$	$Ge_7Sb_2Te_5Se_5$	$Ge_{12}Sb_2Te_{12}Se_3$	$Ge_{12}Sb_2Te_{7.5}Se_{7.5}$
asymmetric unit	$Ge_{0.7}Sb_{0.2}Se_{0.2}Te_{0.8}$	$Ge_{0.7}Sb_{0.2}Se_{0.5}Te_{0.5}$	$Ge_{0.8}Sb_{0.133}Se_{0.2}Te_{0.8}$	$Ge_{0.8}Sb_{0.133}Se_{0.5}Te_{0.5}$
formula weight asymmetric unit (in g mol^{-1})	193.05	178.46	192.15	177.56
F(000)	324.0	302.4	323.1	301.5
crystal system / space group (no.)	cubic / $Fm\bar{3}m$ (225)			
lattice parameters (in Å)	a = 5.919(3)	a = 5.844(2)	a =5.913(2)	a = 5.798(2)
cell volume (in $Å^3$)	207.4(4)	199.6(2)	206.8(6)	194.9(2)
density (X-ray, in g/cm³)	6.182(11)	5.939(6)	6.174(6)	6.052(7)
radiation	Cu-$K_{\alpha 1}$ (λ = 1.540596 Å)			
2θ range (in °)	$22 \leq 2\theta \leq 100$			
parameters (thereof background)	33 (12)		32 (12)*	
R_p / R_{wp}	0.026 / 0.043	0.028 / 0.046	0.023 / 0.034	0.027 / 0.038
GooF / R_{Bragg}	1.515 / 0.013	1.656 / 0.010	1.301 / 0.011	1.469/ 0.007

*1 profile parameter less for $Ge_{12}Sb_2(Te_{1-x}Se_x)_{15}$ (x = 0.2, 0.5)

Table S2. Atom coordinates and isotropic displacement parameters (in Å²) from Rietveld refinements for the $Ge_nSb_2(Te_{1-x}Se_x)_{n+3}$ samples used for thermoelectric measurements (obtained by grinding small parts of the ingots).

	Anions				Cations and vacancies			
	position		occupancy	U_{iso}	position		occupancy	U_{iso}
$Ge_7Sb_2Te_8Se_2$	4*a*	1/2 1/2 1/2	4/5 Te, 1/5 Se	1.36(10)	4*b*	0 0 0	7/10 Ge, 2/10 Sb	3.06(14)
$Ge_7Sb_2Te_5Se_5$	4*a*	1/2 1/2 1/2	1/2 Te, 1/2 Se	1.32(10)	4*b*	0 0 0	7/10 Ge, 2/10 Sb	2.93(13)
$Ge_{12}Sb_2Te_{12}Se_3$	4*a*	1/2 1/2 1/2	4/5 Te, 1/5 Se	1.88(12)	4*b*	0 0 0	12/15 Ge, 2/15 Sb	3.62(15)
$Ge_{12}Sb_2Te_{7.5}Se_{7.5}$	4*a*	1/2 1/2 1/2	1/2 Te, 1/2 Se	1.19(8)	4*b*	0 0 0	12/15 Ge, 2/15 Sb	4.12(13)

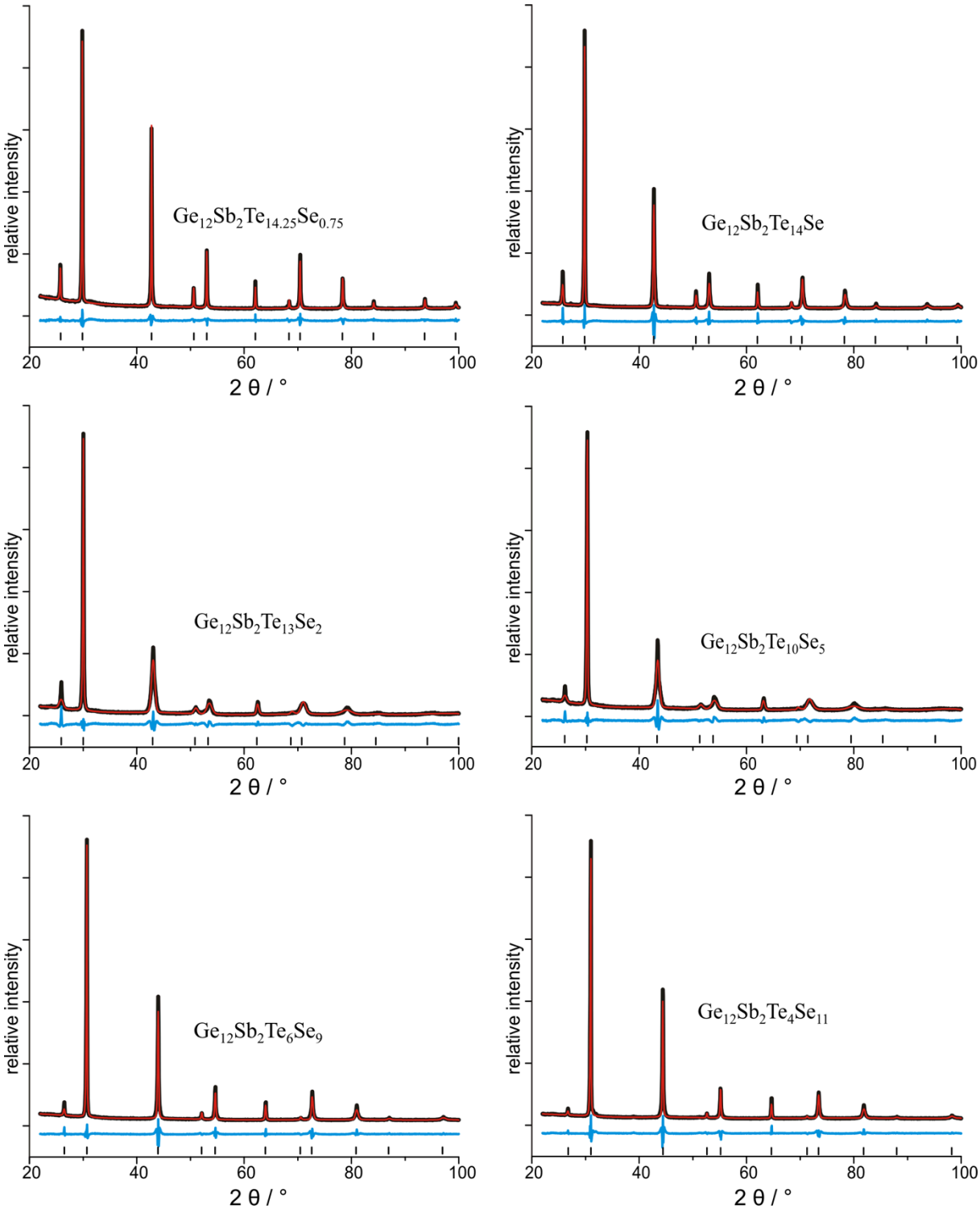

Fig. S2: Profile fits from Rietveld refinements of $Ge_{12}Sb_2(Te_{1-x}Se_x)_{15}$ samples that where prepared by quenching the melt in water, subsequently annealing in the existence range of the cubic HT Phase (580 °C) for 2 days and quenching in water again: experimental (black) and simulated (red) powder patterns, difference plot (blue) and reflection markers (black, bottom); the scaling of the 2 θ axis is the same for all plots and the intensities have been normalized according to the intensity of the strongest reflection of the experimental powder pattern.

Table S3a. Details of the Rietveld refinements for the quenched $Ge_{12}Sb_2(Te_{1-x}Se_x)_{15}$ phases.

	$Ge_{12}Sb_2Te_{14.25}Se_{0.75}$	$Ge_{12}Sb_2Te_{14}Se$	$Ge_{12}Sb_2Te_{13}Se_2$
x	0.05	0.067	0.133
M (in g mol^{-1})	2992.72	2980.56	2931.92
F(000)	334.0	332.8	328.0
crystal system / space group (no.)		cubic / $Fm\bar{3}m$ (225)	
lattice parameters (in Å)	a = 5.9752(3)	a = 5.9811(7)	a =5.951(4)
cell volume (in $Å^3$)	213.33(3)	213.96(7)	210.7(4)
density (X-ray, in g/cm³)	6.2112(8)	6.168(2)	6.161(12)
Radiation		Cu-$K_{\alpha1}$ (λ = 1.540596 Å)	
2θ range (in °)		22 ≤ 2θ ≤ 100	
parameters (thereof background)		33 (12)	
R_p / R_{wp}	0.027 / 0.039	0.042 / 0.073	0.038/ 0.057
GooF / R_{Bragg}	1.516 / 0.008	2.902 / 0.017	2.253 / 0.008

Table S3b. Details of the Rietveld refinements for the quenched $Ge_{12}Sb_2(Te_{1-x}Se_x)_{15}$ phases.

	$Ge_{12}Sb_2Te_{10}Se_5$	$Ge_{12}Sb_2Te_6Se_9$	$Ge_{12}Sb_2Te_4Se_{11}$
x	0.333	0.600	0.733
M (in g mol^{-1})	2786.00	2591.44	2494.16
F(000)	313.6	294.4	284.8
crystal system / space group (no.)		cubic / $Fm\bar{3}m$ (225)	
lattice parameters (in Å)	a = 5.902(4)	a = 5.819(1)	a =5.7625(15)
cell volume (in $Å^3$)	205.5(4)	197.05(12)	191.35(15)
density (X-ray, in g/cm³)	6.001(12)	5.823(3)	5.771(4)
radiation		Cu-$K_{\alpha1}$ (λ = 1.540596 Å)	
2θ range (in °)		22 ≤ 2θ ≤ 100	
parameters (thereof background)		33 (12)	
R_p / R_{wp}	0.034 / 0.053	0.036 / 0.059	0.047 / 0.074
GooF / R_{Bragg}	2.084 / 0.010	2.334 / 0.010	3.096 * / 0.022

*) The slightly worse fit of these data is not hard to recognize in Fig. S2 as it is uniformly distributed over the whole pattern.

Table S4. Atom coordinates and isotropic displacement parameters for the quenched $Ge_{12}Sb_2(Te_{(1-x)}\ Se_x)_{15}$ phases (in Å²).

	anions				cations and vacancies			
	position		occupancy	U_{iso}	position		occupancy	U_{iso}
$Ge_{12}Sb_2Te_{14.25}Se_{0.75}$	4*a*	½ ½ ½	0.95 Te, 0.05 Se	1.09(5)	4*b*	0 0 0	12/15 Ge, 2/15 Sb	3.15(9)
$Ge_{12}Sb_2Te_{14}Se$	4*a*	½ ½ ½	14/15 Te, 1/15 Se	0.94(8)	4*b*	0 0 0	12/15 Ge, 2/15 Sb	3.56(13)
$Ge_{12}Sb_2Te_{13}Se_2$	4*a*	½ ½ ½	13/15 Te, 2/15 Se	1.20(11)	4*b*	0 0 0	12/15 Ge, 2/15 Sb	3.66(15)
$Ge_{12}Sb_2Te_{10}Se_5$	4*a*	½ ½ ½	2/3 Te,1/3 Se	1.26(13)	4*b*	0 0 0	12/15 Ge, 2/15 Sb	3.81(17)
$Ge_{12}Sb_2Te_6Se_9$	4*a*	½ ½ ½	6/15 Te, 9/15 Se	1.27(8)	4*b*	0 0 0	12/15 Ge, 2/15 Sb	3.72(12)
$Ge_{12}Sb_2Te_4Se_{11}$	4*a*	½ ½ ½	4/15 Te,11/15 Se	1.52(9)	4*b*	0 0 0	12/15 Ge, 2/15 Sb	3.58(12)

Table S5. EDX results of $Ge_nSb_2(Te_{1-x}Se_x)_{n+3}$ samples: calculated values: SEM-EDX of samples for thermoelectric (TE) characterization and TEM-EDX of the samples investigated by TEM (in atom-%, one measurement from the region used for HRTEM images, accuracy ~ 1 – 2 atom-%).

weighted composition		Ge	Sb	Te	Se
$Ge_7Sb_2Te_8Se_2$	calculated	36.8	10.5	42.1	10.5
	TE sample	37.1(5)	11.0(3)	41.2(6)	10.6(2)
	TEM	35.7(2.3)	10.6(6)	42.1(1.3)	11.4(3)
$Ge_7Sb_2Te_5Se_5$	calculated	36.8	10.5	26.3	26.3
	TE sample	37.1(7)	10.2(7)	26(1)	27(2)
	TEM	35.0(1)	10.3(7)	27.0(4)	27.6(1.1)
$Ge_{12}Sb_2Te_{12}Se_3$	calculated	41.4	6.9	41.4	10.3
	TE sample *	40.9(5)	6.9(2)	41.5(6)	10.8(3)
	TEM	41.5(4)	7.1(1.3)	41.8(9)	9.6(1.9)
$Ge_{12}Sb_2Te_{7.5}Se_{7.5}$	calculated	41.4	6.9	25.9	25.9
	TE sample	41.7(3)	6.4(1)	27.8(9)	24.0(5)
	TEM	41.4	6.8	25.7	26.0

* Thermoelectric values of a sample prepared under the same conditions as those used for the sample for EDX (here) are given in the paper.

Table S6. EDX results of the $Ge_nSb_2(Te_{1-x}Se_x)_{n+3}$ samples used for the Vegard plot (Fig. 2): calculated values and SEM-EDX (in atom %, the number of point measurements averaged is given in parentheses).

weighted composition		Ge	Sb	Te	Se
$Ge_{12}Sb_2Te_{14}Se$	calculated	41.38	6.90	3.45	48.28
	SEM-EDX (4)*	43(5)	7(4)	2.9(8)	47.5(9)
$Ge_{12}Sb_2Te_{13}Se_2$	calculated	41.38	6.90	6.90	44.83
	SEM-EDX (3)	41.5(1.2)	7.9(1.7)	11.4(1.9)	39.3(2.6)
$Ge_{12}Sb_2Te_{10}Se_5$	calculated	41.38	6.90	17.24	34.48
	SEM-EDX (3)	42.3(1.2)	7.6(7)	16.6(2.3)	33.5(1.8)
$Ge_{12}Sb_2Te_8Se_7$	calculated	41.38	6.90	24.14	27.59
	SEM-EDX (4)	42.4(7)	6.9(5)	27.8(2.39	24.8(2.1)
$Ge_{12}Sb_2Te_6Se_9$	calculated	41.38	6.90	31.03	20.69
	SEM-EDX (4)	41.0(8)	7.6(1.1)	32.1(6)	19.3(5)

* This measurement was done before annealing the sample; the rather large variance probably indicated a slightly inhomogeneous distribution of Ge and Sb; however, the effect might also be due to surface roughness effects.

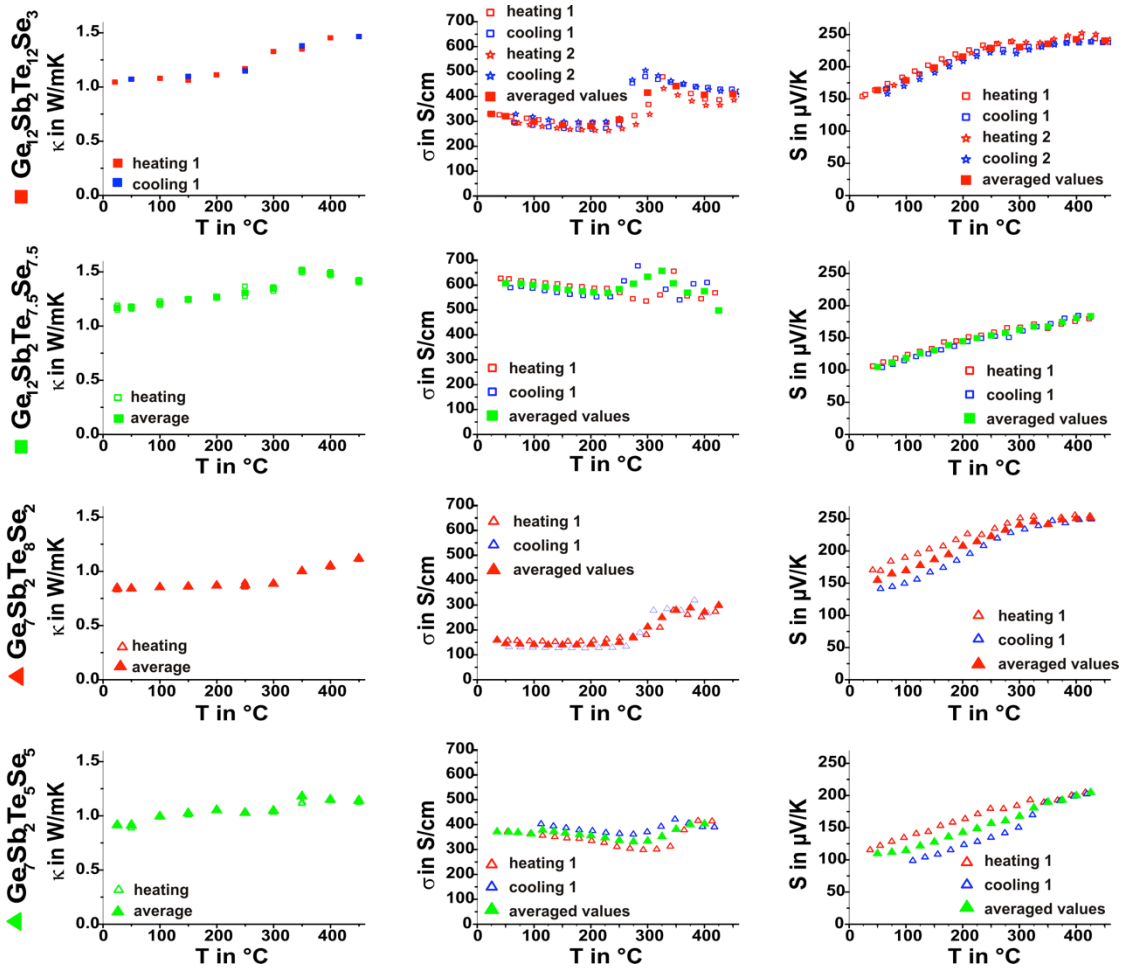

Fig. S3: Thermoelectric characteristics of quenched $Ge_nSb_2(Te_{1-x}Se_x)_{n+3}$ samples: top to bottom $Ge_{12}Sb_2Te_{12}Se_3$, $Ge_{12}Sb_2Te_{7.5}Se_{7.5}$, $Ge_7Sb_2Te_8Se_2$ and $Ge_7Sb_2Te_5Se_5$; from left to right: thermal conductivity (κ), electrical conductivity (σ) and Seebeck coefficient (S)

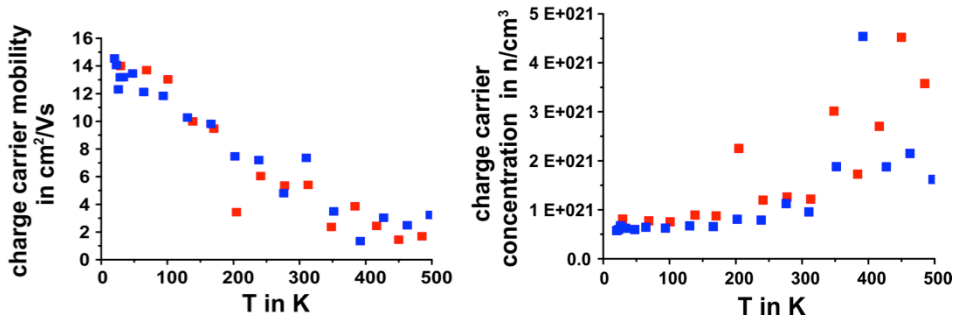

Fig. S4: Charge carrier concentration and charge carrier mobility obtained by Hall measurements of quenched $Ge_{12}Sb_2Te_{15}$.

Appendix to the Experimental Section

Details of the temperature programmed X-ray powder diffraction investigations

Powdered samples were filled intp silica glass capillaries with a diameter of 0.3 mm under Ar atmosphere. These were heated from room temperature up to 750 °C with 10 °C/min and subsequently cooled to room temperature at the same rate. Data were collected every 25°C with 10-20 minutes acquisition time.

Treatment of the thermoelectric data:

The values of (in some cases multiple) heating and cooling cycles were averaged to avoid the over-interpretation of slight variations e.g. due to partially irreversible structural changes, various experimental errors, etc. (cf. Section 3.4). In order to obtain comparable data, equal temperature steps were obtained from the different measurements by linear interpolation.

Uncertanties of the thermoelectric characterization

The estimated experimental uncertainties of individual measurements are 7% for the electrical conductivity (due to the slightly irregular sample geometries, the "standard" value of 5% was increased to account for sample imperfectness) and 5% for the Seebeck coefficient. An experimental error of 3% for the thermal diffusivity and 5% for the heat capacity was considered in the calculation of the uncertainty of the ZT values shown as error bars in Figure 8. This uncertainty of 14% results from the square root of the sum of the squares of the individual errors which is valid given the assumption of independent and statistical individual errors. The uncertainties of the ZT values and the individual measurements are comparable to the values stated in the *International Round-Robin Study* on the transport properties of bulk thermoelectrics.[62,63]

2.3.3.6 References

[1] S. Raoux, R. M. Shelby, J. Joran-Sweet, B. Munoz, M. Salinga, Y.-C. Chen, Y.-H. Shih, E.-K. Lai, M.-H. Lee, *Microelectron. Eng.* **2008**, *85*, 2330.

[2] T. Siegrist, P. Merkelbach, M. Wuttig, *Annu. Rev. Condens. Matter Phys*. **2012**, *3*, 215.

[3] T. Matsunaga, N. Yamada, *Phys. Rev. B*. **2004**, *69*, 104111.

[4] M. Wuttig, S. Raoux, *Z. Anorg. Allg. Chem.* **2012**, *638*, 2455.

[5] D. Lancer, M. Salinga, B. Grabowski, T. Hickel, J. Neugebauer, M. Wuttig, *Nature Mater.* **2008**, *7*, 972.

[6] M. N. Schneider, T. Rosenthal, C. Stiewe, O. Oeckler, *Z. Kristallogr.* **2010**, *225*, 463.

[7] T. Rosenthal, M. N. Schneider, C. Stiewe, M. Döblinger, O. Oeckler, *Chem. Mater.* **2011**, *23*, 4349.

[8] T. L. Anderson, H. B. Krause, *Acta Crystallogr. Sect. C* **1974**, *47*, 1141.

[9] O. G. Karpinsky, L. E. Shelimova, M. A. Kretova, J.-P. Fleurial, *J. Alloys Compd.* **1998**, *268*, 112.

[10] L. E. Shelimova, O. G. Karpinsky, M. A. Kretova, V. I. Kosyakov, V. A. Shestakov, V. S. Zemskov, F. A. Kuznetsov, *Inorg. Mater.* **2000**, *36*, 768.

[11] T. Matsunaga, H. Morita, R. Kojima, N. Yamada, K. Kifune, Y. Kubota, Y. Tabata, J.-J. Kim, M. Kobata, E. Ikenaga, K. Kobayashi, *J. Appl. Phys.* **2008**, *103*, 093511.

[12] S. Raoux, W. Wojciech, D. Ielmini, *Chem. Rev.* **2010**, *110*, 240.

[13] T. Rosenthal, L. Neudert, S. Welzmiller, O. Oeckler, *Z. Kristallogr. Suppl.* **2012**, *32*, 15.

[14] H. Li, K. F. Cai, Y. Du, H. F. Wang, S. Z. Shen, X. L. Li, Y. Y. Wang, C. W. Zhou, *Curr. Appl. Phys*. **2012**, *12*, 188.

[15] M. Schmidt, R. Zybala, K. T. Wojciechowski, *Ceram. Mater.* **2010**, *62*, 465.

[16] K. Wojciechowski, J. Tobola, M. Schmidt, R. Zybala, *J. Phys. Chem. Solids* **2008**, 69, 2748.

[17] K. Wojciechoeski, M. Schmidt, J. Tobola, M. Koza, A. Olech, R. Zybala, *J. Electron. Mater.* **2010**, *39*, 2053.

[18] K. T. Wojciechowski, M. Schmidt, *Phys. Rev. B*, **2009**, *79*, 184202.

[19] B. Du, H. Li, J. Xu, X. Tang, C. Uher, *Chem. Mater.* **2010**, *22*, 5521.

[20] B. Duan, P. Zhai, L. Liu, Q. Zhang, X. Ruan, *J. Solid State Chem.* **2012**, *193*, 8.

[21] B. Duan, P. Zhai, L. Liu, Q. Zhang, *Mater. Res. Bull.* **2012**, *47*, 1670.

[22] B. Duan, P. Zhai, L. Liu, Q. Zhang, *J. Electron. Mater*. **2012**, *41*, 1120.

[23] S. Buller, C. Koch, W. Bensch, P. Zalden, R. Sittner, S. Kremers, M. Wuttig, U. Schürmann, L. Kienle, T. Leichtweiß, J. Janek, B. Schönborn, *Chem. Mater.* **2012**, *24*, 3582.

[24] S. N. Dutta, G. A. Jeffrey, *Inorg. Chem.* **1965**, *4*, 1363.

[25] T. Chattopadhyay, J. X. Boucherle, H. G. von Schnering, *J. Phys. C: Solid State Phys*. **1987**, *20*, 1431.

[26] J. Goldak, C. S. Barrett, D. Innes, W. *J.* Youdelis, *Chem. Phys.* **1966**, *44,* 3323.

[27] K. Schubert, H. *Z.* Fricke, *Naturforsch. A* **1951***, 6,* 781.

[28] K. Schubert, H. *Z.* Fricke, *Metallkd*. **1953**, *44*, 457.

[29] S. Brodas, M. T. Clavaguera-Mora, B. Legendre, C. Hancheng, *Thermochim. Acta* **1986**, *107*, 239.

[30] S. Brodas, M. T. Clavaguera-Mora, B. Legendre, *Thermochim. Acta* **1982**, *56*, 161.

[31] P. Losták, R. Novontný, L. Benes, S. Civis, *J. Crystal Growth* **1989**, *94*, 656.

[32] J. Tomforde, S. Buller, M. Ried, W. Bensch, D. Wamwangi, M. Heidelmann, M. Wuttig, *Solid State Sci.* **2009**, *11*, 683.

[33] *DigitalMicrograph 3.6.1*, Gatan Software, Pleasanton, USA, **1999**.

[34] P. A. Stadelmann, *Ultramicroscopy* **1987**, *21*, 131.

[35] *ESVision*, *4.0.164*, Emispec Systems Inc., Tempe, USA, **1994-2002**.

[36] *WINXPOW*, *v2.12 ed*., Stoe & Cie GmbH, Darmstadt, Germany, **2005**.

[37] *TOPAS-Academic*, *V. 4.1*, Coelho Software, Brisbane, Australia, **2007**.

[38] J.-C. Labiche, O. Mathon, S. Pascarelli, M. A. Newton, G. G. Ferre, C. Curfs, G. Vaughan, A. Homs, D. F. Carreiras, *Rev. Sci. Instrum.* **2007**, *78*, 091301.

[39] G. B. M. Vaughan, J. P. Wright, C. Bytchkov, C. Curfs, C. Grundlach, M. Orlova, L. Erra, H. Gleyzolle, T. Buslaps, A. Götz, G. Suchet, S. Petitdemange, M. Rossat, L. Margulies, W. Ludwig, A. Snigirey, I. Snigireva, H. O. Sørensen, E. M. Lauridsen, U. L. Olsen, J. Oddershede, H. F. Poulsen, *Proc. 31st Risø Int. Symp. Mater. Sci.* **2010**, *521*, 457.

[40] G. Evans, R. F Pettifer, *J. Appl. Crystallogr.* **2001**, *34*, 82.

[41] *IPDS software package*, STOE & Cie GmbH, Darmstadt, Germany, **1997-1999**.

[42] *X-RED32 V. 1.31*, STOE & Cie GmbH, Darmstadt, Germany, **2005**.

[43] *X-SHAPE V. 2.07*, STOE & Cie GmbH, Darmstadt, Germany, **2005**.

[44] J. L. Chambers, K. L. Smith, M. R. Pressprich, Z. Jin, *SMART Version 5.059*, Bruker AXS, Madison (USA) **1997-1998**.

[45] *SAINT V. 6.36A*, Bruker AXS, Madison , USA, **1997-2002**.

[46] *SADABS V. 2.05*, Bruker AXS, Madison, USA, **1999**.

[47] V. Petricek, M. Dusek, Palatinus, L. *JANA2006 – The Crystallographic Computing System*. Institute of Physics, Praha, Czech Republic, **2006**.

[48] G. M. Sheldrick, *Acta Crystallogr. Sect. A* **2008**, *64*, 112.

[49] J. de Boor, C. Stiewe, P. Ziolkowski, T. Dasgupta, G. Karpinski, E. Lenz, F. Edler, E. Müller, *J. Electron. Mater.* **2013**, *42*, 1711.

[50] J. de Boor, E. Müller, *Rev. Sci. Instrum.* **2013**, *84*, 065102.

[51] G. S. Kumar, G. Prasad, R. O. Pohl, *J. Mater. Chem.* **1993,** *28*, 4261.

[52] A. Le Bail, A. Jouanneaux, *J. Appl. Crystallogr*. **1997**, *30*, 265.

[53] unpublished results, deposited at the Fachinformationszentrum Karlsruhe, 76344 Eggenstein-Leopoldshafen, Germany (fax: (+49)7247-808-666; e-mail: crysdata@fiz-karlsruhe.de) as CSD-426863.

[54] A. K. Cheetham, A. P. Wilkinson, *Angew. Chem. Int. Ed.* **1992**, *31*, 1557.

[55] S. Welzmiller, P. Urban, F. Fahrnbauer, L. Erra, O. Oeckler, *J. Appl. Crystallogr.* **2013**, *46*, 769.

[56] J. L. Hodeau, V. Favre-Nicolin, S. Bos, H. Renevier, E. Lorenzo, J. F. Berar, *Chem. Rev.* **2001**, *101*, 1843.

[57] L. Kissel, B. Zhou, S. C. Roy, S. K. Sen Gupta, R. H. Pratt, *Acta Crystallogr. Sect. A* **1995**, *51*, 271.

[58] M. N. Schneider, X. Biquard, C. Stiewe, T. Schröder, P. Urban, O.Oeckler, *Chem. Commun.* **2012**, *48*, 2192.

[59] M. N. Schneider, M. Seibald, P. Lagally, O. Oeckler, *J. Appl. Crystallogr.* **2010**, *43*, 1012.

[60] Y. Chen, T. J. Zhu, S. H. Yang, S. N. Zhang, W. Miao, X. B. Zhao, *J. Electron. Mater.* **2010**, *39*, 1719.

[61] S. H. Yang, T. J. Zhu, C. Yu, J. J. Shen, Z. Z. Yin, X. B. Zhao, *J. Electron. Mater.* **2011**, *40*, 1244.

[62] H. Wang, W. D. Porter, H. Böttner, J. König, L. Chen, S. Bai, T. M. Tritt, A. Mayolet, J. Senawiratne, C. Smith, F. Harris, P. Gilbert, J. W. Sharp, J. Lo, H. Kleinke, L. Kiss, *J. Electron. Mater*. **2013**, *42*, 654.

[63] H. Wang, W. D. Porter, H. Böttner, J. König, L. Chen, S. Bai, T. M. Tritt. A. Mayolet, J. Senawiratne, C. Smith, F. Harris, P. Gilbert, J. W. Sharp, J. Lo, H. Kleinke, L. Kiss, *J. Electron. Mater*. **2013**, *42*, 1073.

3 Real - structure property relationships in thermoelectric chalcogenides

3.1 Overview

The insights concerning the optimization of the thermoelectric properties by substitution and thermal treatment obtained for GST materials (Chapter 2) can be transferred to various related tellurides. The structural chemistry in the system $(GeTe)_nBi_2Te_3$ (GBT materials) is analogous to that of GST materials.[1-3] It is possible to influence the nanostructures and thermoelectric properties of GBT materials by variation of the thermal treatment during high-pressure (HP) synthesis (Chapter 3.2). Thermodynamically stable $GeBi_2Te_4$ and samples that were slowly cooled under HP conditions are metallic. In contrast, samples thermally quenched while maintaining the pressure exhibit semiconducting characteristics of σ(T), since they have higher grain-boundary concentrations compared to slowly cooled ones.

Investigations on other Bi containing compounds such as $In_2Bi_3Se_7I$ and $InBi_2Se_4I$ (Chapter 3.3) reveal that even though their structural motifs are well suited for low thermal conductivity (κ) due to the presence of rather weakly bound heavy atoms (rattlers), low σ values and consequently *ZT* values are observed if all elements exhibit normal valence states. However, delocalized electrons in In_3SbTe_2 result in metallic conductivity, which impedes high *S* and therefore high *ZT* values.[4] In_3SbTe_2 exhibits a rocksalt-type structure with In in a sixfold coordination and randomly disordered Sb and Te on the anion position. No pronounced nanostructures are present; however, TEM investigations and single-crystal X-ray data reveal diffuse streaks caused by static atom displacements from the special position as a result of the different radii of the atoms occupying the anion position. The sixfold coordination of In in metallic In_3SbTe_2 is uncommon as In exhibits a tetrahedral coordination polyhedron at ambient conditions in most of its compounds. However, HP conditions are a way to synthesize homogeneous bulk materials of silver indium antimony telluride (AIST) $Ag_{3.4}In_{3.7}Sb_{76.4}Te_{16}$, which at ambient pressure can only be obtained by melt spinning.[5] Like the GST materials discussed in Chapter 2, $Ag_{3.4}In_{3.7}Sb_{76.4}Te_{16}$ is used as a phase-change material for rewritable data storage.[6,7] Both HP syntheses and melt-spinning yield the A7 (gray As type) structure type, in which In is coordinated in a 3+3 fashion. The preference for the fourfold coordination of In might be an explanation for the formation of chalcopyrite-type $AgInTe_2$ under conventional solid-state synthesis conditions and upon heating the A7-type

material. Whereas it is impossible to synthesize mixed crystals of rocksalt-type $AgSbTe_2$ and chalcopyrite-type $AgInTe_2$ at ambient conditions, HP/HT syntheses lead to rocksalt-type $AgIn_xSb_{1-x}Te_2$, which exhibits a mixed occupation on the cation position which is probably the reason for its extremely low phononic contribution to the thermal conductivities (κ_{ph}) (Chapter 3.4). Alloying $AgSbTe_2$ and $AgInTe_2$ is possible under HP/HT conditions since the latter exhibits a rocksalt-type HP phase in accordance with the pressure-coordination rule.[8] At high temperature, the quaternary compounds decompose to $AgInTe_2$ and $AgSbTe_2$. This decomposition might be utilized to create nano-composite materials with improved thermoelectric properties at room temperature.

The combination of $AgSbTe_2$ with GeTe results in $(GeTe)_nAgSbTe_2$ (TAGS) materials which are well known for their high *ZT* values that mainly result from low thermal conductivities (κ).[9,10] TAGS materials crystallize in the α-GeTe-type structure with random disorder of Ag, Sb and Ge on the cation position. They exhibit phase transitions to a cubic rocksalt-type structure, comparable to GeTe itself, at ~510 K.[11,12] TAGS can be doped with In (up to 3.6 %) by quenching from high temperatures at ambient pressure (Chapter 3.5). $(GeTe)_{5.5}AgIn_{0.5}Sb_{0.5}Te_2$ exhibits a reduced κ up to the decomposition temperature compared to $(GeTe)_{\sim 5.5}AgSbTe_2$ (TAGS-85). This might be explained by the presence of a combination of nanoscopic precipitates with other real-structure effects like dislocations and twinning in $(GeTe)_{5.5}AgIn_{0.5}Sb_{0.5}Te_2$. Above 240 °C the compound decomposes to $(GeTe)_{11}AgSbTe_2$ and chalcopyrite-type $AgInTe_2$. Materials with higher In contents decompose at lower temperatures. For the synthesis of such compounds, HP/HT conditions are required to "force" In in the octahedral coordination. $(GeTe)_{5.5}AgInTe_2$ prepared under HP/HT conditions exhibits higher *ZT* values than TAGS-85 material up to 125 °C. If the Ag/Sb ratio in such materials is smaller than 1, vacancies are present and the structural chemistry is comparable to that of GST materials (Chapter 3.6). The quenched pseudocubic materials exhibit a phase transition to a layered trigonal phase with parallel van der Waals gaps at elevated temperatures and to a cubic HT phase at higher temperatures. TEM investigations reveal parquet-like nanostructures comparable to those in GST materials in the quenched compounds $Ge_{0.53}Ag_{0.13}Sb_{0.27}\square_{0.07}Te_1$ and $Ge_{0.61}Ag_{0.11}Sb_{0.22}\square_{0.06}Te_1$. These materials combine the excellent power factors of conventional TAGS materials without vacancies and the nanostructures known from GST that correlate with low κ values. This results in *ZT* values that are superior to both GST and TAGS at certain temperatures (up to 1.3 at 160 °C for parquet-like nanostructured $Ge_{0.53}Ag_{0.13}Sb_{0.27}\square_{0.07}Te_1$)

References

[1] O. G. Karpinskii, L. E. Shelimova, M. A. Kretova, V. S. Zemskov, *Inorg. Mater.* **2000**, *36*, 1321.

[2] L. E. Shelimova, O. G. Karpinskii, V. S. Zemskov, P. P. Konstantinov, *Inorg. Mater.* **2000**, *36*, 302.

[3] C. Sun, J. Lee, Y. Kim, *Phys. Stat. Sol. A*, **2009**, *206*, 50.

[4] T. Schröder, T. Rosenthal, S. Grott, C. Stiewe, J. de Boor, O. Oeckler, *Z. Anorg. Allg. Chem.* **2013**, *639*, 2536.

[5] T. Schröder, T. Rosenthal, C. Gold, E.-W. Scheidt, W. Schnick, O. Oeckler, *Z. Anorg. Allg. Chem.* **2013**, *15*, 2862.

[6] T. Matsunaga, R. Kojima, N. Yamada, Y. Kubota, K. Kifune, *Acta Crystallogr. Sect. B* **2012**, *68*, 559.

[7] T. Matsunaga, J. Akola, S. Kohara, T. Honma, K. Kobayashi, E. Ikenaga, R. O. Jones, N. Yamada, M. Takata, R. Kojima, *Nat. Mater*. **2011**, *10*, 129.

[8] K.- J. Range, G. Engert, A. Weiss, *Soild State Comm.* **1969**, *7*, 1749.

[9] J. Davidow, Y. Gelbstein, *J. Electron. Mater.* **2013**, *42*, 1542.

[10] G. C. Christakudis, S. K. Plachkova, L. E. Shelimova, E. S. Avilov, *Phys. Status Solidi A* **1991**, *128*, 465.

[11] F. D. Rosi, J. P. Dismukes, E. F. Hockings, *Electr. Eng.* **1960**, *79*, 450.

[12] B. A. Cook, M. J. Kramer, X. Wei, J. L. Harringa, E. M. Levin, *J. Appl. Phys.* **2007**, *101*, 053715.

3.2 Nanostructures in metastable $GeBi_2Te_4$ obtained by high-pressure synthesis and rapid quenching and their influence on physical properties

T. Schröder, M. N. Schneider, T. Rosenthal, A. Eisele, C. Gold, E.-W. Scheidt, W. Scherer, R. Berthold, O. Oeckler

Phys. Rev. B **2011**, *84,* 184104

Abstract

We report on a new metastable modification of $GeBi_2Te_4$ obtained by high-pressure high-temperature synthesis. It crystallizes in the CuPt type, different nanostructures are induced by various temperature programs under a constant pressure of 12 GPa. The particle size changes from < 10 nm in quenched samples to > 100 nm for melts slowly crystallized under high pressure. The smaller the domains the more random is their orientation distribution. The nanostructure has a high impact on the temperature characteristics of the electrical resistivity. The domain size determines whether the compounds are metallic or semiconducting. In the latter case, the semiconducting behavior is due to the scattering of electrons at domain and/or grain boundaries. Intermediate behavior that starts off metal-like and changes to semiconducting at higher temperature has been observed for samples thermally quenched from the solid state at high-pressure. Resistivity measurements of the high-pressure samples involving multiple heating and cooling sequences lead to a significant reduction of internal stress and finally approach a state which is characterized by a $\rho(T)$ hysteresis. Our results show the large influence of the domain size and the grain boundary concentration on the properties of the materials and reveal how properties like the thermoelectric figure of merit (ZT) depend on the preparation technique. By the microstructuring of stable $GeBi_2Te_4$, the ZT value drops by one order of magnitude.

3.2.1 Introduction

Tellurides play important roles in various fields of application such as phase-change materials (PCMs) for data storage as well as a broad range of high-performance thermoelectrics. Interestingly, most of the relevant tellurides are not thermodynamically stable. Metastability is, for example, a crucial property of PCMs used in optical as well as electrical rewritable storage devices (DVD-RW, BD-RE, PC-RAM, etc.).[1,2] The recording and erasing process involves

the fast and reversible switching between amorphous and metastable disordered crystalline phases with simple average structures which exhibit the A7 (gray arsenic) or the rocksalt structure type. Metastability and disorder are essential to reach extremely short switching times for writing or erasing large amounts of data as no long-distance diffusion is required and as both structural states are inert enough to guarantee reliable long-time data storage. The required material properties of PCMs, are, at least in part, similar to those that are crucial in the field of thermoelectrics.[3] However, it remains unclear if the thermoelectric effect itself is important in electrically switchable PCMs.

The long-time goal of most research activities on thermoelectrics, which interconvert thermal and electrical energy, is the generation of electrical energy from waste heat. The efficiency of thermoelectrics depends on the dimensionless figure of merit $ZT = S^2T / \rho\kappa$ (with the Seebeck coefficient S, the electrical resistivity ρ, and the thermal conductivity κ). As all these quantities depend on the charge carrier concentration, they cannot be optimized independently. The electrical resistivity and the electronic part of the thermal conductivity are inversely proportional to each other according to the Wiedemann-Franz law. Therefore, the only way to decrease the overall thermal conductivity without significantly increasing the electrical resistivity is to influence the phononic part of the thermal conductivity. This can be achieved, for instance, by introducing nanostructures. Phase transitions associated with the formation of long-periodically ordered structures, twinning, or (partial) decomposition may yield nanostructures that scatter phonons rather effectively and therefore enhance the thermoelectric properties. Nanostructures are, of course, metastable states, especially if they are obtained by partial stabilization of highly disordered metastable phases. This can be accomplished by various quenching techniques. However, care must be taken not to completely reach the fully ordered equilibrium state.[4-11]

In addition to the common characteristic feature that the compounds are metastable, many efficient thermoelectrics (e.g. $AgPb_mSbTe_{2+m}$ (LAST),[12] $NaPb_mSbTe_{2+m}$ (SALT),[13] $(AgSbTe_2)_{1-m}(GeTe)_m$ (TAGS),[14] or Bi_2Te_3) contain more or less the same chemical elements in similar ratios as well-known PCMs (e.g. $(GeTe)_n(Sb_2Te_3)$ (GST),[15-17] $Ag_{3.4}In_{3.7}Sb_{76.4}Te_{16.5}$ (AIST)).[18] Inspired by GST-based PCMs in PC-RAM and BD-RE devices, the investigation of the thermoelectric properties of $(GeTe)_{12}(Sb_2Te_3)$ yielded ZT values of ~1.3 at 450 °C.[3] These compounds exhibit cubic high-temperature phases with Ge, Sb and vacancies disordered on the cation sites of the rocksalt-type structure, which can be quenched as pseudocubic bulk material. The high ZT value can be related to short-range vacancy ordering effects. Similar metastable rocksalt-type phases of GBT (Ge/Bi/Te)

materials have been reported for thin-film samples obtained by sputtering and exhibit rapid phase-change behavior that can be induced by laser irradiation.[19] However, in this case the rocksalt-type phase does not exist as a stable high-temperature phase (it is in fact unstable at any temperature). Therefore, quenching experiments using bulk samples do not yield cubic or pseudocubic phases, but the stable rhombohedral layered modifications which are similar to stable GST phases. Therefore, it is essential to apply methods beyond conventional solid-state synthesis to obtain metastable GBT compounds as bulk materials. Fast quenching methods such as melt-spinning as well as high-pressure experiments seem promising in order to obtain different nanostructures that can be correlated with the corresponding thermoelectric properties.

In this report, we focus on $GeBi_2Te_4$, which is one of the peritectic compounds that can be found on the pseudo-binary line GeTe-Bi_2Te_3 in the Ge/Bi/Te phase diagram. The stable modification of $GeBi_2Te_4$ crystallizes in a rhombohedral long-range ordered 21*R*-type structure (space group $R\bar{3}m$, no. 166) with 21 hexagonal atom layers in each unit cell (Fig. 1).[20] These 21 layers form three blocks of 7 layers each, which can be described as a distorted cutout of the rocksalt structure type due to the octahedral coordination of the cations. Adjacent blocks are linked via van der Waals gaps by tellurium···tellurium interactions. In contrast to this stable phase, the metastable cubic modification found for thin-film samples experiments corresponds to a rocksalt-type structure $(Ge_{0.25}Bi_{0.5}\square_{0.25})Te$ displaying cation defects.[19,21] A phase transition towards the stable state therefore involves a vacancy rearrangement. Layer-like defect ordering and subsequent relaxation leads to the formation of the van der Waals gaps. Intermediate structures between the cubic and the 21*R*-type phases could be observed for $Ge_2Bi_2Te_5$ in annealing experiments on thin films.[22] They involve a shear deformation which may also be important for the phase-change mechanism.

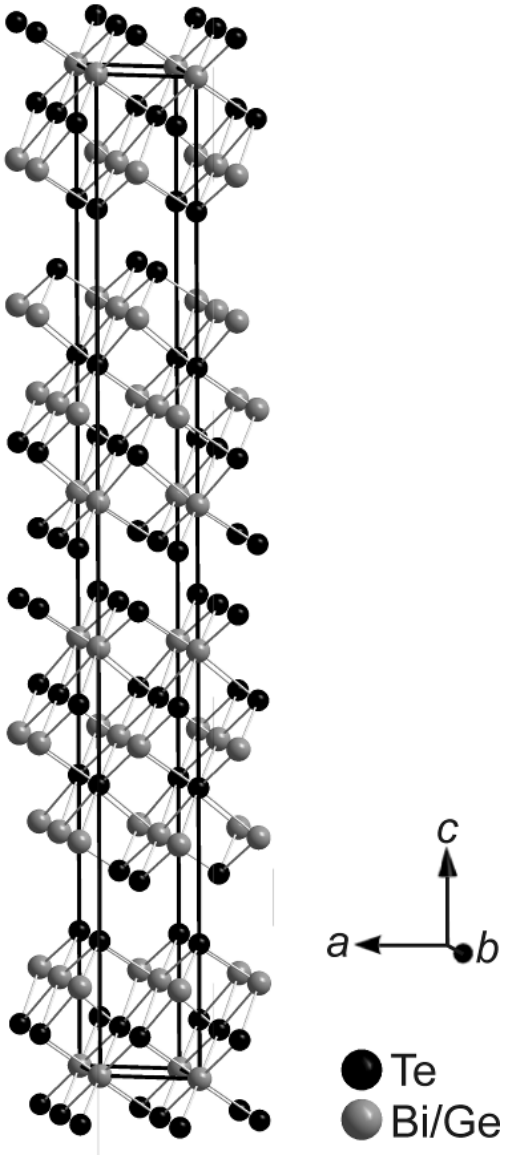

Fig. 1: Crystal structure of stable 21*R*-type $GeBi_2Te_4$ (the small percentage of anti-site disorder is neglected).

3.2.2 Experimental details

3.2.2.1 Synthesis

Bulk samples with the nominal composition $GeBi_2Te_4$ were prepared by heating a stoichiometric mixture (e.g., 0.3 g) of the pure elements (germanium 99.999 %, Sigma Aldrich; bismuth 99.999 %, Smart Elements; tellurium 99.999 %, Alfa Aesar) in sealed silica glass ampoules to 950 °C under argon atmosphere. The resulting melts were quenched to room temperature in water and used as starting material for the following syntheses. After quenching, some ingots were annealed at 500 °C to obtain the stable 21*R*-type modification.

High-pressure experiments were performed using the multi-anvil technique with a hydraulic press (Voggenreiter, Mainleus, Germany).[23-26] Quenched $GeBi_2Te_4$ was powdered, loaded into a cylindrical capsule of hexagonal boron nitride (Henze, Kempten, Germany) and sealed with a BN cap. The capsule was centered within two nested graphite tubes, which acted as an electrical resistance furnace. The remaining volume at both ends of the sample capsule was filled with two cylindrical pieces of magnesium oxide. The arrangement was placed into a zirconia tube and then transferred into a pierced Cr_2O_3-doped MgO octahedron (edge length 14 mm, Ceramic Substrates & Components, Isle of Wight, Great Britain). Eight truncated tungsten carbide cubes (truncation edge length 8 mm) separated by pyrophyllite gaskets served as anvils for the compression of the octahedron. Two plates of molybdenum provided electrical contact for the graphite tubes. The assembly was compressed up to a constant pressure of 12 GPa in 350 minutes. At this pressure, three temperature programs were applied (see Table 1). Samples were prepared by heating to 850 °C and subsequently (1) quenching the melt by turning off the furnace (melt-quenched samples), or (2) cooling the sample to 200 °C within 5 hours and then turning off the furnace (solid-quenched samples). A third type (3) of high-pressure samples was prepared by cooling the samples to room temperature within 4 hours (slowly cooled samples). After the temperature program the pressure was reduced to ambient pressure within 1050 minutes.

Table 1. High-pressure sample overview

denotation	pressure	temperature program
melt-quenched	12 GPa	quenched from melt (850 °C)
solid-quenched	12 GPa	quenched from 200 °C
slowly cooled	12 GPa	slowly cooled from 850 °C to RT

A melt-spinning apparatus (model SC, Bühler, Germany) was used in order to obtain high quenching rates (up to approximately 10^9 K/s) at ambient pressure. Powdered $GeBi_2Te_4$ was loaded into a tantalum blast pipe, which was placed over a rotating copper wheel (60 Hz). Both the tantalum blast pipe and the copper wheel were placed in a recipient, which was evacuated and/or filled with argon. The powder was melted using a water-cooled high-frequency coil (high frequency generator Himmel HIT 12, Himmelwerk Hoch- & Mittelfrequenzanlagen GmbH, Germany) and then sprayed onto the rotating copper wheel under an argon pressure of 500 mbar by applying an excess argon pressure connected to the tantalum blast pipe. The melt hits the copper wheel and solidifies immediately. Flat particles with the size of about $5 \times 2 \times 0.2$ mm^3 were hurled away from the wheel onto a collecting tray.

3.2.2.2 EDX analysis

EDX (energy dispersive X-Ray) spectra were recorded using a JSM-6500F (Jeol, USA) scanning electron microscope with EDX detector (model 7418, Oxford Instruments, Great Britain). For each particle or fragment of the ingot, respectively, the results of five point analyses were averaged and the error limits were estimated from their variance.

3.2.2.3 X-ray diffraction

X-ray powder patterns were recorded with a Huber G670 Guinier camera equipped with a fixed imaging plate and integrated read-out system using Cu-$K_{\alpha 1}$ radiation (Ge monochromator, λ = 1.54059 Å). Specimens were prepared by crushing representative parts of the samples and fixing the powder on Mylar foils using silicone grease. Low-temperature measurements between 10 K and 300 K were obtained using a cryo cooling system (Cooling head, CTI-Cyrogenics, model 22 CP). The phase homogeneity was assessed and lattice parameters were determined by pattern fitting (Rietveld method) using the program TOPAS.[27] Temperature-dependent powder diffraction experiments at temperatures above 300 K were performed with a STOE Stadi P powder diffractometer equipped with an imaging plate detector system using Mo-$K_{\alpha 1}$ radiation (Ge monochromator, λ = 0.71093 Å) in Debye–Scherrer geometry. Powdered specimens were filled into silica glass capillaries with 0.3 mm diameter and sealed with silicone grease under argon atmosphere. During the measurement, the samples were heated up to 600 °C in a graphite furnace and then cooled to room temperature with a heating/cooling rate of 5 K/min.

3.2.2.4 Transmission electron microscopy

For transmission electron microscopy studies, finely ground samples were dispersed in ethanol and distributed on copper grids coated with a holey carbon film (S166-2, Plano GmbH, Germany). The grids were fixed on a double tilt holder. Selected area electron diffraction (SAED) and high resolution transmission electron microscopy (HRTEM) were done on a JEM2011 (Jeol Ltd., Japan) with a tungsten thermal emitter and an acceleration voltage of 200 kV equipped with a TVIPS CCD (model 114, resolution: 1k x 1k). Further HRTEM, SAED and EDX measurements were done on a Titan 80-300 (FEI, USA) with a field emission gun operated at 300 kV equipped with a TEM TOPS 30 EDX spectrometer (EDAX,

Germany). Images were recorded using an UltraScan 1000 camera (Gatan, USA, resolution: 2k × 2k). HRTEM and SAED data was evaluated using the Digital Micrograph and EMS software,[28,29] for STEM and EDX data the program ES Vision was used.[30]

3.2.2.5 Electrical and thermal transport measurements

The temperature dependent resistivity $\rho(T)$ of various stable and metastable $GeBi_2Te_4$ modifications were measured by a standard four-probe dc method employing a constant current of 5 mA and using a physical property measurement system (PPMS, Quantum Design). The data were collected in the temperature range of 2 – 300 K by cooling and heating sequences in which the temperature changed at a rate of 0.5 K/min. The uncertainty of the absolute electrical resistivity values (approx. 20 – 30 %) has been estimated by taking into account the errors in specifying the sample dimensions.
The thermoelectric power $S(T)$ and the thermal conductivity $\kappa(T)$ of samples crystallizing in the stable $GeBi_2Te_4$ modification were measured simultaneously using the commercial thermal transport option of the PPMS. This is based on a relaxation method employing one heater and two thermometers to determine the induced thermal voltage and the temperature gradient along the sample in a temperature range between 4 K and 300 K. These measurements were carried out using bar-shaped samples with typical dimensions of about $1 \times 2 \times 5$ mm^3 during a heating process at a rate of 0.5 K/min. The total accuracy of $S(T)$ and $\kappa(T)$ is about 5%.

3.2.3 Results and discussion

3.2.3.1 Structure of quenched HP-$GeBi_2Te_4$

The powder diffraction pattern of a sample obtained by quenching the melt of $GeBi_2Te_4$ under a constant pressure of 12 GPa (i.e. switching off the furnace) could be indexed assuming a rhombohedral unit cell with a = 4.3508(3) Å and c = 11.234(2) Å. Starting from an α-GeTe-type structure model (space group $R3m$), which allows many degrees of freedom, Ge, Bi and vacancies were placed on the cation position (occupancy factors 0.25 for Ge and 0.5 for Bi) and Te (fully occupied) on the anion position. The occupancy factors were derived from the nominal composition, which is confirmed by the EDX results (for all $GeBi_2Te_4$ samples between $Ge_{0.9(1)}Bi_{2.2(1)}Te_4$ and $Ge_{1.1(1)}Bi_{2.0(1)}Te_4$). The Rietveld refinement (shown in Fig. 2) turned out that there is no evidence for non-centrosymmetry of the average structure, as in

contrast to α-GeTe, all cation-anion distances are equal within two standard deviations. Therefore, the average structure seems not to be layered, and the space group can be identified as $R\bar{3}m$ (no. 166). Details of the Rietveld analysis and the refined atomic parameters are given in Tables 2 and 3, respectively.

Table 2. Crystal data and Rietveld refinement of melt-quenched $GeBi_2Te_4$

sum formula	$GeBi_2Te_4$
molar mass (in g/mol)	1000.97
lattice parameters (in Å)	a = 4.3508(3) Å; c = 11.234(2)
cell volume (in Å³)	184.16(5)
radiation	Cu-$K_{\alpha 1}$ (λ = 1.540596 Å)
density (in g/cm³)	6.769(2)
space group	$R\bar{3}m$ (no. 166)
2 theta range	22° < 2Θ < 95°
number of reflections	32
refined parameters	12 structural / 36 background
constraints	2
profile function	fundamental parameter approach
step width (2θ)	0.005°
R_{wp}; R_p	0.0135; 0.0104

Table 3. Atom positions and displacement parameters of HP-$GeBi_2Te_4$

atom	Wyck.	x y z	s.o.f.	U_{eq}	$U_{11} = U_{22} = 2U_{12}$	U_{33}	U_{13}=U_{23}
Te	3*a*	0 0 0	1	0.15(2)	0.017(11)	0.48(7)	0
Bi/Ge	3*b*	0 0 1/2	Bi 0.5 Ge 0.25	0.18(2)	0.008(11)	0.43(6)	0

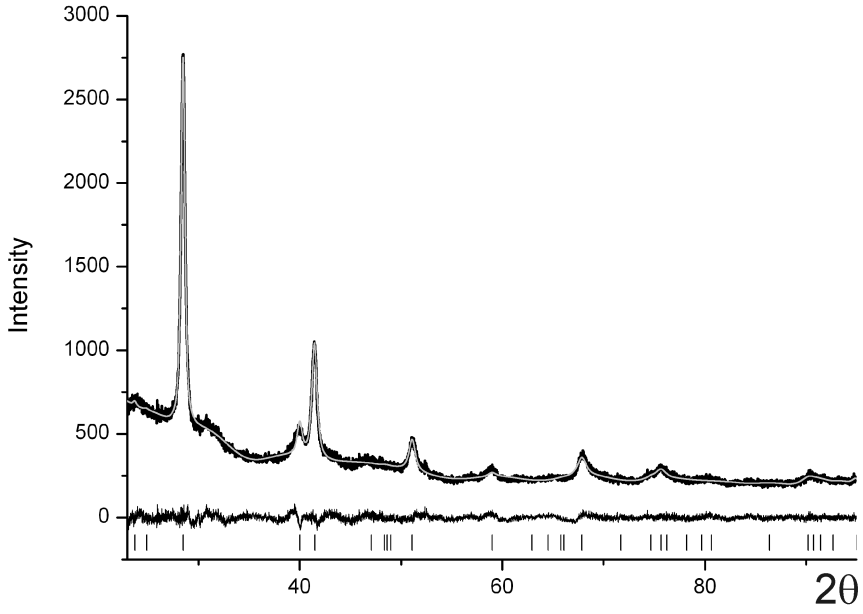

Fig. 2: Rietveld refinement of melt-quenched HP-$GeBi_2Te_4$: experimental powder pattern (black), calculated pattern (gray), and difference plot (black) and tick marks (black, straight lines).

The average structure model derived from Bragg reflections corresponds to the CuPt-type structure, a rhombohedrally distorted variant of the rocksalt type, derived from the latter by stretching the unit cell along <111>. In fact, the powder pattern contains no significant evidence for different scattering densities on anion and cation positions, as disordered germanium, bismuth and vacancies lead to an average electron count of 49.5 at the cation position and tellurium involves 52 electrons on the anion position. Thus, the structure might formally be described assuming the α-Hg type with just one Wyckoff position for all atoms, however, electron diffraction patterns clearly show the CuPt type's reflections *hkl* with *h*, *k*, *l* = 2n+1 whose intensity (similar to the rocksalt case) can only be observed in case of different scattering densities for cation and anion sites (see next section). Of course, a certain degree of anti-site disorder cannot be excluded; however, such phenomena have been thoroughly investigated for Ge/Sb/Te phases, where the amount of anti-site disorder is either very small or not significant.[17,31] Although the refinement fits the experimental data, the structure model does not correspond to an ordered compound; and the disorder goes far beyond the cation disorder itself. The "average" structure from Bragg data can only be described with very prolate atomic displacement ellipsoids as can be seen in Fig. 3; so in fact there is no average structure with, at least in part, "normal" atom positions. These results suggest that a cubic rocksalt-type phase is formed under high pressure, but partially relaxes to a layered trigonal structure as soon as the pressure is released. The short-range order in this phase may locally correspond to the structure of the stable room temperature phase. Obviously, the high vacancy concentration of 25 % on the cation sites does not allow a completely random vacancy distribution at ambient conditions.

The powder diffraction patterns of the slowly cooled and solid-quenched samples, respectively, do not differ significantly from those of samples that were quenched from the melt, although the micro-/nanostructures are significantly different (see below). However, Table 4 shows that the lattice parameters of the average structures vary slightly. All trigonal *c*/*a* ratios are almost equally far from that of the trigonal setting of a unit cell with cubic metrics (2.45).

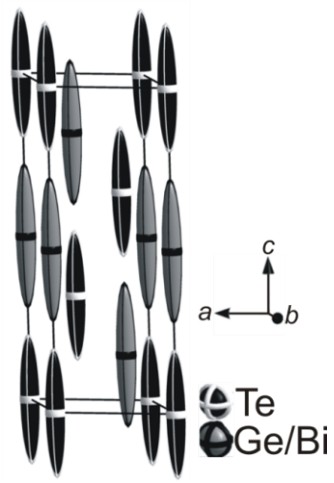

Fig. 3: "Average" structure model of metastable HP-$GeBi_2Te_4$ as determined from Bragg data (displacement ellipsoids for 99% probability).

Table 4. Comparison of the lattice parameters of various high-pressure samples (cf. text)

denotation	*a* (Å)	*c* (Å)	*c*/*a*	Volume (Å^3)
melt-quenched	4.3502(4)	11.234(2)	2.582	184.05(5)
solid-quenched	4.347(2)	11.184(5)	2.573	183.1(2)
slowly cooled	4.3495(5)	11.043(3)	2.539	180.93(7)

Figure 4 shows that temperature-dependent powder diffraction experiments and ex-situ annealing of high-pressure samples (for 36 hours at 300 °C) prove that the high pressure phase is metastable at ambient pressure. The reflections of the layered 21*R*-type structure reappear when the metastable compound is heated over 200 °C.

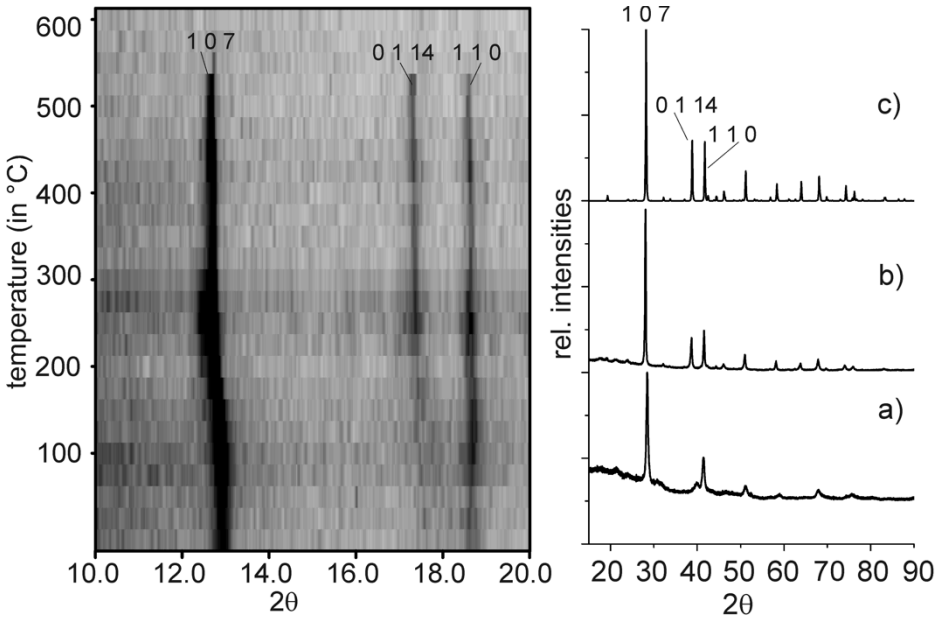

Fig. 4: Temperature-dependent PXRD (left, room temperature to 600 °C, Mo-$K_{\alpha 1}$ radiation - intensity from 0 (white) to maximum (black)) of the melt-quenched HP phase; PXRD (Cu-$K_{\alpha 1}$ radiation) of the melt-quenched sample (right): a) as removed from the press, b) after annealing for 36 h at 300 °C, c) calculated powder pattern of 21*R*-type $GeBi_2Te_4$.

3.2.3.2 Nucleation mechanism and nanostructuring

The nanostructure of the melt-quenched sample which is shown in Fig. 5(a) is characterized by a broad range of different domain orientations with domain sizes < 10 nm. The domains are intergrown, but there are no coherent domain walls. Therefore, the SAED pattern corresponds to the combination of multiple patterns and not to a single crystallite. A few grains with larger domains can be found, but they are rare exceptions. Thus, quenching the melt under a high constant pressure leads to nucleation dominated growth.

The solid-quenched sample exhibits larger and more anisotropic domains with average dimensions ≥ 10 nm. Therefore, it is possible to obtain single crystalline SAED patterns as shown in Fig. 5(b), if larger domains are selected. These patterns contain reflections *hkl* with *h*, *k*, *l* = 2n+1, which implies that there are different scattering densities for anion and cation sites, respectively. There are no pronounced diffuse streaks in the SAED patterns. Thus, there is no pronounced intermediate-range order corresponding to extended vacancy layers or van der Waals gaps within the domains as they are known from the stable trigonal phases.

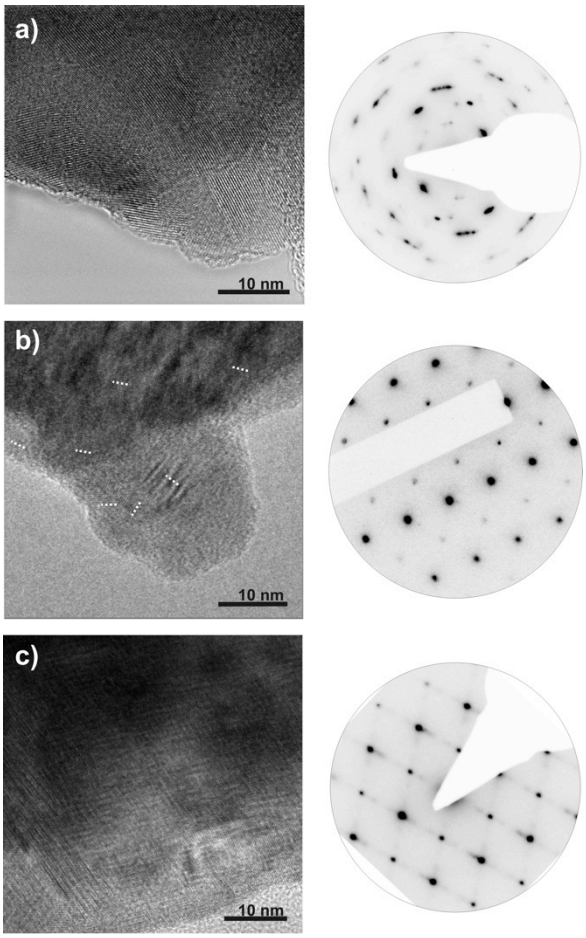

Fig. 5: HRTEM images (left) and the corresponding SAED (right) a) of the melt-quenched sample (Titan 80-300); b) of the solid-quenched sample, some domain orientations are highlighted with white dashed lines (JEM 2011); c) of the slow cooled sample; here different domain orientations overlap (Titan 80-300).

Probably the lack of vacancy ordering limits the maximal domain size as vacancies might aggregate at domain boundaries. The crystallites are larger than the ones in the melt-quenched HP sample; yet, the domains are still randomly oriented. The domain shape is more anisotropic than in the melt-quenched sample.

Fig. 5(c) shows that the slowly cooled sample has large crystallites ≥ 100 nm. Twinned areas next to single-domain areas can be observed. All slowly cooled samples exhibit extended vacancy layers which lead to van der Waals gaps if the adjacent Te atom layers relax. Therefore, diffuse streaks can be observed in the corresponding SAED patterns. These large domains indicate fast growth crystallization rather than nucleation dominated growth. The relative orientation of the twin domains corresponds to the <111> directions of a pseudo-cubic structure. This corroborates the assumption that there is a cubic high-pressure phase of $GeBi_2Te_4$ which, upon a phase transition towards a trigonal phase, involves fourfold twinning according to the *translationengleiche* cubic → rhombohedral group-subgroup relationship.

The powder X-ray diffraction pattern (PXRD) pattern of melt-spun $GeBi_2Te_4$ corresponds to that of the ordered 21*R*-type structure and not to the PXRD patterns of the high pressure samples. Yet, melt-spun $GeBi_2Te_4$ exhibits small intergrown domains, the smallest ones with a diameter of ~10 nm as shown in Fig. 6 larger domains are also present. The domain orientation changes within one grain, however, not as randomly as in the quenched high-pressure samples.

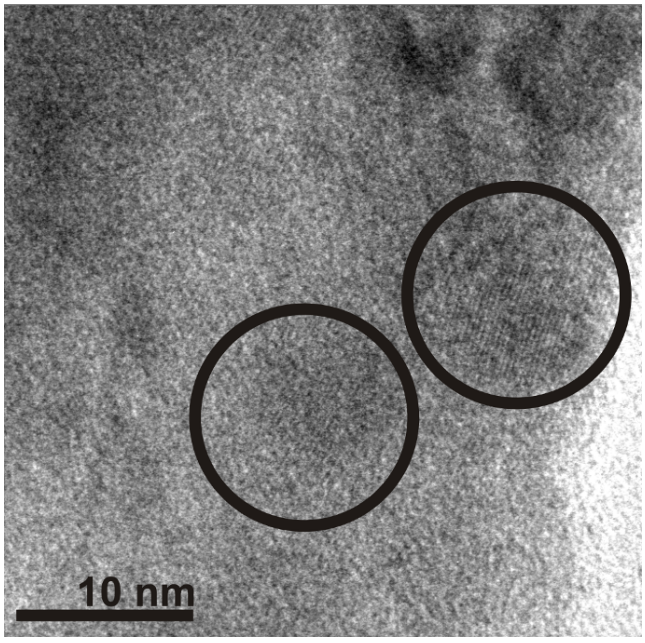

Fig. 6. HRTEM image of a melt-spun sample of $GeBi_2Te_4$; two well-ordered domains of the stable layered phase are highlighted by black circles.

3.2.3.3 Influence of the nanostructure on the electrical resistivity

The following section conduces to the understanding of the influence of the nanostructure of the metastable modifications of HP-$GeBi_2Te_4$ on the temperature dependent resistivity ρ(T). Therefore the resistivity of three different metastable quenched samples – slowly cooled, solid-quenched and melt-quenched – were synthesized and compared with an annealed ingot as well as a melt-spun particle, both crystallizing in the stable modification.

Stable and melt-spun modification of $GeBi_2Te_4$

The resistivity of an annealed ingot of the stable ambient-pressure modification of $GeBi_2Te_4$ is plotted vs. temperature in the range between 2 K and 300 K in Fig. 7a). The decrease of $\rho(T)$ with decreasing temperature suggests metal-like behavior. However, the high residual resistivity ρ_0 of about 0.3 mΩ cm together with the small residual resistivity ratio of RRR = ρ(300 K)/ρ(2 K) = 2.52 suggest the presence of severe disorder. The metallic conductivity behavior depends on two different scattering processes. The temperature independent residual resistivity ρ_0 originates from the scattering of conduction electrons by defects (impurity atoms, grain boundaries etc.). In the present case this is probably due to the Ge/Bi disorder at the cation sites. The second – temperature dependent – process is due to the scattering of conduction electrons by phonon excitations. These two processes yield the description of simple metals via the Bloch-Grüneisen (BG) relation.

$$\rho_{\mathrm{BG}}(T) = \rho_0 + \frac{4B}{\Theta_{\mathrm{D}}}\left(\frac{T}{\Theta_{\mathrm{D}}}\right)^5 \int_0^{\Theta_{\mathrm{D}}/T} \frac{z^5 \mathrm{d}z}{\left(e^z - 1\right)\left(1 - e^{-z}\right)}$$

where B is the temperature-independent electron-phonon interaction strength, Θ_{D} the Debye-temperature and $z = \hbar\omega/k_{\mathrm{B}}T$.

The insert of Fig. 7(a) depicts the resistivity behavior $\rho(T)$ of the stable $GeBi_2Te_4$ modification in comparison with a corresponding data fit employing the Bloch-Grüneisen (BG) relationship. The BG relation fits the experimental sufficiently well only at temperatures below ~ 40 K. For higher temperatures, $\rho(T)$ displays larger values than those expected by the BG relation for metallic behavior. This suggests an onset of semiconducting behavior at elevated temperatures in accordance with the high residual resistivity and the small RRR value. Furthermore, $\rho(T)$ of the annealed ingot reflects fully reversible behavior between cooling and heating sequences only below 40 K in the region where experimental data can be

fitted by the BG relation. This reversibility can also be retrieved in the metastable modifications of $GeBi_2Te_4$ (see subsequent discussion).

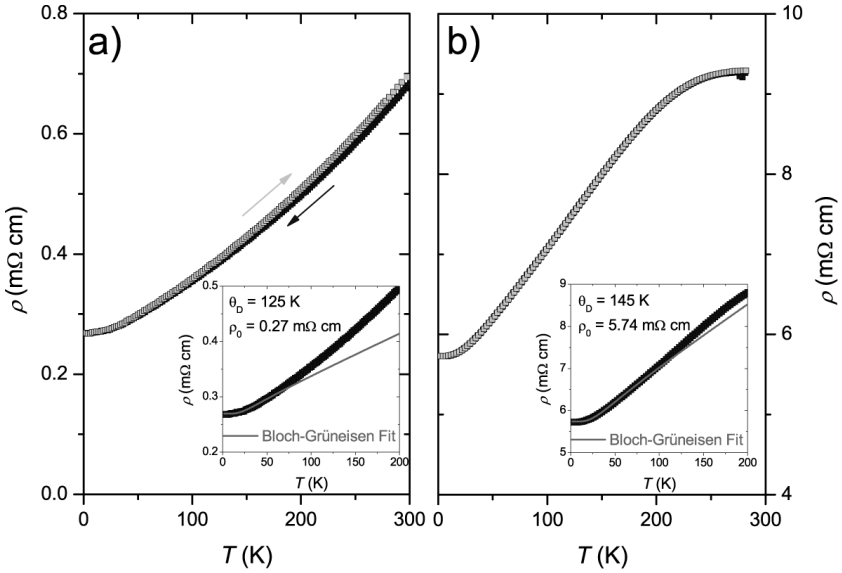

Fig. 7: Comparison of the temperature-dependent resistivity of a) an annealed ingot of 21*R*-type $GeBi_2Te_4$ and of b) a melt-spun particle of $GeBi_2Te_4$. The inserts show the low-temperature behavior together with a fit according to the Bloch-Grüneisen relationship (solid line). The arrows denote cooling and heating sequences, respectively.

The deviation from metallic behavior above a certain temperature, becomes more evident in the resistivity of the melt-spun particle (see Fig. 7.(b)), although in this case the BG relation fits the experimental data well up to ~ 60 K. However, the residual resistivity ρ_0 increases by a factor of 20 in comparison to the annealed ingot. Furthermore, $\rho(T)$ of the melt-spun particle starts to saturate already at ~ 9.3 mΩ cm in the high temperature regime. The higher resistivity can be attributed to the reduction of the grain size (up to 10 nm) and can therefore be related to the increasing number of domain and grain boundaries acting as scattering centers. The saturation below room temperature is in line with a transition from metal-like to a degenerate semiconducting behavior as supported by the description via the BG formalism (see insert Fig. 7b)) at low temperatures which also takes the temperature dependency of the charge carrier density into account.[32] Such a two-regime behavior was recently reported for Ge-based clathrate I compounds as well as Sb-based skutterudites.[33-35]

These results point out that the nanostructure, e.g. the domain size and the relative orientation, influence the temperature characteristics of the resistivity behavior even if the crystal structure is maintained (21*R* type).

Metastable quenched HP-$GeBi_2Te_4$

All three high-pressure samples are characterized by pronounced irreversible temperature dependencies of $\rho(T)$ for repeated cooling and heating cycles in the temperature range between 44 K and 260 K. This is shown for the slowly cooled sample of HP-$GeBi_2Te_4$ in Fig. 8 There is a drastic change of the hysteretic behavior when the $\rho(T)$ sequences of cycle one and two are compared. However, already after the third cooling/heating sequence the hysteresis curves remain rather invariant. There is, however, a subtle decrease of the resistivity (and of the $\rho(T)$ minima at ca. 35 K - 38 K) with increasing number of cooling/heating cycles.

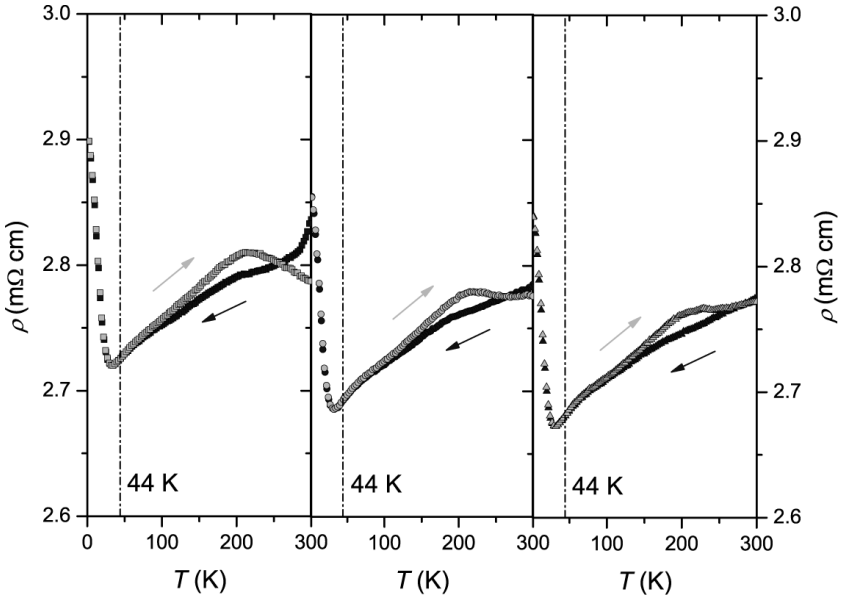

Fig. 8: Temperature-dependent resistivity of a slowly cooled HP-$GeBi_2Te_4$ sample; from left to right three successive cooling (black) and heating (gray) sequences, approaching a final state.

In the final state after more than three successive cooling and heating sequences, the resistivity $\rho(T)$ shows a metal-like behavior above 35 K and an insulating one for lower temperatures, similar to the behavior observed, e.g., for didymium skutterudites $(Pr,Nd)(Fe,Co)_4Sb_{12}$ and $(Pr,Nd)(Fe,Ni)_4Sb_{12}$.[36] Below 44 K heating and cooling curves show reversibility, while above 44 K a hysteresis with a maximal splitting of 0.014 mΩ cm at ~ 208 K occurs. One may speculate that the $\rho(T)$ behavior in the reversible regions is mainly controlled by the intrinsic resistivity of the grains, whereas above 44 K the resistivity of the grain boundaries starts to dominate, as observed in case of in the stable $GeBi_2Te_4$ modification (see previous discussion, Fig. 7(a)).

In Fig. 9 the temperature-dependent resistivity behavior of three metastable high-pressure samples of $GeBi_2Te_4$ obtained by different cooling/quenching procedures is compared. All three samples are characterized by a hysteretic $\rho(T)$ behavior which also depends on the number cooling/heating sequences applied (vide supra; Fig. 8). However, in order to study exclusively the competition between the intrinsic resistivity of the domains with that of the grain boundaries only those $\rho(T)$ cooling/heating curves were depicted in Fig. 9 which remained invariant after several measuring cycles. All of the three samples possess reversible temperature dependence below ~ 40 K. Above that temperature, the temperature characteristics of the resistivity changes from metallic-like (slowly cooled) to semiconducting (melt-quenched sample). Hence, the temperature-dependent resistivity behavior critically depends on the sample history, especially on the cooling/quenching approach applied. In contrast, the hysteretic behavior above 40 K remains a characteristic feature of all the three different samples.

The occurrence of such hysteresis effects could be due to either a first-order phase transition or the presence of internal stress. A first-order phase transition can be excluded based on temperature dependent X-ray experiments, which do not reveal any significant change in the powder diffraction pattern down to 15 K (except for a trivial change of lattice parameters), as well as by specific heat studies (not shown here) which do not indicate any phase transformation. Therefore, the hysteretic $\rho(T)$ behavior is probably due to the internal stress of the grains. The extent of the hysteresis changes drastically with an increasing domain size and the number of their relative orientation in the different samples. Accordingly, the slowly cooled sample is characterized by the smallest hysteresis splitting of all three samples (see Fig. 9(a). This is consistent with the expected small change of internal stress as a consequence of the large domain size ($\geq$ 100 nm) and the presence of only few domain orientations as evidenced by the HRTEM studies. A similar, but more pronounced splitting is therefore found in case of the melt-quenched sample (see Fig. 9(c)) which is characterized by very small particles (< 10 nm) showing many different orientations. However, the solid-quenched sample reveals the strongest splitting of all metastable $GeBi_2Te_4$ compounds (see Fig. 9(b)). This is probably a result of the strongly anisotropic size of the grains.

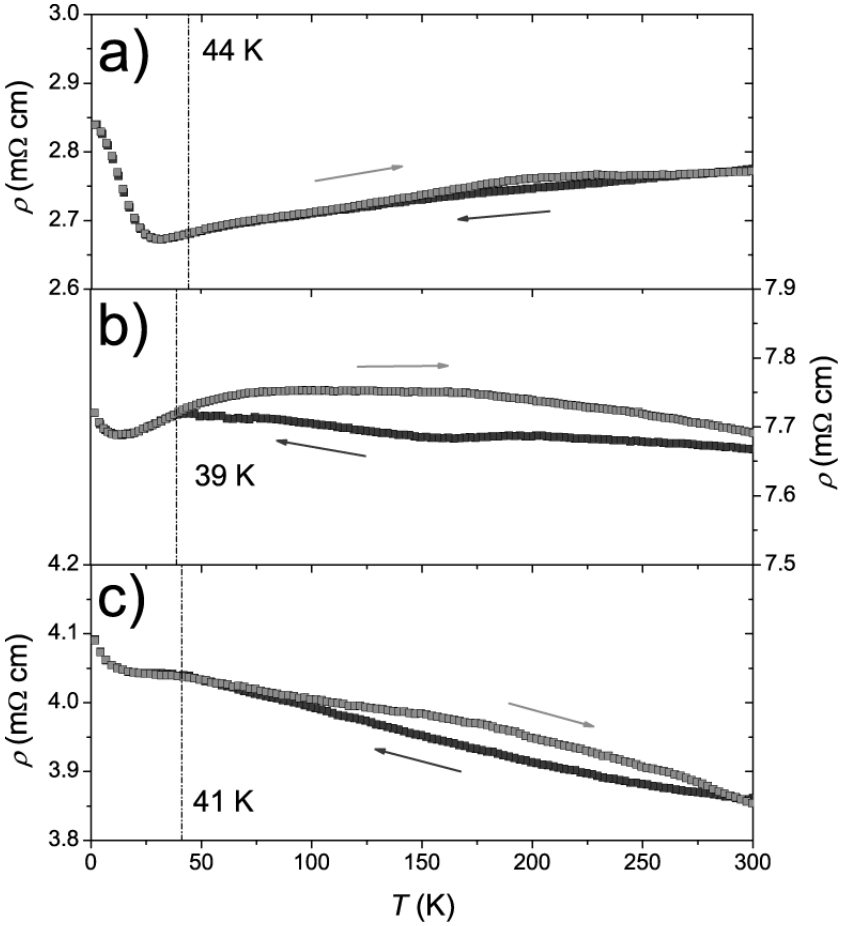

Fig. 9: Final state of the cooling (black) and heating (gray) sequences of the temperature dependent resistivity of a) slowly cooled b) solid-quenched and c) melt-quenched high-pressure samples of $GeBi_2Te_4$

Due to this type of nanostructuring, the total resistivity of these samples is not only affected by the intrinsic structure and disorder of the domains but also by a contribution of the microscopic nature of the domain and/or grain boundaries. The change of the residual resistivity in Fig. 9 suggests that also the dominant scattering mechanisms might differ in the three samples. The slowly cooled high-pressure sample exhibits the lowest residual resistivity and the most pronounced similarity to the stable modification (e.g. metallic conductivity at ambient temperature; see Fig. 7(a). This is basically due to the fact that this sample exhibits the largest domains of the three high-pressure systems and displays a disordered pseudocubic layered structure. The melt-quenched sample, however, shows semiconducting behavior between 41 K and room temperature in spite of the isotropy and rather random orientation of its domains. The temperature dependence of the resistivity is therefore dominated by the grain boundaries' contributions. The solid-quenched sample indicates the highest residual resistivity of all the high-pressure species under investigation. This remarkably high value in combination with the pronounced grain anisotropy implies a coexistence of both scattering

mechanisms discussed (see previous discussion). The $\rho(T)$ behavior of the solid-quenched modification, however, marks an intermediate behavior and thus adopts to the high-temperature behavior of the slowly cooled and mimics the low-temperature behavior of the melt-quenched one.

Influence of grain boundaries on ZT

In order to investigate the influence of the sample preparation techniques on the thermoelectric figure of merit *ZT*, the thermal and electrical transport properties of three characteristic samples were measured between 4 K and room temperature. In this respect, the annealed ingot of stable 21*R*-type $GeBi_2Te_4$ represents a benchmark sample which is compared with two pellet samples (samples two and three). Sample two is a pellet pressed of 21*R*-$GeBi_2Te_4$ powder while the third sample is a pellet composed of cold-pressed powder of the melt-spun 21*R*-$GeBi_2Te_4$. It was not possible to perform such measurements with the high-pressure samples due to their small sample volumes.

A comparison of the $\rho(T)$ behavior of these three samples is plotted in Fig. 10(a)-10(c). The $\rho(T)$ behavior of the annealed ingot and that of the melt spun sample were already characterized as metal-like in Fig. 7. In contrast, $\rho(T)$ of the two pellets do not shows metal-like conductivity behavior. In addition, ρ_0 increases by a factor of about 30 and 60 in case of both pellet samples, irrespective of the sample's origin (stable modification or melt-spun 21*R*-$GeBi_2Te_4$ sample, respectively). Two closely related control parameters might be responsible for observation of semiconducting behavior, namely the nano- or microstructure formation by different synthesis routes and the process of pellet pressing itself. Both lead to an increasing number of grain boundaries and therefore trigger the increase of ρ_0 and the change of the $\rho(T)$ behavior.

These observations are consistent with the thermal conductivity $\kappa(T)$ behavior shown in Fig. 11(a) and (b). The total thermal conductivity κ_{total} of solids can be expressed as the sum of an electrical κ_{el} as well as a phononic κ_{ph} contribution. The electrical contribution was estimated from the electrical resistivity (cf. Fig. 10) via the Wiedemann-Franz law. Subtracting this part from the experimentally determined total thermal conductivity yields the phononic contribution.

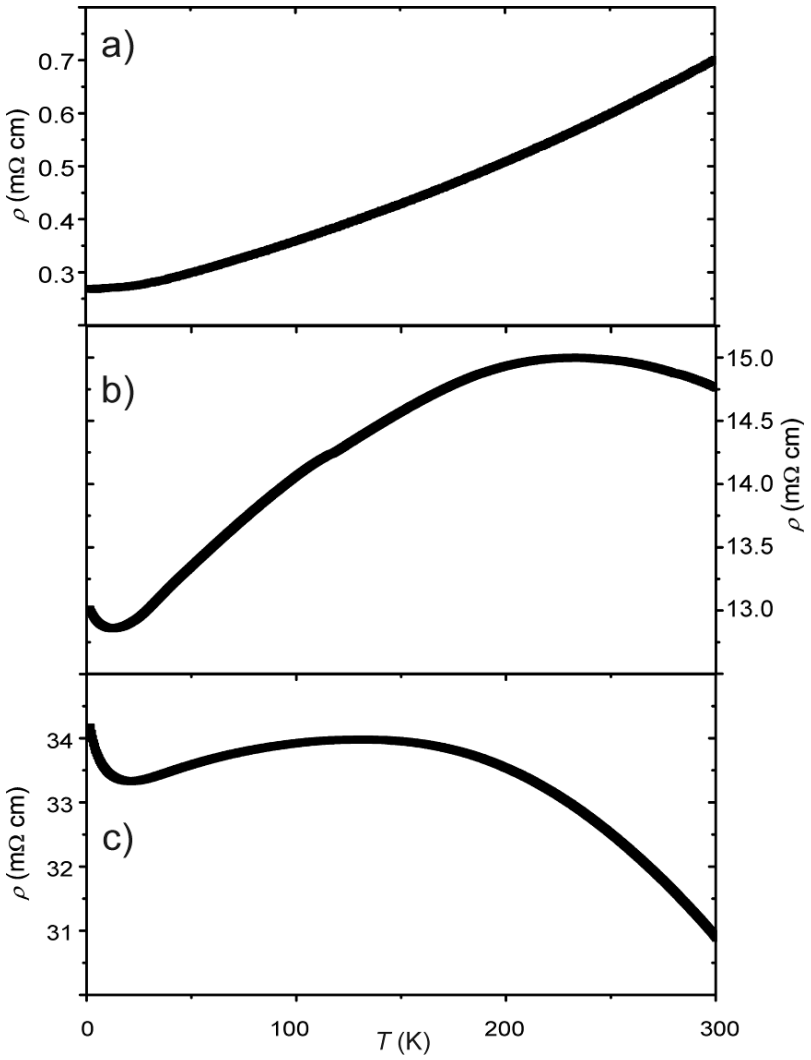

Fig. 10: Comparison of the temperature dependent resistivity ρ(T) (heating from 2 to 300 K) of a) an annealed ingot of $GeBi_2Te_4$, b) a pressed powder pellet of 21*R*-$GeBi_2Te_4$ and c) a pressed powder pellet of melt-spun $GeBi_2Te_4$.

In Fig. 11(a), κ_{total} of the annealed ingot of the stable modification is composed of significant contributions from κ_{ph} and κ_{el}. While at room temperature both parts coexist and contribute approximately by the amount to κ_{total}, a phonon dominated state is observed below 50 K. The maximum of κ_{ph} at about 13 K displays the onset of phonon umklapp scattering which effectuates a decrease of κ_{ph} above a certain temperature. Such kind of maximum depends only weakly on the Debye temperature and occurs well below $\Theta_D/10$. The low-temperature slope of κ_{ph} thus indicates defect scattering and becomes large when the number of defects is small.

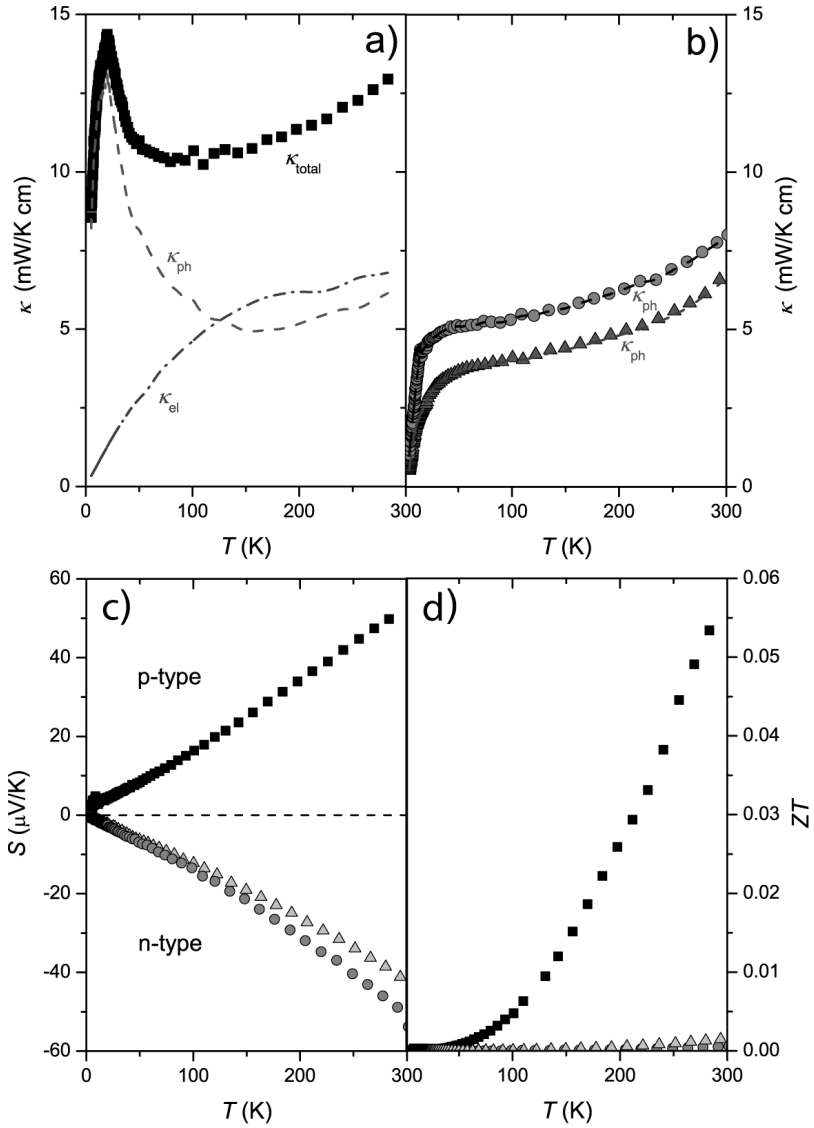

Fig. 11. Temperature characteristics a) of the total thermal conductivity, κ_{total}, (black squares), the phonon contribution, κ_{ph}, (dashed line) and electronic contribution, κ_{el}, (dashed and dotted line) for the annealed ingot of $GeBi_2Te_4$; b) of κ_{total} for the pressed powder pellet of 21*R*-type $GeBi_2Te_4$ (gray circles) and the powder pressed pellet of melt-spun $GeBi_2Te_4$ (gray triangles) and the phonon contributions (dashed lines, dark gray); c) of the Seebeck coefficient and d) of the *ZT* value for the annealed ingot (black squares), the pressed powder pellet of 21*R*-type $GeBi_2Te_4$ (gray circles) and the pressed powder pellet of melt-spun $GeBi_2Te_4$ (light gray triangles).

A comparison with the $\kappa(T)$ results of the two pellets indicate an overall and significant reduction of $\kappa_{total}(T)$ (Fig. 11(b)). Generally, κ_{ph} of the thermal conductivity of both samples follows the pattern of κ_{total} while the κ_{el} contribution vanishes as expected in the light of the high resistivity values observed. Furthermore, the change of the low-temperature slope of κ_{ph} hints to an increase of phonon scattering at boundaries and/or point defects. Hence, the reduced thermal conductivity of the pellet-pressed samples originates mainly from the enhancement of these scattering processes.

The thermopower $S(T)$ of the three samples is depicted in Fig. 11(c). For the annealed ingot of the stable modification, an increase of the thermopower up to about + 50 μV/K at room temperature can be observed. The positive sign of $S(T)$ between 4 K and 300 K reveals the characteristic behavior of a p-type material. The featureless, almost linear temperature dependence of $S(T)$ indicates the absence of any significant correlations within the charge carriers and is expected for the diffusion thermopower above the Debye temperature (125 K). In this temperature region electron-phonon scattering is the dominant scattering mechanism and given by

$$S_{\mathrm{d}}(T > \Theta_{\mathrm{D}}) = \frac{\pi^2 {k_{\mathrm{B}}}^2 2m_{\mathrm{e}}}{|e|\hbar^2 (3n\pi^2)^{2/3}} \cdot T$$

with $k_{\mathrm{B}} = 1.38065 \cdot 10^{-23}$ J/K, $m_{\mathrm{e}} = 9.10938 \cdot 10^{-31}$ kg, $e = 1.60218 \cdot 10^{-19}$ C, and $h = 6.62607 \cdot 10^{-34}$ Js. According to this equation, the slope below 300 K yields a density of charge carriers of $3.4 \cdot 10^{21}$ cm^{-3}.

In contrast to its influence on $\rho(T)$ and $\kappa(T)$, the method of synthesis has no drastic influence on $S(T)$ except for the remarkable change of sign in the thermopower of the pellets from positive (p-type) to negative (n-type). The absolute values of $S(T)$ as well as the carrier concentration (~ 10^{21} cm^{-3}) of the pellet samples remain more or less the same.

The ZT values, for the three samples, calculated from the present results are shown in Fig. 11(d). For the annealed ingot of the stable modification a ZT value of 0.055 was reached at room temperature. The ZT values of both pellet samples where found to be one order of magnitude lower, which disqualifies these sample from thermoelectric applications. Significant scattering of the charge carriers on grain boundaries results in high resistivity values for the micro- or nanostructured samples and, as a consequence, in a small electronic contribution to the thermal conductivity.

3.2.4 Conclusion

Quenching melts of $GeBi_2Te_4$ at high pressure yields metastable samples whose average structure is related to the rocksalt type, similar to samples obtained by laser irradiation of thin films for PCM applications. Partial relaxation towards the stable trigonal layered modification leads to a rhombohedrally distorted crystal structure. The metastable state can be completely relaxed by annealing. Concerning PCMs, the nucleation mechanisms are important. “Nucleation dominated growth” begins spontaneously at different spots in the amorphous phase and therefore leads to a multitude of grains, which have no crystallographic relation to

each other. We have shown that the crystallization of melts during rapid quenching is very similar, an intermediate solid amorphous phase might be discussed for bulk samples as well, but cannot be confirmed by our experiments. The domain size and therefore probably the nucleation mechanism depends on the temperature regime, including quenching rates, which were applied under a constant pressure of 12 GPa. The nanostructures obtained and especially the corresponding domain and grain boundaries have a large influence on the temperature characteristics of the electrical resistivity. In the high pressure compounds, the characteristics of the electrical resistivity changes from metal-like to semiconducting behavior with decreasing domain size and more randomly oriented domains, because the resistivity becomes more dominated by scattering of the electrons at the domain or grain boundaries. The temperature regime during the synthesis therefore determines at which temperature this type of scattering becomes dominant. However, multiple heating and cooling sequences in course of the resistivity measurements show that the system seems to approach a final state. Apparently, internal stress needs to be reduced before the measurements yield invariant $\rho(T)$ sequences, but even after the stabilization a hysteretic behavior remains.

As a consequence, the preparation technique has a large influence on the *ZT* value as shown by measurements on samples that exhibit the stable layered structure. The thermal conductivity is influenced by the electronic contribution, which decreases significantly in pressed pellets with many grain boundaries; however, it is accompanied by the corresponding increase of the electrical resistivity. Therefore, the *ZT* value drops by more than an order of magnitude because the phononic contribution becomes dominant. These findings illustrate the importance of the thermal conditioning of thermoelectrics, especially in order to ensure sufficient electrical conductivity. It is often difficult to reproduce thermoelectric materials with distinct properties; because different methods of synthesis (like hot press, high pressure experiments or conventional solid-state preparation techniques), annealing times and temperatures lead to various amounts of grain boundaries and therefore strong deviations in *ZT*.

Acknowledgements

We thank T. Miller and M. Rotter for the temperature-dependent powder diffraction experiments, C. Minke for SEM operation and EDX analyses, and M. Döblinger for help with TEM operation. We are indebted to Dr. G. Kreiner for providing access to the melt-spinner and gratefully acknowledge Prof. Dr. W. Schnick's generous support of this work. This investigation was funded by the Deutsche Forschungsgemeinschaft (grants OE530/1-2 and SCHE487/12-1) and the Studienstiftung des deutschen Volkes.

3.2.5 References

[1] W. Bensch, M. Wuttig, *Chem. Unserer Zeit* **2010**, *44*, 92.

[2] S. Raoux, *Annu. Rev. Mater. Res.* **2009**, *39*, 9.

[3] M. N. Schneider, T. Rosenthal, C. Stiewe, O. Oeckler, *Z. Kristallogr.* **2010**, *225*, 463.

[4] J. Sommerlatte, K. Nielsch, H. Böttner, *Phys. J.* **2007**, *6*, 35.

[5] A. Bulusu, D. G. Walker, *Superlattice Microstruct.* **2008**,*44*, 36.

[6] A. Majumdar, *Science* **2004**, *303*, 777.

[7] M. S. Dresselhaus, G. Chen, M. Y. Tang, R. Yang, H. Lee, D. Wang, Z. Ren, J.-P. Fleurial, P. Gogna, *Adv. Mater.* **2007**, *19*, 1.

[8] D. L. Medlin, G. J. Snyder, *Curr. Opin. Colloid Interface Sci.* **2009**, *14*, 226.

[9] M. G. Kanatzidis, *Chem. Mater.* **2010**, *22*, 648.

[10] Y. C. Lan, A. J. Minnich, G. Chen, Z. F. Ren, *Adv. Funct. Mater.* **2010**, *20*, 357.

[11] J. R. Sootsman, D. Y. Chung, M. G. Kanatzidis, *Angew. Chem. Int. Ed.* **2009**, *48*, 8616.

[12] B. A. Cook, M. J. Kramer, J. L. Harringa, M.-K. Han, D.-Y. Chung, M. G. Kanatzidis, *Adv. Funct. Mater.* **2009**, *19*, 1254.

[13] P. F. P. Poudeu, J. D'Angelo, A. D. Downey, J. L. Short, T. P. Hogan, and M. G. Kanatzidis, *Angew. Chem. Int. Ed.* **2006**, *45*, 3835.

[14] F. D. Rosi, J. P. Dismukes, E. F. Hockings, *Electron Eng.* **1960**, *79*, 450.

[15] T. Matsunaga, N. Yamada, *Phys. Rev. B* **2004**, *69*, 104111.

[16] T. Matsunaga, N. Yamada, Y. Kubota, *Acta Crystallogr. Sect. B* **2004**, *60*, 685.

[17] T. Matsunaga, R. Kojima, N. Yamada, K. Kifune, Y. Kubota, Y. Tabata, M. Takata, *Inorg. Chem.* **2006**, *45*, 2235.

[18] T. Matsunaga, Y. Umetani, N. Yamada, *Phys. Rev. B* **2001**, *64*, 184116.

[19] T. Matsunaga, N. Yamada, Jpn. *J. Appl. Phys.* **2004**, *43*, 4704.

[20] L. E. Shelimova, O. G. Karpinskii, P. P. Konstantinov, E. S. Avilov, M. A. Kretova, V. S. Zemskov, *Inorg. Mater.* **2004**, *5*, 451.

[21] S.-I. Shamoto, N. Yamada, T. Matsunaga, T. Proffen, *Phys. B.* **2006**, *385-386*, 574.

[22] C. W. Sun, J. Y. Lee, Y. T. Kim, *Phys. Stat. Sol. RRL* **2009**, *3***,** 254.

[23] D. Walker, M. A. Carpenter, C. M. Hitch, *Am. Mineral.* **1990**, *75*, 1020.

[24] D. Walker, *Am. Mineral.* **1991**, *76*, 1092.

[25] D. C. Rubie, *Phase Trans.* **1999**, *68*, 431.

[26] H. Huppertz, *Z. Naturforsch. B* **2001**, *56*, 697.

[27] *TOPAS-Academic*, *V. 4.1*, Coelho Software, Brisbane, Australia, **2007**.

[28] *DigitalMicrograph 3.6.1*, Gatan Software, Pleasanton, USA, **1999**.

[29] P. A. Stadelmann, *Ultramicroscopy* **1987**, *21*, 131.

[30] *ESVision*, *4.0.164*, Emispec Systems Inc., Tempe, USA, **1994-2002**.

[31] P. P. Konstantinov, L. E. Shelimova, E. S. Avilov, M. A. Kretova, V. S. Zemskov, *Inorg. Mater.* **2001**, *37*, 662.

[32] N. Melnychenko-Koblyuk, A. Grystsiv, St. Berger, H. Kaldarar, H. Michor, F. Röhrbacher, E. Royanian, E. Bauer, P. Rogl, H. Schmid, G. Giester, *J. Phys. Condens. Matter* **2007**, *19*, 046203.

[33] C. Candolfi, U. Aydemir, M. Baitinger, N. Oeschler, F. Steglich, Y. Grin, *J. Electron. Mater.* **2010**, *39*, 2039.

[34] A. Grytsiv, P. Rogl, St. Berger, Ch. Paul, H. Michor, E. Bauer, G. Hilscher, C. Godart, P. Knoll, M. Musso, W. Lottermoser, A. Saccone, R. Ferro, T. Roisnel, H. Noel, *J. Phys. Condens. Matter* **2002**, *14*, 7071.

[35] G. Rogl, A. Grytsiv, E. Bauer, P. Rogl, M. Zehetbauer, *Intermetallics* **2010**, *18*, 394.

[36] G. Rogl, A. Grytsiv, E. Bauer, P. Rogl, M. Zehetbauer, *Intermetallics* **2010**, *18*, 57.

3.3 Structural features and physical properties of $In_2Bi_3Se_7I$, $InBi_2Se_4I$ and BiSeI

T. Rosenthal, M. Döblinger, P. Wagatha, C. Gold, E.-W. Scheidt, W. Scherer, O. Oeckler
Z. Anorg. Allg. Chem. **2011**, *637,* 2239–2245.

Abstract

The quaternary compounds $In_2Bi_3Se_7I$ and $InBi_2Se_4I$ have been synthesized via gas phase reactions. They decompose above ca. 400 °C, losing iodine and forming binary compounds. Their crystal structures have been solved and refined using single crystal X-ray diffraction data ($In_2Bi_3Se_7I$: space group *Pnma*, a = 13.6720(2), b = 4.0893(3), c = 16.7070(2) Å; $InBi_2Se_4I$: space group *Pnma*, a = 26.6039(14), b = 4.1285(2), c = 13.5031(9) Å). Both compounds show structural features related to those found in alkali metal bismuth chalcogenides known for their good thermoelectric properties such as β-$K_2Bi_8Se_{13}$. All these structures contain rocksalt-like building blocks as well as CdI_2-like fragments and loosely bound anions (selenide halides) or cations (alkali metal selenides), respectively, located in rather large cavities which suggests the possibility of phonon scattering by rattling. The electrical resistivity of $In_2Bi_3Se_7I$ and $InBi_2Se_4I$ conforms to semiconducting behavior. The total thermal conductivity of sintered pellets of In_2BiSe_4I exhibits a maximum of 0.7 W K^{-1} m^{-1} at 22 K. The rather high electrical resistivity of $In_2Bi_3Se_7I$ and In_2BiSe_4I is probably a consequence of the different electronegativities of the constituting elements in combination with the balanced valence states. The related compound BiSeI has a lower electrical resistivity and a higher thermal conductivity featuring a maximum of 10.3 W K^{-1} m^{-1} at 8.2 K; its Seebeck coefficient (S) amounts to -55 μV K^{-1} at 295 K.

3.3.1 Introduction

The efficiency of thermoelectric materials depends on the combination of a high Seebeck coefficient, low thermal conductivity and low electrical resistivity. Therefore, it is crucial to understand how certain structural features are related to physical properties in order to improve existing materials or – as a long-term goal – to synthesize tailor-made materials for specific applications. Bi_2Te_3 has been one of the main starting points for the development of thermoelectric materials since the 1950s.[1] Mixing the isostructural Bi_2Se_3 with alkali metals

provides another intriguing perspective to control its physical properties. Indeed, it has been demonstrated that $K_2Bi_8S_{13}$ displays a significantly lower electrical resistivity at room temperature than its parent compound Bi_2S_3.[2] Assuming that the replacement of S by the heavier Se results in reduced occupancy disorder between K^+ and Bi^{3+} and decreased thermal conductivity, β-$K_2Bi_8Se_{13}$ was synthesized by Kanatzidis and coworkers.[3] The resulting positive effect on the thermoelectric properties has been revealed by comparing the isostructural compounds $K_2Bi_8S_{13}$ and β-$K_2Bi_8Se_{13}$. The α-phase of $K_2Bi_8Se_{13}$ is a wide-band semiconductor with a band gap of 0.76 eV.[4] β-$K_2Bi_8Se_{13}$ is a narrow-gap semiconductor with mixed K/Bi occupancy and interesting thermoelectric properties; it has an electrical resistivity of 4 mΩcm and a Seebeck coefficient of -200 μV/K at room temperature resulting in a *ZT* value of 0.23.[3]

This compound was found during an exploratory synthesis program based on the assumption that more complex structures may lead to complex electronic structures which possibly result in high thermoelectric power factors combined with low thermal conductivities.

The compounds in the quaternary system In-Bi-Se-X (X = I, Br) exhibit structural features related to those found in many alkali metal bismuth chalcogenides such as the above mentioned α-$K_2Bi_8Se_{13}$ and β-$K_2Bi_8Se_{13}$ [3,4] and might as well help to understand the underlying structure-property relationships. Wang first synthesized $InBi_2Se_4Br$[5] and $In_2Bi_3Se_7I$[6] and elucidated their crystal structures. All these structures consist of complex partial structures with rocksalt-like and CdI_2-like fragments and loosely bound anions (selenide halides) or cations (alkali metal selenides), respectively, located in rather large cavities which opens the possibility of phonon scattering by rattling. Due to the structural similarity to alkali bismuth chalcogenides it seems interesting to investigate the compounds in the system In/Bi/Se/I and their thermoelectric properties, especially as the high atomic weight of all elements present should further decrease the phonon propagation.

3.3.2 Results and Discussion

3.3.2.1 Synthesis and stability of $In_2Bi_3Se_7I$ and In_2BiSe_4I

Samples of In_2BiSe_4I can be prepared by annealing a stoichiometric mixture of In_2Se_3 and BiSeI obtained by quenching or air-cooling a corresponding melt of the elements. $In_2Bi_3Se_7I$ was synthesized in a two-zone furnace with the reactants, i.e. a mixture of the elements, in the hot zone. Details are given in the *Experimental Section*. The gas phase obviously plays an

important role in the synthesis of both $In_2Bi_3Se_7I$ and In_2BiSe_4I. The long and delicate needle-shaped habit of the lustrous dark grey crystalline products is typical for chemical vapor transport reactions, and the formation of the product on the surface of apparently unchanged ingots (In_2BiSe_4I) or next to the starting material ($In_2Bi_3Se_7I$) further corroborates this assumption. Both compounds cannot be obtained by simply melting stoichiometric mixtures of the elements.

In_2BiSe_4I crystals are formed on the surface of the In_2Se_3/BiSeI ingots during the annealing process and large amounts of them can be collected in order to obtain pure samples. A Rietveld fit of the experimental powder diffraction pattern using the structure model of In_2BiSe_4I derived from the single crystal X-ray diffraction data proves the phase purity of the product (cf. Figure S1 in the *Supporting Information*) and yields $R_p = 0.0575$. According to differential thermal analysis and thermogravimetry (DTA-TG) in an open crucible, In_2BiSe_4I shows a reduction in mass of 13 % between 400 °C and 450 °C, associated with an endothermic heat flow. In powder X-ray diffraction (PXRD) patterns of the samples after thermal analysis, In_2Se_3, Bi_2Se_3 as well as small amounts of InSeI and BiSeI were found. The decomposition might correspond to the reaction $6In_2BiSe_4I \rightarrow 5In_2Se_3 + 3Bi_2Se_3 + 2InI_3$. However, the evaporation of InI_3 would mean a weight loss of 18.7%. The amount of InI_3 that formally remains in the samples forms MSeI = $M_2Se_3{\cdot}InI_3$ (M = In, Bi). A second endothermic signal in the heat flow at approximately 715 °C may be credited to the melting of Bi_2Se_3 (melting temperature 706 °C [7]) or the phase transition γ-$In_2Se_3 \rightarrow \delta$-$In_2Se_3$, reported to occur at 730 °C.[8]

$In_2Bi_3Se_7I$ is not obtained with quantitative yield; however, the Rietveld fit using the structure model of $In_2Bi_3Se_7I$ from the single crystal X-ray diffraction data shows the phase purity of the product (cf. Figure S2 in the *Supporting Information*, $R_p = 0.0144$). $In_2Bi_3Se_7I$ shows a reduction in mass of 8 % starting at 430 °C and peaking around 470 °C, concurring with an endothermic heat flow. In the corresponding PXRD, In_2Se_3 and Bi_2Se_3 could be identified. In analogy to In_2BiSe_4I, this can be explained by $6In_2Bi_3Se_7I \rightarrow 5In_2Se_3 + 9Bi_2Se_3 + 2InI_3$, again with some MSeI as a byproduct. A second endothermic signal at approximately 700 °C coincides with the melting of Bi_2Se_3 (melting temperature 706 °C[9]), In_2Se_3 remains solid in the measured temperature range (melting temperature 880 °C[8]).

3.3.2.2 Crystal structure of In_2BiSe_4I

In_2BiSe_4I crystallizes in the orthorhombic space group *Pnma*. Atomic parameters are listed in Table 1, anisotropic displacement parameters are given in Table S1 in the *Supplementary Information*. Crystal data and details of the refinement are summarized in Table 2.

Table 1. Wyckoff positions, atomic coordinates and isotropic displacement parameters (in Å) for In_2BiSe_4I

atom	Wyckoff position	***x***	***y***	***z***	U_{eq}
Bi (1)	4***c***	0.54283(4)	0.25	0.61052(3)	0.02061(13)
I (1)	4***c***	0.06245(7)	0.25	0.27815(6)	0.0253(2)
In (1)	4***c***	0.24027(8)	0.25	0.50210(6)	0.0212(2)
In (2)	4***c***	0.39286(8)	0.25	0.13975(7)	0.0239(2)
Se (1)	4***c***	0.10806(10)	0.25	0.04080(8)	0.0191(3)
Se (2)	4***c***	0.22002(11)	0.25	0.66588(9)	0.0231(3)
Se (3)	4***c***	0.32093(10)	0.25	0.35705(8)	0.0197(3)
Se (4)	4***c***	0.88775(11)	0.25	0.51611(9)	0.0217(3)

Table 2. Crystallographic data and structure refinement of In_2BiSe_4I and $In_2Bi_3Se_7I$ at 293 K

Formula	In_2BiSe_4I	$In_2Bi_3Se_7I$
Formula mass (in $gmol^{-1}$)	881.36	1536.20
Crystal system / Space group	orthorhombic, *Pnma*	orthorhombic, *Pnma*
Cell parameters (in Å)	*a* = 13.6720(2) Å *b* = 4.0893(3) Å *c* = 16.7070(2) Å	*a* = 26.6039(14) Å *b* = 4.1285(2) Å *c* = 13.5031(9) Å
Cell volume (in $Å^3$)	934.07(19)	1483.10(14)
X-ray density (in gcm^{-3})	6.267	6.880
Absorption coefficient (in mm^{-1})	22.829	31.224
Formula units per unit cell (Z)	4	4
F(000)	1480	2552
Diffractometer	Stoe IPDS I	Stoe IPDS I
Radiation	Ag-$K_{\alpha1}$ (λ = 0.56085 Å)	Ag-$K_{\alpha1}$ (λ = 0.56085 Å)
2ϑ range (in °)	$0 \leq 2\theta \leq 50$	$0 \leq 2\theta \leq 45$
Absorption correction	numerical	numerical
Measured reflections	11973	14384
Independent data / parameters	1871 / 50	2208 / 80
Refinement	full-matrix least-squares on F^2	full-matrix least-squares on F^2
R(int) / R(σ)	0.0987 / 0.0651	0.0506 / 0.0267
R indices [$I > 2\sigma(I)$]	R1 = 0.0399, wR2 = 0.0742	R1 = 0.0184, wR2 = 0.0354
R indices [all data]	R1 = 0.0747, wR2 = 0.0835	R1 = 0.0270, wR2 = 0.0375
GooF [all data]	0.929	0.979
$\Delta\rho_{min}$ / $\Delta\rho_{max}$ ($eÅ^{-3}$)	−2.246 / +1.986	−1.468 / +1.085

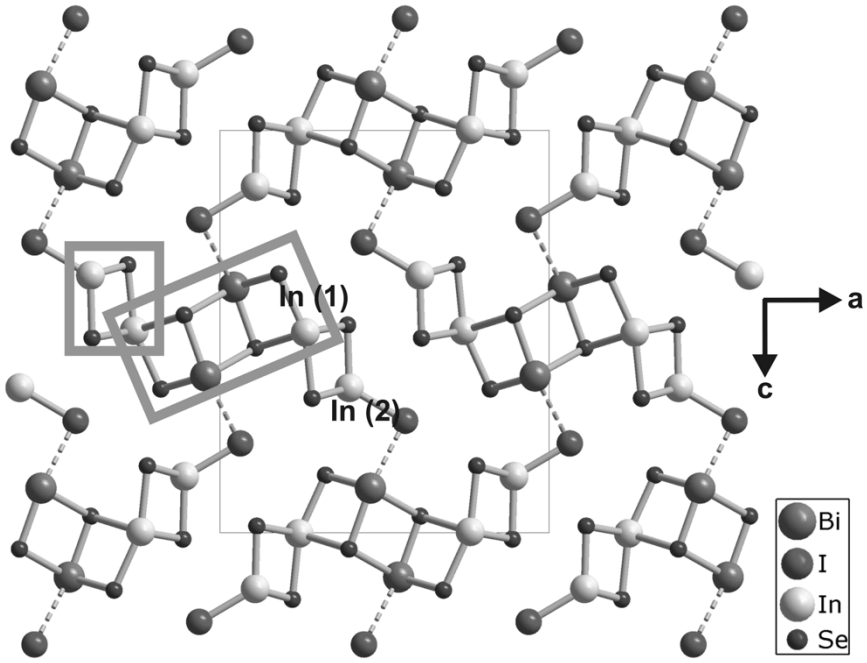

Fig. 1. Projection of the structure of In_2BiSe_4I along [010], Typical NaCl-like (larger) and CdI_2-like (smaller) building blocks are marked by gray boxes. The unit cell is indicated by thin lines, displacement ellipsoids are scaled to include a probability of 98%.

The structure is built up of one-dimensional infinite strands running along [010] (Figure 1). The strands are interconnected by I atoms. They contain two structure motifs that can be described as a distorted rocksalt-type strand in the center and two CdI_2-like strands that share the In(1) atoms on both sides with the rocksalt-like strand.

Bi is 5+2 coordinated by five Se and two I atoms corresponding to the notation $[Bi^{3+}{}_{1/1}Se^{2-}{}_{3/5}Se^{2-}{}_{2/3}I^{-}{}_{2/3}]^{1/5-}$. The Bi coordination polyhedrons share faces and edges. Bi–Se bond lengths range from 2.681 Å to 3.129 Å, varying around the values of 2.990 Å and 3.061 Å observed in Bi_2Se_3.[10] The Bi coordination polyhedrons share edges with the In(1) coordination octahedrons. In occupies two crystallographically and chemically different atom sites. In(1) is coordinated in a distorted octahedral fashion by six Se atoms. The octahedrons share common edges corresponding to the notation $[In^{3+}{}_{1/1}Se^{2-}{}_{2/5}Se^{2-}{}_{4/3}]^{7/15-}$. In(2) is coordinated by a distorted tetrahedron consisting of three Se atoms and one I atom. The tetrahedrons are linked via the edges by common Se atoms, corresponding to the notation $[In^{3+}{}_{1/1}Se^{2-}{}_{3/3}I^{-}{}_{1/3}]^{2/3+}$. The In(1) coordination octahedrons are edge-linked to the In(2) coordination tetrahedron. The In–Se bond lengths range from 2.599 Å to 2.983 Å, comparable to the bond lengths 2.521 and 2.940 in In_2Se_3.[11] The In–I bond length of 2.694 Å is in compliance with the terminal In–I bond lengths of 2.641 Å - 2.643 Å in In_2I_6.[12] Se occupies four chemically and crystallo-

graphically independent atom sites. Se(1) is coordinated by three In atoms, Se(2) is coordinated by three Bi atoms and two In atoms, Se(3) is coordinated by two Bi atoms and one In atom, Se(4) is coordinated by three In atoms. The interatomic distance Bi–I of 3.754 Å is significantly longer than the Bi-I distances in the binary BiI_3 (3.054 Å, 3.125 Å) [13] but below the sum of the van der Waals radii of these atoms (4.05 Å[14]). It is comparable with other long Bi–I bonds, e.g. 3.742 Å in BiSI[15], 3.790 Å in BiSeI[16] and 3.822 Å in SbSeI.[17] Neglecting the Bi-I interaction the calculated bond valence sum[22] of iodine is smaller (-0.84) than the formal oxidation state -I, in accordance with a weak bonding condition of the I atoms. Taking the Bi-I bond into consideration, the valence sum of I increases to -1.00; however, at the same time the valence sum of Bi increases from 3.07 to 3.23. In general, all bond valence sums are in a reasonable range (2.63 to 2.94 for In, -1.74 to -2.4 for Se) for a compound that is not very ionic.

3.3.2.3 Structure of $In_2Bi_3Se_7I$

The structure of $In_2Bi_3Se_7I$ was first described by Wang.[6] The accessibility of these data is limited as they have not been published in a journal and, moreover, they are not very precise. Therefore we redetermined the structure. The structure refinement presented here is much more accurate with a final R1 (observed reflections) of 0.018 compared to 0.078 for the original refinement. $In_2Bi_3Se_7I$ crystallizes in the orthorhombic space group *Pnma*. Crystal data and details of refinement are summarized in Table 2. Fractional atomic coordinates and equivalent isotropic displacement parameters are given in Table 3, anisotropic displacement parameters are given in Table S2 in the *Supporting Information*.

$In_2Bi_3Se_7I$ is built up of layers containing two different building blocks with the iodine atoms pointing towards the interlayer space. One building block corresponds to the distorted rocksalt-like, the other one to the CdI_2-like fragment also present in In_2BiSe_4I (see above). However, in $In_2Bi_3Se_7I$ there are different types of CdI_2-like blocks distinguished by their connectivity. The one containing In(1) shares one In position with the rocksalt-type block as described for In_2BiSe_4I. The other CdI_2-like block contains In(2) and is connected to the rocksalt-type block along the (001) plane by a three-coordinated Se atom. The interlayer Bi–I distance (dotted line in Figure 2) is 3.586 Å, corresponding to a weak interaction, so that the layers adhere mainly by van der Waals type bonding. The overall weak bonding of the iodine atoms results in a calculated bond valence sum (-0.65) that is 35% smaller than the formal

valence sum of -1. The other bond valence sums are in reasonable ranges (2.77 to 2.84 for In, 2.99 to 3.17 for Bi, -1.84 to -2.22 for Se).

Table 3. Wyckoff positions, atomic coordinates and isotropic displacement parameters (in Å) for $In_2Bi_3Se_7I$

atom	Wyckoff position	*x*	*y*	*z*	U_{eq}
In (1)	4*c*	0.03383(2)	0.25	0.58439(4)	0.02334(12)
In (2)	4*c*	0.44764(2)	0.25	0.54308(5)	0.02714(13)
Bi (1)	4*c*	0.186068(10)	0.25	0.425180(19)	0.01966(7)
Bi (2)	4*c*	0.190731(10)	0.25	0.049321(19)	0.02002(7)
Bi (3)	4*c*	0.343750(9)	0.25	0.20446(2)	0.01920(7)
Se (1)	4*c*	0.00991(3)	0.25	0.12187(5)	0.01906(14)
Se (2)	4*c*	0.02755(3)	0.25	0.38917(5)	0.01971(15)
Se (3)	4*c*	0.08705(2)	0.25	0.74802(5)	0.01515(13)
Se (4)	4*c*	0.23125(2)	0.25	0.60733(5)	0.01476(13)
Se (5)	4*c*	0.24091(2)	0.25	0.87243(5)	0.01599(13)
Se (6)	4*c*	0.36424(2)	0.25	0.44888(5)	0.01559(13)
Se (7)	4*c*	0.38011(2)	0.25	0.01920(5)	0.01558(13)
I (1)	4*c*	0.366341(19)	0.25	0.73411(3)	0.02175(10)

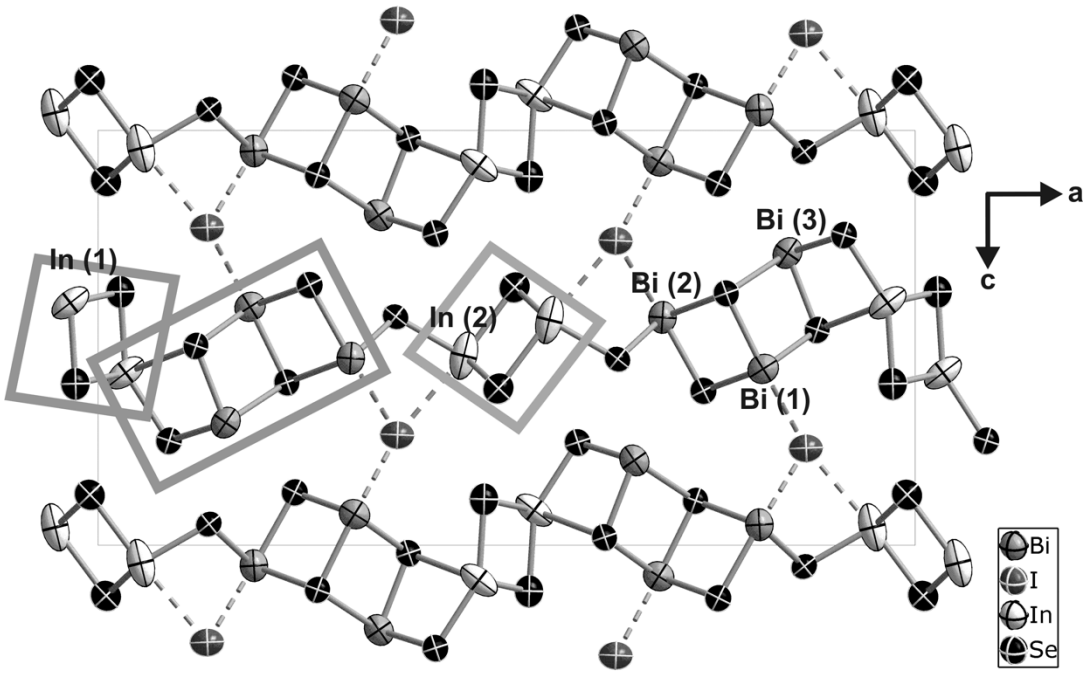

Fig. 2: Projection of the structure of $In_2Bi_3Se_7I$ viewed along [010]. Typical NaCl-like (larger) and CdI_2-like (smaller) building units are highlighted by the gray boxes. The unit cell is indicated by thin lines, displacement ellipsoids are scaled to include a probability of 98%.

In $In_2Bi_3Se_7I$, In(1) atoms are coordinated by six Se atoms corresponding to the notation $[In^{3+}{}_{1/1}Se^{2-}{}_{2/5}Se^{2-}{}_{4/3}]^{7/15-}$ like in In_2BiSe_4I. In(2) is coordinated in a trigonal bipyramidal fashion by four Se atoms and one I atom corresponding to the notation $[In^{3+}{}_{1/1}Se^{2-}{}_{4/3}I^{-}{}_{1/5}]^{2/15+}$.

The In(1) as well as the In(2) coordination polyhedrons are edge linked along [010]. In–Se bond lengths range from 3.207 Å to 2.557 Å with the longest In–Se bond being 0.267 Å longer than the corresponding one in In_2Se_3,[11] the shorter bond lengths In–Se are similar in the quaternary and binary compounds. The distance In–I (3.366 Å) is significantly larger than the longest In-I bonds in In_2I_6 (2.839 Å), but smaller than the sum of the van der Waals radii (3.91 Å),[14] confirming the weak bonding of the iodine atoms as suggested by the bond valence sum mentioned above. Bi occupies three crystallographically independent atom sites. Bi(1) is 5+2 coordinated by five Se atoms and two I atoms corresponding to the notation $[Bi^{3+}_{1/1}Se^{2-}_{2/3}Se^{2-}_{3/5}I^{-}_{2/5}]^{1/15+}$. Bi(2) is 5+2 coordinated by five Se atoms and two I atoms corresponding to the notation $[Bi^{3+}_{1/1}Se^{2-}_{3/3}Se^{2-}_{2/5}I^{-}_{2/5}]^{3/15-}$. Bi(3) is coordinated by five Se atoms corresponding to the notation $[Bi^{3+}_{1/1}Se^{2-}_{3/5}Se^{2-}_{2/3}]^{7/15+}$. Bi–Se bond lengths range from 2.682 Å to 3.156 Å. The two different Bi–I bond lengths are very similar (3.576 Å and 3.586 Å) and a little shorter than those in In_2BiSe_4I.

3.3.2.4 Common structural features in the systems Bi-In-Se-I and X-Bi-Se (X = alkali metal)

The structures of In_2BiSe_4I and $In_2Bi_3Se_7I$ exhibit similar building units. Both contain distorted rocksalt-type blocks and characteristic entities that can be described as small cut-outs of the $CdCl_2$ type. These structural features are also present in alkali metal bismuth chalcogenides that exhibit interesting thermoelectric properties. Kanatzidis et al. describe β-$K_2Bi_8Se_{13}$ as a 3D network built up from Bi_2Te_3, CdI_2 and NaCl rod-like fragments,[3] which are also common in other chalcogenides (cf. Figure S3 in the *Supporting Information*). As Bi_2Te_3 blocks can be considered as distorted NaCl-like fragments, all these structures can be described as 3D-networks containing more or less distorted cut-outs of the rocksalt-type atom arrangement and of CdI_2-like fragments. While most of the known alkali metal bismuth chalcogenides consist of an anionic framework with weakly bound alkali metals, the formally cationic infinite strands or sheets in In_2BiSe_4I and $In_2Bi_3Se_7I$, respectively, are interconnected by weakly bound I atoms as indicated by the bond lengths and the low bond valence. One might expect that this reduces the phonon propagation between the sheets or strands and leads to a low lattice thermal conductivity.

3.3.2.5 Thermoelectric Properties

Due to the structural similarity with well-known thermoelectric materials, the physical properties of $In_2Bi_3Se_7I$ and In_2BiSe_4I were examined. The total thermal conductivity (κ) of In_2BiSe_4I ranges from 0.16 W K^{-1} m^{-1} at 3.5 K to 0.3 W K^{-1} m^{-1} at room temperature, with a maximum of 0.7 W K^{-1} m^{-1} at 22 K. The electrical resistivity increases from 3.3 kΩ cm at 300 K to 325 kΩ cm at 222 K (Figure 3a). The corresponding Arrhenius plot reveals semiconducting behavior with a band gap of 0.72 eV between 250 K and 300 K (insert Figure 3a). The electrical resistivity of $In_2Bi_3Se_7I$ drops from 136 kΩ cm at 4 K to 94 Ω cm at 300 K (Figure 3b). The calculated band gap of 0.19 eV results from an Arrhenius plot in the same temperature range as specified for In_2BiSe_4I. Due to this high electrical resistivity, measurements of the thermal conductivity and the thermopower were considered futile. As a consequence, no reliable figure of merit *ZT* could be determined for $In_2Bi_3Se_7I$ and In_2BiSe_4I.

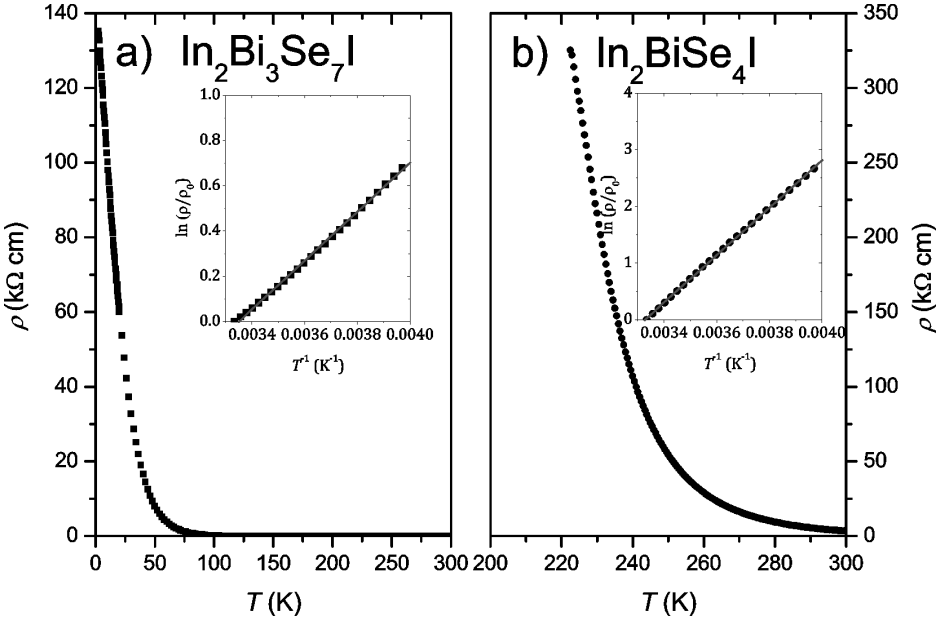

Fig. 3: Electrical resistivity of a) In_2BiSe_4I and b) $In_2Bi_3Se_7I$. The inserts pictures an Arrhenius plot for the temperature range between 250K and 300 K.

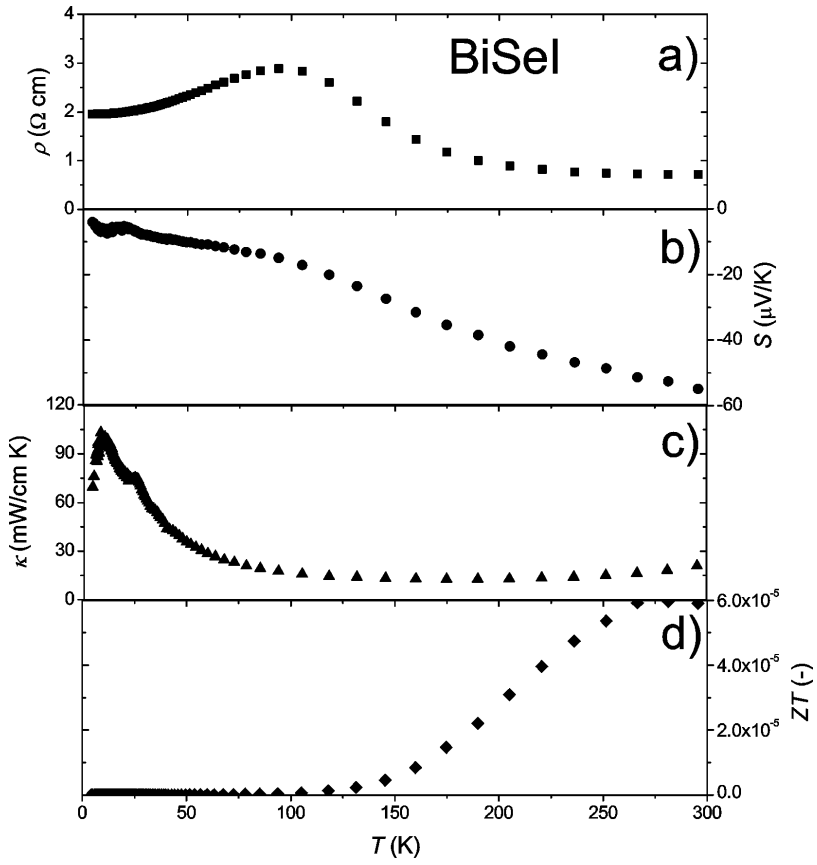

Fig. 4: Thermoelectric properties of BiSeI; a) electrical resistivity (ρ); b) Seebeck coefficient (S); c) thermal conductivity (κ)**;** d) thermoelectric figure of merit (ZT).

The electrical resistivity of both compounds is much larger compared with the characteristic values displayed by structurally related alkali metal bismuth chalcogenides.[3,4] The reason for this discrepancy may be explained by the differences in the respective electronic structures. The ionicity in $In_2Bi_3Se_7I$ and In_2BiSe_4I is rather high and the compounds are characterized by balanced valence states. In contrast, the actual composition of β-$K_2Bi_8Se_{13}$ from single crystal structure refinement is $K_{2.06}Bi_{7.94}Se_{13}$, yielding a charge mismatch of 0.12 electrons per formula unit. Therefore, the valence states are not balanced which, in combination with a lower degree of ionicity, is reflected in a lower electrical resistivity.

The related compound BiSeI,[16] which contains CdI_2-like strands of Bi and Se atoms with weakly bound terminal I atoms, is structurally similar but exhibits slightly better thermoelectric properties (Figure 4). In comparison with the quaternary compounds $In_2Bi_3Se_7I$ and $InBi_2Se_4I$, the total resistivity at 4 K is reduced by three orders of magnitude. Semiconducting behavior (band gap 0.06 eV) can only be observed in the high-temperature region well above 100 K. The absolute value of the Seebeck coefficient rises from nearly 0 $\mu V\ K^{-1}$ at 4K to -55 $\mu V\ K^{-1}$ at 295 K in accordance with n-type conductivity. The thermal

conductivity of BiSeI is 70 mW K^{-1} cm^{-1} at 4 K and decreases to 21 mW K^{-1} cm^{-1} at 295 K. The maximum at 8.2 K is probably due to phonon *umklapp* scattering – a phenomenon typically observed in pure crystalline materials. The resulting thermoelectric figure of merit (*ZT*) reaches 6 10^{-5} at 295 K. Hence, the lower degree of condensation in BiSeI is probably responsible for the enhancement of the *ZT* value relative to the quaternary indium bismuth selenide iodides. However, the nominal value achieved is rather small.

3.3.3 Conclusion

$In_2Bi_3Se_7I$ and In_2BiSe_4I exhibit structural features similar to several alkali metal bismuth chalcogenides that are known for their thermoelectric properties, e.g. β-$K_2Bi_8Se_{13}$. These features include a three-dimensional network with some weakly bonded heavy atoms as well as rocksalt-like and CdI_2-like building blocks and loosely bound atoms. Although this might reduce the lattice thermal conductivity, good thermoelectric properties are impeded by the high electrical resistivity of $In_2Bi_3Se_7I$ and In_2BiSe_4I which again is probably a consequence of the significantly different electronegativities of the elements in combination with the balanced valence states. Therefore, the rather high ionicity of these ternary phases is reflected in poor electrical conductivity. On contrary, the deviation of β-$K_2Bi_8Se_{13}$ samples from their formal composition with balanced valence states and their lower ionicity might be the key parameters responsible for the lower electrical resistivity observed in these non-stoichiometric compounds. The deviation of the actual composition from the idealized composition with balanced valence states is a common feature found in structurally related compounds that have been discussed as thermoelectric materials, e.g. $K_{2.5}Bi_{8.5}Se_{14}$ showing an actual composition of $K_{2.36}Bi_{8.64}Se_{14}$ and a resulting charge mismatch of 0.28 per formula unit.[3] This shows the strong influence of slight variations from the balanced valence state on the electrical resistivity and thus on the thermoelectric properties. Therefore, increasing the metallic character by doping, e.g. with alkali metals, might significantly enhance the thermoelectric properties in the system In-Bi-Se-X (X = I, Br).

3.3.4 Experimental Section

3.3.4.1 Synthesis

All samples were prepared from stoichiometric mixtures of the elements indium (99.999%, Smart Elements, Vienna, Austria), bismuth (99.999%, Smart Elements, Vienna, Austria), selenium (shots, amorphous, 99.999+%, Alfa Aesar), and iodine (99.9%, AppliChem, Germany, dried with conc. H_2SO_4). Samples of In_2BiSe_4I were prepared by melting the mixtures in a tube furnace in silica glass ampoules (11 mm diameter) under argon. The resulting ingots consist of In_2Se_3 and BiSeI. They were ground and annealed at 425 °C for 36 h under argon. Coarse metallic gray needles of In_2BiSe_4I could be mechanically separated, with approximately 10% In_2Se_3 as a side phase. $In_2Bi_3Se_7I$ was synthesized in a two-zone furnace. A stoichiometric mixture of the elements was sealed at a pressure of $< 5\times10^{-3}$ mbar and heated to 380 °C / 330 °C for 7 days with the reactants in the hot zone, and subsequently quenched to room temperature. The product consists of fine metallic gray needles of $In_2Bi_3Se_7I$ on the hot side of the tube, near the starting material. Pellets for thermoelectric measurements (6 mm diameter) were pressed with a force of 21 kN and annealed for 24 h at 420 °C under Ar atmosphere to reduce the amount of grain boundaries. Pellets for physical property measurements of BiSeI were prepared by melting a stoichiometric mixture of the elements in a flat-bottom silica glass tube (22 mm diameter) at 600 °C for 15 h followed by quenching to room temperature, resulting in a dark grey ingot of BiSeI, which was polished to a pellet-like shape. All operations at reduced pressure were conducted under dry ice cooling to prevent iodine sublimation.

3.3.4.2 EDX analyses

The composition of the compounds was verified by energy-dispersive X-ray spectroscopy (EDX) with a JSM-6500F (Jeol, USA) scanning electron microscope (SEM) equipped with a model 7418 EDX detector (Oxford Instruments, Great Britain). Spectra were acquired using an acceleration voltage of 24 kV and 80 seconds accumulation time. 3 to 7 point analyses were averaged and the uncertainties estimated from the variance.

The ingot for thermoelectric measurements with the nominal composition BiSeI yielded an average composition of $Bi_{0.9(1)}Se_1I_{0.8(1)}$. The EDX results of the samples of In_2BiSe_4I and $In_2Bi_3Se_7I$ used for physical property measurements were $In_{2.0(2)}Bi_{1.1(2)}Se_4I_{1.1(2)}$ and $In_{1.9(1)}Bi_{2.9(2)}Se_7I_{1.0(1)}$ respectively. The phase purity of the samples was verified by PXRD prior to the physical property measurements.

3.3.4.3 Thermal Analysis

Differential thermal analysis and thermogravimetry (DTA-TG) was performed on finely ground samples using a Setaram TG-92 thermal analyzer, equipped with a protected DTA-TG rod. The measurements were conducted under helium at a scanning rate of 10 °C min^{-1} using alumina crucibles.

3.3.4.4 X-ray Diffraction

For X-ray powder diffraction, finely ground samples were fixed on Mylar foils using silicone grease. Data were collected on a G670 (Huber, Germany) X-ray powder diffractometer with Guinier geometry, equipped with a position-sensitive imaging plate detector using Cu-$K_{\alpha 1}$ radiation (1.54051 Å, Ge(111) monochromator). Powder patterns were evaluated using the program WINXPOW.[18]

Single crystals were mounted on glass fibers and checked for quality by Laue photographs using a Buerger precession camera (Huber, Germany). Data were collected on an IPDS-I (Stoe & Cie GmbH, Germany) diffractometer equipped with an imaging plate detector using graphite monochromated Ag-$K_{\alpha 1}$ (0.56086 Å) radiation. Numerical absorption correction based on measured crystal faces was performed on all samples using the X-RED/X-SHAPE software.[19,20] The structures were solved by direct methods and refined by full-matrix least-squares techniques using the SHELX-97 software.[21] The crystallographic information files (cif) are available from the Fachinformationszentrum Karlsruhe, D-76344 Eggenstein-Leopoldshafen (Germany), e-mail: crysdata@fiz-karlsruhe.de, by quoting the deposition numbers CSD-423015 (In_2BiSe_4I) and CSD-423016 ($In_2Bi_3Se_7I$), respectively, the name of the authors and the citation of the paper.

The formal charge distribution according to bond valence sums was calculated with VaList.[22] The calculation was based on the structure parameters from single-crystal data.

3.3.4.5 Thermoelectric Measurements

For thermoelectric measurements, a commercial PPMS (Quantum Design, USA) was used. The electrical resistivity measurements were performed by a standard four-probe dc method with a constant current of 5 mA where the temperature changes at a rate of 0.7 K min^{-1}. The thermal conductivity and the Seebeck coefficient were measured using the thermal transport option on bar-shaped samples in a four-point setup (one heater, two thermometers). All measurements were performed in the temperature range between 3 K and room temperature.

Acknowledgement

We thank T. Miller for the single-crystal data collection, C. Minke for SEM operation and EDX analyses and S. Makowski for thermal analyses. We gratefully acknowledge Prof. Dr. W. Schnick's generous support of this work.

3.3.5 Supplementary Information:

A) Powder diffraction

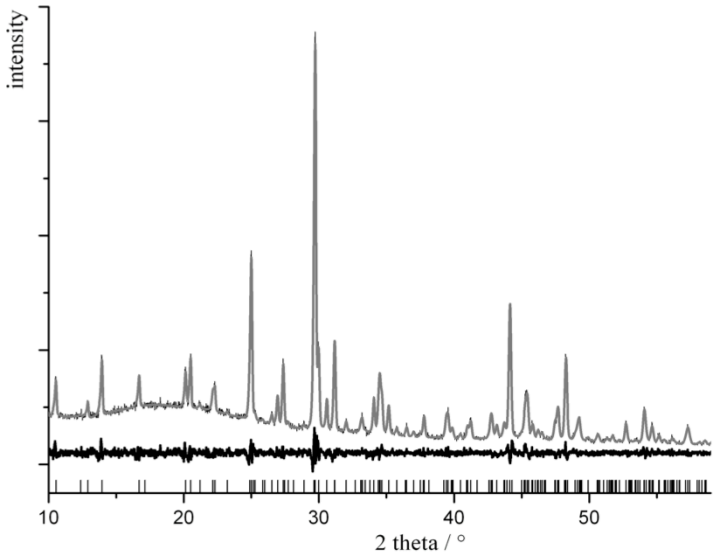

Figure S1: Result of a Rietveld fit (gray) based on a structure model of In_2BiSe_4I derived from the single crystal X-ray diffraction data, showing the experimental powder diffraction pattern of In_2BiSe_4I (black), a difference plot and reflection markers (bottom). The fit converged at Rp = 0.0575 and Rwp = 0.0754, respectively.

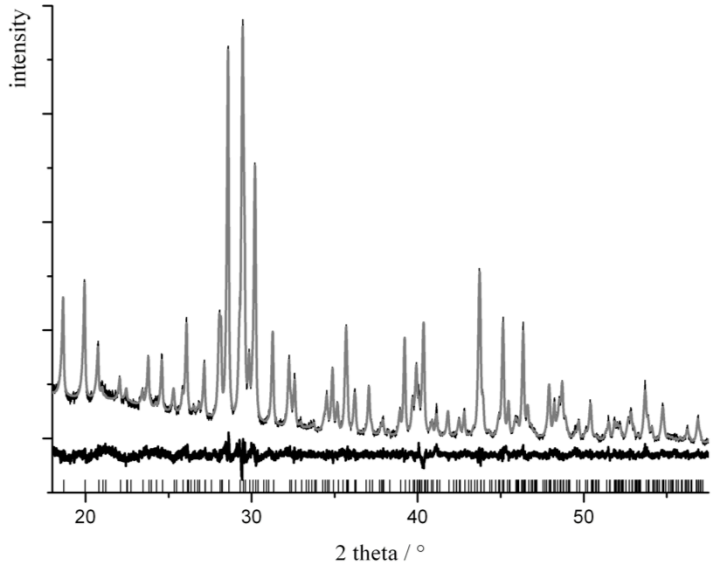

Figure S2: Result of a Rietveld fit (grey) based on a structure model of $In_2Bi_3Se_7I$ derived from the single crystal X-ray diffraction data, showing the experimental powder diffraction pattern of $In_2Bi_3Se_7I$ (black), a difference plot and reflection markers (bottom). The fit converged at Rp = 0.0144 and Rwp = 0.0183, respectively.

B) Anisotropic displacement parameters

Table S1. Anisotropic displacement parameters (in Å²) for In_2BiSe_4I

atom	U_{11}	U_{22}	U_{33}	U_{13}	$U_{23} = U_{12}$
Bi (1)	0.0204(2)	0.0195(2)	0.0220(2)	0.00309(19)	0
I (1)	0.0197(4)	0.0317(6)	0.0246(5)	0.0028(3)	0
In (1)	0.0235(5)	0.0184(5)	0.0219(5)	0.0082(4)	0
In (2)	0.0251(5)	0.0188(5)	0.0278(5)	-0.0087(4)	0
Se (1)	0.0172(5)	0.0206(7)	0.0194(6)	-0.0015(5)	0
Se (2)	0.0233(6)	0.0186(7)	0.0272(7)	-0.0015(5)	0
Se (3)	0.0177(6)	0.0197(7)	0.0218(6)	-0.0014(5)	0
Se (4)	0.0202(6)	0.0203(7)	0.0245(6)	-0.0009(5)	0

Table S2. Anisotropic displacement parameters (in Å²) for $In_2Bi_3Se_7I$

atom	U_{11}	U_{22}	U_{33}	U_{13}	$U_{23} = U_{12}$
In (1)	0.0299(3)	0.0170(3)	0.0231(2)	-0.0130(2)	0
In (2)	0.0173(3)	0.0146(3)	0.0495(4)	-0.0084(2)	0
Bi (1)	0.02061(12)	0.01924(15)	0.01914(12)	-0.00156(9)	0
Bi (2)	0.01692(11)	0.02059(15)	0.02255(13)	0.00036(9)	0
Bi (3)	0.01884(11)	0.01769(15)	0.02106(12)	0.00296(9)	0
Se (1)	0.0212(3)	0.0147(4)	0.0213(3)	0.0013(2)	0
Se (2)	0.0187(3)	0.0171(4)	0.0234(3)	0.0001(2)	0
Se (3)	0.0154(3)	0.0135(4)	0.0165(3)	-0.0004(2)	0
Se (4)	0.0147(3)	0.0136(4)	0.0159(3)	0.0005(2)	0
Se (5)	0.0158(3)	0.0160(4)	0.0161(3)	-0.0002(2)	0
Se (6)	0.0152(3)	0.0171(4)	0.0145(3)	0.0015(2)	0
Se (7)	0.0145(3)	0.0159(4)	0.0163(3)	0.0007(2)	0
I (1)	0.0259(2)	0.0221(3)	0.0173(2)	0.00034(17)	0

C) Additional figure

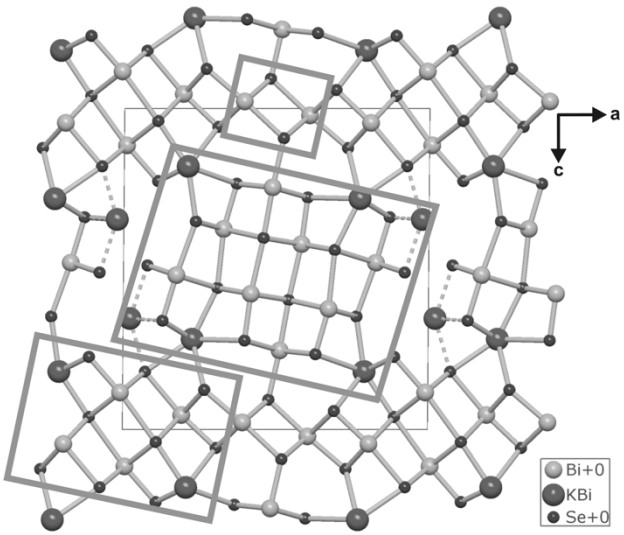

Figure S3: Projection of the structure of β-$K_2Bi_8Se_{13}$ viewed along [010]. Typical NaCl (large and middle) and CdI_2 (smaller) building units are highlighted by gray boxes. The unit cell is indicated by thin lines. (according to D. Y. Chung, K. S. Choi, L. Iordanidis, J. L. Schindler, P. W. Brazis, C. R. Kannewurf, B. X. Chen, S. Q. Hu, C. Uher, M. G. Kanatzidis, *Chem. Mater.* **1997**, *9*, 3060-3071).

3.3.6 References

[1] G. J. Snyder, E. S. Toberer, *Nat. Mater*. **2008**, *7*, 105.

[2] M. G. Kanatzidis, T. J. McCarthy, T. A. Tanzer, L. –H. Chen, L. Iordanidis, T. Hogan, C. R. Kannewurf, C. Uher, B. Chen, *Chem. Mater*. **1996**, *8*, 1465.

[3] D. Y. Chung, K. S. Choi, L. Iordanidis, J. L. Schindler, P. W. Brazis, C. R. Kannewurf, B. X. Chen, S. Q. Hu, C. Uher, M. G. Kanatzidis, *Chem. Mater.* **1997**, *9*, 3060.

[4] D. I. Bilc, S. D. Mahanti, T. Kyratsi, D. Y. Chung, M. G. Kanatzidis, P. Larson *Phys. Rev. B*, **2005**, *71*, 085116.

[5] L. Wang, S.-J. Hwu, *Chem. Mater.* **2007**, *19*, 6212.

[6] L. Wang, Dissertation thesis, Clemson University, Clemson, USA, **2007**.

[7] U. Petasch, H. Göbel, H. Oppermann, *Z. Anorg. Allg. Chem.* **1998**, *624*, 1767.

[8] S. Popovic, A. Tonejc, B. Grzetaplenkovic, B. Celustka, R. Trojko, *J. Appl. Crystallogr.* **1979**, *12*, 416.

[9] U. Petasch, H. Göbel, H. Oppermann, *Z. Anorg. Allg. Chem.* **1998**, *624*, 1767.

[10] S. A. Semiletov, Z. G. Pinsker, *Dokl. Akad. Nauk SSSR* **1955,** *100*, 1079.

[11] A. Likforman, D. Carre, R. Hillel, *Acta Crystallogr. Sect. B: Struct. Sci.* **1978**, *34*, 1.

[12] J. D. Forrester, A. Zalkin, D. H. Templeton, *Inorg. Chem.* **1964**, *3*, 63.

[13] J. Trotter, T. Zobel, *Z. Kristallogr.* **1966**, *123*, 67.

[14] M. Mantina, A. C. Chamberlin, R. Valero, C. J. Cramer, D. G. Truhlar, *J. Phys. Chem. A* **2009**, *113*, 5806.

[15] W. Haase-Wessel, *Naturwissenschaften* **1973**, *60*, 474.

[16] V. A. Trifonov, A. V. Shevel'kov, E. V. Dikarev, B. A. Popovkin, *Russ. J. Inorg. Chem.* **1999**, *44*, 5.

[17] G. P. Voutsas, P. J. Rentzeperis, *Z. Kristallogr.* **1982**, *161*, 111.

[18] *WINXPOW*, *v2.12 ed*., Stoe & Cie GmbH, Darmstadt, Germany, **2005**.

[19] *X-RED32 V. 1.31*, STOE & Cie GmbH, Darmstadt, Germany, **2005**.

[20] *X-SHAPE V. 2.07*, STOE & Cie GmbH, Darmstadt, Germany, **2005.**

[21] G. M. Sheldrick, *Acta Crystallogr. Sect. A* **2008**, *64*, 112.

[22] A. S. Wills, *VaList Version 3.0.13*, University College London, UK, **1998-2008**.

3.4 A high-pressure route to thermoelectrics with low thermal conductivity: the solid solution series $AgIn_xSb_{1-x}Te_2$ (x = 0.1 - 0.6)

T. Schröder, T. Rosenthal, D. Souchay, C. Petermayer, S. Grott, E.-W. Scheidt, C. Gold, W. Scherer, O. Oeckler

J. Solid State Chem. **2013**, *206*, 20 - 26.

Abstract

Metastable rocksalt-type phases of the solid solution series $AgIn_xSb_{1-x}Te_2$ (x = 0.1, 0.2, 0.4, 0.5 and 0.6) were prepared by high-pressure synthesis at 2.5 GPa and 400 °C. In these structures, the coordination number of In^{3+} is six, in contrast to chalcopyrite ambient-pressure $AgInTe_2$ with fourfold In^{3+} coordination. Transmission electron microscopy shows that real-structure phenomena and a certain degree of short-range order are present, yet not very pronounced. All three cations are statistically disordered. The high degree of disorder is probably the reason why $AgIn_xSb_{1-x}Te_2$ samples with $0.4 < x < 0.6$ exhibit very low thermal conductivities with a total $\kappa < 0.5$ W/Km and a lattice contribution of $\kappa_{ph} \sim 0.3$ W/Km at room temperature. These are lower than those of other rocksalt-type tellurides at room temperature; e.g., the well-known thermoelectric $AgSbTe_2$ ($\kappa \sim 0.6$ W/Km). The highest *ZT* value (0.15 at 300 K) is observed for $AgIn_{0.5}Sb_{0.5}Te_2$, mainly due to its high Seebeck coefficient of 160 μV/K. Temperature-dependent X-ray powder patterns indicate that the solid solutions are metastable at ambient pressure. At 150 °C, the quaternary compounds decompose into chalcopyrite-type $AgInTe_2$ and rocksalt-type $AgSbTe_2$.

3.4.1 Introduction

The interconversion of thermal and electrical energy by means of thermoelectrics is intensely researched, the long-term goal being the efficient generation of electrical energy from waste heat and the development of novel materials for Peltier coolers or small heating devices. The dimensionless figure of merit $ZT = S^2\sigma T / \kappa$ (Seebeck coefficient *S*, electrical conductivity σ, thermal conductivity κ)[1] is a measure of the efficiency of the conversion process. All quantities involved depend on the charge carriers' concentration and mobility and therefore cannot be optimized independently. According to the Wiedemann-Franz law, σ and the electronic part of the thermal conductivity (κ_{el}) are proportional to each other. Increasing the mobility of the charge carriers and thus σ, in addition, usually lowers the absolute value of *S*.

Therefore, a common approach to improving thermoelectrics aims at decreasing the phononic part of the thermal conductivity (κ_{ph}) without significantly interfering with the electronic properties. This paradigm suggests that effective phonon scattering is important, which can be achieved by creating nano-domain structures, e.g. twin domains in TAGS, i.e.,$(AgSbTe_2)_{1-n}(GeTe)_n$,[2-4] or short-range ordered defect layers in GST materials, i.e. $(GeTe)_nSb_2Te_3$.[5,6] Domain structures often result from phase transitions or, in case of heterogeneous systems, from partial phase separation.[7-14] Exsolution may lead to endotactic nanodots, e.g. in LAST ($AgPb_nSbTe_{2+n}$).[15] As nanostructures and other real-structure effects as well as phase transitions play an important role, transmission electron microscopy and temperature-dependent X-ray diffraction are very valuable tools for structure elucidation.

Synthetic approaches to lowering κ_{ph} may include the application of high pressure or fast quenching (e.g. melt spinning) during crystallization. Stress as well as short crystallization times usually yield smaller grain sizes (i.e. more grain boundaries) and more pronounced real-structure effects. Both features may scatter phonons more effectively than electrons.[16,17]

A large number of ternary I-V-VI_2 phases exhibit very low intrinsic thermal conductivities (< 1 W/Km),[18,19] the most prominent compound being $AgSbTe_2$ with $\kappa \approx 0.6$ W/Km at room temperature (RT). It is characterized by ZT values of ~0.3 at RT and up to 1.3 at 400 °C, respectively;[20] and represents both the end member of TAGS solid solutions and the matrix of LAST materials.[2-4,15] All of these materials, including nanostructured ones, exhibit cation disorder in sometimes distorted rocksalt-type crystal structures.

In contrast to $AgSbTe_2$, $AgInTe_2$ crystallizes in the chalcopyrite structure type, a superstructure of the sphalerite type where all cations are tetrahedrally coordinated by Te. In accordance with the pressure-coordination rule, $AgInTe_2$ transforms to a rocksalt-type structure under high pressure; however, phases with tetrahedrally coordinated In^{3+} are formed again after decompression within a few days.[21] For $AgInSe_2$, rocksalt-type high-pressure phases are metastable at ambient pressure when In is partially substituted by Sb.[22] Thus, one can expect that cation-disordered rocksalt-type members of a solid solution series $AgInTe_2$-$AgSbTe_2$ are accessible by high-pressure high-temperature syntheses and may be metastable at ambient conditions. For these phases, no thermoelectric data are available. However, chalcopyrite-type $AgInTe_2$ exhibits a thermal conductivity of ~ 2 W/Km at 300 K,[14,23] more than three times higher than that of $AgSbTe_2$. The thermal conductivities of quaternary solid solutions may be expected to be even lower than those of ternary I-V-VI_2 compounds due to the fact that the number of disordered cation types is higher.

The element combination Ag/In/Sb/Te ("AIST") is an intriguing one as it plays an important role in the field of phase-change materials for rewritable optical data storage (e.g. $Ag_{3.4}In_{3.7}Sb_{76.4}Te_{16.5}$ on CD-RWs).[24] As the required material properties for phase-change materials are comparable to those for thermoelectrics,[5] the present study aims at characterizing the thermoelectric properties and structural features as well as stability ranges of AIST materials prepared by high-pressure high-temperature synthesis.

3.4.2 Experimental

3.4.2.1 Synthesis

Bulk samples with the nominal compositions $AgIn_xSb_{1-x}Te_2$ (x = 0.1, 0.2, 0.4, 0.5 and 0.6) were prepared by heating stoichiometric mixtures (e.g., 1.5 g) of the pure elements (silver 99.9999%, Alfa Aesar; indium 99.999%, Smart Elements; antimony 99.9999%, Smart Elements; tellurium 99.999 %, Alfa Aesar) in sealed silica glass ampoules to 950 °C under argon atmosphere. The resulting melts were quenched to RT in water. They contain mixtures of chalcopyrite-type $AgInTe_2$ and rocksalt-type $AgSbTe_2$ and were used as starting materials for high-pressure syntheses.

High-pressure experiments were performed using a multi-anvil hydraulic press (Voggenreiter, Mainleus, Germany).[25-28] Quenched $AgIn_xSb_{1-x}Te_2$ was powdered, loaded into a cylindrical crucible made of hexagonal BN (Henze, Kempten, Germany) and sealed with a BN cap. In order to obtain an electrical resistance furnace; the capsule was centered within two nested graphite tubes. The remaining volume at both ends of the outer graphite tube was filled with two MgO discs. The arrangement, surrounded by a zirconia tube, was then placed into a pierced truncated Cr_2O_3-doped MgO octahedron (edge length 25 mm, Ceramic Substrates & Components, Isle of Wight, Great Britain). Eight truncated tungsten carbide cubes (truncation edge length 17 mm) served as anvils for the compression of the truncated octahedron, they were separated by pyrophyllite gaskets. The graphite tubes were electrically contacted by two Mo plates. The assembly was compressed up to a pressure of 2.5 GPa in 2 h. At this constant pressure, samples were prepared by annealing at 400 °C for 5 h and subsequently quenching the sample by turning off the furnace. After quenching the sample, the pressure was maintained for 1 h to ensure that RT was reached. Subsequently, the pressure was reduced to ambient pressure within 6 h.

3.4.2.2 EDX analysis

EDX (energy dispersive X-Ray) spectra of representative pieces of crushed bulk samples were recorded using a JSM-6500F (Jeol, USA) scanning electron microscope with EDX detector (model 7418, Oxford Instruments, Great Britain). For each sample, the results of five point analyses were averaged and the errors were estimated from their variance (see Table 1).

Table 1. EDX results for $AgIn_xSb_{1-x}Te_2$ (averaged from 5 point analyses each)

sum formula	atom-% (calc.)	atom-% (EDX)
$AgIn_{0.6}Sb_{0.4}Te_2$	Ag: 25; In: 15; Sb: 10; Te: 50	Ag: 23.1(7); In: 14.8(4); Sb: 11.6(3); Te: 50.5(9)
$AgIn_{0.5}Sb_{0.5}Te_2$	Ag: 25; In: 12.5; Sb: 12.5; Te: 50	Ag: 24.2(3); In: 12.1(6); Sb: 13.5(5); Te: 50.2(5)
$AgIn_{0.4}Sb_{0.6}Te_2$	Ag: 25; In: 10; Sb: 15; Te: 50	Ag: 24.9(5); In: 8.9(3); Sb: 16.0(5); Te: 50.2(6)
$AgIn_{0.2}Sb_{0.8}Te_2$	Ag: 25; In: 5; Sb: 20; Te: 50	Ag: 24.5(4); In: 4.5(3); Sb: 20.9(3); Te: 50.1(4)
$AgIn_{0.1}Sb_{0.9}Te_2$	Ag: 25; In: 2.5; Sb: 22.5; Te: 50	Ag: 24.5(5); In: 2.2(5); Sb: 23.5(5); Te: 49.7(6)

3.4.2.3 X-ray diffraction

X-ray powder patterns were recorded with a Huber G670 Guinier camera equipped with a fixed imaging plate and integrated read-out system using Cu-$K_{\alpha 1}$ radiation (Ge monochromator, λ = 1.54051 Å). Specimens were prepared by crushing representative parts of the samples and fixing the powder on Mylar foils using vacuum grease. The phase homogeneity was evaluated and lattice parameters were determined by pattern fitting (Rietveld method) using the program TOPAS.[29] Temperature-dependent powder diffraction experiments were performed with a STOE Stadi P powder diffractometer equipped with an imaging plate detector system using Mo-$K_{\alpha 1}$ radiation (Ge monochromator, λ = 0.71093 Å) in a modified Debye–Scherrer geometry. Powdered specimens were filled into silica glass capillaries with 0.3 mm diameter and sealed with vacuum grease under argon atmosphere. During the measurement, the samples were heated up to 600 °C in a graphite furnace with a heating rate of 5 K/min.

3.4.2.4 Transmission electron microscopy

For transmission electron microscopy, finely ground samples were dispersed in ethanol and distributed on copper grids coated with a holey carbon film (S166-2, Plano GmbH, Germany). The grids were fixed on a double-tilt holder. Selected area electron diffraction (SAED), high resolution transmission electron microscopy (HRTEM) and EDX measurements were done on a Titan 80-300 (FEI, USA) with a field emission gun operated at 300 kV equipped with a TEM TOPS 30 EDX spectrometer (EDAX, Germany). Images were recorded using an UltraScan 1000 camera (Gatan, USA, resolution: 2k x 2k). HRTEM and SAED data were evaluated using the programs Digital Micrograph[30] and EMS,[31] EDX data were processed with ES Vision.[32]

3.4.2.5 Electrical and thermal transport measurements

The temperature-dependent conductivities $\sigma(T)$ of the samples were measured by a standard four-probe dc method employing a constant current of 5 mA with a physical property measurement system (PPMS, Quantum Design). The data were collected in the temperature range of 2 – 300 K by cooling and heating sequences in which the temperature changed at a rate of 0.5 K min^{-1}. The uncertainty of the absolute electrical resistivity has been estimated by taking into account the errors in specifying the sample dimensions; it amounts to ~ 20 %. The thermoelectric power $S(T)$ and the thermal conductivity $\kappa(T)$ of samples were measured simultaneously using the thermal transport option of the PPMS. This is based on a relaxation method employing one heater and two thermometers to determine the induced thermal voltage and the temperature gradient along the sample in a temperature range between 4 K and 300 K. These measurements were carried out using bar-shaped samples with typical dimensions between 4 and 7 mm^3 during a heating process at a rate of 0.5 $Kmin^{-1}$. The total accuracy of the $S(T)$ and $\kappa(T)$ values is about 5%.

3.4.3 Results and discussion

3.4.3.1 Crystal structure

The powder diffraction patterns of the compounds of the solid solution series $AgIn_xSb_{1-x}Te_2$ with x = 0.1, 0.2, 0.4, 0.5 and 0.6, which were obtained by thermal quenching under a constant pressure of 2.5 GPa, could be indexed assuming cubic metrics. For x > 0.6, the

samples were inhomogeneous. The average structure (for $x \leq 0.6$) derived from Bragg reflections corresponds to the rocksalt type (space group $Fm\bar{3}m$, no. 225), which has been reported for $AgSbTe_2$ (x = 0) at ambient pressure and for the high-pressure phase of $AgInTe_2$ (x = 1).[33,20] The powder patterns contain little evidence for different scattering densities on anion and cation positions due to the similar electron counts; however, very weak intensities can be observed for the NaCl type's reflections hkl with h, k, l = 2n+1 (more pronounced in electron diffraction patterns, see below). Thus, Ag, In and Sb were placed on the cation position (occupancy factors 0.5 for Ag, $^{x}/_{2}$ for In and $0.5 - {}^{x}/_{2}$ for Sb), whereas full occupancy by Te was assumed on the anion site. The occupancy factors were set according to the nominal composition of the starting materials, which was confirmed by EDX measurements (see Table 1). A common isotropic displacement parameter was used for the cations; the one for Te was refined separately. Slight preferred orientation was taken into account using the March-Dollase algorithm. Representative profile fits resulting from Rietveld refinements for $AgIn_{0.5}Sb_{0.5}Te_2$ and $AgIn_{0.6}Sb_{0.4}Te_2$ are shown in Fig. 1 (the Rietveld fit for x = 0.1, 0.2 and 0.4 can be found in the Supplementary Information). Crystal data and the refined atomic parameters are given in Tables 2 and 3, respectively. Further details of the crystal structure investigations may be obtained from Fachinformationszentrum Karlsruhe, 76344 Eggenstein-Leopoldshafen, Germany (fax: (+49)7247-808-666; e-mail: crysdata@fiz-karlsruhe.de, http://www.fiz-karlsruhe.de /request_for_deposited_data.html) on quoting the depository numbers CSD-426090, CSD-426089, CSD-426086, CSD-426088 and CSD-426087 for x = 0.1, 0.2, 0.4, 0.5 and 0.6, respectively.

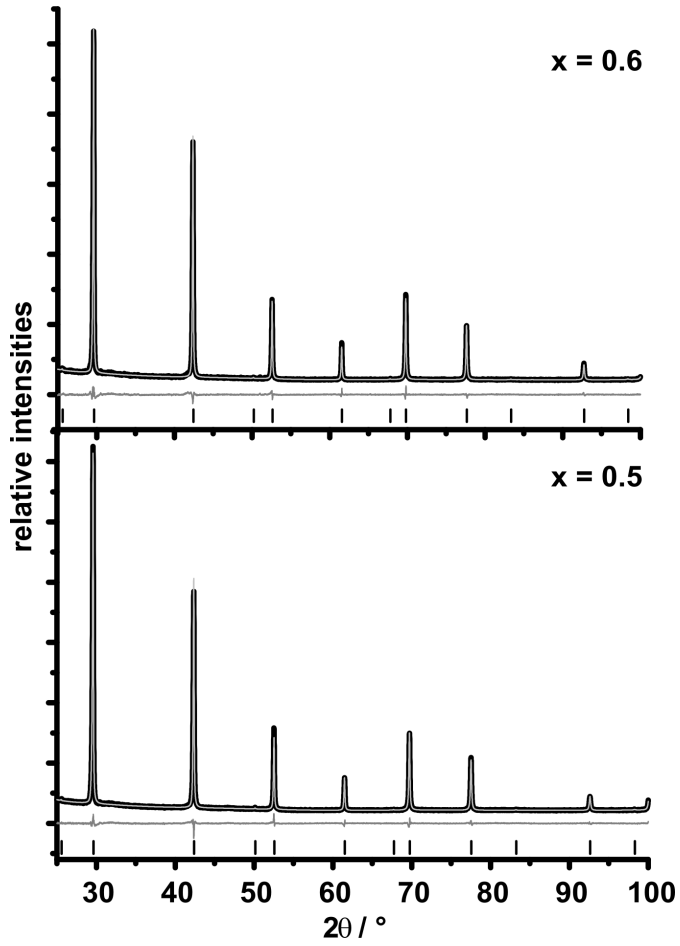

Fig. 1: Rietveld fits for $AgIn_{0.5}Sb_{0.5}Te_2$ (bottom) and $AgIn_{0.6}Sb_{0.4}Te_2$ (top); experimental (black) and calculated data (gray); difference plot (gray, below), peak positions (black, vertical lines).

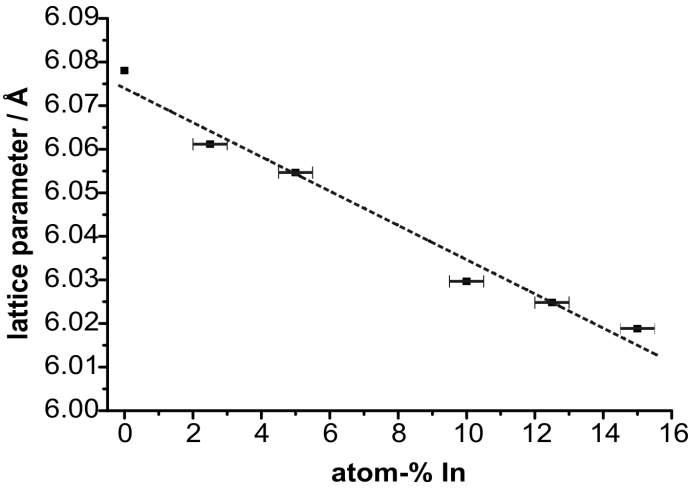

Fig. 2: Vegard's plot for $AgIn_xSb_{1-x}Te_2$ (dotted line: least-squares fit) with estimated error bars of 0.5 atom-% (see text); the atom-% refer to the sum formula (i.e. $AgInTe_2$ would correspond to 25 atom-% In); value for $AgSbTe_2$ from ref. [32].

Table 2. Results of the Rietveld refinements for $AgIn_{0.1}Sb_{0.9}Te_2$, $AgIn_{0.2}Sb_{0.8}Te_2$, $AgIn_{0.4}Sb_{0.6}Te_2$, $AgIn_{0.5}Sb_{0.5}Te_2$, and $AgIn_{0.6}Sb_{0.4}Te_2$.

Sum formula	$AgIn_{0.1}Sb_{0.9}Te_2$	$AgIn_{0.2}Sb_{0.8}Te_2$	$AgIn_{0.4}Sb_{0.6}Te_2$	$AgIn_{0.5}Sb_{0.5}Te_2$	$AgIn_{0.6}Sb_{0.4}Te_2$
Molar mass / g mol^{-1}	484.13	483.44	482.05	481.36	480.66
$F(000)$	403.6	403.2	402.4	402	401.6
Crystal system / space group (no.)	cubic / $Fm\bar{3}m$ (no.225)				
Lattice parameter / Å	6.06114(2)	6.05464(2)	6.02965(2)	6.02483(2)	6.01881(2)
Cell volume / Å^3	222.671(2)	221.955(2)	219.218(2)	218.693(2)	218.038(2)
Density (X-ray) / g cm^{-3}	7.221	7.234	7.303	7.310	7.321
Radiation	Cu-$K_{\alpha 1}$ (λ = 1.540596 Å)				
2θ range / °	$20 \leq 2\theta \leq 100$				
Profile function	fundamental parameter approach				
Constraints	2				
Number of reflections	15				
Refined parameters / thereof background	23 / 12	23 / 12	23 / 12	23 / 12	23 / 12
R_p / R_{wp}	0.0168 / 0.0239	0.0186 / 0.0259	0.0149 / 0.0209	0.0173 / 0.0238	0.0170 / 0.0244
Gof	0.841	0.937	0.743	0.888	0.890

Table 3. Atom positions, occupancy and displacement parameters (B_{eq}) for $AgIn_{0.1}Sb_{0.9}Te_2$, $AgIn_{0.2}Sb_{0.8}Te_2$, $AgIn_{0.4}Sb_{0.6}Te_2$, $AgIn_{0.5}Sb_{0.5}Te_2$, and $AgIn_{0.6}Sb_{0.4}Te_2$.

Sum formula	Atom	Wyckoff position	x y z	s.o.f.	B_{eq}
$AgIn_{0.1}Sb_{0.9}Te_2$	Ag/In/Sb	4*a*	0 0 0	0.5/0.05/0.45	2.36(2)
	Te	4*b*	$^1/_2$ $^1/_2$ $^1/_2$	1	1.57(2)
$AgIn_{0.2}Sb_{0.8}Te_2$	Ag/In/Sb	4*a*	0 0 0	0.5/0.1/0.4	2.34(3)
	Te	4*b*	$^1/_2$ $^1/_2$ $^1/_2$	1	1.58(2)
$AgIn_{0.4}Sb_{0.6}Te_2$	Ag/In/Sb	4*a*	0 0 0	0.5/0.2/0.3	1.53(2)
	Te	4*b*	$^1/_2$ $^1/_2$ $^1/_2$	1	1.18(2)
$AgIn_{0.5}Sb_{0.5}Te_2$	Ag/In/Sb	4*a*	0 0 0	0.5/0.25/0.25	1.35(2)
	Te	4*b*	$^1/_2$ $^1/_2$ $^1/_2$	1	0.90(2)
$AgIn_{0.6}Sb_{0.4}Te_2$	Ag/In/Sb	4*a*	0 0 0	0.5/0.3/0.2	1.29(2)
	Te	4*b*	$^1/_2$ $^1/_2$ $^1/_2$	1	0.83(2)

The lattice parameters approximately fulfill Vegard's law (see Fig. 2) up to x = 0.6; indicating a solid solution series. The standard deviations of the lattice parameters are negligible compared to the uncertainties of the composition of high-pressure samples. The latter were estimated from the variance of EDX analyses and their deviation from the starting compositions. The lattice parameter of $AgSbTe_2$ deviates slightly more from the least-squares fit than the other values. This might be due to the fact that $AgSbTe_2$ cannot be synthesized without minor amounts of Ag_2Te so that its actual composition has been given as $Ag_{19}Sb_{29}Te_{52}$.[34]

3.4.3.2 Thermal behavior

Temperature-dependent powder X-ray diffraction patterns (Fig. 3 middle and bottom, additional ones in the Supplementary Information) show that, for instance, $AgIn_{0.5}Sb_{0.5}Te_2$ and $AgIn_{0.1}Sb_{0.9}Te_2$ decompose upon heating. The higher the In concentration, the lower the temperature that is required for the transition to the stable state, which corresponds to a mixture of rocksalt-type $AgSbTe_2$ and chalcopyrite-type $AgInTe_2$. The decomposition of $AgIn_xSb_{1-x}Te_2$ starts at 120 °C for x = 0.6, at 140 °C for x = 0.5 and 0.4, at 160 °C for x = 0.2 and at 200 °C for x = 0.1. This is consistent with the fact that samples with x > 0.6 are not long-term stable even at RT.

Chalcopyrite-type $AgInTe_2$ begins to form while the diffraction pattern is still dominated by the reflections of the rocksalt-type phase. The intensity of the latter's Bragg peaks is rather invariant, however, the reflection positions shift upon heating. This is due to the formation of $AgSbTe_2$ which has the same structure type but displays a slightly different lattice parameter (a = 6.078 Å).[32] It might still contain small amounts of In. As indicated by the dashed rectangles in Fig. 3, an additional reflection is observed at intermediate temperature which disappears when the rocksalt-type reflections of (possibly In-doped) $AgSbTe_2$ become stronger at higher temperature. This single reflection is not sufficient to decide if the rocksalt-type phase is distorted (reflection splitting) or if an additional intermediate phase (e.g. a silver telluride) is present. The diagram for x = 0.1 shows that at least at high temperatures, small amounts of In are soluble in $AgSbTe_2$ as the chalcopyrite-type reflections disappear without another phase being formed.

3.4.3.3 Electron microscopy of $AgIn_{0.5}Sb_{0.5}Te_2$

Electron microscopy studies of $AgIn_{0.5}Sb_{0.5}Te_2$ confirm the results of the Rietveld refinements. The *d*-values observed in selected area electron diffraction (SAED) patterns (Fig. 4) are consistent with those found in the Rietveld fit of the corresponding X-ray powder data (cf. Fig. 1, bottom). The rocksalt type's reflections with h, k, l = 2n+1 are clearly visible. Samples are chemically homogeneous according to TEM-EDX. There are just very weak diffuse intensities; this means that there are no pronounced short-range cation ordering phenomena, atomic size effect[35] or other real-structure features. However, the scattering contrast between the elements involved is small, so that a possible small degree short-range order without relaxation is hard to detect. There are no discrete maxima between the Bragg reflections in SAEDs which would indicate a tendency to form a superstructure.

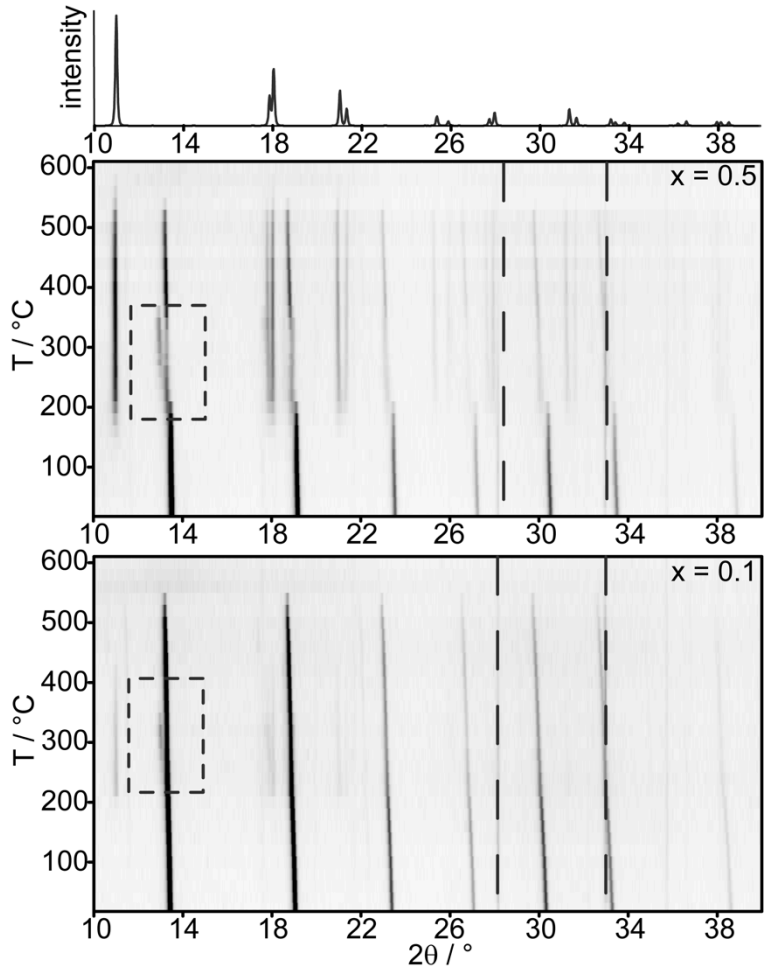

Fig. 3: Simulated powder X-ray diffraction pattern of chalcopyrite-type $AgInTe_2$ at ambient conditions (top), temperature dependent powder X-ray diffraction patterns of $AgIn_{0.5}Sb_{0.5}Te_2$ (middle) and $AgIn_{0.1}Sb_{0.9}Te_2$ (bottom); reflections caused by the furnace material are indicated by dashed lines; the decomposition of the rocksalt-type phase is marked by dashed rectangles.

In the HRTEM images in Figures 4 and 5, few planar defects can be observed in the fringe areas of the crystallites. In contrast to the Fourier transforms of these areas, the SAED patterns of whole small crystallites or of thicker areas exhibit less pronounced diffuse intensities. Therefore, such defects are rather rare effects in thin areas. It remains unclear whether they are due to the high-pressure high-temperature synthesis or induced by the TEM sample preparation.

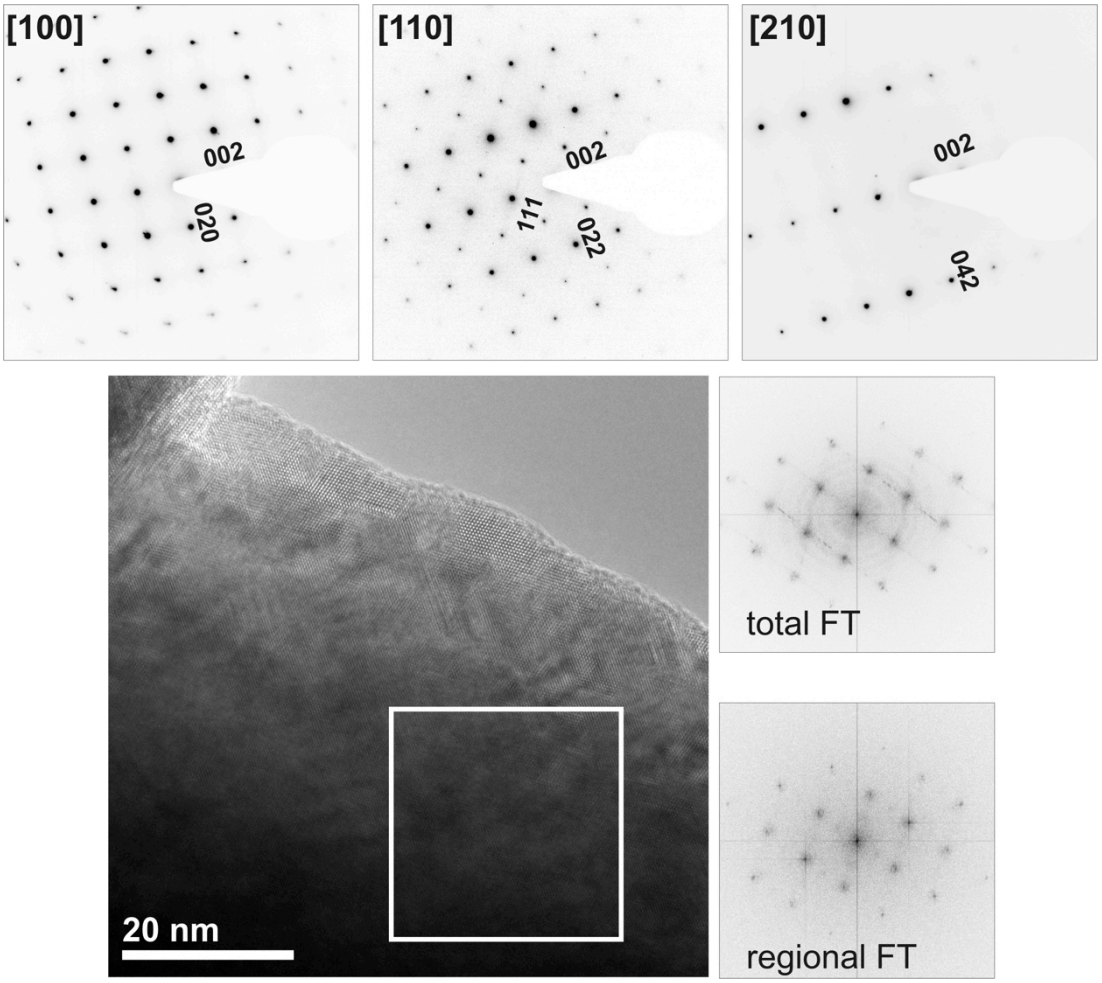

Fig. 4: SAED patterns of the zone axes [100], [110] and [210] (top) of rocksalt-type $AgIn_{0.5}Sb_{0.5}Te_2$; HRTEM image of $AgIn_{0.5}Sb_{0.5}Te_2$ (bottom, left) with the corresponding Fourier transforms of the whole image (middle right) and of the region marked with the white square (bottom right).

3.4.3.4 Thermoelectric properties

All investigated compounds of the series $AgIn_xSb_{1-x}Te_2$ are p-type semiconductors. The electrical conductivity (Figure 6, top) increases with x, although at low temperatures the values for x = 0.4 and 0.5 are similar. For x = 0.6, σ is higher by one order of magnitude compared to the other samples. Below RT, κ of all samples is very low (Figure 6; third from top), less than 0.5 W/Km. In line with the electrical contribution to κ, the absolute values of the thermal conductivities exhibit a comparable trend with respect to x as the electrical conductivities. For all samples, κ_{ph} at 300 K is in the same range of 0.35 - 0.29 W/Km. Due to the low σ of x = 0.4 and 0.5, the electrical contribution κ_{el} to the total κ is rather small (cf. Figure 6). The thermal conductivity of all samples is lower than that of both $AgSbTe_2$ (~ 0.6 W/Km at 300 K) and $AgInTe_2$ (~ 2 W/Km at 300 K).[18] This strong decrease in κ, especially κ_{ph}, upon doping might be caused by the increased disorder at the cation position.

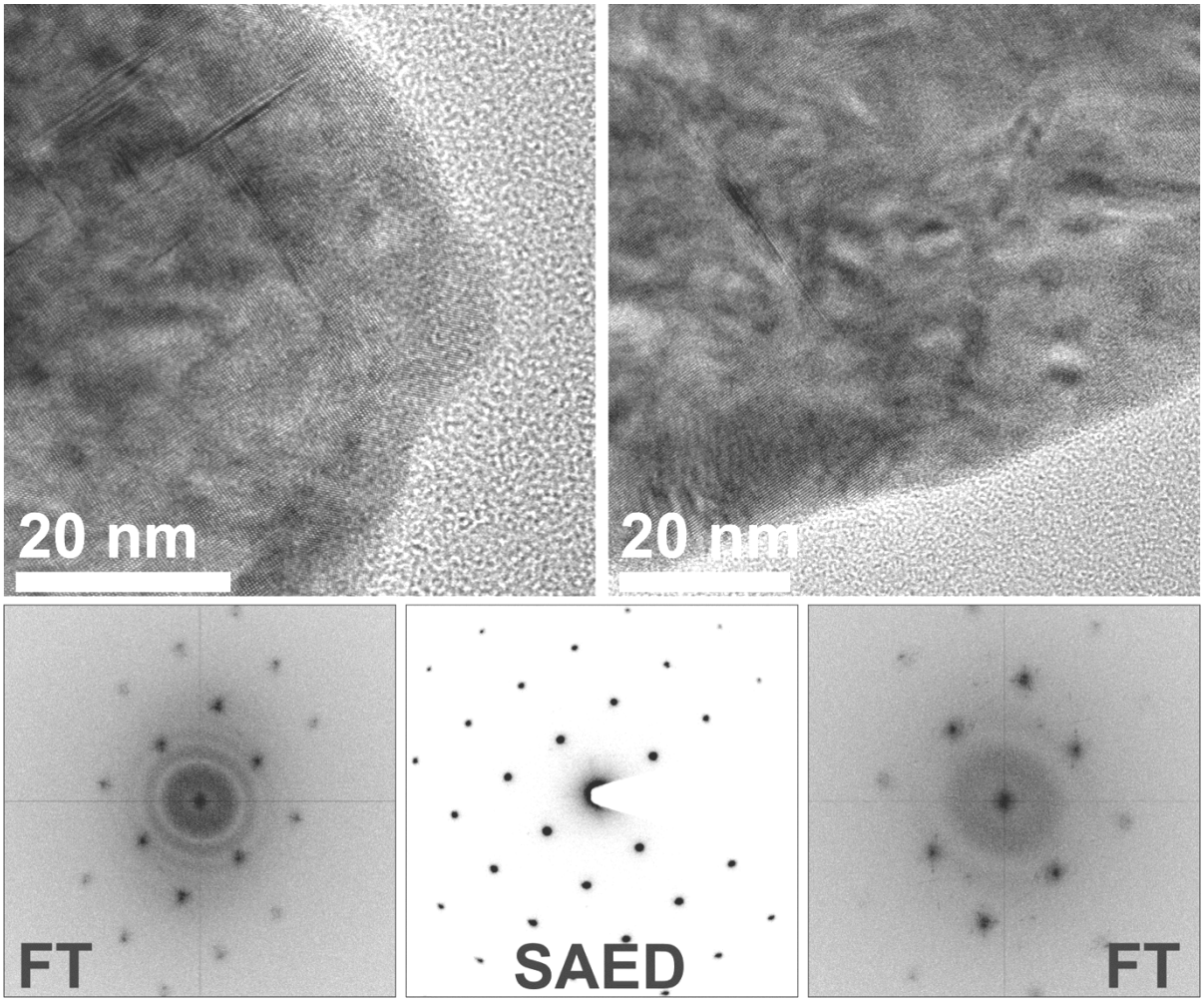

Fig. 5: Electron microscopy $AgIn_{0.5}Sb_{0.5}Te_2$ (zone axis [100]): HRTEM images of two different areas of the same crystallite (top) with the corresponding Fourier transforms (FT, bottom) and the SAED pattern (bottom, middle) of the crystallite. The rather strong contrasts originate from thickness variations (the sample was crushed from an ingot obtained under high-pressure conditions).

$AgIn_{0.5}Sb_{0.5}Te_2$ exhibits the highest Seebeck coefficient (Figure 6; second from top) of the quaternary samples; at RT it amounts to 160 μV/K. This probably indicates a rather high charge carrier concentration. The differences in the *ZT* values of the samples investigated are mainly due to the different Seebeck coefficients; thus, $AgIn_{0.5}Sb_{0.5}Te_2$ exhibits the highest *ZT* value (0.15 at 300K) (Figure 6; bottom). This is lower than that of $AgSbTe_2$ (*ZT* = ~0.3 at 300 K) because of the latter's higher Seebeck coefficient (~240 μV/K at 300 K). However, the observed *ZT* value of $AgIn_{0.5}Sb_{0.5}Te_2$ falls in the same range as corresponding values of other tellurium-based high-performance p-type thermoelectrics at 300 K.[14] In comparison, the thermoelectric properties of chalcopyrite-type $AgInTe_2$, which exhibits a maximum *ZT* value of 0.06 at 600 K and <0.01 at 300 K,[23] are less suitable for potential applications.

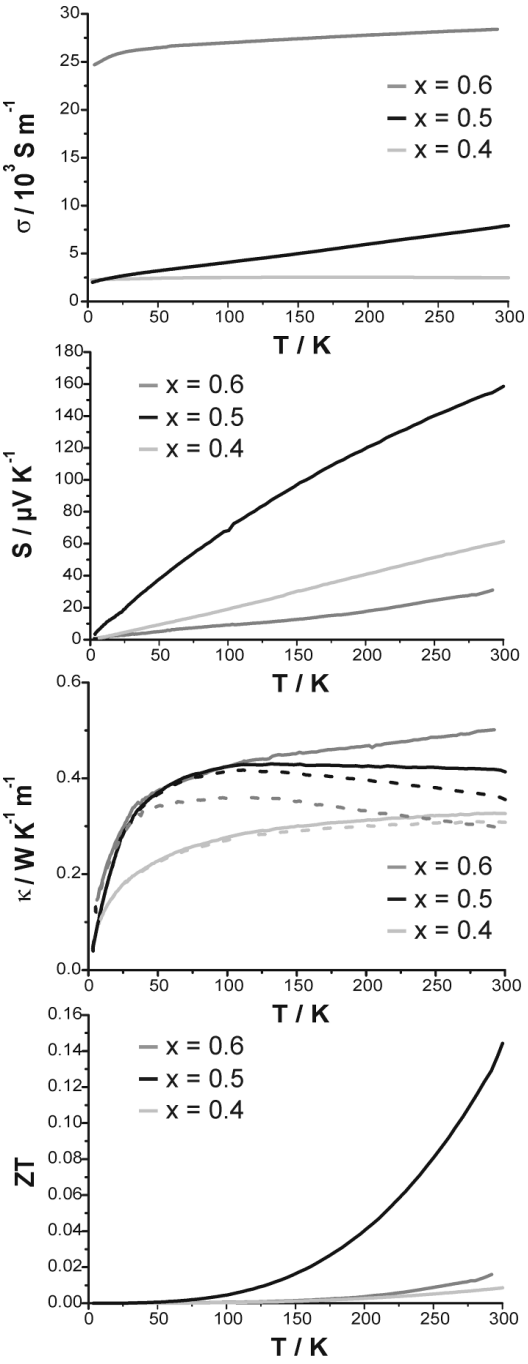

Fig. 6: Electrical conductivity (top), Seebeck coefficients (second from top), total (solid lines) and phononic (broken lines) thermal conductivities (third from top), and *ZT* values (bottom) of $AgIn_{0.4}Sb_{0.6}Te_2$ (light gray), $AgIn_{0.5}Sb_{0.5}Te_2$ (black) and $AgIn_{0.6}Sb_{0.4}Te_2$ (dark gray).

3.4.4 Conclusion

High-pressure high-temperature syntheses have been shown to lead to solid solutions $AgIn_xSb_{1-x}Te_2$ that are metastable at ambient conditions and are yet not accessible by other synthetic approaches. The novel phases exhibit thermoelectric figures of merit *ZT* up to 0.15 which are comparable to many high-performance thermoelectrics and outperform those of chalcopyrite-type $AgInTe_2$, but are still lower than in the benchmark system $AgSbTe_2$ at room temperature ($ZT \sim 0.3$).[20] Most likely, the cation disorder is the true physical origin of the significantly reduced thermal conductivity in the solid solutions, especially as the phononic contribution is dominant. Thus, further optimization of the power factor $S^2\sigma$, possibly by additional doping, might lead to materials with better performance than $AgSbTe_2$ at low temperatures. To the best of our knowledge, the quenched high-pressure phases exhibit the lowest thermal conductivities among all rocksalt-type tellurides (e.g. $NaSbTe_2$, $AgSbTe_2$ or $NaBiTe_2$) at room temperature.

In general, high-pressure phase transitions may be an intriguing way towards novel thermoelectrics. As high pressure favors higher coordination numbers, solid solutions may be accessible in many systems that are characterized by immiscibility gaps. Although the decomposition of the quenched high-pressure phase $AgIn_{0.5}Sb_{0.5}Te_2$ into $AgInTe_2$ and $AgSbTe_2$ is a drawback for high-temperature applications, careful annealing may be used to produce materials that are heterogeneous on the nanoscale and possibly exhibit endotactic nano-precipitates. As the exsolution of chalcopyrite type $AgInTe_2$ starts before the cubic compound decomposes, such nanostructuring of the material by nanodots comparable to LAST materials may be achieved in a controllable fashion. In addition, phase transitions may further produce favorable domain structures. The synthesis of nanostructured solid solutions displaying low thermal conductivities is thus a promising approach which warrants further exploration.

Acknowledgments

We thank T. Miller for the temperature-dependent powder diffraction experiments, C. Minke for SEM operation and EDX analyses. We are deeply grateful to Prof. Dr. W. Schnick for his generous support of this study, especially for providing the high-pressure equipment. This investigation was funded by the Deutsche Forschungsgemeinschaft (grant OE530/1-2) and the Studienstiftung des deutschen Volkes.

3.4.5 Supplementary information

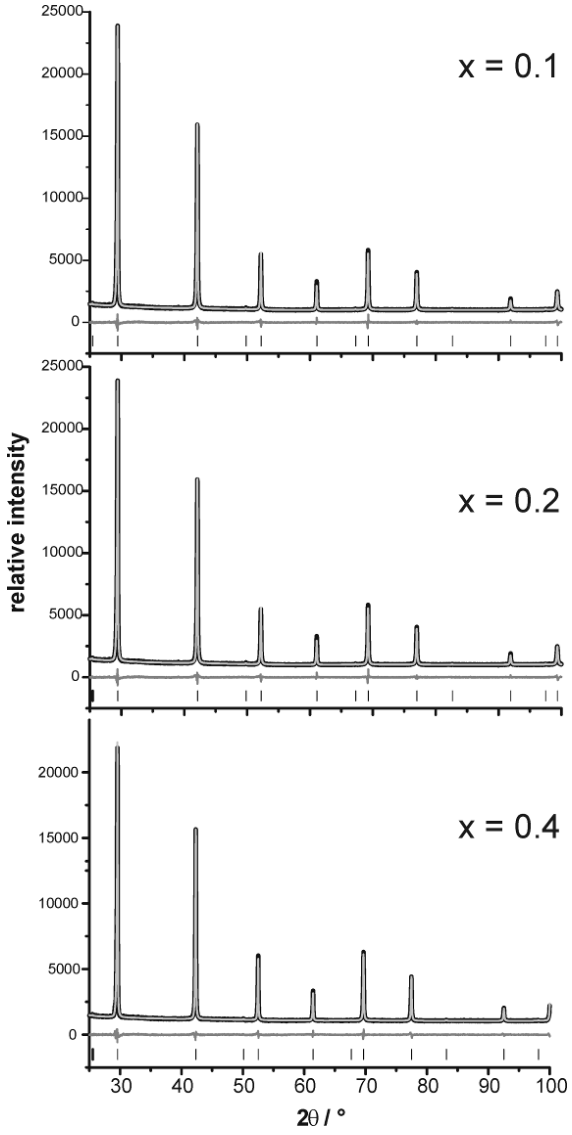

Fig. S1: Rietveld fits for $AgIn_{0.1}Sb_{0.9}Te_2$ (top), $AgIn_{0.2}Sb_{0.8}Te_2$ (middle) and $AgIn_{0.4}Sb_{0.6}Te_2$ (bottom); experimental data (black); calculated data (light gray); difference plot (gray, below), peak positions (black, vertical lines).

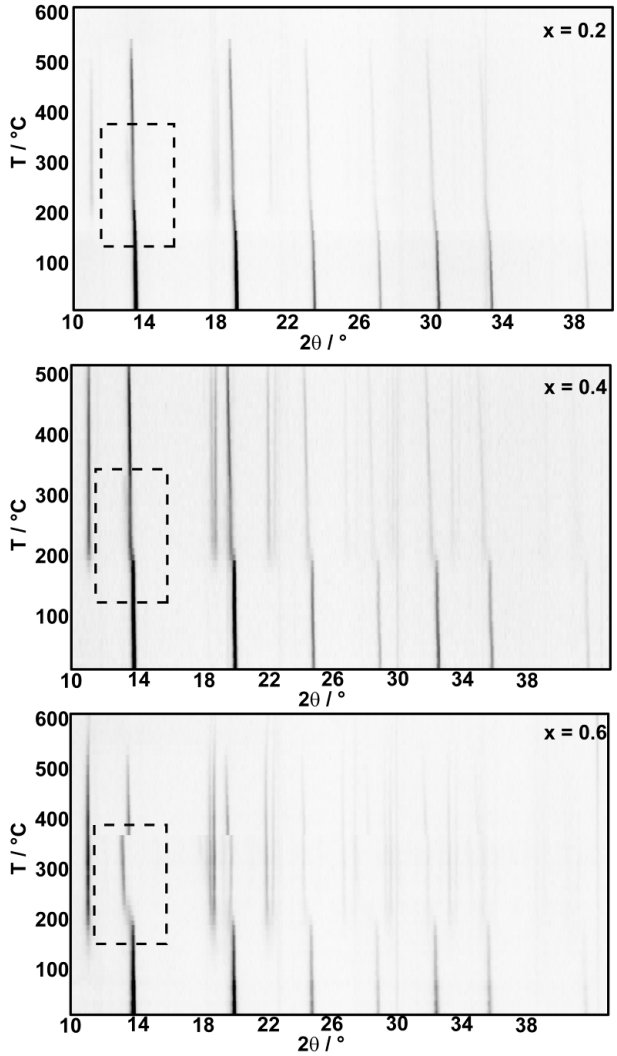

Fig. S2: Temperature dependent powder X-ray diffraction patterns of $AgIn_{0.2}Sb_{0.8}Te_2$ (top), $AgIn_{0.4}Sb_{0.6}Te_2$ (middle) and $AgIn_{0.6}Sb_{0.4}Te_2$ (bottom); the decomposition of the rocksalt-type phase is marked by dashed rectangles.

3.4.6 References

[1] H. J. Goldsmid, *Thermoelectric Refrigeration*, Plenum Press, New York, **1964**.

[2] S. H. Yang, T. J. Zhu, T. Sun, J. He, S. N. Zhang, X. B. Zhao, *Nanotechnology* **2008**, *19*, 245707.

[3] F. D. Rosi, J. P. Dismukes, E. F. Hockings, *Electron. Eng.* **1960**, *79*, 450.

[4] S. K. Plachkova, *Phys. Status Solidi A* **1984**, *83*, 349.

[5] M. N. Schneider, T. Rosenthal, C. Stiewe, O. Oeckler, *Z. Kristallogr.* **2010**, *225*, 463.

[6] T. Rosenthal, M. N. Schneider, C. Stiewe, M. Döblinger, O. Oeckler, *Chem. Mater.* **2011**, *23*, 4349.

[7] J. Sommerlatte, K. Nielsch, H. Böttner, *Phys. J.* **2007**, *6*, 35.

[8] A. Bulusu, D. G. Walker, *Superlattice Microst.* **2008**, *44*, 1.

[9] A. Majumdar, *Science* **2004**, *303*, 777.

[10] M. S. Dresselhaus, G. Chen, M. Y. Tang, R. Yang, H. Lee, D. Wang, Z. Ren, J.-P. Fleurial, P. Gogna,

Adv. Mater. **2007**, *19*, 1.

[11] D. L. Medlin, G. J. Snyder, *Curr. Opin. Colloid Interface Sci.* **2009**, *14*, 226.

[12] M. G. Kanatzidis, *Chem. Mater.* **2010**, *22*, 648.

[13] Y. C. Lan, A. J. Minnich, G. Chen, Z. F. Ren, *Adv. Funct. Mater.* **2010**, *20*, 357.

[14] J. R. Sootsman, D. Y. Chung, M. G. Kanatzidis, *Angew. Chem. Int. Ed.* **2009**, *48*, 8616.

[15] B. A. Cook, M. J. Kramer, J. L. Harringa, M.-K. Han, D.-Y. Chung, M. G. Kanatzidis, *Adv. Funct. Mater.***2009**, *19*, 1254.

[16] G. Rogl, D. Setman, E. Schafler, J. Horky, M. Kerber, M. Zehetbauer, M. Falmbigl, P. Rogl, E. Royanian, E. Bauer, *Acta Mater.* **2012**, *60*, 2146.

[17] T. Schröder, M. N. Schneider, T. Rosenthal, A. Eisele, C. Gold, E.-W. Scheidt, W. Scherer, R. Berthold, O. Oeckler, *Phys. Rev. B* **2011**, *84*, 184104.

[18] D. T. Morelli, V. Jovovic, J. P. Heremans, *Phys. Rev. Lett.* **2008**, *101*, 035901.

[19] M. D. Nielsen, V. Ozolins, J. P. Heremans, *Energy Environ. Sci.* **2013**, *6*, 570.

[20] C. Wood, *Rep. Prog. Phys.* **1988**, *51*, 459.

[21] K. J. Range, G. Engert, A. Weiss, *Sol. State Comm.* **1969**, *7*, 1749.

[22] W. Schanow, K. J. Range, *Mater. Res. Bull.* **1983**, *18*, 39.

[23] Y. Aikebaier, K. Kurosaki, T. Sugahara, Y. Ohishi, H. Muta, S. Yamanaka, *Mater. Sci. Eng. B* **2012**, *177*, 999.

[24] T. Matsunaga, J. Akola, S. Kohara, T. Honma, K. Kobayashi, E. Ikenaga, R. O. Jones, N. Yamada, M. Takata, R. Kojima, *Nature Mater.* **2011**, *10*, 129.

[25] D. Walker, M. A.Carpenter, C. M. Hitch, *Am. Mineral.* **1990**, *75*, 1020.

[26] D. Walker, *Am. Mineral.* **1991**, *76*, 1092.

[27] D. C. Rubie, *Phase Trans.* **1999**, *68*, 431.

[28] H. Huppertz, *Z. Naturforsch. B* **2001**, *56*, 697.

[29] *TOPAS-Academic*, *V. 4.1*, Coelho Software, Brisbane, Australia, **2007**.

[30] *DigitalMicrograph 3.6.1*, Gatan Software, Pleasanton, USA, **1999**.

[31] P. A. Stadelmann, *Ultramicroscopy* **1987**, *21*, 131.

[32] *ESVision*, 4.0.164, Emispec Systems Inc., Tempe, USA, **1994-2002**.

[33] S. Geller, J. H. Wernick, *Acta Crystallogr.* **1959**, *12*, 46.

[34] R. Marin-Ayral, B. Legendre, G. Brun, B. Liautard, J. Tedenac, *Thermochim. Acta* **1988**, *131*, 37.

[35] M. Pasciak, R. Welberry, *Z. Kristallogr.* **2011**, *226*, 113.

3.5 TAGS-related indium compounds and their thermoelectric properties – the solid solution series $(GeTe)_xAgIn_ySb_{1-y}Te_2$ (x = 1 – 12; y = 0.5 and 1)

T. Schröder, T. Rosenthal, N. Giesbrecht, S. Maier, E.-W. Scheidt, W. Scherer, G. J. Snyder, W. Schnick, O. Oeckler

J. Mater. Chem. A **2014**, *2*, 6384-6395.

Abstract

Various members of the solid solution series $(GeTe)_xAgIn_ySb_{1-y}Te_2$ can be obtained by quenching high-temperature phases (x = 12 for y = 1 and x > 5 for y = 0.5). In contrast, high-temperature high-pressure conditions (2.5 GPa, 350 °C) are required for the synthesis of members with In contents > 3.6 atom-% (such as x < 12 for y = 1 and x < 5 for y = 0.5) in order to avoid the formation of $AgInTe_2$. The latter exhibits tetrahedrally coordinated indium atoms at ambient conditions and therefore does not form mixed crystals with tellurides of germanium and antimony that are characterized by sixfold coordinated atom sites. Solid solutions with $x \leq 5$ crystallize in rocksalt-type structures with octahedrally coordinated indium, whereas the ones with x > 5 adopt the α-GeTe structure type (3+3 coordination). Thus, in all samples investigated, 3 or 4 cations are disordered at one Wyckoff position. The quenched high-temperature or high-pressure phases, respectively, are almost homogeneous. Their powder X-ray diffraction patterns suggest pure phases; yet, high-resolution electron microscopy occasionally reveals a very small extent of nanoscopic precipitates as well as dislocations and twinning. $(GeTe)_{5.5}AgIn_{0.5}Sb_{0.5}Te_2$ shows a maximal ZT value of 0.75 even when (partial) decomposition into the TAGS material $(GeTe)_{11}AgSbTe_2$ and chalcopyrite-type $AgInTe_2$ has occurred at 300 °C. $(GeTe)_{5.5}AgInTe_2$ prepared under high-pressure conditions exhibits a ZT value of 0.6 at 125 °C, i.e. far below the decomposition temperature and thus is an interesting new low-temperature thermoelectric material.

3.5.1 Introduction

Under ambient conditions, In is tetrahedrally coordinated by Te in chalcopyrite-type $AgInTe_2$.[1] A rocksalt-type high-pressure polymorph with octahedral coordination of In has been described; however, upon decompression, this phase cannot be obtained as a metastable

material as it transforms back to the chalcopyrite structure type.[2] This shows the strong tendency of In to be tetrahedrally coordinated. It is possible to obtain comparable metastable, i.e. kinetically inert, compounds with octahedrally coordinated In by partially substituting In in $AgInTe_2$ by Sb; however, high-pressure conditions are always required to synthesize these compounds.[3] This substitution leads to the rocksalt-type solid solution series $AgIn_ySb_{1-y}Te_2$. Its member $AgIn_{0.5}Sb_{0.5}Te_2$ exhibits a dimensionless thermoelectric figure of merit $ZT = S^2\sigma T/\kappa$ (with the Seebeck coefficient S, the electrical conductivity σ, the temperature T and the thermal conductivity κ)[4] of 0.15 at room temperature (RT). Due to the solid-solution alloying, the low thermal conductivities of both end members $AgInTe_2$ and $AgSbTe_2$ (κ ~ 2 W/Km and 0.6 W/Km,[5] respectively) are further reduced to 0.4 W/Km at RT. These compounds decompose to chalcopyrite-type $AgInTe_2$ and rocksalt-type $AgSbTe_2$ at temperatures > 150 °C. In general, tellurides crystallizing in these structure types exhibit very good thermoelectric properties: rocksalt-type compounds mainly due to their low lattice thermal conductivities,[6] and materials with structures derived from sphalerite (e.g. $Cu_2Zn_{1-x}Fe_xGeSe_4$, $CuGaTe_2$, $CuInTe_2$) predominantly due to their high Seebeck coefficients.[7-10]

Despite the lower κ of$AgIn_{0.5}Sb_{0.5}Te_2$, the ZT value of $AgSbTe_2$ at RT (~ 0.3) is higher due to its a higher Seebeck coefficient.[11] It is well known that the thermoelectric properties of $AgSbTe_2$ can further be improved in solid solutions with GeTe,[12,13] resulting in so-called TAGS materials $(GeTe)_x(AgSbTe_2)$.[14-17] These compounds have been the subject of many investigations because of their high ZT values (up to 1.7) at elevated temperatures.[18,19] Further optimization of TAGS materials was achieved by substituting Ge by Sn as well as by doping with rare-earth elements.[20-22] However, to the best of our knowledge, the substitution of Sb with In has not been investigated, probably because many of these compounds cannot be obtained by classical solid-state synthesis as they would contain octahedrally coordinated In.

Consequently, solid solutions between GeTe, $AgInTe_2$ and additional $AgSbTe_2$ are intriguing as they would probably combine the effects known from TAGS with the low thermal conductivity of $AgIn_{0.5}Sb_{0.5}Te_2$ and thus might exhibit high ZT values. Here we report on solid solutions $(GeTe)_x(AgInTe_2)$ which we call TIGS in analogy to TAGS and on compounds $(GeTe)_xAgIn_{0.5}Sb_{0.5}Te_2$, i.e. TAGS materials in which half of the Sb is substituted by In.

3.5.2 Experimental

3.4.2.1 Synthesis

Samples of $(GeTe)_xAgIn_ySb_{1-y}Te_2$ (x = 1 – 12; y = 0.5, 1) were prepared by reacting stoichiometric mixtures of the elements (germanium 99.999%, Sigma-Aldrich; silver 99.9999%, Alfa Aesar; antimony 99.9999%, Smart Elements; indium 99.996%, Smart Elements; tellurium 99.999%, Alfa Aesar) at 950 °C for 12 h in sealed silica ampoules under argon atmosphere. The ampoules containing the resulting melts were quenched in water and subsequently annealed for 3 days at 550 °C. After that, the ampoules containing the annealed ingots were quenched in water. This synthesis route yielded $(GeTe)_xAgIn_ySb_{1-y}Te_2$ samples with x = 12 and y = 1 as well as those with x = 5, 5.5, 7 or 12 and y = 0.5 which were homogeneous according to powder X-ray diffraction patterns (cf. section *Crystal structure*). Samples with higher overall In contents, i.e. x = 1, 5, 5.5, 7 and y =1 or x = 1 and y = 0.5 were not single-phase (see below); they were used as starting materials for further high-pressure (HP) synthesis.

A multi-anvil hydraulic press (Voggenreiter, Mainleus, Germany) was used for the HP experiments.[23-26] The finely ground starting materials were densely loaded in crucibles sealed with caps (material: hexagonal boron nitride, Henze, Kempten, Germany). These were centered in two nested graphite tubes, which acted as a resistance furnace. In order to keep the inner graphite tube in place, the remaining volume at both ends of the outer tube was filled with MgO discs. This arrangement was surrounded by a zirconia tube and placed in pierced Cr_2O_3-doped MgO octahedron (edge length 25 mm, Ceramic Substrates & Components, Isle of Wight, Great Britain). In order to electrically contact the graphite tubes, Mo plates were used that were connected to two of the eight truncated tungsten carbide cubes (truncation edge length 17 mm), which served as anvils for the compression. These cubes were separated by pyrophyllite gaskets. Within two hours, this assembly was compressed to 2.5 GPa. At this pressure, the temperature was raised to 350 °C within 30 min and the samples were subsequently kept at this temperature for 8 h. Afterwards, the samples were quenched to room temperature by switching off the furnace. The arrangement was kept under pressure for another hour to ensure that the sample was cooled down completely before reducing the pressure to ambient conditions within 6 h.

3.4.2.2 X-ray diffraction

Powder X-ray diffraction (PXRD) patterns of the finely ground samples fixed between Mylar foils on a flat sample holder with vacuum grease were collected using a Huber G670 Guinier camera (Cu-$K_{\alpha 1}$ radiation, Ge(111) monochromator, λ = 1.54051 Å) with a fixed imaging plate and an integrated read-out system.

Temperature-dependent PXRD patterns were measured using a STOE Stadi P diffractometer (Mo-$K_{\alpha 1}$ radiation, Ge(111) monochromator, λ = 0.71093 Å) with an imaging plate detector system in a modified Debye-Scherrer geometry. The powdered samples were filled into silica glass capillaries (0.3 mm diameter) under argon atmosphere and sealed with vacuum grease. Data were measured up to 600 °C with a heating rate of 10 °C/min in 20 °C steps. For $(GeTe)_{5.5}AgIn_{0.5}Sb_{0.5}Te_2$, further diffraction patterns were recorded from 600 °C to RT with a cooling rate of 5 °C/min.

Phase homogeneity was evaluated using WINXPOW[27] and Rietveld refinements were carried out using the program TOPAS.[28]

3.4.2.3 Electron microscopy, diffraction and X-ray spectroscopy

A JSM-6500F (Jeol, USA) scanning electron microscope (SEM) equipped with an energy dispersive X-ray (EDX) detector (model 7418, Oxford Instruments, Great Britain) was used for the collection of X-ray spectra of representative parts of the samples. The results of 5 - 15 point analyses were averaged. The compositions determined can be found in Table S1 and S2 in the Supplementary Information.

For high-resolution transmission electron microscopy (HRTEM), the samples were ground, dispersed in ethanol and distributed on copper grids coated with a holey carbon film (S166-2, Plano GmbH, Germany) which were subsequently fixed on a double-tilt holder. HRTEM images and selected area electron diffraction (SAED) patterns were recorded using a Titan 80-300 (FEI, USA) with a field-emission gun operated at 300 kV equipped with a TEM TOPS 30 EDX spectrometer (EDAX, Germany). The images were recorded using an UltraScan 1000 camera (Gatan, USA, resolution 2k x 2k). For HRTEM and SAED data evaluation, the Digital Micrograph and EMS software packages were used;[29,30] EDX data were evaluated with ES Vision.[31]

3.4.2.4 Thermoelectric characterization

The thermoelectric properties of $(GeTe)_{5.5}AgIn_{0.5}Sb_{0.5}Te_2$ prepared by quenching the sample from 550 °C were determined from 25 °C to 500 °C. The electrical conductivity σ was measured in 50 K steps at a heating rate of 150 K/h using the van der Pauw method[32] and pressure-assisted Nb contacts in an in-house built facility at Caltech.[33] The Seebeck coefficient S was determined using Chromel-Nb thermocouples in steps of 61 K at a heating rate of 150 K/h and a temperature oscillation rate of ± 7.5 K.[34] The thermal diffusivity D_{th} was measured using a LFA457 MicroFlash (Netzsch, Germany) laser flash system. The thermal conductivity was calculated according to $\kappa = D_{th} \cdot C_p \cdot d$ with a calculated heat capacity C_p using the Dulong-Petit approximation and the density d determined by weighing the sample and measuring its dimensions. The combined uncertainty of the measurements is ca. 20% for the ZT value.

The thermoelectric properties of a $(GeTe)_{5.5}AgInTe_2$ sample prepared under high-pressure conditions were characterized between 4 K and 400 K using a physical property measurement system (PPMS, Quantum Design). The temperature dependent electrical resistivity ρ was measured using a standard four-probe dc method by employing a constant current of 5 mA with a cooling/heating rate of 2 K/min, the estimated uncertainty of ρ amounts to ca. 10 %. The thermal transport option of the PPMS with a cooling/heating rate of 0.5 K/min was used to measure the κ and S values simultaneously. The measurements relied on a relaxation method employing one heater and two thermometers to determine the induced thermal voltage and the temperature gradient along the sample. The uncertainty of these values is approximately 5%.

3.5.3 Results and Discussion

3.5.3.1 Sample characterization and optimal conditions for syntheses

The present investigation focuses on compounds $(GeTe)_xAgIn_ySb_{1-y}Te_2$ with x = 1, 5, 5.5, 7 and 12 for y = 0.5 and 1, which cover a broad range of In-substituted TAGS materials. The stoichiometry includes In contents from 16.7 atom-% in $(GeTe)AgInTe_2$ down to 1.8 atom-% in $(GeTe)_{12}AgIn_{0.5}Sb_{0.5}Te_2$. Quenched melts with In-rich compositions such as $(GeTe)_xAgInTe_2$ (x = 1 - 7) contain mixtures of chalcopyrite-type $AgInTe_2$ and GeTe. In contrast, related homogeneous TAGS materials, i.e. $(GeTe)_xAgSbTe_2$, are easily obtained.[15] However, syntheses under high-pressure high-temperature conditions (2.5 GPa and 350 °C for all high-pressure experiments mentioned in this article) yield samples of, for instance, $(GeTe)AgInTe_2$ and $(GeTe)AgIn_{0.5}Sb_{0.5}Te_2$ with rocksalt type structure whose PXRD patterns exhibit no reflections of side phases (cf. section *Crystal structure*).

The compositional range investigated allows one to elucidate the influence of In on the reaction products under various synthesis conditions. It turned out that samples of $(GeTe)_xAgInTe_2$ with $x < 12$ and $(GeTe)_xAgIn_{0.5}Sb_{0.5}Te_2$ with $x < 5$, all of which contain more than 3.6 atom-% In, consist of mixtures of $AgInTe_2$ and GeTe or $(GeTe)_{2x}AgSbTe_2$, respectively, both after quenching the melt and after quenching solid ingots after annealing them at 550 °C. For such In-rich compounds, high-pressure conditions are required to obtain samples that are single-phase according to their PXRD patterns. In contrast, single-phase compounds (according to PXRD) with In contents ≤ 3.6 atom-%, i.e. $(GeTe)_{12}AgInTe_2$ and $(GeTe)_xAgIn_{0.5}Sb_{0.5}Te_2$ $x \geq 5$, respectively, can be obtained by quenching the samples after annealing them at 550 °C (existence range of high-temperature (HT) phases, cf. *Thermal behavior* section).

The chemical compositions of all compounds whose PXRD patterns show no side phases were determined by SEM-EDX measurements. They agree very well with the nominal composition (cf. Tables S1 and S2 in the Supplementary Information).

3.5.3.2 Crystal structure

PXRD patterns of $(GeTe)_xAgIn_ySb_{1-y}Te_2$,samples (cf. Fig. 1 and 2) without reflections from side phases (synthesis with or without HP depending on the In content as described above) could be indexed assuming cubic metrics for $x \leq 5.5$; however, for x = 5.5 the structure is

rhombohedral (see below). Samples with $x > 5.5$ clearly show reflection splittings in conformity with rhombohedral unit-cell dimensions. All structures were refined using the Rietveld method. Even if the metrics is cubic, rhombohedral structures must be considered as suggested by the reflection splittings for $x > 5.5$. Symmetry reduction is not unusual in comparable compounds that are pseudocubic from the point of view of lattice parameters. Therefore, refinements in space groups with rhombohedral symmetry were tested, especially in *R*3*m*, which corresponds to the α-GeTe type.[12,13] In the trigonal setting, the *z* parameter of the cations is a measure for the formation of layers when the anions of the polar structure are fixed on the origin. If *z* deviates significantly from 0.5, GeTe-type layers are formed which correspond to a binary variant of the A7 structure type of gray arsenic.

The cation positions in all structure models were occupied according to the nominal composition with Ge, Ag, In, and Sb if present, refining a common displacement parameter for all cations on a shared Wyckoff site (i.e. a common *z* parameter in rhombohedral compounds); the anion position was occupied with Te whose displacement parameter was refined individually. Due to the use of a flat sample holder, preferred orientation had to be taken into account, using 4th order spherical harmonics with a single parameter for $x \leq 5$ (cubic) and with 3 parameters for $x \geq 5.5$ (trigonal). Anisotropic broadening of the reflection profiles was refined for $(GeTe)_xAgInTe_2$ (with x = 5.5, 7 and 12) and $(GeTe)_xAgIn_{0.5}Sb_{0.5}Te_2$ (with x = 7 and 12) using the LeBail-Jouanneaux algorithm.[35] In addition to the profile fits of the Rietveld refinements in Fig. 1 and 2, crystal data and details of the structure refinement as well as the atomic parameters are given in Tables 1 and 2, respectively, for the TIGS compounds and in Tables 3 and 4, respectively, for the quinary compounds. Further details of the crystal structure investigations may be obtained from Fachinformationszentrum Karlsruhe, 76344 Eggenstein-Leopoldshafen, Germany (fax: (+49)7247-808-666; e-mail: crysdata@fiz-karlsruhe.de, http://www.fiz-karlsruhe.de/request_for_deposited_data.html) on quoting the depository numbers CSD 426809, 426800, 426805, 426808 and 426803 for $(GeTe)_xAgInTe_2$ with x = 1, 5, 5.5, 7 and 12, respectively, or CSD 426807, 426801, 426804, 426802 and 426806 for $(GeTe)_xAgIn_{0.5}Sb_{0.5}Te_2$ with x = 1, 5, 5.5, 7 and 12, respectively.

It turned out that the average structure of the samples with $x \leq 5$ corresponds to the rocksalt structure type. The atom positions refined in trigonal space groups (for testing purposes) do not deviate from those of the rocksalt type, which in combination with the cubic unit cell confirms the assumption of a cubic average structure. In these compounds, the lattice parameter *a* and thus the average cation-anion distance, which corresponds to *a*/2, decreases with increasing Ge content both for TIGS compounds as well as for the quinary

$(GeTe)_xAgIn_{0.5}Sb_{0.5}Te_2$ phases. The lattice parameters of the latter phases are slightly larger than those of the corresponding Sb-free TIGS samples.

The compounds with x > 5 display, however, rhombohedral symmetry. Although for x = 5.5, the refined *c*/*a* ratios (2.451 for $(GeTe)_{5.5}AgInTe_2$ and 2.459 for $(GeTe)_{5.5}AgIn_{0.5}Sb_{0.5}Te_2$) deviate only slightly from that of the rhombohedral setting of a cubic unit cell (*c*/*a* = 2.449), the *z* parameter of the cations clearly indicates the formation of α-GeTe-type layers which precludes cubic symmetry. This becomes more pronounced for increasing GeTe contents (x > 5.5) where, in addition, the reflection splittings in the PXRD patterns strongly support rhombohedral structures. With increasing GeTe content, i.e. from x = 5.5 to x = 12, the *a* lattice parameters become smaller and the *c* lattice parameters become larger. These opposite trends lead to a non-linear change of the unit-cell volumes.

Table 1. Crystal data and results of the Rietveld refinements of $(GeTe)AgInTe_2$, $(GeTe)_5AgInTe_2$, $(GeTe)_{5.5}AgInTe_2$, $(GeTe)_7AgInTe_2$ and $(GeTe)_{12}AgInTe_2$.

compound	$(GeTe)AgInTe_2$	$(GeTe)_5AgInTe_2$	$(GeTe)_{5.5}AgInTe_2$	$(GeTe)_7AgInTe_2$	$(GeTe)_{12}AgInTe_2$
asymmetric unit	$Ge_{1/3}Ag_{1/3}In_{1/3}Te$	$Ge_{5/7}Ag_{1/7}In_{1/7}Te$	$Ge_{11/15}Ag_{2/15}In_{2/15}Te$	$Ge_{7/9}Ag_{1/9}In_{1/9}Te$	$Ge_{12/14}Ag_{1/14}In_{1/14}Te$
molar mass (of asymmetric unit) / g mol^{-1}	225.94	211.29	210.44	208.81	205.64
F(000)	378.5	354.3	264.7	262.7	258.7
crystal system / space group (no.)	cubic / $Fm\bar{3}m$ (225)			trigonal / $R3m$ (160)	
Z	4			3	
lattice parameters / Å	5.96391(2)	5.95766(3)	*a* = 4.21824(2) *c* =10.3378(1)	*a* = 4.20056(2) *c* = 10.4188(1)	*a* = 4.18692(3) *c* = 10.5211(1)
cell volume / Å^3	212.126(2)	211.460(3)	159.302(2)	159.207(2)	159.728(3)
density (X-ray) / g cm^{-3}	7.075	6.637	6.581	6.534	6.413
absorption coefficient / mm^{-1}	163.93	140.433	138.55	135.87	130.40
radiation	Cu-$K_{\alpha 1}$ (λ = 1.540596 Å)				
2θ range / °	20 – 100				
no. of data points	16001				
no. of reflections	13			30	
constraints	2			4	
refined parameters / thereof background	23 / 12			39 / 12	
R_p / R_{wp}	0.0151 / 0.0216	0.0195 / 0.0277	0.0170 / 0.0255	0.0148 / 0.0204	0.0206 / 0.0306
R_{Bragg}	0.0156	0.0108	0.0117	0.0120	0.0062
Goof	0.746	0.974	0.941	0.684	1.101

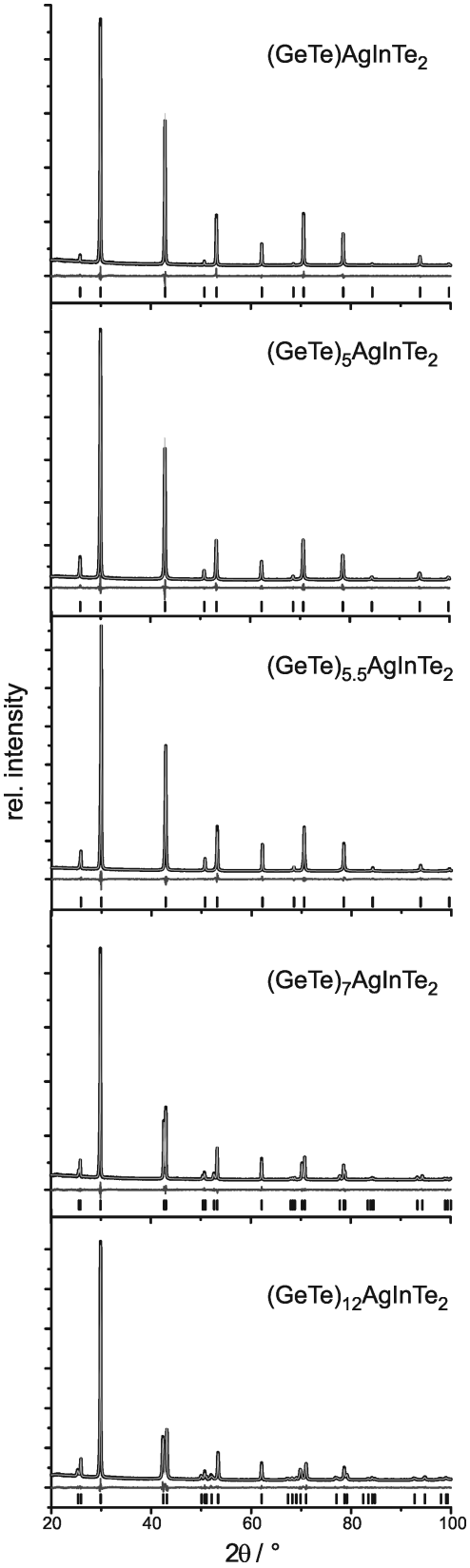

Fig. 1: Rietveld fits for $(GeTe)_xAgInTe_2$ (x = 1, 5, 5.5, 7 and 12; from top to bottom – HP synthesis except for x = 12): experimental (black) and calculated data (gray); difference plot (gray, below); peak positions (black, vertical lines).

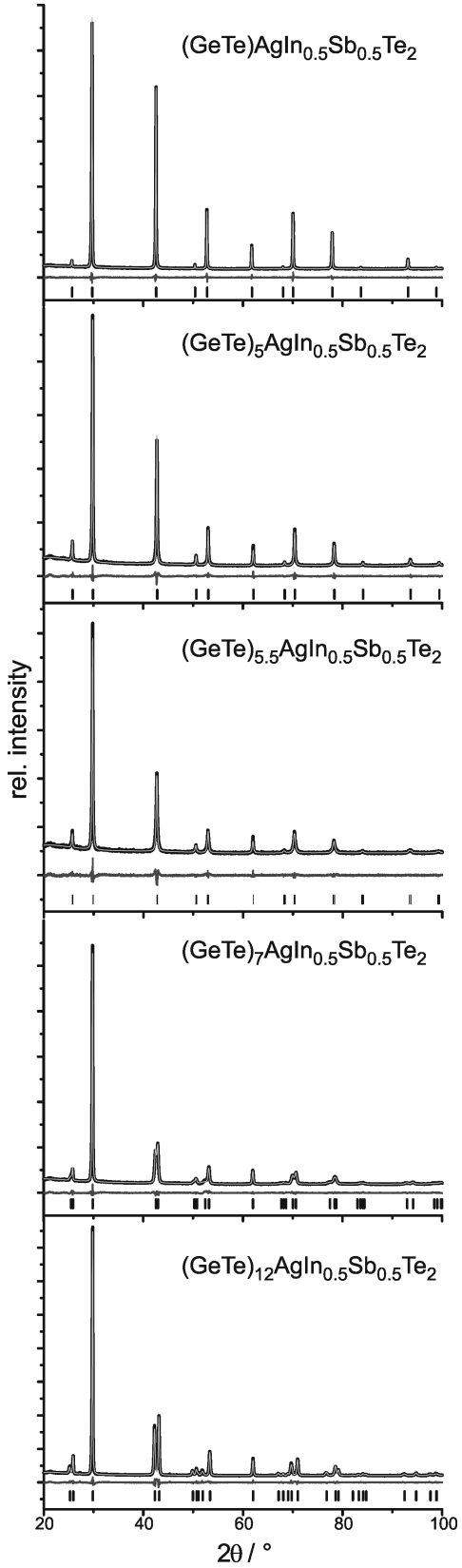

Fig. 2: Rietveld fits for $(GeTe)_xAgIn_{0.5}Sb_{0.5}Te_2$ (x = 1, 5, 5.5, 7 and 12; from top to bottom – HP synthesis for x = 1): experimental (black) and calculated data (gray); difference plot (gray, below); peak positions (black, vertical lines).

Table 2. Atom positions, occupancy factors and isotropic displacement parameters (B_{iso} in Å^2) for $(GeTe)AgInTe_2$, $(GeTe)_5AgInTe_2$, $(GeTe)_{5.5}AgInTe_2$, $(GeTe)_7AgInTe_2$ and $(GeTe)_{12}AgInTe_2$.

sample	atom positions	x y z	s.o.f.	B_{iso}
$(GeTe)AgInTe_2$	Ge/Ag/In	0 0 0	1/3 1/3 1/3	1.508(15)
	Te	0.5 0.5 0.5	1	0.797(12)
$(GeTe)_5AgInTe_2$	Ge/Ag/In	0 0 0	5/7 1/7 1/7	1.980(14)
	Te	0.5 0.5 0.5	1	0.810(11)
$(GeTe)_{5.5}AgInTe_2$	Ge/Ag/In	0 0 0.4834(4)	11/15 2/15 2/15	1.28(6)
	Te	0 0 0	1	1.11(2)
$(GeTe)_7AgInTe_2$	Ge/Ag/In	0 0 0.48596(18)	7/9 1/9 1/9	2.05(3)
	Te	0 0 0	1	1.057(14)
$(GeTe)_{12}AgInTe_2$	Ge/Ag/In	0 0 0.47877(16)	12/14 1/14 1/14	1.81(3)
	Te	0 0 0	1	0.847(18)

Table 3. Crystal data and results of the Rietveld refinements of $(GeTe)AgIn_{0.5}Sb_{0.5}Te_2$, $(GeTe)_5AgIn_{0.5}Sb_{0.5}Te_2$, $(GeTe)_{5.5}AgIn_{0.5}Sb_{0.5}Te_2$, $(GeTe)_7AgIn_{0.5}Sb_{0.5}Te_2$ and $(GeTe)_{12}AgIn_{0.5}Sb_{0.5}Te_2$.

compound	$(GeTe)AgIn_{0.5}Sb_{0.5}Te_2$	$(GeTe)_5AgIn_{0.5}Sb_{0.5}Te_2$	$(GeTe)_{5.5}AgIn_{0.5}Sb_{0.5}Te_2$	$(GeTe)_7AgIn_{0.5}Sb_{0.5}Te_2$	$(GeTe)_{12}AgIn_{0.5}Sb_{0.5}Te_2$
asymmetric unit	$Ge_{1/3}Ag_{1/3}In_{1/6}Sb_{1/6}Te$	$Ge_{5/7}Ag_{1/7}In_{1/14}Sb_{1/14}Te$	$Ge_{11/15}Ag_{2/15}In_{1/15}Sb_{1/15}Te$	$Ge_{7/9}Ag_{1/9}In_{1/18}Sb_{1/18}Te$	$Ge_{12/14}Ag_{1/14}In_{1/28}Sb_{1/28}Te$
molar mass (of asymmetric unit)/ g mol^{-1}	227.21	211.67	211.02	209.31	206.00
$F(000)$	380	354.7	265.2	263.1	259.1
crystal system / space group (no.)	cubic / $Fm\bar{3}m$ (225)		trigonal / $R3m$ (160)	trigonal / $R3m$ (160)	
Z	4		3		
lattice parameters / Å	a = 5.99892(1)	a = 5.97300(4)	a = 4.2218(1) c = 10.3821(4)	a = 4.20712(5) c = 10.4602(2)	a = 4.18601(3) c = 10.5582(1)
cell volume / Å^3	215.883(1)	213.097(4)	160.255(11)	160.340(6)	160.222(3)
density (X-ray) / g cm^{-3}	6.991	6.598	6.560	6.503	6.405
absorption coefficient / mm^{-1}	163.48	140.28	138.75	135.78	130.58
radiation	Cu-$K_{\alpha 1}$ (λ = 1.540596 Å)				
2θ range / °	20 - 100				
no. of data points	16001				
no. of reflections	13		30	30	
constraints	3		6	6	
refined parameters / thereof background	23 / 12		27 / 12	39 / 12	
R_p / R_{wp}	0.0150 / 0.0210	0.0217 / 0.0313	0.0165 / 0.0241	0.0183 / 0.0252	0.0233 / 0.0355
R_{Bragg}	0.0032	0.0043	0.0064	0.0082	0.0064
Goof	0.7220	1.120	0.781	0.889	1.310

Table 4. Atom positions, occupancy factors and isotropic displacement parameters (B_{iso} in Å^2) for $(GeTe)AgIn_{0.5}Sb_{0.5}Te_2$, $(GeTe)_5AgIn_{0.5}Sb_{0.5}Te_2$, $(GeTe)_{5.5}AgIn_{0.5}Sb_{0.5}Te_2$, $(GeTe)_7AgIn_{0.5}Sb_{0.5}Te_2$ and $(GeTe)_{12}AgIn_{0.5}Sb_{0.5}Te_2$.

sample	atom positions	x y z	s.o.f.	B_{iso}
$(GeTe)AgIn_{0.5}Sb_{0.5}Te_2$	Ge/Ag/In/Sb	0 0 0	1/3 1/3 1/6 1/6	2.176(12)
	Te	0.5 0.5 0.5	1	1.462(10)
$(GeTe)_5AgIn_{0.5}Sb_{0.5}Te_2$	Ge/Ag/In/Sb	0 0 0	5/7 1/7 1/14 1/14	2.37(2)
	Te	0.5 0.5 0.5	1	0.810(18)
$(GeTe)_{5.5}AgIn_{0.5}Sb_{0.5}Te_2$	Ge/Ag/In/Sb	0 0 0.4857(8)	11/15 2/15 1/15 1/15	2.00(11)
	Te	0 0 0	1	1.14(5)
$(GeTe)_7AgIn_{0.5}Sb_{0.5}Te_2$	Ge/Ag/In/Sb	0 0 0.4813(2)	7/9 1/9 1/18 1/18	1.65(4)
	Te	0 0 0	1	1.32(2)
$(GeTe)_{12}AgIn_{0.5}Sb_{0.5}Te_2$	Ge/Ag/In/Sb	0 0 0.47722(14)	12/14 1/14 1/28 1/28	1.71(3)
	Te	0 0 0	1	0.991(19)

For the rhombohedral TIGS compounds, the unit-cell volumes are smaller than those of the quinary $(GeTe)_xAgIn_{0.5}Sb_{0.5}Te_2$ compounds. Yet, the shortest cation-tellurium bond lengths are slightly larger in the TIGS samples e.g. 2.8609(9) Å for $(GeTe)_{12}AgInTe_2$ and 2.8546(8) Å for $(GeTe)_{12}AgIn_{0.5}Sb_{0.5}Te_2$, which can be explained by a less pronounced tendency towards layered structures in TIGS.

Also note that the cations' *z* parameter value of $(GeTe)_7AgInTe_2$ does not lie between those of $(GeTe)_{5.5}AgInTe_2$ and $(GeTe)_{12}AgInTe_2$, which is probably related to the fact that $(GeTe)_{5.5}AgInTe_2$ and $(GeTe)_7AgInTe_2$ had to be synthesized under HP conditions, whereas $(GeTe)_{12}AgInTe_2$ was synthesized by quenching the sample after annealing it at 550 °C.

3.5.3.3 Electron microscopy and diffraction

HRTEM and SAED were performed on $(GeTe)_{5.5}AgIn_{0.5}Sb_{0.5}Te_2$ and $(GeTe)_7AgIn_{0.5}Sb_{0.5}Te_2$ which were both synthesized by annealing the samples at 550 °C and subsequent quenching through a two phase region (cf. *Thermal behavior* section). The former's metrics are very close to cubic, the latter's are clearly rhombohedral. Although the angle between the directions [012]* and [01 $\bar{4}$]* (which correspond to cubic [110]* and [001]*, respectively) of $(GeTe)_{5.5}AgIn_{0.5}Sb_{0.5}Te_2$ is calculated as 89.7° from the structure model obtained by Rietveld refinement, the SAED patterns in Fig. 3 show more pronounced deviations from 90°. This may be due to local variations of the composition – possibly as a consequence of the fast quenching – or metric relaxation in the small crystallites investigated. In quenched bulk samples the domains may be strained and thus the metrics remains closer to the one of the HT phase.

Although the samples appear homogeneous in PXRD patterns, the HRTEM images in Fig. 4 and 5 show two different kinds of precipitates. Both $(GeTe)_{5.5}AgIn_{0.5}Sb_{0.5}Te_2$ and $(GeTe)_7AgIn_{0.5}Sb_{0.5}Te_2$ contain Ag-rich precipitates (Fig. 4). These may consist of Ag_2Te, which was observed as a side phase in $AgSbTe_2$,[36] or Ag_7Te_4,[37] which might be an intermediate phase during the formation of Ag_2Te. Both compounds exhibit d values (e.g. 6.8 Å, 3.4 Å) close to those observed in SAED patterns and Fourier transforms of HRTEM images. Fig. 5 shows In-rich precipitates in $(GeTe)_7AgIn_{0.5}Sb_{0.5}Te_2$ which most likely correspond to $AgInTe_2$ which is also expected from the temperature-dependent phase equlibria (see below). However, only very few precipitates can be observed and they are too small to contribute significantly to the PXRD patterns. The formation of precipitates also causes slight deviations in the compositions of the matrix crystallites which might contribute to the deviating metrics

observed in the SAED patterns in Fig. 3 as the most pronounced metric deviations occur next to the precipitates. In addition, characteristic dislocations and twinning have also been observed in these materials (cf. Fig. S1 in the Supplementary Information and also weak additional maxima in Fig. 3a).

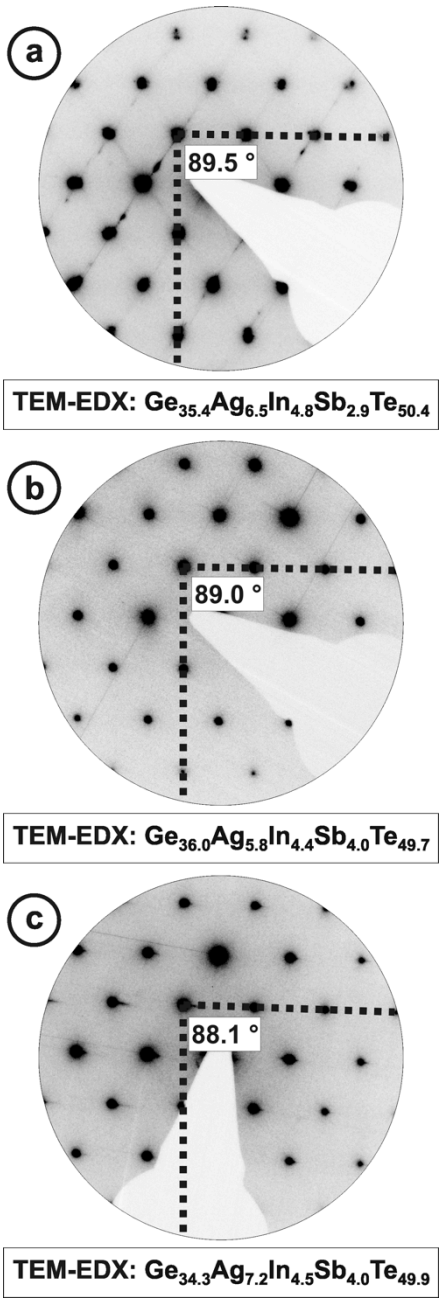

Fig. 3: SAED patterns of the <100> zone axis of different crystallites in a sample of $(GeTe)_{5.5}AgIn_{0.5}Sb_{0.5}Te_2$ (a and b: different areas of the same crystallite, c: other crystallite). The [012]* (horizontal) and [01 $\bar{4}$]* (vertical) directions are marked with dotted lines and the angle between them is given; TEM-EDX analyses of the corresponding areas are given below each SAED (calculated composition: $Ge_{36.7}Ag_{6.7}In_{3.3}Sb_{3.3}Te_{50}$).

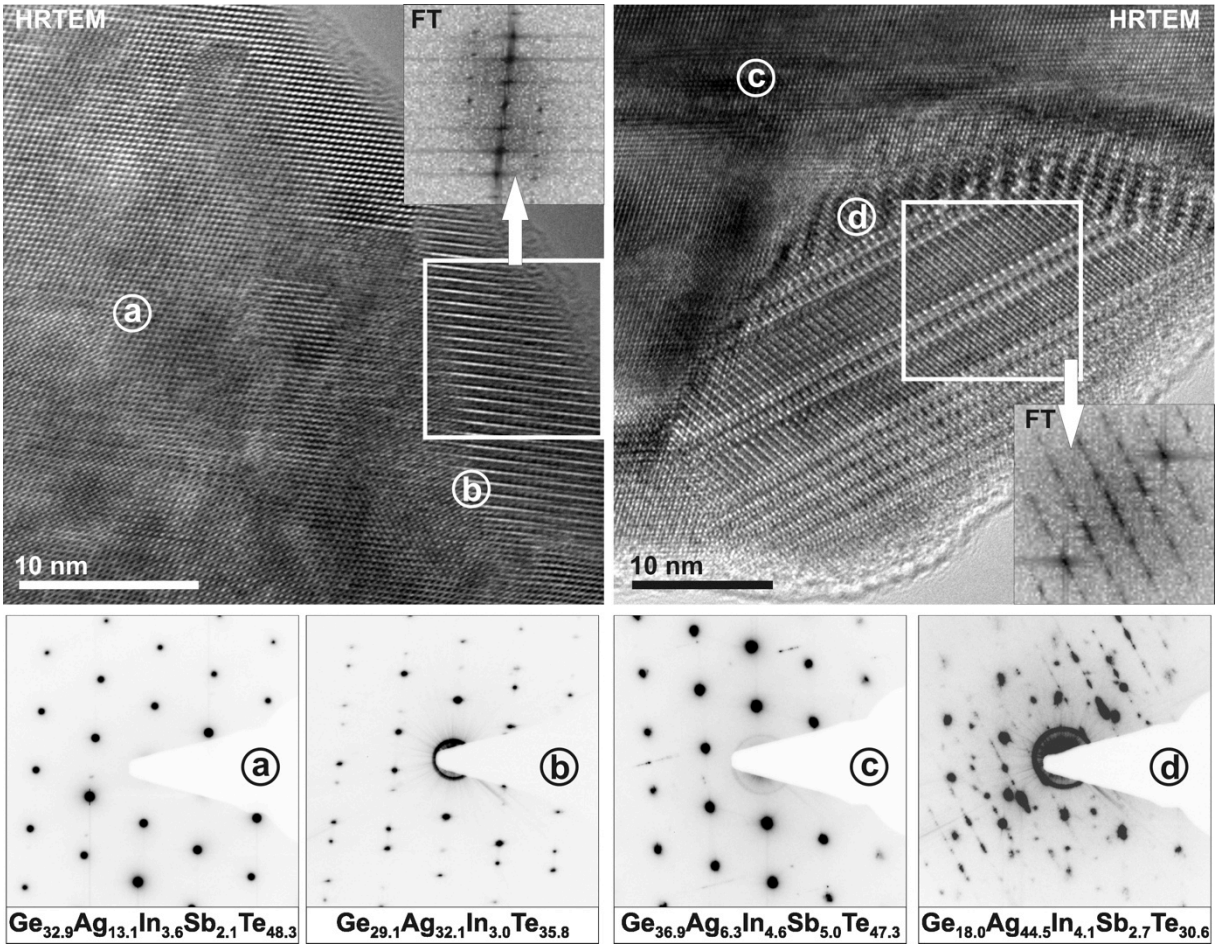

Fig. 4: HRTEM images (zone axis <100> with respect to the rhombohedral matrices, top) of silver-rich precipitates in $(GeTe)_{5.5}AgIn_{0.5}Sb_{0.5}Te_2$ (left) and in $(GeTe)_7AgIn_{0.5}Sb_{0.5}Te_2$ (right) with corresponding Fourier transforms of the precipitates (insets) and SAED patterns (irradiated area ca. 50 - 100 nm, bottom) with composition (in atom-%, from TEM-EDX, irradiated area ca. 10 - 20 nm) of the matrix areas (a, c) and areas that contain the matrix and the precipitates (b, d; b also shows twinning of the matrix, see also Fig. S1 in the Supplementary Information).

3.5.3.4 Thermal behavior

The fact that In-poor $(GeTe)_xAgIn_ySb_{1-y}Te_2$ compounds with x = 12 for y =1 and $x \geq 5$ for y = 0.5 can be synthesized without applying HP by annealing at 550 °C and subsequent quenching may be explained by the existence of thermodynamically stable, homogeneous HT phases. The PXRD patterns in Fig. 6 show the temperature-dependent phase transitions of four rocksalt-type samples during the heating process: $(GeTe)AgInTe_2$, $(GeTe)AgIn_{0.5}Sb_{0.5}Te_2$ and $(GeTe)_5AgInTe_2$, which were prepared under HP conditions, and $(GeTe)_5AgIn_{0.5}Sb_{0.5}Te_2$, which was prepared by quenching from 550 °C. Upon heating, the cubic phases decompose by forming chalcopyrite-type $AgInTe_2$. Assuming complete decomposition as a reasonable approximation, the main phase is GeTe or $(GeTe)_{2x}AgSbTe_2$, respectively. However, these

might be doped with small amounts of In. (GeTe)$AgInTe_2$ decomposes into $AgInTe_2$ and GeTe at ~150 °C. No HT phase is formed, both compounds melt at individual temperatures. For (GeTe)$AgIn_{0.5}Sb_{0.5}Te_2$, the decomposition reaction into $AgInTe_2$ and $(GeTe)_2AgSbTe_2$ starts at ~200 °C. The intensity of the strongest reflection of $AgInTe_2$ at ~11° 2θ becomes weaker at around 520 °C, which might be attributed to melting or a reaction with $(GeTe)_2AgSbTe_2$, which however does not result in a homogeneous quinary HT phase. $(GeTe)_5AgInTe_2$ shows a similar decomposition reaction as (GeTe)$AgInTe_2$ starting at ~220 °C; however, a quaternary HT phase is formed at ~480 °C and the reflections of $AgInTe_2$ vanish completely. This re-reaction is also confirmed by the non-linear increase in the lattice parameter *a* of the rocksalt-type phase (best visible for the reflections at 31° and 34° 2θ). Although a HT phase exists at 550 °C, quenching it does not yield a homogeneous compound; $AgInTe_2$ was always found as a side phase so that HP synthesis was necessary as described above (Section *Sample characterization and optimal conditions for synthesis*). Probably, the cooling rate is not sufficient to avoid the partial decomposition. As expected, $(GeTe)_5AgIn_{0.5}Sb_{0.5}Te_2$ decomposes into $AgInTe_2$ and $(GeTe)_{10}AgSbTe_2$ at ~240 °C. A quinary HT phase is formed which can be quenched to obtain a metastable sample which is homogeneous according to its PXRD pattern.

Temperature dependent PXRD of $(GeTe)_{5.5}AgIn_{0.5}Sb_{0.5}Te_2$ (see Fig. 7, also concerning the numbering of the transitions) reveal that in addition to the decomposition, structural phase transitions of the trigonal compounds occur during heating and cooling. At ~100 °C (1) the phase transition from trigonal (α-GeTe type) to cubic (rocksalt type) takes place in the quinary quenched compound. At ~240 °C (2) the compound decomposes into $AgInTe_2$ and – assuming complete decomposition – $(GeTe)_{11}AgSbTe_2$. The homogeneous HT phase begins to form at 400 °C (3), whereas upon slow cooling, the decomposition into $AgInTe_2$ and $(GeTe)_{11}AgSbTe_2$ starts at ~340 °C (4). The different temperatures for the formation and decomposition of the HT phase, respectively, probably reflect time and particle-size dependence. During heating (3), relatively large grains of $AgInTe_2$ react with $(GeTe)_{11}AgSbTe_2$ while during cooling (4) $AgInTe_2$ grains need to nucleate and to grow, and the very broad reflections of nanoscale precipitates may not be visible in PXRD patterns. As discussed above, there may be very small amounts of other nanoscale precipitates that do not

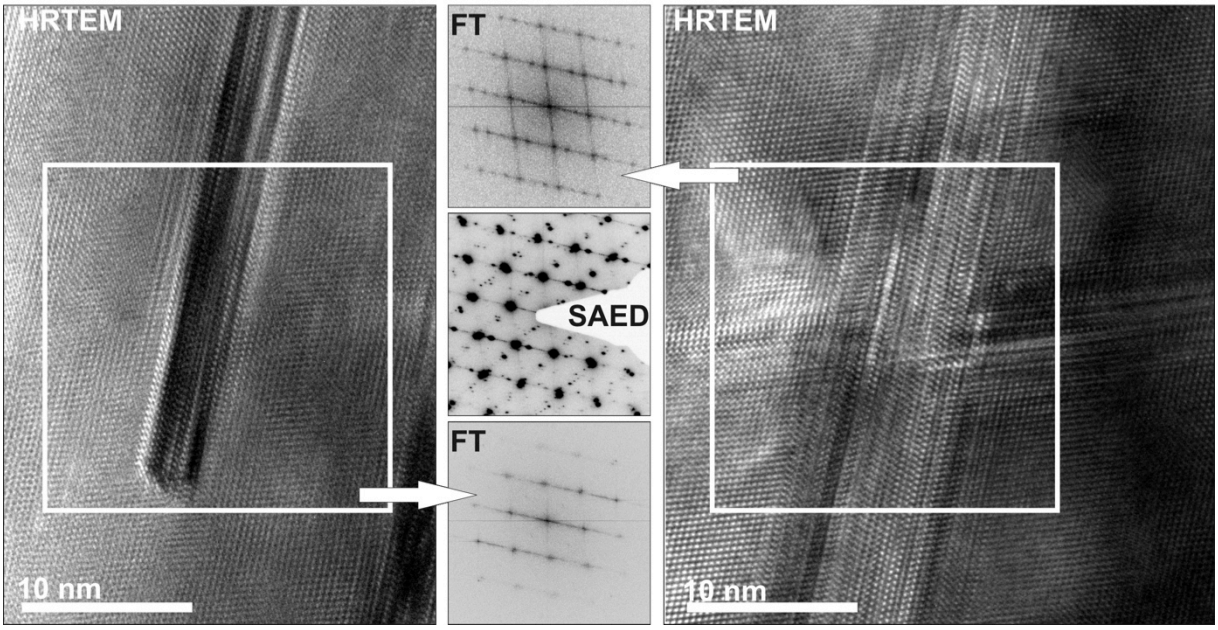

Fig. 5: HRTEM images viewed along the <100> zone axis of two different crystal areas of rhombohedral $(GeTe)_7AgIn_{0.5}Sb_{0.5}Te_2$ with $AgInTe_2$ precipitates, the corresponding Fourier transforms (FT) and an SAED pattern from the crystallite corresponding to the HRTEM on the right side; TEM-EDX of areas containing the precipitates yield $Ge_7Ag_5In_{26}Sb_6Te_{56}$ (left) and $Ag_{26}In_{23}Te_{51}$ (right), these analyses only show a trend as the beam cannot be focused exclusively on the precipitates.

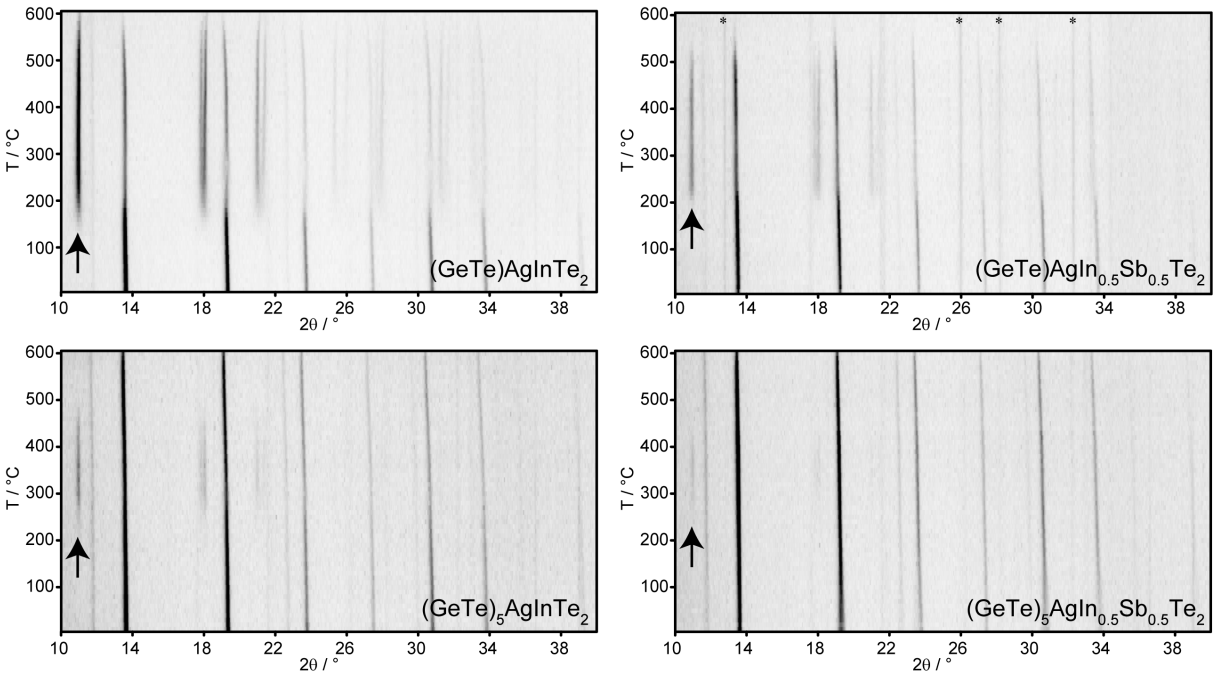

Fig. 6: Temperature-dependent X-ray powder diffraction patterns of $(GeTe)_xAgIn_ySb_{1-y}Te_2$ for x = 1 (top) and 5 (bottom); y = 1 (left) and 0.5 (right); asterisks (*) mark reflections caused by the furnace; the arrows mark the strongest reflection of $AgInTe_2$.

contribute to the PXRD patterns, especially when quenching leads through a two-phase region. While $AgInTe_2$ remains present, the cubic to trigonal phase transition (5) of the main phase $(GeTe)_{11}AgSbTe_2$ takes place at ~140 °C. The difference between the trigonal to cubic (1) and cubic to trigonal (5) phase transition temperatures is due to the change of the main phase's composition from $(GeTe)_{5.5}AgIn_{0.5}Sb_{0.5}Te_2$ to $(GeTe)_{11}AgSbTe_2$. Therefore, the phase transition temperatures increases and gets closer to the one of pure GeTe.[38]

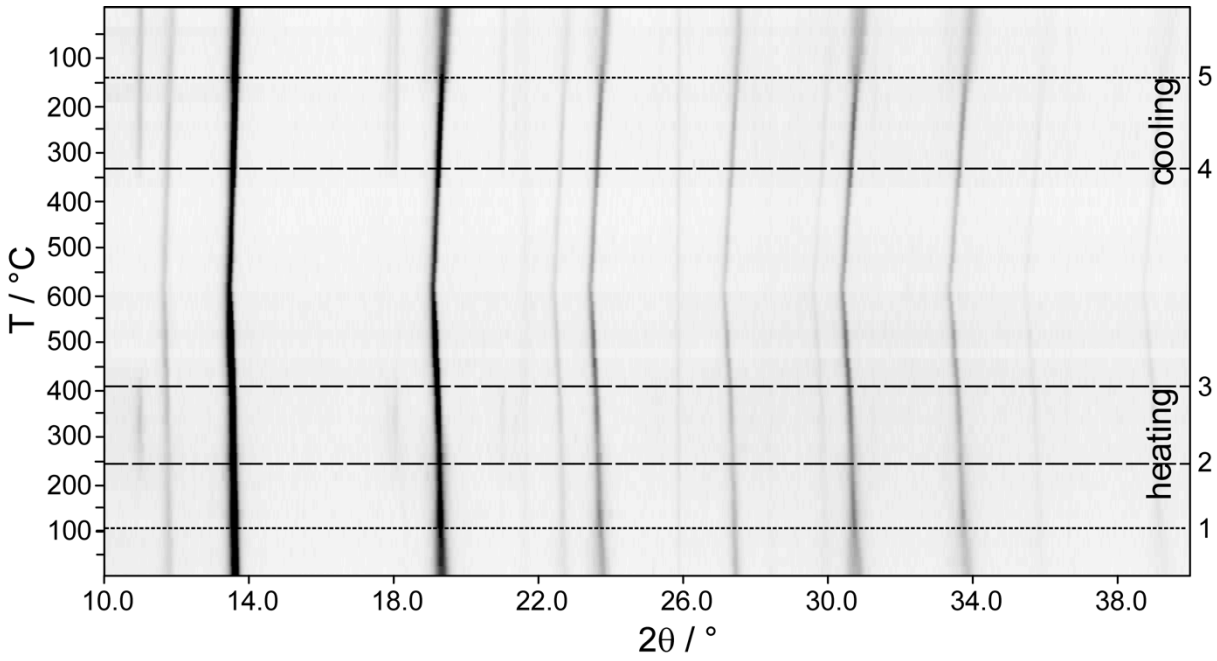

Fig. 7: Temperature-dependent X-ray powder diffraction pattern of $(GeTe)_{5.5}AgIn_{0.5}Sb_{0.5}Te_2$: (1) the reflections become sharper as the rhombohedral splitting of the α-GeTe type's pattern vanishes during the phase transition to the rocksalt-type structure; (2) decomposition to $AgInTe_2$ and $(GeTe)_{11}AgSbTe_2$; (3) formation of a cubic quinary HT phase; (4) decomposition to $AgInTe_2$ and $(GeTe)_{11}AgSbTe_2$; (5) cubic to trigonal phase transition of $(GeTe)_{11}AgSbTe_2$.

3.5.3.5 High-temperature thermoelectric properties of $(GeTe)_{5.5}AgIn_{0.5}Sb_{0.5}Te_2$

The thermoelectric properties of $(GeTe)_{5.5}AgIn_{0.5}Sb_{0.5}Te_2$ (cf. Fig. 8), which was prepared by annealing at 550 °C (stability region of the quinary HT phase) and subsequent quenching can be understood by the temperature dependent PXRD pattern in Fig. 7. During heating, σ exhibits metallic characteristics and decreases from 1100 to 750 S/cm; this is only slightly affected by the decomposition into chalcopyrite-type $AgInTe_2$ and $(GeTe)_{11}AgSbTe_2$. However, for the quinary cubic HT phase σ increases again, probably because the interfaces caused by nanoscopic $AgInTe_2$ precipitates (cf. Section *Electron microscopy and diffraction*) vanish and thus do not scatter electrons anymore. Upon cooling, the characteristics of σ is

parallel to the heating curve. The heating and cooling curves of κ are very similar. In the two-phase region the slope of κ is not as steep as for lower and higher temperatures. However, this part of the κ curve should not be over-interpreted as the assumption of constant heat capacity (according to Dulong-Petit) may not be a good approximation during the decomposition reaction. S increases up to a maximum at ~300 °C, i.e. in the two-phase area. For the quinary cubic HT phase, S decreases slightly with increasing temperature. Upon cooling, S is slightly larger than at the same temperatures during heating. This is a consequence of the above mentioned reactions and phase transitions. In general, the characteristics of the thermoelectric properties nicely reflect the phase transitions observed in the temperature dependent PXRD pattern. The discussion of the maximal ZT should be restricted to the cooling curve below 350 °C. During heating and in the two-phase regions, the absolute values of the properties are not reliable (no well-defined heat capacity, see above) and there may be a pronounced time dependence due to reactions and nucleation processes. The highest ZT value of 0.75 at 300 °C can be observed close to the decomposition into $AgInTe_2$ and $(GeTe)_{11}AgSbTe_2$. Low-temperature experiments are not promising, because the ZT value has already dropped to 0.35 at room temperature.

3.5.3.6 Low-temperature thermoelectric properties of $(GeTe)_{5.5}AgInTe_2$

The thermoelectric properties of the TIGS sample $(GeTe)_{5.5}AgInTe_2$ (Fig. 9) were measured from RT down to 4 K and then up to 400 K, i.e. far below the decomposition temperature. The heating and cooling curves for all properties are almost similar within the experimental errors and do not indicate pronounced irreversible processes (the slight deviation between the κ values during cooling and heating sequences between 50 and 150 K is probably due to contact problems). The subtle hysteretic behavior between 40 and 300 K may be comparable to that observed in metastable modifications of $GeBi_2Te_4$ where the extent of the hysteresis could be correlated with the average domain size of the crystalline samples.[39] The high residual resistivity of 1.015 mΩcm together with the remarkably small residual resistivity ratio of RRR = ρ(300 K) / ρ(2 K) = 1.08 clearly confirms the presence of significant disorder in $(GeTe)_{5.5}AgInTe_2$. Furthermore, the sequential change of the sign of the slope, dρ/dT supports the presence of a crossover-scenario between a degenerated semiconducting and metallic-like behavior of $(GeTe)_{5.5}AgInTe_2$. This observation may be due to different scattering processes caused (*i*) by the temperature independent residual resistivity originating from electron-impurity scattering (impurity atoms, grain boundaries, etc.) and (*ii*) the

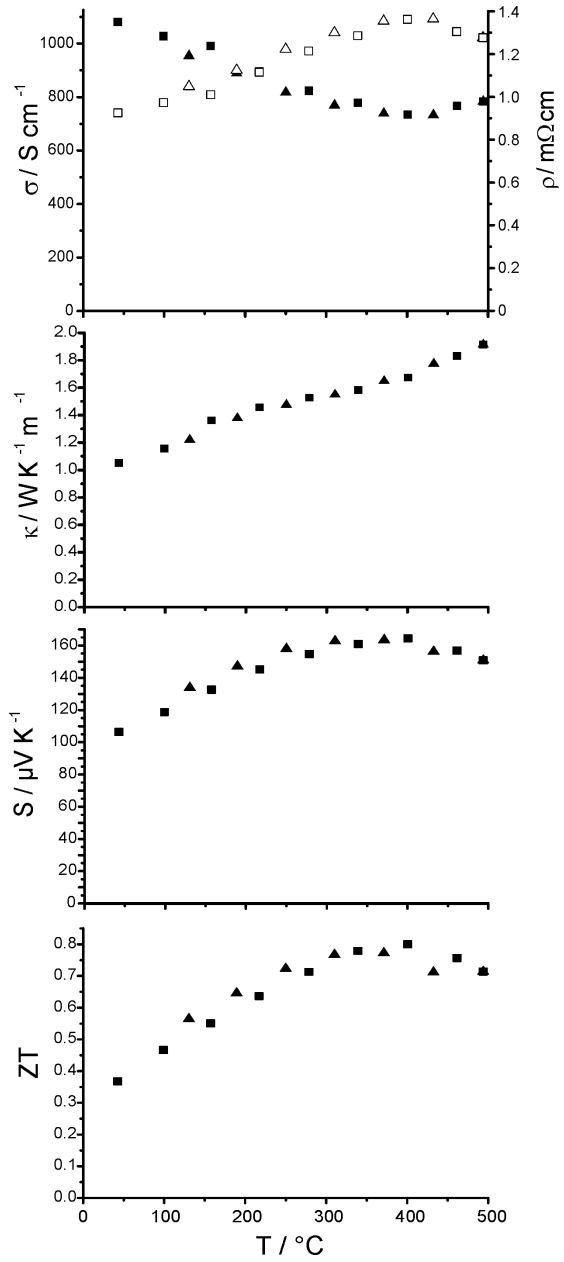

Fig. 8: Thermoelectric properties of $(GeTe)_{5.5}AgIn_{0.5}Sb_{0.5}Te_2$ (heating curves: ■; cooling curves: ▲), from top to bottom: electrical conductivity and resistivity (solid and empty symbols, respectively), thermal conductivity, Seebeck coefficient and ZT value in comparison to values for TAGS-85 (asterisks) taken from reference [19].

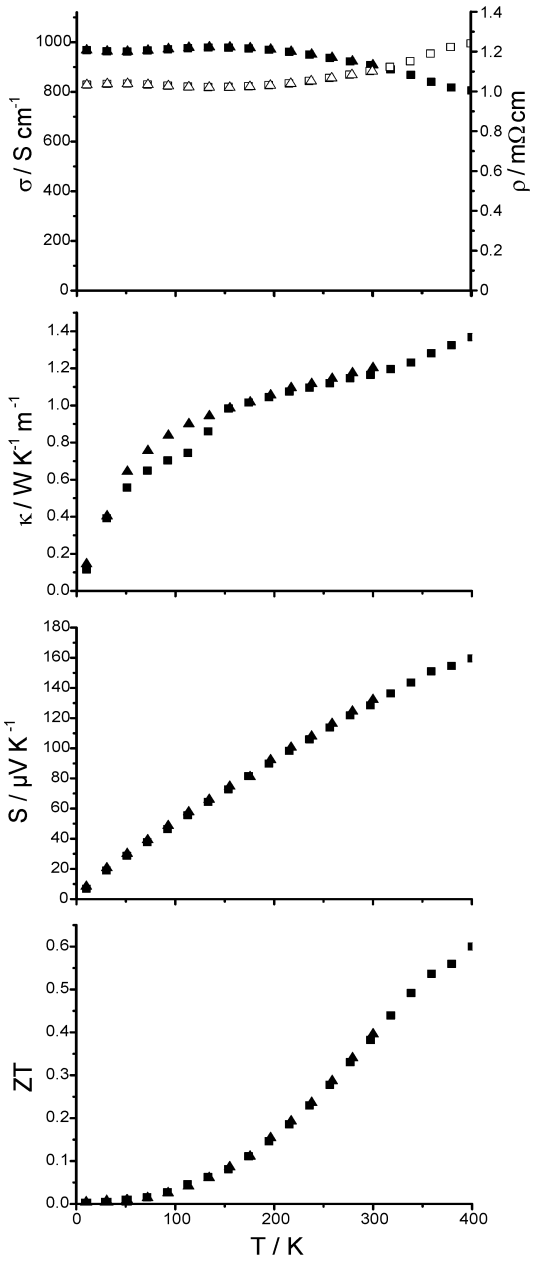

Fig. 9: Thermoelectric properties of $(GeTe)_{5.5}AgInTe_2$ (heating curve: ■; cooling curve: ▲), from top to bottom: electrical conductivity and resistivity (solid and empty symbols, respectively), thermal conductivity, Seebeck coefficient and ZT value in comparison to values for TAGS-85 (asterisks) taken from reference [19].

temperature dependent contribution due to electron-phonon scattering. From 150 K to 400 K, σ(T) exhibits metallic-like characteristics and the absolute values between RT and 400 K are approximately in the same range as the corresponding ones of $(GeTe)_{5.5}AgIn_{0.5}Sb_{0.5}Te_2$. The absolute κ values of the TIGS sample are slightly larger compared with the ones in

$(GeTe)_{5.5}AgIn_{0.5}Sb_{0.5}Te_2$ at room temperature. This hints for a less pronounced disorder in $(GeTe)_{5.5}AgInTe_2$ *vs*. $(GeTe)_{5.5}AgIn_{0.5}Sb_{0.5}Te_2$. The increase of S is steeper for TIGS than for $(GeTe)_{5.5}AgIn_{0.5}Sb_{0.5}Te_2$ which compensates the higher κ and leads to a higher ZT value of 0.6 at 400 K.

3.5.4 Conclusion

Members of the solid solution series between GeTe and $AgInTe_2$ or $AgIn_{0.5}Sb_{0.5}Te_2$, respectively, crystallize in disordered rocksalt-type structures for GeTe contents $1 < x \leq 5$ and in disordered α-GeTe-type structures for $5 < x < 12$. In such $(GeTe)_xAgIn_ySb_{1-y}Te_2$ phases, In is octahedrally coordinated by Te or exhibits a 3+3 coordination in a trigonal antiprismatic fashion, respectively, whereas in general, In prefers to be tetrahedrally coordinated by Te. Thus, the synthesis of homogeneous In-rich samples with more than 3.6 atom-% In (i.e. $x < 12$ for $y = 1$ and $x < 5$ for $y = 0.5$) requires high-pressure conditions, because the octahedral coordination of In is energetically favored under HP conditions (pressure-coordination rule). Samples with an In content ≤ 3.6 atom-% (i.e. $x = 12$ for $y = 1$ and $x \geq 5$ for $y = 0.5$) do not require HP synthesis and can be obtained by quenching after annealing the samples at 550 °C. All $(GeTe)_xAgIn_ySb_{1-y}Te_2$ phases investigated decompose into chalcopyrite-type $AgInTe_2$ and GeTe or $(GeTe)_{2x}AgSbTe_2$ for $y = 1$ or 0.5, respectively, upon heating at ambient pressure. The decomposition temperature depends on the In content and is higher for samples with lower In contents. However, the cubic HT phases of GeTe or $(GeTe)_{2x}AgSbTe_2$ react with small amounts of $AgInTe_2$. At high temperature, solid solutions are favored by entropy as indicated by the observation of rocksalt-type HT phases for In contents up to 7-8 atom-% at temperatures above ~450 °C (the exact temperature depends on the In content). Although no side phase can be observed in the PXRD patterns, quenching leads to nanoscopic precipitates of $AgInTe_2$ and Ag-rich domains. Thus, the applied quenching rates cannot completely suppress the nucleation of $AgInTe_2$ during the decomposition reaction. $(GeTe)_{5.5}AgIn_{0.5}Sb_{0.5}Te_2$ quenched from the rocksalt-type HT phase exhibits a maximum ZT value of 0.75 at 300 °C close to the decomposition into $AgInTe_2$ and $(GeTe)_{11}AgSbTe_2$ but only 0.5 at 125 °C where $(GeTe)_{5.5}AgInTe_2$ prepared under HP conditions exhibits ZT = 0.6. As expected the latter's κ is slightly higher than that of the quinary compound, but this is outbalanced by the higher Seebeck coefficient. TIGS's ZT value is higher than that of the corresponding TAGS-85[19] in the investigated temperature range.

Both the $(GeTe)_xAgIn_{0.5}Sb_{0.5}Te_2$ as well as the TIGS samples show promising new ways towards high-performance thermoelectric materials. While TIGS compounds prepared under

high-pressure conditions exhibit remarkable ZT values close to RT and up to 125 °C, both the more pronounced disorder and the decomposition of $(GeTe)_{5.5}AgIn_{0.5}Sb_{0.5}Te_2$ might provide possible control parameters to decrease the thermal conductivity without significantly affecting the electrical conductivity.

Acknowledgement

We thank Christian Minke and Dr. Markus Seibald for SEM operation and EDX analyses and Thomas Miller (LMU Munich) for the temperature-dependent powder diffraction experiments. Furthermore, we thank Fivos Drymiotis (California Institute of Technology) for help with the thermoelectric measurements and PD Dr. Gerald Wagner (Leipzig University) for his help with the HRTEM interpretation. This investigation was funded by the Deutsche Forschungsgemeinschaft (grant OE530/1-2) and the Studienstiftung des deutschen Volkes (scholarship for T.S.).

3.5.5 Supplementary information

Table S1. Results of the SEM-EDX analyses (averaged from 5 - 15 point analyses per sample) of $(GeTe)AgInTe_2$, $(GeTe)_5AgInTe_2$, $(GeTe)_{5.5}AgInTe_2$, $(GeTe)_7AgInTe_2$ and $(GeTe)_{12}AgInTe_2$.

sample	atom-% calc.	atom-% found
$(GeTe)AgInTe_2$	Ge: 16.7; Ag: 16.7; In: 16.7; Te: 50.0	Ge: 17.9(4); Ag: 16.0(4); In: 16.5(4); Te: 49.6(6)
$(GeTe)_5AgInTe_2$	Ge: 35.7; Ag: 7.1; In: 7.1; Te: 50.0	Ge: 36.0(14); Ag: 7.2(4); In: 7.3(4); Te: 50(1)
$(GeTe)_{5.5}AgInTe_2$	Ge: 36.7; Ag: 6.7; In: 6.7; Te: 50.0	Ge: 37.1(15); Ag: 6.5(4); In: 6.9(4); Te: 49.5(8)
$(GeTe)_7AgInTe_2$	Ge: 38.9; Ag: 5.6; In: 5.6; Te: 50.0	Ge: 39.7(16); Ag: 5.5(5); In: 5.4(6); Te: 49.4(8)
$(GeTe)_{12}AgInTe_2$	Ge: 42.9; Ag: 3.6; In: 3.6; Te: 50.0	Ge: 44(1); Ag: 3.2(7); In: 3.6(4); Te: 49.3(7)

Table S2. Results of the SEM-EDX analyses (averaged from 5 - 15 point analyses per sample) of $(GeTe)AgIn_{0.5}Sb_{0.5}Te_2$, $(GeTe)_5AgIn_{0.5}Sb_{0.5}Te_2$, $(GeTe)_{5.5}AgIn_{0.5}Sb_{0.5}Te_2$, $(GeTe)_7AgIn_{0.5}Sb_{0.5}Te_2$.and $(GeTe)_{12}AgIn_{0.5}Sb_{0.5}Te_2$

sample	atom-% calc.	atom-% found
$(GeTe)AgIn_{0.5}Sb_{0.5}Te_2$	Ge: 16.7; Ag: 16.7; Sb: 8.3; In: 8.3; Te: 50.0	Ge: 17.3(7); Ag: 16.2(5); Sb: 9.0(6); In: 8.0(5); Te: 49.6(4)
$(GeTe)_5AgIn_{0.5}Sb_{0.5}Te_2$	Ge: 35.7; Ag: 7.1; Sb: 3.6; In: 3.6; Te: 50.0	Ge: 37.7(9); Ag: 6.6(1); Sb: 3.9(4); In: 3.3(3); Te: 48.5(7)
$(GeTe)_{5.5}AgIn_{0.5}Sb_{0.5}Te_2$	Ge: 36.7; Ag: 6.7; Sb: 3.3; In: 3.3; Te: 50.0	Ge: 37.1(1); Ag: 6.5(5); Sb: 3.5(1); In: 3.3(1); Te: 49.6(5)
$(GeTe)_7AgIn_{0.5}Sb_{0.5}Te_2$	Ge: 38.9; Ag: 5.6; Sb: 2.8; In: 2.8; Te: 50.0	Ge: 40(1); Ag: 5.2(4); Sb: 2.9(4); In: 2.7(3); Te: 48.9(9)
$(GeTe)_{12}AgIn_{0.5}Sb_{0.5}Te_2$	Ge: 42.9; Ag: 3.6; In: 1.8; Sb: 1.8 Te: 50.0	Ge: 41.8(9); Ag: 3.8(3); In: 1.9(3); Sb: 2.2(5) Te: 50.3(7)

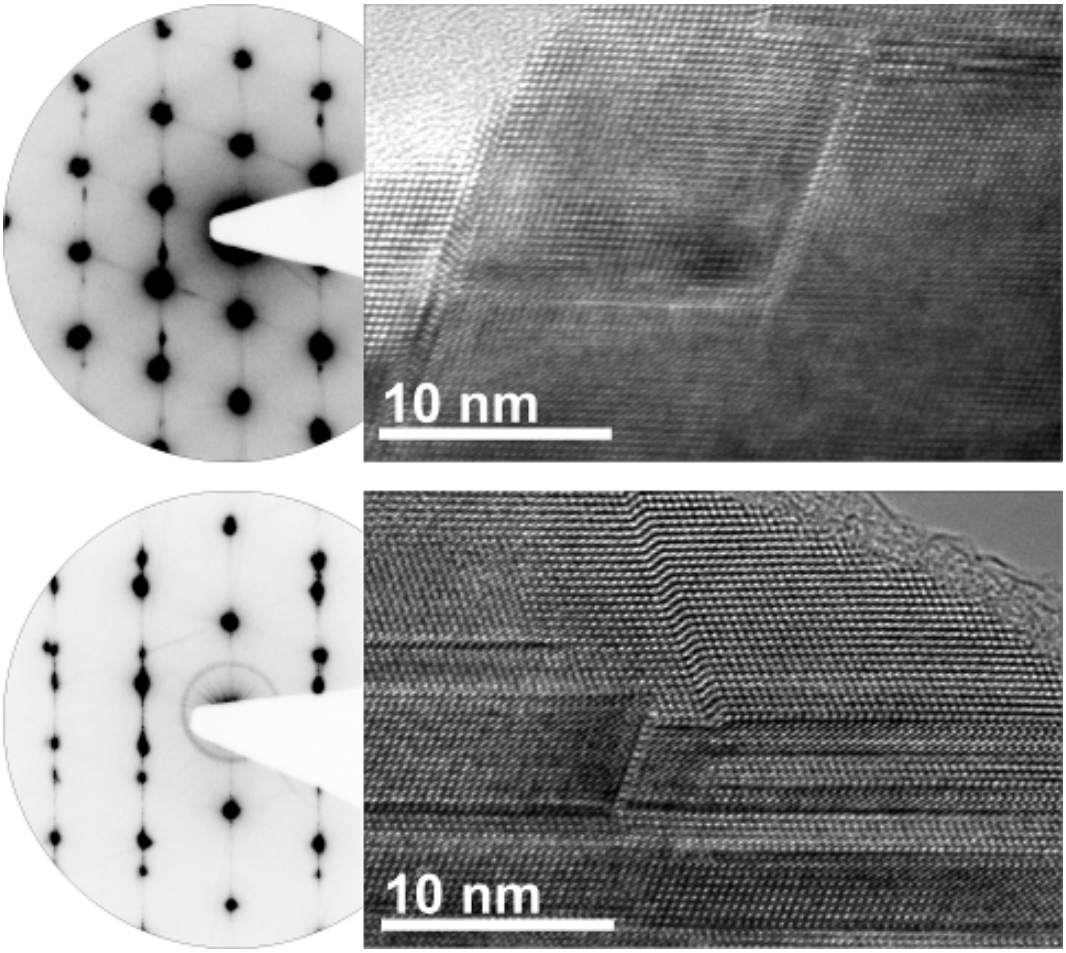

Fig. S1. HRTEM images (right) and the corresponding SAED patterns (left) of crystal areas with dislocations and twin domains: $(GeTe)_{5.5}AgIn_{0.5}Sb_{0.5}Te_2$ (top) and $(GeTe)_7AgIn_{0.5}Sb_{0.5}Te_2$ (bottom).

3.5.6 References

[1] H. Hahn, G. Frank, W. Klingler, A. D. Meyer, G. Störger, *Z. Anorg. Allg. Chem.* **1953**, *271*, 153.

[2] K. J. Range, G. Engert, A. Weiss, *Solid State Commun.* **1969**, *7*, 1749.

[3] T. Schröder, T. Rosenthal, D. Souchay, C. Petermayer, S. Grott, E.-W. Scheidt, C. Gold, W. Scherer, O. Oeckler, *J. Solid State Chem.* **2013**, *206*, 20.

[4] H. J. Goldsmid, *Thermoelectric Refrigeration*, Plenum Press, New York, **1964**.

[5] D. T. Morelli, V. Jovovic, J. P. Heremans, *Phys. Rev. Lett.* **2008**, *101*, 035901.

[6] M. D. Nielsen, V. Ozolins, J. P. Heremans, *Energy Environ. Sci.* **2013**, *6*, 570.

[7] W. G. Zeier, Y. Z. Pei, G. Pomrehn, T. Day, N. Heinz, C. P. Heinrich, G. J. Snyder, W. Tremel, *J. Am. Chem. Soc.* **2013**, *135*, 726.

[8] A. Yusufu, K. Kurosaki, Y. Ohishi, H. Muta, S. Yamanaka, *Jpn. J. Appl. Phys.* **2013**, *52*, 081801.

[9] T. Plirdpring, K. Kurosaki, A. Kosuaga, T. Day, S. Firdosy, V. Ravi, G. J. Snyder, A. Harnwunggmoung, T. Sugahara, Y. Ohishi, H. Muta, S. Yamanaka, *Adv. Mater.* **2012**, *24*, 3622.

[10] R. Liu, L. Xi, H. Liu, X. Shi, W. Zhang, L. Chen, *Chem. Commun.* **2012**, *48*, 3818.

[11] C. Wood, *Rep. Prog. Phys.* **1988**, *51*, 459.

[12] W. Klemm, G.Frischmuth, *Z. Anorg. Allg. Chem.* **1934**, *218*, 249.

[13] J. Goldak, C. S. Barrett, D. Innes, W. Youdelis, *J. Chem. Phys.* **1966**, *44*, 3323.

[14] B. A. Cook, M. J. Kramer, X. Wei, J. L. Harringa, E. M. Levin, *J. Appl. Phys.* **2007**, *101*, 053715.

[15] S. K. Plachkova, *Phys. Status Solidi A* **1984**, *83*, 349.

[16] S. H. Yang, T. J. Zhu, T. Sun, S. N. Zhang, X. B. Zhao, J. He, *Nanotechnol.* **2008**, *19*, 245707.

[17] F. D. Rosi, J. P. Dismukes, E. F. Hockings, *Electron. Eng.* **1960**, *79*, 450.

[18] G. C. Christakudis, S. K. Plachkova, L. E. Shelimova, E. S. Avilov, *Phys. Status Solidi A* **1991**, *128*, 465.

[19] J. Davidow, Y. Gelbstein, *J. Electron. Mater.* **2013**, *42*, 1542.

[20] X. Shi, J. R. Salvador, J. Yang, H. Wang, *Sci. Adv. Mater.* **2011**, *3*, 667.

[21] E. M. Levin, B. A. Cook, J. L. Harringa, S. L. Bud'ko, R. Venkatasubramanian, K. Schmidt-Rohr, *Adv. Funct. Mater.* **2011**, *21*, 441.

[22] E. M. Levin, S. L. Bud'ko, K. Schmidt-Rohr, *Adv. Funct. Mater.* **2012**, *22*, 2766.

[23] D. Walker, M. A.Carpenter, C. M. Hitch, *Am. Mineral.* **1990**, *75*, 1020.

[24] D. Walker, *Am. Mineral.* **1991**, *76*, 1092.

[25] D. C. Rubie, *Phase Trans.* **1999**, *68*, 431.

[26] H. Huppertz, *Z. Naturforsch. B* **2001**, *56*, 697.

[27] *WINXPOW*, *v2.12 ed*., Stoe & Cie GmbH, Darmstadt, Germany, **2005**..

[28] *TOPAS-Academic*, *V. 4.1*, Coelho Software, Brisbane, Australia, **2007**.

[29] *DigitalMicrograph 3.6.1*, Gatan Software, Pleasanton, USA, **1999**.

[30] P. A. Stadelmann, *Ultramicroscopy* **1987**, *21*, 131.

[31] *ESVision*, *4.0.164*, Emispec Systems Inc., Tempe, USA, **1994-2002**.

[32] L. J. van der Pauw, *Philips Res. Rep.* **1958**, *13*, 1.

[33] K. A. Borup, E. S. Toberer, L. D. Zoltan, G. Nakatsukasa, M. Errico, J. P. Fleurial, B. B. Iversen, G. J. Snyder, *Rev. Sci. Instrum.* **2012**, *83*, 123902.

[34] S. Iwanaga, E. S. Toberer, A. LaLonde, G. J. Snyder, *Rev. Sci. Instrum.* **2011**, *82*, 063905.

[35] A. LeBail, A. Jouanneaux, *J. Appl. Crystallogr.* **1997**, *30*, 265.

[36] R. Marin-Ayral, B. Lendre, G. Brun, B.Liautard, J. Tedenac, *Thermochim. Acta* **1988**, *131*, 37.

[37] R. M. Imamov, Z. G. Pinsker, *Sov. Phys. Crystallogr.* **1966**, *11*, 182.

[38] T. Chattopadhyay, J. Boucherle, H. von Schnering, *J. Phys. C* **1987**, *20*, 1431.

[39] T. Schröder, M. N. Schneider, T. Rosenthal, A. Eisele, C. Gold, E.-W. Scheidt, W. Scherer, R. Berthold, O. Oeckler, *Phys. Rev. B* **2011**, *84*, 184104.

3.6 Nanostructures in TAGS thermoelectric materials induced by phase transitions associated with vacancy ordering

T. Schröder, T. Rosenthal, N. Giesbrecht, M. Nentwig, S. Maier, H. Wang, G. J. Snyder, O. Oeckler

Inorg. Chem. **2014**, *53*, 7722-7729.

Abstract

TAGS materials with rather high concentrations of cation vacancies exhibit improved thermoelectric properties as compared to corresponding conventional TAGS (with constant Ag/Sb ratio of 1) due to a significant reduction of the lattice thermal conductivity. There are different vacancy ordering possibilities depending on the vacancy concentration and the history of heat treatment of the samples. In contrast to the average α-GeTe-type structure of TAGS materials with cation vacancy concentrations < ~3%, quenched compounds like $Ge_{0.53}Ag_{0.13}Sb_{0.27}\square_{0.07}Te_1$ and $Ge_{0.61}Ag_{0.11}Sb_{0.22}\square_{0.06}Te_1$ exhibit "parquet-like" multi-domain nanostructures with finite intersecting vacancy layers. These are perpendicular to the pseudo-cubic <111> directions but not equidistantly spaced, comparable to the nanostructures of compounds $(GeTe)_nSb_2Te_3$. Upon heating, the nanostructures transform into long-periodically ordered trigonal phases with parallel van der Waals gaps. These phases are slightly affected by stacking disorder but distinctly different from the α-GeTe-type structure reported for conventional TAGS materials. Deviations from this structure type are evident only from HRTEM images along certain directions or very weak intensities in diffraction patterns. At temperatures above ~ 400 °C, a rocksalt-type high-temperature phase with statistically disordered cation vacancies is formed. Upon cooling, the long-periodically trigonal phases are reformed at the same temperature. Quenched nanostructured $Ge_{0.53}Ag_{0.13}Sb_{0.27}\square_{0.07}Te_1$ and $Ge_{0.61}Ag_{0.11}Sb_{0.22}\square_{0.06}Te_1$ exhibit *ZT* values as high as 1.3 and 0.8, respectively, at 160 °C, which is far below the phase transition temperatures. After heat treatment, i.e. without pronounced nanostructure and when only reversible phase transitions occur, the *ZT* values of $Ge_{0.53}Ag_{0.13}Sb_{0.27}\square_{0.07}Te_1$ and $Ge_{0.61}Ag_{0.11}Sb_{0.22}\square_{0.06}Te_1$ with extended van der Waals gaps amount to 1.6 at 360 °C and 1.4 at 410 °C, respectively, which is at the top end of the range of high-performance TAGS materials.

3.6.1 Introduction

Facing the current energy problems, many ways of increasing the efficiency of energy transformation processes have been evaluated, among them the interconversion of heat and electrical energy by thermoelectric materials. Their efficiency is characterized by the dimensionless figure of merit $ZT = S^2\sigma T/\kappa$ (with the Seebeck coefficient S, the electrical conductivity σ, the temperature T and the thermal conductivity κ). At moderately high temperatures between 150 and 600 °C, chalcogenides with high *ZT* values are the materials of choice.[1] Many different materials, e.g. tellurides with rocksalt-type structure like $AgSbTe_2$[2,3] or $AgIn_xSb_{1-x}Te_2$[4,5] as well as heterogeneous $(PbTe)_mAgSbTe_2$ (LAST)[6] materials were recently investigated, along with chalcogenides derived from the sphalerite structure type, such as $Cu_2Zn_{1-x}Fe_xGeSe_4$,[7] $CuGaTe_2$,[8,9] or $CuInTe_2$.[10] The so-called TAGS-x materials $(GeTe)_x(AgSbTe_2)_{100-x}$, which crystallize in the α-GeTe structure type at ambient conditions and exhibit rocksalt-type high-temperature (HT) phases represent some of the classical and best characterized thermoelectric materials with *ZT* values above 1.[11-14] They can be understood as quasi-binary solid solutions between $AgSbTe_2$ and GeTe[15,16] and reach *ZT* values of up to 1.7 at 500 °C.[17] In order to optimize the thermoelectric properties of TAGS, many different substitution variants were investigated, e.g. Ge^{2+} was replaced by Sn^{2+} in $(SnTe)_xAgSbTe_2$,[18] Ag^+ by Li^+ in $(GeTe)_x(LiSbTe_2)_2$[19] and Sb^{3+} by In^{3+} in $(GeTe)_xAgInTe_2$ and $(GeTe)_xAgIn_{0.5}Sb_{0.5}Te_2$.[20] Even doping with rare earth metals was considered.[21,22] Extending the compositional range of TAGS materials beyond pseudobinary solid solutions $(GeTe)_x(AgSbTe_2)_{100-x}$ leads to compounds $(GeTe)_x[(Ag_2Te)_y(Sb_2Te_3)_{1-y}]_{100-x}$,[23] where the Ag/Sb ratio is variable. This approach leads to improved thermoelectric properties in high-performance TAGS materials like $(GeTe)_{85}(Ag_ySbTe_{y/2+1.5})_{15}$, where the thermal conductivity is reduced without significantly affecting the electrical conductivity[24] and the power factor is increased due to an optimized charge carrier concentration without decreasing the carrier mobility.[25,26] This extension involves cation vacancies for all values of $y < 1$, because y atoms of Ag but only y/2 atoms of Te are removed as compared to TAGS-x, which results in a larger number of anions than cations. The impact and the ordering possibilities of cation vacancies have not been taken into consideration so far in the literature. In compounds $(GeTe)_nSb_2Te_3$ (n = 12, 19), which correspond to TAGS $(GeTe)_x(Ag_ySbTe_{y/2+1.5})_{100-x}$ with y = 0 and consequently exhibit maximal cation vacancy concentrations, different cation vacancy ordering motifs were described, depending on the composition (n) and the thermal treatment.[27] Upon quenching, these compounds $(GeTe)_nSb_2Te_3$ form metastable pseudo-cubic phases in contrast to the α-

GeTe-type structure of vacancy-free TAGS, whose cubic HT phase cannot be retained at ambient temperature by quenching as the phase transition is displacive. The reason for the formation of such pseudo-cubic structures lies in their "parquet-like" nanoscale domain structures produced by short-range vacancy ordering in layers perpendicular to the cubic <111> directions.[28] These layers are not equidistantly spaced, which results in diffuse streaks along <111>* in diffraction patterns. Upon heating, the atoms next to the vacancy layers rearrange to form extended parallel van der Waals gaps. Stacking disorder is typical and results in an α-Hg-type average structure. At higher temperatures (typically above ~500 °C), a rocksalt-type HT phase with randomly disordered cation vacancies is formed. If this is slowly cooled, the above mentioned trigonal phase is formed.

The formation of comparable "parquet-like" nanostructures can be expected to be beneficial for the thermoelectric properties of high-performance TAGS materials, too, although the existence of multiple phase transitions might be a drawback for the thermal cycling behavior of these materials. In the present work, the effects of the cation vacancy concentration on the structure, stability and properties of TAGS materials with cation vacancies are studied.

3.6.2 Experimental

3.6.2.1 Synthesis

Samples with the nominal compositions $Ge_{0.53}Ag_{0.13}Sb_{0.27}Te_1$, $Ge_{0.61}Ag_{0.11}Sb_{0.22}Te_1$ and $Ge_{0.77}Ag_{0.07}Sb_{0.13}Te_1$ were synthesized by melting stoichiometric mixtures (typically 2.0 g) of the pure elements (silver 99.9999%, Alfa Aesar; germanium 99.999%, Sigma-Aldrich; antimony 99.9999%, Smart Elements; tellurium 99.999 %, Alfa Aesar) at 900 °C under Ar atmosphere in silica glass ampoules for 1 day and subsequently quenching the ampoules to room temperature (RT) by removing from the furnace. The samples were then annealed at 500 °C for 3 days and again quenched to RT in the same fashion. Samples for thermoelectric characterization were synthesized in the same manner; however, larger ampoules (diameter 1.2 cm) with a flat bottom were used to quench the melts in order to obtain ingots with dimensions as required for the measurements. The disc-shaped ingots were subsequently ground down until the round faces were parallel and finally polished. For these discs, homogeneity and absence of side phases were verified in the same manner as for all samples; the synthesis is well reproducible.

3.6.2.2 Diffraction methods

A Huber G670 Guinier camera equipped with a fixed imaging plate and integrated read-out system using Cu-$K_{\alpha 1}$ radiation (Ge(111) monochromator, λ = 1.54051 Å) was used for the collection of powder X-ray diffraction (PXRD) patterns of representative parts of the crushed samples, which were fixed between two Mylar foils using vacuum grease. A STOE Stadi P powder diffractometer equipped with an imaging-plate detector system using Mo-$K_{\alpha 1}$ radiation (Ge(111) monochromator, λ = 0.71093 Å) in a modified Debye–Scherrer geometry equipped with a graphite furnace was used for the collection of temperature-dependent powder diffraction patterns from RT to 600 °C with a heating rate of 10 K/min and from 600 °C back to RT with cooling rate of 5 K/min (faster cooling is impossible with the setup used). For these temperature-dependent measurements, powdered samples were filled into silica glass capillaries (0.3 mm diameter), which were then sealed with vacuum grease under argon atmosphere. Rietveld refinements were carried out using the program TOPAS,[29] phase homogeneity and the temperature-dependent powder diffraction patterns were evaluated using WINXPOW.[30]

3.6.2.3 Electron microscopy, diffraction and X-ray spectroscopy

X-ray spectra of representative parts of the samples were recorded with an energy dispersive X-ray (EDX) detector (model 7418, Oxford Instruments, Great Britain) mounted on a JSM-6500F (Jeol, USA) scanning electron microscope (SEM). The results of 6 point analyses were averaged. Detailed results are given in Table S1 in the Supplementary Information.

Finely ground samples were dispersed in ethanol and distributed on copper grids coated with holey carbon film (S166-2, Plano GmbH, Germany) for high-resolution transmission electron microscopy (HRTEM). The copper grids were subsequently fixed on a double-tilt holder and investigated in a Titan 80-300 (FEI, USA) equipped with a TEM TOPS 30 EDX spectrometer (EDAX, Germany) and a field-emission gun operated at 300 kV. Selected-area electron diffraction (SAED) patterns and HRTEM images were recorded using an UltraScan 1000 camera (Gatan, USA, resolution 2k x 2k). The Digital Micrograph[31] and EMS software packages[32] were used for HRTEM and SAED data evaluation; EDX data were evaluated with ES Vision.[33]

3.6.2.4 Thermoelectric characterization

For the characterization of the thermoelectric properties of $Ge_{0.53}Ag_{0.13}Sb_{0.27}\square_{0.07}Te_1$ and $Ge_{0.61}Ag_{0.11}Sb_{0.22}\square_{0.06}Te_1$ between 50 °C and 450 °C, three samples of each composition were synthesized as irreversible phase transitions (see thermal behavior section) were expected, which affect the transport properties. In order to obtain reliable *ZT* values for quenched samples at low temperatures, i.e. where the nanostructure is inert, each property was measured using a sample that had not undergone previous heating cycles. All analytical methods applied did not indicate any differences between samples with the same composition and thermal treatment. The electrical conductivity σ was measured in-plane using pressure-assisted Nb contacts in an in-house built facility at Caltech[34] using the van der Pauw method[35] (heating rate 150 K/h, measurement in 50 K steps). A LFA457 MicroFlash (Netzsch, Germany) laser flash system was used for the out-of-plane measurement the thermal diffusivity D_{th}. The thermal conductivity was calculated as $\kappa = D_{th} \cdot C_p \cdot \rho$ (C_p: calculated heat capacity using the Dulong-Petit approximation, i.e. 0.226 J/gK for $Ge_{0.53}Ag_{0.13}Sb_{0.27}\square_{0.07}Te_1$ and 0.230 J/gK for $Ge_{0.61}Ag_{0.11}Sb_{0.22}\square_{0.06}Te_1$; ρ: density determined by weighing the sample and measuring its dimensions). The Seebeck coefficient *S* was determined out-of-plane using Chromel-Nb thermocouples in steps of 61 K at a heating rate of 150 K/h and a temperature oscillation rate of ± 7.5 K.[36] The combined uncertainty of the measurements is ca. 20% for the ZT value.

3.6.3 Results and discussion

3.6.3.1 Overview and sample characterization

In principle, there are three ways (and combinations of them) of introducing cation vacancies (□) in TAGS materials without affecting the overall charge neutrality: (1) the exchange of 1 Ag^+ by 0.5 Ge^{2+} and 0.5 □, (2) the exchange of 1 Ag^+ by 1/3 Sb^{3+} and 2/3 □ and (3) the exchange of 1 Ge^{2+} by 2/3 Sb^{3+} and 1/3 □. These different possibilities make it difficult to maintain the widespread TAGS-x nomenclature (with x given by $(GeTe)_x(AgSbTe_2)_{100-x}$). For example, $Ge_{0.53}Ag_{0.13}Sb_{0.27}\square_{0.07}Te_1$ may be written as $Ge_4AgSb_2Te_{7.5}$, which on the one hand could be understood as a variant of TAGS-80 = $(GeTe)_{80}(AgSbTe_2)_{20}$ = $(GeTe)_4AgSbTe_2$ = $Ge_4AgSbTe_6$ with additional 0.5 Sb_2Te_3 per formula unit, on the other hand it can also be viewed as TAGS-85 = $(GeTe)_{85}(AgSbTe_2)_{15} \approx (GeTe)_{5.5}AgSbTe_2$ = $Ge_{5.5}AgSbTe_{7.5}$ with 1.5 Ge^{2+} being replaced by 1 Sb^{3+}. Therefore, the comparison of vacancy-containing compounds with conventional TAGS-x is not unequivocal. Similarly, a given vacancy concentration is not

sufficient to characterize modified TAGS materials, because there are different element combinations that correspond to the same amount of cation vacancies. For the sake of clarity, we use normalized formulas that immediately show the vacancy concentration as a consequence of the site occupancies in possibly distorted rocksalt-type structures that are characteristic for all compounds discussed here: they exhibit just one cation and one anion position. For example $Ge_4AgSb_2Te_{7.5}$ is written as $Ge_{0.53}Ag_{0.13}Sb_{0.27}\square_{0.07}Te_1$.

Many experiments have shown that all of these variations lead to single-phase samples as long as charge neutrality is not violated. If the anion and cation charges are not balanced, binary side phases or remaining elemental Ge or Te are observed. All samples discussed in this manuscript are single-phase as shown by Rietveld refinements (cf. next section), typically the weight of the ingot differs from that of the mixture of starting materials by less than 1%. The composition and homogeneity are further confirmed by SEM-EDX results (cf. Table S1 in the Supplementary Information).

3.6.3.2 Crystal structures of the quenched compounds

All reflections in the PXRD patterns of $Ge_{0.53}Ag_{0.13}Sb_{0.27}\square_{0.07}Te_1$ and $Ge_{0.61}Ag_{0.11}Sb_{0.22}\square_{0.06}Te_1$ can be indexed assuming the rocksalt type's cubic metrics. In contrast, reflection splitting indicates that $Ge_{0.77}Ag_{0.07}Sb_{0.13}\square_{0.03}Te_1$ is rhombohedral; the unit cell corresponds to the α-GeTe type. The latter compound is discussed in order to demonstrate the influence of the vacancy concentration on the average structure in the case of high Ge contents; however, it was not further characterized as its expected low Seebeck coefficient (already lowered for $Ge_{0.53}Ag_{0.13}Sb_{0.27}\square_{0.07}Te_1$ compared to $Ge_{0.61}Ag_{0.11}Sb_{0.22}\square_{0.06}Te_1$; see thermoelectric properties section) precludes promising thermoelectric properties. Rietveld refinements for $Ge_{0.53}Ag_{0.13}Sb_{0.27}\square_{0.07}Te_1$ and $Ge_{0.61}Ag_{0.11}Sb_{0.22}\square_{0.06}Te_1$ confirm the presence of rocksalt-type average structures. In order to exclude rhombohedral structures with pseudocubic metrics, which have been reported in the Ag/Ge/In/Sb/Te system,[20] various test refinements were performed. Layer formation like in α-GeTe reduces the symmetry from $Fm\bar{3}m$ to $R3m$. A measure of this layer formation is the z parameter of the cations which is 0.5 in the trigonal setting of the cubic unit cell. No significant deviations from this value were detected. In the final refinements, common atom coordinates and displacement parameters were refined for all cations. Cation site occupancies were taken from the nominal composition and not refined; tentative refinements did not indicate significant changes. The Te anion position was assumed as completely occupied with an independent displacement parameter.

For the refinements in the space group *R*3*m*, preferred orientation was considered as a flat sample holder was used (4th order spherical harmonics with 3 parameters). The profile fits are depicted in Fig. 1, the results of the refinement and the atomic parameters are given in Tables 1 and 2, respectively. Further details of the crystal structure investigations may be obtained from Fachinformationszentrum Karlsruhe, 76344 Eggenstein-Leopoldshafen, Germany (fax: (+49)7247-808-666; e-mail: crysdata@fiz-karlsruhe.de, http://www.fiz-karlsruhe.de/request_for_deposited_data.html) on quoting the depository numbers CSD 427403, 427405 and 427404 for $Ge_{0.53}Ag_{0.13}Sb_{0.27}\square_{0.07}Te_1$, $Ge_{0.61}Ag_{0.11}Sb_{0.22}\square_{0.06}Te_1$ and $Ge_{0.77}Ag_{0.07}Sb_{0.13}\square_{0.03}Te_1$, respectively.

The rocksalt-type average structure of $Ge_{0.53}Ag_{0.13}Sb_{0.27}\square_{0.07}Te_1$ and $Ge_{0.61}Ag_{0.11}Sb_{0.22}\square_{0.06}Te_1$ is an uncommon observation for TAGS materials, because usually it is not possible to quench their cubic HT phase due to the displacive character of the phase transition. This hints at the crucial role of cation vacancy ordering in the compounds investigated (see below). With increasing GeTe content, the lattice parameter decreases. In addition to the metrics indicated by reflection splitting, the α-GeTe type structure of $Ge_{0.77}Ag_{0.07}Sb_{0.13}\square_{0.03}Te_1$ is corroborated by the cation z parameter of 0.4834(2) which indicates pronounced layer formation.

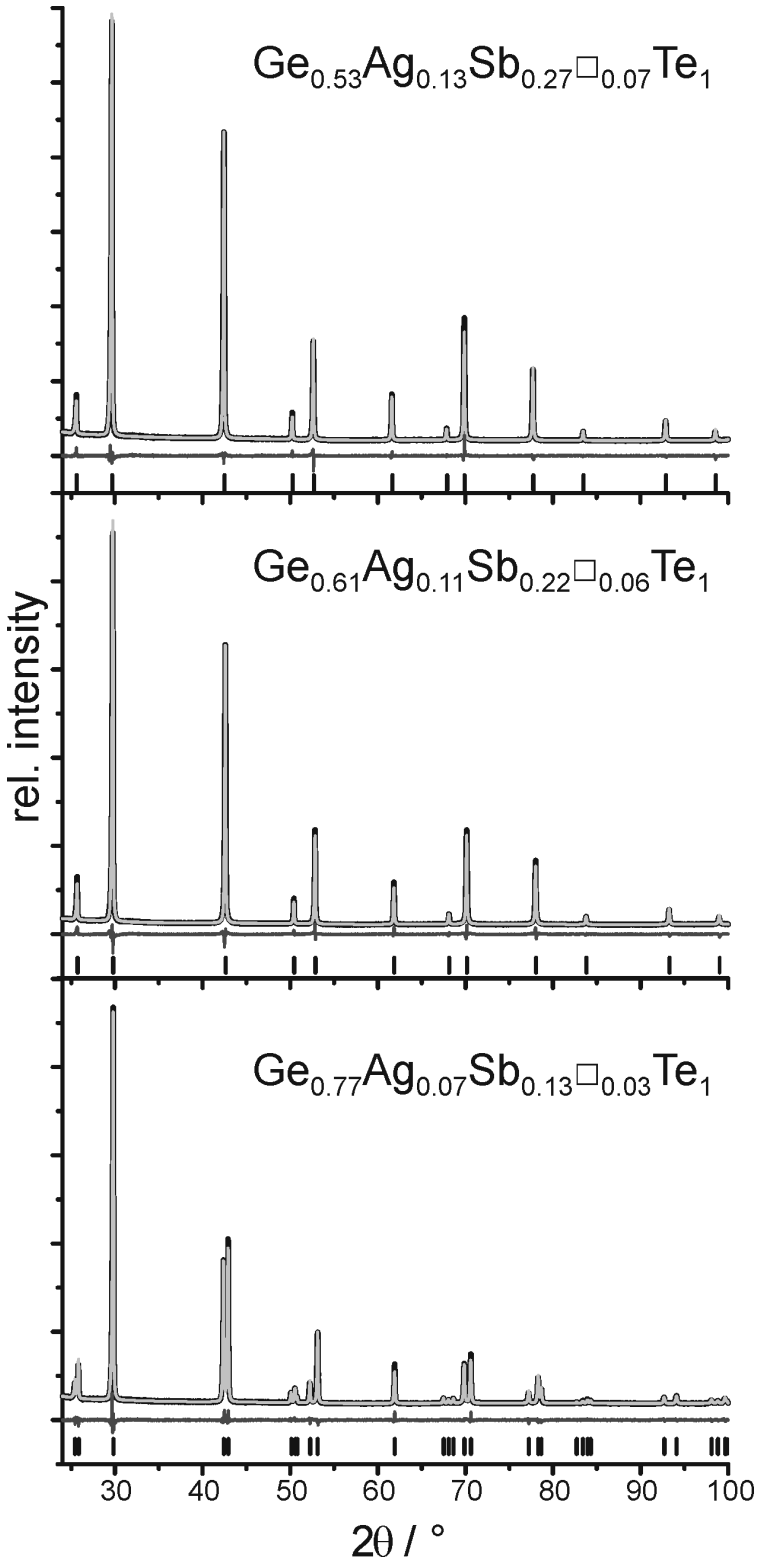

Fig. 1: Experimental (black) and calculated (light gray) powder diffraction patterns according to the Rietveld refinement of $Ge_{0.53}Ag_{0.13}Sb_{0.27}\square_{0.07}Te_1$, $Ge_{0.61}Ag_{0.11}Sb_{0.22}\square_{0.06}Te_1$ and $Ge_{0.77}Ag_{0.07}Sb_{0.13}\square_{0.03}Te_1$ (top to bottom), with difference plots (black, below the profiles) and peak positions (black lines).

Table 1. Crystal data and results of the Rietveld refinement of $Ge_{0.53}Ag_{0.13}Sb_{0.27}\square_{0.07}Te_1$, $Ge_{0.61}Ag_{0.11}Sb_{0.22}\square_{0.06}Te_1$ and $Ge_{0.77}Ag_{0.07}Sb_{0.13}\square_{0.03}Te_1$.

Sample	$Ge_{0.53}Ag_{0.13}Sb_{0.27}\square_{0.07}Te_1$	$Ge_{0.61}Ag_{0.11}Sb_{0.22}\square_{0.06}Te_1$	$Ge_{0.77}Ag_{0.07}Sb_{0.13}\square_{0.03}Te_1$
molar mass (of asymmetric unit) / g mol^{-1}	213.16	210.97	206.71
crystal system / spacegroup (no.)	cubic / $Fm\bar{3}m$ (no. 225)		trigonal / $R3m$
Z	4		3
$F(000)$	355.7	352.4	259.4
lattice parameters / Å	6.01175(2)	5.99253(2)	a = 4.20935(2) c = 10.4922(1)
cell volume / Å^3	217.272(2)	215.194(2)	161.001(3)
density (X-ray) / g cm^{-3}	6.52	6.51	6.40
absorption coefficient / mm^{-1}	147.2	143.9	134.8
radiation	Cu-$K_{\alpha 1}$ (λ = 1.540596 Å)		
2θ range / °	24 – 100		
no. of data points	15201		
no. of reflections	13		31
constraints	2		4
refined parameters / thereof background	22 / 12		27 / 12
R_p / R_{wp}	0.0173 / 0.0275	0.0254 / 0.0371	0.0181 / 0.0280
R_{Bragg}	0.0139	0.0182	0.0147
Goof	0.997	1.430	0.947

Table 2. Atom positions, occupancy factors (s.o.f.), and displacement parameters (B_{iso} in Å^2) of $Ge_{0.53}Ag_{0.13}Sb_{0.27}\square_{0.07}Te_1$, $Ge_{0.61}Ag_{0.11}Sb_{0.22}\square_{0.06}Te_1$ and $Ge_{0.77}Ag_{0.07}Sb_{0.13}\square_{0.03}Te_1$.

sample	atom	x y z	s.o.f.	B_{iso}
$Ge_{0.53}Ag_{0.13}Sb_{0.27}\square_{0.07}Te_1$	Ge/Ag/Sb	0 0 0	0.533/0.133/0.267	2.66(1)
	Te	0.5 0.5 0.5	1	0.96(1)
$Ge_{0.61}Ag_{0.11}Sb_{0.22}\square_{0.06}Te_1$	Ge/Ag/Sb	0 0 0	0.611/0.111/0.222	2.76(2)
	Te	0.5 0.5 0.5	1	1.05(1)
$Ge_{0.77}Ag_{0.07}Sb_{0.13}\square_{0.03}Te_1$	Ge/Ag/Sb	0 0 0.4834(2)	0.767/0.067/0.133	2.12(3)
	Te	0 0 0	1	1.35(2)

3.6.3.3 Transmission electron microscopy

HRTEM investigations (cf. Figure 2) reveal the ordering of cation defects in a sample of $Ge_{0.61}Ag_{0.11}Sb_{0.22}\square_{0.06}Te_1$, which was quenched after being annealed in the stability range of the cubic HT phase (see section below). The nanostructure is comparable to the one observed for Ag-free $(GeTe)_nSb_2Te_3$ thermoelectric materials.[28] The average lateral extension of the defect layers (measured in HRTEM images) is 9(2) nm in good agreement with the lateral extension of 11(3) nm observed for $(GeTe)_7Sb_2Te_3$, which exhibits a similar cation vacancy concentration.[37] The defect layers in both compounds are perpendicular to the cubic <111> directions; they intersect and thereby form a "parquet-like" multi-domain nanostructure (cf. Figure 2, top). The observation that the defect layers form van der Waals gaps at higher temperatures (see next section) and the fact that the average structure of the investigated compound is cubic ($Fm\bar{3}m$) corroborates that the planar defects correspond to cation vacancy layers as opposed to twin boundaries in conventional trigonal TAGS materials (corresponding to the symmetry reduction from $Fm\bar{3}m$ to $R3m$ upon cooling the HT phase). The average distance between the vacancy layers is 4(1) nm; however, they are not equidistant as corroborated by diffuse streaks that interconnect Bragg reflections along <111>* in the SAED patterns taken along the [110] zone axis and the corresponding Fourier transforms of HRTEM images. This nanostructure is not limited to thin fringes of the particles, but extends over the whole crystallites (cf. Fig. S2 bottom in the Supplementary Information). Due to their special orientation, defect layers and corresponding diffuse intensities cannot be observed in HRTEM images or SAED patterns along most zone axes (e.g. [100], cf. Fig. S2 top). The same type of nanostructure is also observed in quenched $Ge_{0.53}Ag_{0.13}Sb_{0.27}\square_{0.07}Te_1$ (cf. Fig. S1).

Larger areas with parallel defect layers (lateral extension > 25 nm), which are more regularly spaced (average spacing: 3.5(5) nm) and correspond to extended van der Waals gaps, were observed after prolonged exposure to the electron beam (cf. Figure 2, bottom). This indicates a tendency towards long-range order comparable to that in annealed samples of $(GeTe)_nSb_2Te_3$.[28]

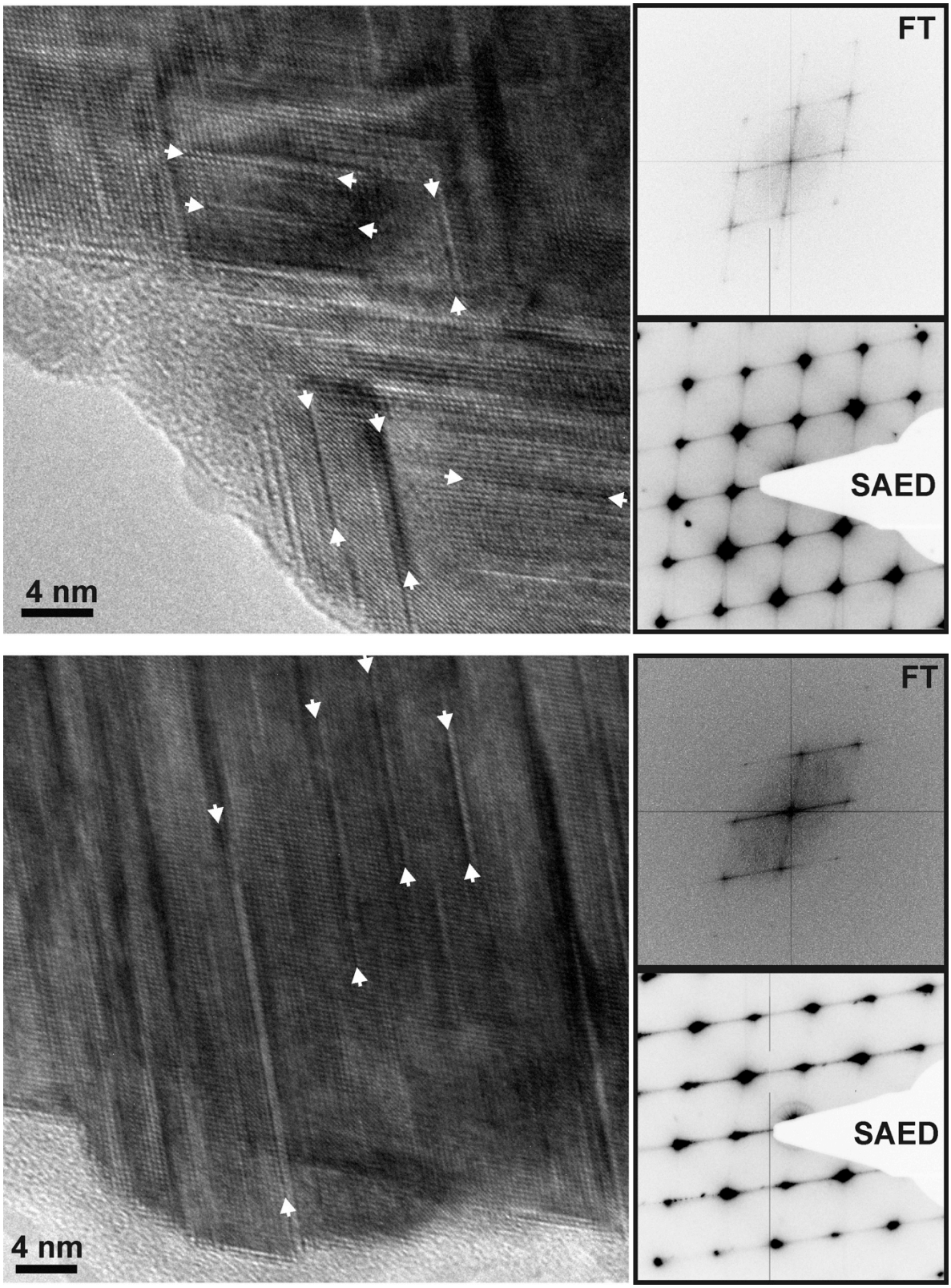

Fig. 2: HRTEM images of quenched $Ge_{0.61}Ag_{0.11}Sb_{0.22}\square_{0.06}Te_1$ (top) and a different area of the same crystallite after prolonged exposure to the electron beam (bottom) with the corresponding Fourier transforms (FT) and SAED patterns of the crystallite (all along the zone axis [110] with respect to cubic indexing). Some selected vacancy layers are highlighted by white arrows and their arrangement is indicated.

3.6.3.4 Stability ranges and phase transitions

Temperature-dependent PXRD patterns of quenched $Ge_{0.53}Ag_{0.13}Sb_{0.27}\square_{0.07}Te_1$ and $Ge_{0.61}Ag_{0.11}Sb_{0.22}\square_{0.06}Te_1$ (see Fig. 3) show that upon heating in both compounds the pseudocubic phase (with "parquet-like" multi-domain nanostructure) transforms to a trigonal, long-periodically ordered phase at ca. 200 °C. This is indicated by reflection splitting and additional weak reflections, e.g. at 2θ = 14° and 20°. During heating, these reflections are rather broad, which indicates severe stacking disorder and impedes the assignment of a distinct structure type. At ca. 400 °C, both compounds form their rocksalt-type HT phases with statistically disordered cation vacancies. Upon cooling, they retransform to the trigonal long-periodically ordered structures. A schematic illustration of the rearrangements of the vacancy layers is depicted in Fig. 4. Owing to the slow cooling process, the weak reflections of the trigonal phase are sharper that during the heating process. Therefore, the $Ge_5As_2Te_8$ structure type with a 15*P* stacking sequence (space group $P\bar{3}m1$ (no. 164), a = 4.2136(3) Å; c = 27.711(4) Å) can be assigned for $Ge_{0.53}Ag_{0.13}Sb_{0.27}\square_{0.07}Te_1$ (cf. Fig. S3 and Table S2 in the Supplementary Information). This structure can be understood as a sequence of slightly distorted 15-layer slabs cut out of the rocksalt-type structure, which are terminated by Te atom layers and separated by van der Waals gaps (cf. Fig. S4). Around the latter, the Te-Te stacking sequence corresponds to a hexagonal ABAB one. This rearrangement of cation vacancies corresponds to a reconstructive phase transition. For such layered phases, the number of layers between the van der Waals gaps can be estimated from the vacancy concentration as detailed in the literature.[38] In the case of $Ge_{0.53}Ag_{0.13}Sb_{0.27}\square_{0.07}Te_1$ the expected number of layers (1/0.067 = 15) corresponds exactly the observed one.

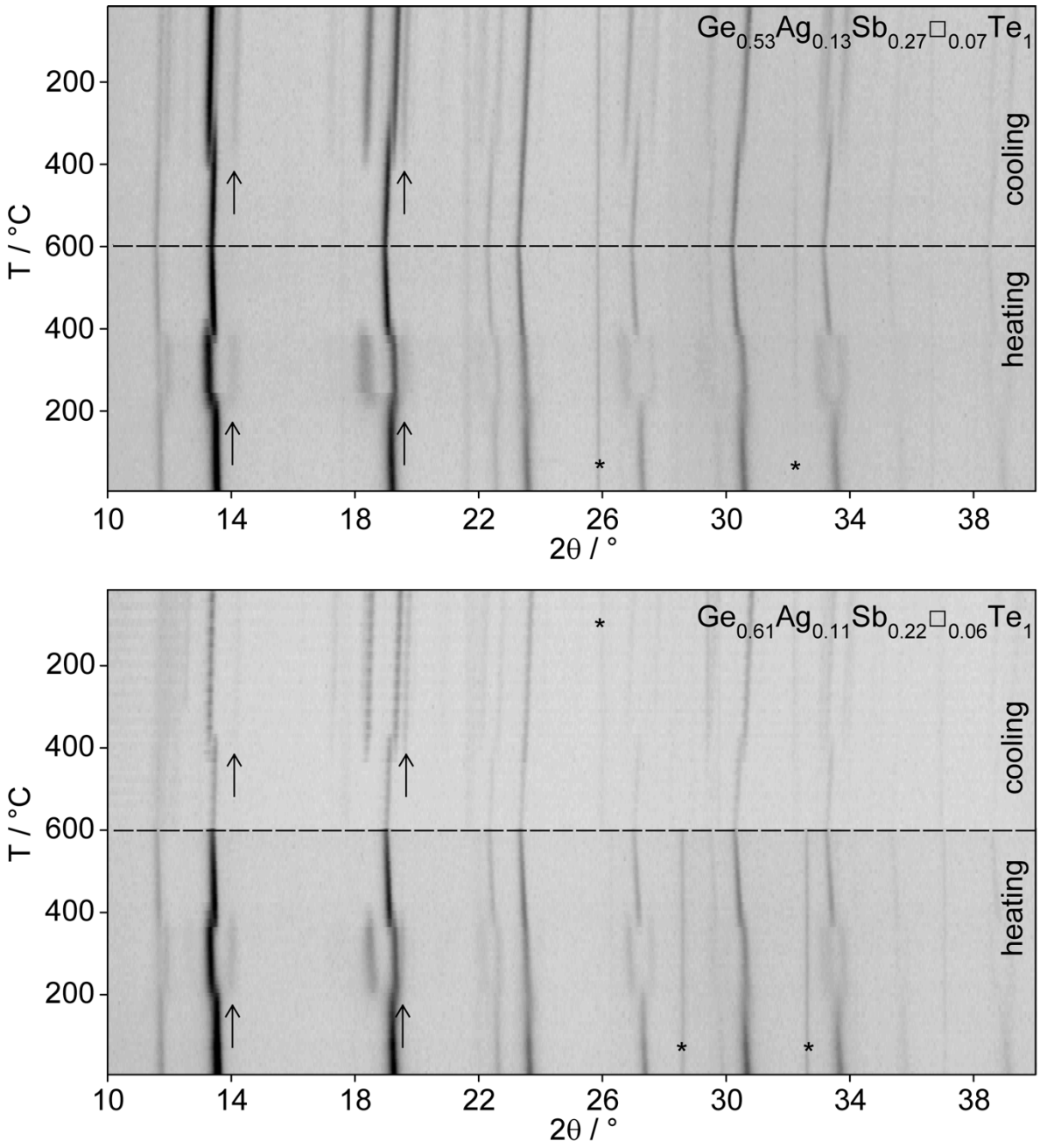

Fig. 3: Temperature-dependent PXRD patterns of $Ge_{0.53}Ag_{0.13}Sb_{0.27}\square_{0.07}Te_1$ (top) and $Ge_{0.61}Ag_{0.11}Sb_{0.22}\square_{0.06}Te_1$ (bottom, note that different contrast of the cooling section is due to the use of another measurement, asterisks mark the positions of reflections caused by the furnace); two of the strongest additional reflections that indicate the formation of a long-periodically ordered trigonal phase are marked with arrows; the dashed horizontal line marks the highest temperature.

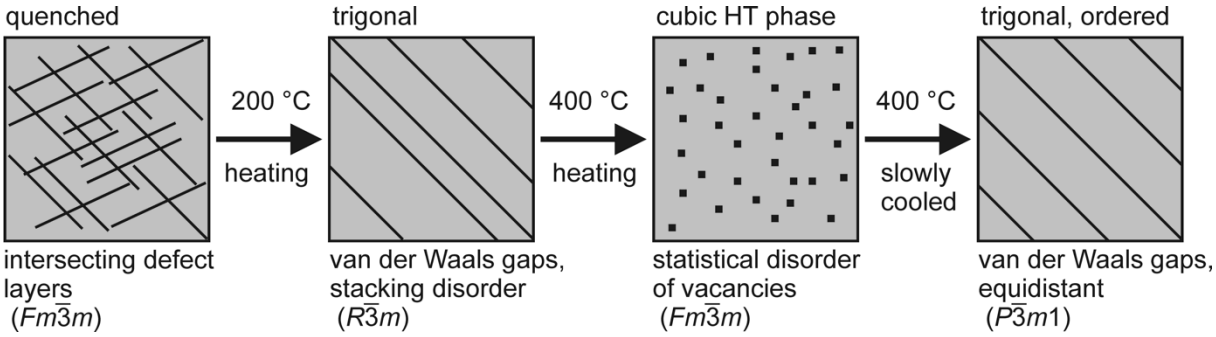

Fig. 4: Schematic illustration of the rearrangement of the vacancies during heating and cooling.

3.6.3.5 Thermoelectric properties of $Ge_{0.53}Ag_{0.13}Sb_{0.27}\square_{0.07}Te_1$ and $Ge_{0.61}Ag_{0.11}Sb_{0.22}\square_{0.06}Te_1$

The thermoelectric properties of nanostructured $Ge_{0.53}Ag_{0.13}Sb_{0.27}\square_{0.07}Te_1$ and $Ge_{0.61}Ag_{0.11}Sb_{0.22}\square_{0.06}Te_1$ (cf. Fig. 5) as measured at the beginning of the first heating cycle change after heating over 200 °C as expected by the phase transitions as described above, when the finite intersecting defect layers become extended and parallel. As the structural changes during the first heating measurement between 200 °C and 450 °C can be viewed as a slow ongoing ordering process, the measured properties in this range shall not be discussed as they may be extremely time-dependent and during a phase transition, assuming a constant C_p is not justified. Subsequent heating and cooling cycles show no further significant irreversibility within the accuracy of the measurements, which is expected because without further quenching steps the samples that were heated once retain only one reversible phase transition at 400 °C from a long periodically trigonal phase to the cubic HT phase. The density of the samples does not change significantly among the differently ordered variants of the compounds after the phase transitions. Both quenched and HT phases are cubic so that anisotropy effects should not affect the measurements; they may, however, occur in the trigonal phase in the same way as they do in “classical” TAGS materials.

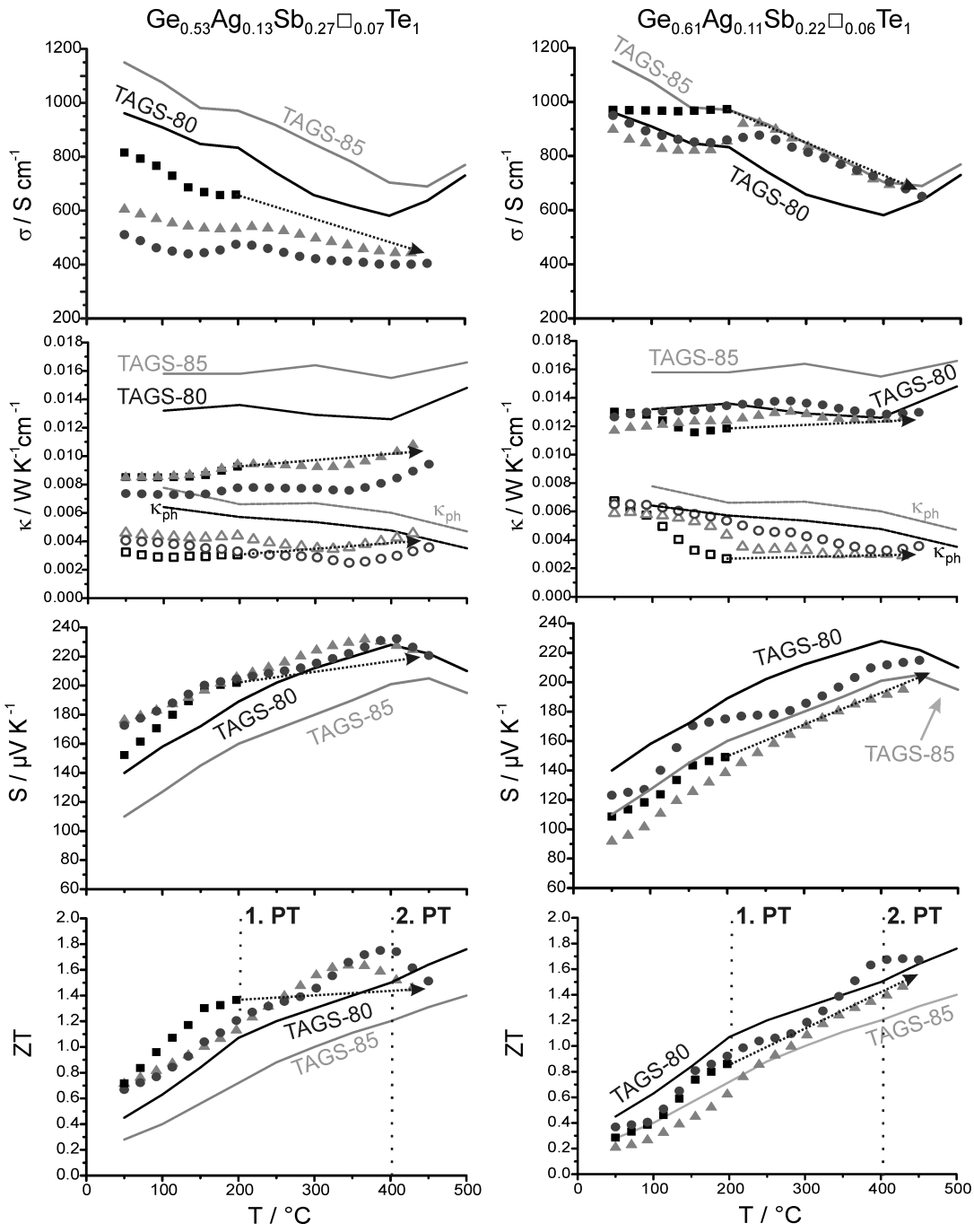

Fig. 5: Electrical conductivity σ, thermal conductivity κ (phononic contribution κ_{ph} with empty symbols), Seebeck coefficient S and ZT values (top to bottom; first heating cycle: black squares, first cooling cycle: gray triangles, second heating cycle: dark gray circles – some slight offsets are within the error limits of the methods and result from re-mounting the samples) of $Ge_{0.53}Ag_{0.13}Sb_{0.27}\square_{0.07}Te_1$ (left) and $Ge_{0.61}Ag_{0.11}Sb_{0.22}\square_{0.06}Te_1$ (right) in comparison to TAGS-80 (black line) and TAGS-85 (gray line) as taken from ref. [19] with recalculated κ_{ph} (marked by black/gray κ_{ph} for TAGS-80 and TAGS-85, respectively); in the ZT plot the phase transition temperatures (1. and 2. PT as discussed in the text) are marked by dotted lines; the values between 200 °C and 450 °C during the first heating cycle are not shown (the arrows just indicate further heating) because they are strongly affected by slow irreversible phase transitions (see discussion).

Below 200 °C, $Ge_{0.53}Ag_{0.13}Sb_{0.27}\square_{0.07}Te_1$ outperforms both TAGS-80, TAGS-85 and other recently reported high-performance TAGS materials.[17,24] The properties of the isotropic nanostructured modification at the beginning of the first heating cycle are remarkable although they could only be exploited if the samples are never heated over 200 °C. The *ZT* value of 1.3 at 160 °C, i.e. below any phase transition temperature, is higher than that of TAGS-80 (or any other TAGS sample) at the same temperature. While σ and *S* of $Ge_{0.53}Ag_{0.13}Sb_{0.27}\square_{0.07}Te_1$ are comparable to those of TAGS-80, the high *ZT* value is due to the low thermal conductivity; especially its phononic contribution (calculated with a Lorenz number as reported for TAGS materials with vacancies of $2 \cdot 10^{-8}$ V^2K^{-2})[24] is significantly reduced in comparison to TAGS materials without vacancies. However, these favorable values may additionally be associated with a change in the carrier concentration and mobility, which is another consequence of the adjusted Ag/Sb ratio.[26] For the consecutive cooling and heating cycle, the *ZT* values are in good accordance with the values recently published for TAGS materials with Ag/Sb rations deviating from 1.[24,26]

For $Ge_{0.61}Ag_{0.11}Sb_{0.22}\square_{0.06}Te_1$, consecutive heating and cooling cycles vary less than for the sample with the slightly higher cation vacancy concentration. The lattice contribution to the thermal conductivity is again lower than the one observed for conventional TAGS materials, but not as low as for $Ge_{0.53}Ag_{0.13}Sb_{0.27}\square_{0.07}Te_1$, and increases when the nanostructure vanishes. σ and *S* are comparable to TAGS-85, while κ corresponds to TAGS-80. This leads to slightly higher *ZT* values than those of TAGS-85, but it does not outperform TAGS-80 and other high-performance TAGS materials. These observations clearly show the huge influence of minor changes of the vacancy concentration.

3.6.4 Conclusion

The best conventional vacancy-free TAGS materials, i.e. TAGS-80 and TAGS-85 differ only little concerning their chemical composition: by 6 atom% for Ge and 3 atom% for Ag and Sb. Thus, there is a rather limited compositional range for further optimization. We focus on two homogeneous compounds with optimized Ag/Sb ratio, involving the presence of cation vacancies. According to the present investigation, the enhanced thermoelectric properties result from these more or less short-range ordered cation vacancies. They might act as phonon scattering centers as indicated by the significant reduction of the phononic contribution to the thermal conductivity while the good electrical properties remain almost unchanged in comparison to conventional vacancy-free TAGS materials. The cation vacancy concentration

also plays a crucial role concerning the structural chemistry of TAGS materials. For high cation vacancy concentrations, the structures are in remarkable contrast to those reported for conventional TAGS materials.[11-14,19] Both $Ge_{0.53}Ag_{0.13}Sb_{0.27}\square_{0.07}Te_1$ and $Ge_{0.61}Ag_{0.11}Sb_{0.22}\square_{0.06}Te_1$ can be quenched to form metastable compounds with a rocksalt-type average structure and layer-like short-range ordered vacancies. In contrast, lower vacancy concentrations as in $Ge_{0.77}Ag_{0.07}Sb_{0.13}\square_{0.03}Te_1$ lead to a TAGS-like α-GeTe-type structure which implies that cation ordering effects do not play an important role.

Quenched, nanostructured compounds with high cation vacancy concentrations exhibit two phase transitions. An irreversible transition leads from a (pseudo-)cubic "parquet-like" multi-domain nanostructure to a long-periodically ordered trigonal one and a second, reversible transition to a cubic rocksalt-type HT phase. Although the partial irreversibility and phase transitions in general may be viewed as drawbacks concerning thermal cycling, nanostructured $Ge_{0.53}Ag_{0.13}Sb_{0.27}\square_{0.07}Te_1$ may be applied far below any phase transition temperature, where it exhibits a *ZT* value of 1.3 at 160 °C. Annealed samples, or those heated over 200 °C just once, exhibit only one reversible phase transition. Their thermoelectric properties still differ from conventional vacancy-free TAGS, as do their structures. These findings are in good accordance with the values recently published for high-performance TAGS materials.[23,24,26] Our results clearly illustrate how the structural chemistry of this multinary system can be significantly changed even when the composition is varied only slightly as this involved a much more pronounced relative change of the vacancy concentration. In addition to altered charge carrier concentrations, different short- or long-range ordering variants of the cation vacancies significantly influence the thermoelectric properties and are one reason for the high performance of TAGS material with an Ag/Sb ratio differing from 1. It remains an open question if conventional TAGS materials, despite the fact that their chemical formulas formally suggest vacancy-free structures, may also exhibit a certain amount of vacancies that contribute to their performance.

Acknowledgement

We thank Thomas Miller and Christian Minke (LMU Munich) for the temperature-dependent powder diffraction experiments and for SEM-EDX analyses, respectively. We are grateful to Prof. Dr. W. Schnick (LMU Munich) for the generous support of this work. Furthermore, we thank Fivos Drymiotis (California Institute of Technology) for help with the thermoelectric measurements. This investigation was funded by the Deutsche Forschungsgemeinschaft (grant OE530/1-2) and the Studienstiftung des deutschen Volkes (scholarship for T.S.).

3.6.5 Supplementary information

Table S1. Results from EDX analyses (SEM, 6 point analyses averaged per compound).

sample	atom-% (calculated)	atom-% (experimental)
$Ge_{0.53}Ag_{0.13}Sb_{0.27}\square_{0.07}Te_1$	Ge: 27.6; Ag: 6.9; Sb: 13.8; Te: 51.7	Ge: 29.0(12); Ag: 6.5(3); Sb: 14.6(4); Te: 49.9(7)
$Ge_{0.61}Ag_{0.11}Sb_{0.22}\square_{0.06}Te_1$	Ge: 31.4; Ag: 5.7; Sb: 11.4; Te: 51.4	Ge: 32.8(9); Ag: 5.2(2); Sb: 12.4(3); Te: 49.7(7)
$Ge_{0.77}Ag_{0.07}Sb_{0.13}\square_{0.03}Te_1$	Ge: 39.0; Ag: 3.4; Sb: 6.8; Te: 50.8	Ge: 39.9(4); Ag: 3.6(3); Sb: 6.9(3); Te: 49.8(6)

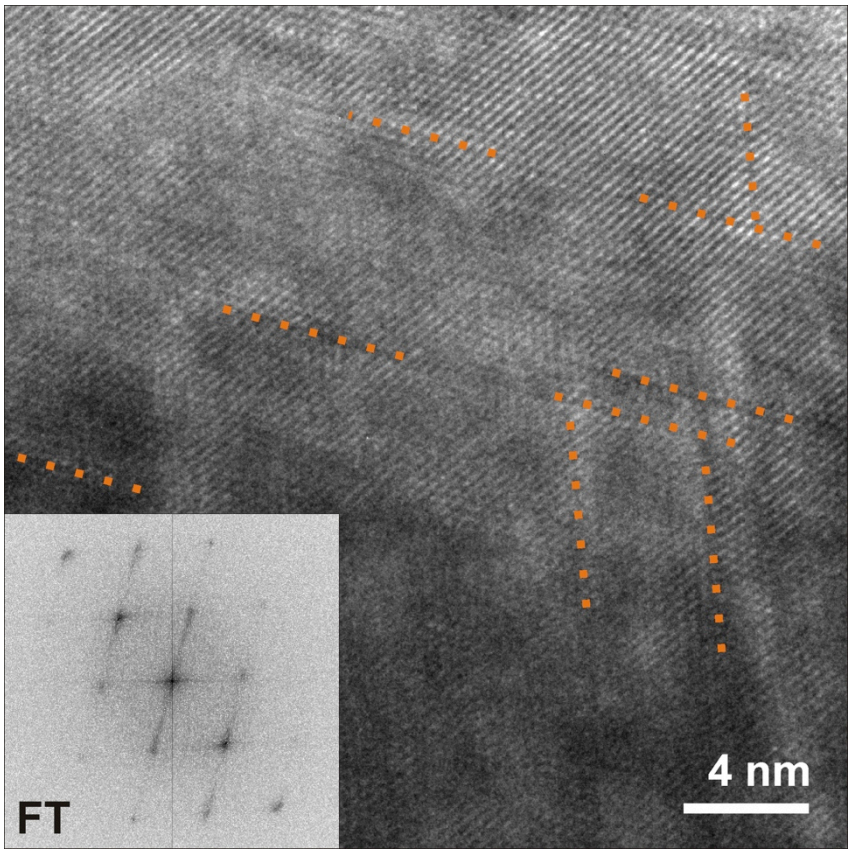

Fig. S1: HRTEM image of quenched $Ge_{0.53}Ag_{0.13}Sb_{0.27}\square_{0.07}Te_1$ (zone axis [110]) with the corresponding Fourier transform (inset). Some vacancy layers are highlighted (dotted orange lines).

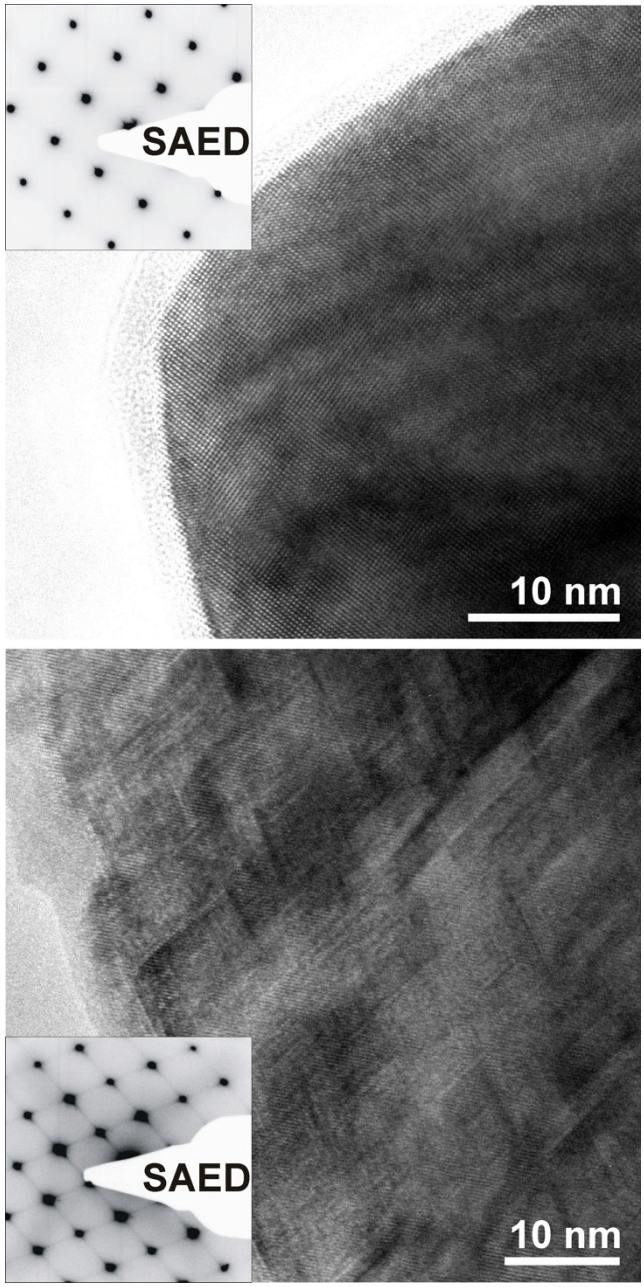

Fig. S2: HRTEM images of quenched $Ge_{0.61}Ag_{0.11}Sb_{0.22}\square_{0.06}Te_1$ (top: zone axis [100], bottom: zone axis [110]) with the corresponding selected-area electron diffraction patterns of the crystallites (insets).

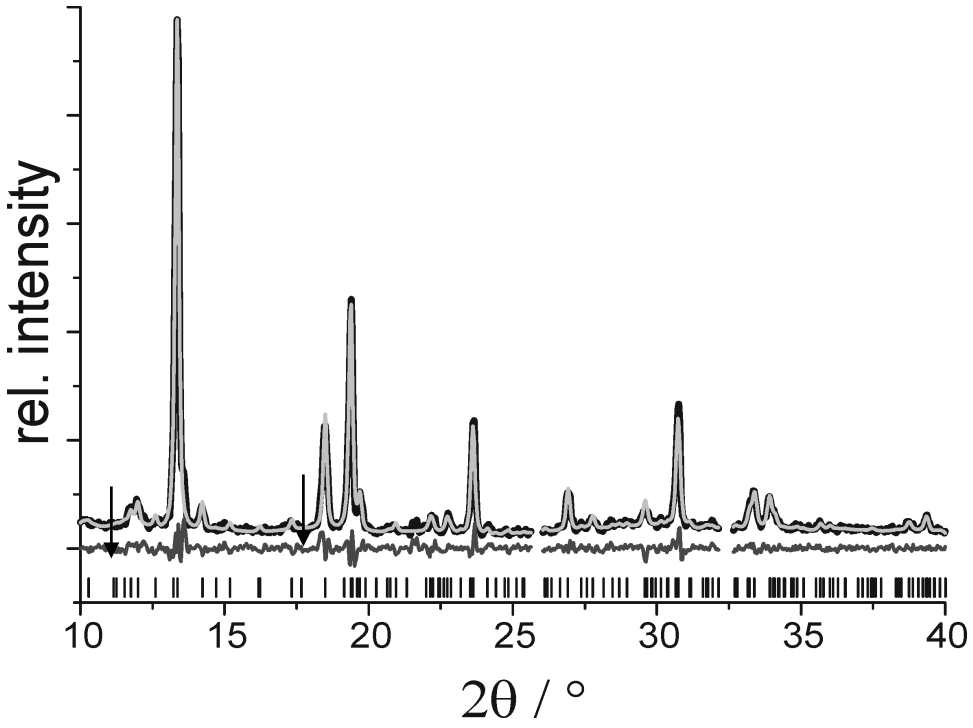

Fig. S3: Rietveld refinement of $Ge_{0.53}Ag_{0.13}Sb_{0.27}\square_{0.07}Te_1$ in its trigonal long-periodically ordered layered 15*P*-$Ge_5As_2Te_8$ type structure (slowly cooled from the HT phase after the heating experiment): experimental (black) and calculated (light gray) powder diffraction patterns, difference plots (dark gray) and peak positions (black lines); space group *P*3*m*1 (no. 164), a = 4.2136(3) Å; c = 27.711(4) Å, R_p = 0.0812, R_{wp} = 0.1087, R_{Bragg} = 0.0275. Reflections caused by the furnace at ca. 26° and 32.4° 2θ were excluded; arrows highlight the most significant reflections indicating long-range order (also visible and highlighted in the temperature-dependent PXRD patterns in the text).

Table S2. Atom positions, occupancy factors (s.o.f., atom distribution not refined), and displacement factors (B_{iso} in Å^2, common for cations and anions respectively) of $Ge_5As_2Te_8$ type $Ge_{0.53}Ag_{0.13}Sb_{0.27}\square_{0.07}Te_1$

sample	atom	x y z	s.o.f.	B_{iso}
$Ge_{0.53}Ag_{0.13}Sb_{0.27}\square_{0.07}Te_1$	Ge Ag Sb	0 0 0	4/7 1/7 2/7	1.6(3)
	Te	2/3 1/3 0.064(1)	1	0.8(2)
	Ge Ag Sb	1/3 2/3 0.136(1)	4/7 1/7 2/7	1.6(3)
	Te	0 0 0.191(1)	1	0.8(2)
	Ge Ag Sb	2/3 1/3 0.254(2)	4/7 1/7 2/7	1.6(3)
	Te	1/3 2/3 0.320(1)	1	0.8(2)
	Ge Ag Sb	0 0 0.392(2)	4/7 1/7 2/7	1.6(3)
	Te	2/3 1/3 0.447(1)	1	0.8(2)

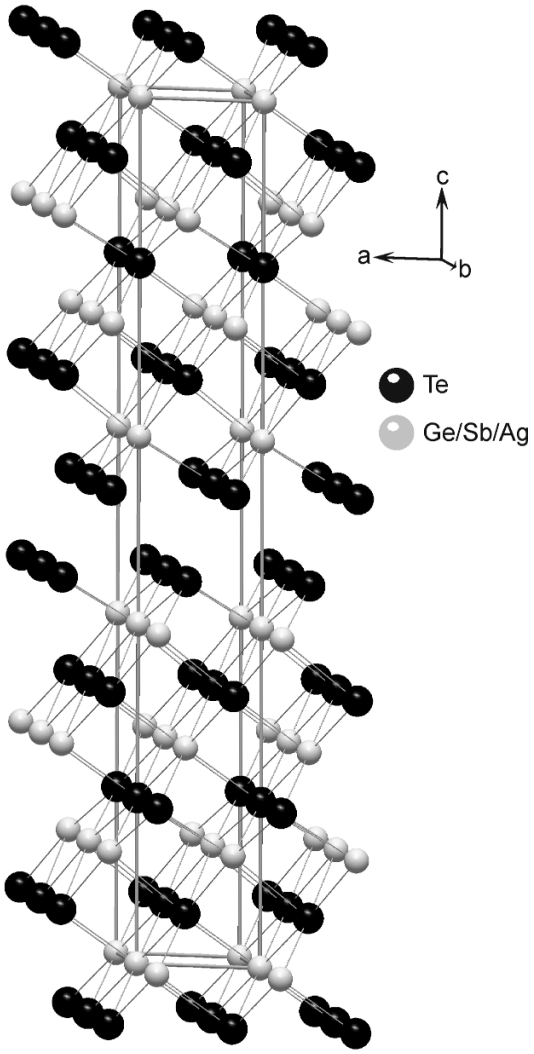

Fig. S4: Crystal structure of 15*P*-type $Ge_{0.53}Ag_{0.13}Sb_{0.27}\square_{0.07}Te_1$, formed after slowly cooling the cubic high-temperature phase to room temperature.

3.6.6 References

[1] J. R. Sootsman, D. Y. Chung, M. G. Kanatzidis, *Angew. Chem. Int. Ed.* **2009**, *48*, 8616.

[2] C. Wood, *Rep. Prog. Phys.* **1988**, *51*, 459.

[3] D. T. Morelli, V. Jovovic, J. P. Heremans, *Phys. Rev. Lett.* **2008**, *101*, 035901.

[4] T. Schröder, T. Rosenthal, D. Souchay, C. Petermayer, S. Grott, E.-W. Scheidt, C. Gold, W. Scherer, O. Oeckler, *J. Solid State Chem.* **2013**, *206*, 20.

[5] R. Mohanraman, R. Sankar, K. M. Boopathi, F.-C. Chou, C.-W. Chu, C.-H. Lee, Y.-Y. Chen, *J. Mater. Chem. A* **2014**, *2*, 2839.

[6] K. F. Hsu, S. Loo, F. Guo, W. Chen, J. S. Dyck, C. Uher, T. Hogan, E. K. Polychroniadis, M. G. Kanatzidis, *Science* **2004**, *303*, 818.

[7] W. G. Zeier, Y. Z. Pei, G. Pomrehn, T. Day, N. Heinz, C. P. Heinrich, G. J. Snyder, W. Tremel, *J. Am. Chem. Soc.* **2013**, *135*, 726.

[8] A. Yusufu, K. Kurosaki, Y. Ohishi, H. Muta, S. Yamanaka, *Jpn. J. Appl. Phys.* **2013**, *52*, 081801.

[9] T. Plirdpring, K. Kurosaki, A. Kosuaga, T. Day, S. Firdosy, V. Ravi, G. J. Snyder, A. Harnwunggmoung, T. Sugahara, Y. Ohishi, H. Muta, S. Yamanaka, *Adv. Mater.* **2012**, *24*, 3622.

[10] R. Liu, L. Xi, H. Liu, X. Shi, W. Zhang, L. Chen, *Chem. Commun.* **2012**, *48*, 3818.

[11] B.A. Cook, M. J. Kramer, X. Wei, J. L. Harringa, E. M. Levin, *J. Appl. Phys.* **2007**, *101*, 053715.

[12] S. K. Plachkova, *Phys. Status Solidi A* **1984**, *83*, 349.

[13] S. H. Yang, T. J. Zhu, T. Sun, S. N. Zhang, X. B. Zhao, J. He, *Nanotechnol.* **2008**, *19*, 245707.

[14] F. D. Rosi, J. P. Dismukes, E. F. Hockings, *Electron. Eng.* **1960**, *79*, 450.

[15] W. Klemm, G. Frischmuth, *Z. Anorg. Allg. Chem.* **1934**, *218*, 249.

[16] J. Goldak, C. S. Barrett, D. Innes, W. Youdelis, *J. Chem. Phys.* **1966**, *44*, 3323.

[17] J. Davidow, Y. Gelbstein, *J. Electron. Mater.* **2013**, *42*, 1542.

[18] X. Shi, J. R. Salvador, J. Yang, H. Wang, *Sci. Adv. Mater.* **2011**, *3*, 667.

[19] T. Schröder, S. Schwarzmüller, C. Stiewe, J. de Boor, M. Hölzel, O. Oeckler, *Inorg. Chem.* **2013**, *52*, 11288.

[20] T. Schröder, T. Rosenthal, N. Giesbrecht, S. Maier, E.-W. Scheidt, W. Scherer, G. J. Snyder, W. Schnick, O. Oeckler, *J. Mater. Chem. A* **2014**, *2*, 6384.

[21] E. M. Levin, B. A. Cook, J. L. Harringa, S. L. Bud'ko, R. Venkatasubramanian, K. Schmidt-Rohr, *Adv. Funct. Mater.* **2011**, *21*, 441.

[22] E. M. Levin, S. L. Bud'ko, K. Schmidt-Rohr, *Adv. Funct. Mater.* **2012**, *22*, 2766.

[23] G. C. Christakudis, S. K. Plachkova, L. E. Shelimova, E. S. Avilov, *Phys. Status Solidi A* **1991**, *128*, 465.

[24] T. Zhu, H. Gao, Y. Chen, X. B. Zhao, *J. Mater. Chem. A* **2014**, *2*, 3251.

[25] Y. Chen, B. He, T. J. Zhu, X. B. Zhao, *J. Phys. D: Appl. Phys.* **2012**, *45*, 115302.

[26] Y. Chen, C. M. Jaworski, Y. B. Gao, H. Wang, T. J. Zhu, G. J. Snyder, J. P. Heremans, X. B. Zhao, *New J. Phys.* **2014**, *16*, 013057.

[27] M. N. Schneider, T. Rosenthal, C. Stiewe, O. Oeckler, *Z. Kristallogr.* **2010**, *225*, 463.

[28] T. Rosenthal, M. N. Schneider, C. Stiewe, M. Döblinger, O. Oeckler, *Chem. Mater.* **2011**, *23*, 4349.

[29] *TOPAS-Academic*, *V. 4.1*, Coelho Software, Brisbane, Australia, **2007**.

[30] *WINXPOW*, *v2.12 ed.*, Stoe & Cie GmbH, Darmstadt, Germany, **2005**.

[31] *DigitalMicrograph 3.6.1*, Gatan Software, Pleasanton, USA, **1999**.

[32] P. A. Stadelmann, *Ultramicroscopy* **1987**, *21*, 131.

[33] *ESVision*, *4.0.164*, Emispec Systems Inc., Tempe, USA, **1994-2002**.

[34] K. A. Borup, E. S. Toberer, L. D. Zoltan, G. Nakatsukasa, M. Errico, J. P. Fleurial, B. B. Iversen, G. J. Snyder, *Rev. Sci. Instrum.* **2012**, *83*, 123902.

[35] L. J. van der Pauw, *Philips Res. Rep.* **1958**, *13*, 1.

[36] S. Iwanaga, E. S. Toberer, A. LaLonde, G. J. Snyder, *Rev. Sci. Instrum.* **2011**, *82*, 063905.

[37] T. Rosenthal, P. Urban, K. Nimmrich, L. Schenk, J. de Boor, C. Stiewe, O. Oeckler, *Chem. Mater.* **2014**, *26*, 2567.

[38] M. N. Schneider, O. Oeckler, *Z. Anorg. Allg. Chem.* **2008**, *634*, 2557.

4 Synergism of electron microscopy and synchrotron diffraction methods

4.1 Overview

Electron and X-ray methods often deliver complementary structural information. While X-ray diffraction can be used to elucidate the average structure as well as temperature-dependent phase transitions, electron microscopy is the most efficient way to analyze real-structure effects and assign small grains in inhomogeneous samples. If such crystallites are not large enough for conventional single-crystal X-ray diffraction, a combination of transmission electron microscopy (TEM) and X-ray synchrotron microdiffraction is an efficient way to determine the crystal structure (Chapter 4.2). The high spatial resolution could also be used to track reaction mechanism as well as nucleation phenomena. The combination of synchrotron methods and electron diffraction can be employed to obtain detailed information on site occupancies, e.g. in long-periodically ordered structures of germanium antimony tellurides (GST materials) and substitution variants with Sn or In. Nevertheless, due to the similar electron counts of Sn, In and Sb and the resulting lack of scattering contrast, the use of resonant diffraction is required to determine the element variation in powder samples (Chapter 4.3) and in single crystals (Chapter 4.4 as well as references [1] and [2]) of Sn- or In-containing GST materials. Synchrotron radiation is suitable to reach wavelengths near the adsorption edges of the elements as required for resonant scattering. The corresponding structure refinements show that Sb preferably occupies the position near the van der Waals gaps in the long-periodically ordered GST compounds and Sn- or In-substituted variants thereof. In shows a tendency to occupy the positions at the center of the rocksalt-type slabs,[1] while the Sn distribution differs with the thickness of the rocksalt-type building blocks (Chapters 4.3 and 4.4). In Sb-rich $M_{0.067}Sb_{0.667}Te_{0.266}$ (M = Ge, Sn) that consists consist of Sb_2Te_3 slabs alternating with four antimony layers that represent the gray arsenic type, high resolution TEM (HRTEM) images show a contrast variation that corresponds to a changing element distribution. Resonant scattering reveals the partial substitution of Sb by GeTe and SnTe.[2] TEM investigations of thinned single crystals of $(Ge_{0.5}Sn_{0.5}Te)_4Sb_2Te_7$ reveal a new superstructure of the cubic basis structure and a complex hierarchical nanostructure that consists of slabs with a parallel arrangement of equidistant defect layers corresponding to the thermodynamically stable layered structure embedded in a matrix with the parquet-like structure (Chapter 4.3).

References

[1] F. Fahrnbauer, P. Urban, S. Welzmiller, T. Schröder, T. Rosenthal, O. Oeckler, *Solid State Sci.* **2013**, *208*, 20.

[2] M. N. Schneider, F. Fahrnbauer, T. Rosenthal, M. Döblinger, C. Stiewe, O. Oeckler, *Chem. Eur. J.* **2012***, 18,* 1209.

4.2 Complementary use of electron microscopy and synchrotron diffraction for structure analysis

The structure determination of novel compounds has always been a major field of research in solid-state chemistry. The easiest and most common way to elucidate the structure of unknown materials is single-crystal X-ray diffraction. However, the required crystal size remains a constraint for various materials where such single crystals cannot be obtained. As long as the materials are crystalline on the microscale, X-ray powder diffraction can often be used for the structure determination if phase-pure materials are obtained or if sufficient information about the side phases is available. Without optimizing the synthesis conditions, which may be very time-consuming, new materials are often neither phase pure nor exhibit "large" crystals. Precipitates with diameters of less than one micrometer are often desirable for example for the reduction of the phonon proliferation in thermoelectric materials. Also the investigation of reaction mechanisms, e.g. nucleation phenomena during phase transitions, would greatly benefit from the possibility of investigating sub-micrometer crystals. In recent years, electron crystallography has become a powerful tool to overcome the scatter power restrictions of X-ray diffraction. Due to the strong interaction of electrons with matter, crystallites of down to 20 nm diameter can be investigated. Novel methods like automated diffraction tomography (ADT)[1-3] or rotation electron diffraction (RED)[4] generate and process electron-diffraction data analogous to conventional X-ray single-crystal diffraction methods. The elucidation of various structures like that of the oxonitridophosphates SrP_3N_5O[5] and $Ba_6P_{12}N_{17}O_9Br_3$[6] as well as the complex intergrown zeolite ITQ-39[7] have demonstrated the potential of these methods. A wide variety of data from structures with different complexity ranging from elemental Mn over $BaSO_4$ and $Eu_2Si_5N_8$ to unknown oxonitridophosphates obtained at the electron microscopes available at the LMU Munich show that without the use of precession electron diffraction (PED), the structure solution is often ambiguous. PED patterns resemble those based on the kinematic approximation since multiple scattering is significantly reduced by precessing the electron beam.[8] The data manually acquired with tilt ranges between 45° and 120° and tilt steps down to 0.2° can be processed by the ADT software package.[1-3] Straightforward determination of the lattice parameters is, in most cases, possible even with tilt ranges of only 60°. The best data sets collected of $BaSO_4$ and $Eu_2Si_5N_8$ (tilt range 120°) are sufficient for structure solution. The main problem is that the "classical" computer programs for structure determination do not

consider the dynamical effects which often strongly affect the intensities in electron-diffraction patterns. Even when PED patterns of very thin specimens are available, atom parameters with a precision comparable to that of single-crystal X-ray structure analyses are not accessible. Synchrotron radiation with high brilliance can be used to obtain high-quality kinematical data for crystals with diameters smaller than 1 micrometer. A major problem in dealing with such small crystals is their selection and alignment in the synchrotron beam. The problem can be overcome by the combined use of synchrotron and TEM experiments.

Electron microscopy can be used to preselect the desired crystals according to their diffraction patterns (crystallinity and d-values) and composition. Thereby one can confirm that the crystals are not affected by real-structure phenomena and that a selected region is well crystallized. The crystal position on the grid is recorded by images with different magnifications so that it can be recovered at the synchrotron facility, where a data set is measured from which the structure can be solved and refined.

This method was successfully applied to different chemical systems where inhomogeneous samples with small crystals cannot be measured with laboratory single-crystal diffraction methods. Synchrotron microfocus data were acquired at the beamline ID11 (ESRF, Grenoble). The preselected crystals were optically positioned in the beam and the centering was optimized by fluorescence scans.

The structure of $Pb_8Sb_8S_{15}Te_5$ ($P4_1$, a = 8.0034(11) Å, c = 15.022(3) Å) was solved and refined from data obtained with a beam diameter of 0.7 x 1.5 μm. The refined atom parameters are comparable to state-of-the-art single-crystal structure refinements; they are sufficient for all common discussions, e.g. bond valence sum calculations. This compound is the first lead antimony sulfide telluride. It is isostructural to Tl_3PbCl_5, detailed information is provided in Ref.[9,10].

The structure of a melam-melem co-crystal was elucidated using a sample that consisted of crystals of melem, melam and the co-crystals. Due to pronounced reflection overlap, structure analysis from X-ray powder diffraction was not possible. From SAED patterns as well as from ADT measurements only the unit-cell metrics of the co-crystal could be determined due to significant beam damage during the prolonged exposure to the electron beam. However, it was possible to preselect a co-crystal according to its metrics and to obtain data sets at the synchrotron from which the structure was solved and refined ($P\bar{1}$, a = 4.56(2) Å, b = 19.34(8) Å, c = 21.58(11) Å, α = 73.34(11)°, β = 89.1(2)°, γ = 88.4(2)°). It consists of 4 melam and 4 melem molecules in the unit cell as shown in Figure 1.

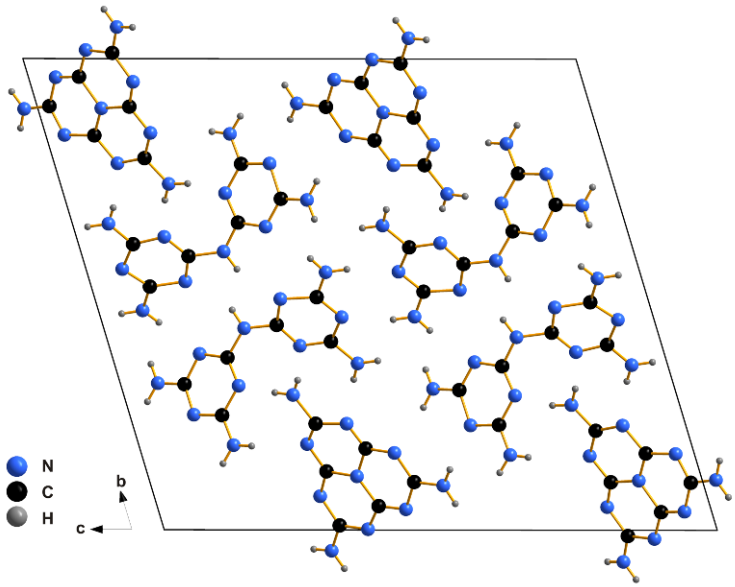

Fig. 1: Structure of the melam-melem co-crystal (zone axis [100]) with 4 melam and 4 melem molecules in the unit cell (black)

With the same strategy, the structure of the novel oxonitridophosphate "$(Ca,Mg)_7P_{18}ON_{34}$" was elucidated from a data set obtained from a crystallite of several micrometer with a well crystallized areas of only 1.5 x 1.5 µm which was obtained as a side-phase during high-pressure syntheses.[11] The preliminary composition was derived from the experimental data under the assumption of charge balance. The compound ($P6_3/m$, a = 14.122(2) Å, c = 8.1068(16) Å) crystallizes in a network of corner-sharing $P(O,N)_4$ tetrahedra and Ca/Mg atoms (Figure 2).

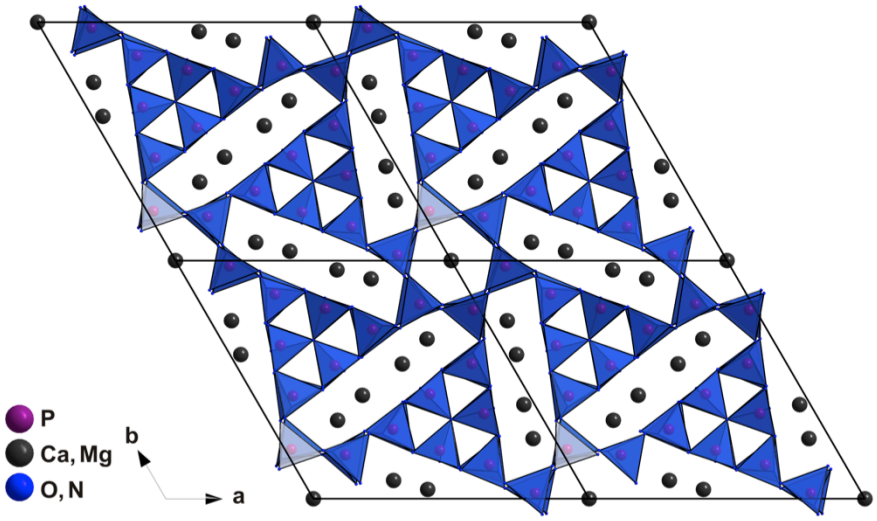

Fig. 2: Structure of "$(Ca,Mg)_7P_{18}ON_{34}$"; viewing direction along [001]; the $P(N,O)_4$ tetrahedra are shown; O and N are not distinguished

Especially in thermoelectric materials the identification of precipitates by TEM, followed by the collection of datasets of the matrix and the precipitates by means of synchrotron micro-diffraction is very interesting. The structure models of both precipitates and matrix shall be used to simulate HRTEM images and identify how the matrix and the precipitates are intergrown. According to this approach, the distortion of the characteristic Sb_4 units of skutterudite-type precipitates in a GST matrix (as shown in Figure 3) can be correlated with the degree of substitution of Sb by GeTe.[12] The GST matrix exhibits a rocksalt-type structure with neither split positions nor symmetry reduction.

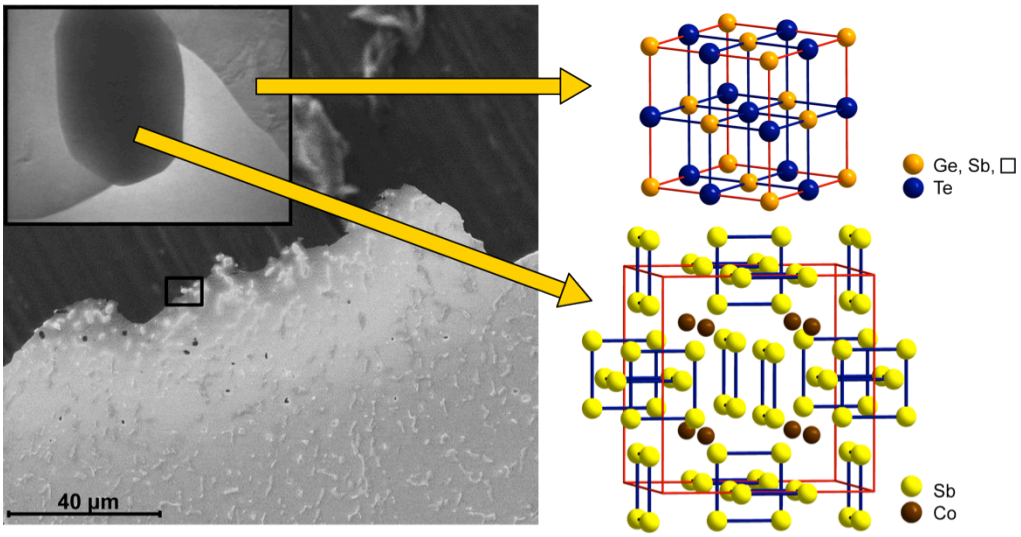

Fig. 3: Scanning electron micrograph with STEM inset of a skutterudite-type precipitate in a GST matrix (left side); structure models of the rocksalt-type GST matrix (top right) and the skutterudite-type precipitate (bottom right); the Sb_4 units of skutterudite are marked with blue rectangles.

Reference

[1] U. Kolb, T. Gorelik, C. Kübel, M. T. Otten, D. Hubert, *Ultramicroscopy* **2007**, *107*, 507.

[2] U. Kolb, T. Gorelik, M. T. Otten, *Ultramicroscopy* **2008**, *108*, 763.

[3] E. Mugnaioli, T. Gorelik, U. Kolb, *Ultramicroscopy* **2009**, *109*, 758.

[4] D. Zhang, P. Oleynikov, S. Hovmöller, X. D. Zou, *Z. Kristallogr.* **2010**, 225, 94.

[5] S. J. Sedlmaier, E. Mugnaioli, O. Oeckler, U. Kolb, W. Schnick, *Chem. Eur. J.* **2011**, *17*, 11258.

[6] E. Mugnaioli, S. J. Sedlmaier, O. Oeckler, U. Kolb, W. Schnick, *Eur. J. Inorg. Chem.* **2012**, 121.

[7] T. Willhammar, J. Sun, W. Wan, P. Oleynikov, D. Zhang, X. D. Zou, M. Moliner, J. Gonzalez, C. Martinez, F. Rey, A. Corma, *Nature Chem.* **2012**, *4*, 188.

[8] P. Oleynikov, S. Hovmöller, X. D. Zou, *Ultramicroscopy* **2007**, *107*, 523.

[9] T. Schmutzler, *Masterarbeit*, **2013**, IMKM Leipzig

[10] F. Fahrnbauer, T. Rosenthal, T. Schmutzler, G. Wagner, G. Vaughan, J. Wright, O. Oeckler, *unpublished results*

[11] F. Fahrnbauer, P. Schultz, *unpublished results*

[12] F. Fahrnbauer, *unpublished results*

4.3 Novel superstructure of the rocksalt type and element distribution in germanium tin antimony tellurides

T. Rosenthal, S. Welzmiller, L. Neudert, P. Urban, A. Fitch, O. Oeckler

J. Solid. State Chem. **2014**, *219*, 108-117.

Abstract

A superstructure of the rocksalt-type observed in quenched CVT-grown single crystals of $Ge_{3.25(7)}Sn_{1.10(3)}Sb_{1.10(3)}Te_6$ was elucidated by X-ray diffraction using fourfold twinned crystals (space group $P\bar{3}m1$, a = 4.280(1) Å, c = 20.966(3) Å). The structure is built up of distorted rocksalt-type building blocks typical for long-range ordered GST materials and substitution variants thereof. In contrast to those phases, an exclusive ABC-type cubic stacking sequence of the Te-atom layers is present. High-resolution electron microscopy reveals spheroidal domains with this structure (average diameter 25 nm) whose stacking direction is perpendicular to the <111> directions of the basic rocksalt-type structure. Additional slab-like domains with a lateral extension up to 1 µm occasionally result in a hierarchical structure motif. Due to the similar electron counts of the elements involved, resonant diffraction was used in order to elucidate the element distribution in rocksalt-type building blocks of the stable layered compound 39*R*-$Ge_3SnSb_2Te_7$ ($R3m$, a = 4.24990(4) Å, c = 73.4677(9) Å). Sb tends to occupy the atom site close to the van der Waals gaps while Ge concentrates in the center of the building blocks.

4.3.1 Introduction

Germanium antimony tellurides $(GeTe)_nSb_2Te_3$ (GST materials) are widely used as phase-change materials (PCMs) in rewritable optical data storage media.[1,2] The substitution with Sn in thin films of $(GeTe)_nSb_2Te_3$, which was predominantly studied for n = 2, decreases the melting point and increases the crystallization speed and thereby the performance of these PCMs.[3-11] For the same reasons, the substitution with Sn is also beneficial for the application in PCRAM devices.[12,13] The low thermal conductivities that are typical for PCMs are also desirable for thermoelectric materials.[14] Sn substitution in compounds with n = 1 or 2 leads to lower thermal conductivities; however, 21*R*-$Ge_{0.6}Sn_{0.4}Sb_2Te_4$ and 9*P*-$Ge_{1.3}Sn_{0.7}Sb_2Te_5$ exhibit only slightly higher thermoelectric figures of merit (*ZT*)

than the unsubstituted variants.[15] The *ZT* value describes the efficiency of thermoelectric materials and is determined by the Seebeck coefficient (*S*), the electrical conductivity (σ) and the thermal conductivity (κ): $ZT = S^2 \cdot \sigma \cdot \kappa^{-1} \cdot T$, where T is the absolute temperature. For $Ge_1Sb_2Te_4$ and $Ge_2Sb_2Te_5$ (i.e. n = 1 and 2), the Seebeck coefficients are not affected by the substitution of Ge by Sn and reach a maximum of ~85 μV/K, resulting in *ZT* values of up to 0.25 at 400 °C.[15] Higher GeTe contents in $(GeTe)_nSb_2Te_3$ with n = 7, 12, 19 are associated with higher Seebeck coefficients and, as a rule, higher *ZT* values.[16,17] The positive effect of the Sn substitution on the *ZT* values is especially pronounced for samples with n = 4 and n = 7 where a 50% substitution of Ge with Sn results in doubled and tripled *ZT* values at 400 °C, respectively.[17] For these GeTe contents, the lattice thermal conductivity of the Sn-substituted samples is by 0.4-0.5 W/m K higher compared to the unsubstituted samples up to 250 °C. The lattice contributions to the thermal conductivity converge to ~ 1.0 W/m K for both substituted and unsubstituted samples above 250 °C and when slowly cooled to room temperature.

For GST materials with GeTe contents n > 3, stable high-temperature (HT) phases contain randomly disordered cation vacancies in a cubic rocksalt-type structure. In these cases, the structure of quenched samples differs from that of the thermodynamically stable layered phases. Quenching the HT phase involves short-range ordering of the vacancies which, in general, leads to thermal conductivities that are lower than those of the layered phases. The latter are present in slowly cooled samples and also in quenched bulk samples with n = 1 and 2. They are trigonal and consist of rocksalt-type slabs separated by van der Waals gaps with a hexagonal stacking (i.e. ABAB) of the Te-atom layers across the gaps. The thickness of the rocksalt-type slaps is determined by the GeTe content (n). These layered phases are comparable to the members of the binary system $(Sb_2Te_3)_m(Sb_2)_n$ where additional Sb_2 layers instead of the additional GeTe layers are introduced between the Sb_2Te_3 slabs, which has been shown to result in higher thermoelectric power factors compared to Sb_2Te_3 (up to 80 μV/K at 650 °C for SbTe and Sb_8Te_9).[18] Electron diffraction patterns revealed rather large translation periods in $Ge_8Sb_2Te_{11}$;[19] its structure corresponds that of $Ge_5As_2Te_8$ with a hexagonal stacking of the Te layers across the van der Waals gaps.[20] In quenched bulk samples $(GeTe)_nSb_2Te_3$ with $n \geq 3$, diffusion pathways required to reach the trigonal structure are longer than for n = 1 or 2 and therefore only short-range ordering occurs during rapid cooling. The vacancies form defect layers with limited lateral extension which are oriented perpendicular to the <111> directions of the cubic phase. Metastable solid solutions $(Ge_{1-x}Sn_xTe)_nSb_2Te_3$ (n = 4, 7, 12; $0 \leq x \leq 1$) obtained by quenching also exhibit such defect

layers that may intersect.[16,17] More pronounced ordering of the vacancies results in parallel defect layers whose lateral extension depends on the vacancy concentration and atom mobility. These determine the size of the domains with parallel defect layers and, as a consequence, the degree of relaxation which is present at the defect layers. The thermodynamic equilibrium is reached when all vacancies are arranged in equidistant parallel defect layers which can then be viewed as van der Waals gaps. Their formation involves a change from the cubic ABC stacking of the Te-atom layers in the rocksalt type to a hexagonal ABAB one around the gaps, which also enables the blocks to move closer together and thus relieves strain that is present in quenches samples.[21]

The arrangement of vacancy layers and the element distribution in the distorted rocksalt-type building blocks are crucial in the chemistry of GST materials and Sn-substituted variants thereof. In quenched thin films of $Ge_2Sb_2Te_5$,[22] for example, scanning transmission electron microscopy (STEM) using a high-angle annular dark field (HAADF) detector revealed non-equidistant defect layers with limited lateral extension around which, according to simulations based on a rocksalt-type model, there is no significant relaxation and the cubic stacking of the HT phase is preserved. Their spatial arrangement perpendicular to all cubic <111> directions, which correspond to the [001] directions of the individual trigonal domains, is comparable to the situation in quenched bulk samples of GST materials with n = 3-19[16] and $(Ge_{1-x}Sn_xTe)_nSb_2Te_3$ (n= 4, 7, 12; $0 \leq x \leq 1$).[17] Like in many related compounds,[23] Sb in the layered trigonal compounds 21*R*-$Ge_{0.6}Sn_{0.4}Sb_2Te_4$ and 9*P*-$Ge_{1.3}Sn_{0.7}Sb_2Te_5$ concentrates near the van der Waals gaps while Ge prefers positions in the center of the rocksalt-type slabs.[15] Sn shows a slight preference for the position near the van der Waals gaps. The Te-Te distances at these gaps are nearly the same for 21*R*-$GeSb_2Te_4$,[24,25] 21*R*-$Ge_{0.6}Sn_{0.4}Sb_2Te_4$,[15] 21*R*-$SnSb_2Te_4$,[26] 9*P*-$Ge_{1.3}Sn_{0.7}Sb_2Te_5$,[15] 9*P*-$Ge_2Sb_2Te_5$[27] and 33*R*-$Ge_{4-x}Sb_{2-y}Te_7$ (x, y ≈ 0.1)[28] whereas the cation-anion bond lengths increase slightly with increasing Sn content.

Phase transitions in $(Ge_{1-x}Sn_xTe)_4Sb_2Te_3$ (x = 0.25 - 0.5) are comparable to those in the corresponding pure GST materials;[17] however, the local structure in the vicinity of the defect layers and the element distribution have not been elucidated yet. Diffraction patterns of Sn-doped GST materials discussed in this study indicate the presence of a novel superstructure of the rocksalt type.

4.3.2 Experimental

4.3.2.1 Synthesis

Samples were prepared by melting stoichiometric mixtures of the elements Ge (99.999 %, Sigma Aldrich), Sb (99.999 %, Smart Elements), Sn (99.999 %, Smart Elements), and Te (99.999 %, Alfa Aesar) in silica glass ampoules under argon atmosphere and subsequently quenching the ampoules in water. Samples with the nominal composition $Ge_2Sn_2Sb_2Te_7$ were melted at 950 °C for 1.5 h, annealed at 590 °C for 20 h and subsequently quenched in water again. Crystals were grown from ~ 90 mg of this product by chemical vapor transport (CVT) with ~ 15 mg iodine (99.9 %, AppliChem, dried over conc. H_2SO_4) from the hot side (595 °C) to the cold side (525 °C) of the ampoules (diameter 11 mm, length ~25 cm) in 3 days and subsequently cooled by removing them from the furnace. 39*R*-$Ge_3SnSb_2Te_7$ samples were prepared by melting a stoichiometric mixture at 950°C for 9 d, subsequent annealing at 380 °C for 9 d and cooling to room temperature (RT) by turning off the furnace (~ 2 h to RT).

4.3.2.2 Analytical methods

The phase purity of the samples was analyzed by powder X-ray diffraction which was performed on crushed samples fixed on Mylar foils. The data were collected on a Huber G670 powder diffractometer with an imaging plate detector in Guinier geometry using Cu-$K_{\alpha1}$ radiation (λ = 1.54051 Å, Ge(111) monochromator). The powder diffraction patterns were evaluated with TOPAS-Academic.[29]

Single crystals were mounted on glass fibers with vacuum grease and their quality was assessed with Laue photographs using a Buerger precession camera (Huber, Germany). X-ray data of the single crystals were obtained with Ag-$K_{\alpha1}$ radiation (λ = 0.56086 Å, graphite monochromator) on an IPDS-I diffractometer (Stoe, Germany) with an imaging plate detector. Reciprocal lattice sections were reconstructed using the diffractometer software. As detailed below and as evident from Fig. 2, crystals with the approximate composition $Ge_{3.26}Sb_{1.1}Sb_{1.1}Te_6$ exhibit a sixfold superstructure of the rocksalt type along one of its <111> directions. This involves fourfold twinning; however, all reflections of the diffraction pattern can be indexed on the basis of a common face-centered cubic "twin lattice" with a = 36.314(6) Å. Reflection intensities were integrated based on this lattice. For the refinement, data corresponding to the four twin-domain orientations were identified using the corresponding transformation matrices that describe the transition from the NaCl structure type to the superstructure observed. These data were combined in a SHELX HKLF 5 format

file,[30] the zero-intensity data at twin lattice nodes that did not correspond to any reflection of one of the domains were discarded. Semiempirical absorption correction based on the intensities of equivalent reflections was done using XPREP.[31] The refinement strategy is described in Section 3.2.

Resonant X-ray diffraction was done at beamline ID31 of the ESRF (Grenoble, France) on powdered samples in glass capillaries with diameters of 0.3 mm that were rotated during the measurements in order to improve particle distribution statistics. Data at wavelengths of the K-edges of the elements Te, Sb and Sn (cf. Table 1) and at a wavelength far away from these K-edges (λ = 0.354198(10) Å) were acquired with a bank of 9 point detectors (2° apart from each other), each one preceded by a Si(111) analyzer crystal.[32] The data was recorded in a continuous scan mode and afterwards merged, using a Si 670c standard sample (NIST) to calibrate the offset and the wavelength.[33] The lattice parameters and other wavelengths were refined against this reference. X-ray fluorescence as a function of the wavelength was measured with an energy-dispersive AXAS solid state detector (Ketek GmbH). From these data, the dispersion correction terms $\Delta f'$ and $\Delta f''$ of the elements at the wavelengths corresponding to their absorption edges were calculated with the program CHOOCH[34] based on the Kramers-Kronig transform.[35] These were used without further refinement; they are given in Table 1. Other dispersion correction terms were taken from Ref. [36]. The structure was refined taking into account all four datasets simultaneously. Reflection profiles were fitted with a fundamental parameters approach using TOPAS-Academic.[29] Preferred orientation (using 6^{th} order spherical harmonics) and strain parameters were considered individually for each data set. Anisotropic broadening of the reflections was refined according to Stephens's method[37] with one set of parameters for each data set (since data were obtained from different specimens of the same sample because of temperature-dependent measurements not reported here). The occupancy factors were refined assuming a fixed sum formula as derived from the nominal composition and verified by energy-dispersive X-ray spectroscopy (EDX, see below). Thus, mixed occupancy of cation positions is possible, but no additional vacancies may be taken into account. A common displacement parameter was refined for all anion sites whereas individual ones were used for each cation positions in order not to obtain unrealistically small standard deviations for the occupancy factors.

For TEM investigations, finely ground samples were drop cast on copper grids coated with a holey carbon film. In addition, single crystals were embedded in two-component glue and thinned by grinding, dimpling (dimple grinder model 650, Gatan) with diamond paste and precision argon ion polishing (PIPS model 691, Gatan) until holes were fabricated. The

composition of the samples was determined by an EDX detector system TOPS 30 (EDAX) attached to a FEI Titan 80-300 transmission electron microscope. The microscope was equipped with a Gatan UltraScan 1000 camera with a resolution of 2k x 2k and the field emission gun was operated at 300 kV. Selected-area electron diffraction (SAED) patterns and high-resolution transmission electron microscopy (HRTEM) images were evaluated with the Digital Micrograph[38] software package. For EDX analyses, the ES Vision[39] software was used. HRTEM image simulations were carried out with the JEMS[40] program package using the multi-slice approach (C_S = 0.6 mm, C_C = 1.2 mm, energy spread 0.9 eV), whereas the kinematical approximation was used for the calculation of electron diffraction patterns. Additional EDX spectra were obtained with an EDX detector (Inca system, Oxford Instruments) attached to a LEO 1530 Gemini (Zeiss) scanning electron microscope.

4.3.3 Results and discussion

4.3.3.1 Overview and strategy

As stated in Section 1, the thermoelectric properties of some Sn-doped GST materials outperform those of the corresponding Sn-free phases near RT.[17] HRTEM images showed planar defects; however, structural details on these phases have not yet been reported. The stacking sequence of Te-atom layers around such defect planes may be derived from HRTEM images, but in order to obtain precise interatomic distances, single-crystal X-ray data are the method of choice. Using $Ge_2Sn_2Sb_2Te_7$ as starting material, crystals could be obtained by CVT. Their Ge content is higher than in the starting material and cannot be easily influenced. Numerous TEM-EDX analyses of the CVT-grown single crystals (cf. Table S1 in the Supplementary Information) yield approximately the same Sn and Sb contents, but more Ge. In combination with the assumption of charge neutrality and taking into account the structure refinement (Section 3.2b), the approximate composition of the crystals can be given as $Ge_{3.25}Sn_{1.1}Sb_{1.1}Te_6$. Crystals with lower GeTe contents $(GeTe)_nSb_2Te_3$ (n = 1, 2) obtained by CVT were also shown to exhibit higher Ge contents than the starting materials.[15] As shown in Section 3.2, $Ge_{3.25}Sn_{1.1}Sb_{1.1}Te_6$ crystals form a novel superstructure of the rocksalt type upon quenching, whose structure parameters were refined using data of a twinned crystal. Its structure is characterized by defect planes that present a realistic model for those in quenched samples. This is confirmed by TEM data, which show that the structures of the CVT-grown crystals exhibit a higher degree of ordering than ingots obtained by quenching; however, the

structure near the defect planes is very similar. In addition, there are hierarchical nanostructures with additional slab-like domains (Section 3.3).

However, the information from CVT-grown crystals is incomplete. Sb, Sb and Te cannot be distinguished by conventional X-ray diffraction due to their similar electron counts. Furthermore, the long-range order of the superstructure is not perfect in the domain crystals, especially when the extended slab-like domains with a more relaxed structure are present. Thus, the study was completed with a resonant diffraction (Section 3.4) study using powder from a rather Ge-rich well-ordered annealed ingot of $Ge_3SnSb_2Te_7$ which approximates the Ge/Sn ratio of the CVT-grown crystals. The mass of the ingots usually differed less than 1% from that of the starting materials (EDX data cf. Table S1). The corresponding joint Rietveld refinement provides reliable information about the element distribution in rocksalt-type slabs of Sn-doped GST materials although the stacking of the layers differs from that of the superstructure observed in CVT-grown crystals.

4.3.3.2 Superstructure of the rocksalt type

a) construction of a structure model

Both X-ray as well as electron diffraction data of the CVT-grown crystals (cf. Fig. 1) show superstructure reflections along the cubic <111> directions. These indicate a sixfold superstructure of the NaCl type along c_{trigonal} in the trigonal setting of its *cF* lattice ($a_{\text{trigonal}} = a_{\text{cubic}} / \sqrt{2}$, $c_{\text{trigonal}} = \sqrt{3}\, a_{\text{cubic}}$). The diffraction patterns show superstructure reflections along all cubic <111> directions which correspond to the [001] direction of the individual domains according to the trigonal setting. This can be explained by fourfold twinning by reticular pseudo-merohedry; it involves superstructure reflections which belong to the individual twin domains and the reflections of the NaCl aristotype which contain contributions from all twin domains. The whole diffraction pattern can be indexed assuming a *cF* lattice with with a = 36.314(6) Å as used for the data integration (cf. Section 2.2). The individual lattices of the trigonal twin domains can be obtained from this "twin lattice" by transformation matrices like e.g. (0 1/12 1/12 | 1/12 -1/12 0 | 1/3 1/3 -1/3). Whereas, in principle, the refinement of such a twinned structure poses no problem, the overlap of all strong reflections impedes a straightforward structure solution.

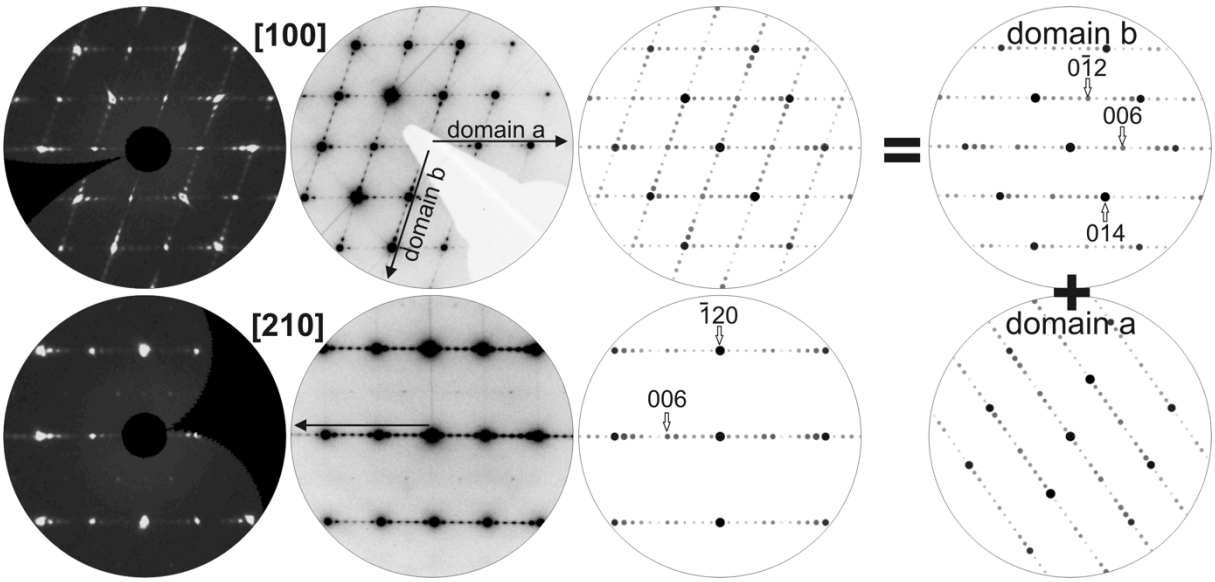

Fig. 1: Comparison of the superstructure reflections in "$Ge_{3.25}Sn_{1.1}Sb_{1.1}Te_6$" in diffraction patterns along the zone axes <100> and <210> according to the trigonal setting (cf. Table 1): reciprocal lattice sections reconstructed from single crystal X-ray diffraction data (left), SAED patterns (middle) and simulations based on the trigonal structure model for the long-range ordered structure: the pattern corresponding to the <100> zone axis is a twin-like superposition of those of domains that result from vacancy ordering in layers perpendicular to their [001] directions during quenching. The cubic [001] direction is indicated for all domains by black arrows in the SAED patterns.

Therefore, an initial structure model was constructed starting from the NaCl type. The sixfold superstructure implies a stacking of 12 atom layers along one of the NaCl-type lattice's <111> directions, which equals [001] of the trigonal superstructure. This corresponds to a structure in the space group $P\bar{3}m1$ with $a \approx 4.28$ Å and $c \approx 20.97$ Å. Due to the overlap of all strong reflections, the crystal data preclude the detection of small deviations from the cubic metrics of the basic structure. As powder diffraction patterns from crushed crystals show no significant reflection splitting, the unit cell parameters calculated from those of the pseudocubic twin lattice by the matrix given above were used for all further data evaluation.

HRTEM images clearly show vacancy layers (see below) as known from GST materials and substitution variants containing Sn, In, Se.[13,17,43,44] Therefore, one cation layer was replaced by a vacancy layer and *z* coordinates of the six anion and 5 cation layers (3 independent Wyckoff sites each) were manually altered so that reasonable interatomic distances were obtained. These were approximated by comparable values from similar compounds (cf. Section 1). However, as the average structure corresponds to the NaCl type, the stacking sequence of Te-atom layers must be a "cubic" (ABC) one.[41] This is also corroborated by contrasts in HRTEM images, comparable to investigations on thin films of $Ge_2Sb_2Te_5$.[22] The corresponding Te-Te distance across the vacancy layer was taken from $Ge_4Bi_2Te_7$,[41] which exhibits a comparable environment in highly disordered crystals. Thus, the corresponding

model shown in Fig. 2 exhibits an 11*P* stacking sequence with the composition $M_3Sb_2Te_6$ (M = Ge, Sn) in analogy to $Ge_3Sb_2Te_6$ which, however, is characterized by a 33*R* stacking sequence (space group $R\bar{3}m$) as the Te-atom layers exhibit a "hexagonal" ABAB stacking around its van der Waals gaps (which can be viewed as defect layers, cf. Section 1). The latter is not a superstructure of the NaCl type in a strict crystallographic sense. The good fit between diffraction patterns calculated on the basis of the constructed 11*P* structure (cf. Fig.1) indicates that the model with the exclusively ABC-type stacking of Te-atom layers is suitable.

b) structure refinement on X-ray data

The structure model described above was refined taking into account all four twin domains and the fact that all of them contribute to the reflections of the aristotype. The refined interatomic distances differ very little from those of the constructed model (see above). From a plethora of comparable structures it is obvious that the concentration of anti-site defects is negligible so that the Te positions can clearly be identified. As Sn and Sb cannot be distinguished and as equal amounts of them were detected by EDX (Table S1), cation positions were constrained to full occupancy with equal amounts of Sn and Sb and a refined percentage of Ge. This is, of course, only an approximation. However, the refined Ge content is highest in the center of the rocksalt-type slabs as in all GST and related materials because Sb concentrates near the vacancy layers. Difference Fourier syntheses revealed small residual electron densities in the vacancy layers. Due to their short distance to neigboring Te atoms, these were assumed to be Ge atoms; their occupancy was refined. This is also an approximation as these densities are most likely due to the fact that the lateral extension of the defect layers is in the range of the X-ray's length of coherence. Thus, these disordered atoms with large displacement parameters represent areas where the vacancies are not fully ordered. This refinement yields a chemical formula close to $Ge_{3.25}Sn_{1.1}Sb_{1.1}Te_6$, which was constrained to be charge balanced; however, this constraint did not change the refined composition significantly. There are no significant residual electron densities, especially none that would indicate any deviation from the ABC-type Te-atom layer stacking sequence. Crystal data and refinement details are given in Table 1, the refined atom parameters are listed in Table 2. The structure is depicted in Fig. 2, which also shows the relevant interatomic distances. Further details of the crystal structure investigation may be obtained from Fachinformationszentrum Karlsruhe, 76344 Eggenstein-Leopoldshafen, Germany (Fax: +49 7247 808 666; email: crysdata@fiz-karlsruhe.de, http://www.fiz-karlsruhe.de/request_for_deposited_data.html) on quoting the deposity number CSD-427753.

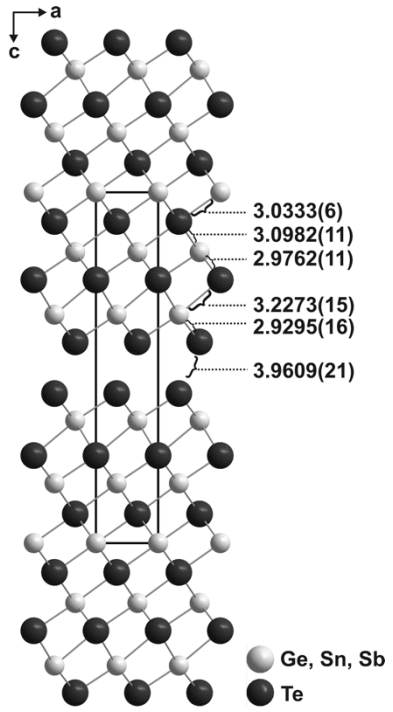

Fig. 2: Crystal structure of "$Ge_{3.25}Sn_{1.1}Sb_{1.1}Te_6$" as refined from X-ray diffraction data of a twinned crystal (selected interatomic distances are given in Å); partially occupied Ge positions in the vacancy layer (cf. text) are not shown.

Table 1. Crystallographic data and structure refinement of "$Ge_{3.25}Sn_{1.1}Sb_{1.1}Te_6$" at RT

Formula (refined)	$Ge_{3.25(7)}Sn_{1.10(3)}Sb_{1.10(3)}Te_6$
Formula mass (in $gmol^{-1}$)	1266.73
Crystal system / Space group	trigonal, $P\bar{3}m1$
Cell parameters (in Å)	a = 4.028(1) Å, c = 20.966(3) Å
Cell volume (in $Å^3$)	332.61(19)
X-ray density (in gcm^{-3})	6.32
Absorption coefficient (in mm^{-1})	12.838
Formula units per unit cell (Z)	1
F(000)	527.1
Radiation	Ag-$K_{\alpha 1}$ (λ = 0.56085 Å)
2ϑ range (in °)	$4.6 \leq 2\theta \leq 43.8$
Independent data / parameters / restraints	389 / 34 / 4
R(σ)	0.0401
R indices [I > 2σ(I)] *	R1 = 0.058, wR2 = 0.167
R indices [all data] *	R1 = 0.128, wR2 = 0.217
GooF [all data]	0.919
$\Delta\rho_{min}$ / $\Delta\rho_{max}$ ($eÅ^{-3}$)	−1.86 / +3.29

*) $R1 = \frac{\sum \| |F_o| - |F_c| \|}{\sum |F_o|}$, $wR2 = \left(\frac{\sum \left[w\left(F_o^2 - F_c^2\right)^2 \right]}{\sum \left[w\left(F_o^2\right)^2 \right]} \right)^{\frac{1}{2}}$, $w = 1/[\sigma^2 F_o^2 + (0.1P)^2]$ with $P = [F_c^2 + \mathrm{Max}(F_o^2, 0)]/3$

Table 2. Coordinates, equivalent isotropic and anisotropic displacement parameters and site occupancies (s.o.f.) of "$Ge_{3.25}Sn_{1.1}Sb_{1.1}Te_6$" at RT ($U_{eq}$ = 1/3[U_{33} + 4/3(U_{11} + U_{22} – U_{12})]; U_{13} = U_{23} = 0; U / Å^2).

Atom	Wyckoff position	*x*	*y*	*z*	s.o.f.**	U_{eq}	$U_{11} = U_{22} = 2\ U_{12}$	U_{33}
Ge1/Sb1/Sn1	1*a*	0	0	0	0.617(12)/0.192(6)/0.192(6)	0.0407(5)	0.0411(6)	0.0399(9)
Te1	2d	1/3	2/3	0.08392(4)	1	0.0368(2)	0.0363(4)	0.0378(6)
Ge2/Sb2/Sn2	2*d*	2/3	1/3	0.17303(7)	0.615(10)/0.193(5)/0.193(5)	0.0431(4)	0.0415(4)	0.0463(8)
Te2	2*d*	0	0	0.25214(4)	1	0.0383(3)	0.0387(4)	0.0376(6)
Ge3/Sb3/Sn3	2*d*	1/3	2/3	0.35117(10)	0.482(11)/0.259(6)/0.259(6)	0.0445(6)	0.0414(4)	0.0507(12)
Te3	2*d*	2/3	1/3	0.42618(9)	1	0.0466(4)	0.0454(5)	0.0489(6)
Ge4*	2*d*	0	0	0.4804(14)	0.226(5)	0.214(13)	-	-

* residual electron densities in the vacancy layers assumed to be Ge

* s.o.f. (Sn) = s.o.f. (Sb)

The coordination of cations by Te is closer to a regular octahedron in the center of the slabs and becomes more distorted towards the defect layers. The Te-Te distance across the defect layers in the present ABC stacking is only slightly shorter than the sum of the van der Waals radii (ca. 4.0 Å, the exact value depends on the method of calculation);[42] it amounts to 3.96 Å. This is significantly longer than in stable long-range ordered structures with ABAB stacking, e.g. $Ge_{0.6}Sn_{0.4}Sb_2Te_4$ (3.720 Å) and $Ge_{1.3}Sn_{0.7}Sb_2Te_5$ (3.728 Å),[15] as well as $Ge_3SnSb_2Te_7$ (cf. Section 3.4).

c) HRTEM image simulations

HRTEM images obtained from crushed single crystals were simulated based on the trigonal 11*P* structure model in $P\bar{3}m1$ with a cubic ABC-type stacking of the Te-atom layers across the van der Waals gaps (Fig. 3). The differences between the defocus values used are similar to those that were applied experimentally. The contrast variation in the simulations matches the observed one. At all defocus values, the expected defect layers are clearly visible and it is evident that the stacking sequence does not change across the gaps but resembles those within the blocks. The slightly smaller distance of similar structural features across the defect layers compared to that within the distorted rocksalt-type slabs reflects the shorter distances between Te-atom layers (3.96 Å and 4.30-4.41 Å, respectively).

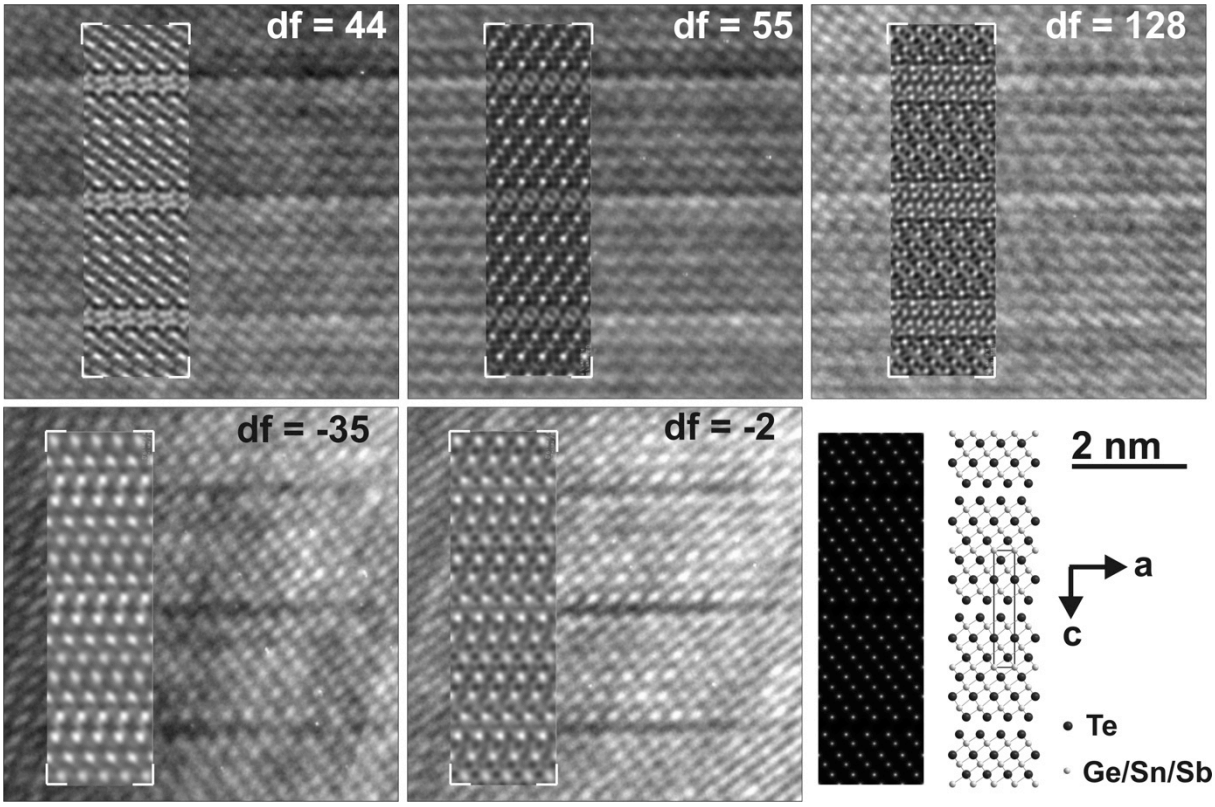

Fig. 3: Fourier filtered HRTEM images at various defocus values (two different areas of the same crystallite) of crushed crystals of "$Ge_{3.25}Sn_{1.1}Sb_{1.1}Te_6$" (zone axis <100> according to trigonal setting)which show the "cubic" ABC-type Te-atom layer stacking sequence around the defect layers; the insets show simulations based on the model discussed in Section 3.2 (thickness: top images 6.4 nm, bottom images 9.0 nm, other parameters used for the simulations are provided in the experimental section); bottom right: projected potential as well as the structure model used for the simulations. A comparison of the Fourier filtered HRTEM images and the unfiltered ones is provided in the Fig. S6 in the Supplementary Information.

4.3.3.3 Domain size and hierarchical structure in $Ge_2Sn_2Sb_2Te_7$

Most diffraction patterns of single crystals grown by CVT show the superstructure described above; diffuse streaks are observed only occasionally. In contrast, crystallites from quenched ingots of $Ge_2Sn_2Sb_2Te_7$ show superstructure reflections only in SAED patterns of few areas. As shown in ref. [17], they usually exhibit the typical diffuse intensities that correspond to "parquet-like" domain structures, which can be understand as tweed-like domains, as observed e.g. for $Sb_2Te_3(GeTe)_n$ (n = 4.5 - 19)[16] and substitution variants with Sn, In and Se.[17,43,44]. The average lateral extension of the defect layers in the parquet-like areas is 11.3 ± 3.0 nm for the CVT-grown crystals and 9.1 ± 2.6 nm for the polycrystalline samples, i.e. approximately the same as in unsubstituted quenched ingots of $Ge_4Sb_2Te_7$ with 10.1 ± 2.6 nm (derived from the data shown in ref. [44]). These values were obtained by measuring a total of ~ 100 defect layers in several HRTEM images for each compound.

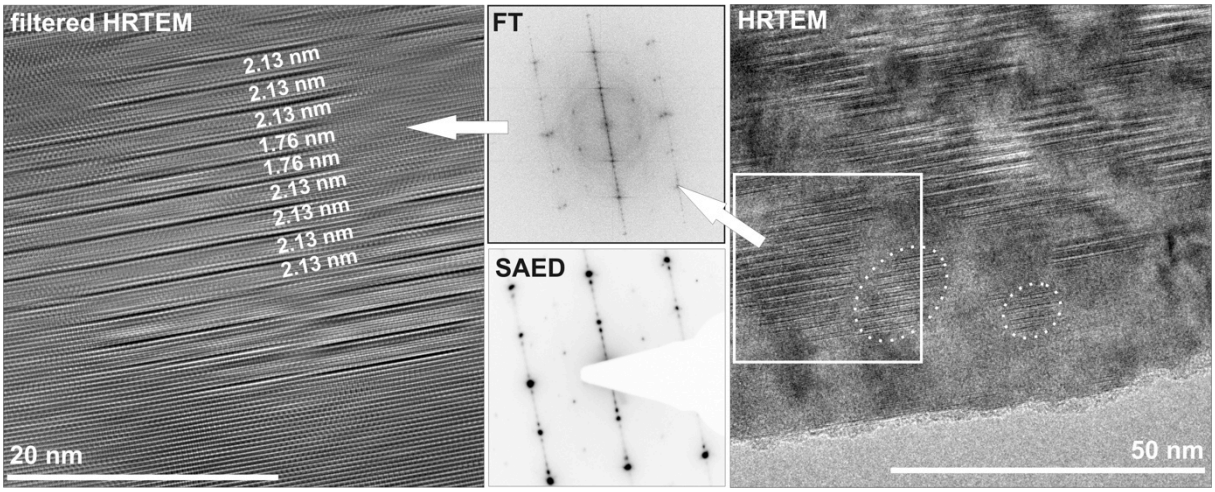

Fig. 4: TEM of $Ge_2Sn_2Sb_2Te_7$ quenched from the melt (zone axis <210> according to trigonal setting): HRTEM with spheroidal domains (two domains are highlighted with white dotted lines) with average diameter of ~ 25 nm (right); superstructure reflections in the corresponding SAED pattern (diameter of irradiated area ca. 150 nm) and Fourier transform (middle) as well as Fourier-filtered HRTEM of the highlighted area with selected spacings of the defect layers (left, based on an image with higher magnification).

Crystals with superstructure reflections exhibit spheroidal domains with parallel defect layers perpendicular to the [001] direction of these trigonal domains, which correspond to the cubic <111> directions, with an average diameter of ~ 25 nm (Fig. 4). Most defect layers in these domains are equidistantly spaced; however, some slabs differ in thickness (typically by one GeTe-type layer). The boundaries between the individual spheroidal domains are expected to be twin boundaries but appear rather diffuse. CVT-grown crystals occasionally exhibit additional domains with much larger lateral extension (500 to 1200 nm) that are embedded as large slabs in a "matrix" consisting of the spheroidal domains. This can lead to a hierarchical structure motif as shown in Fig. 5. For sequences of rocksalt-type building blocks with identical numbers of atom layers, the translation period along the stacking direction ([001] in trigonal setting) in the extended slab-like domains tends to be slightly shorter than in the domain structure sandwiched between them. This indicates a higher degree of relaxation; as a consequence, the structure of the slab-like domains approaches that of the corresponding trigonal phase with hexagonal (ABAB) stacking of the Te-atom layers around van der Waals gaps. The composition of these domains does not differ significantly from that of the spheroidal domains as evidenced by EDX analyses that focus on different parts of the hierarchical structure as shown in Fig. S1 and Table S2 in the Supplementary Information. SAED patterns from the hierarchical structure (Fig. S2 in the Supplementary Information) exhibit similar superstructure reflections and the same metrics (deviation less than 0.5%) as areas without the slab-like domains (cf. Fig. 1).

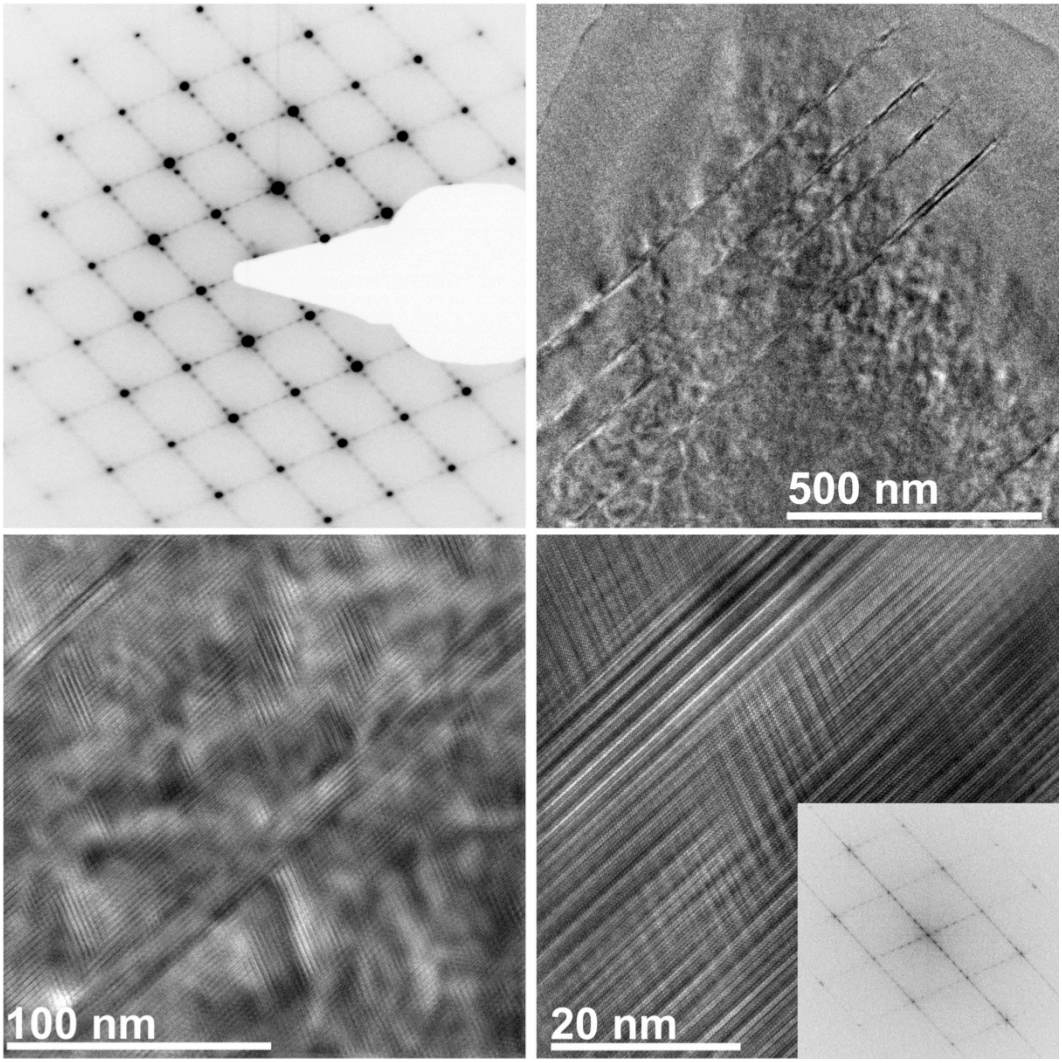

Fig. 5: Thinned section of a CVT-grown crystal of "$Ge_{3.25}Sn_{1.1}Sb_{1.1}Te_6$" (zone axis <110> according to cubic setting of the rocksalt type): SAED pattern with superstructure reflections along the <111> directions of the cubic average structure which correspond to the [001] directions of the trigonal domains with different orientations (top left) and HRTEM images – obtained with different magnifications from the same area of the crystallite – that show the hierarchical structure of extended slab-like domains with parallel "defect layers" sandwiching arrays of spheroidal domains with a diameter of ~ 25 nm and the structure described in the text; Fourier transform of the HRTEM image as inset (bottom right corner).

4.3.3.4 Element distribution $Ge_3SnSb_2Te_7$

As Sn, Sb and Te exhibit similar electron counts, they cannot easily be distinguished by conventional X-ray diffraction; however, anomalous dispersion near absorption edges leads to a change of the atom form factors that increases the scattering contrast. Such resonant diffraction experiments were carried out using powder data of the long-periodically ordered layered phase 39*R*-$Ge_3SnSb_2Te_7$ in order to elucidate the element distribution. The composition of this sample approximates that of the above mentioned CTV-grown crystals and phase transition temperatures do not show significant differences for slight variations in

Sn content.[17] Therefore, the element distribution in powder samples of 39*R*-$Ge_3SbSn_2Te_7$ should be a good model for that in the CVT-grown crystals despite the fact that the stacking sequences and slab thicknesses are not identical. Details of the refinement (cf. Experimental Section), which yielded unambiguous site occupancies and no significant residual electron density in the van der Waals gap, are provided in Tables 3 and 4. A profile fit for the data collected at 0.354198 Å is shown in Fig. 6, further ones for the data sets obtained with wavelengths close to the K-edges of Sb, Sn, and Te are shown in the Supplementary Information (Fig. S3-S5). Further details of the crystal structure investigation may be obtained from Fachinformationszentrum Karlsruhe (contact data cf. Section 3.2b) on quoting the deposity number CSD-427688.

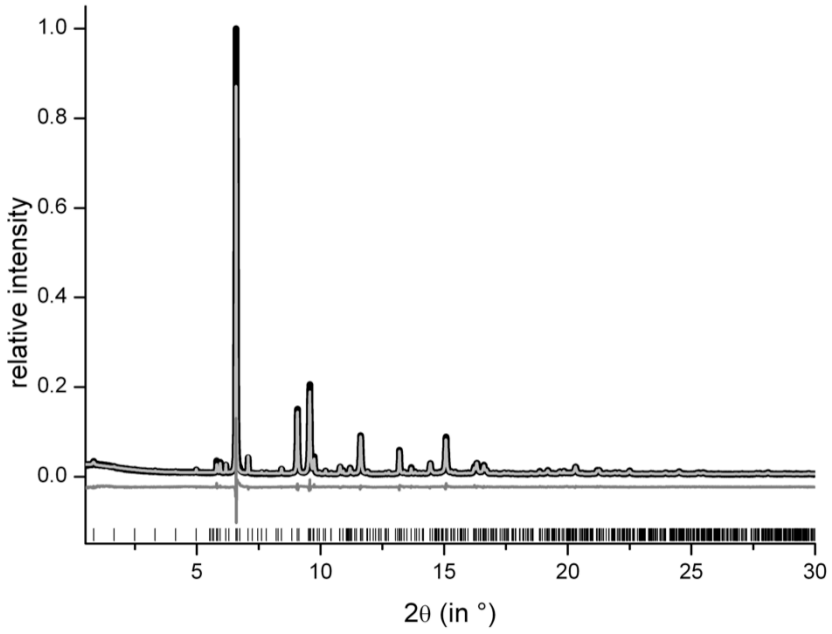

Fig. 6: Profile fit for the data away from the K-edges (λ = 0.354198(10)Å) from the joint Rietveld refinement of 39*R*-$Ge_3SnSb_2Te_7$ (the other data are shown in the Supplementary Information): experimental (black) and calculated pattern (gray) and difference plot (below); vertical lines indicate calculated reflection positions.

According to the structure refinement, slowly cooled $Ge_3SnSb_2Te_7$ exhibits the 39*R*-type structure known for $Ge_4As_2Te_7$[20] as shown in Fig. 7. This structure is expected from the stoichiometry, whereas in contrast to predictions based on the cation/anion ratio, a 33*R*-type stacking sequence was reported for $Ge_4Sb_2Te_7$, possibly as a consequence of disorder and slight deviations from the idealized composition.[28] 39*R*-$Ge_3SnSb_2Te_7$ consists of distorted rocksalt-type slabs that exhibit an alternating arrangement of 6 cation and 7 anion layers. Like in the structure of "$Ge_{3.25}Sn_{1.1}Sb_{1.1}Te_6$", the octahedral coordination polyhedra are almost regular in the center of the slabs and more distorted near the van der Waals gaps. The distance

between the Te atoms terminating the slabs is 3.7508(14) Å in good agreement with the corresponding distances in $Ge_{0.6}Sn_{0.4}Sb_2Te_4$ (3.720 Å) and $Ge_{1.3}Sn_{0.7}Sb_2Te_5$ (3.728 Å) or other 21*R*-type structures of MSb_2Te_4 with M = Ge[24], Sn[26], Pb[45] where the distance does not differ more than 2 % from the ones reported here. The cation positions in the centre of the slabs (C3 and C2) are predominantly occupied by Ge and Sn while Sb concentrates at the position near the van der Waals gaps. This element distribution resembles the one in long-range ordered 21*R*-$Ge_{0.6}Sn_{0.4}Sb_2Te_4$ and 9*P*-$Ge_{1.3}Sn_{0.7}Sb_2Te_5$.[15] In contrast to the latter compounds with lower GeTe content, the position next to the van der Waals gap (C1) contains almost no Sn in $Ge_3SnSb_2Te_7$ where it is occupied by similar amounts of Ge and Sb.

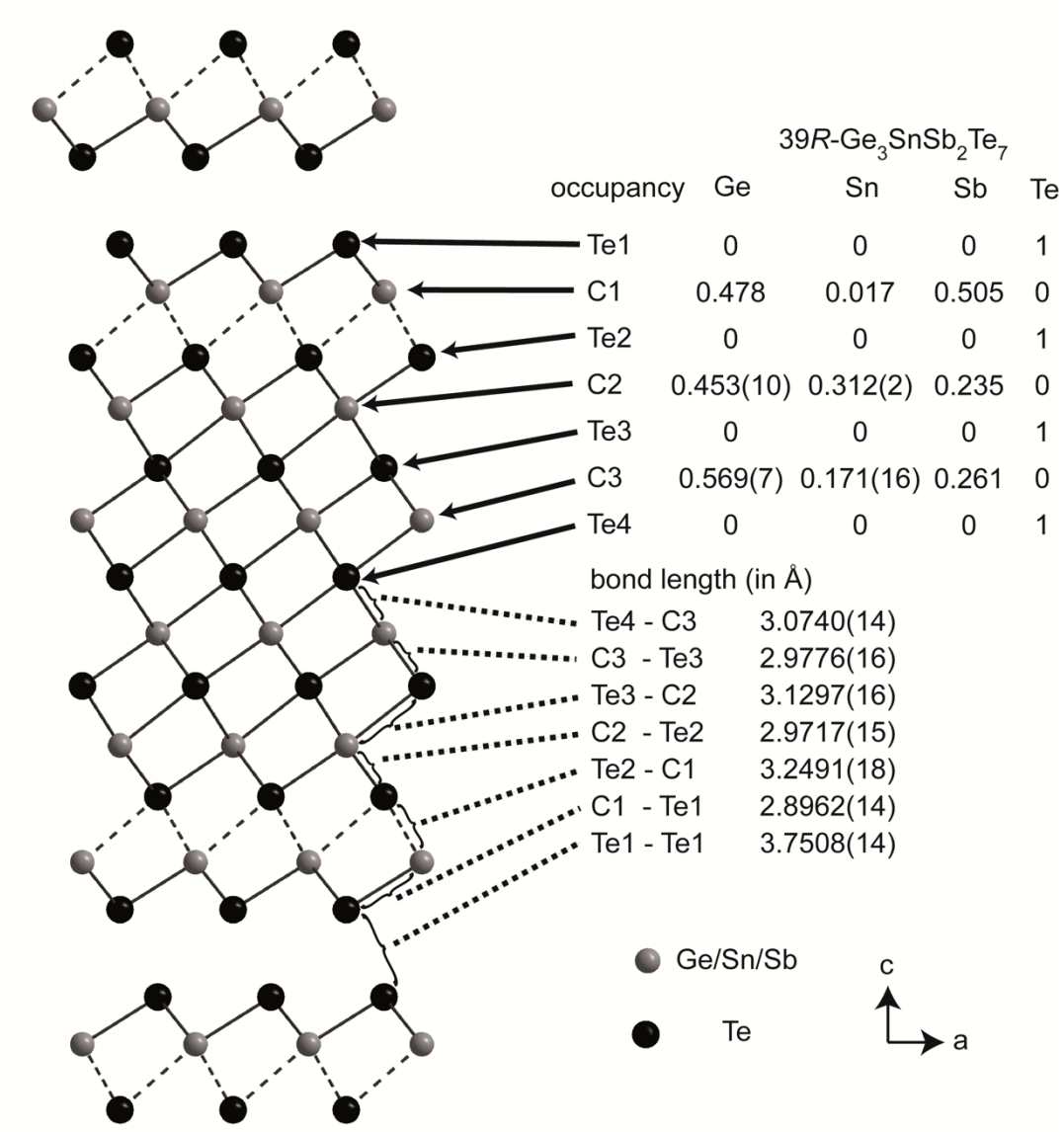

Fig 7: Atom distribution (occupancy factors, missing esd's are a consequence of constraints) for each position and bond lengths in the refined model of 39*R*-$Ge_3SnSb_2Te_7$ (only one slab and its vicinity is shown) at 293 K.

Table 3. Crystallographic data from the structure refinement of 39*R*-$Ge_3SnSb_2Te_7$ at RT.

		39*R*-$Ge_3SnSb_2Te_7$		
Formula mass (in g mol^{-1})		1473.26		
Crystal system / space group		trigonal / $R\bar{3}m$		
Cell parameters (in Å)		a = 4.24990(4), c = 73.4677(9)		
Cell volume (in Å^3)		1149.17(3)		
X-ray density (in g cm^{-3})		6.38		
Formula units (per unit cell)		4		
F(000)		1836		
	far	Te-K edge	Sb-K edge	Sn-K edge
Wavelength (in Å)	0.354198(10)*	0.389937(9)	0.406879(6)	0.424833(5)
Energy (in keV)	35.00422	31.79597	30.47202	29.18423
Measured reflections	613	654	622	641
Absorption coefficient μ (in mm^{-1})	1.5	9.3	6.9	5.9
2θ range (in °)	0.5 – 30	0.5 – 34	0.5 – 35	0.5 – 37
$\sin\theta_{max}$ / λ in Å^{-1}	0.73	0.75	0.74	0.75
Δf' / Δf'' of the element corresponding to the respective edge		-8.29 / 2.51	-9.16 / 2.86	-8.99 / 2.34
Parameters / thereof background	120 / 48	120 / 48	120 / 48	120 / 48
R_{Bragg}	0.018	0.012	0.019	0.016
R_{exp}	0.026	0.031	0.027	0.018
R_p	0.053	0.042	0.054	0.047
R_{wp}	0.072	0.054	0.076	0.067
GooF	2.73	1.74	2.77	3.68
R_p / R_{wp} / GooF (all datasets)		0.049 / 0.068 / 2.84		

* In contrast to the other e.s.d.'s, this one is not from the Rietveld refinenemt (where this wavelength was kept constant) but from the refinement against a standard (cf. Section 2.2).

Table 4. Structure parameters of 39*R*-$Ge_3SnSb_2Te_7$ at RT: atom positions and coordinates, site occupancies (s.o.f., those with no e.s.d.'s given follow from the others due to the constraints applied) and isotropic displacement parameters (B_{eq} in Å^2)

atom	position	Wyckoff position	x	y	z	occupancy	B_{eq}
Te	Te1	6*c*	0	0	0.14736(2)	1	1.11(2)
Te	Te2	6*c*	0	0	0.23591(2)	1	= B_{eq} (Te1)
Te	Te3	6*c*	0	0	0.38150(2)	1	= B_{eq} (Te1)
Te	Te4	3*a*	0	0	0	1	= B_{eq} (Te1)
Ge/Sn/Sb	C1	6*c*	0	0	0.45975(3)	0.478 / 0.017 / 0.505	2.50(6)
Ge/Sn/Sb	C2	6*c*	0	0	0.07461(3)	0.453(10) / 0.312(2) / 0.235	1.85(7)
Ge/Sn/Sb	C3	6*c*	0	0	0.30813(3)	0.569(7) / 0.171(16) / 0.261	1.88(5)

4.3.4 Conclusion

Quenched CVT-grown crystals with the approximate composition $Ge_{3.25}Sn_{1.1}Sb_{1.1}Te_6$ exhibit a superstructure of the rocksalt type. The building blocks present resemble the stable trigonal phases of GST materials. However, probably due to the quenching process, the ABC-type stacking of the Te-atom layers present in the cubic HT phase is retained. The higher degree of order of quenched Sn-substituted single crystals compared to the unsubstituted samples may be explained by the assumption that the lower bond energy of Sn-Te compared to Ge-Te outweighs the lower mobility during quenching of the Sn-substituted compounds resulting from the lower phase transition temperatures. The existence of a long- or intermediate-range ordered superstructure that combines elements of both stable phases (i.e. HT and RT) hints at the mechanism of the phase transition between them. During cooling, the randomly distributed vacancies order in defect layers as visible in the pseudocubic quenched samples.[16,17] When these defect layers grow larger, the spacing between the adjacent Te-atom layers decreases but the cubic stacking is preserved. The superstructure of the rocksalt-type reported here may be viewed as model of this intermediate state. 2D extended defect ordering renders the relaxation to the stable trigonal RT phase possible, which involves a shift of the consecutive building blocks perpendicular to the stacking direction. Such a process would be strongly determined by the atom mobility (i.e., bonding energies of the atoms and transition temperatures) and may explain many changes in the nanostructure that are associated with substitutions in GST materials.

In quenched crystals of $Ge_{3.25}Sn_{1.1}Sb_{1.1}Te_6$, domains with different degrees of structural relaxation coexist, depending on the lateral extension of the domains. Slab-like domains with a lateral extension of ~ 1μm exhibit the same number of atom layers in each building block and the same composition as the nanodomain "matrix" around them; they deviate only with respect to the degree of relaxation. This opens new possibilities for structuring GST materials on the nanoscale as well as on the microscale which is expected to be associated with lower thermal conductivities compared to long-range ordered compounds. The "matrix" contains spheroidal domains with an average diameter of ~ 25 nm. These share a common anion sublattice and exhibit no diffuse intensities in diffraction patterns. This is a promising feature concerning thermoelectric properties since twin domains with different orientations should reduce phonon propagation while the common anion lattice may enable high electrical conductivities.

The mobility might also influence the formation of the layered thermodynamically stable phases. For phases $(MTe)_nX_2Te_3$ (M = Sn, Ge; X = Sb, In, Bi) with high defect concentrations ($n \leq 3$), the number of atom layers in the building block is usually $2n + 5$.[15,24-28] For samples with higher values of n, the observed structures often exhibit fewer atom layers per translation period than predicted.[11,28,46] This is probably a consequence of incomplete ordering and residual vacancies within the building blocks or the presence of atoms remaining in the "vacancy layers" as observed in the superstructure of $Ge_{3.25}Sn_{1.1}Sb_{1.1}Te_6$. The higher mobility in the Sn-substituted sample would also explain the fact that $Ge_3SnSb_2Te_7$ crystallizes in a 39*R*-type as expected while $Ge_4Sb_2Te_7$ adopts a 33*R*-type,[28] which would be expected for compounds with n = 3. The element distribution of layered 39*R*-$Ge_3SnSb_2Te_7$ is comparable to $(Ge_{1-x}Sn_xTe)_nSb_2Te_3$ (n = 1, 2) with the formally higher charged Sb^{3+} concentrating on the position near the defect layers in order to compensate the unsaturated coordination of the Te atoms at the outer face of the building blocks. Very likely, this is a suitable model for the blocks in the "intermediate phases" with ABC-type Te-atom stacking.

Acknowledgement

The authors thank Felix Hennersdorf (Leipzig University, Germany) and Thorsten Schröder (LMU Munich, Germany) for their help during the collection of the resonant powder diffraction data as well as Pirmin Ganter for the synthesis of the sample used and Gerald Wagner (IMKM, Leipzig, Germany) for the conduction of SEM-EDX experiments. We are indebted to Prof. Dr W. Schnick (LMU Munich, Germany) as well as the ESRF (project HS-4826) for their generous support of this study. This work was funded by the Deutsche Forschungsgemeinschaft (Grant OE530/1-2).

4.3.5 Supplementary Information

Table S1. EDX analyses of crystals grown by CVT from $Ge_2Sn_2Sb_2Te_7$ as a starting material (in atom %).

samples	number of point analyses	Ge	Sn	Sb	Te
calculated composition for $Ge_2Sn_2Sb_2Te_7$	-	15.4	15.4	15.4	53.8
calculated composition for $Ge_3Sn_1Sb_2Te_7$	-	23.1	7.7	15.4	53.8
calculated composition for $Ge_{3.25}Sn_{1.1}Sb_{1.1}Te_6$	-	28.4	9.6	9.6	52.4
ingot of $Ge_2Sn_2Sb_2Te_7$ (quenched)	4 (TEM)	16.0(6)	17.8(5)	15.8(7)	50.3(11)
ingot of $Ge_3Sn_1Sb_2Te_7$ (annealed)	12 (SEM)	25.5(21)	7.5(6)	15.4(5)	51.7(15)
crushed CVT-grown crystal	14 (TEM)	24.0(26)	14.1(12)	12.3(15)	49.6(23)
ion-thinned CVT-grown crystals	10 (TEM)	23.4(22)	13.6(8)	14.0(11)	49.0(21)

Table S2. Results of TEM-EDX measurements for different sample areas as shown in Figure S1 (in atom %).

area	structure	Ge	Sb	Sn	Te
1	small (spheroidal) domains, "matrix"	19.7	12.5	13.2	54.46
2	small (spheroidal) domains, "matrix"	20.7	13.1	14.4	51.7
3	slab-like domain with parallel defect layers	18.6	14.2	13.0	54.3
4	slab-like domain with parallel defect layers	19.5	12.9	11.8	55.8
5	slab-like domain with parallel defect layers	20.0	12.8	13.6	53.6
a	"matrix" far away from slab-like domain	19.9	13.1	14.2	52.8
e	"matrix" far away from slab-like domain	21.4	11.9	15.0	51.3
b	"matrix" close to slab-like domain	21.4	11.8	14.7	52.2
d	"matrix" close to slab-like domain	23.4	10.9	14.9	50.8
c	slab-like domain with parallel defect layers	20.7	14.3	12.9	52.1
average (12 points)	"matrix" close to slab-like domain	22.3(1.7)	13.2(1.6)	14.1(1.0)	50.6(2.7)
average (7 points)	slab-like domains with parallel defect layers	21.3(2.4)	13.3(1.8)	13.1(1.2)	52.2(2.7)

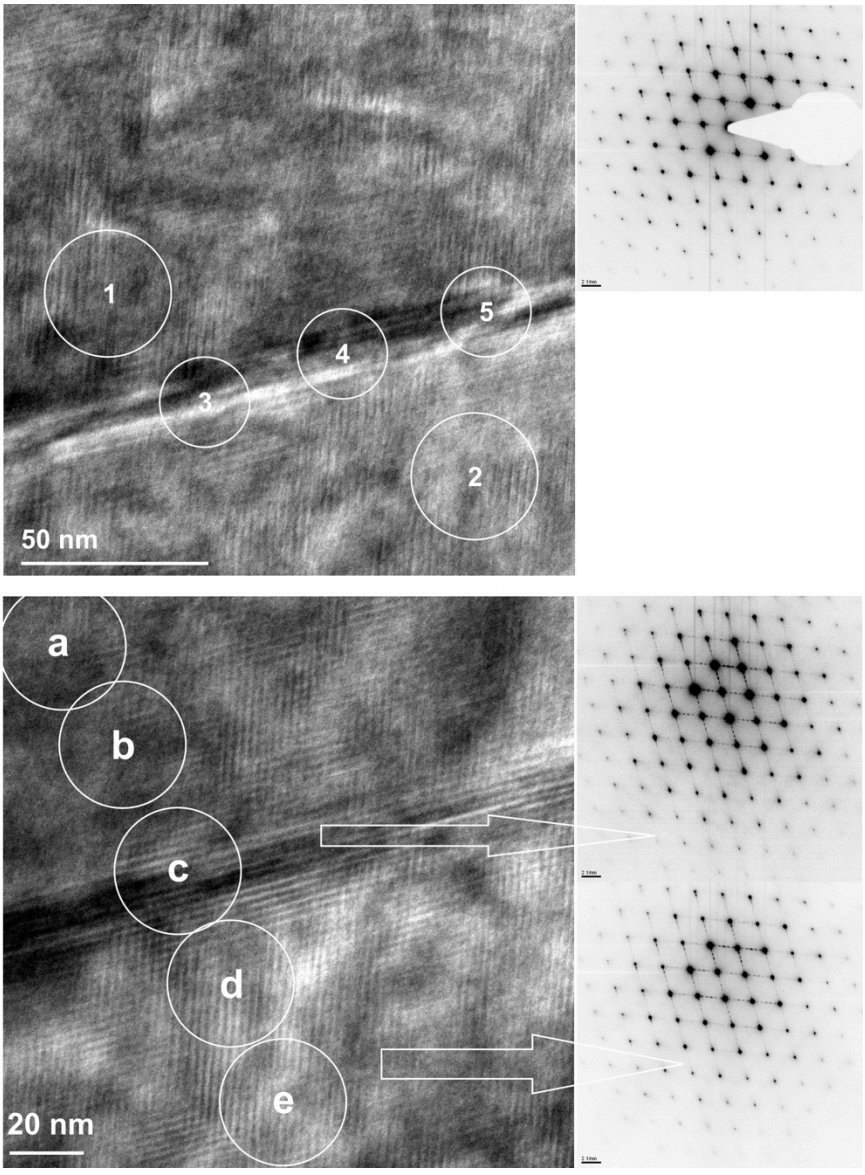

Fig. S1: Thinned sections of a crystal of "$Ge_{3.25}Sn_{1.1}Sb_{1.1}Te_6$"; local EDX analyses from various areas of the hierarchical structure (marked spots, the EDX results are given in Table S2) and SAED patterns.

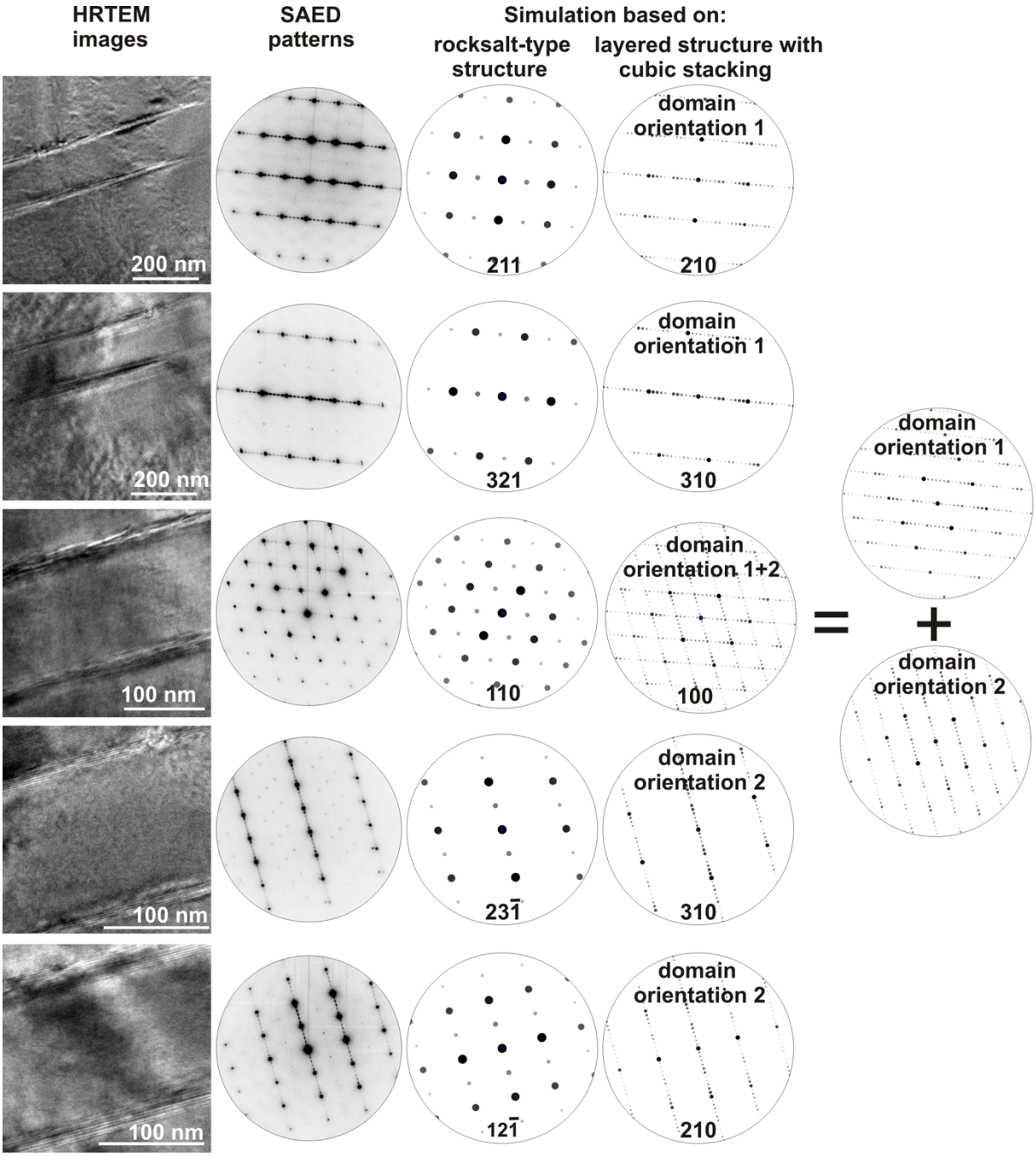

Fig. S2: Different orientations of the same area of a CVT-grown crystal of "$Ge_{3.25}Sn_{1.1}Sb_{1.1}Te_6$" that exhibits the hierarchical structure described in the text: HRTEM images (left) with corresponding SAED patterns (second column); simulated SAED patterns based on the average cubic rocksalt-type structure and indexed accordingly (third column) as well as based on the layered structure model developed for "$Ge_{3.25}Sn_{1.1}Sb_{1.1}Te_6$" (consisting of rocksalt type building blocks with 11 atom layers and a cubic stacking of the Te atom layers terminating the slabs) and indexed accordingly (fourth column); the pattern of the zone axis [100] can be explained by superimposing those of the domains.

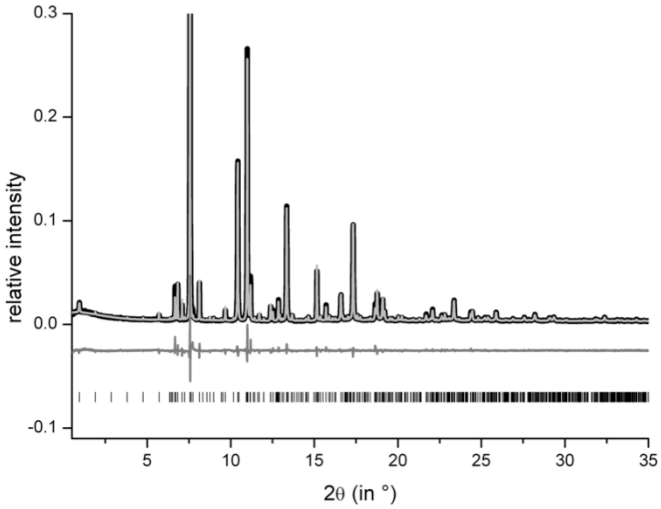

Fig. S3: Rietveld refinement of 39R-$Ge_3SnSb_2Te_7$ (the strongest reflection is cut off) near the K-edge of Sb at 0.406879Å; vertical lines indicate calculated reflection positions, experimental (black) and calculated pattern (gray) and difference plot (below) are shown.

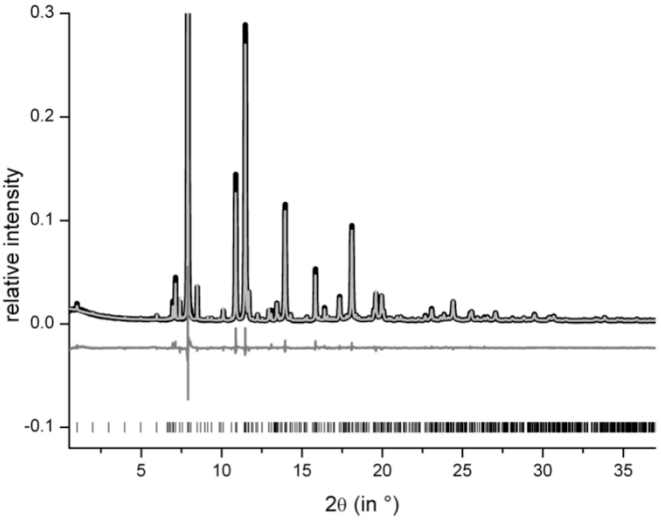

Fig. S4: Rietveld refinement of 39R-$Ge_3SnSb_2Te_7$ (the strongest reflection is cut off) near the K-edge of Sn at 0.424833 Å; representation like in Figure S3.

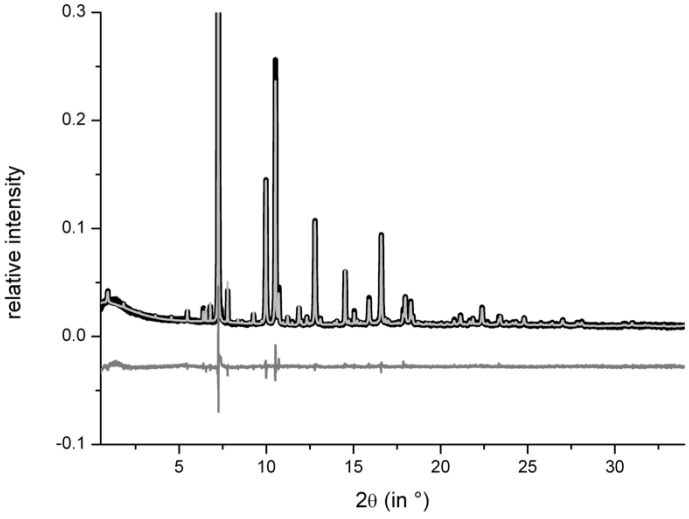

Fig. S5: Rietveld refinement of 39R-$Ge_3SnSb_2Te_7$ (the strongest reflection is cut off) near the K-edge of Te at 0.389937Å; representation like in Figure S3.

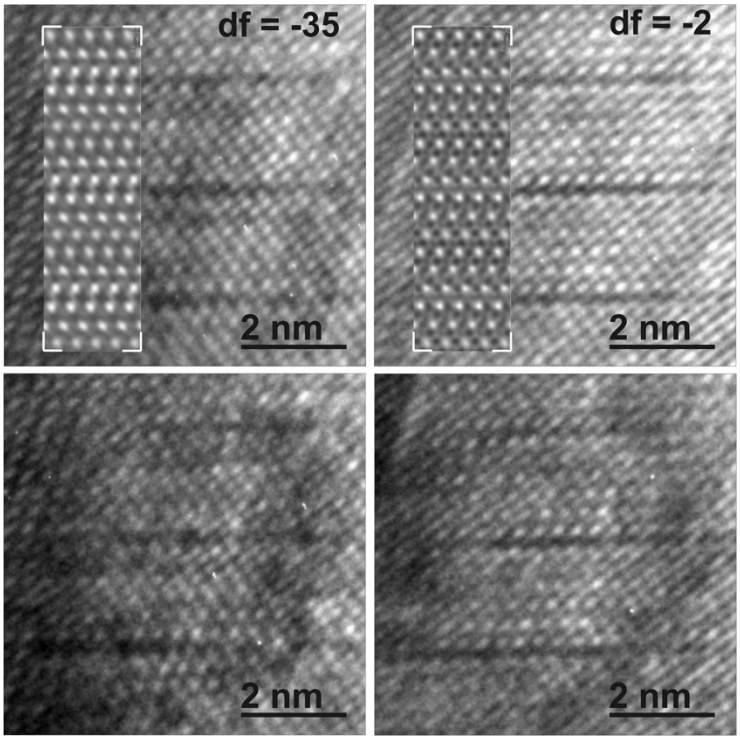

Fig. S6: Comparison of fourier filtered HRTEM images (top) and raw data (bottom) at two different defocus values of crushed crystals of "$Ge_{3.25}Sn_{1.1}Sb_{1.1}Te_6$" (zone axis <100>); the insets show simulations based on the model discussed in 3.2 (thickness: 9.0 nm, other parameters used for the simulations are provided in the experimental section)

4.3.6 References

[1] T. Siegrist, P. Merkelbach, M. Wuttig, *Annu. Rev. Condens. Matter Phys.* **2012**, *3*, 215.

[2] S. Raoux, W. Welnic, D. Ielmini, *Chem. Rev.* **2010**, *110*, 240.

[3] K. Wang, D. Wamwangi, S. Ziegler, C. Steimer, M. J. Kang, S. Y. Choi, M. Wuttig, *Phys. Stat. Sol. (a)* **2004**, *201*, 3087.

[4] R. Kojima, N. Yamada, *Jpn. J. Appl. Phys.* **2001**, *40*, 5930.

[5] K. Wang, C. Steimer, D. Wamwangi, S. Ziegler, M. Wuttig, J. Tomforde, W. Bensch, *Microsyst. Technol.* **2007**, *13*, 203.

[6] C. Xu, B. Liu, Z.-T. Song, S.-L. Feng, B. Chen, *Chinese Phys. Lett.* **2005**, *22*, 2929.

[7] J. Xu, F. Rao, Z. Song, M. Xia, C. Peng, Y. Gu, M. Zhu, L. Wu, B. Liu, S. Feng, *Electrochem. Solid-State Lett.* **2012**, *15*, H59.

[8] D.-H. Kim, F. Merget, M. Laurenzis, P. H. Bolivar, H. Kurz, *J. Appl. Phys.* **2005**, 97, 083538.

[9] M. L. Lee, K. T. Yong, C. L. Gan, L. H. Ting, S. B. M. Daud, L. P. Shi, *J. Phys. D: Appl. Phys.* **2008**, *41*, 215402.

[10] M. L. Lee, K. T. Yong, C. L. Gan, L. H. Ting, L. P. Shi, *Jpn. J. Appl. Phys*. **2009**, *48*, 03A063.

[11] S. Buller, C. Koch, W. Bensch, P. Zalden, R. Sittner, S. Kremers, M. Wuttig, U. Schürmann, L. Kienle, T. Lichtweiß, J. Janek, B. Schönborn, *Chem. Mater.* **2012**, *24*, 3582.

[12] W. D. Song, L. P. Shi, X. S. Miao, C. Chong, *Appl. Phys. Lett.* **2007**, *90*, 91904.

[13] T. J. Park, D. H. Kim, S. M. Yoon, K. J. Choi, N. Y. Lee, B. G. Yu, S. Y. Choi, *Jpn. J. Appl. Phys.* **2006**, *45*, L1273.

[14] M. N. Schneider, T. Rosenthal, C. Stiewe, O. Oeckler, *Z. Kristallogr.* **2010**, *225*, 463.

[15] S. Welzmiller, T. Rosenthal, P. Ganter, L. Neudert, F. Fahrnbauer, P. Urban, C. Stiewe, J. de Boor, O. Oeckler, *Dalton Trans.* **2014**, DOI: 10.1039/c4dt00336e

[16] T. Rosenthal, M. N. Schneider, C. Stiewe, M. Döblinger, O. Oeckler, *Chem. Mater*. **2011**, *23*, 4349.

[17] T. Rosenthal, L. Neudert, P. Ganter, J. de Boor, C. Stiewe, O. Oeckler, *J. Solid State Chem.* **2014,** *215*, 231.

[18] P. F. P. Poudeu, M. G. Kanatzidis, *Chem. Commun.*, **2005**, *21*, 2672.

[19] U. Schürmann, V. Duppel, S. Buller, W. Bensch, L Kienle, *Cryst. Res. Technol.* **2011**, *46*, 561.

[20] H. W. Shu, S. Jaulmes, J. Flahaut, *J. Solid State Chem.* **1988**, *74*, 277.

[21] M. N. Schneider, P. Urban, A. Leinweber, M. Döblinger, O. Oeckler, *Phys. Rev. B* **2010**, *81*, 184102.

[22] U. Ross, A. Lotnyk, E. Thelander, B. Rauschenbach, *Appl. Phys. Lett.* **2014**, *104*, 121904.

[23] F. Fahrnbauer, P. Urban, S. Welzmiller, T. Schröder, T. Rosenthal, O. Oeckler, *Solid State Sci.* **2013**, *208*, 20.

[24] O. G. Karpinsky, L. E. Shelimova, M. A. Kretova, J.-P. Fleurial, *J. Alloys Comp.* **1998**, *268*, 112.

[25] T. Matsunaga, N. Yamada, *Phys. Rev. B* **2004**, 69, 104111.

[26] O. Oeckler, M. N. Schneider, F. Fahrnbauer, G. Vaughan, *Solid State Sci.* **2011**, *13*, 1157.

[27] P. Urban, M. N. Schneider, L. Erra, S. Welzmiller, F. Fahrnbauer, O. Oeckler, *CrystEngComm*, **2013**, *15*, 4823.

[28] M. N. Schneider, O. Oeckler, *Z. Anorg. Allg. Chem.* **2008**, *634*, 2557.

[29] *TOPAS-Academic*, *V. 4.1*, Coelho Software, Brisbane, Australia, **2007**.

[30] G. M. Sheldrick, *Acta Crystallogr. Sect. A* **2008**, *64*, 112.

[31] *XPREP, V. 6.12*, Siemens Analytical X-ray Instruments Inc, Madison, USA, **1996**.

[32] J.-L. Hodeau, P. Bordet, M. Anne, A. Prat, A. N. Fitch, E. Dooryhee, G. Vaughan, A. Freund, *Proc. SPIE* **1998**, *3448*, 353.

[33] J. P. Wright, G. B. M. Vaughan, A. N. Fitch, *IUCr Computing Commission Newsletter* **2003**, *1*, 92.

[34] G. Evans, R. F. Pettifer, *J. Appl. Crystallogr*. **2001**, *34*, 82.

[35] R. de L. Kronig, *J. Opt. Soc. Am.* **1926**, *12*, 547.

[36] B. L. Henke, E. M. Gullikson, J. C. Davis, *Atom. Data. Nucl. Data* **1993**, *54*, 181.

[37] P. W. Stephens, *J. Appl. Crystallogr.* **1999**, *32*, 281.

[38] *DigitalMicrograph 3.6.1*, Gatan Software, Pleasanton, USA, **1999**.

[39] *ESVision*, *4.0.164*, Emispec Systems Inc., Tempe, USA, **1994-2002**.

[40] P. Stadelmann; *JEMS*, *V. 3.3525U2008*, CIME-EPFL, Switzerland, **1999 -2008**.

[41] P. Urban, A. Simonov, T. Weber, O. Oeckler, *submitted*.

[42] S. S. Basanov, *Inorg. Mater.* **2001**, *37*, 871.

[43] T. Rosenthal, S. Welzmiller, O. Oeckler, *Solid State Sci.* **2013**, *25*, 118.

[44] T. Rosenthal, P. Urban, K. Nimmrich, L. Schenk, J. de Boor, C. Stiewe, O. Oeckler, *Chem. Mater.* **2014**, *26*, 2567.

[45] L. E. Shelimova, O. G. Karpinskii, T. E. Svechnikova, E. S. Avilov, M. A. Kretova, V. S. Zemskov, *Inorg. Mater*. **2004**, *40*, 1264.

[46] T. Matsunaga, H. Morita, R. Kojima, N. Yamada, K. Kifune, Y. Kubota, Y. Tabata, J.-J. Kim, M. Kobata, E. Ikenaga, K. Kobayashi *J.Appl. Phys.* **2008**, *103*, 093511.

4.4 Layered germanium tin antimony tellurides: element distribution, nanostructures and thermoelectric properties

S. Welzmiller, T. Rosenthal, P. Ganter, L. Neudert, F. Fahrnbauer, P. Urban, C. Stiewe, J. de Boor, O. Oeckler

Dalton Trans. **2014**, *43*, 10529-10540.

Abstract

In the system Ge-Sn-Sb-Te, there is a complete solid solution series between $GeSb_2Te_4$ and $SnSb_2Te_4$. As $Sn_2Sb_2Te_5$ does not exist, Sn can only partially replace Ge in $Ge_2Sb_2Te_5$; samples with 75% or more Sn are not homogeneous. The joint refinement of high-resolution synchrotron data measured at the K-absorption edges of Sn, Sb and Te combined with data measured at off-edge wavelengths unambiguously yields the element distribution in 21*R*-$Ge_{0.6}Sn_{0.4}Sb_2Te_4$ and 9*P*-$Ge_{1.3}Sn_{0.7}Sb_2Te_5$. In both cases, Sb predominantly concentrates on the position near the van der Waals gaps between distorted rocksalt-type slabs whereas Ge prefers the position in the middle of the slabs. No significant antisite disorder is present. Comparable trends can be found in related compounds; they are due to the single-side coordination of the Te atoms at the van der Waals gap, which can be compensated more effectively by Sb^{3+} due to its higher charge in comparison to Ge^{2+}. The structure model of 21*R*-$Ge_{0.6}Sn_{0.4}Sb_2Te_4$ was confirmed by high-resolution electron microscopy and electron diffraction. In contrast, electron diffraction patterns of 9*P*-$Ge_{1.3}Sn_{0.7}Sb_2Te_5$ reveal a significant extent of stacking disorder as evidenced by diffuse streaks along the stacking direction. The Seebeck coefficient is unaffected by the Sn substitution but the thermal conductivity drops by a factor of 2 which results in a thermoelectric figure of merit ZT = ~0.25 at 450 °C for both $Ge_{0.6}Sn_{0.4}Sb_2Te_4$ and $Ge_{1.3}Sn_{0.7}Sb_2Te_5$, which is higher than ~0.20 for unsubstituted stable layered Ge-Sb-Te compounds.

4.4.1 Introduction

Compounds in the system Ge-Sb-Te (so-called GST materials) with the general formula $(GeTe)_nSb_2Te_3$ are widely used as phase-change materials (PCM) on rewritable optical data storage media and in non-volatile PCRAM devices.[1-4] Data is stored by means of a reversible phase transition from a metastable crystalline to an amorphous phase of PCMs, which involves significant changes of the optical and electrical properties. Consequently, erasing

corresponds to recrystallization. The performance mainly depends on kinetic effects as a fast transition between the amorphous and crystalline phases is crucial for efficient write-erase cycles. The substitution of thin-film GST materials with Sn [5-10] increases the crystallization speed which enables fast erasing. It additionally decreases the melting point, which is favourable since it means that less energy is required for the amorphization. Both effects are due to the lower average bond dissociation energy of Sn-Te compared to Ge-Te.[11] As the materials properties required for PCMs are, at least in part, similar to those of good thermoelectrics,[12] GST materials turned out to exhibit thermoelectric figures of merit *ZT* up to 1.3.[13] *ZT* depends on the Seebeck coefficient *S*, the electrical σ and the thermal conductivity κ; $ZT = S^2\sigma T\kappa^{-1}$. Approaches to improving the *ZT* values focus on either influencing κ or the power factor $S^2\sigma$ However, both are interdependent according to the Wiedemann-Franz law ($\lambda/\sigma = LT$; with Lorenz number *L*). Sn doping should influence the thermoelectric properties as phonon scattering is enhanced when an element with a different atomic number is included on the same Wyckoff position.[14] In $(GeTe)_nSb_2Te_3$ phases with $n \geq 3$, quenching the disordered rocksalt-type high-temperature phase (stable above ~500 °C), which corresponds to the metastable crystalline phase of PCMs, yields metastable pseudo-cubic materials with pronounced nanostructures. They are often characterized by irregularly spaced and often intersecting defect layers [13-16] with limited lateral extension whose concentration depends on the GeTe content n. The highest *ZT* values (1.3 at ~450 °C) were observed for quenched phases with n = 12 or 19.[13]

At temperatures below ~500 °C – the exact temperature mainly depending on n –, layered trigonal phases of $(Ge_{1-x}Sn_xTe)_nSb_2Te_3$ are thermodynamically stable. They are formed by long-term annealing at temperatures below the existence range of the cubic high-temperature phase or during very slow cooling. These phases contain distorted rocksalt-type slabs with alternating anion (Te) and cation layers (Ge/Sb) which are separated by van der Waals gaps. In the case of 9*P*-$Ge_2Sb_2Te_5$ or 21*R*-$GeSb_2Te_4$, these slabs consist of 9 or 7 alternating anion and cation layers, respectively (compare Figures 3 and 7).[17, 18]

Sn-doped GST materials are a challenge for crystal structure determination as elements with similar electron counts (Sb, Sn, Te) are often disordered in comparable systems. The almost non-existing scattering contrast requires resonant X-ray diffraction to determine the element distribution over the Wyckoff sites present.[19-21] In diffraction experiments with wavelengths near the absorption edges, anomalous dispersion significantly changes the atom form factors of the respective elements and thus enhances the scattering contrast. The element distribution in single crystals of multinary tellurides has been unambiguously investigated by means of

resonant X-ray diffraction, e.g. for 39*R*-$M_{0.067}Sb_{0.667}Te_{0.266}$ (M=Ge, Sn),[22] 21*R*-$SnSb_2Te_4$[23] and 9*P*-$Ge_2Sb_2Te_5$[24]Therefore, it is a promising method to get a deeper insight in the structure-properties relationship of thermoelectric Sn-doped GST materials.

4.4.2 Results and Discussion

4.4.2.1 The solid solution series $(Ge_{1-x}Sn_x)Sb_2Te_4$ (x = 0-1)

Samples with the compositions $(Ge_{1-x}Sn_x)Sb_2Te_4$ (x = 0.25, 0.40, 0.50, 0.75) were obtained from stoichiometric melts of the elements. Rietveld refinements prove that they are single-phase and that all members of the solid solution series exhibit a 21*R*-type structure (space group $R\bar{3}m$), they are isostructural to the end members $GeSb_2Te_4$ [25] and $SnSb_2Te_4$.[23] The trend of the lattice parameters is linear according to Vegard's law over the whole region of the solid solution (Figure 1). The occupancy factors were chosen according to the results of the single-crystal structure analysis based on resonant scattering data (see below). The occupancy of Sb on each cation's Wyckoff position was fixed to the value of $Ge_{0.6}Sn_{0.4}Sb_2Te_4$ and the difference to full occupancy was filled with Ge and Sn according to their site preference ratio from the resonant single crystal refinement. With increasing Sn content, the bond lengths between cation and anion positions slightly increase according to the Rietveld refinement results; however, the standard deviations are rather large (cf. Fig. S1 in the ESI). Yet, this reflects the larger ionic radius of Sn in comparison to Ge. Fig. 2 shows the result of the Rietveld refinement for $Ge_{0.5}Sn_{0.5}Sb_2Te_4$, the other plots are given in the ESI (Fig. S2 – S4). Crystallographic data are summarized in Table 1, the refined parameters are given in Table 2.

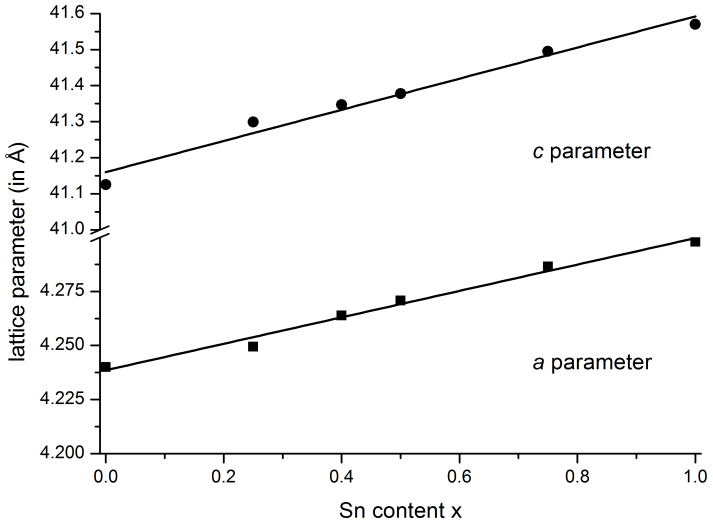

Fig. 1: Vegard's plot of compounds in the series $(Ge_{1-x}Sn_x)Sb_2Te_4$ (x = 0 - 1); *c* parameter (top) and *a* parameter (bottom); values for $GeSb_2Te_4$[25] ans $SnSb_2Te_4$[23] taken from literature.

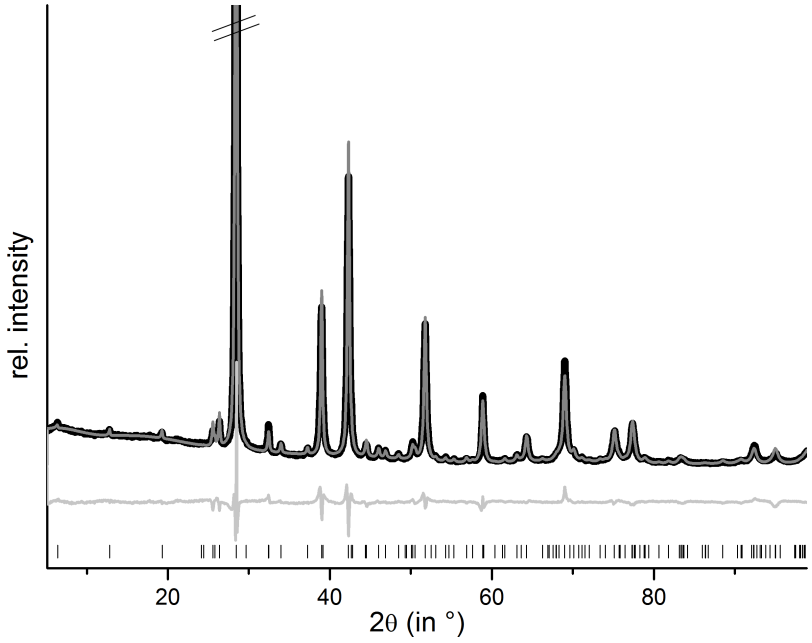

Fig. 2: Rietveld refinement of 21*R*-$Ge_{0.5}Sn_{0.5}Sb_2Te_4$ (the strongest reflection is cut off); vertical lines indicate calculated reflection positions, experimental (black) and calculated pattern (gray) and difference plot (below) are shown.

In order to precisely determine the element distribution, a single crystal for resonant diffraction experiments was grown by chemical transport (cf. Experimental Section). Energy-dispersive X-ray spectroscopy (EDX) yields a composition of $Ge_{9.5(5)}Sn_{6.0(5)}Sb_{28.7(3)}Te_{55.8(4)}$ (averaged from 3 point analyses). Taking into account normal valence states, this corresponds to the formula $Ge_{0.6}Sn_{0.4}Sb_2Te_4$ (calculated atom-%: $Ge_{8.6}Sn_{5.7}Sb_{28.6}Te_{57.1}$). This compound forms a 21*R* In_3Te_4-type structure with distorted rocksalt-type slabs as described above, which is depicted in Fig. 3.[25-29] The three slabs per unit cell are separated by van der Waals gaps with Te-Te distances (between the atoms A2, cf. Table 4 and Fig. 3) of 3.720 Å which indicate a partially covalent interaction (sum of van der Waals radii: 4.42 Å).[30] This is comparable to the corresponding Te-Te distances in 21*R*-type phases like $GeSb_2Te_4$[25], $SnSb_2Te_4$[23] or $PbSb_2Te_4$.[31] Among all these phases, these distances do not differ more than about 2%. The bond lengths in the distorted 3 + 3 coordination of the cations (C2) next to the van der Waals gap are 2.959 Å towards the gap (C2-A2) and 3.2117 Å towards the center of the slabs (C2-A1), respectively (cf. Fig. 3); the bond angles are A2-C2-A2: 92.19°; A1-C2-A1: 83.18 and A1-C2-A2: 92.15°. The cation-centered octahedra in the middle of the slabs are almost regular with bond lengths of 3.045 Å and angles of 88.88° and 91.12° respectively (A1-C1-A1). While Sn is almost uniformly distributed over both cation positions (occupancy factors 11.8% on position C2 and 16.3% on C1, respectively, cf. Fig. 3), Sb clearly prefers the position near the van der Waals gap (77.1% on position C2). In contrast, the position in the

centre of the rocksalt-type slab (C1) shows almost equal amounts of Ge (37.8%) and Sb (45.8%). The same trend can be found in comparable compounds like $GeSb_2Te_4$,[25] $SnSb_2Te_4$,[23] $PbSb_2Te_4$[31] and $GeBi_2Te_4$.[32] Tables 3 and 4 summarize the crystal data and give parameters of the refinement. The atomic coordinates obtained from the single-crystal data and from the corresponding Rietveld refinement are very similar, taking into account their standard deviation, the single-crystal values are of course more precise.

Table 1. Results from the Rietveld refinements for $(Ge_{1-x}Sn_x)Sb_2Te_4$ compounds with x = 0.25, 0.4, 0.5, 0.75

Compound	$Ge_{0.75}Sn_{0.25}Sb_2Te_4$	$Ge_{0.6}Sn_{0.4}Sb_2Te_4$	$Ge_{0.5}Sn_{0.5}Sb_2Te_4$	$Ge_{0.25}Sn_{0.75}Sb_2Te_4$
Formula mass (in g mol^{-1})	838.06	844.97	849.58	861.11
F(000)	1039.5	1048	1053	1066.5
Crystal system / space group	trigonal / $R\bar{3}m$ (no. 166)			
Z	3			
Cell parameters (in Å)	a = 4.24950(12) c = 41.299(3)	a = 4.26384(14) c = 41.346(3)	a = 4.27072(13) c = 41.376(3)	a = 4.28656(14) c = 41.495(4)
Cell volume (in Å^3)	645.87 (6)	650.973(7)	653.66(6)	660.30(7)
X-ray density (in g·cm^{-3})	6.46	6.47	6.48	6.50
Absorption coefficient (in mm^{-1})	162.24	163.77	164.97	167.88
Wavelength (in Å)	Cu-$K_{\alpha1}$ (λ = 1.540596 Å)			
2θ range (in °)	$5 \le 2\theta \le 99$			
Profile function	fundamental parameters (direct convolution approach)			
Restraints	6			
Reflections	115	117	117	119
Parameters / thereof background	37 / 18	37 / 18	37 / 18	37 / 18
R_p / R_{wp}	0.0235 / 0.0349	0.0234 / 0.0340	0.0238 / 0.0342	0.0246 / 0.0369
R_{Bragg}	0.0350	0.0331	0.0333	0.0332
GooF	1.326	1.436	1.451	1.567

Table 2. Wyckoff positions, atom coordinates, occupancy factors and isotropic displacement parameters B_{iso} (in Å^3) for $(Ge_{1-x}Sn_x)Sb_2Te_4$ compounds with x = 0.25, 0.4, 0.5, 0.75.

Atom	Formula	Position	Wyckoff position	x y z	Occupancy	B_{iso}
Ge/Sn/Sb	$Ge_{0.75}Sn_{0.25}Sb_2Te_4$	C1	3*a*	0 0 0	0.4065 / 0.1355/ 0.458	1.56(13)
	$Ge_{0.6}Sn_{0.4}Sb_2Te_4$			0 0 0	0.378 / 0.1634 / 0.458	1.33(13)
	$Ge_{0.5}Sn_{0.5}Sb_2Te_4$			0 0 0	0.271 / 0.271 / 0.458	1.10(9)
	$Ge_{0.25}Sn_{0.75}Sb_2Te_4$			0 0 0	0.1355 / 0.4065 / 0.458	1.90(14)
Ge/Sn/Sb	$Ge_{0.75}Sn_{0.25}Sb_2Te_4$	C2	6*c*	0 0 0.42746(16)	0.1718 / 0.0572 / 0.771	1.56(13)
	$Ge_{0.6}Sn_{0.4}Sb_2Te_4$			0 0 0.42740(16)	0.1107 / 0.1183 / 0.771	1.34(13)
	$Ge_{0.5}Sn_{0.5}Sb_2Te_4$			0 0 0.42725(14)	0.1145 / 0.1145 / 0.771	1.10(9)
	$Ge_{0.25}Sn_{0.75}Sb_2Te_4$			0 0 0.4277(2)	0.0572 / 0.1718 / 0.771	1.90(14)
Te	$Ge_{0.75}Sn_{0.25}Sb_2Te_4$	A1	6*c*	0 0 0.13205(15)	1	1.61(11)
	$Ge_{0.6}Sn_{0.4}Sb_2Te_4$			0 0 0.13208(15)	1	1.21(11)
	$Ge_{0.5}Sn_{0.5}Sb_2Te_4$			0 0 0.13251(14)	1	1.58(12)
	$Ge_{0.25}Sn_{0.75}Sb_2Te_4$			0 0 0.1324(2)	1	1.55(12)
Te	$Ge_{0.75}Sn_{0.25}Sb_2Te_4$	A2	6*c*	0 0 0.2900(2)	1	1.61(11)
	$Ge_{0.6}Sn_{0.4}Sb_2Te_4$			0 0 0.2904(2)	1	1.21(11)
	$Ge_{0.5}Sn_{0.5}Sb_2Te_4$			0 0 0.28993(18)	1	1.58(12)
	$Ge_{0.25}Sn_{0.75}Sb_2Te_4$			0 0 0.2898(3)	1	1.55(12)

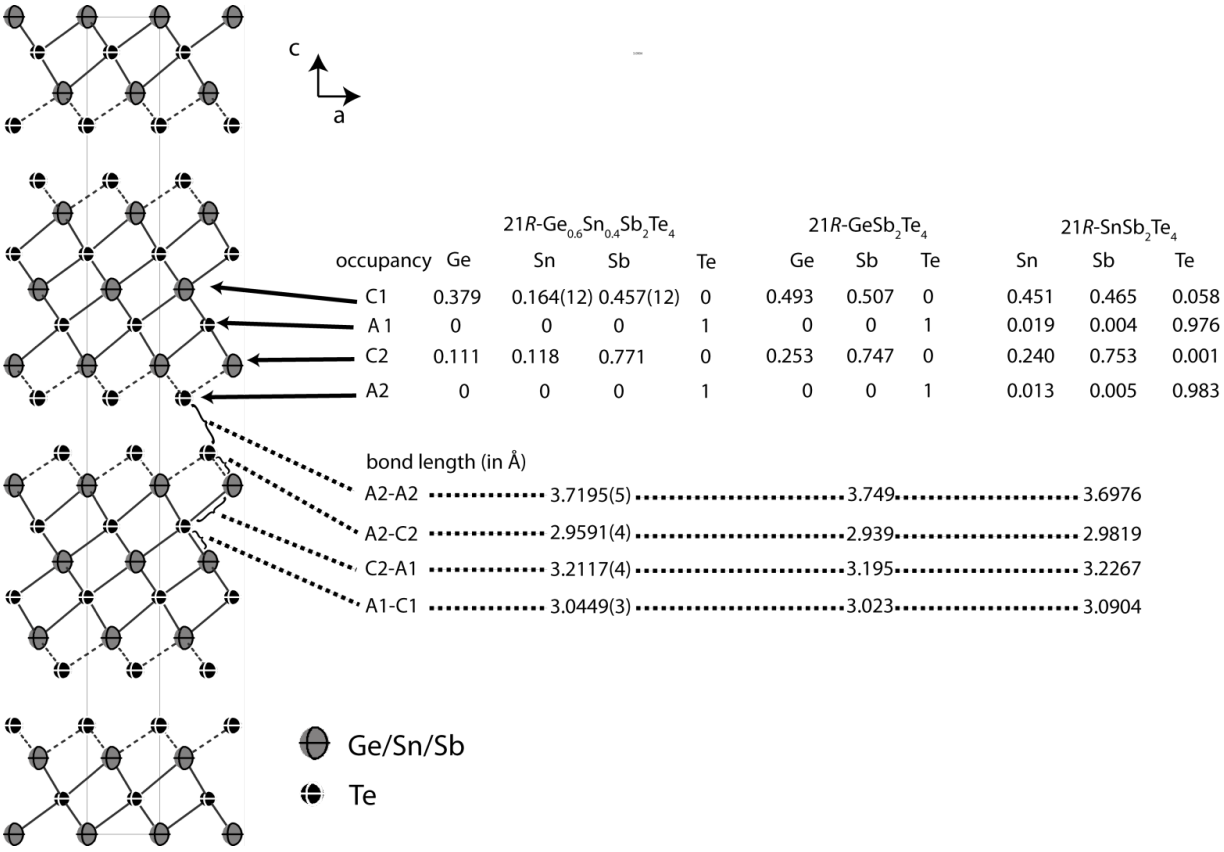

Fig. 3: Atom distribution (occupancy factors, missing esd's are a consequence of constraints) for each positon and bond lengths in the refined model of 21*R*-$Ge_{\sim 0.6}Sn_{\sim 0.4}Sb_2Te_4$ at 293 K (displacement ellipsoids drawn at 99 % probability level) compared with $GeSb_2Te_4$[25] and $SnSb_2Te_4$[23] (cation-anion antisite disorder is not significant in $SnSb_2Te_4$, the e.s.d.'s of the occupancy factors are ~ 0.006).

Table 3. Crystallographic data on the structure refinement of 21R-$Ge_{0.6}Sn_{0.4}Sb_2Te_4$ at 293 K; residual electron density averaged over all datasets.

	$Ge_{0.6}Sn_{0.4}Sb_2Te_4$					
Formula mass (in g mol^{-1})	844.97					
Cell parameters (in Å)	a = 4.26384(14) , c = 41.346(3)					
Cell volume (in $Å^3$)	650.973(7)					
Crystal system / space group	trigonal, $R\ \bar{3}m$ (no. 166)					
X-ray density (in gcm^{-3})	6.466					
F(000)	1048					
Formular units (per unit cell)	3					
crystal size (in mm)	0.10 · 0.09 · 0.01					
Wavelength (in Å)	0.71073	0.56356	0.42468	0.40681	0.38979	all datasets
sin(q)/l	0.70	0.75	0.65	0.55	0.60	
Absorption coefficient (in mm^{-1})	22.47	11.91	5.55	9.34	12.04	
Measured / independent reflections	2667 / 370	2112 / 366	5351 / 790	5334 / 383	8716 / 370	
R_{int}	0.0634	0.0408	0.0310	0.0401	0.0392	
R_σ	0.0268	0.0374	0.0252	0.0380	0.0277	
Parameters / restraints	22 / 15					
Residual electron density (min / max) (in $eÅ^{-3}$)	-1.91 / +3.36					
$R_{(obs)}$ [(a)]	0.0370	0.0533	0.0419	0.0473	0.0366	0.0362
$wR_{(obs)}$ [(b)]	0.0544	0.1082	0.0898	0.1021	0.0754	0.0509
$R_{(all)}$ [(a)]	0.0424	0.0596	0.0500	0.0536	0.0513	0.0411
$wR_{(all)}$ [(b)]	0.0563	0.1092	0.0918	0.1053	0.0811	0.0516
$GooF_{(obs)}$	1.25	2.25	1.93	2.24	1.53	1.59
$GooF_{(all)}$	1.15	2.04	1.73	2.08	1.41	1.46

[(a)] $R=\sum|F_o-F_c|/\sum|F_o|$.
[(b)] $wR=[\sum[w(F_0-F_c)^2]/\sum[w(F_0)^2]]^{1/2}$; $w=1/[\sigma^2(F_0)+0.0004\ (F_0^2)]$.

Table 4. Structure parameters of 21*R*-$Ge_{0.6}Sn_{0.4}Sb_2Te_4$ at 293 K: atom positions and coordinates, occupancy factors (on each position two parameters were refined and the other is calculated from the difference to full occupancy), equivalent isotropic (u_{eq} in $Å^2$) and anisotropic displacement parameters (u_{ij} in $Å^2$; $u_{23} = u_{13} = 0$)

Atom	Position	Wyckoff	x	y	z	Occupancy	u_{eq}	$u_{11} = u_{22} = 2 \cdot u_{12}$	u_{33}
Ge/Sn/Sb	C1	3*a*	0	0	0	Ge 0.379			
						Sb 0.457(12)	0.02466(17)	0.0235(2)	0.0269(3)
						Sn 0.164(12)			
Ge/Sn/Sb	C2	6*c*	0	0	0.426568(11)	Ge 0.111			
						Sb 0.771	0.02434(12)	0.02234(14)	0.0284(2)
						Sn 0.118			
Te	A1	6*c*	0	0	0.132947(8)	Te 1	0.01858(11)	0.01922(13)	0.01729(17)
Te	A2	6*c*	0	0	0.289989(7)	Te 1	0.01581(10)	0.01666(13)	0.01412(17)

HRTEM images and diffraction patterns of a thinned crystal of $Ge_{0.75}Sn_{0.25}Sb_2Te_4$ whose composition was confirmed by TEM-EDX (measured $Ge_{12.2(7)}Sn_{5.5(11)}Sb_{29(2)}Te_{53(2)}$; calculated $Ge_{10.7}Sn_{3.6}Sb_{28.6}Te_{57.1}$) match well with simulations (Fig. 4 and 5). The average *c* parameter from TEM experiments is 41(1) Å in accordance with the 41.346(3) Å obtained by X-ray diffraction (Table 1). No phase separation or exsolution was observed; the sample is homogeneous. In the SAED patterns, as well as in the Fourier transform of the HRTEM image every seventh reflection is strong, which indicates that there are seven layers per rocksalt-type slab corresponding to a trigonal structure ($R\bar{3}m$) with a 21*R* stacking sequence. The variance of the interatomic distances derived from X-ray data is also visible in the HRTEM images; they show sequences of 7 atom layers are separated by van der Waals gaps (Fig. 4). This is confirmed by image simulations based on the structure model of $Ge_{0.75}Sn_{0.25}Sb_2Te_4$ determined by Rietveld refinement on X-ray powder data. No diffuse intensities along [001]* are visible in the SAED patterns; therefore, no stacking disorder is present.

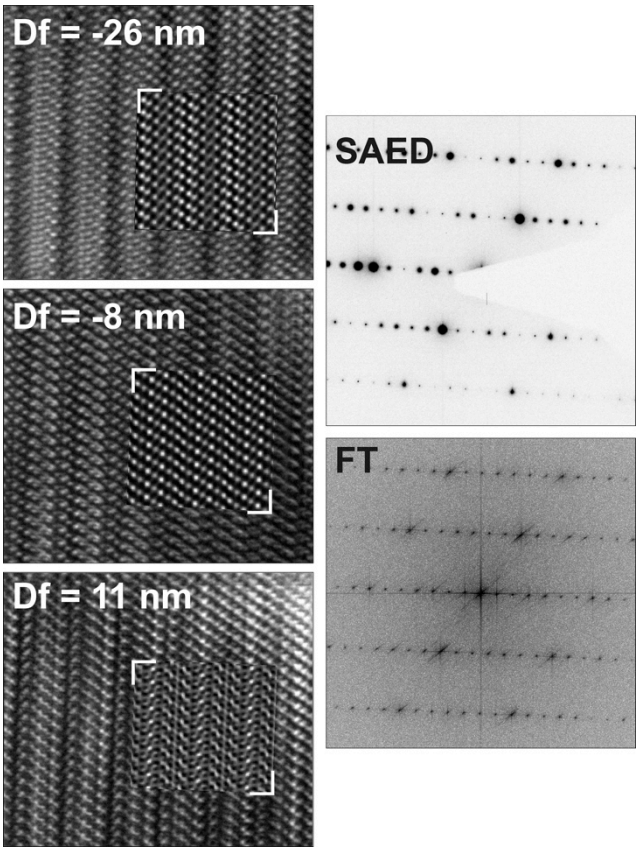

Fig. : Fourier filtered HRTEM images (zone axis <100>, different defocus values) with inserted image simulations (thickness 6 unit cells along the viewing direction, *C*s = 1.2, spread of defocus 2.14 nm, beam semiconvergence angle of 0.4 mrad) based on the structure model for $Ge_{0.75}Sn_{0.25}Sb_2Te_4$ determined by Rietveld refinement on X-ray powder data (left); corresponding Fourier transform (for df = -8 nm) and SAED pattern (right).

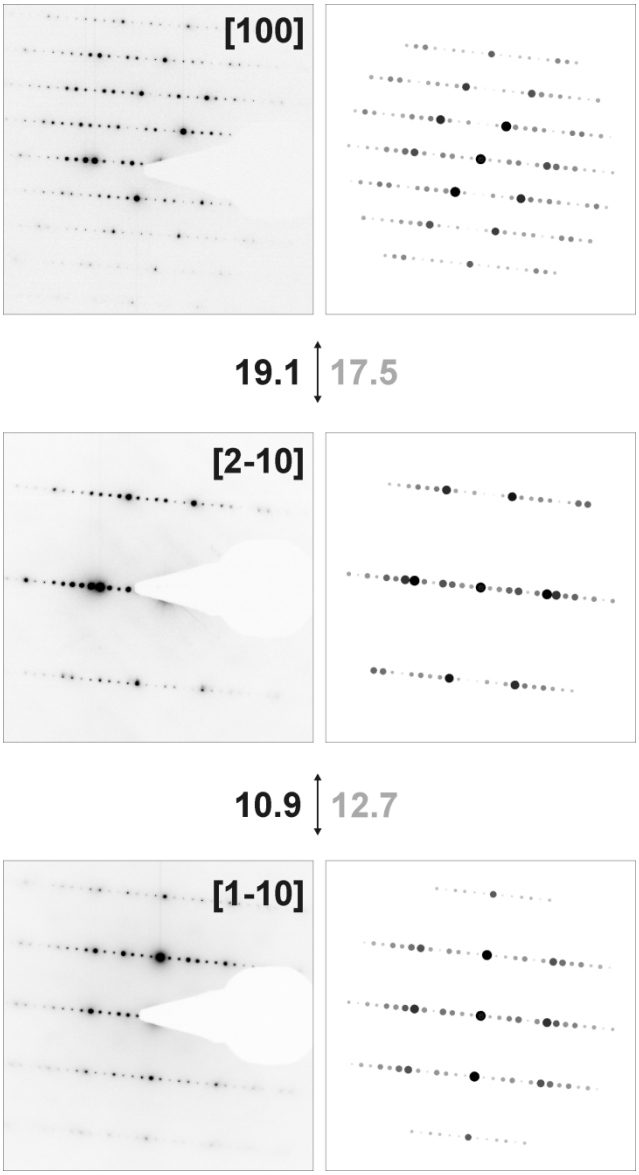

Fig. 5: SAED patterns of $Ge_{0.75}Sn_{0.25}Sb_2Te_4$ and corresponding simulations (kinematical intensities) based on the corresponding structure model determined by Rietveld refinement (cf. Tables 1 and 2) with calculated (black) and measured (gray) tilt angles between the zone axes.

4.4.2.2 Mixed crystals $(Ge_{1-x}Sn_x)_2Sb_2Te_5$ (x= 0.35, 0.5)

Rietveld refinements comfirm that homogemeous samples of $(Ge_{1-x}Sn_xTe)_2Sb_2Te_3$ with x = 0.50 and 0.35 could be obtained by melting stoichiometric amounts of the pure elements, quenching in water and subsequently annealing them. The compounds are isostructural to the end member 9*P*-$Ge_2Sb_2Te_5$; however, the other end member $Sn_2Sb_2Te_5$ does not exist. A sample with x = 0.75 contains a small amount of a side phase. This is most likely due to a partial decomposition,[8] probably into $Ge_{1-x}Sn_xSb_2Te_4$ and $Ge_{1-x}Sn_xTe$. Structure refinements using the Rietveld method were carried out with powder diffraction data of $GeSnSb_2Te_5$ and

$Ge_{1.3}Sn_{0.7}Sb_2Te_5$ (cf. Experimental section). Constraints concerning the sum formula and element distribution set up in the same way as explained above for $(Ge_{1-x}Sn_x)Sb_2Te_4$. Figure 6 shows the result of the Rietveld refinement of $GeSnSb_2Te_5$, the corresponding data for $Ge_{1.3}Sn_{0.7}Sb_2Te_5$ are presented in the ESI (Figure S5). Further information about the refinements of $GeSnSb_2Te_5$ and $Ge_{1.3}Sn_{0.7}Sb_2Te_5$ powder samples is given in Table 5, the refined atom parameters are listed in Table 6.

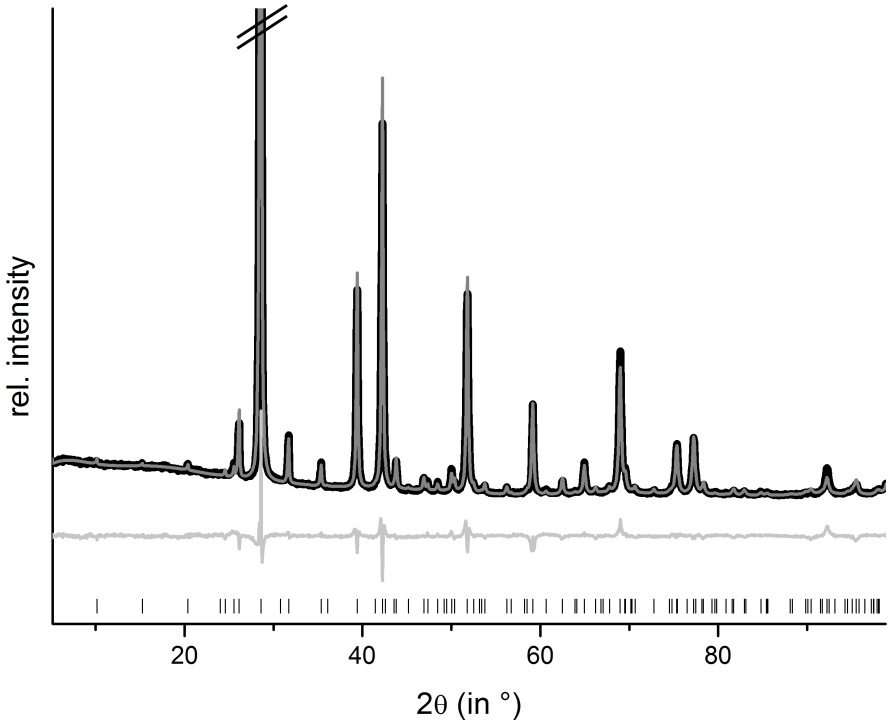

Fig. 6: Rietveld refinement of 9*P*-$GeSnSb_2Te_5$; (the strongest reflection is cut off); vertical lines indicate calculated reflection positions, experimental (black) and calculated pattern (gray) and difference plot (below) are shown.

A single crystal obtained by chemical transport was used for resonant diffraction experiments in order to precisely determine the element distribution. The composition of the single crystal was determined by SEM-EDX. Taking into account electroneutrality, the formula is very close to $Ge_{1.3}Sn_{0.7}Sb_2Te_5$ (experiment: $Ge_{15.7(10)}Sn_{8.2(2)}Sb_{21.6(4)}Te_{54.4(14)}$, calculated: $Ge_{14.4}Sn_{7.8}Sb_{22.2}Te_{55.6}$).

Similar to $Ge_2Sb_2Te_5$, $Ge_{1.3}Sn_{0.7}Sb_2Te_5$ forms the 9*P*-$Pb_2Bi_2Se_5$ structure type with 9 alternating anion and cation layers, respectively, per distorted rocksalt-type slab and unit cell. The slabs contain two additional layers compared to 21*R*-$GeSb_2Te_4$ but their arrangement is very similar (cf. Fig. 7). Further information about the structure analysis is given in the Experimental section, Table 7 presents details of the refinement; refined atom parameters are given in Table 8.

Fig. 7 gives an overview of the structure and the element distribution in comparison with $Ge_2Sb_2Te_5$. The Te atoms at the van der Waals gap (A3) have a distance of 3.728 Å to the next slab, which is slightly larger than for $Ge_{0.6}Sn_{0.4}Sb_2Te_4$ (3.720 Å). The bond length alteration in the rocksalt-type slabs is comparable to 21*R*-type $(Ge_{1-x}Sn_x)Sb_2Te_4$ phases described above. The coordination sphere of cations near the van der Waals gap (C2) corresponds to distorted octahedrons with shorter bonds (2.939 Å) to the unsaturated Te atoms at the van der Waals gap (A3) and longer ones to the Te atom in the middle of the slab (A2, 3.232) Å; the bond angles indicate pronounced distortion (A3-C2-A3: 92.82°, A3-C2-A2: 92.17°, A2-C2-A2: 82.40°). The C1 octahedrons closer to the center of the slab are more regular with bond lengths of 2.996 and 3.082 Å to the Te atoms A1 and A2, respectively (bond angles: A1-C1-A1: 87.38°, A2-C1-A2: 90.57°; A2-C1-A1: 91.00°). In $Ge_{1.3}Sn_{0.7}Sb_2Te$, all bonds are slightly longer than in $Ge_{0.6}Sn_{0.4}Sb_2Te_4$ and $Ge_2Sb_2Te_5$.[24] This is due to the higher Sn content (ionic radii: Sn 0.69 Å, Ge 0.53 Å].[30] The larger Sb with its higher oxidation state concentrates on the position C2 near the van der Waals gap (occupancy 59.8%), where Sn (22.4%) is also slightly preferred in comparision to Ge (17.8%). The cation position C1 is occupied by more Ge (47.2%) than Sb (40.2%) and a little Sn (12.6%). The atomic coordinates of $Ge_{1.3}Sn_{0.7}Sb_2Te_5$ obtained from single crystal refinement and Rietveld analysis, respectively, differ by up to 10σ. This is probably due to the fact that standard deviations are often underestimated in Rietveld method.

Table 5. Results from the Rietveld refinements for $GeSnSb_2Te_5$.and $Ge_{1.3}Sn_{0.7}Sb_2Te_5$

Sum formula	$Ge_{1.3}Sn_{0.7}Sb_2Te_5$	$GeSnSb_2Te_5$
Formula mass (in g mol^{-1})	1059.01	1072.84
F(000)	386.6	392
Crystal system / space group	trigonal / $P\ \bar{3}m1$ (no. 164)	
Z	1	
Cell parameters (in Å)	a = 4.25792(11) c = 17.3657(14)	a = 4.27486(7) c = 17.4165(8)
Cell volume (in $Å^3$)	272.66(3)	275.635(16)
X-ray density (in gcm^{-3})	6.45	6.46
Absorption coefficient (in mm^{-1})	158.50	161.19
Wavelength (in Å)	Cu-$K_{\alpha1}$ (λ = 1.540596 Å)	
2θ (in °)	$5 \le 2\theta \le 99$	
Profile function	fundamental parameters (direct convolution approach)	
Restraints	6	
Reflections	148	148
Parameters / thereof background	38 / 18	38 / 18
R_p / R_{wp}	0.0258 / 0.0375	0.0226 / 0.0340
R_{Bragg}	0.0212	0.0158
GooF	1.660	1.430

Table 6. Wyckoff-positions, atom coordinates, occupancy factors, isotropic temperature factors (in Å^3) for $GeSnSb_2Te_5$.and $Ge_{1.3}Sn_{0.7}Sb_2Te_5$ from powder data

Atom	Formula	Position	Wyckoff position	x y z	Occupancy	B_{iso}
Te	$Ge_{1.3}Sn_{0.7}Sb_2Te_5$	A1	1a	0 0 0	1	1.56(10)
	$GeSnSb_2Te_5$			0 0 0	1	1.41(8)
Ge/Sn/Sb	$Ge_{1.3}Sn_{0.7}Sb_2Te_5$	C1	2d	2/3 1/3 0.1190(11)	0.472 / 0.126 / 0.402	1.70(13)
	$GeSnSb_2Te_5$			2/3 1/3 0.1097(9)	0.299 / 0.299 / 0.402	2.26(10)
Te	$Ge_{1.3}Sn_{0.7}Sb_2Te_5$	A2	1a	1/3 2/3 0.2065(8)	1	1.56(10)
	$GeSnSb_2Te_5$			1/3 2/3 0.2082(6)	1	1.41(8)
Ge/Sn/Sb	$Ge_{1.3}Sn_{0.7}Sb_2Te_5$	C2	2c	0 0 0.3235(6)	0.178 / 0.224 / 0.598	1.70(13)
	$GeSnSb_2Te_5$			0 0 0.3244(5)	0.201 / 0.201 / 0.598	2.26(10)
Te	$Ge_{1.3}Sn_{0.7}Sb_2Te_5$	A3	2d	2/3 1/3 0.4183(8)	1	1.56(10)
	$GeSnSb_2Te_5$			2/3 1/3 0.4189(6)	1	1.41(8)

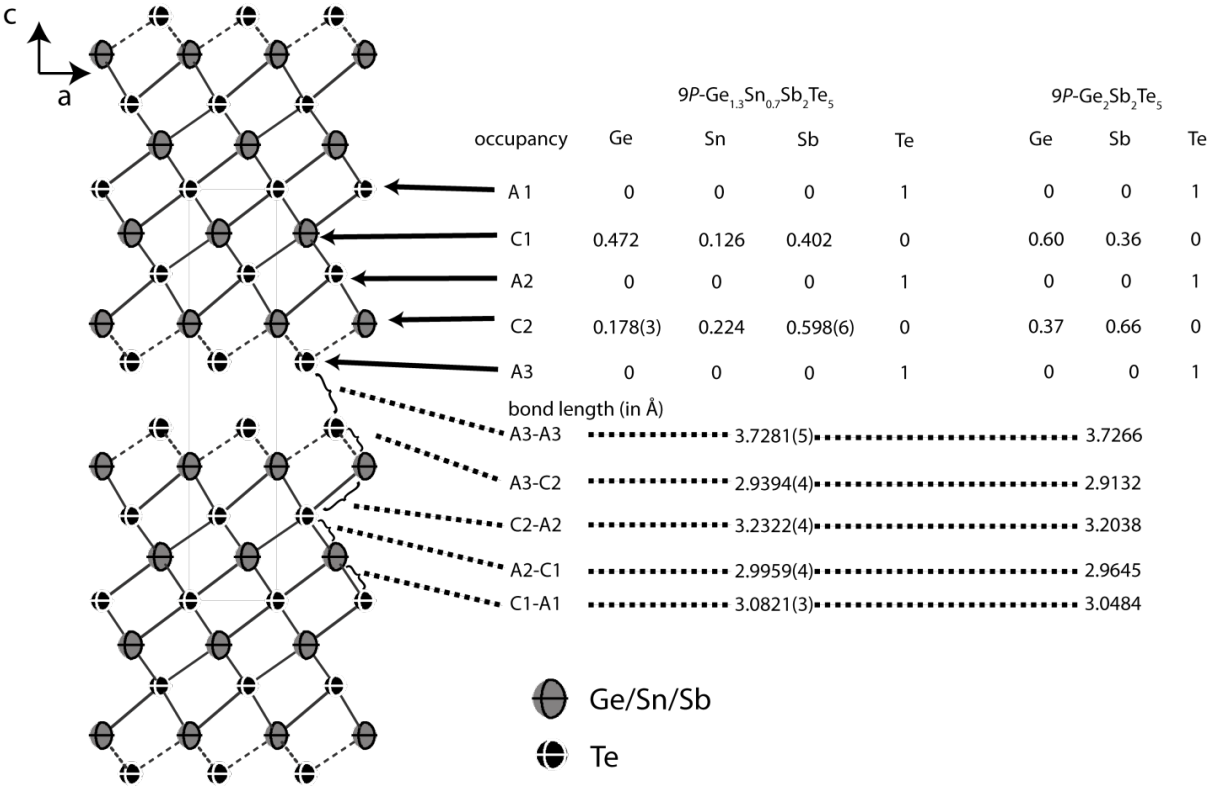

Fig 7: Atom distribution (occupancy factors, missing esd's are a consequence of constraints) for each element and bond lengths in the refined model of $Ge_{1.3}Sn_{0.7}Sb_2Te_5$ at 293 K (displacement ellipsoids drawn at 99 % probability level) compared with $Ge_2Sb_2Te_5$.[24]

TEM investigations of quenched bulk samples of $GeSnSb_2Te_5$ corroborate the structure and composition of this quarternary trigonal phase, TEM-EDX measurements yield $Ge_{12.1(2)}Sn_{12.3(2)}Sb_{23.2(5)}Te_{52.5(5)}$ (calculated for $GeSnSb_2Te_5$: $Ge_{11.1}Sn_{11.1}Sb_{22.2}Te_{55.5}$). For a crushed fragment of the ingot with the nominal composition $Ge_{1.3}Sn_{0.7}Sb_2Te_5$ used for thermoelectric characterization (see below), EDX yields $Ge_{14.8(2)}Sn_{9.5(2)}Sb_{21.6(5)}Te_{54.0(5)}$

(calculated for $Ge_{1.3}Sn_{0.7}Sb_2Te_5$: $Ge_{14.4}Sn_{7.8}Sb_{22.2}Te_{55.5}$). HRTEM images as well as SAED patterns of the same sample show a *d*-value of 17 Å which corresponds to the [001]* direction of 9*P*-$Ge_{2-x}Sn_xSb_2Te_5$. Diffuse streaks along [001]* (cf. Fig. 8) indicate a certain degree of stacking disorder or the presence of rocksalt-type slabs with varying thickness.

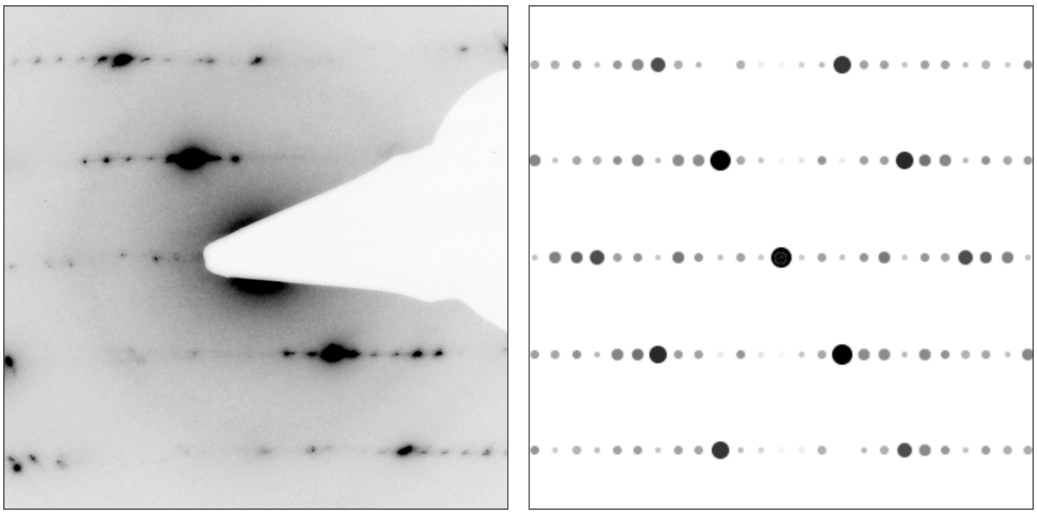

Fig. 8: Experimental SAED pattern (zone axis <110>, left) of a crystal from a bulk sample of $Ge_{1.3}Sn_{0.7}Sb_2Te_5$ and a corresponding calculated one (right) based on the structure model from $Ge_{1.3}Sn_{0.7}Sb_2Te_5$.

Table 7. Crystallographic data on the structure refinement of 9*P*-$Ge_{1.3}Sn_{0.7}Sb_2Te_5$ at 293 K; residual electron density averaged over all datasets.

Formular	$Ge_{1.3}Sn_{0.7}Sb_2Te_5$					
Formula mass (in g mol^{-1})	1058.96					
Cell parameters (in Å)	a = 4.25793(11) , c = 17.3657(14)					
Cell volume (in Å^3)	270.83(7)					
Crystal system / space group	trigonal, $P\ \bar{3}m1$ (no. 164)					
X-ray density (in gcm^{-3})	6.45					
F(000)	439					
Z	1					
crystal size (in mm)	0.20 · 0.09 · 0.03					
Wavelength (in Å)	0.71073	0.56356	0.42468	0.40681	0.38979	all datasets
sin(q)/l	0.71	0.70	0.52	0.70	0.50	
Absorption coefficient (in mm^{-1})	23.23	12.31	6.81	9.32	12.12	
Measured/independent reflections	2667 / 370	2112 / 366	5351 / 790	5334 / 383	8440 / 950	
R_{int}	0.0634	0.0406	0.0310	0.0401	0.0391	
R_σ	0.0268	0.0374	0.0252	0.0383	0.0254	
Parameters/restraints	19 / 13					
Residual electron density (min/max) (in eÅ^{-3})	-1.95 / +2.64					
$R_{(obs)}$ [(a)]	0.0362	0.0516	0.0382	0.0436	0.0350	0.0393
$wR_{(obs)}$ [(b)]	0.0532	0.0771	0.0763	0.0814	0.0700	0.0722
$R_{(all)}$ [(a)]	0.0416	0.0579	0.0463	0.0498	0.0456	0.0470
$wR_{(all)}$ [(b)]	0.0552	0.0786	0.0786	0.0745	0.0745	0.0753
$GooF_{(obs)}$	1.22	1.60	1.64	1.78	1.46	1.53
$GooF_{(all)}$	1.12	1.46	1.48	1.69	1.37	1.41

[(a)] $R=\sum|F_o-F_c|/\sum|F_o|$.
[(b)] $wR=[\sum[w(F_0-F_c)^2]/\sum[w(F_0)^2]]^{1/2}$; $w=1/[\sigma^2(F_0)+0.0016(F_0^2)]$

Table 8. Structure parameters of 9*P*-$Ge_{1.3}Sn_{0.7}Sb_2Te_5$ at 293 K: atom positions and coordinates, occupancy factors (on each position two parameters were refined and the other is calculated from the difference to full occupancy), equivalent isotropic (u_{eq} in Å^2) and anisotropic displacement parameters (u_{ij} in Å^2; $u_{23} = u_{13} = 0$)

Atom	Position	Wyckoff	x	y	z	Occupancy	u_{eq}	$u_{11} = u_{22} = 2 \cdot u_{12}$	u_{33}
Te1	A1	1a	0	0	0	Te 1	0.01699(10)	0.01752(13)	0.01593(17)
Ge/Sn/Sb2	C1	2d	2/3	1/3	0.10705(3)	Sb 0.402(6)	0.02547(13)	0.02393(16)	0.0286(2)
						Ge 0.472(3)			
						Sn 0.126(7)			
Te3	A2	2d	1/3	2/3	0.205655(18)	Te 1	0.01729(9)	0.01789(11)	0.01608(15)
Ge/Sn/Sb4	C2	2c	0	0	0.32650(3)	Sb 0.598(6)	0.02326(10)	0.02144(13)	0.02692(18)
						Ge 0.178(3)			
						Sn 0.224(7)			
Te5	A3	2d	2/3	1/3	0.41930(2)	Te 1	0.02015(9)	0.02072(12)	0.01900(16)

4.4.2.3 Thermoelectric properties

$Ge_{0.6}Sn_{0.4}Sb_2Te_4$ and $Ge_{1.3}Sn_{0.7}Sb_2Te_5$, for which single-crystal data are available, as well as $GeSnSb_2Te_5$ show metallic behavior of the electrical conductivity σ the absolute values are similar and lie in the range of poor metals (cf. Fig. 9). Compared to water-quenched $GeSb_2Te_4$ and $Ge_2Sb_2Te_5$, which exhibit the crystal structure of the corresponding stable phase, the values of the Sn-containing samples are lower by a factor of 3;.[33] σ of $Ge_{0.6}Sn_{0.4}Sb_2Te_4$ is about 50% of that of melt-spun, i.e. rapidly solidified $GeSb_2Te_4$ at room temperature and 75% at 700 K, respectively, while the values of melt-spun $Ge_2Sb_2Te_5$ [33] are more or less equal to those of quenched $Ge_{1.3}Sn_{0.7}Sb_2Te_5$ as reported here. The Seebeck coefficients *S* of the samples investigated are very similar. The values for $Ge_{1.3}Sn_{0.7}Sb_2Te_5$ and $GeSnSb_2Te_5$ are in the same range as those of water-quenched $Ge_2Sb_2Te_5$ and ~25% lower than those of the rapidly solidified (melt spun) compound between 180 K and 380 K.[33] This might be due to grain boundaries or anti-site defects in the melt spun sample.

The difference in the *ZT* values is a consequence of the different thermal conductivities κ. These are only 67% ($Ge_{1.3}Sn_{0.7}Sb_2Te_5$) and 56% ($Ge_{0.6}Sn_{0.4}Sb_2Te_4$), respectively, of those of unsubstituted samples (3.2 W/mK for $GeSb_2Te_4$ and 3.0 W/mK for $Ge_2Sb_2Te_5$ at room temperature).[34] The phononic part κ_L of the thermal conductivity (electronic part calculated using $L = 2.44 \bullet 10^{-8}\ V^2K^{-2}$ which is a typical value for good metals and degenerate semiconductors[35]) decreases slightly with increasing temperature for $Ge_{0.6}Sn_{0.4}Sb_2Te_4$ and $Ge_{1.3}Sn_{0.7}Sb_2Te_5$ while it increases for $GeSnSb_2Te_5$. Therefore, Sn substitution reduces κ for lower substitution rates ($Ge_{1.3}Sn_{0.7}Sb_2Te_5$ and $Ge_{0.6}Sn_{0.4}Sb_2Te_4$ compared with $Ge_2Sb_2Te_5$ and

$GeSb_2Te_4$), which results in higher *ZT* values up to 0.25 than those of the unsubstituted samples (*ZT* up to 0.2).[33] Since κ of $GeSnSb_2Te_5$ increases with the temperature, its *ZT* value at high temperatures is significantly lower than that of $Ge_{1.3}Sn_{0.7}Sb_2Te_5$

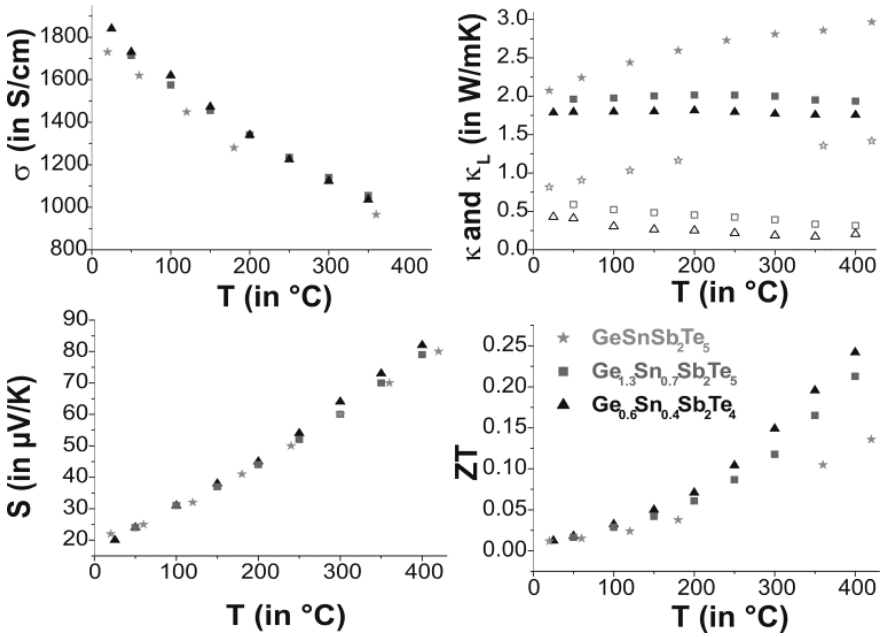

Fig. 9: Thermoelectric properties of $Ge_{0.6}Sn_{0.4}Sb_2Te_4$, $Ge_{1.3}Sn_{0.7}Sb_2Te_5$ and $GeSnSb_2Te_5$: electrical conductivity and Seebeck coefficient (left side top to bottom); lattice thermal conductivity (κ bold and κ_L open faced) and thermoelectric figure of merit (right side top to bottom).

4.4.3 Conclusion

Homogeneous bulk samples of Sn-substituted GST materials have so far been investigated predominantly as thin films, because their performance as PCMs can be enhanced by substituting Sn into the structure.[5 6, 10] Compounds with a similar composition but a different structure could be obtained as bulk samples by quenching stoichiometric melts of elements involved. The layered phases $Ge_{0.6}Sn_{0.4}Sb_2Te_4$ and $Ge_{1.3}Sn_{0.7}Sb_2Te_5$ show improved thermoelectric properties compared to $GeSb_2Te_4$ and $Ge_2Sb_2Te_5$ since the thermal conductivity is decreased while the Seebeck coefficient remains nearly unaffected at high temperatures (~400 °C). The lower thermal conductivity might be due to the introduction of an additional element in the cation substructure that can act as a phonon scattering center. Detailed structural data on the element distribution obtained from single crystals grown by chemical transport reactions show that the cations are not randomly distributed but exhibit clear preferences for certain positions. $Ge_{1-x}Sn_xSb_2Te_4$ and $(Ge_{1-x}Sn_x)_2Sb_2Te_5$ form layered phases comparable to those known from the corresponding stable modifications of GST materials. The trend of the element distribution is comparable in the new Sn-containing

compounds as well as in unsubstituted $GeSb_2Te_4$, $Ge_2Sb_2Te_5$.and other compounds with the same structure type like $SnSb_2Te_4$, $PbSb_2Te_4$ and $GeBi_2Te_4$.[23-25, 31, 32] The position near the van der Waals gap is preferably occupied by Sb, whereas the position in the center of the distorted rocksalt-type slabs is shared by almost equal amounts of Sb and Ge. Sn shows a slight preference for the position near the van der Waals gap. This element distribution can be explained by the unsaturated coordination of the Te atoms next to the van der Waals gaps, which can be compensated more effectively by Sb^{3+} than by Ge^{2+} due to the higher formal charge. The polarizability and covalent bonding character may also play a role and explain why the behavior of Sn is comparable to that of Sb, yet to a lesser extent. The Te-Te distances at the van der Waals gaps are nearly the same for all of the 21*R*-type and 9*P*-type compounds whereas the cation-anion bond lengths increase slightly with increasing Sn content.

Layered GST materials substituted with Sn open a field of easily accessible thermoelectrics which can be produced as bulk material in large amounts. The use of Sn instead of much more expensive Ge may also reduce the cost significantly. As these layered phases are thermodynamically stable, the thermoelectric properties are not influenced by changing nanostructures or by decomposition. The results concerning the element distribution and the distortion of coordination polyhedra may also be valuable as a model for PCMs in order to describe the local environment in amorphous and crystalline thin films of Sn-doped GST materials.

4.4.4 Experimental Section

4.4.4.1 Sample preparation

Bulk samples were prepared by melting stoichiometric mixtures of the elements Ge (99.999%, Aldrich), Sn (99.99%, Alfa Aesar), Sb (99.9999%, Smart Elements) and Te (99.999%, Alfa Aesar) in sealed silica glass ampoules under argon atmosphere at 950 °C (for 2 h - 24 h) and quenching in water. Subsequently, the samples were annealed about 48 h at temperatures between 450 °C and 590 °C (detailed information can be found in Table S1 in the ESI). Samples for thermoelectric measurements (ca. 3-4 g) were melted at 950 °C (2 h) in ampoules with a flat bottom, quenched in air, annealed ($Ge_{0.6}Sn_{0.4}Sb_2Te_4$: 6 d at 540 °C; $Ge_{1.3}Sn_{0.7}Sb_2Te_5$: 2 d at 490 °C; $GeSnSb_2Te_5$: 20 h at 550 °C) and subsequently quenched in air. Single crystals of $Ge_{0.6}Sn_{0.4}Sb_2Te_4$ and $Ge_{0.75}Sn_{0.25}Sb_2Te_4$ were grown by chemical transport reactions in sealed silica glass ampoules under vacuum using ~20 mg of I_2 with temperature gradients from ca. 580 °C to 500 °C for 1 d (composition of the starting material:

$Ge_{0.5}Sn_{0.5}Sb_2Te_4$ and $GeSnSb_2Te_5$, respectively). $Ge_{1.3}Sn_{0.7}Sb_2Te_5$ crystals were grown at ~600 °C (20 h) using the intrinsic gradient of a tube furnace for 20 h from $GeSnSb_2Te_5$ as starting material, adding 20 mg of SbI_3 as a transport agent. In all cases, plate-like single crystals could be obtained from the cold end of the ampoule; residual transport agent was removed by washing with acetone.

4.4.4.2 Electron microscopy and X-ray spectroscopy

The composition of the single crystals used for structure determination was confirmed by energy dispersive X-ray spectroscopy (EDX) on planar crystal faces using a Jeol JSM-6500F scanning electron microscope with EDX detector (model 7418, Oxford Instruments).
For TEM investigations on $Ge_{1.3}Sn_{0.7}Sb_2Te_5$, a finely powdered part of the sample used for thermoelectric measurements was dispersed on a copper grid coated with holey carbon film. Single crystals of $Ge_{0.75}Sn_{0.25}Sb_2Te_4$ (EDX analysis see above) grown by chemical transport were embedded in two-component glue and placed between silicon wafers and glass panels. These "sandwiches" were fixed in brass tubes with an inner diameter 2 mm. Slices of 0.2 mm thickness were cut from the tube and polished to 80-90 μm thickness using SiC coated sand papers. In the middle of the disks, conical cavities were produced using a dimple grinder (model 650, Gatan) and diamond polishing paste (Electron Microscopy Science) and holes were fabricated using a precision argon ion polishing system (model 691, Gatan). The samples were mounted on a double-tilt holder with maximum tilt angles of ±30°. The measurements were performed on a FEI Titan 80–300 equipped with a field-emission gun operating at 300 kV, a Gatan UltraScan 1000 (2k x 2k) camera and an EDX detector system TOPS 30 (EDAX). The results were evaluated using the Digital Micrograph[36] and ES Vision[37] software packages. SAED patterns were calculated applying the kinematical approximation and HRTEM images were simulated using the multislice method as implemented in the JEMS[38] and EMS program package.[39]

4.4.4.3 X-ray powder diffraction

X-ray powder patterns were recorded on a Huber G670 Guinier camera equipped with a fixed imaging plate and integrated read-out system using Cu-$K_{\alpha 1}$ radiation (Ge(111) monochromator, $\lambda = 1.54056$ Å). Specimens were prepared by crushing representative parts of the samples and fixing powders on Mylar foils using hair-fixing spray. Lattice parameters

were determined by pattern fitting (Rietveld method) using TOPAS ACADEMIC[40] with structure models obtained from the single-crystal structure analyses. Shifted Chebychev background functions were used, crystallite strain was described using a Voigt function and preferred orientation was refined with spherical harmonics of the 6th order. All functions are implemented in the TOPAS program suite. Atomic coordinates were set equal for atoms sharing one position and one common isotropic displacement parameter each was used for anions and cations, respectively. Further details of the Rietveld refinements are available from the Fachinformationszentrum Karlsruhe, D-76344 Eggenstein-Leopoldshafen (Germany), on quoting the depository numbers CSD-426668 ($Ge_{0.75}Sn_{0.25}Sb_2Te_4$), CSD-426672 ($Ge_{0.5}Sn_{0.5}Sb_2Te_4$), CSD-426667 ($Ge_{0.25}Sn_{0.75}Sb_2Te_4$) and CSD-426669 ($GeSnSb_2Te_5$) as well as the names of the authors and citation of the paper (Fax: +49-7247-808-666; E-mail: crysdata@fiz-karlsruhe.de).

4.4.4.4 Single crystal and synchrotron diffraction methods

Laboratory single crystal datasets were recorded on an IPDS I diffractometer (Stoe & Cie.) with an imaging plate detector using Mo-K_α radiation (graphite monochromator, λ= 0.71073 Å). Synchrotron data of the same crystals were collected at beamline ID11[41]of the ESRF (Grenoble) on a heavy-duty diffractometer (Huber) with vertical rotation axis equipped with a Frelon2K CCD detector. The beamline provides a beam tuneable by undulators in the required energy range from 22 keV to 32 keV (0.56 Å to 0.39 Å) near the K absorption edges of Sn (29.195 keV, 0.42468 Å), Sb (30.477 keV, 0.40681 Å), Te (31.818 keV, 0.38979 Å) and far away from the edges (22.00 keV, 0.56357 Å). In order to measure high-angle data, a detector offset was used. The datasets were indexed and integrated using SMART[42] and SAINT[43] Laboratory datasets were absorption corrected numerically using XRED[44] and XSHAPE[45]; synchrotron data consisted of several different datasets, which were combined and absorption corrected semiempirically using SADABS.[46] In both cases, the Laue symmetry $\bar{3}m$ was applied. Joint least-squares refinements employing multiple datasets[19] were carried out with JANA2006.[47] The dispersion correction terms $\Delta f'$ and $\Delta f''$ were calculated from X-ray fluorescence spectra (energy-dispersive XFlash detector; Rontec) via the Kramers-Kronig transform[48] using the program CHOOCH.[49] The refinement aimed at determining the element distribution in the compounds simultaneously for each element on each crystallographic position; full total occupancy was assumed on all atom positions as suggested by the results of previous investigations.[22-24] Occupancy factors were constrained

in order to fix the sum formula according to the result of the EDX measurements to prevent the overall scale factor from diverging. Elements with occupancy factors close to zero within their standard deviation (or slightly negative) were deleted on the respective positions until only elements with occupancy factors > 3 σ were present. Atomic coordinates and ADPs of atoms occupying the same site were set equal. Cell parameters determined from powder samples have been used due to their higher precision. Further details of the single-crystal structure investigation are available from the Fachinformationszentrum Karlsruhe, D-76344 Eggenstein-Leopoldshafen (Germany), on quoting the depository number, CSD-426670 ($Ge_{0.6}Sn_{0.4}Sb_2Te_4$) and CSD-42671 ($Ge_{1.3}Sn_{0.7}Sb_2Te_5$) as well as the names of the authors and citation of the paper (Fax: +49-7247-808-666; E-mail: crysdata@fiz-karlsruhe.de).

4.4.4.5 Thermoelectric properties

Commercial and in-house-built facilities of the DLR (Cologne) were used to determine the temperature dependence of the electrical and thermal conductivities as well as the Seebeck coefficient from room temperature up to approximately 500 °C under He atmosphere. Peltier influences on the measurement of the electrical conductivity were reduced by a four-point-probe setup using an AC method (low frequency method using 7 Hz). The electrical resistivity was calculated according to $\rho = (1/G_F) \cdot R$ (G_F: correction of cross section and thickness of the sample as well as distance between probe tips). For the determination of the Seebeck coefficient a small-temperature gradient across the sample was established while slowly changing the environment temperature in order to obtain Seebeck coefficients for each mean sample temperature. Type-N thermocouples were directly attached to the sample in order to measure both the Seebeck voltage and the temperature.[50, 51] The thermal conductivity was calculated from the thermal diffusivity (measured using a laser-flash apparatus Netzsch LFA 427), the heat capacity (determined by differential scanning calorimetry Netzsch DSC 404), and the density of the samples (measured using a Mohr's balance). The experimental errors were estimated at 5% for the electrical conductivity, 5% for the Seebeck coefficient, and 8% for the thermal conductivity. The data were calculated by averaging between heating and cooling measurements; the values were interpolated to get 50 °C steps in order to calculate *ZT* and κ_L.

Acknowledgements

We thank T. Miller for laboratory single-crystal data collections, C. Minke for SEM operation and EDX analyses and W. Schönau for technical support with the thermal conductivity measurements. Special thanks go to Dr. Gavin Vaughan and Dr. Jonathan Wright for their help during synchrotron data collection and evaluation as well as to Dr. Loredana Erra for her support during measurements at ESRF. Preliminary studies by Dr. M. N. Schneider are acknowledged. We gratefully acknowledge Prof. Dr. W. Schnick's generous support of this work. This investigation was funded by the Deutsche Forschungsgemeinschaft (grant OE530/1-2) and the ESRF (project HS-4363). Part of the project was also financed by the European Union (European Social Fund, NFG "Effiziente Energienutzung: Neue Konzepte und Materialien").

4.4.5 Supplementary Information

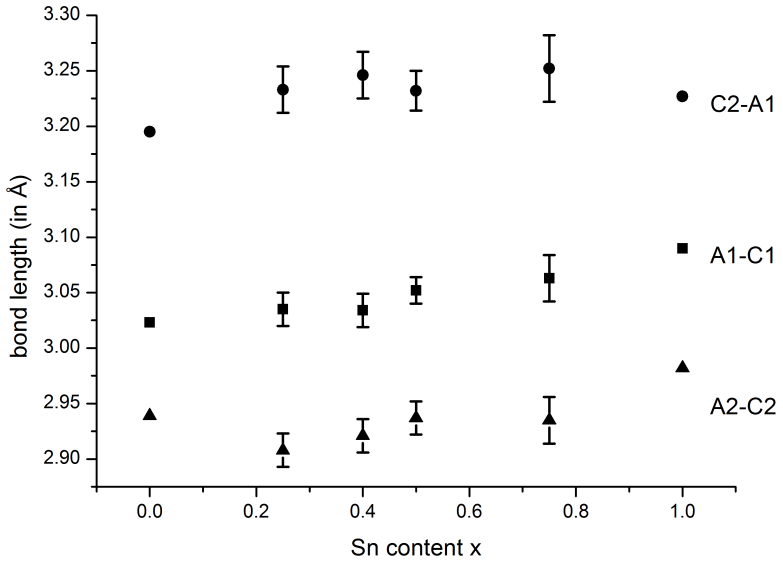

Fig. S1: Trend of the cation-anion bond lengths (labelling cf. Fig. 4) with increasing Sn content x; error bars corrspond to 3 standard deviations; bond lengths for $GeSb_2Te_4$ and $SnSb_2Te_4$ taken from literature (refs. [20] and [22]).

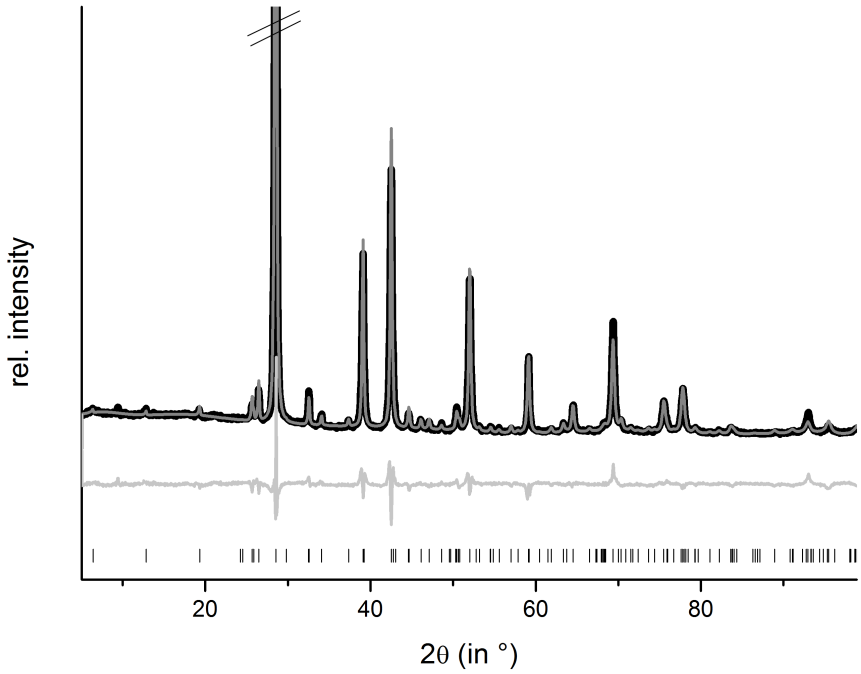

Fig. S2: Rietveld refinement of 21*R*-$Ge_{0.75}Sn_{0.25}Sb_2Te_4$ (the strongest reflection is cut off); vertical lines indicate calculated reflection positions, experimental (black) and calculated pattern (gray) and difference plot (below) are shown.

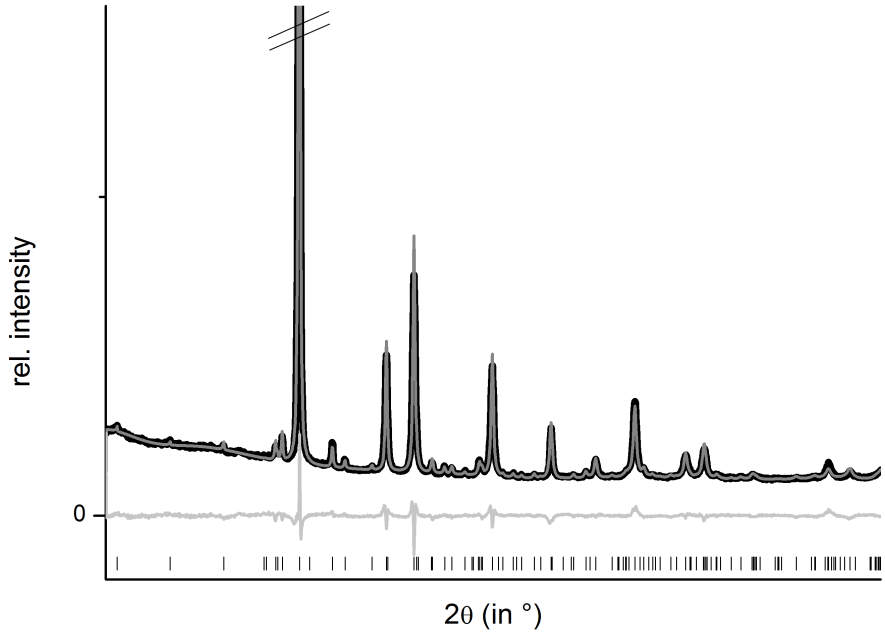

Fig. S3: Rietveld refinement of 21*R*-$Ge_{0.6}Sn_{0.4}Sb_2Te_4$ (the strongest reflection is cut off); vertical lines indicate calculated reflection positions, experimental (black) and calculated pattern (gray) and difference plot (below) are shown.

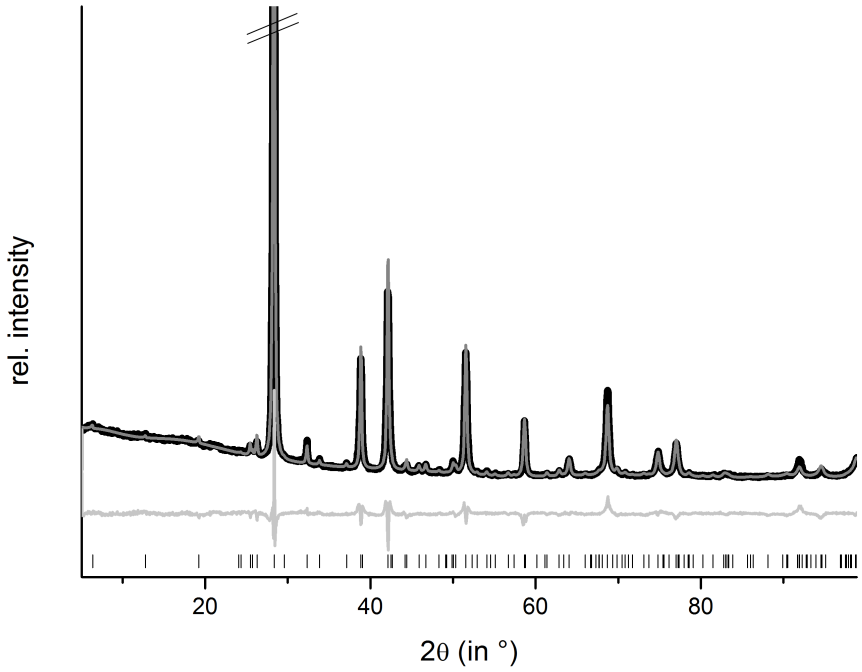

Fig. S4: Rietveld refinement of 21*R*-$Ge_{0.25}Sn_{0.75}Sb_2Te_4$ (the strongest reflection is cut off); vertical lines indicate calculated reflection positions, experimental (black) and calculated pattern (gray) and difference plot (below) are shown.

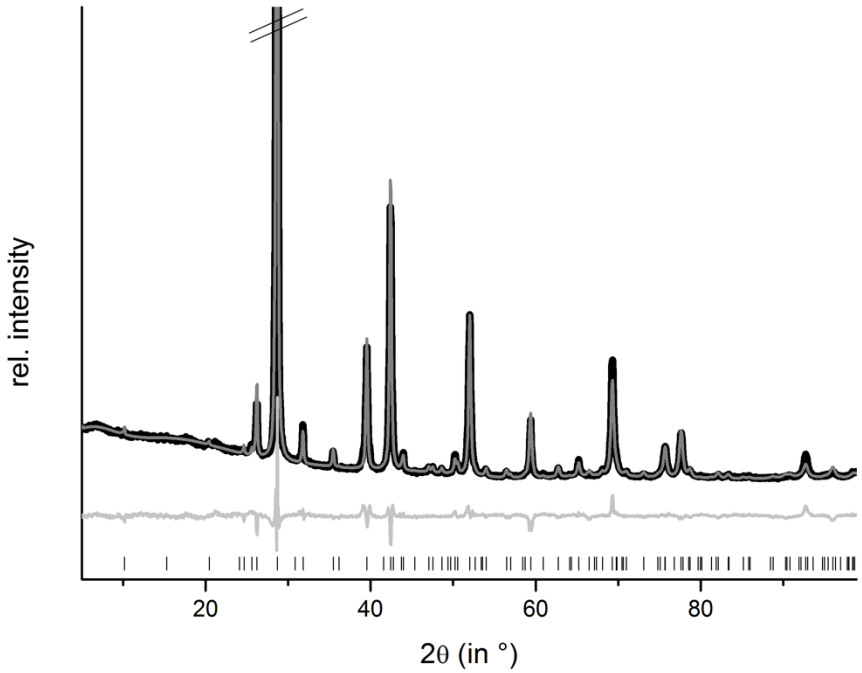

Fig. S5: Rietveld refinement of 9*P*-$Ge_{1.3}Sn_{0.7}Sb_2Te_5$; (the strongest reflection is cut off); vertical lines indicate calculated reflection positions, experimental (black) and calculated pattern (gray) and difference plot (below) are shown

Table S1: Specific annealing conditions of samples used for structure determination by Rietveld refinement; note that the exact temperatures and annealing times have little influence on the powder diffraction patterns and that many more samples with almost the same diffraction patterns were obtained at slightly different conditions.

Formula	Annealing time (in h)	Temperature (in °C)
$Ge_{0.75}Sn_{0.25}Sb_2Te_4$	46	560
$Ge_{0.6}Sn_{0.4}Sb_2Te_4$	144	540
$Ge_{0.5}Sn_{0.5}Sb_2Te_4$ *	20	550
$Ge_{0.25}Sn_{0.75}Sb_2Te_4$	46	560
$Ge_{1.3}Sn_{0.7}Sb_2Te_5$	46	490
$GeSnSb_2Te_5$	39	570

* The TEM-EDX measurements for $Ge_{0.5}Sn_{0.5}Sb_2Te_4$ were done with a sample that was anneales at 620 °C for 72 h and subsequently at 590 °C for 120 h.

4.4.6 References

[1] M. Wuttig, S. Raoux, *Z. Anorg. Allg. Chem.* **2012**, ***638***, 2455.

[2] S. Raoux, *Annu. Rev. Mater. Res*. **2009**, *39*, 25.

[3] T. Siegrist, P. Merkelbach, P. Wuttig, *Annu. Rev. Condens. Matter Phys.* **2012**, *3*, 215.

[4] T. Matsunaga, H. Morita, R. Kojima, N. Yamada, K. Kifune,Y. Kubota, Y. Tabata, J.-J. Kim, M. Kobata, E. Ikenaga, K. Kobayashi, *J. Appl. Phys.* **2008**, *103*, 093511.

[5] K. Wang, D. Wamwangi, S. Ziegler, C. Steimer, M. J. Kang, S. Y. Choi, M. Wuttig, *Phys. Stat. Sol. A* **2004**, *201*, 3087.

[6] R. Kojima, N. Yamada, *Jpn. J. Appl. Phys.* **2001**, *40*, 5930.

[7] C. Xu, B. Liu, Z.-T. Song, S.-L. Feng, B. Chen, *Chinese Phys. Lett.* **2005**, *22*, 2929.

[8] W. D. Song, L. P. Shi, X. S. Miao, C. Chong, *Appl. Phys. Lett.* **2007**, *90*, 91904.

[9] J. Xu, F. Rao, Z. Song, M. Xia, C. Peng, Y. Gu, M. Zhu, L. Wu, B. Liu, S. Feng, *Electrochem. Solid St.* **2012**, *15*, H59.

[10] K. Wang, C. Steimer, D. Wamwangi, S. Ziegler, M. Wuttig, J. Tomforde, W. Bensch, *Microsyst Technol.* **2007**, *13*, 203.

[11] D. R. Lide, *CRC Handbook of Chemistry and Physics*, *82nd ed*., CRC, New York, **2001**.

[12] M. N. Schneider, T. Rosenthal, C. Stiewe, O. Oeckler, *Z. Kristallogr.* **2010**, *224*, 463.

[13] T. Rosenthal, M. N. Schneider, C. Stiewe, M. Döblinger, O. Oeckler, *Chem. Mater.* **2011**, *23*, 4349.

[14] G. J. Snyder, E. S. Toberer, *Nat. Mater*. **2008**, *7,* 105.

[15] T. Matsunaga, H. Morita, R. Kojima, N. Yamada, K. Kifune, Y. Kubota, Y. Tabata, J.-J. Kim, M. Kobata, E. Ikenaga, K. Kobayashi, *J. Appl. Phys.* **2008**, *103*, 093511.

[16] S. Roux, W. Wojciech, D. Ielmini, *Chem. Rev.* **2010**, *110*, 240.

[17] T. Matsunaga, N. Yamada, Y. Kubota, *Acta Crystallogr. Sect. B* **2004**, *60*, 685.

[18] O. G. Karpinsky, L. E. Shelimova, M. A. Kretova, J.-P. Fleurial, *J. Alloys Compd*. **1998**, *268*, 112.

[19] S. Welzmiller, P. Urban, F. Fahrnbauer, L. Erra, O. Oeckler, *J.Appl.Crystallogr.* **2013**, *46*, 769.

[20] J. L. Hodeau, V. Favre-Nicolin, S. Bos, H. Renevier, E. Lorenzo, J. F. Berar, *Chem. Rev.* **2001**, *101*, 1843.

[21] A. K. Cheetham, A. P. Wilkinson, *Angew. Chem.Int. Ed.* **1992**, *31*, 1557.

[22] M. N. Schneider, F. Fahrnbauer, T. Rosenthal, M. Döblinger, C. Stiewe, O. Oeckler, *Chem. Eur. J.* **2012**, *18*, 1209.

[23] O. Oeckler, M. N. Schneider, F. Fahrnbauer, G. Vaughan, *Solid State Sci.* **2011**, *13*, 1157.

[24] P. Urban, M. N. Schneider, L. Erra, S. Welzmiller, F. Fahrnbauer, O. Oeckler *CrystEngComm* **2013**, *15*, 4823.

[25] L. E. Shelimova, O. G. Karpinskii, T. E. Svechnikova, I. Y. Nikhezina, E. S. Avilov, M. A. Kretova, V. S. Zemskov, *Inorg. Mater.* **2008**, *44*, 371.

[26] H. W. Shu, S. Jaulmes, J. Flahaut, *J. Solid State Chem.* **1988**, *74*, 277.

[27] A. G. Talybov, *Soviet Phys. Crystallogr*. **1961**, *6*, 40.

[28] G. Concas, T. M. de Pascale, L. Garbato, F. Ledda, F. Meloni, A. Rucci, M. Serra, *J. Phys Chem. Solids* **1992**, *53*, 791.

[29] T. B. Zhukova, A. I. Zaslavskii, *Soviet Phys. Crystallogr.* **1972**, *16*, 796.

[30] R. D. Shannon, *Acta Crystallogr. Sect. A* **1976**, *32*, 751.

[31] L. E. Shelimova, O. G. Karpinskii, T. E. Svechnikova, E. S. Avilov, M. A. Kretova, V. S. Zemskov, *Inorg. Mater*. **2004**, *40*, 1264.

[32] O. G. Karpinsky, L. E. Shelimova, M. A. Kretova, J.-P. Fleurial, *J. Alloys Compd*. **1998**, *265*, 170.

[33] F. Yan, T. J. Zhu, X. B. Zhao, S. R. Dong, *Appl. Phys.* **2007**, *A88*, 425.

[34] P. P. Konstantinov, L. E. Shelimova, M. A. Avilov, M. A. Kretova, V. S. Zemskov, *Inorg. Mater* **2001**. *37*, 662.

[35] G.S. Kumar, G. Prasad, R.O. Pohl, *J. Mater. Chem*. **1993**, *28*, 4261.

[36] *DigitalMicrograph 3.6.1*, Gatan Software, Pleasanton, USA, **1999**.

[37] *ESVision*, *4.0.164*, Emispec Systems Inc., Tempe, USA, **1994-2002**.

[38] P. Stadelmann; *JEMS*, *V. 3.3525U2008*, CIME-EPFL, Switzerland, **1999 -2008**.

[39] P. A. Stadelmann, *Ultramicroscopy,* **1987**, *21*, 131.

[40] *TOPAS-Academic*, *V. 4.1*, Coelho Software, Brisbane, Australia, **2007**.

[41] G. B. M. Vaughan, J. P. Wright, A. Bytchkov, C. Curfs, C. Gundlach, M. Orlova, L. Erra, H. Gleyzolle, T. Buslaps, A. Götz, G. Suchet, S. Petitdemange, M. Rossat, L. Margulies, W. Ludwig, A. Snigirev, I. Snigireva, H. Sørensen, E. M. Lauridsen, U. L. Olsen, J. Oddershede, H. F. Poulsen, *Proceedings of the 31st Risø International Symposium on Materials Science: Challenges in materials science and possibilities in 3D and 4D characterization techniques* **2010**, *521*, 457.

[42] J. L. Chambers, K. L. Smith, M. R. Pressprich, Z. Jin, *SMART*, *V.5.625*. Bruker AXS, Madison, USA, **1997-2001**.

[43] *SAINT V. 6.36A*, Bruker AXS, Madison , USA, **1997-2002**.

[44] *X-RED32 V. 1.31*, STOE & Cie GmbH, Darmstadt, Germany, **2005**.

[45] *X-SHAPE V. 2.07*, STOE & Cie GmbH, Darmstadt, Germany, **2005**.

[46] *SADABS V. 2.05*, Bruker AXS, Madison, USA, **1999**.

[47] V. Petricek, M. Dusek, L. Palatinus, JANA2006 - The CrystallographicComputing System. Institute of Physics, Praha, Czech Republic, **2006**.

[48] R. de L. Kronig, *J. Opt. Soc. Am.* **1926**, *12*, 547.

[49] G. Evans, R. F. Pettifer, *J. Appl. Crystallogr.* **2001**, *34*, 82.

[50] J. de Boor, C. Stiewe, P. Ziolkowski, T. Dasgupta, G. Karpinski, E. Lenz, F. Edler, E. Müller, *J. Electron. Mater.* **2013**, *42*, 1711.

[51] J. de Boor, E. Müller, *Rev. Sci. Instrum*. **2013**, *84*, 065102.

5 Complementary use of electron and X-ray methods for the structure elucidation of luminescent oxonitridosilicates

5.1 Overview

The oxonitridosilicate phosphors $Sr_{1-x}Ba_xSi_2O_2N_2:Eu^{2+}$ ($0 \leq x \leq 1$) are well suited for application in phosphor-converted light-emitting diodes (pc-LEDs) due to their high thermal and chemical stability combined with excellent quantum efficiencies.[1-3] They exhibit intense emission from blue to yellow when exited by UV to blue radiation (Chapter 1.2). A comprehensive comparison of the $Sr_{1-x}Ba_xSi_2O_2N_2:Eu^{2+}$ ($0 \leq x \leq 1$) phases reveals that all compounds are layered oxonitridosilicates with corrugated or planar metal-atom sheets that alternate with silicate layers built up of condensed $SiON_3$ tetrahedra. Although the topology of the silicate layers is similar for all Sr/Ba ratios (x), there is no complete solid-solution series. Variations of the relative orientations of the silicate layers perpendicular to the stacking direction result in the formation of polytypes and pronounced real-structure effects. The higher individual symmetry of the metal-atom and silicate layers, respectively, compared to the overall crystal structure, results in twinning, anti-phase boundaries and intergrowth of domains with different structures as well as domains with the same structure but different orientations (Figure 1). The best way of elucidating such real-structure phenomena, which dominate the structural chemistry in these materials, is by transmission electron microscopy (TEM). Due to the special metrics relation and similar interatomic vectors of the $Sr_{1-x}Ba_xSi_2O_2N_2:Eu^{2+}$ ($0 \leq x \leq 1$) phases, the X-ray powder diffraction patterns resemble each other especially since the intensities of the reflections are often strongly influenced by disorder and preferred orientation. Since it is often impossible to obtain phase pure samples, these structures can only be distinguished unambiguously by detailed structural analysis. The combined use of TEM and X-ray investigations is well suited for the in-depth structural analysis of this class of materials. A comprehensive overview of all $Sr_{1-x}Ba_xSi_2O_2N_2:Eu^{2+}$ ($0 \leq x \leq 1$) phases, their real structures, luminescence properties, synthesis routes as well as a critical discussion of the literature can be found in Ref [4].

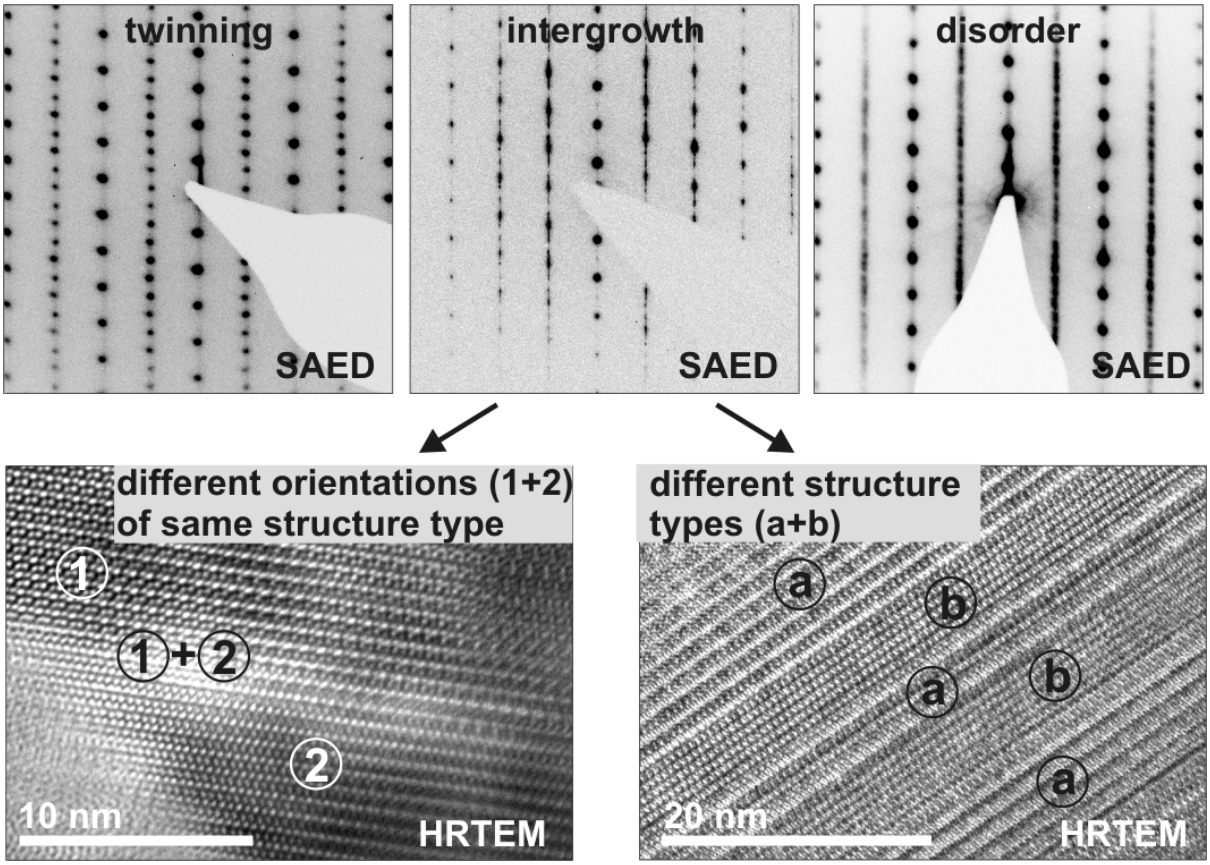

Fig. 1: Real-structure effects typically observed in $Sr_{1-x}Ba_xSi_2O_2N_2:Eu^{2+}$ ($0 \leq x \leq 1$): SAED of $SrSi_2O_2N_2$ (zone axis [10 $\bar{1}$]) with twinned domains (top left) and domains with stacking disorder (top right); SAED indicating intergrowth of domains (top center); HRTEM image of intergrowth of $SrSi_2O_2N_2$ domains of the zone axes [001] (1) and [100](2) (bottom left); HRTEM images of oriented intergrowth of domains with (a) the $BaSi_2O_2N_2$-type structure (zone axis [001]) and (b) domains with $SrSi_2O_2N$-type structure (zone axis [10 $\bar{1}$]) (bottom right); this figure was taken from Ref [4]

For $SrSi_2O_2N_2:Eu^{2+}$, there are two maximum degree of order (MDO) polytypes. The yellow-green emitting triclinic polymorph (space group *P*1) exhibits a quantum efficiency of more than 90%.[5,6] The recently discovered monoclinic modification (space group $P2_1$) described in Chapter 5.2 exhibits a doubled translation period along the stacking direction. This originates from a 180° rotation of consecutive silicate layers, which results in a structure that can be described as a "maximally twinned" variant of the triclinic form, every silicate layer being a twin boundary. The emission maximum of this monoclinic polytype is shifted to lower wavelengths by 5 nm compared to that of the triclinic one. Powder samples that consist of both polytypes exhibit even higher quantum efficiencies than the triclinic modification. $BaSi_2N_2O_2$ crystallizes in the orthorhombic space group *Pbcn*;[7] however, additional domains with the idealized space group $Cmc2_1$ are present. SAED patterns reveal that $Sr_{0.25}Ba_{0.75}Si_2O_2N_2:Eu^{2+}$ consists of intergrown domains corresponding to the $SrSi_2N_2O_2$-type structure and domains with metrics comparable to $BaSi_2N_2O_2$ but with additional metal-atom ordering (Chapter 5.3). The small average domain sizes impede the collection of single-

crystal data from exclusively one domain. Therefore, electron microscopy was used for the determination of the metrics of the individual domains and their relative orientation. HRTEM investigations reveal the ordering of the metal atoms in the domains with $BaSi_2N_2O_2$ metrics. This can be described in the space group *P*1 with 4 metal atom positions, of which one is occupied by Sr and the other three by Ba. Metal-atom layers occupied with Sr and Ba are more corrugated than those containing only Ba. Due to its similar atomic radius,[8] Eu^{2+} is expected to occupy exclusively the Sr position. This single-site occupancy with Eu^{2+} is the main reason why $Sr_{0.25}Ba_{0.75}Si_2O_2N_2:Eu^{2+}$ exhibits the smallest full width at half maximum (37 nm) known for Eu^{2+}-doped silicate phosphors. These investigations demonstrate that since the luminescence properties are mainly determined by the coordination sphere of the rear-earth atom, they can only be understood based on a profound knowledge about the crystal structure. Due to the presence of various real-structure effects, detailed investigations of Eu^{2+}-doped $Sr_{1-x}Ba_xSi_2O_2N_2$ ($0 \leq x \leq 1$) compounds (Chapter 5.2 and 5.3), which are necessary to explain their luminescence, rely on the combined use of electron and X-ray diffraction methods. When the Ba content in $Sr_{1-x}Ba_xSi_2O_2N_2$ is increased, a red shift of the emission to the yellow green spectral region is observed as long as the $SrSi_2O_2N_2$-type structure is present, e.g. for $Sr_{0.5}Ba_{0.5}Si_2O_2N_2:Eu^{2+}$.[9] This is a consequence of the shorter bond lengths between Eu^{2+} and the oxygen ligands, because the introduction of larger Ba atoms lead to a compression of the Sr coordination spheres and Eu^{2+} preferably occupies the Sr site as described above. $Sr_{0.25}Ba_{0.75}Si_2O_2N_2:Eu^{2+}$ is expected to show an even stronger red shift due to the further increased Ba content. However, the structure changes to a distorted variant of the $BaSi_2O_2N_2$ type and therefore a shift of the emission maxima to the blue spectral region compared to the compounds with lower Ba contents occurs. As observed for samples with $SrSi_2O_2N_2$-type structure, a red shift of the emission with respect to $BaSi_2O_2N_2$ itself is expected for increasing Sr contents. However, the corrugated metal-atom layers in $Sr_{0.25}Ba_{0.75}Si_2O_2N_2:Eu^{2+}$ (they are planar in $BaSi_2O_2N_2$) in combination with the slight shift of consecutive silicate layers against each other perpendicular to the stacking direction result in larger distances between Eu^{2+} and the oxygen ligands. Therefore intense blue emission with an overall emission wavelength of 472 nm is observed.

References

[1] Y. Q. Li, A. C. A. Delsing, G. de With, H. T. Hintzen, *Chem. Mater.* **2005**, *17*, 3242.

[2] V. Bachmann, C. Ronda, O. Oeckler, W. Schnick, A. Meijerink, *Chem. Mater.* **2009**, *21*, 316.

[3] M. Zeuner, S. Pagano, W. Schnick, *Angew. Chem.* **2011**, *123*, 7898; *Angew. Chem. Int. Ed.* **2011**, *50*, 7754.

[4] M. Seibald, T. Rosenthal, O. Oeckler, W. Schnick, *Crit. Rev. Solid State Mater. Sci.* **2014**, *39*, 215.

[5] H. A. Höppe, *Dissertation*, **2003**, LMU Munich.

[6] O. Oeckler, F. Stadler, T. Rosenthal, W. Schnick, *Solid State Sci.* **2007**, *9*, 205.

[7] J. A. Kechele, O. Oeckler, F. Stadler, W. Schnick, *Solid State Sci.* **2009**, *11*, 537.

[8] R. D. Shannon, *Acta Crystallogr. Sect. A* **1976**, 32, 751.

[9] M. Seibald, O. Oeckler, V. R. Celinski, P. J. Schmidt, A. Tücks, W. Schnick, *Solid State Sci.* **2011**, *13*, 1769.

5.2 New polymorph of the highly efficient LED-phosphor $SrSi_2O_2N_2:Eu^{2+}$ – polytypism of a layered oxonitridosilicate

M. Seibald, T. Rosenthal, O. Oeckler, C. Maak, A. Tücks, P. J. Schmidt, D. Wiechert, W. Schnick

Chem. Mater. **2013**, *25*, 1852-1857.

Abstract

$SrSi_2O_2N_2:Eu^{2+}$ is an outstanding yellow emitting phosphor material with practical relevance for application in high power phosphor-converted light-emitting diodes. The triclinic compound exhibits high thermal and chemical stability and quantum efficiency above 90 % and can be excited by GaN-based UV to blue LEDs efficiently. We have now discovered a hitherto unknown monoclinic polymorph of $SrSi_2O_2N_2$, synthesized by solid-state reaction, which is characterized by an alternating stacking sequence of silicate layers made up of condensed $SiON_3$ tetrahedra and metal-ion layers. As proven by single-crystal X-ray diffraction, the arrangement of the silicate layers is significantly different from the triclinic polymorph. The translation period along the stacking direction is doubled in the monoclinic modification ($P2_1$, $Z = 8$, $a = 7.1036(14)$, $b = 14.078(3)$, $c = 7.2833(15)$ Å, $\beta = 95.23(3)°$, $V = 725.3(3)$ Å^3). TEM investigations in combination with HRTEM-image simulations confirm the structure model. The powder X-ray diffraction pattern shows that the volume fractions of the monoclinic and triclinic modifications are approximately equal in the corresponding powder sample. The emission wavelength of 532 nm (fwhm ~2600 cm^{-1}) as determined by single-crystal luminescence measurements of the monoclinic phase exhibits a shift to smaller wavelengths by ~5 nm compared to the triclinic polymorph. Differences of the luminescence properties between the monoclinic and triclinic phase are interpreted with respect to the differing coordination of Eu^{2+} in both phases. The new monoclinic $SrSi_2O_2N_2:Eu^{2+}$ polymorph is a very attractive phosphor material for enhancement of color rendition of white-light pc-LEDs.

5.2.1 Introduction

Phosphor-converted light-emitting diodes (pc-LEDs) are attractive candidates to replace incandescent light bulbs because of their much more efficient conversion of electric energy to visible light.[1-4] In order to improve the performance and energy-saving potential of pc-LEDs, there is a huge demand for novel efficient phosphors as well as for improvement of the properties of existing materials.[5,6] Various luminescent solid-state materials with emission from the blue to the red spectral region have been described.[2,6-14] Analysis of their properties in relation to composition and crystal structure of the host material has revealed general requirements for phosphors to be used for pc-LED applications.[12] The detailed knowledge of the crystal structure is a prerequisite as properties of such optical materials cannot be fully predicted from the material's composition alone.[15]

According to these specifications, the material class of (oxo)nitridosilicates is well suited for application as host lattices because high quantum efficiencies (> 90%) can be achieved, a small Stokes shift is possible due to the rigidity of silicate substructures and pronounced thermal and chemical stability is present.[16] $SrSi_2O_2N_2$ is a host lattice showing excellent luminescence properties when doped with Eu^{2+}. $SrSi_2O_2N_2$:Eu^{2+} exhibits intense broad-band emission in the yellow-green spectral region due to the parity allowed $4f^6(^7F)5d^1 \rightarrow 4f^7(^8S_{7/2})$ transition when excited by UV to blue light.[4,10,17-35] The disordered crystal structure consists of alternating metal-ion and silicate layers. Both the idealized ordered structure as well as the average structure of the disordered variant are triclinic (a = 7.0802(2), b = 7.2306(2), c = 7.2554(2) Å, α = 88.767(3), β = 84.733(2), γ = 75.905(2)°, V = 358.73(2) Å^3, space group $P1$). The metal-ion layers are strongly affected by disorder phenomena, i.e. polysynthetic twinning, antiphase boundaries, or oriented intergrowth. The silicate layers are built up of vertex-sharing $SiO^{[1]}N^{[3]}_3$ tetrahedra forming *dreier* rings perpendicular to [010]*.[36] The reflection positions in powder X-ray diffraction (PXRD) patterns, in principle, resemble those reported by Zhu (X_2-phase)[37] and Hintzen[28] although these authors have proposed different metrics. However, some powder patterns of our samples and also those in the literature show a number of reflections that are inconsistent with the triclinic structure model of $SrSi_2O_2N_2$ discussed in literature.[20,29,31,35,38-41] Surprisingly, samples with such "impurity phases" exhibit excellent overall luminescence properties. Whenever peak emission wavelengths of $SrSi_2O_2N_2$:Eu^{2+} powder samples are reported to be significantly smaller than 537 nm the corresponding PXRD patterns show unknown, additional reflections.[20,29,31,35,38,39] In this contribution, we clarify the nature of the additional phase that leads to these reflections and further investigate its impact on luminescence properties.

5.2.2 Experimental Section

5.2.2.1 Synthesis

$SrSi_2O_2N_2:Eu^{2+}$ (2 mol% Eu) was prepared by heating a stoichiometric mixture of $Sr_2SiO_4:Eu^{2+}$ and Si_3N_4 (UBE, > 98%) for 16 h to 1540 °C in forming gas atmosphere ($N_2:H_2$ = 95:5) according to eq. 1. The starting materials were placed on tungsten foil within a molybdenum crucible and heated to the final temperature with 300 °C/h (T < 1000 °C) and 150 °C/h (T > 1000 °C), respectively.

$$Sr_2SiO_4:Eu^{2+} + Si_3N_4 \longrightarrow 2\ SrSi_2O_2N_2:Eu^{2+} \qquad \text{(Eq. 1)}$$

5.2.2.2 X-ray Spectroscopy

The chemical composition of several crystallites was analyzed by energy dispersive X-ray (EDX) spectroscopy using a JSM-6500F scanning electron microscope (SEM, Jeol) with a Si/Li EDX detector (Oxford Instruments, model 7418). The SEM was also used to collect images of particles to study their morphology. Further analyses were performed using the EDX system (TEM Tops 30, Edax) of the transmission electron microscope mentioned below.

5.2.2.3 Powder X-ray Diffraction

PXRD data were collected on a STOE STADI P diffractometer (Cu-$K_{\alpha 1}$ radiation, Ge(111) monochromator, position sensitive detector) in transmission geometry using a flat sample holder with thin film of investigated powder material. Rietveld refinement was carried out using the TOPAS package.[42]

5.2.2.4 Single-Crystal X-ray Diffraction

Selected green luminescent single crystals of $SrSi_2O_2N_2:Eu^{2+}$ were mounted on glass fibers and checked for quality on a Buerger precession camera. Intensity data were collected on a Nonius Kappa-CCD diffractometer with graded multilayer X-ray optics (Mo-K_α radiation, λ = 0.71093 Å). The structure was solved by direct methods and refined by full-matrix least-squares methods.[43] Further details of the crystal structure investigation may be obtained from Fachinformationszentrum Karlsruhe, 76344 Eggenstein-Leopoldshafen, Germany (fax, (+49)7247-808-666; e-mail, crysdata@fiz-karlsruhe.de, http://www.fiz-karlsruhe.de /request_for_deposited_data.html) on quoting the depository number CSD-425649.

5.2.2.5 Transmission Electron Microscopy

Selected area electron diffraction (SAED) patterns and high-resolution (HR) images were recorded on a Fei Titan 80-300 (acceleration voltage 300 kV) transmission electron microscope (TEM). Tilt series of diffraction patterns were obtained using a double-tilt sample holder with a maximum tilt angle of ±30°. For preliminary experiments, ground powder samples were dispersed in ethanol and drop cast on copper grids coated with a holey carbon film. Since such samples showed pronounced preferred orientation, the powder was mixed with a two-component glue, placed between silicon wafers and glass panels, and then fixed in brass tubes (inner diameter 2 mm). These were cut into slices perpendicular to the tube elongation (thickness approx. 200 µm) and polished to 80-90 µm using different SiC coated sand papers (grain size: 40-5 µm). Finally, the thickness in the middle of the disk was reduced to approximately 10 µm using a dimple grinder (type 650, Gatan) and diamond polishing paste (Electron Microscopy Science). Subsequently, a hole in the glue matrix was fabricated using a precision ion polishing system (type 691, Gatan). Crystallites at the perimeter of the hole (partially free of glue) were randomly oriented and suitable for TEM investigations. For simulations of SAED patterns and HRTEM images EMS program was used.[44] In order to ensure comparability to results from single-crystal and powder investigations, the same sample was used for TEM analysis.

5.2.2.6 Luminescence

Luminescence investigations were done using a luminescence microscope consisting of a HORIBA Fluoromax4 spectrofluorimeter system attached to an Olympus BX51 microscope via fiber optical bundles. The samples were measured inside a glass capillary (outer diameter approx. 0.2 mm). The excitation wavelength was chosen to 420 nm with a spectral width of 10 nm. The emission spectra were collected in the wavelength range between 450 nm and 750 nm with 2 nm step size. This range was also used for color-point calculations.

5.2.3 Results and Discussion

5.2.3.1 Synthesis and chemical analysis

In powder samples of $SrSi_2O_2N_2:Eu^{2+}$ (2 mol% Eu) prepared by the above-mentioned synthesis, which exhibit additional reflections in PXRD patterns (referring to triclinic structure model), two different types of particle morphology can be found in SEM images. Particles of type 1 (Figure 1, left) are built up of stacked platelet-like crystals. Due to the well-known real-structure effects,[36] such morphology seems to be reasonable for the triclinic $SrSi_2O_2N_2$ structure type. Particles of type 2 (Figure 1, right) show crystals with approximately isometric polyhedral shape with diameters of > 10 μm as required for X-ray structure analysis, which is surprising for $SrSi_2O_2N_2$. EDX yields an average composition (7 measurements), normalized according to the overall metal content, of $Sr_{0.98}Eu_{0.02}Si_{2.35(3)}O_{2.6(2)}N_{2.3(6)}$ for crystals of type 2. This is in accordance with the nominal composition $SrSi_2O_2N_2$ taking into account the typical uncertainty intervals (Sr/Si signal overlap).

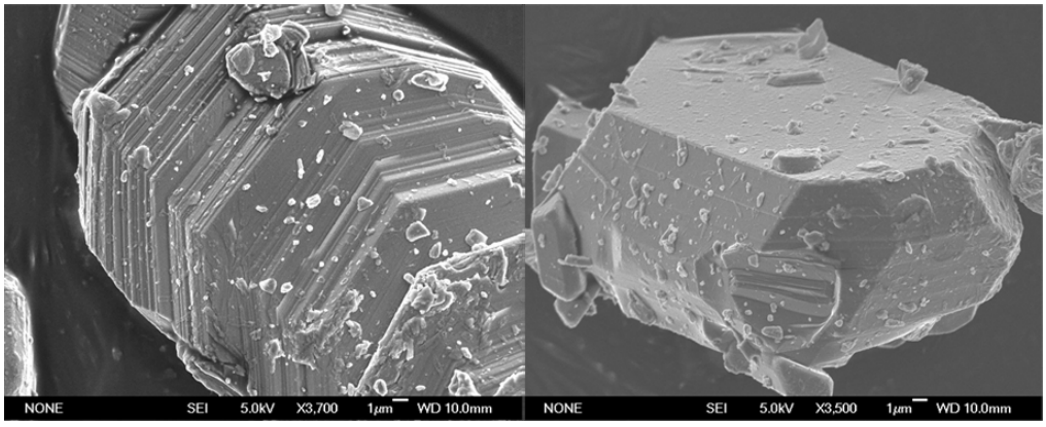

Fig. 1: SEM images of two typical $SrSi_2O_2N_2:Eu^{2+}$ particles in the powder sample. Stacked platelet-like crystals (left) and polyhedral single crystals (right) can clearly be distinguished.

5.2.3.2 Single-Crystal Structure Analysis

Diffraction data of a green luminescent polyhedral crystal (type 2) were collected and the corresponding crystal structure of monoclinic $SrSi_2O_2N_2:Eu^{2+}$ was refined in space group $P2_1$.[43] The Eu^{2+} content (2 mol%) was neglected because of its insignificant contribution to the scattering density. A separate scale factor was used for the broadened reflections with $h = 2n + 1$, and inversion twinning was taken into account. Crystallographic data are summarized in Table 1. Similar to triclinic $SrSi_2O_2N_2$, the crystal structure exhibits alternating

metal-ion and silicate layers, the latter ones built up from highly condensed $SiO^{[1]}N^{[3]}_3$ tetrahedra forming *dreier* rings.[36,45-48] In contrast to the triclinic structure, the tetrahedra orientation changes in consecutive silicate layer, which are rotated against each other by 180°, consistent with a 2_1 screw axis and the doubled translation period along the [010]* stacking direction compared to the triclinic structure (Figure 2).[36] The cations are coordinated in a trigonal prismatic way by O atoms, similar to the triclinic model.

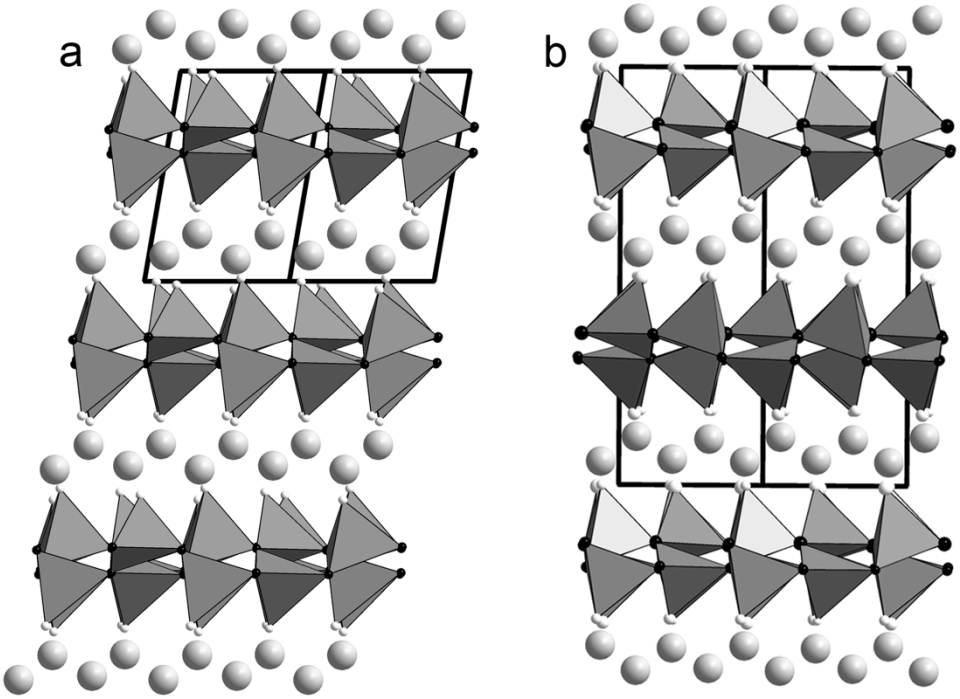

Fig. 2: Crystal structures (metal atoms: gray spheres, unit-cells outlined) of (a) triclinic $SrSi_2O_2N_2$ (projection along [101]) and (b) monoclinic $SrSi_2O_2N_2$ (projection along [10$\bar{1}$]). The orientation of consecutive silicate layers ($SiON_3$ tetrahedra: gray, oxygen: white spheres, nitrogen: black spheres) differs in both models.

The 180° rotation of two consecutive silicate layers corresponds to the structure of twin boundaries as they are present in the real structure of $Sr_{0.5}Ba_{0.5}Si_2O_2N_2$, which is isotypic to triclinic $SrSi_2O_2N_2$.[47] There, such twin boundaries occur approximately every 100 nm. Significantly smaller twin domains dramatically change the PXRD pattern as they involve a different average structure. Monoclinic $SrSi_2O_2N_2$, however, can be regarded as a maximally twinned form of the triclinic modification with “domains” of just one layer thickness in an ordered stacking sequence. This yields higher symmetry and different unit-cell metrics.

Table 1. Crystallographic data for $SrSi_2O_2N_2$.

Crystal system	monoclinic
Space group	$P2_1$ (no. 4)
Lattice parameters [Å]	a = 7.1036(14)
	b = 14.078(3)
	c = 7.2833(15)
	β = 95.23(3)°
Cell volume [Å^3]	725.3(3)
Z	8
Formula weight [g mol^{-1}]	203.82
ρ_{calcd} [g cm^{-3}]	3.733
Absorption coefficient μ [mm^{-1}]	15.358
F(000)	768
2θ range [°]	3.16 – 26.00
Radiation λ [Å]	0.71073 (Mo-K_α)
Reflections (total)	5572
Independent reflections	1468
Observed reflections	1145
Goodness of fit	1.077
$R1$ / $wR2$ (all reflections)	0.0850 / 0.1743
$R1$ / $wR2$ ($F_o^2 \geq 2\sigma(F_o^2)$)	0.0633 / 0.1573
min / max residual electron density [eÅ^{-3}]	- 1.58 / 2.74

5.2.3.3 Lattice Energy Calculations

The consistency of the structure model is corroborated by lattice energy calculations (MAPLE, Madelung part of lattice energy).[49-52] The assignment of O and N atoms was done in analogy to other $Sr_{1-x}Ba_xSi_2O_2N_2$ phases with the same silicate layer topology.[36,45-48] This is confirmed by the calculated values listed in Table 2 which are close to typical partial MAPLE values.[16] The comparison between the calculated total MAPLE value and the sum of MAPLE values corresponding to the reference reaction equation, starting from the respective binaries, shows a difference of only 0.06 %. This is in good agreement to the value calculated for $EuSi_2O_2N_2$ also based on single crystal data (Δ = 0.1 %).

Table 2. Results of MAPLE Calculations (in kJ/mol) for Monoclinic $SrSi_2O_2N_2$: Partial MAPLE Values, Total MAPLE Sum and Difference to Theoretical Total MAPLE Value Corresponding to a Reference Equation[a]

Sr^{2+}	Si^{4+}	$O^{[1]2-}$	$N^{[3]3-}$	Total MAPLE	Δ
1929-2070	9373-9617	2227-2432	6093-6268	37923	0.06 %
Total MAPLE ($SrO + 0.5\ SiO_2 + 0.5\ Si_3N_4$): 37946					

[a]Typical MAPLE values (in kJ/mol): Sr^{2+}: 1500-2100; Si^{4+}: 9000-10200; $O^{[1]2-}$: 2000-2800; $N^{[3]3-}$: 5000-6200.

5.2.3.4 Rietveld Refinement

In order to evaluate the proportion of monoclinic $SrSi_2O_2N_2$ in the powder sample, a two-phase Rietveld refinement using TOPAS[42] was done (Figure 3). Weighted distance restraints for Si-O/N tetrahedra in monoclinic $SrSi_2O_2N_2$ were used to ensure comparability to other $Sr_{1-x}Ba_xSi_2O_2N_2$ phases with the same kind of silicate layers.[36,45-48] Thereby all atomic coordinates could be refined. The remaining misfit was significantly reduced after adding the triclinic structure of $SrSi_2O_2N_2$ as a second phase. For the latter, only Sr and Si atom positions were refined.[36] Some 2θ regions were excluded because they are strongly affected by diffuse scattering as a consequence of real-structure effects in triclinic $SrSi_2O_2N_2$[47] (stacking disorder) which cannot be described by the Rietveld method. The degree of cation disorder, i.e. value of antiphase transitions in %, was refined to 40 % using split positions as described for the triclinic average structure.[36,47] As expected, both diffraction patterns are rather similar since basically only the N positions in every second silicate layer are different in the two structure models. Nevertheless, the patterns can clearly be distinguished by reflections at 14.0, 17.8, 20.9, 22.7, and especially at 29.4° 2θ because there are no contributions from the triclinic structure (see Figure 3). The results confirm that the described stacking sequence in monoclinic $SrSi_2O_2N_2$ is present in a significant portion of the powder particles. The amounts of both modifications are approximately equal, and no further unexplained reflections occur in PXRD pattern.

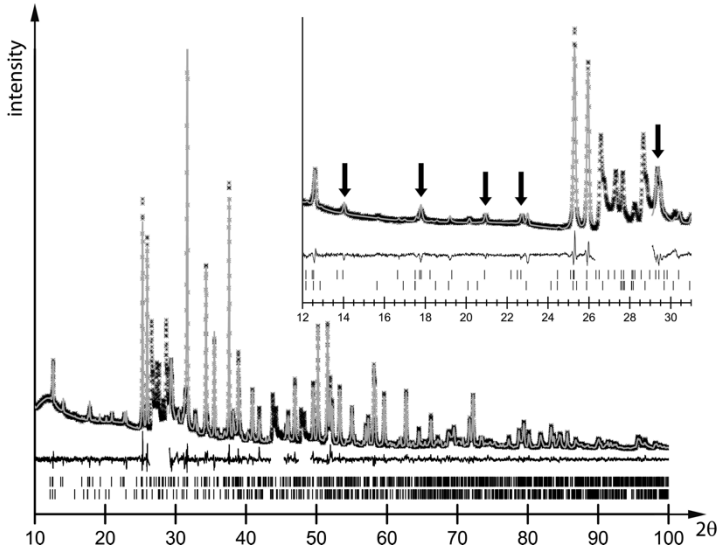

Fig. 3: Two-phase Rietveld fit (R_P = 0.041, wR_P = 0.055; 8367 data points) of the PXRD pattern of $SrSi_2O_2N_2:Eu^{2+}$ with measured histogram (black crosses), calculated pattern (gray solid line), difference curve (black solid line) and positions of reflections (bars): top monoclinic $SrSi_2O_2N_2$ (48 %, ρ_{calcd} [g cm^{-3}] = 3.7083(5)), bottom triclinic $SrSi_2O_2N_2$ (52 %, ρ_{calcd} [g cm^{-3}] = 3.7043(2)). The excluded regions (no difference curve) correspond to maxima due to diffuse scattering. Selected reflections exclusively belonging to monoclinic phase are marked by black arrows in enlarged pattern (upper right).

5.2.3.5 Transmission Electron Microscopy and Electron Diffraction

In TEM samples prepared by dispersing powder on Cu grids with carbon film, all plate-like crystallites exhibited approximately the same orientation of the stacking direction, perpendicular to the grid, as it is typical for layered compounds. This, of course, impedes the determination of the stacking periodicities. Such texture effects are not significant if the powder is embedded in glue, where crystallites with a translation period of ~14 Å, typical for monoclinic $SrSi_2O_2N_2$, could easily be found. TEM-EDX yielded an average formula of $Sr_{0.98}Eu_{0.02}Si_{2.01(8)}O_{2.3(5)}N_{1.6(3)}$ for the crystallites investigated. Traces of $SrSiO_3$ were found, although the corresponding reflections cannot be observed in PXRD data. Various SAED patterns showing translation periods of 14 Å can be simulated based on the results from single-crystal analysis. Calculated tilt angles between different zone axes correspond to the expected ones (Figure 4).[44] Experimental SAEDs contain 0*k*0 reflections with $k = 2n + 1$ (kinematically absent for $2_1 \parallel [010]$) because of dynamic effects.

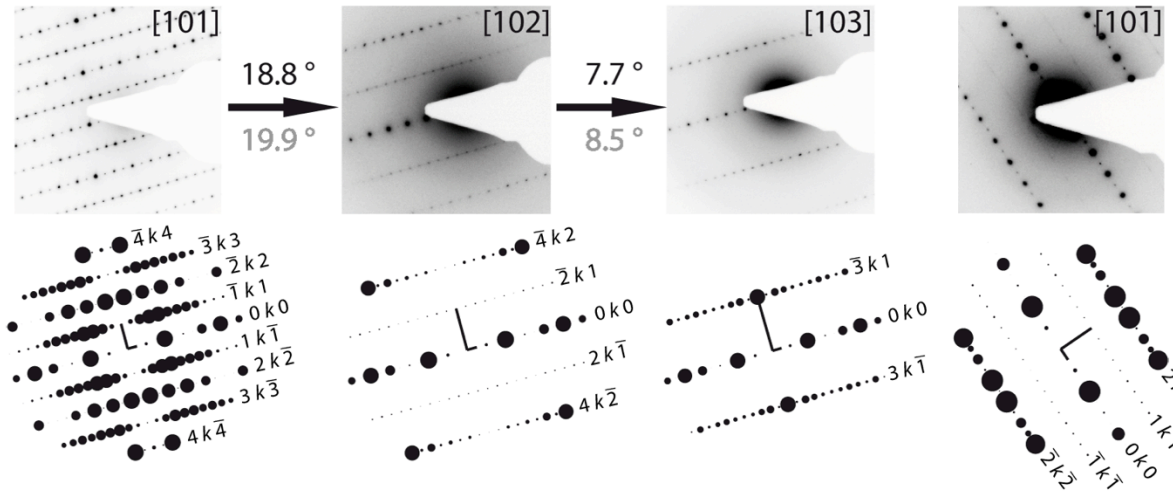

Fig. 4: Experimental SAED patterns (top) of monoclinic $SrSi_2O_2N_2:Eu^{2+}$ with the corresponding zone axes and simulated ones (bottom, calculated from single-crystal data). Experimental tilt angles (black) between zone axes match calculated ones (gray). The [10$\bar{1}$] pattern was recorded using another crystallite due to the limited tilt range of the sample holder.

Although the monoclinic model for $SrSi_2O_2N_2$ is appropriate to simulate experimental SAED images, the local stacking sequence might differ since the beam diameter for SAED patterns (Ø = 100 nm) is significantly larger than the smallest area (10 unit cells ≈ 10 nm) that may be described by an ordered structure model. Figure 5 shows an HRTEM image of a crystallite fringe. As the Fourier transform (FT) of the marked area (diagonal 10 nm) corresponds to the SAED pattern, this area is representative for the whole area contributing to SAED patterns; no or few defects are expected.

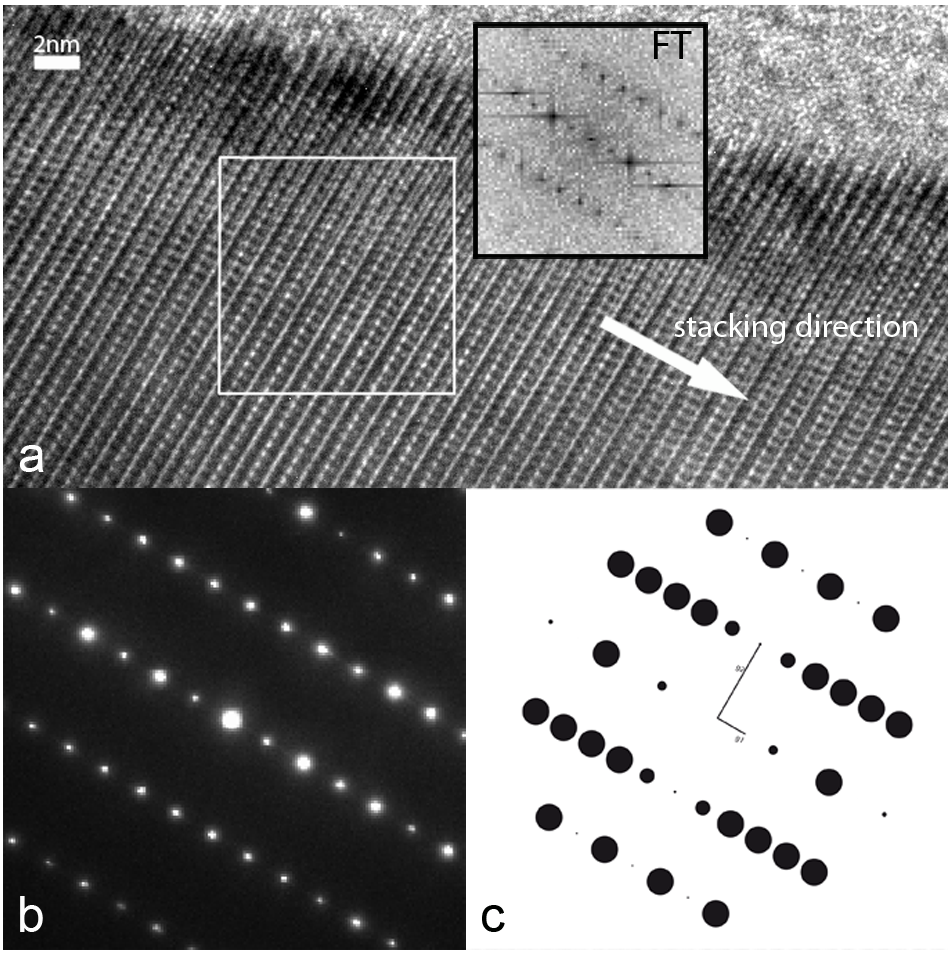

Fig. 5: (a) HRTEM image of monoclinic $SrSi_2O_2N_2:Eu^{2+}$ (zone axis [101]); approximately 10 unit cells (~10 nm) along stacking direction (white frame), the corresponding FT is shown (black frame); (b) experimental SAED pattern (beam diameter ~100 nm); (c) SAED pattern simulated using $SrSi_2O_2N_2$ (monoclinic) single-crystal data.

HRTEM image simulations using the multislice method correlate the structure model to experimental images of a defocus series, passing the Scherzer defocus.[44] The defocus value in Figure 6a (zone axis [10$\bar{1}$]) is -52 nm, i.e. close to the Scherzer defocus so that contrasts can directly be correlated to atom positions.

The simulation fits all features of the experimental image quite well, which is also true for the other HRTEM simulations in Figure 6. In summary, the results of TEM investigations confirm the existence of the monoclinic stacking variant of $SrSi_2O_2N_2$ derived from single-crystal X-ray diffraction analysis.

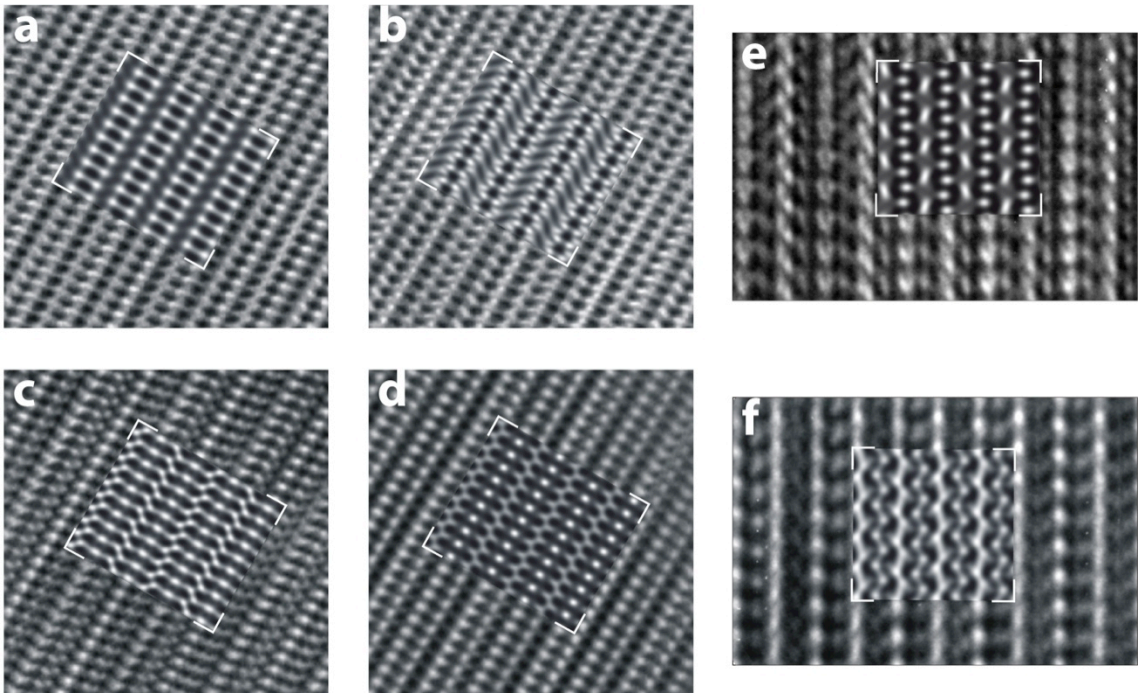

Fig. 6: HRTEM (accelerating voltage = 300 kV) images of monoclinic $SrSi_2O_2N_2:Eu^{2+}$ crystallites of zone axis [101] (a-d) and [10$\bar{1}$] (e,f) with inserted image simulations (a: Δf = -52 nm; b: Δf = -72 nm; c: Δf = -92 nm; d: Δf = -112 nm; e: Δf = +19 nm; f: Δf = +40 nm; for all simulations: aperture diameter = 20 nm^{-1}, c_s = 1.2 mm, spread of focus = 2.14 nm, beam semi-convergence = 0.60 mrad, layer thickness approx. 4 nm).

5.2.3.6 Luminescence

The emission wavelength of green (presumably) triclinic $SrSi_2O_2N_2:Eu^{2+}$ (no additional reflections in PXRD pattern belonging to monoclinic modification) was reported in a range of ~537-540 nm for doping with 2 mol% Eu,[4,17,21,24,27,53,54] which leads to high quantum efficiency (QE > 90%).[24] Regarding the enhancement of color rendition of white-light pc-LEDs that make use of mixtures of green and red emitting phosphors, a shift of the peak emission wavelength towards shorter wavelengths (~ 530 nm) would be desirable.[14] The color point of "triclinic" $SrSi_2O_2N_2:Eu^{2+}$ can be changed by variation of the Eu-doping level[19,26,28-30,34] or substitution of Sr by Ca or Ba.[11,23,24,26,34,55-57] Nevertheless, all changes of the host-lattice composition shift the emission wavelength towards smaller energies. For $Sr_{1-x}Ba_xSi_2O_2N_2:Eu^{2+}$ with $x \geq 0.75$, a shift to higher energies can be achieved; however, its emission spectrum is located in the blue-green spectral region due to the different structure type.[28,46] The determination of luminescence properties of monoclinic $SrSi_2O_2N_2:Eu^{2+}$ cannot be done using powder samples because all obtained samples were inhomogeneous (see section: Rietveld refinement). In order to avoid averaging of emission signals of both modifications, the emission spectrum of the single crystal, which was already used for structure analysis, was measured (Figure 7).

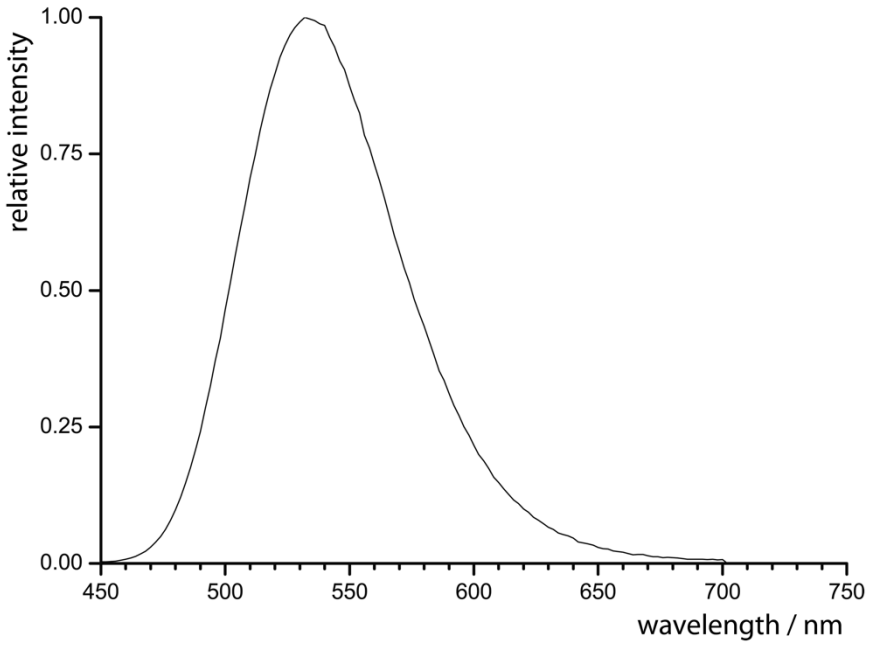

Fig. 7: Emission spectrum of the $SrSi_2O_2N_2:Eu^{2+}$ (2 mol% Eu) single crystal (λ_{exc} = 420 nm, λ_{em} = 532 nm, fwhm ~2600 cm^{-1}); CIE color coordinates: x = 0.314, y = 0.621.

The peak position was determined at λ_{em} = 532 nm by exciting with UV to blue radiation. This means that the emission wavelength of the single crystal of monoclinic $SrSi_2O_2N_2:Eu^{2+}$ is shifted at least 5 nm towards smaller wavelengths in comparison to powder material of $SrSi_2O_2N_2:Eu^{2+}$ which do not show additional reflections in PXRD pattern belonging to monoclinic modification. In order to prove whether this fact is intrinsic or caused by reabsorption of emitted high-energetic radiation in the powder sample (i.e. excitation of another Eu^{2+}-ion by re-emitted photons due to overlap of absorption and emission band), various crystallites (independent of crystal symmetry) with anisotropic morphology were investigated. If the emission wavelength is affected by the length of the radiation pathway through a crystal (i.e. number of activator centers along the pathway, maximal for macroscopic powder sample) different values for λ_{em} are expected for varying orientations of crystallites. The more centers are involved, the more the macroscopically composed emission signal gets shifted to smaller energies. In the present case, λ_{em} was constant for various orientations of three investigated anisotropic crystallites with different sizes. Thus, the red-shifted emission wavelength of $SrSi_2O_2N_2:Eu^{2+}$ powder samples ("triclinic" modification, i.e. no additional reflections in PXRD patterns belonging to monoclinic modification), compared to $SrSi_2O_2N_2:Eu^{2+}$ single crystal (monoclinic modification), is not caused by reabsorption effects. Therefore, the observed differences in measured λ_{em}-values for $SrSi_2O_2N_2:Eu^{2+}$ (single crystal, monoclinic) and $SrSi_2O_2N_2:Eu^{2+}$ (powder, no additional reflections in PXRD pattern

belonging to monoclinic modification) are significant. In order to draft a possible reason for the shift on the basis of the crystal structures, we focus on lattice parameters of triclinic and monoclinic modification. In contrast to the triclinic phase, monoclinic $SrSi_2O_2N_2$ has larger *a* and *c* lattice parameters which represent the periodicity of silicate layers because corresponding settings are equal for both crystal structures. As a direct consequence, interatomic distances increase which corresponds to less corrugated chains of condensed $SiON_3$ tetrahedra. Furthermore, Sr-O distances are also increased which should lead to a decreased 5d-orbital splitting in case of substitution of Sr by an Eu activator ion and an increase of the energetic separation of the $4f^7 5d^0$ and $4f^6 5d^1$ states, equivalent to a blue-shifted maximum of the emission band for monoclinic $SrSi_2O_2N_2:Eu^{2+}$ compared to the triclinic modification. For both modifications, average activator-ligand distances are slightly longer than the sum of the ionic radii.[52] This hardly leads to lattice relaxation in the case of excited Eu^{2+}. As a consequence, less electron-phonon coupling may result in reduced Stokes shift and narrower fwhm, which decreases thermal quenching of luminescence.[58] Luminescence properties of the above-mentioned $SrSi_2O_2N_2:Eu^{2+}$ powder (mixture of triclinic and monoclinic phase) were also measured while reabsorption effects for the powder were minimized by extrapolating the emission properties of a dilution series (silicone suspensions) to zero phosphor concentration, in order to ensure comparability of single-crystal and powder data. An emission wavelength of λ_{em} = 535 nm was determined supporting the thesis that the emission band of the monoclinic modification is blue-shifted in comparison to samples without additional reflections in the PXRD pattern (537-540 nm).

5.2.5 Conclusion

A new monoclinic modification of $SrSi_2O_2N_2$ has been characterized applying a combination of X-ray diffraction and electron-microscopy methods. For the first time, single-crystal data could be obtained for samples with this composition. The triclinic and monoclinic modifications are, in fact, polytypes. Phase formation might therefore be controlled by kinetics. Polytypism was occasionally discussed for layered $M^{II}Si_2O_2N_2$ (M = Ca, Sr, Ba) phases; now we have described two distinct maximum degree of order (MDO) polytypes. The emission wavelength of a single crystal of the Eu-doped monoclinic modification is shifted by ~5 nm towards smaller wavelengths (λ_{em} = 532 nm) compared to that of triclinic $SrSi_2O_2N_2:Eu^{2+}$ (2 mol%) whose emission wavelength cannot be tuned to that value by host-lattice modification because substitution of Sr by Ca as well as Ba always leads to red-shifted emission bands. The triclinic and monoclinic polytypes only differ by the orientation of

consecutive symmetrically equivalent silicate layers. A dependence of luminescence properties on layer orientation in polytypes has not yet been discussed for phosphor materials in the literature. As the triclinic and monoclinic modifications are so closely related, it is not clear if phase pure samples of any $SrSi_2O_2N_2$ modification can be prepared. The results from our contribution complement the understanding of structure-property relationships for frequently used phosphor material $SrSi_2O_2N_2:Eu^{2+}$.

Acknowledgment

The authors thank Dr. Peter Mayer for collecting single-crystal data and Dr. Florian Stadler for preliminary work (both LMU Munich) as well as Petra Huppertz (LDCA Aachen) for single-crystal luminescence measurements. Financial support by the Fonds der Chemischen Industrie (FCI) is gratefully acknowledged.

5.2.6 References

[1] M. Mikami, H. Watanabe, K. Uheda, S. Shimooka, Y. Shimomura, T. Kurushima, N. Kijima, *IOP Conf. Ser.: Mater. Sci. Eng.* **2009**, *1*, 012002.

[2] S. Ye, F. Xiao, Y. X. Pan, Y. Y. Ma, Q. Y. Zhang, *Mater. Sci. Eng., R* **2010**, *71*, 1.

[3] C. C. Lin, R.-S. Liu, *J. Phys. Chem. Lett.* **2011**, *2*, 1268.

[4] R. Mueller-Mach, G. Mueller, M. R. Krames, H. A. Höppe, F. Stadler, W. Schnick, T. Juestel, P. Schmidt, *Phys. Status Solidi A* **2005**, *202*, 1727.

[5] A. A. Setlur, *Electrochem. Soc. Interface* **2009**, *18*, 32.

[6] R.-J. Xie, N. Hirosaki, T. Takeda, T. Suehiro, *ECS J. Solid State Sci. Technol.* **2013**, *2*, R3031.

[7] R.-J. Xie, N. Hirosaki, Y. Li, T. Takeda, *Materials* **2010**, *3*, 3777.

[8] X.-H. He, N. Lian, J.-H. Sun, M.-Y. Guan, *J. Mater. Sci.* **2009**, *44*, 4763.

[9] R.-J. Xie, N. Hirosaki, T. Takeda, *J. Korean Ceram. Soc.* **2012**, *49*, 375.

[10] R.-J. Xie, N. Hirosaki, *Sci. Technol. Adv. Mater.* **2007**, *8*, 588.

[11] D. P. Dutta, A. K. Tyagi, *Solid State Phenomena* **2009**, *155*, 113.

[12] P. F. Smet, A. B. Parmentier, D. Poelman, *J. Electrochem. Soc.* **2011**, *158*, R37.

[13] H. A. Höppe, *Angew. Chem.* **2009**, *121*, 3626; *Angew. Chem. Int. Ed.* **2009**, *48*, 3572.

[14] J. M. Phillips, M. E. Coltrin, M. H. Crawford, A. J. Fischer, M. R. Krames, R. Mueller-Mach, G. O. Mueller, Y. Ohno, L. E. S. Rohwer, J. A. Simmons, J. Y. Tsao, *Laser & Photon. Rev.* **2007**, *1*, 307.

[15] M. Mikami, N. Kijima, *Optical Materials* **2010**, *33*, 145.

[16] M. Zeuner, S. Pagano, W. Schnick, *Angew. Chem.* **2011**, *123*, 7898; *Angew. Chem. Int. Ed.* **2011**, *50*, 7754.

[17] J. Botterman, K. Van den Eeckhout, A. J. J. Bos, P. Dorenbos, P. F. Smet, *Opt. Mater. Express* **2012**, *2*, 341.

[18] K. Machida, *IOP Conf. Ser.: Mater. Sci. Eng.* **2011**, *18*, 052001.

[19] Y. H. Song, W. J. Park, D. H. Yoon, *J. Phys. Chem. Solids* **2010**, *71*, 473.

[20] X. Song, H. He, R. Fu, D. Wang, X. Zhao, Z. Pan, *J. Phys. D: Appl. Phys.* **2009**, *42*, 065409.

[21] C.-C. Yang, C.-M. Lin, Y.-J. Chen, Y.-T. Wu, S.-R. Chuang, *Appl. Phys. Lett.* **2007**, *90*, 123503.

[22] Y. Zhang, X. Liu, B. Lei, H. Wang, Q. Sun, *Energy Procedia* **2012**, *16*, 391.

[23] B. Y. Han, K.-S. Sohn, *Electrochem. Solid-State Lett.* **2010**, *13*, J62.

[24] V. Bachmann, C. Ronda, O. Oeckler, W. Schnick, A. Meijerink, *Chem. Mater.* **2009**, *21*, 316.

[25] M. Zhang, J. Wang, Z. Zhang, Q. Zhang, Q. Su, *Appl. Phys. B: Lasers Opt.* **2008**, *93*, 829.

[26] B.-G. Yun, Y. Miyamoto, H. Yamamoto, *J. Electrochem. Soc.* **2007**, *154*, J320.

[27] X. Yang, H. Song, L. Yang, X. Xu, *J. Am. Ceram. Soc.* **2011**, *94*, 28.

[28] Y. Q. Li, A. C. A. Delsing, G. De With, H. T. Hintzen, *Chem. Mater.* **2005**, *17*, 3242.

[29] Y. Song, X. Xu, H. Zou, Y. Sheng, H. You, *J. Alloys Compd.* **2012**, *513*, 86.

[30] B.-G. Yun, K. Machida, H. Yamamoto, *J. Ceram. Soc. Jpn.* **2007**, *115*, 619.

[31] Y.-C. Fang, P.-C. Kao, Y.-C. Yang, S.-Y. Chu, *J. Electrochem. Soc.* **2011**, *158*, J246.

[32] K. Y. Jung, J. H. Seo, *Electrochem. Solid-State Lett.* **2008**, *11*, J64.

[33] S. D. Jee, K. S. Choi, J. S. Kim, *Met. Mater. Int.* **2011**, *17*, 655.

[34] G. Anoop, I. H. Cho, D. W. Suh, J. S. Yoo, *Phys. Status Solidi A* **2012**, *209*, 2635.

[35] X.-K. Meng, J. Tan, T. Lei, W. Zhang, W. Yan, C.-M. Li, X.-W. Sun, *Chinese J. Inorg. Chem.* **2012**, *28*, 893.

[36] O. Oeckler, F. Stadler, T. Rosenthal, W. Schnick, *Solid State Sci.* **2007**, *9*, 205.

[37] W. H. Zhu, P. L. Wang, W. Y. Sun, D. S. Yan, *J. Mater. Sci. Lett.* **1994**, *13*, 560.

[38] X. Song, R. Fu, S. Agathopoulos, H. He, X. Zhao, R. Li, *J. Electrochem. Soc.* **2010**, *157*, J34.

[39] X. Song, R. Fu, S. Agathopoulos, H. He, X. Zhao, J. Zeng, *Mater. Sci. Eng., B* **2009**, *164*, 12.

[40] J.-Y. Tang, X.-F. Yang, C. Zhan, L.-Y. Hao, X. Xu, W.-H. Zhang, *J. Mater. Chem.* **2012**, *22*, 488.

[41] J. Ruan, R.-J. Xie, N. Hirosaki, T. Takeda, *J. Electrochem. Soc.* **2012**, *159*, H66.

[42] *TOPAS-Academic*, *V. 4.1*, Coelho Software, Brisbane, Australia, **2007**.

[43] G. M. Sheldrick, *Acta Crystallogr. Sect. A* **2008**, *64*, 112.

[44] P. A. Stadelmann, *Ultramicroscopy* **1987**, *21*, 131.

[45] J. A. Kechele, O. Oeckler, F. Stadler, W. Schnick, *Solid State Sci.* **2009**, *11*, 537.

[46] M. Seibald, T. Rosenthal, O. Oeckler, F. Fahrnbauer, A. Tücks, P. J. Schmidt, W. Schnick, *Chem.-Eur. J.* **2012**, *18*, 13446.

[47] M. Seibald, O. Oeckler, V. R. Celinski, P. J. Schmidt, A. Tücks, W. Schnick, *Solid State Sci.* **2011**, *13*, 1769.

[48] F. Stadler, O. Oeckler, H. A. Höppe, M. H. Möller, R. Pöttgen, B. D. Mosel, P. Schmidt, V. Duppel, A. Simon, W. Schnick, *Chem.–Eur. J.* **2006**, *12*, 6984.

[49] R. Hoppe, *Angew. Chem.* **1966**, *78*, 52; *Angew. Chem. Int. Ed.* **1966**, *5*, 95.

[50] R. Hoppe, *Angew. Chem.* **1970**, *82*, 7; *Angew. Chem. Int. Ed.* **1970**, *9*, 25.

[51] R. Hübenthal, *Madlung Part of Lattice Energy*, version 4, **1993**, University of Gießen (Germany).

[52] R. D. Shannon, *Acta Crystallogr. Sect. A* **1976**, *32*, 751.

[53] V. Bachmann, T. Juestel, A. Meijerink, C. Ronda, P. J. Schmidt, *J. Lumin.* **2006**, *121*, 441.

[54] C.-W. Yeh, Y. Li, J. Wang, R.-S. Liu, *Opt. Express* **2012**, *20*, 18031.

[55] H. Yamamoto, M. Yamauchi, J. Iizuka, B. G. Yun, K. Machida, N. Kijima, *ECS Trans.* **2011**, *33*, 109.

[56] B. Lei, K. Machida, T. Horikawa, H. Hanzawa, *Chem. Lett.* **2011**, *40*, 140.

[57] I. H. Cho, G. Anoop, D. W. Suh, S. J. Lee, J. S. Yoo, *Opt. Mater. Express* **2012**, *2*, 1292.

[58] G. Blasse, B. C. Grabmaier, *Luminescent Materials*, Springer, Berlin, Germany, **1994**

5.3 Unexpected luminescence properties of $Sr_{0.25}Ba_{0.25}Si_2O_2N_2:Eu^{2+}$ – a narrow blue emitting oxonitridosilicate with cation ordering

M. Seibald, T. Rosenthal, O. Oeckler, F. Fahrnbauer, A. Tücks, P. J. Schmidt, W. Schnick
Chem. Eur. J. **2012**, *18*, 13446-13452.

Abstract

Due to parity allowed $4f^6(^7F)5d^1 \rightarrow 4f^7(^8S_{7/2})$ transition, powders of the nominal composition $Sr_{0.25}Ba_{0.75}Si_2O_2N_2:Eu^{2+}$ (2 mol % Eu^{2+}) show surprising intense blue emission (λ_{em} = 472 nm) when excited by UV to blue radiation. Similarly to other phases in the system $Sr_{1-x}Ba_xSi_2O_2N_2:Eu^{2+}$, the described compound is a promising phosphor material for pc-LED applications as well. The FWHM of the emission band is 37 nm, representing the smallest value found for blue emitting (oxo)nitridosilicates so far. A combination of electron and X-ray diffraction methods was used to determine the crystal structure of $Sr_{0.25}Ba_{0.75}Si_2O_2N_2:Eu^{2+}$. HRTEM images reveal the intergrowth of nanodomains with $SrSi_2O_2N_2$ and $BaSi_2O_2N_2$-type structures, which leads to pronounced diffuse scattering. Taking into account the intergrowth, the structure of the $BaSi_2O_2N_2$-type domains was refined on single-crystal diffraction data. In contrast to coplanar metal atom layers which are located between layers of condensed $SiON_3$-tetrahedra in pure $BaSi_2O_2N_2$, in $Sr_{0.25}Ba_{0.75}Si_2O_2N_2:Eu^{2+}$ corrugated metal atom layers occur. HRTEM image simulations indicate cation ordering in the final structure model, which, in combination with the corrugated metal atom layers, explains the unexpected and excellent luminescence properties.

5.3.1 Introduction

In times of economic crises, shortage of resources and increased sensibility of people to their environment, there is a huge demand for new materials or improved applications to enhance energy and cost efficiency together with environmental compatibility. One possible strategy is the replacement of conventional incandescent bulbs and fluorescent lamps by phosphor converted (pc)-LED applications that leads to energy saving and positive environment effects.[1-5] White light can be generated by pc-LEDs employing the combination of a blue pump LED with yellow-green and orange-red solid-state luminescent materials (phosphors) for light conversion. Therefore, the interest and research on host lattices for rare earth activators rapidly increased during the last few years. Beside oxidic garnet phosphors

especially (oxo)nitrido(alumo)silicates are being investigated in this respect.[1-7] Their crystal structures show higher variability compared to pure oxosilicates, because N atoms can bridge up to four tetrahedra leading to a higher degree of condensation.[7] As a consequence, emission variable within the entire visible optical spectrum can be achieved with these materials. The oxonitridosilicate phases $Sr_{1-x}Ba_xSi_2O_2N_2$ (examples of so called 1-2-2-2 phases) are promising host lattices since excellent luminescence properties in the yellow-green spectral region are observed upon doping with Eu^{2+} ions.[8-17] For instance, $SrSi_2O_2N_2:Eu^{2+}$ can be used in white high power pc-LED applications achieving a high luminous efficiency, excellent color quality and high color stability.[18] The corresponding crystal structures exhibit various real-structure effects on different length scales, e.g. intergrowth, microtwinning and stacking disorder.[8,15,19] Single crystals for structure elucidation could only be obtained for $EuSi_2O_2N_2$ (isotypic to $SrSi_2O_2N_2$).[20] As a consequence, routine strategies for structure determination could not be used for the related Sr and Ba compounds as well as the respective mixed phases.[8,15,19] The compounds $Sr_{1-x}Ba_xSi_2O_2N_2:Eu^{2+}$ exhibit outstanding luminescence properties. They show an unexpected red-shifted luminescence for increasing Ba^{2+} content.[10,11] Usually, substitution of Sr^{2+} by larger Ba^{2+} ions causes a shift to shorter emission wavelengths due to lower Eu^{2+} 5d-orbital splitting when Eu^{2+} randomly occupies the metal positions. Rietveld refinement on powder X-ray diffraction (PXRD) data in combination with transmission electron microscopy (TEM) showed that $Sr_{0.5}Ba_{0.5}Si_2O_2N_2:Eu^{2+}$ is highly disordered and multiply twinned.[15] Its crystal structure is very similar to that of $SrSi_2O_2N_2:Eu^{2+}$, which exhibits a lower degree of disorder. Substitution of Sr^{2+} by Ba^{2+} leads to a deformation of the layered crystal structure. The Sr-O distances in the pure Sr phase are larger than the sum of the ionic radii, however, Ba integration leads to shorter Sr-O distances in the mixed phase compared to non-substituted $SrSi_2O_2N_2:Eu^{2+}$. The dopant Eu^{2+} preferably occupies these Sr positions, resulting in more pronounced structural relaxation and a larger Stokes shift.[15] Preferred occupation of Sr sites, i.e. sites with shorter metal-ligand distances, by Eu^{2+} was also reported for $Ba_{3-x}Sr_xSi_6O_{12}N_2:Eu^{2+}$ where the unexpected small FWHM of the emission band was explained by a favored occupation of one of the two independent alkaline earth sites.[21] The detailed knowledge of the crystal structure thus allows to explain the luminescence properties, which appear surprising at first glance. Apparently, the impact of cation substitution on the deformation of the crystal structure is difficult to predict, so that the luminescence properties may be unexpected. This is most pronounced for systems which do not form solid solutions with a broad compositional range (e.g. $SrSi_2O_2N_2$ and $BaSi_2O_2N_2$). As shown for

$Sr_{0.5}Ba_{0.5}Si_2O_2N_2:Eu^{2+}$, PXRD patterns of very similar structures may look significantly different; both additional and "missing" intensities do result from real structure effects. The coherent interference of scattered waves can change the pattern dramatically if nanodomains are present.[15] Therefore, nanotwinning may affect the intensities in powder diffraction patterns whereas "classical" twinning (domain sizes larger than the X-ray's length of coherence) has no influence. Here, we present the structure of $Sr_{1-x}Ba_xSi_2O_2N_2:Eu^{2+}$ (x = 0.75) which was elucidated by combining X-ray and electron diffraction and high-resolution TEM (HRTEM). The material exhibits complex real structure effects as well as excellent luminescence properties.

5.3.2 Results and Discussion

5.3.2.1 Synthesis and Chemical Analysis

Two different approaches for sample synthesis have been applied: (1) Powder samples of $Sr_{1-x}Ba_xSi_2O_2N_2:Eu^{2+}$ (x = 0.75) suitable for TEM investigations were prepared by heating a stoichiometric mixture (1:3; ball milled) of $(Sr_{0.25}Ba_{0.75})_2SiO_4:Eu^{2+}$ and Si powder (Cerac, 99.999%) at maximum temperatures of 1400 °C in a stream of forming gas (N_2:H_2 = 95:5) using a molybdenum crucible.
(2) Samples with crystals suitable for single-crystal analysis were obtained by heating a stoichiometric mixture of $(Sr_{0.25}Ba_{0.75})_2SiO_4:Eu^{2+}$ and α-Si_3N_4 (UBE, >95 %) at maximum temperatures of 1400 °C using a tungsten crucible positioned in a radio-frequency (RF) furnace [22] with stationary forming gas (N_2:H_2 = 95:5) atmosphere (equation 1).

$$(Sr_{1-x}Ba_x)_2SiO_4:Eu^{2+} + Si_3N_4 \longrightarrow 2\,(Sr_{1-x}Ba_x)Si_2O_2N_2:Eu^{2+} \qquad \text{(Eq. 1)}$$

EDX analysis of the $Sr_{1-x}Ba_xSi_2O_2N_2:Eu^{2+}$ powder, obtained in a forming gas stream, yielded x = 0.74(1) (average of seven measurements of crystallites with typical platelet morphology) as expected. For single crystals (RF furnace synthesis), x was determined to be 0.75(1) as an average of five measurements. From TEM-EDX, x = 0.73(2) was obtained as an average of eight measurements on crystallites with typical morphology. Accordingly, the value of x = 0.75 (within experimental standard deviation 2 - 4 at. %) is confirmed by EDX measurements so that results from electron and X-ray diffraction data are comparable. A minor impurity phase with $BaSi_6N_8O$ structure type[23] was detected, which is typical for thermal decomposition of 1-2-2-2 phases.[15]

5.3.2.2 Electron Microscopy

In samples prepared by dispersing powder on Cu grids with carbon film, all crystallites with the expected composition exhibited approximately the same orientation due to the platelet particle morphology typical for layered compounds. This impedes the determination of lattice parameters. Although in general tilting the sample changes the diffraction pattern significantly, in this case tilting (overall up to 48 °) did not result in a variation of the zone axis visible in selected area electron diffraction (SAED) patterns. However, the intensity of the "reflections" varies (Figure 1).

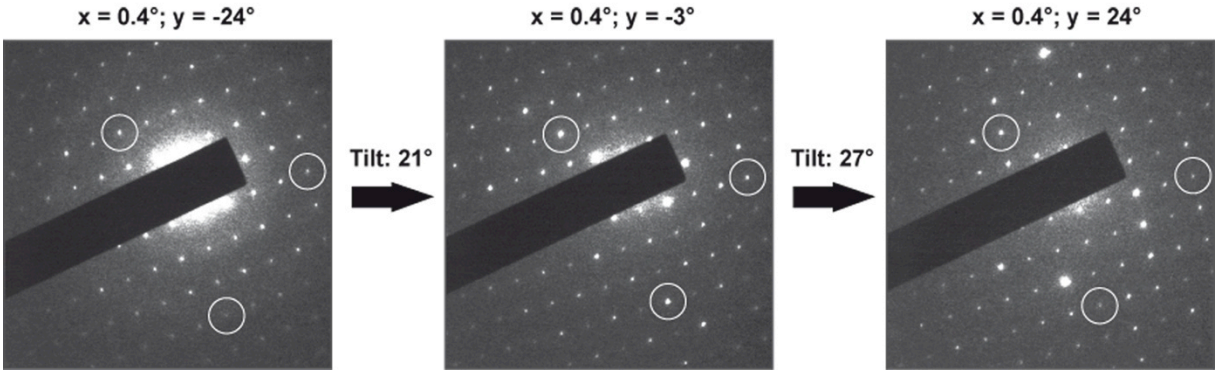

Fig. 1: SAED patterns of a tilt series (along y; overall 48° tilt angle; x and y are absolute tilt angles of the TEM sample holder). Exemplary "reflections" with changing intensities are marked by white circles.

This effect can be explained by assuming continuous diffuse streaks interconnecting the Bragg positions along the viewing direction. The maximum of the measured (real) lattice spacing during the tilt is d = 5.46 and 4.80 Å, respectively, which is close to d values determined by single-crystal analysis (*next section*) and include an angle of 90.5°, corresponding to the unit mesh dimension within the silicate layer (Figure 2).

To diminish texture effects (to accomplish more statistical distribution of particles) and directly observe diffuse streaks, powder samples, embedded in two-component glue, were used. Intense diffuse streaks interconnecting Bragg reflections were observed. The lattice spacing along the streaks correspond to the unit cell dimension of $BaSi_2O_2N_2$.

In HRTEM images, a domain structure can be observed (Figure 3). The metrics of the crystal structure of both domain types were determined using SAED patterns (Figure 4). A subset of the reflections can be described by the metrics of the $BaSi_2O_2N_2$ type. The elongated maxima between these Bragg reflections cannot be indexed by this lattice; they require a second lattice, resembling that of $SrSi_2O_2N_2$.

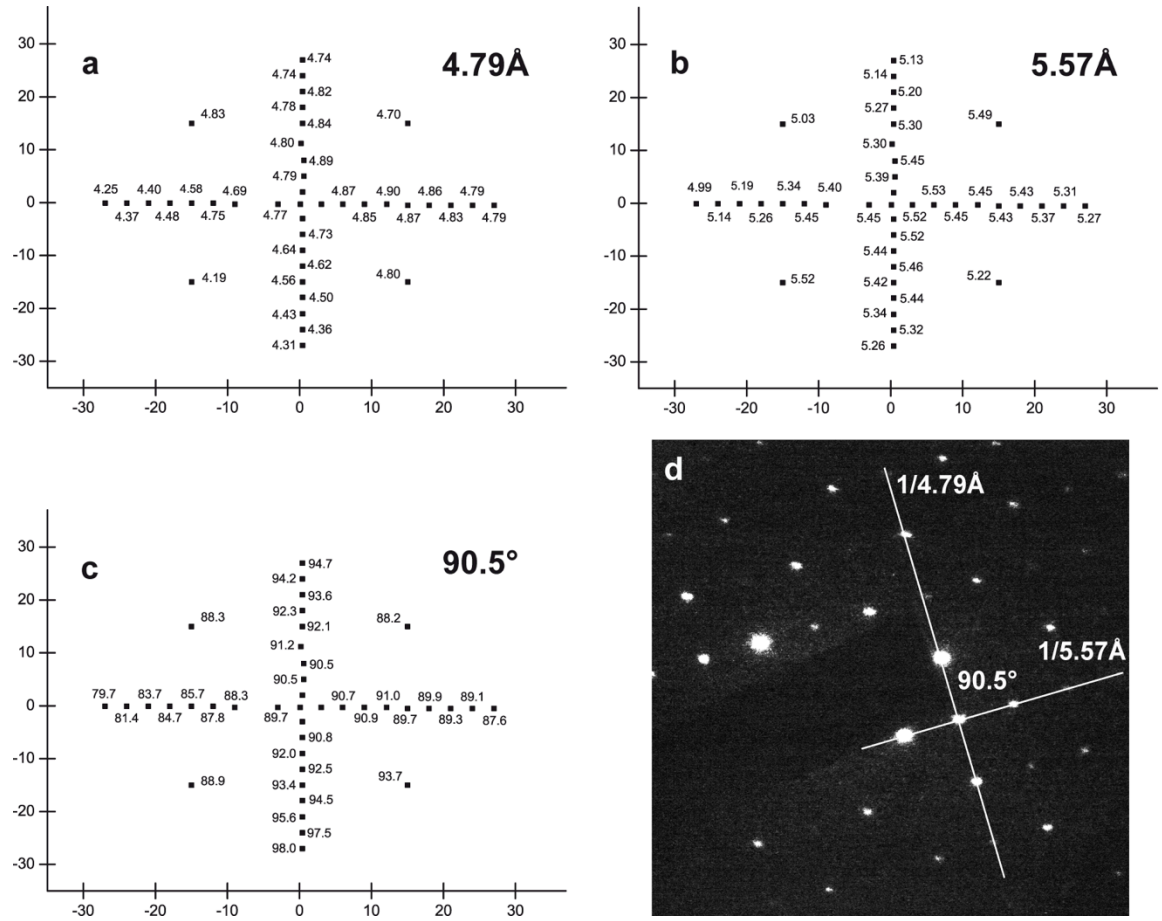

Fig. 2: ”Pseudo” lattice spacing (a, b) and corresponding angle (c) of $Sr_{0.25}Ba_{0.75}Si_2O_2N_2:Eu^{2+}$ dependent on tilt angle of TEM sample holder (axes of coordinate systems). Due to platelet morphology of crystallites, the tilt angles of the sample holder are approx. 0° in both directions for the maximal d values. Typical SAED pattern (d) close to 0 ° tilt angle of sample holder.

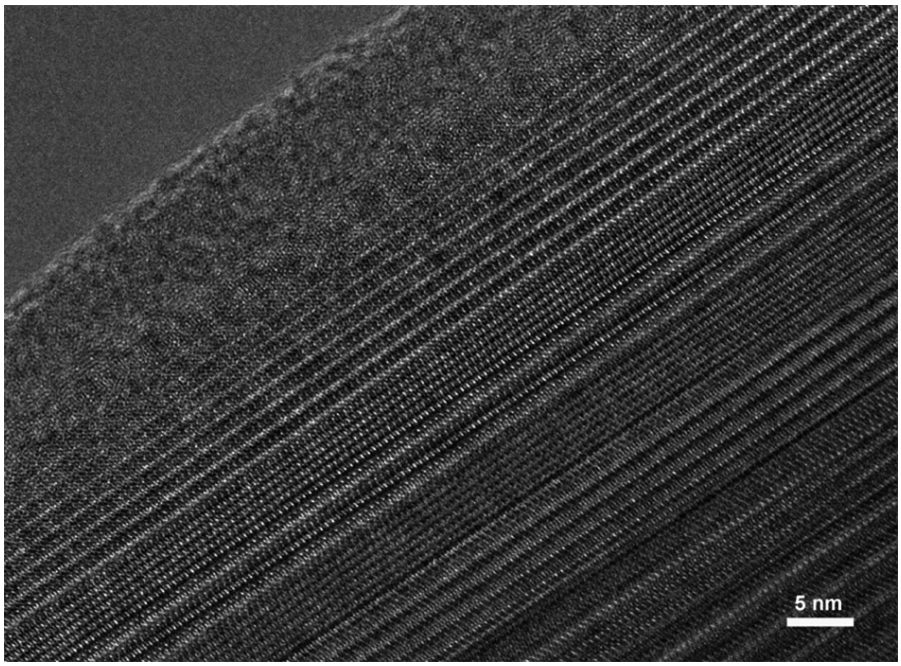

Fig. 3: Typical HRTEM image of $Sr_{0.25}Ba_{0.75}Si_2O_2N_2:Eu^{2+}$ with layered domain structure.

Results of TEM-EDX analyses corroborate the presence of domains with higher Sr content which can be expected to exhibit the $SrSi_2O_2N_2$ structure type. This variation of the Sr distribution cannot be detected in SEM-EDX measurements because the domain sizes are much smaller than the area investigated. Both lattices share one direction: d_{010} of the $BaSi_2O_2N_2$ type (14.00 Å; 14.28 Å from single-crystal data; black unit cell) is twice d_{010} of the $Sr_{0.5}Ba_{0.5}Si_2O_2N_2$ type (7.00 Å; 7.17 Å from PXRD,[15] white unit cell). Both lattice vectors are parallel and correspond to the stacking direction of silicate layers. The second smallest spacing of each lattice corresponds to d_{100} of $BaSi_2O_2N_2$ type (5.53 Å; 5.47 Å from single-crystal analysis,) and d_{101} of $Sr_{0.5}Ba_{0.5}Si_2O_2N_2$ type (5.34 Å; 5.29 Å from PXRD,[15] respectively. The corresponding angles ($BaSi_2O_2N_2$ type: 90°; single crystal orthorhombic; $Sr_{0.5}Ba_{0.5}Si_2O_2N_2$ type: 75°; 76° from PXRD)[15] also match well. The deviations between lattice parameters from electron and X-ray diffraction data are consistent within experimental errors of both methods.

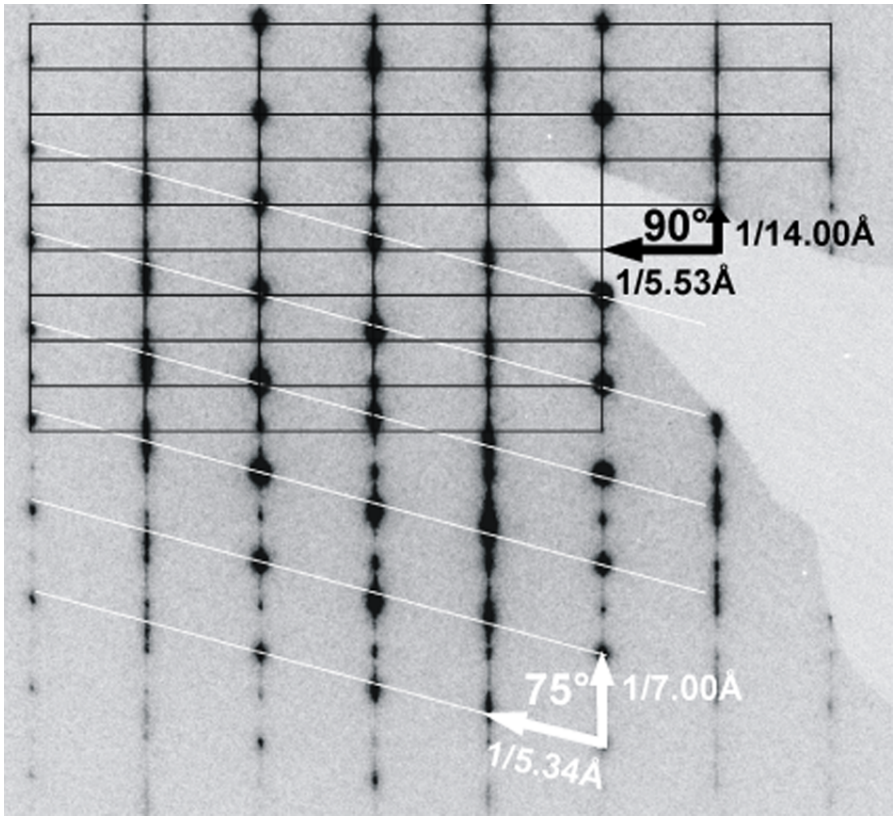

Fig. 4: SAED pattern representing a superposition (middle) of the [001] zone axis of the $BaSi_2O_2N_2$ type (black, top) and the $[10\bar{1}]$ zone axis of the $SrSi_2O_2N_2$ type (white, bottom). For both, d values and corresponding angles are shown. In every third vertical row, some Bragg reflections of both compounds overlap completely. Diffuse streaks interconnect the reflections.

Some reflections of $SrSi_2O_2N_2$ and $BaSi_2O_2N_2$ lattice types overlap completely and therefore the intensity of affected sharp Bragg reflections (in every third row) is the sum of two contributions and thus contains information from both systems. Therefore, diffraction patterns do not show orthorhombic Laue symmetry (see $BaSi_2O_2N_2$ [8] structure type). The $SrSi_2O_2N_2$ structure type [19] is triclinic (space group *P*1) and the superposition with any other pattern yields overall triclinic Laue symmetry.

5.3.2.3 Single-Crystal Structure Analysis

As shown in Figure 3, $Sr_{0.25}Ba_{0.75}Si_2O_2N_2:Eu^{2+}$ exhibits a domain structure with 2D extended domains, which are only a few nanometers thick. Single crystals show pronounced diffuse scattering in reciprocal lattice sections. Because the domains are very thin, the scattered waves superimpose coherently which means that overlapping intensities contain information on both domain types (see Figure 4). These overlapping reflections were discarded for the refinement of the structure of the blue emitting material (based on $BaSi_2O_2N_2$ lattice parameters). The relative orientation of both domain types does not change, so "single crystal" methods can be used for such crystals when reflections with contributions from different domain types are neglected. The scheme in Figure 5, which was derived from different reciprocal lattice sections, shows that all rows along [010] with exclusively sharp reflections (see Figure 4) are involved. This corresponds to 1/3 of all reflections.

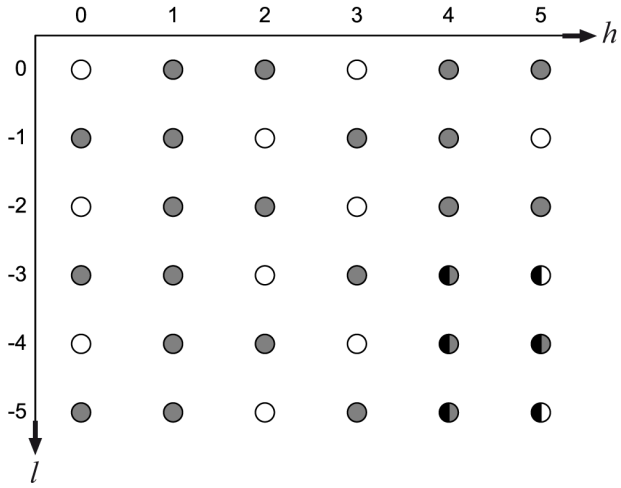

Fig 5: Schematic view of the overlap of the reciprocal lattice of $BaSi_2O_2N_2$ with that of the $SrSi_2O_2N_2$ structure type. As derived from reciprocal lattice sections, rows along [010] of the $BaSi_2O_2N_2$ type show either exclusively sharp reflections or elongated, diffuse intensities. Referring to Figure 4, rows with only sharp reflections overlap for both lattice types (white spheres) while the others exclusively belong to the $BaSi_2O_2N_2$ lattice type (gray spheres). As the resolution of the reciprocal lattice sections available was limited, some rows (black-gray spheres, black-white spheres) were extrapolated.

The crystal structure of $Sr_{0.25}Ba_{0.75}Si_2O_2N_2:Eu^{2+}$ was refined in space group $Pna2_1$ (no. 33) with $a = 5.470(2)$, $b = 14.277(3)$, $c = 4.791(1)$ Å and $V = 374.2(2)$ Å^3 (see Figure 7). Refinement converged finally to $R1 = 0.0924$. Comparable refinements in *Pnma* show disordered silicate layers as described for $BaSi_2O_2N_2$ [8] but with significantly higher *R*-values. The absence of disorder in the crystal structure is corroborated by the Fourier transforms of individual domains in HRTEM images, which exhibit no diffuse intensities. In the refined structure model, the silicate layers are built up of vertex sharing $SiON_3$-tetrahedra and shifted against each other along the stacking direction [010]. The metal atom layers in between them are corrugated instead of being coplanar as in $BaSi_2O_2N_2$.[8] As the Bragg reflections used for the structure refinement are located on diffuse streaks, their absolute intensities are biased. Mixed occupation of the metal atom position was set to an atomic ratio Sr:Ba = 1:3 as suggested by the EDX analysis. The doping with 2 mol% Eu was neglected during refinement. Distance restraints for the $SiON_3$-tetrahedra were implemented in order to ensure their comparability to the values in $SrSi_2O_2N_2$ and $BaSi_2O_2N_2$. The similarity of tetrahedra topology within the silicate layers is the reason for the intergrowth of $Sr_{0.25}Ba_{0.75}Si_2O_2N_2$ domains in zone axis orientation [001] with $SrSi_2O_2N_2$ structure type domains in $[10\bar{1}]$ respectively, as determined from superimposed diffraction patterns like the one in Figure 4. Related anionic substructures can for example also be observed in $(Sr_{0.94}Eu_{0.06})(Al_{0.3}Si_{0.7})_4(N_{0.8}O_{0.2})_6$, an alumosilicate with stacking faults.[24]

5.3.2.4 Cation Ordering as Derived from HRTEM

HRTEM image simulations[25] were compared to experimental images (Figure 6). They show that a structure model with one mixed occupied metal atom position ($Pna2_1$) does not well describe all significant features of the HRTEM images (Figure 6b).

Horizontal rows with bright white contrasts (indicated by black arrows, Figure 6a) are strongly affected by the metal atom positions so that the periodic varying contrast in every second of these rows indicates deviations from space group $Pna2_1$ as it is not consistent with mirror planes and mixed occupation of a single metal atom position. A convincing fit was obtained employing space group *P*1 and full occupation of one of the four resulting metal atom positions with Sr, which is consistent with the chemical composition Sr:Ba = 1:3 (Figure 6c, 6d).

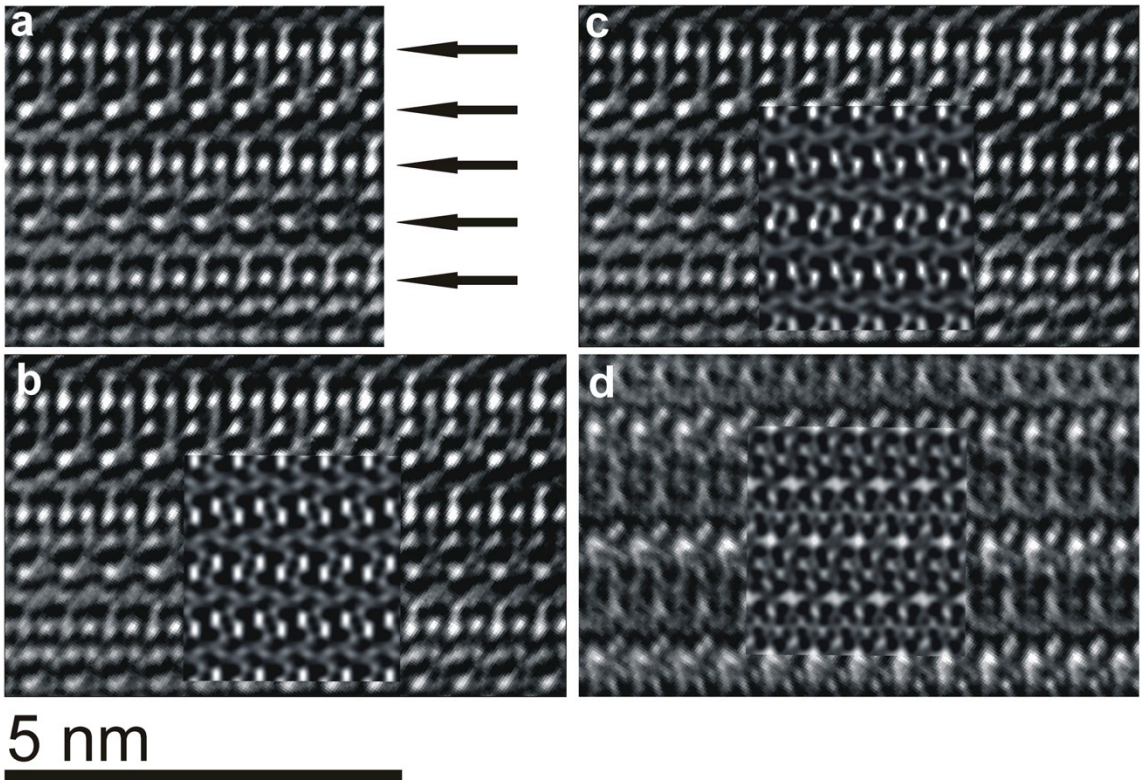

Fig. 6: HRTEM images of $Sr_{0.25}Ba_{0.75}Si_2O_2N_2:Eu^{2+}$ with: black arrows indicating horizontal contrasts mainly affected by metal atom layers (a), simulation for the refined structure in space group $Pna2_1$ (b, defocus value -81 nm), simulation for structure in space group P1 (c, cation ordering, defocus value -81 nm) and simulation for structure in P1 (d, cation ordering, defocus value -119 nm). For all simulations the following values were used: accelerating voltage = 300 kV, aperture diameter = 20 nm^{-1}, c_s = 1.2 mm, spread of focus = 2.14 nm, beam semi-convergence = 0.60 mrad, layer thickness approx. 4 nm (8 unit cells in corresponding viewing direction).

Additionally, the position of the metal atoms was slightly shifted, because of different ionic radii and consequently different coordination spheres of Sr and Ba (compare trigonal prismatic in $SrSi_2O_2N_2$ vs. cuboid in $BaSi_2O_2N_2$). This means that rows exclusively occupied by Ba atoms are less corrugated than rows containing alternating Ba and Sr atoms and Ba-Sr bond lengths are shorter than the Ba-Ba bond lengths (Figure 7). The relaxation of surrounding light atoms was neglected because it affects only slightly the simulated images. Simulated images for two defocus values reproduce the main features (Figure 6c, 6d) quite well.

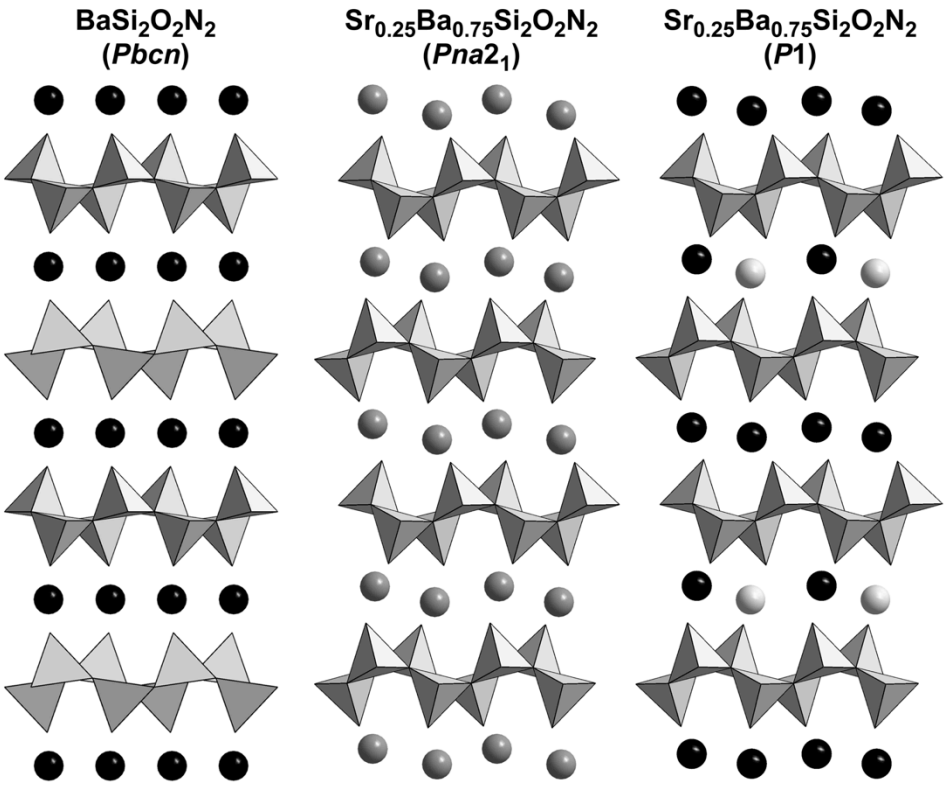

Fig 7: Projections of the crystal structures of $BaSi_2O_2N_2$ (left),[8] $Sr_{0.25}Ba_{0.75}Si_2O_2N_2$ ("average" structure from single-crystal data, middle) and $Sr_{0.25}Ba_{0.75}Si_2O_2N_2$ (local cation ordering according to TEM, right) perpendicular to stacking direction. Silicate layers of condensed $SiON_3$-tetrahedra are illustrated gray, Ba atoms black, Sr/Ba mixed occupied positions dark gray and Sr atoms light gray.

The consistency of the structure model is corroborated by lattice energy calculations (MAPLE, Madelung part of lattice energy).[26-29] The assignment of O and N atoms was done in analogy to other $Sr_{1-x}Ba_xSi_2O_2N_2$ phases with the same silicate layer topology.[8,15,19] The calculated values listed in Table 1 are close to typical partial MAPLE values.[7] The total MAPLE values calculated for the refined structure and the structure model containing ordered cations are compared to that of a theoretical reference reaction equation starting from the respective binary compounds. The deviation is almost half the value for the structure model with cation ordering compared to the structure model refined on X-ray data.

Table 1. Results of MAPLE calculations (in kJ/mol) for $Sr_{0.25}Ba_{0.75}Si_2O_2N_2$ and increment calculations: partial MAPLE values, total MAPLE sum and difference to theoretical total MAPLE value.[a]

	Sr^{2+}	Ba^{2+}	Si^{4+}	$O^{[1]2-}$	$N^{[3]3-}$	Total MAPLE	Δ
$Pna2_1$	1896 (mixed)		9408-9566	2219-2276	6174-6206	37745	0.064 %
*P*1	1916	1871-1900	9249-9755	2144-2386	6051-6331	37755	0.037 %
Total MAPLE (0.25 SrO + 0.75 BaO + 0.5 SiO_2 + 0.5 Si_3N_4): 37769							

[a] Typical MAPLE values (in kJ/mol): Ba^{2+}: 1500-2000; Sr^{2+}: 1500-2100; Si^{4+}: 9000-10200; $O^{[1]2-}$: 2000-2800; $N^{[3]3-}$: 5000-6200.[7]…

5.3.2.5 Luminescence

Eu^{2+}-doped samples of $Sr_{0.25}Ba_{0.75}Si_2O_2N_2$ show unexpected intense narrow band blue emission when excited with UV to blue radiation as a consequence of the parity allowed $4f^6(^7F)5d^1 \rightarrow 4f^7(^8S_{7/2})$ transition.

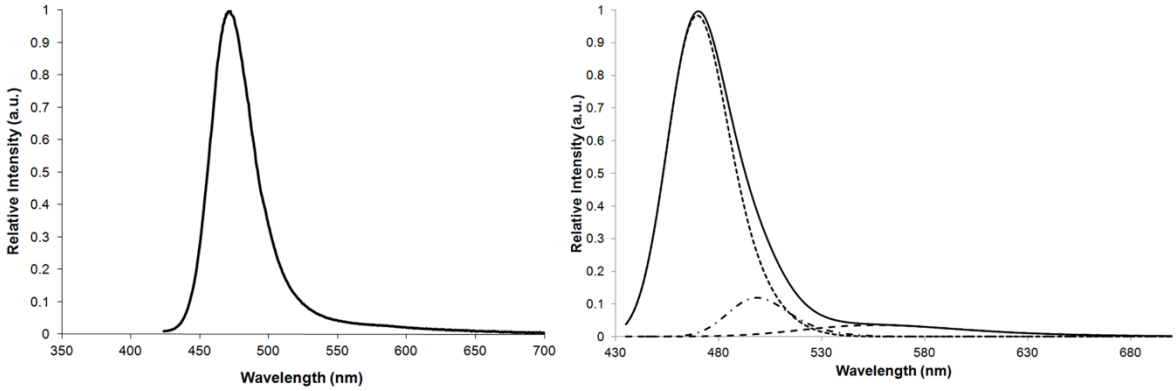

Fig. 8: Left: emission spectrum of $Sr_{0.25}Ba_{0.75}Si_2O_2N_2:Eu^{2+}$ (2 mol %) powder sample (λ_{exc} = 400 nm, λ_{em} = 472 nm, FWHM = 37 nm). Right: Least-square refinement of measured emission spectrum (black solid line) with three individual curves (1: λ_{em} = 469 nm, FWHM = 36 nm, line: dashed; 2: λ_{em} = 498 nm, FWHM = 35 nm, line: dashed and dotted; 3: λ_{em} = 555 nm, FWHM = 90 nm, line: dashed).

As shown for the $SrSi_2O_2N_2$ structure type, the substitution of Sr by Ba leads to an unexpected increase of the Stokes shift (i.e. a shift of emission wavelength from green to yellow spectral region), e.g. for $Sr_{0.5}Ba_{0.5}Si_2O_2N_2:Eu^{2+}$.[15] $Sr_{0.25}Ba_{0.75}Si_2O_2N_2:Eu^{2+}$ is supposed to show an even larger Stokes shift,[10,11] which, at first glance, seems obvious because of the increasing amount of Ba. For this composition, however, the structure changes towards the $BaSi_2O_2N_2$ structure type as mentioned above. In relation to $BaSi_2O_2N_2:Eu^{2+}$, a larger Stokes shift is expected for $Sr_{0.25}Ba_{0.75}Si_2O_2N_2:Eu^{2+}$ due to more pronounced local structure relaxation of Eu^{2+} sites in the excited state in case of increasing Sr content. However, a comparable Stokes shift is observed, leading to an overall emission wavelength of 472 nm and a shifted lowest lying absorption band towards higher energies for this material. The explanation for this behavior is based on structure deformation. In the crystal structure of $Sr_{0.25}Ba_{0.75}Si_2O_2N_2$ there are corrugated metal atom layers while they are coplanar in $BaSi_2O_2N_2$. Additionally, the silicate layers are slightly shifted against each other perpendicular to stacking direction. As a consequence, there are longer Eu-O (also Eu-N) distances than in $BaSi_2O_2N_2:Eu^{2+}$ because of distorted cuboid metal atom coordination. The overall Eu^{2+} coordination explains the shift of absorption and emission bands towards higher

energies. The similarity of the ionic radii results obviously in a preferred occupation of Eu^{2+} on the single Sr^{2+} site, causing the narrow band width of only 37 nm. This is the smallest value found so far for blue emitters of this material class. A second emission band can be assigned to the yellow conversion of primary radiation by domains with $SrSi_2O_2N_2:Eu^{2+}$ structure type with its typical broad band emission (see Figure 8). To improve the refinement of measured values, a sharp profile according to Eu^{2+} emission in $BaSi_2O_2N_2$ host lattice was included (see Figure 8). $BaSi_6N_8O:Eu^{2+}$ is not present in this case, because there is no quantitative excitation at 400 nm.[30]

5.3.3 Conclusion

Within the series of $Sr_{1-x}Ba_xSi_2O_2N_2:Eu^{2+}$ phosphor materials, $Sr_{0.25}Ba_{0.75}Si_2O_2N_2:Eu^{2+}$ is a remarkable example that complex analytic methods are required to determine the crystal structure when dealing with real structure effects. Only detailed knowledge of atomic arrangement qualifies to describe reliable structure-property relations. Integration of Ba^{2+} in $Sr_{1-x}Ba_xSi_2O_2N_2$ leads to an intergrowth of domains of the $SrSi_2O_2N_2$ and $BaSi_2O_2N_2$ structure type, respectively, for $x = 0.75$, as there is no solid solution series. Fourier transforms of individual domains in HRTEM images do not show diffuse streaks. Therefore, the diffuse scattering in electron diffraction patterns presumably results from this intergrowth. Based on HRTEM image simulations, there is only one crystallographic site exclusively occupied by Sr^{2+} ions in the final structure model of $Sr_{0.25}Ba_{0.75}Si_2O_2N_2:Eu^{2+}$. According to very similar ionic radii, also preferred single-site occupation for the Eu^{2+} ions can be expected. In accordance with the results observed for $SrSi_6N_8:Eu^{2+}$ [31] and $BaSi_2O_2N_2:Eu^{2+}$, occupation of only one site with Eu^{2+} is obviously a main reason for a very sharp emission band in phosphor materials. $Sr_{0.25}Ba_{0.75}Si_2O_2N_2:Eu^{2+}$ exhibits the smallest value for FWHM (37 nm) known so far for blue emitters of this material class. The narrow band emission in the blue spectral region qualifies this material for applications in pc-LEDs, e.g. white LEDs with high color rendering index, blue LEDs (UV irradiation) or blue pump-LEDs closing the cyan spectral gap. Layered $Sr_{1-x}Ba_xSi_2O_2N_2:Eu^{2+}$ phases are good examples how conformation and arrangement of metal atoms and the Si-O/N partial structure affect luminescence properties.

5.3.4 Experimental Section

5.3.4.1 Synthesis and Chemical Analysis

Powder samples of $Sr_{1-x}Ba_xSi_2O_2N_2:Eu^{2+}$ (x = 0.75) suitable for TEM investigations were prepared by heating a stoichiometric mixture (1:3; ball milled) of $(Sr_{0.25}Ba_{0.75})_2SiO_4:Eu^{2+}$ and Si powder (Cerac, 99.999%) for 5 h to 1350 °C in a stream of forming gas (N_2:H_2 = 95:5) using a molybdenum crucible. The product was ground (ball milled using agate balls in cyclohexane) and reheated to 1400 °C for another 5 h under forming gas and ground again. The final product was washed with diluted HCl and ethanol to remove remaining oxosilicate byproducts. Samples with crystals suitable for single-crystal analysis were obtained by heating a stoichiometric mixture of $(Sr_{0.25}Ba_{0.75})_2SiO_4:Eu^{2+}$ and α-Si_3N_4 (UBE, >95 %) using a tungsten crucible positioned in a radio-frequency (RF) furnace [22] with stationary forming gas (N_2:H_2 = 95:5) atmosphere. The temperature was increased to 1350 °C (22 °C/ min) and held for 3 h. After heating to 1400 °C (10 °C/ min) and keeping this temperature for 3 h, the temperature was reduced to 650 °C (1.1 °C/ min). The starting material $(Sr_{0.25}Ba_{0.75})_2SiO_4:Eu^{2+}$ was synthesized by heating a mixture (ball milled) of $SrCO_3$ (Solvay, SL300), $BaCO_3$ (Solvay, L500), SiO_2 (Evonik, Aerosil OX 50) and Eu_2O_3 (Rhodia, 99,99 %, dopant, 2 mol %) for 2 h in a stream of forming gas (N_2:H_2 = 95:5). The chemical composition of the crystalline product was analyzed by energy dispersive X-ray spectroscopy (EDX) using a JSM-6500F scanning electron microscope (SEM, Joel) with a Si/Li EDX detector (model 7418, Oxford Instruments).

5.3.4.2 Single-Crystal X-ray Diffraction

Blue luminescent crystals obtained by RF furnace synthesis were mounted on glass fibers and checked for quality on a Buerger precession camera. Intensity data were collected on a Nonius Kappa-CCD diffractometer with graded multilayer X-ray optics (λ = 0.71093 Å). The structure was solved by direct methods [32] and refined by full-matrix least-squares method using anisotropic displacement parameters for the metal atoms.[33] Due to intergrowth with $SrSi_2O_2N_2$ intensity data were corrected (*section single-crystal structure analysis*).[34]

5.3.4.3 Transmission Electron Microscopy

For preliminary experiments, ground powder samples were dispersed in ethanol in order to deposit them on copper grids coated with a holey carbon film. Since such samples showed preferred orientation, the powder was mixed with two-component glue, placed between silicon wafers and glass panels, and then fixed in brass tubes (inner diameter 2 mm). These were cut into slices perpendicular to the tube elongation (thickness approx. 200 µm) and polished to 80-90 µm using different SiC coated sand papers (grain size: 40 - 5 µm). Finally, the thickness in the middle of the disk was reduced to approx. 20 µm using a dimple grinder (type 650, Gatan) and diamond grind (Electron Microscopy Science). Subsequently, a hole within the glue matrix samples was fabricated using an argon ion precision ion polishing system (type 691, Gatan). Crystallites near the hole, which are partially free of glue, are suitable for TEM investigations. SAED patterns and/or high-resolution images were recorded on transmission electron microscopes Jeol JEM-2011 (200 kV) and Fei Titan 80-300 (300 kV), respectively. The latter one was equipped with an EDX system (TEM Tops 30, Edax). Tilt series of diffraction patterns were obtained using a double tilt sample holder with maximum tilt angle of ±30°.

Acknowledgements

The authors thank Dr. Peter Mayer (LMU Munich) for collection of single-crystal data, Dr. Markus Döblinger (LMU Munich) for support concerning TEM investigations as well as Peter Käshammer and Roman Pobel (both LMU Munich) for preliminary work. Financial support by the Fonds der Chemischen Industrie (FCI), Germany, is gratefully acknowledged.

5.3.5 References

[1] R.-J. Xie, N. Hirosaki, *Sci. Technol. Adv. Mater.* **2007**, *8*, 588.

[2] X.-H. He, N. Lian, J.-H. Sun, M.-Y. Guan, *J. Mater. Sci.* **2009**, *44*, 4763.

[3] S. Ye, F. Xiao, Y. X. Pan, Y. Y. Ma, Q. Y. Zhang, *Mater. Sci. Eng., R* **2010**, *71*, 1.

[4] P. F. Smet, A. B. Parmentier, D. Poelman, *J. Electrochem. Soc.* **2011**, *158*, R37.

[5] C. C. Lin, R.-S. Liu, *J. Phys. Chem. Lett.* **2011**, *2*, 1268.

[6] R.-J. Xie, N. Hirosaki, K. Sakuma, N. Kimura, *J. Phys. D: Appl. Phys.* **2008**, *41*, 144013.

[7] M. Zeuner, S. Pagano, W. Schnick, *Angew. Chem.* **2011**, *123*, 7898; *Angew. Chem. Int. Ed.* **2011**, *50*, 7754.

[8] J. A. Kechele, O. Oeckler, F. Stadler, W. Schnick, *Solid State Sci.* **2009**, *11*, 537.

[9] Y. Q. Li, A. C. A. Delsing, G. de With, H. T. Hintzen, *Chem. Mater.* **2005**, *17*, 3242.

[10] V. Bachmann, C. Ronda, O. Oeckler, W. Schnick, A. Meijerink, *Chem. Mater.* **2009**, *21*, 316.

[11] B.-G. Yun, Y. Miyamoto, H. Yamamoto, *J. Electrochem. Soc.* **2007**, *154*, J320.

[12] B. Lei, K. Machida, T. Horikawa, H. Hanzawa, *Chem. Lett.* **2011**, *40*, 140.

[13] Y. H. Song, W. J. Park, D. H. Yoon, *J. Phys. Chem. Solids* **2010**, *71*, 473.

[14] X. Song, H. He, R. Fu, D. Wang, X. Zhao, Z. Pan, *J. Phys. D: Appl. Phys.* **2009**, *42*, 065409.

[15] M. Seibald, O. Oeckler, V. R. Celinski, P. J. Schmidt, A. Tücks, W. Schnick, *Solid State Sci.* **2011**, *13*, 1769.

[16] V. Bachmann, T. Jüstel, A. Meijerink, C. Ronda, P. J. Schmidt, *J. Lumin.* **2006**, *121*, 441.

[17] P. Schmidt, A. Tuecks, H. Bechtel, D. Wiechert, R. Mueller-Mach, G. Mueller, W. Schnick, *Proc. SPIE-Int. Soc. Opt. Eng.* **2008**, *7058*, 70580L (Eighth International Conference on Solid State Lighting, 2008).

[18] R. Mueller-Mach, G. Mueller, M. R. Krames, H. A. Höppe, F. Stadler, W. Schnick, T. Juestel, P. Schmidt, *Phys. Status Solidi A* **2005**, *202*, 1727.

[19] O. Oeckler, F. Stadler, T. Rosenthal, W. Schnick, *Solid State Sci.* **2007**, *9*, 205.

[20] F. Stadler, O. Oeckler, H. A. Höppe, M. H. Möller, R. Pöttgen, B. D. Mosel, P. Schmidt, V. Duppel, A. Simon, W. Schnick, *Chem. Eur. J.* **2006**, *12*, 6984.

[21] C. Braun, M. Seibald, S. L. Börger, O. Oeckler, T. D. Boyko, A. Moewes, G. Miehe, A. Tücks, W. Schnick*, Chem. Eur. J.* **2010**, *16*, 9646.

[22] W. Schnick, H. Huppertz, R. Lauterbach, *J. Mater. Chem.* **1999**, *9*, 289.

[23] F. Stadler, R. Kraut, O. Oeckler, S. Schmid, W. Schnick, *Z. Anorg. Allg. Chem.* **2005**, *631*, 1773.

[24] H. Yamane, S. Shimooka, K. Uheda, *J. Solid State Chem.* **2012**, *190*, 264.

[25] P. A. Stadelmann, *Ultramicroscopy* **1987**, *21*, 131.

[26] R. Hoppe, *Angew. Chem.* **1966**, *78*, 52; *Angew. Chem. Int. Ed.* **1966**, *5*, 95.

[27] R. Hoppe, *Angew. Chem.* **1970**, *82*, 7; *Angew. Chem. Int. Ed.* **1970**, *9*, 25.

[28] R. Hübenthal, *Madlung Part of Lattice Energy*, V. 4, University of Gießen, Germany, **1993**.

[29] R. D. Shannon, *Acta Crystallogr. Sect. A* **1976**, *32*, 751.

[30] R.-J. Xie, N. Hirosaki, Y. Li, T. Takeda, *J. Lumin.* **2010**, *130*, 266.

[31] K. Shioi, N. Hirosaki, R.-J. Xie, T. Takeda, Y. Li, *J. Mater. Sci.* **2008**, *43*, 5659.

[32] M. C. Burla, M. Camalli, B. Carrozzini, G. L. Cascarano, C. Giacovazzo, G. Polidori, R. Spagna, *J. Appl. Crystallogr.* **2003**, *36*, 1103.

[33] G. M. Sheldrick, *Acta Crystallogr. Sect. A* **2008**, *64*, 112.

[34] Further details of the crystal structure investigation may be obtained from Fachinformationszentrum Karlsruhe, 76344 Eggenstein-Leopoldshafen, Germany (fax: (+49)7247-808-666; e-mail, crysdata@fiz-karlsruhe.de, http://www.fiz-karlsruhe.de/request_for_deposited_data.html) on quoting the depository number CSD-424289 ($Sr_{0.25}Ba_{0.75}Si_2O_2N_2$).

6 Conclusion and prospects

In the present thesis, complementary information obtained from electron microscopy and X-ray diffraction is combined in different ways in order to elucidate average crystal structures, as well as a broad variety of real-structure effects. The latter have a decisive influence on the thermoelectric properties of telluride-based thermoelectrics and detailed knowledge about them is equally necessary to understand the luminescence properties of $Sr_{1-x}Ba_xSi_2O_2N_2:Eu^{2+}$ ($0 \leq x \leq 1$) phases.

In germanium antimony telluride (GST), germanium bismuth telluride (GBT) and silver germanium antimony telluride (TAGS) materials, diffusion processes during synthesis and the resulting short-range order of cation vacancies strongly determine the thermoelectric properties. These kinds of real-structure phenomena are clearly visible in high-resolution transmission electron microscopy (HRTEM) images. The Z contrast provided by scanning TEM (STEM) using a high-angle annular dark field (HAADF) detector is used to prove the nature of such vacancy layers. The limited statistical relevance of TEM investigations is overcome by the matching of selected area electron diffraction (SAED) patterns and reciprocal lattice sections from single-crystal X-ray data in order to verify that the region investigated by TEM is representative for the bulk material.

In GST materials, the thermal treatment, vacancy concentration and substitution determine the diffusion processes during the “partial” phase transitions between the high-temperature (HT) phase and the thermodynamically stable state and therefore the resulting nanostructures of the compounds (Chapter 2.2, Chapter 2.3). The highest *ZT* values (up to 1.5 at 450 °C) are observed for quenched GST materials with rather low vacancy concentrations (n = 12, 19) where the vacancies are short-range ordered in intersecting defect layers with limited lateral extension. This nanostructure is associated with a lower phononic contribution to the thermal conductivity (κ_L) compared to slowly cooled samples with a parallel arrangement of the “defect layers”. Investigations on GBT emphasize the importance of the thermal treatment under various conditions, including high-pressure (HP), on the nanostructure and the characteristics and absolute values of the thermoelectric properties (Chapter 3.2). Experiments on In_3SbTe_2,[1] $In_2Bi_3Se_7I$ and $InBi_2Se_4I$ (Chapter 3.3) highlight the importance of charge balance of the anions and cations and/or ionicity for sufficient electrical conductivities.

Substitutions with In, Sn and Se in GST alter the phase transition temperatures as well as the atom mobility and thereby the thermal stability and the degree of order of the nanostructure. HRTEM and STEM reveal smaller average lateral extensions of the vacancy layers and a

higher variance in their spacing for compounds with lower mobility during quenching (e.g. for Se-substituted samples). Statistical information about these vacancy ordering phenomena are obtained from the diffuse intensity distribution in SAED and single-crystal X-ray diffraction patterns. In contrast to these diffuse intensities, the presence of superstructure reflections in Sn-substituted GST crystals prepared by chemical vapor transport reveal the first long-range ordered GST phase where the rocksalt-type building blocks of the thermodynamically stable layered phase is combined with the cubic stacking of the HT phase. This highlights the existence of additional phases GST and substitution variants thereof which have not been reported so for (Chapter 4.3). The interplay of the changes in the Seebeck coefficient (*S*) and σ with κ results in higher *ZT* values for the nanostructured Sn-substituted samples, especially at temperatures above 300 °C. The substitution with In improves *S* and, as a consequence, *ZT* values below 300 °C, where the nanostructure does not change as diffusion processes are not significant (Chapter 2.3). A combined substitution with both elements is therefore promising in order to improve the *ZT* values in the whole temperature range. Additional anion substitution with Se can be used to shift the *S*(T) curve to higher values which, especially for intermediate vacancy concentrations (n = 7), results in higher *ZT* values. The introduction of hierarchical nanostructures as present in single crystals of Sn substituted GST materials might be used to further reduce κ_L (Chapter 4.3).

Quenched TAGS materials with a Sb/Ag ratio < 1 exhibit intersecting defect layers comparable to GST (Chapter 3.6). The resulting low κ_L values compared to vacancy-free TAGS in combination with the higher *S* compared to the corresponding GST materials, result in *ZT* values of up to 1.3 at 160 °C, which outperforms comparable GST and vacancy free TAGS materials. This illustrates the potential of transferring the nanostructuring mechanisms investigated for GST and substitution variants thereof to other systems with vacancies and intrinsically high (*S*) and σ values.

Besides the arrangement of cation vacancies which is crucial for the detailed understanding of the structures and the consequences of substitution on the thermoelectric properties, the distribution of the cations in long-range ordered GST materials and Sn, In or Se substituted variants is also an important issue. Due to the similar electron counts of the elements resonant X-ray diffraction is often necessary to elucidate their distribution (Chapter 4.3, 4.4 and reference [2]).

HP syntheses extend this field to compounds with octahedrally coordinated In, e.g. bulk material corresponding to the well known PCM material $Ag_{3.4}In_{3.7}Sb_{76.4}Te_{16}$[3] or In-substituted $AgSbTe_2$. The latter, e.g. $AgIn_{0.5}Sb_{0.5}Te_2$, exhibits extremely low κ and high *S*

values (Chapter 3.4). $AgInTe_2$ precipitates in In-substituted TAGS revealed by electron microscopy explain the low thermal conductivity of theses compounds (Chapter 3.5). In analogy to GST, the substitution with In is correlated with increased *S* for $(GeTe)_{5.5}AgInTe_2$ compared to the unsubstituted TAGS material. The decomposition into $AgInTe_2$ and $AgSbTe_2$ at elevated temperatures might be used to introduce additional nanostructures which render this class of compounds an intriguing subject of future studies. The structure and orientation of precipitates in such nanostructured systems can be efficiently investigated by combining TEM and synchrotron micro-diffraction as described for skutterudite-type precipitates in a GST matrix in Chapter 4.2. This combination also enables the elucidation of otherwise hardly accessible structures of compounds whose crystals are not suitable for laboratory X-ray diffraction (Chapter 4.2). The combined use of electron crystallography and synchrotron experiments might also be ideally suited for needle-shaped crystals that often form bunches. In such samples there may be several crystals irradiated even by a 1 µm synchrotron beam. An initial ADT measurement of a single crystal might be used to deduce an approximate structure model. This might then be refined on a data set acquired from multiple crystals at the same time with synchrotron radiation in order to obtain reliable interatomic distances, site occupancy factors and thermal displacement parameters.

While the real-structure effects determine the properties of thermoelectric tellurides, they do not affect the excellent luminescence properties of most $Sr_{1-x}Ba_xSi_2O_2N_2:Eu^{2+}$ ($0 \leq x \leq 1$) compounds since the highly symmetric coordination of the rare-earth atoms is often maintained in their disordered structures (Chapter 5). The monoclinic $SrSi_2O_2N_2$ maximum degree of order polytype, which was elucidated by a combination of electron microscopy and X-ray diffraction methods, exhibits excellent luminescence properties in the same spectral region as the triclinic polytype, because both phases have identical metal-atom coordination polyhedra although the orientation of consecutive silicate layers differs (Chapter 5.2). Therefore, in this case it is not necessary to apply complex and costly synthesis routes in order to obtain phase-pure compounds since powder samples containing both polytypes also exhibit quantum efficiencies above 95%. In contrast, the small full width at half maximum (37 nm) of $Sr_{0.25}Ba_{0.75}Si_2O_2N_2:Eu^{2+}$, which is inhomogeneous on the nanoscale, is most likely determined by the real-structure phenomena. This results from the ordering of Sr and Ba atoms and the resulting occupation with Eu^{2+} on only one crystallographic position in the distorted $BaSi_2O_2N_2$-type domains (Chapter 5.3). The determination of the metrics of intergrown domains by electron microscopy which enabled the structure elucidation form single-crystal

data obtained from both domains simultaneously highlights the benefits of the complementary use of both methods.

These examples give a comprehensive insight into the importance of real-structure determination for the systematic development of new materials for increasing the efficiency in the use of energy and the quality of pc-LED light sources. The further elucidation of unknown new phases comparable to $Sr_{0.25}Ba_{0.75}Si_2O_2N_2:Eu^{2+}$ or polymorphs should benefit from TEM due to the high probability that such phases are intergrown. Based on the detailed structure determination, improved synthesis conditions can be derived in order to obtain compounds with desired phase ratios and or phase-pure phosphors which are necessary to optimize the color rendition of white pc-LEDs.

References

[1] T. Schröder, T. Rosenthal, S. Grott, C. Stiewe, J. de Boor, O. Oeckler, *Z. Anorg. Allg. Chem.* **2013**, *639*, 2536.

[2] M. N. Schneider, F. Fahrnbauer, T. Rosenthal, M. Döblinger, C. Stiewe, O. Oeckler, *Chem. Eur. J.* **2012***, 18,* 1209.

[3] T. Schröder, T. Rosenthal, C. Gold, E.-W. Scheidt, W. Schnick, O. Oeckler, *Z. Anorg. Allg. Chem.* **2013**, *15*, 2862.

7 Summary

7.1 From phase-change materials to thermoelectrics?

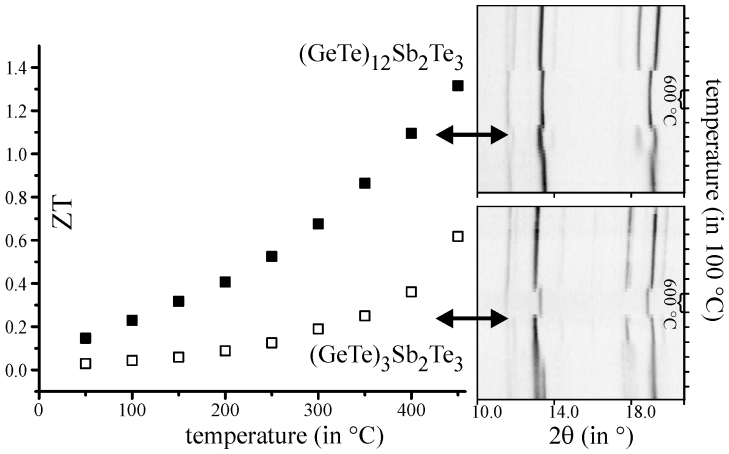

Due to their small bandgap and low thermal conductivity, germanium antimony tellurides (GST) known as phase-change materials for data storage are promising thermoelectric materials. For $(GeTe)_nSb_2Te_3$ ($n \geq 3$), a rocksalt-type phase with randomly distributed vacancies on the cation positions is stable at high temperatures (HT). The concentration of the vacancies is determined by the GeTe content n. At room temperature (RT), stable materials exhibit layered trigonal phases comparable to the tetradymite type for high vacancy concentrations such as n = 3 whereas for low vacancy concentrations (e.g. n = 12) a α-GeTe-type layered structure is formed. A partial phase transition between the cubic HT phase and the layered phases can be utilized to introduce nanostructures. X-ray studies reveal diffuse intensities along <111> (cubic setting) in quenched $Ge_{12}Sb_2Te_{15}$ whereas at 550 °C (stability range of the cubic phase) no short-range vacancy ordering is observed. Transmission electron microscopy (TEM) of quenched $Ge_{12}Sb_2Te_{15}$ reveals diffuse intensities in selected area electron diffraction (SAED) patterns comparable to those present in the X-ray data and corresponding high resolution transmission microscopy (HRTEM) images show intersecting defect layers with limited lateral extension oriented perpendicular to the (pseudo)cubic <111> directions. Temperature-dependent powder diffraction proves the metastability of such samples. Quenched samples of $(GeTe)_n(Sb_2Te_3)$ (n = 12) exhibit thermoelectric figures of merit of up to ZT = 1.3 at 450 °C.

7.2 Real structure and thermoelectric properties of GeTe-rich germanium antimony tellurides

Nanostructured $(GeTe)_nSb_2Te_3$ (n = 3-19) materials can be obtained by quenching their HT rocksalt-type phases with randomly distributed vacancies on the cation position. The GeTe content (n) determines the nanostructures of quenched samples. Higher vacancy concentrations are correlated to longer diffusion pathways towards the thermodynamically

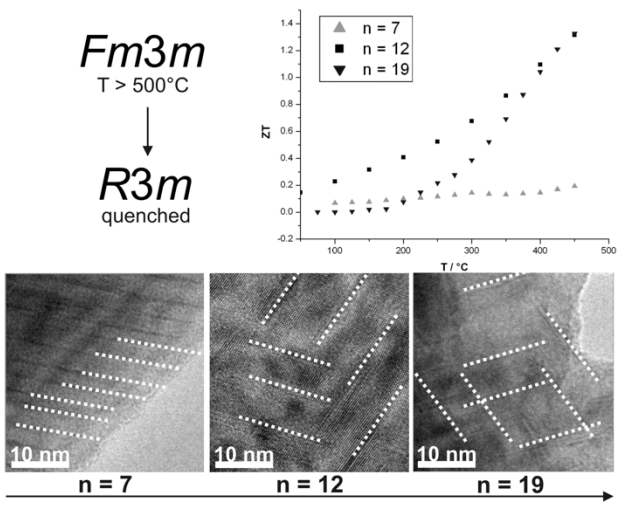

stable phases, which consist of rocksalt-type building blocks with 5+2n layers connected by van der Waals gaps, corresponding to a parallel arrangement of infinite extended "vacancy layers". Therefore, the quenched samples with higher n exhibit a lower number of defect layers with more irregular spacing and, in addition, a more pronounced parquet-like structure formed by intersecting defect layers with limited lateral extension perpendicular to the cubic <111> directions. Such materials exhibit lower phononic contribution to the thermal conductivities (κ_{Ph}) and thus higher *ZT* values compared to samples with exclusively parallel arranged defect layers and the same composition. As a rule, the increase of the Seebeck coefficient (*S*) with the temperature is more pronounced for higher n, which results in *ZT* values of up to 1.3 at 450 °C for $(GeTe)_nSb_2Te_3$ (n = 12, 19).

7.3 The solid solution series $(GeTe)_{12}M_2Te_3$ (M = Sb, In): nanostructures and thermoelectric properties

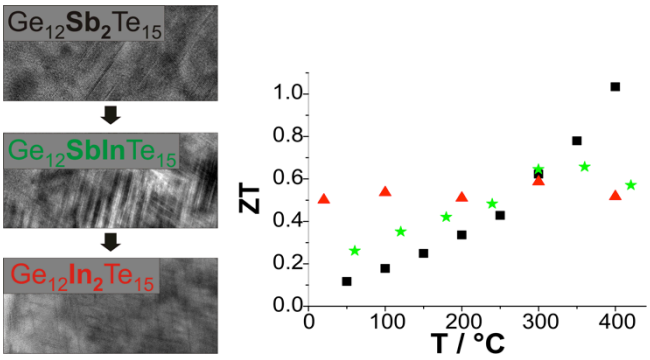

Substitution of Sb with In in GST materials results in the solid solution series of quenched $(GeTe)_{12}M_2Te_3$ (M = Sb, In) with pseudocubic structures. For samples with higher In contents, the metrics of the quenched samples is closer to cubic since they exhibit lower transition temperatures between the cubic HT phase with randomly disordered vacancies and the layered trigonal phases thermodynamically stable at RT. At low temperatures, κ_{Ph} is almost unaffected by the substitution since all quenched samples exhibit similar short-range order in the form of a parquet-like nanostructure. The *ZT* values at temperatures below 300 °C are higher for the In-substituted samples. This is mainly due to a strongly increased *S* compared to $Ge_{12}Sb_2Te_{15}$. The substitution is also correlated with a change from metallic to semiconducting characteristics of the electrical conductivity (σ) and therefore the substitution with In can be used to influence the electronic properties rather independently from the thermal transport properties.

7.4 Nanostructures and thermoelectric properties of the solid solution series $(Ge_{1-x}Sn_xTe)_nSb_2Te_3$ (n = 4, 7, 12; $0 \leq x \leq 1$)

Pseudo-cubic samples with a parquet-like structure comparable to GST materials can be obtained by quenching members of the solid solution series $(Ge_{1-x}Sn_xTe)_nSb_2Te_3$ (n = 4, 7, 12; $0 \leq x \leq 1$). The substitution of Ge with Sn results in significantly lower transition temperatures between the cubic HT phase and the layered RT phases. For low defect concentrations (n = 7, 12) the metrics of the substituted samples remains closer to the cubic HT phase compared to GST so that it is easier to obtain (pseudo-)cubic phases. For $(Ge_{0.5}Sn_{0.5}Te)_nSb_2Te_3$ with n = 4 and 7 the absolute values of σ are up to 3 times higher than for GST and result in higher *ZT* values in a broad temperature range. For $(Ge_{0.5}Sn_{0.5}Te)_7Sb_2Te_3$, *S* is also improved, resulting in *ZT* values of up to 0.7 at 400 °C compared to 0.2 for $(GeTe)_7Sb_2Te_3$.

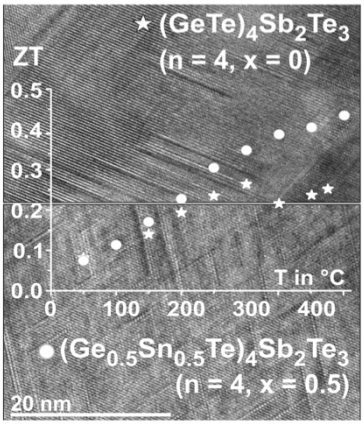

7.5 Enhancing the thermoelectric properties of germanium antimony tellurides by substitution with selenium in compounds $Ge_nSb_2(Te_{1-x}Se_x)_{n+3}$ ($0 \leq x \leq 0.5$; $n \geq 7$)

The substitution of Te by Se in GST bulk samples results in solid solution series of quenched $Ge_nSb_2(Te_{1-x}Se_x)_{n+3}$ with $0 \leq x < 0.75$ for $n \geq 7$. Quenching samples with n = 19 yields α-GeTe-type structures, which exhibit a pronounced deviation from cubic metrics, while for samples with n = 7 and 12 a pseudocubic modification is obtained. For n = 7 and 12 the substitution reduces the transition temperature between the cubic HT phase and the trigonal phase stable at ambient conditions. This leads to a reduced mobility of the atoms during the quenching process and therefore a less pronounced lateral extension of the defect layers. However, the Se-containing pseudocubic samples exhibit parquet-like nanostructures, comparable to GST itself. The lower κ values resulting from the mixed occupation on the anion position are combined with higher *S* especially for substitution rates of 20%. Therefore $Ge_7Sb_2(Te_{1-x}Se_x)_{10}$ compounds with (x = 0.2 and 0.5) exhibit 5-6 times higher *ZT* values at 400 °C compared to $Ge_7Sb_2Te_{10}$. Those samples also exhibit an increased thermal stability of the metastable nanostructured phase.

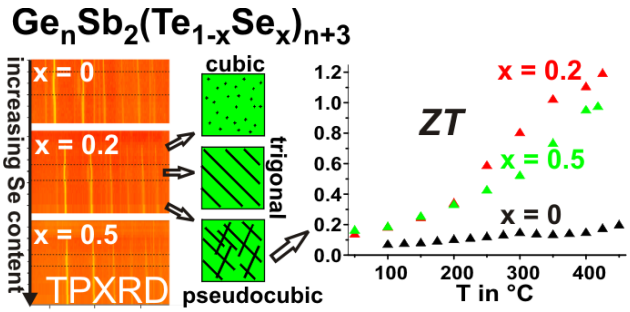

7.6 Nanostructures in metastable $GeBi_2Te_4$ obtained by high-pressure synthesis and rapid quenching and their influence on physical properties

A metastable CuPt-type modification of $GeBi_2Te_4$ can be obtained by high-pressure high-temperature (HP/HT) synthesis. Electron microscopy reveals that the size of individual domains is smaller (down to < 10 nm) for higher cooling rates at 12 GPa. The determination of the domain size is crucial for the understanding of the temperature characteristic of the electrical conductivity that is strongly influenced by the domain size and resulting grain boundary concentration. Randomly oriented domains with small average sizes result in semiconducting behavior for quenched samples, while larger domains in samples that were slowly cooled under high-pressure result in metal-like characteristics of σ. This investigation emphasizes the importance of the thermal treatment in the preparation of thermoelectric materials under high pressure.

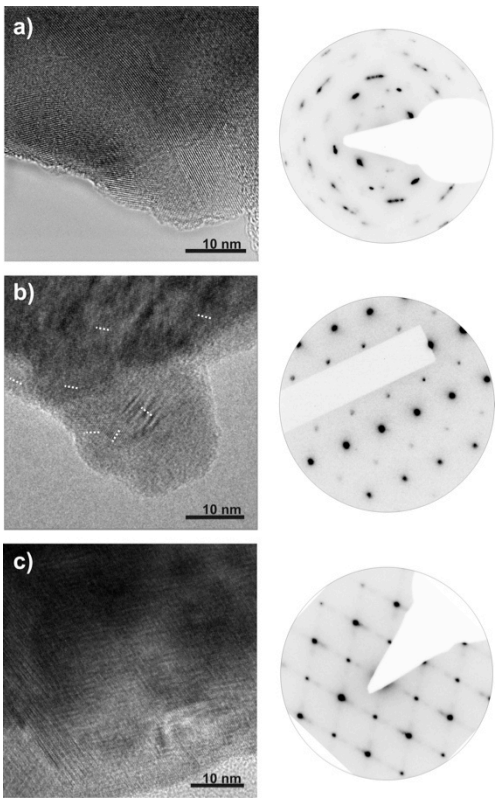

7.7 Structural features and physical properties of $In_2Bi_3Se_7I$, $InBi_2Se_4I$ and BiSeI

The structures of the quaternary compounds $In_2Bi_3Se_7I$ (*Pnma*, a = 13.6720(2), b = 4.0893(3), c = 16.7070(2) Å) and $InBi_2Se_4I$ (*Pnma*, a = 26.6039(14), b = 4.1285(2), c = 13.5031(9) Å) consist of three-dimensional networks built up from rocksalt-like and CdI_2-like blocks as well as loosely bound iodine atoms in rather large cavities. They resemble structures found in alkali metal bismuth chalcogenides known for their thermoelectric properties. The electrical conductivity of $In_2Bi_3Se_7I$ and $InBi_2Se_4I$ is, however, insufficiently low for thermoelectric applications probably due to the high ionicity in combination with balanced valence states. These experiments, including the thermoelectric properties of BiSeI for comparison, emphasize the necessity for slight variations from the normal valencies in such kind of structures in order to obtain high thermoelectric performance.

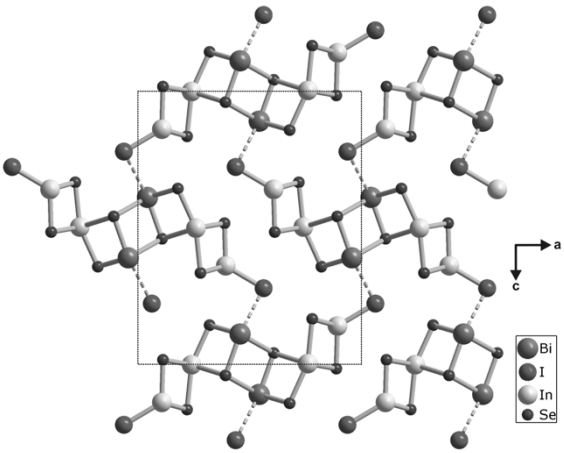

7.8 A high-pressure route to thermoelectrics with low thermal conductivity: the solid solution series $AgIn_xSb_{1-x}Te_2$ (x = 0.1 - 0.6)

Samples of the solid solutions $AgIn_xSb_{1-x}Te_2$ can be obtained by HP/HT synthesis. Their thermal conductivities are among the lowest ones known for rocksalt-type tellurides at RT. In these samples, In^{3+} is sixfold coordinated, in contrast to the fourfold coordination in chalcopyrite-type $AgInTe_2$ at ambient pressure. Electron microscopy confirms the structure and chemical homogeneity of $AgIn_{0.5}Sb_{0.5}Te_2$ and reveals the occasional presence of real-structure effects like short-range cation ordering. The decomposition of the quaternary quenched samples into $AgInTe_2$ and $AgSbTe_2$ at high temperatures opens opportunities for further improvement of the thermoelectric performance at RT since the growth of nano-precipitates could be utilized to introduce nanostructures.

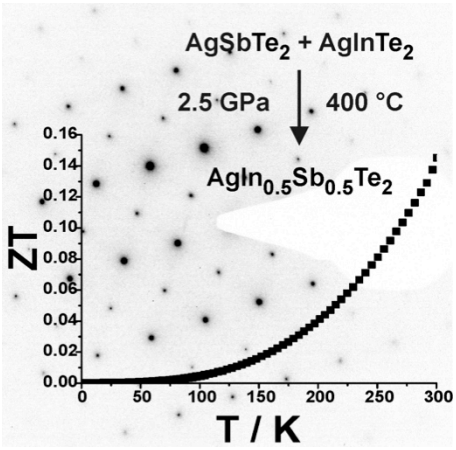

7.9 TAGS-related indium compounds and their thermoelectric properties – the solid solution series $(GeTe)_xAgIn_ySb_{1-y}Te_2$ (x = 1 – 12; y = 0.5 and 1)

Quenching the corresponding HT phases yields the solid solution series $(GeTe)_xAgIn_ySb_{1-y}Te_2$ (x = 12 for y = 1 and x > 5 for y = 0.5). Since In prefers a fourfold coordination at ambient conditions, the synthesis of members with In contents > 3.6 atom-% requires HT/HP conditions (2.5 GPa, 350 °C) in order to stabilize In in the octahedral coordination. For $x \leq 5$, a disordered rocksalt-type structure is obtained while the samples with x > 5 exhibit a disordered α-GeTe structure type. HRTEM reveals the presence of nanoscopic $AgInTe_2$ and Ag-rich precipitates not visible in X-ray powder diffraction patterns as well as dislocations and twinning. Local variations of the composition are reflected in the deviating metrics indicated by SAED patterns of the <100> zone axes – especially near the precipitates – compared to diffraction patterns calculated from X-ray powder diffraction data. $(GeTe)_{5.5}AgIn_{0.5}Sb_{0.5}Te_2$ exhibits a maximal (*ZT*) value of 0.75 at 300 °C, where (partial) decomposition into $(GeTe)_{11}AgSbTe_2$ and chalcopyrite-type $AgInTe_2$ is already present. For $(GeTe)_{5.5}AgInTe_2$ prepared under high-pressure conditions the *ZT* value is 0.6 at 125 °C, i.e. far below the decomposition temperature.

7.10 Nanostructures in TAGS thermoelectric materials induced by phase transitions associated with vacancy ordering

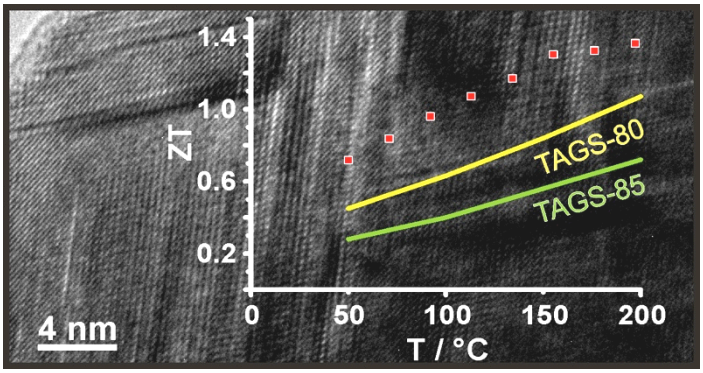

The introduction of cation vacancies by employing Ag/Sb ratios deviating from 1 may optimize the thermoelectric properties of silver germanium antimony tellurides (TAGS). TEM investigations reveal the presence of parquet-like nanostructures resulting from a short-range ordering of the vacancies similar to those of GST materials. Quenched samples with higher vacancy concentrations such as $Ge_{0.53}Ag_{0.13}Sb_{0.27}\square_{0.07}Te_1$ and $Ge_{0.61}Ag_{0.11}Sb_{0.22}\square_{0.06}Te_1$ undergo a phase transitions analogous to those of GST during heating. The nanostructured pseudocubic phase transforms to a long-periodically ordered trigonal structure and upon further heating to a cubic one. The nanostructured phase $Ge_{0.53}Ag_{0.13}Sb_{0.27}\square_{0.07}Te_1$ exhibits higher ZT values compared to GST and TAGS materials (up to 1.3 at 160 °C). This result from reduced κ_{ph} values compared to vacancy-free TAGS materials in combination with comparable σ and S values.

7.11 Complementary use of electron microscopy and synchrotron microfocus diffraction for structure analysis

The combined use of TEM and synchrotron microfocus diffraction is a promising method to elucidate the crystal structure of compounds that can only be obtained as very small crystals in samples with additional unknown impurity phases. The preselection of desired crystals in the TEM followed by the synchrotron data collection resulted in the elucidation of the crystal structures of a melam-melem co-crystal ($P\,\bar{1}$, a = 4.56(2) Å, b = 19.34(8) Å, c = 21.58(11) Å, α = 73.34(11)°, β = 89.1(2)°, γ = 88.4(2)°, Z = 4), the first antimony lead sulfide telluride $Pb_8Sb_8S_{15}Te_5$ ($P4_1$, a = 8.0034(11) Å, c = 15.022(3) Å) and the oxonitridophosphate $(Ca,Mg)_7P_{18}ON_{34}$. The correlation between the degree of GeTe substitution and the distortion of the Sb_4 units of skutterudite-type precipitates in a GST matrix has been elucidated by the combined use of TEM and synchrotron diffraction.

7.12 Novel superstructure of the rocksalt type and element distribution in germanium tin antimony tellurides

The structure of a new metastable yet long-range ordered Sn-doped germanium antimony telluride is elucidated from single crystal X-ray data. In this structure, distorted rocksalt-type building blocks which are typical for long-range ordered thermodynamically stable GST phases and substitution variants thereof is combined with the cubic Te-atom layer stacking present in the HT phases. SAED and single-crystal X-ray diffraction patterns of "$Ge_{3.25}Sn_{1.1}Sb_{1.1}Te_6$" crystals grown by chemical vapor transport exhibit superstructure reflections along the <111> directions of the rocksalt-type basis structure in contrast to the typical diffuse scattering of corresponding GST crystals. Electron microscopy shows that crystals exhibiting the superstructure consist of spheroidal domains with an average diameter of 25 nm. The structure of these domains is similar to 33*R*-$Ge_4Sb_2Te_7$ with a total of 11 alternating anion and cation layers separated by van der Waals gaps. While the latter compound exhibits a hexagonal Te-atom layer stacking across the van der Waals gaps, a cubic stacking is present in "$Ge_{3.25}Sn_{1.1}Sb_{1.1}Te_6$", which involves a larger spacing of the Te-atom layers. HRTEM images reveal the occasional presence of a hierarchical structure motif consisting of slabs with exclusively parallel van der Waals gaps and a much larger lateral extension (500- 1200 nm), which is sandwiched by much thicker slabs with spheroidal domains. Space-resolved EDX measurements show no significant variation of the chemical composition between the different domain types.

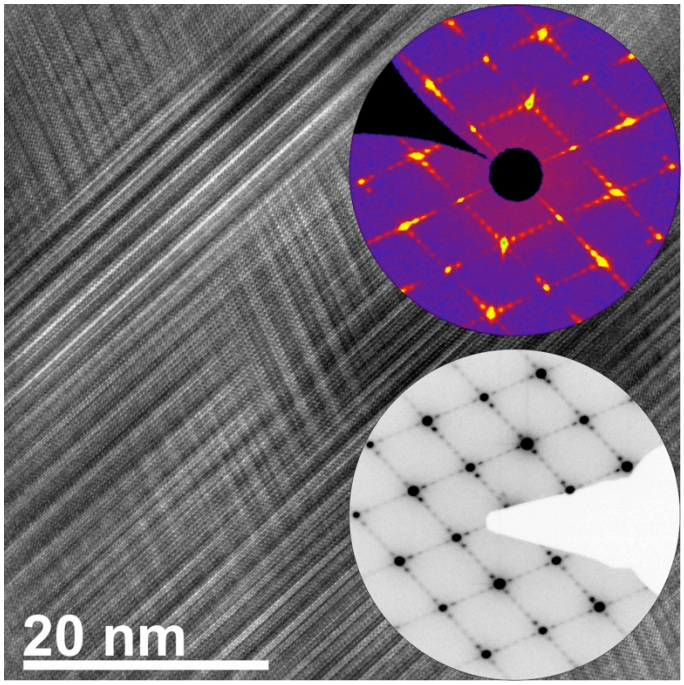

7.13 Layered germanium tin antimony tellurides: element distribution, nanostructures and thermoelectric properties

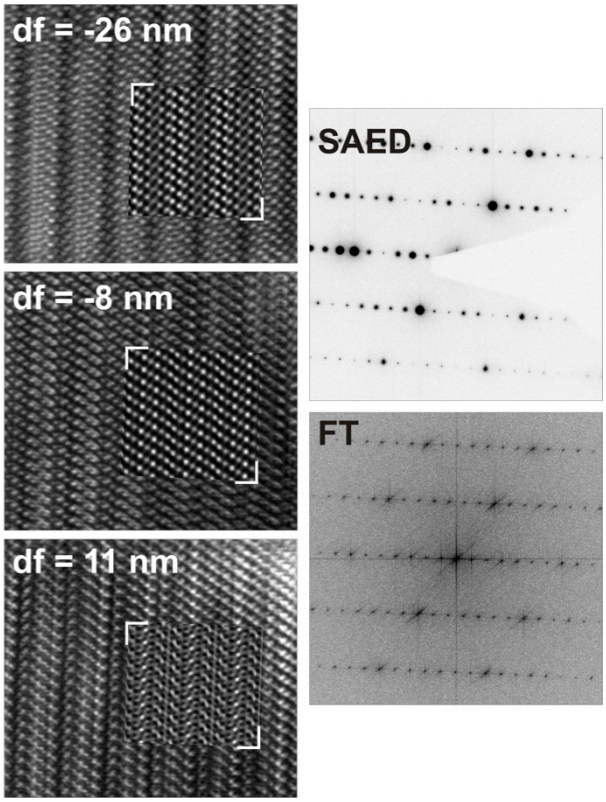

Single-crystal synchrotron data measured at absorption edges reveal that Sb is concentrated near the van der Waals gaps in 21*R*-$Ge_{0.6}Sn_{0.4}Sb_2Te_4$ and 9*P*-$Ge_{1.3}Sn_{0.7}Sb_2Te_5$, comparable to the unsubstituted samples $GeSb_2Te_4$ and $Ge_2Sb_2Te_5$. This can be explained by Sb^{3+} saturating Te atoms at the van der Waals gaps more efficiently than Ge^{2+}. Sn shows a slight preference for the position near the van der Waals gap. The structure model of 21*R*-$Ge_{0.6}Sn_{0.4}Sb_2Te_4$ is verified by simulations of HRTEM images and SAED patterns. The material is homogeneous, there are no indications of decomposition reactions. Diffuse intensities along the stacking direction reveal the presence of significant stacking disorder in 9*P*-$Ge_{1.3}Sn_{0.7}Sb_2Te_5$. The substitution of Ge with Sn in the layered compounds does not alter the *S* but the *ZT* values are higher since the thermal conductivity of $Ge_{1.3}Sn_{0.7}Sb_2Te_5$ and $Ge_{0.6}Sn_{0.4}Sb_2Te_4$ is only half of that of unsubstituted samples.

7.14 New polymorph of the highly efficient LED-phosphor $SrSi_2O_2N_2:Eu^{2+}$ – polytypism of a layered oxonitridosilicate

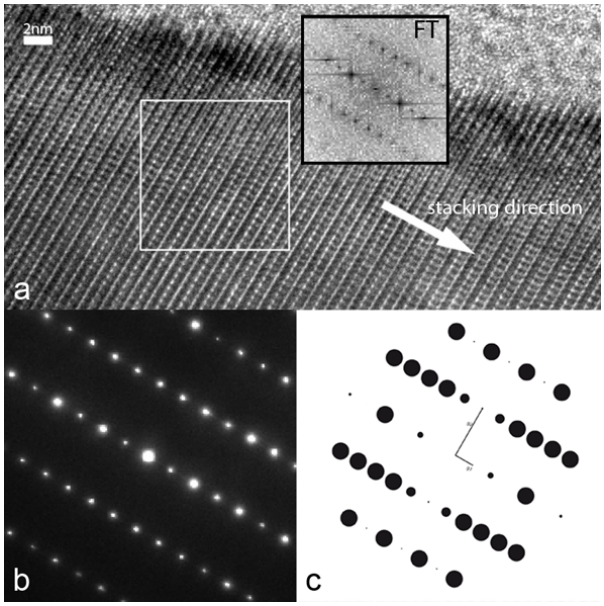

In addition to the typical triclinic modification, a new monoclinic polymorph of $SrSi_2O_2N_2$ ($P2_1$, $a = 7.1036(14)$, $b = 14.078(3)$, $c = 7.2833(15)$ Å, $\beta = 95.23(3)°$, $V = 725.3(3)$ Å^3) is characterized by a different stacking sequence with alternatingly rotated silicate layers interconnected by metal-ion layers. This leads to a doubled translation period along the stacking direction. A shift of the emission maximum to smaller wavelengths

by ~5 nm compared to the triclinic polymorph renders the monoclinic polymorph very attractive for the enhancement of color rendition of white-light phosphor converted light emitting diodes. The structure of the monoclinic polymorph is elucidated by a combination of X-ray and TEM investigations. A structure model obtained from single-crystal data is verified by comparison of metrics and intensity variations with SAED patterns along various orientations. Simulations based on this model are used to interpret HRTEM defocus series in which the stacking sequence is visible. This investigation illustrates the polymorphism of $SrSi_2O_2N_2$:Eu^{2+} and gives insights on the dependence of the luminescent properties on the nanostructure and the orientation of adjacent silicate layers, respectively.

7.15 Unexpected luminescence properties of $Sr_{0.25}Ba_{0.75}Si_2O_2N_2$:$Eu^{2+}$ - a narrow blue emitting oxonitridosilicate with cation ordering

The structure of $Sr_{0.25}Ba_{0.75}Si_2O_2N_2$:$Eu^{2+}$ ($Pna2_1$, a = 5.470(2), b = 14.277(3), c = 4.791(1) Å, V = 374.2(2) Å^3) is elucidated by a combination of X-ray and TEM methods. The lattice parameters are similar to those of $BaSi_2O_2N_2$, but metal-atom layers are corrugated instead of planar. TEM investigations on samples embedded in a two-component matrix reveal the intergrowth of nanodomains with $SrSi_2O_2N_2$-type and $BaSi_2O_2N_2$-type structures, which leads to pronounced diffuse scattering. Consequently, the structure of the $BaSi_2O_2N_2$-type domains is refined on X-ray diffraction data from an intergrown and disordered crystal. Cation ordering in the corrugated metal atom layers is determined by simulations of HRTEM images at various defocus values. The material exhibits intense blue emission (λ_{em} = 472 nm) with the smallest full width at half maximum (FWHM) of the emission band (37 nm) observed for blue emitting (oxo-)nitridosilicates so far. This results from the occupation of Eu^{2+} exclusively on the Sr position which is ordered on one metallic site which results from the ordering of the metal atoms.

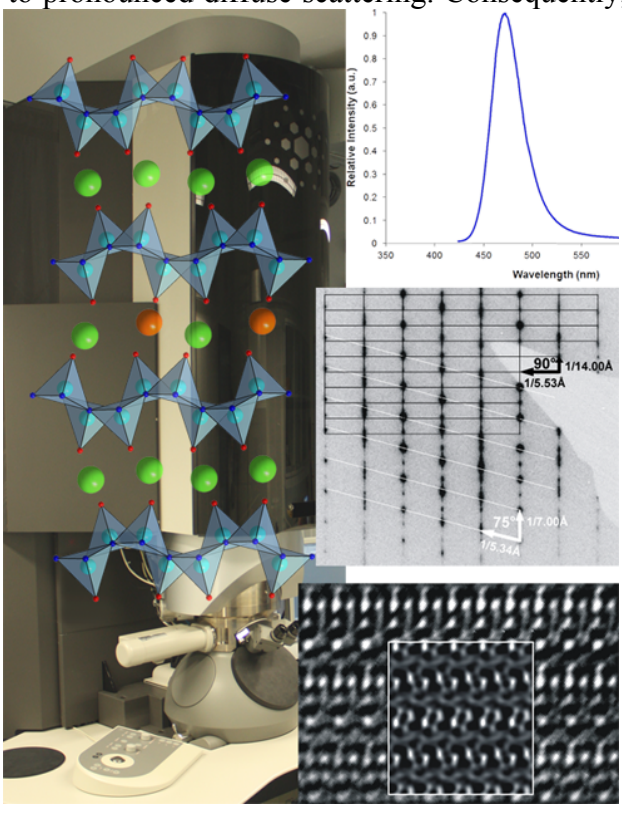

8 Appendix

8.1 Publications within this thesis

All publications included in this thesis and the contributions of the individual authors are listed in the following sections to the best of my knowledge. All manuscripts were revised by Oliver Oeckler, who also initiated the projects and contributed to their development. Manuscripts no. 9, 13 and 14 were also discussed with and revised by Wolfgang Schnick. Low-temperature thermoelectric measurements of the thermoelectric properties for publications no. 6, 7, 8 and 9 were carried out by Ernst-Wilhelm Scheidt, Christian Gold (except no. 9) and Wolfgang Scherer, who also contributes to the discussion. High-temperature thermoelectric measurements were done by Christian Stiewe (publication 2) in cooperation with Johannes de Boor (publications no. 4, 5, and 12).

1) From phase-change materials to thermoelectrics?

M. N. Schneider, T. Rosenthal, C. Stiewe, O. Oeckler

Z. Kristallogr. **2010**, *225,* 463–470.

In this manuscript the evaluation of the TEM data and physical properties measurements for thermoelectric characterization was done by Tobias Rosenthal in cooperation with Mathias Schneider who also formulated the manuscript.

2) Real structure and thermoelectric properties of GeTe-rich germanium antimony tellurides

T. Rosenthal, M. N. Schneider, C. Stiewe, M. Döblinger, O. Oeckler

Chem. Mater. **2011**, *23*, 4349-4356 **.**

The majority of samples were prepared by Tobias Rosenthal who also characterized the samples by powder X-ray investigations, EDX spectroscopy and TEM. He also formulated the text. Additional samples especially for thermoelectric measurements were prepared by Matthias Schneider who also revised the manuscript. Markus Döblinger helped with the operation of the TEM. The treatment of the raw data of the thermoelectric measurements was done by Christian Stiewe. The evaluation of the thermoelectric measurements was carried out by Tobias Rosenthal.

3) The solid solution series $(GeTe)_{12}M_2Te_3$ (M = Sb, In): nanostructures and thermoelectric properties

T. Rosenthal, S. Welzmiller, O. Oeckler

Solid State Sci. **2013**, *25*, 118-123.

Tobias Rosenthal formulated the text and carried out the TEM investigations, Rietveld refinements and evaluation of the EDX measurements, thermoelectric measurements, and temperature dependent powder X-ray investigations. The measurement of the thermoelectric properties was done by Jörg Frohrig (Linseis GmbH, Selb, Germany) for $Ge_{12}InTe_{15}$ and Christian Stiewe and Johannes de Boor for $Ge_{12}InSbTe_{15}$ who are mentioned in the Acknowledgement section of the article. Sample preparation was done by Tobias Rosenthal and Simon Welzmiller who also revised the manuscript.

4) Nanostructures and thermoelectric properties of the solid solution series $(Ge_{1-x}Sn_xTe)_nSb_2Te_3$ (n = 4, 7, 12; $0 \leq x \leq 1$)

T. Rosenthal, L. Neudert, P. Ganter, J. de Boor, C. Stiewe, O. Oeckler

J. Solid State Chem. **2014**, *215*, 231 -240.

The samples were prepared by Tobias Rosenthal and the research interns Lukas Neudert and Pirmin Ganter under his supervision. Electron microscopy was done by Tobias Rosenthal who also evaluated and obtained all other experimental data and formulated the manuscript.

5) Enhancing the thermoelectric properties of germanium antimony tellurides by substitution with selenium in compounds $Ge_nSb_2(Te_{1-x}Se_x)_{n+3}$ ($0 \leq x \leq 0.5$; $n \geq 7$)

T. Rosenthal, P. Urban, K. Nimmrich, L. Schenk, J. de Boor, C. Stiewe, O. Oeckler

Chem. Mater. **2014**, *26*, 2567-2578.

The manuscript was formulated by Tobias Rosenthal who also prepared the samples with the help of the research interns Kathleen Nimmrich and Ludwig Schenk. Tobias Rosenthal also conducted the EDX spectroscopy, X-ray powder diffraction, evaluation of thermoelectric properties, and TEM investigations. The single-crystal data obtained at the synchrotron (beamline ID11, ESRF, Grenoble, France) were evaluated by Philipp Urban who also revised the manuscript.

6) Nanostructures in metastable $GeBi_2Te_4$ obtained by high-pressure synthesis and rapid quenching and their influence on physical properties

T. Schröder, M. N. Schneider, T. Rosenthal, A. Eisele, C. Gold, E.-W. Scheidt, W. Scherer, R. Berthold, O. Oeckler

Phys. Rev. B **2011**, *84,* 184104

Tobias Rosenthal contributed TEM experiments and their evaluation. The TEM related figures and text were developed in collaboration with Thorsten Schröder who formulated the rest of the text and performed all experiments and evaluation of all data except TEM and thermoelectric property data. Andreas Eisele contributed with preliminary experiments under the supervision of Matthias Schneider. Rico Berthold helped with melt-spinning experiments.

7) Structural features and physical properties of $In_2Bi_3Se_7I$, $InBi_2Se_4I$ and BiSeI

T. Rosenthal, M. Döblinger, P. Wagatha, C. Gold, E.-W. Scheidt, W. Scherer, O. Oeckler

Z. Anorg. Allg. Chem. **2011***, 637,* 2239–2245.

The *structure determination from single X-ray data as well as the Rietveld refinements, bond valence calculations and the evaluation of the thermoelectric properties were done by Tobias Rosenthal who also formulated the manuscript. The samples were prepared with the help of Peter Wagatha and based on preliminary studies by Markus Döblinger. Oliver Oeckler contributed to the structure solution from single-crystal data.*

8) A high-pressure route to thermoelectrics with low thermal conductivity: the solid solution series $AgIn_xSb_{1-x}Te_2$ (x = 0.1 - 0.6)

T. Schröder, T. Rosenthal, D. Souchay, C. Petermayer, S. Grott, E.-W. Scheidt, C. Gold, W. Scherer, O. Oeckler

J. Solid State Chem. **2013**, *206*, 20-26.

The manuscript was formulated by Thorsten Schöder and revised by Tobias Rosenthal. Electron microscopy was done by Tobias Rosenthal. Thorsten Schröder evaluated all experimental data. Daniel Souchay, Christian Petermayer and Sebastian Grott helped with the high-pressure high-temperature synthesis of the samples.

9) TAGS-related indium compounds and their thermoelectric properties – the solid solution series $(GeTe)_xAgIn_ySb_{1-y}Te_2$ (x = 1 – 12; y = 0.5 and 1)

T. Schröder, T. Rosenthal, N. Giesbrecht, S. Maier, E.-W. Scheidt, W. Scherer, G. J. Snyder, W. Schnick, O. Oeckler

J. Mater. Chem. A **2014**, *2*, 6384-6395.

The text was formulated by Thorsten Schröder and revised by Tobias Rosenthal. Thorsten Schröder synthesized the samples and evaluated the experimental data with the support of the research interns Nadja Giesbrecht and Stefan Maier, who also performed the high-temperature thermoelectric measurements under the supervision of G. Jeffrey Snyder. Figures and text concerning transmission electron microscopy were developed in a close collaboration with Tobias Rosenthal, who acquired all TEM data.

10) Nanostructures in TAGS thermoelectric materials induced by phase transitions associated with vacancy ordering

T. Schröder, T. Rosenthal, N. Giesbrecht, M. Nentwig, S. Maier, H. Wang, G. J. Snyder, O. Oeckler

Inorg. Chem. **2014**, *53*, 7722-7729.

The TEM investigations were conducted by Tobias Rosenthal. The manuscript was formulated by Thorsten Schröder who prepared the samples, and conducted all other experiments with his research interns Nadja Giesbrecht, Markus Nentwig and Stefan Maier. G. J. Snyder and H. Wang supervised the thermoelectric measurements at the California Institute of Technology and revised the manuscript.

11) Novel superstructure of the rocksalt type and element distribution in germanium tin antimony tellurides

T. Rosenthal, S. Welzmiller, L. Neudert, P. Urban, A. Fitch, O. Oeckler

J. Solid. State Chem. **2014**, *219*, 108-117.

The manuscript was formulated by Tobias Rosenthal and Oliver Oeckler. All samples were synthesized and prepared for TEM investigations by Tobias Rosenthal and, under his supervision, by Lukas Neudert as a research intern. Acquisition and evaluation of all TEM data as well as the evaluation of laboratory powder X-ray

diffraction patterns was done by Tobias Rosenthal. The structure model was determined from single-crystal X-ray diffraction data by Oliver Oeckler and Tobias Rosenthal using a preliminary model from Philipp Urban, who also performed the data collection. Powder diffraction experiments with synchrotron radiation were carried and out and evaluated by Simon Welzmiller with help by Andy Fitch.

12) Layered germanium tin antimony tellurides: element distribution, nanostructures and thermoelectric properties

S. Welzmiller, T. Rosenthal, P. Ganter, L. Neudert, F. Fahrnbauer, P. Urban, C. Stiewe, J. de Boor, O. Oeckler

Dalton Trans. **2014**, *43*, 10529-10540.

The sample preparation for TEM and thermoelectric measurements as well as the characterization of these samples by Rietveld methods and EDX spectroscopy were done by Tobias Rosenthal with the support of the research interns Pirmin Ganter and Lukas Neudert under his supervision. Electron microscopy as well as the evaluation of the thermoelectric measurements was carried out by Tobias Rosenthal. The synthesis of further samples including the single crystals and the evaluation of the resonant single crystal data came from Simon Welzmiller who also formulated the text. The formulation of the thermoelectric and electron microscopy part of the paper were contributed by Tobias Rosenthal and revised by Simon Welzmiller. Resonant diffraction data were acquired by Felix Fahrnbauer, Philipp Urban, Simon Welzmiller and Oliver Oeckler.

13) New polymorph of the highly efficient LED-phosphor $SrSi_2O_2N_2:Eu^{2+}$ – polytypism of a layered oxonitridosilicate

M. Seibald, T. Rosenthal, O. Oeckler, C. Maak, A. Tücks, P. J. Schmidt, D. Wiechert, W. Schnick

Chem. Mater. **2013**, *25*, 1852-1857.

TEM data for this manuscript were obtained by Tobias Rosenthal. For such investigations, the samples were embedded and prepared in cooperation with Christian Maak and Markus Seibald. Phase characterization and the simulation and evaluation of the TEM data were carried out in a close collaboration by Tobias Rosenthal and Markus Seibald. Further analysis and single crystal data evaluation

and formulation of the manuscript were contributed by Markus Seibald. Oliver Oeckler helped with the refinement of the single crystal data and revised the manuscript together with Tobias Rosenthal. Luminescence investigations were done in LDC Aachen (Tücks, Schmidt, Wiechert).

14) Unexpected luminescence properties of $Sr_{0.25}Ba_{0.25}Si_2O_2N_2:Eu^{2+}$ – a narrow blue emitting oxonitridosilicate with cation ordering

M. Seibald, T. Rosenthal, O. Oeckler, F. Fahrnbauer, A. Tücks, P. J. Schmidt, W. Schnick

Chem. Eur. J. **2012**, *18*, 13446-13452.

The preparation of the samples for TEM investigations as well as the collection and evaluation of SAED, TEM-EDX and HRTEM images with various defocus values was done by Tobias Rosenthal. The simulation of the HRTEM images and design of the TEM related figures result from a collaboration with Markus Seibald. He also did literature research and the formulation of the manuscript while Tobias Rosenthal revised it. Luminescence investigations were done in LDC Aachen (Tücks, Schmidt).

8.2 Publications not reprinted as part of this thesis

1) Disorder and transport properties of In_3SbTe_2 – an X-ray, neutron and electron diffraction study

T. Schröder, T. Rosenthal, S. Grott, C. Stiewe, J. de Boor, O. Oeckler

Z. Anorg. Allg. Chem. **2013**, *639*, 2536-2541.

Acquisition and evaluation of the TEM experiments were contributed by Tobias Rosenthal, including the corresponding figures. Thorsten Schröder formulated the text, evaluated all data except TEM measurements and synthesized all samples. Sebastian Grott helped with the synthesis of the samples for thermoelectric characterization. Christain Stiewe and Johannes de Boor contributed the high-temperature thermoelectric measurements.

2) Two synthetic approaches to $Ag_{3.4}In_{3.7}Sb_{76.4}Te_{16.5}$ bulk samples and their transport properties

T. Schröder, T. Rosenthal, C. Gold, E.-W. Scheidt, W. Schnick, O. Oeckler

Z. Anorg. Allg. Chem. **2013**, *15*, 2862-2874.

TEM data were acquired by Tobias Rosenthal who also helped Thorsten Schröder with their evaluation. Thorsten Schröder formulated the text, evaluated the X-ray data and synthesized all samples. Low-temperature measurements of the thermoelectric properties were carried out by Ernst-Wilhelm Scheidt, Christian Gold.

3) $(GeTe)_nSbInTe_3$ ($n \leq 3$) – Element distribution and thermal behavior

F. Fahrnbauer, P. Urban, S. Welzmiller, T. Schröder, T. Rosenthal, O. Oeckler

J. Solid State Chem. **2013**, *208*, 20-26.

Tobias Rosenthal prepared some of the samples and investigated the thermal behavior together with Felix Fahrnbauer. Thorsten Schröder contributed the powder diffraction data and helped with the refinement of some structures. Felix Fahrnbauer formulated the manuscript and evaluated all other experimental data. Philipp Urban help with the evaluation of the resonant synchrotron diffraction data and their acquisition. Simon Welzmiller prepared the samples for these synchrotron experiments and helped with the data collection.

4) Elemental distribution and thermoelectric properties of layered tellurides 39*R*-$M_{0.067}Sb_{0.667}Te_{0.266}$ (M = Ge, Sn)

M. N. Schneider, F. Fahrnbauer, T. Rosenthal, M. Döblinger, C. Stiewe, O. Oeckler
Chem. Eur. J. **2012***, 18,* 1209 – 1218.

Tobias Rosenthal evaluated the TEM data and helped Matthias Schneider with the formulation of the TEM-related parts of the manuscript. Markus Döblinger performed the TEM experiments. Felix Fahrnbauer helped with the acquisition of the resonant single crystal X-ray data at the ID11 beamline in Grenoble. Sample preparation, evaluation of the experimental data and formulation of the manuscript were carried out by Matthias Schneider. High-temperature thermoelectric measurements were done by Christain Stiewe.

5) Highly efficient pc-LED phosphors $Sr_{1-x}Ba_xSi_2O_2N_2:Eu^{2+}$ ($0 \leq x \leq 1$) - crystal structures and luminescence properties revisited

M. Seibald, T. Rosenthal, O. Oeckler, W. Schnick
Crit. Rev. Solid State Mater. Sci. **2014,** *39*, 215-229.

Acquisition and evaluation of the TEM investigations and the resulting real structure effects was done by Tobias Rosenthal. The relevant literature was evaluated by Markus Seibald. The review article was formulated by Markus Seibald and revised by Wolfgang Schnick, Oliver Oeckler and Tobias Rosenthal.

6) Real Structure of $SrSi_2O_2N_2$

O. Oeckler, F. Stadler, T. Rosenthal, W. Schnick
Solid State Sci. **2007**, *9*, 205-212.

The synthesis of the samples and the formulation of the manuscript as well as the evaluation of the experimental data with the exception of the TEM investigation were done by Florian Stadler. The TEM experiments were evaluated by Tobias Rosenthal in the course of his Bachelor's thesis under the supervision of Oliver Oeckler who also contributed to the evaluation of the single crystal data and revised the manuscript together with Wolfgang Schnick.

8.3 Contributions to conferences

1*) **Influencing the thermoelectric properties of germanium antimony tellurides (GST) by substitution with In, Sn and Se**
T. Rosenthal, T. Schröder, P. Urban, S. Welzmiller, C. Stiewe, O. Oeckler
32th International Conference on Thermoelectrics, Kobe (Japan) **2013**

2) **Tuning the thermoelectric properties of quaternary tellurides by varying the vacancy concentration**
T. Schröder, T. Rosenthal, S. Maier, M. Nentwig, O. Oeckler
32th International Conference on Thermoelectrics, Kobe (Japan) **2013**

3) **Combining TEM and synchrotron microdiffraction – a novel lead antimony telluride, and more examples**
O. Oeckler, F. Fahrnbauer, T. Rosenthal, T. Schmutzler, G. Wagner
28th European Crystallographic Meeting, Warwick (England) **2013**

4) **Structure determination of multinary chalcogenides using transmission electron microscopy and microfocus diffraction with synchrotron radiation**
F. Heinke, F. Fahrnbauer, G. Wagner, T. Schmutzler, O. Oeckler, T. Rosenthal, G. Vaghan, J. Wright
Wissenschaftsforum, Darmstadt **2013**

5) **Real-structure effects of quaternary and quinary germanium antimony telluride thermoelectrics caused by doping with silver and indium**
L. Neudert, T. Rosenthal, T. Schröder, M. Döblinger, O. Oeckler
Microscopy Conference 2013, Regensburg **2013**

6) **$CoSb_3$ precipitates in nanostructured Ge-Sb-Te materials as novel promising thermoelectrics**
F. Fahrnbauer, T. Rosenthal, S. Maier, M. Nentwig, M. Grundei, G. Wagner, G. J. Snyder, O. Oeckler
11th European Conference on Thermoelectrics, Noordwijk (Netherlands) **2013**

* oral presentation

7) Optimizing thermoelectric properties of germanium antimony tellurides in different temperature ranges by substitution

S. Welzmiller, T. Rosenthal, T. Schröder, F. Schleife, S. Schwarzmüller, L. Neudert, K. Nimmrich, P. Ganter, P. Huth, B. Kersting, O. Oeckler

11th European Conference on Thermoelectrics, Noordwijk (Netherlands) **2013**

8) Kombination von TEM und Synchrotron-Mikrofokusdiffraktion

L. Neudert, G. Wagner, F. Fahrnbauer, T. Rosenthal, A. Marchuk, P. Urban, T. Schmutzler, W. Schnick, O. Oeckler

Hirschegg-Seminar für Festkörperchemie, Hirschegg (Austria) **2013**

9) Skutterudit in Ge/Sb/Te und Ge/As/Te

F. Fahrnbauer, T. Rosenthal, S. Maier, M. Kasprick, T. Schröder, O. Oeckler

Hirschegg-Seminar für Festkörperchemie, Hirschegg (Austria) **2013**

10) Optimierung thermoelektrischer Eigenschaften von Germanium-Antimon-Telluriden durch Substitution mit Hauptgruppenelementen

F. Heinke, T. Rosenthal, S. Welzmiller, P. Urban, O. Oeckler

Mitteldeutsches Anorganiker-Nachwuchs-Symposium, Dresden **2013**

11*) Se in (GS)TE – Modifikation thermoelektrischer Telluride

T. Rosenthal, P. Urban, C. Stiewe, O. Oeckler

Hemdsärmelkolloquium, Freiburg **2013**

12) Mit Kanonen auf Spatzen geschossen? – Struktur von $Pb_8Sb_8S_{15}Te_5$

O. Oeckler, T. Schmutzler, G. Wagner, T. Rosenthal, F. Fahrnbauer, O. Oeckler

Hemdsärmelkolloquium, Freiburg **2013**

13) Weißblaue GeSCHICHTEN – Erleuchtung aus Bayern

M. Seibald, T. Rosenthal, O. Oeckler, W. Schnick

Hemdsärmelkolloquium, Freiburg **2013**

* oral presentation

14) Tuning real-structure effects and physical properties of germanium antimony tellurides by substitution

S. Welzmiller, T. Rosenthal, T. Schröder, F. Schleife, S. Schwarzmüller, L. Neudert, P. Ganter, P. Huth, B. Kersting, O. Oeckler

XIVth European Conference on Solid State Chemistry, Bordeaux (France) **2013**

15) Structure analysis on the microscale - Characterization of multigrain $CoSb_3$/Ge-Sb-Te materials

F. Fahrnbauer, T. Rosenthal, S. Maier, G. Wagner, O. Oeckler

2nd EuCheMS Inorganic Chemistry Congress, Jerusalem (Israel) **2013**

16) Thermoelectric germanium antimony tellurides: Tuning nanostructures and properties by partial vacancy ordering and doping

O. Oeckler, T. Rosenthal, S. Welzmiller, T. Schröder, L. Neudert

2nd EuCheMS Inorganic Chemistry Congress, Jerusalem (Israel) **2013**

17) Struktur und Eigenschaften Sn- und In-substituierter GST-Materialien

S. Welzmiller, T. Rosenthal, F. Fahrnbauer, P. Urban, L. Erra, O. Oeckler

Hirschegg-Seminar für Festkörperchemie, Hirschegg (Austria) **2012**

18*) Strukturaufklarung an lumineszierendem $Sr_{1-x}Ba_xSi_2O_2N_2:Eu^{2+}$ durch Kombination von TEM- und Röntgen- Methoden

T. Rosenthal, M. Seibald, O. Oeckler

Hirschegg-Seminar für Festkörperchemie, Hirschegg (Österreich) **2012**

19) Thermoelectric properties and element distribution in multinary antimony tellurides

S. Welzmiller, T. Rosenthal, T. Schröder, P. Urban, F. Fahrnbauer, C. Stiewe, O. Oeckler

18th International Conference on Ternary and Multinary Compounds, Salzburg (Österreich) **2012**

* oral presentation

20) Nanostrukturierung von Ge/Sb/Te-Materialien durch $CoSb_3$-Prazipitate – neue vielversprechende Thermoelektrika?

F. Fahrnbauer, T. Rosenthal, S. Maier, R. Berthold, T. Schröder, O. Oeckler

Mitteldeutsches Anorganiker-Nachwuchs-Symposium, Jena **2012**

21) Element- und Leerstellenverteilung in multinären Telluriden und deren physikalische Eigenschaften

O. Oeckler, S. Welzmiller, T. Rosenthal, T. Schröder, F. Fahrnbauer

16. Vortragstagung der Fachgruppe Festkörperchemie und Materialforschung der Gesellschaft Deutscher Chemiker, Darmstadt **2012**

22) Unerwartete Lumineszenzeigenschaften von $Sr_{1-x}Ba_xSi_2O_2N_2:Eu^{2+}$

M. Seibald, T. Rosenthal, O. Oeckler, W. Schnick

16. Vortragstagung der Fachgruppe Festkörperchemie und Materialforschung der Gesellschaft Deutscher Chemiker, Darmstadt **2012**

23) $AgIn_xSb_{1-x}Te_2$ – Über Hochdrucksynthesen zu neuen Thermoelektrika

T. Schröder, T. Rosenthal, D. Souchay, C. Petermayer, S. Grott, O. Oeckler

16. Vortragstagung der Wöhler-Vereinigung, Göttingen **2012**

24) $CoSb_3$ precipitates in GST materials – a combination of two promising thermoelectric compounds

F. Fahrnbauer, T. Rosenthal, S. Maier, T. Schröder, C. Stiewe, O. Oeckler

31st International Conference on Thermoelectrics, Aalborg (Denmark) **2012**

25) Influence of Sn, In and Li substitution on the structure and the thermoelectric properties of $(GeTe)_n(Sb_2Te_3)$ $(1 < n < 20)$

T. Schröder , S. Schwarzmüller, T. Rosenthal, S. Welzmiller, C. Stiewe, O. Oeckler

31st International Conference on Thermoelectrics, Aalborg (Denmark) **2012**

* oral presentation

26) Substituted Ge-Sb-Te materials: structure, element distribution and thermoelectric properties

S. Welzmiller, T. Rosenthal, T. Schröder, P. Urban, F. Fahrnbauer, C. Stiewe, O. Oeckler

27th European Crystallographic Meeting, Bergen (Norway) **2012**

27) Ternary metastable rocksalt-type tellurides

O. Oeckler, T. Schröder, T. Rosenthal, S. Schwarzmüller, C. Petermayer, D. Souchay, S. Grott

27th European Crystallographic Meeting, Bergen (Norway) **2012**

28*) Varying the nanostructure of ternary germanium tellurides and its influence on thermoelectric properties

T. Rosenthal, T. Schröder, M. N. Schneider, C. Stiewe, O. Oeckler

4th EuCheMS Chemistry Congress, Prag (Czech Republic) **2012**

29) New thermoelectrics by combination of $CoSb_3$ with Ge/Sb/Te materials

F. Fahrnbauer, T. Rosenthal, S. Maier, T. Schröder, O. Oeckler

4th EuCheMS Chemistry Congress, Prag (Czech Republic) **2012**

30) Nanostructures of thermoelectric Ge/Sb/Te materials and the effect of Se, In and Sn substitution

T. Rosenthal, S. Welzmiller, L. Neudert, K. Nimmrich, P. Ganter, O. Oeckler

15th European Microscopy Congress, Manchester (England) **2012**

31) Influencing the nanostructures and thermoelectric properties of germanium antimony tellurides

T. Rosenthal, O. Oeckler

International Symposium on X-ray and Electron Crystallography, Stockholm (Schweden) **2012**

* oral presentation

32*) Structure elucidation of germanium tin antimony tellurides by TEM and X-ray methods

T. Rosenthal, L. Neudert, S. Welzmiller, O. Oeckler

20th Annual Meeting of the German Crystallographic Society, München **2012**

33) Thermoelectric properties of metastable Ge/Sb/Te and Ge/Bi/Te compounds

T. Schröder, M. N. Schneider, T. Rosenthal, P. Urban, F. Fahrnbauer, C. Stiewe, C. Gold, E.-W. Scheidt, W. Scherer, O. Oeckler

9th European Conference on Thermoelectrics, Thessaloniki (Greece) **2011**

34) Influence of real-structure effects on the properties of metastable tellurides

O. Oeckler, T. Schröder, T. Rosenthal, M. N. Schneider

Trilateral Seminar "Advances in Inorganic Crystal Chemistry", St. Petersburg (Russia) **2011**

35) Real structure of $Sr_{1-x}BaSi_2O_2N_2:Eu^{2+}$ (0.5<x<0.8) phosphors by TEM and XRD

O. Oeckler , T. Rosenthal, M. Seibald, W. Schnick

International Union of Crystallography (IUCr) 22th Congress and General Assembly, Madrid (Spain) **2011**

36) Structural features and physical properties of $In_2Bi_3Se_7I$ and $InBi_2Se_4I$

T. Rosenthal, M. Döblinger, P. J. Wagatha, O. Oeckler

International Union of Crystallography (IUCr) 22th Congress and General Assembly, Madrid (Spain) **2011**

37) The influence of the microstructure on the thermoelectric properties of $(GeTe)_nSb_2Te_3$ (4 < n < 20) compounds – a TEM investigation

T. Rosenthal, M.N. Schneider, O. Oeckler

Wissenschaftsforum, Bremen **2011**

38) Fehlordnungsvarianten und Nanostrukturen von $GeBi_2Te_4$ und deren Einfluss auf den elektrischen Widerstand

T. Schröder, M. N. Schneider, T. Rosenthal, A. Eisele, C. Gold, E.-W. Scheidt, W. Scherer, O. Oeckler

15. Vortragstagung der Wöhler-Vereinigung, Freiburg **2010**

* oral presentation

39) Real structure of metastable Ge-Sb-Te and Ge-Bi-Te materials
M. N. Schneider, T. Rosenthal, T. Schröder, O. Oeckler
European Phase Change and Ovonics Symposium, Mailand (Spain) **2010**

40) Einfluss der Mikro- und Nanostruktur auf thermoelektrische Eigenschaften von Germaniumantimontelluriden
O. Oeckler, M. N. Schneider, T. Rosenthal, C. Stiewe
15. Vortragstagung der Fachgruppe Festkorperchemie und Materialforschung der Gesellschaft Deutscher Chemiker, Berlin **2010**

41) From phase-change materials to thermoelectrics?
O. Oeckler, M. N. Schneider, T. Schröder, T. Rosenthal, F. Fahrnbauer, C. Stiewe
3rd International Symposium on Structure-Property Relationships in Solid State Materials, Stuttgart **2010**

42) Real-structure effects, diffusion processes and thermoelectric properties of tetradymite-type tellurides and related compounds
O. Oeckler, M. N. Schneider, T. Rosenthal, T. Schröder, P. Urban, F. Fahrnbauer, C. Stiewe, M. Döblinger
Minerals as Advanced Materials II, Kirovsk (Russia) **2010**

43) Real-structure effects of luminescent layered oxonitridosilicates
O. Oeckler, M. Seibald, J. A. Kechele, F. Stadler, T. Rosenthal, H. Koss, W. Schnick
26th European Crystallographic Meeting, Darmstadt **2010**

44) Transmission electron microscopy on stable and metastable Ge/Sb/Te phases
T. Rosenthal, M. N. Schneider, O. Oeckler
26th European Crystallographic Meeting, Darmstadt **2010**

45*) TEM-Untersuchungen zur Nanostruktur GeTe-reicher Germaniumantimontelluride und deren partieller Defektausordnung
T. Rosenthal, M. N. Schneider, O. Oeckler
Hirschegg-Seminar für Festkorperchemie, Hirschegg (Austria) **2010**

* oral presentation

46) Crystal chemistry of disordered layer-like oxonitridosilicates

O. Oeckler, J. A. Kechele, F. Stadler, T. Rosenthal, H. Koss, W. Schnick

24th European Crystallographic Meeting, Marrakesch (Marocco) **2007**

* oral presentation